

AD-A285 937



Ferroic Materials:

Design,

Preparation,

and

Characteristics



Edited by

A. S. Bhalla

R. N. W. Norrish

H. Y. Yoon

H. Y. Yoon

D. A.

DTIC
SELECTED
NOV 04 1994
F

*Ceramic
Transactions*

Volume 43

This document has been approved
for public release and sale; its
distribution is unlimited.

Ferroic Materials:

Design,

Preparation,

and

Characteristics

Accession For	
NTIS CRA&I	<input checked="" type="checkbox"/>
DTIC TAB	<input type="checkbox"/>
Unannounced	<input type="checkbox"/>
Justification	
By	
Distribution	
Availability Codes	
Dist	Avail and/or Special
A-1	

Related titles published by the American Ceramic Society:

Ceramic Transactions, Volume 41: Grain Boundaries and Interfacial Phenomena in Electronic Ceramics

Edited by Lionel M. Levinson and Shin-ichi Hirano

© 1994, ISBN 0-944904-73-4

Ceramic Transactions, Volume 38: Advances in Ceramic-Matrix Composites

Edited by Narottam P. Bansal

© 1993, ISBN 0-944904-69-6

Ceramic Transactions, Volume 36: Microwaves: Theory and Application in Materials Processing II

Edited by David E. Clark, Wayne R. Tinga, and Joseph R. Laia, Jr.

© 1993, ISBN 0-944904-66-1

Ceramic Transactions, Volume 33: Materials in Microelectronic and Optoelectronic Packaging

Edited by Hung C. Ling, Koichi Niwa, and Vishwa N. Shukla

© 1993, ISBN 0-944904-63-7

Ceramic Transactions, Volume 32: Dielectric Ceramics: Processing, Properties, and Applications

Edited by K.M. Nair, J.P. Guha, and A. Okamoto

© 1993, ISBN 0-944904-60-2

Phase Equilibria Diagrams, Phase Diagrams for Ceramists, Volume IX: Semiconductors and Chalcogenides

Edited by Gerald B. Stringfellow

© 1992, ISBN 0-944904-50-5

Ceramic Transactions, Volume 26: Forming Science and Technology for Ceramics

Edited by Michael J. Cima

© 1992, ISBN 0-944904-48-3

Ceramic Transactions, Volume 25: Ferroelectric Films

Edited by A.S. Bhalla and K.M. Nair

© 1992, ISBN 0-944904-47-5

Phase Diagrams for High T_c Superconductors

Edited by John D. Whitler and Robert S. Roth

© 1991, ISBN 0-944904-41-6

For information on ordering titles published by the American Ceramic Society, or to request a publications catalog, please call 614-890-4700, or write to Customer Service Department, 735 Ceramic Place, Westerville, OH 43081.

Ferroic Materials: Design, Preparation, *and* Characteristics



Edited by

A.S. Bhalla

The Pennsylvania State University

K.M. Nair

E.I. du Pont de Nemours & Co., Inc.

I.K. Lloyd

University of Maryland

H. Yanagida

University of Tokyo

D.A. Payne

University of Illinois



Ceramic
Transactions

Volume 43

Published by

The American Ceramic Society

735 Ceramic Place

Westerville, Ohio 43081

437g



94 11 3 05 6

Proceedings of the International Symposium on Ferroelectric Thin Films, the International Symposium on Materials for Intelligent/Smart Systems and Adaptive Structures, and the Processing of Thin Films symposium, presented at the PAC RIM Meeting, held in Honolulu, HI, November 7-10, 1993.

Library of Congress Cataloging-in-Publication Data

Ferroic materials : design, preparation, and characteristics / edited
by A.S. Bhalla . . . [et al.]

p. cm. -- (Ceramic transactions, ISSN 1042-1122 ; v. 43)

"Proceedings of the International Symposium on Ferroelectric Thin
Films, the International Symposium on Materials for
Intelligent/Smart Systems and Adaptive Structures . . . presented at
the PAC RIM Meeting held in Honolulu, HI, Nov. 7-10, 1993"--T.p.
verso.

Includes index.

ISBN 0-944904-77-7

1. Ferroelectric devices--Materials--Congresses. 2. Ferroelectric
crystals--Congresses. 3. Thin films--Materials--Congresses.

4. Ceramic materials--Congresses. 5. Smart materials--Congresses.

I. Bhalla, A.S. II. International Symposium on Ferroelectric Thin
Films (1993 : Honolulu, Hawaii) III. International Symposium on
Materials for Intelligent/Smart Systems and Adaptive Structures
(1993 : Honolulu, Hawaii) IV. Series.

III. Title. IV. Series.

TK7872.F44F47 1994

621.3815'2--dc20

94-27689

CIP

Copyright © 1994, The American Ceramic Society. All rights reserved.

No part of this book may be reproduced, stored in a retrieval system, or transmitted in
any form or by any means, electronic, mechanical, photocopying, microfilming,
recording, or otherwise, without written permission from the publisher.

Permission to photocopy for personal or internal use beyond the limits of Sections 107
and 108 of the U.S. Copyright Law is granted by the American Ceramic Society,
provided that the base fee of US\$5.00 per copy, plus US\$.50 per page, is paid directly to
the Copyright Clearance Center, 27 Congress Street, Salem MA 01970, USA. The fee code
for users of the Transactional Reporting Service for *Ceramic Transactions Volume 43* is 0-
944904-77-7/94 \$5.00+\$.50. This consent does not extend to other kinds of copying, such
as copying for general distribution, for advertising or promotional purposes, or for
creating new collective works. Requests for special photocopying permission and reprint
requests should be directed to the Director of Publications, The American Ceramic
Society, 735 Ceramic Place, Westerville OH 43081, USA.

Printed in the United States of America.

1 2 3 4-98 97 96 95 94

ISSN 1042-1122

ISBN 0-944904-77-7

Contents

Preface	ix
---------------	----

Thin Films: Preparation and Characteristics

Preparation and Evaluation of Ferroelectric Thin Films	3
Toshio Ogawa	

Preparation of (Pb,Lu)TiO ₃ Thin Films by Multiple Cathode Sputtering	15
Kiyoshi Okazaki, Hiroshi Maiwa, and Noboru Ichinose	

Growth and Properties of PZT Thin Films on a 6-8-in. Wafer by MOCVD	27
Tadashi Shiosaki, C.S. Kang, Masaru Shimizu, Mitsuru Fukagawa, Kenichi Nakaya, and Eiki Tanikawa	

Sputter Deposition of Ferroelectric PbTiO ₃ Thin Films on MgO(100) Substrates	37
Sangsub Kim, Youngmin Kang, and Sunggi Baik	

Deposition and Dielectric Properties of Ion-Beam-Assisted Bismuth Titanate Film	55
M. Azimi and P.K. Ghosh	

Dielectric Properties of (Ba,Sr)TiO ₃ Films by RF Sputtering	67
N. Mikami, T. Horikawa, T. Makita, K. Sato, T. Kuroiwa, T. Honda, and H. Watarai	

Preparation of a Metallorganic Deposition Precursor for Barium Titanate	73
Allen W. Apblett, Galina D. Georgieva, and Isobel Raygoza-Maceda	

Synthesis and Characterization of Group IV Metal Adamantanol Alkoxides as Potential PZT Precursors	79
Timothy J. Boyle, Aaron T. Pearson, and Robert W. Schwartz	

Crystallization Behavior and Improved Properties for Sol-Gel-Derived PZT and PLZT Thin Layers Processed with a Lead Oxide Cover Coating	89
Toshihiko Tani, Charles D.E. Lakeman, Jie-Fang Li, Zhengkui Xu, and David A. Payne	

Metal Alkoxide-Derived Oriented and Epitaxial Ferroelectric Thin Films	107
Keiichi Nashimoto	
Sol-Gel Technology for Ferroelectric Thin Films	123
You Song Kim and Hyun M. Jang	
Decrease of Defects of Sol-Gel-Derived PbTiO_3 Thin Film and Its Grain Size Effect on Ferroelectric Properties	131
K. Saegusa and Y. Suzuki	
Processing and Characteristics of Spin-Cast Ferroelectric $\text{Bi}_4\text{Ti}_3\text{O}_{12}$ Thin Films	137
Relva C. Buchanan and Peir-Yung Chu	
Densification and Crystallization of Zirconia Thin Films Prepared by Sol-Gel Processing	145
R.W. Schwartz, J.A. Voigt, C.D. Buchheit, and T.J. Boyle	
Microstructure of Epitaxial Ferroelectric/Metal Oxide Electrode Thin-Film Heterostructures on LaAlO_3 and Silicon	165
Subodh G. Ghonge, Edward Goo, R. Ramesh, R. Haakenaasen, and D.K. Fork	
Microstructure Development in Particulate Ceramic Coatings	183
Y.J. Kim, N.M. Wara, B.V. Velamakanni, and L.F. Francis	
Role of Macrodefects in PZT Thin Films for Microelectromechanical Systems	197
T.G. Cooney, E.A. Hachfeld, and L.F. Francis	

Design and Properties of Materials

Nonlinear Conduction Mechanism in Perovskite-Type Ceramics	207
N. Ichinose	
Conduction Mechanism of SrTiO_3 Thin Films by RF Sputtering	219
T. Kuroiwa, T. Honda, H. Watarai, N. Mikami, T. Horikawa, T. Makita, and K. Sato	
Dielectric, Structural, and Microstructural Characteristics of Tetragonal-Structured PLZT Relaxors	225
Xunhu Dai, Z. Xu, and Dwight Viehland	
Hydroacoustic Evaluation of 1-3 Piezocomposite Plate and Ring Structures	231
Robert Y. Ting, Thomas R. Howarth, and Kurt M. Rittenmyer	
Fabrication and Properties of 1-3 PZT-Polymer Composites	239
R.L. Gentilman, D.F. Fiore, H.T. Pham, K.W. French, and L.J. Bowen	

Applicability of Ceramics for Cryogenic Use	249
S. Nishijima, A. Nakahira, K. Niihara, and T. Okada	
Modeling of the Metal-Ferroelectric-Metal Capacitor: Part I— Theoretical Considerations	255
G. Teowee and D.R. Uhlmann	
Modeling of the Metal-Ferroelectric-Metal Capacitor: Part II— Experimental Verifications	267
G. Teowee and D.R. Uhlmann	
Piezoelectric Ceramics and Ceramic Composites for Intelligent Mechanical Behaviors	277
Hongyu Wang and Raj N. Singh	
Photostriction and Its Applications	287
Kenji Uchino and Sheng-Yuan Chu	
Effects of Heat Treatments on Photostriction in PLZT Ceramics	295
Kazuhiro Nonaka, Akira Takase, Tadahiko Watanabe and Hisayoshi Yoshida	
Temperature Modulation of the Electro-Optic Effect in BaTiO ₃ and LiNbO ₃ —A Theoretical Approach	301
G. Zavala-Enriquez and P.K. Ghosh	
 Sensor Characteristics	
Smart/Intelligent Sensors	315
Tsuneharu Nitta and Shunichiro Kawashima	
Optical Hydrogen Sensor Using Pd/MoO _x Films	331
Jun-ichi Hamagami, Ben Huybrechts, Yuichi Watanabe, and Masasuke Takata	
Gas Sensing by AC Impedance Under DC Bias of CuO/ZnO pn Heterocontact	343
Kazuyasu Hikita, Masaru Miyayama, and Hiroaki Yanagida	
Relationship Between Crystal Orientation and Gas Sensing Property of Sputtered SnO ₂ Films	357
Masasuke Takata	
Evaluation of the Gas Response of ZnO/La ₂ CuO ₄ Heterocontacts with Different Electrode Materials	365
Enrico Traversa, Masaru Miyayama, and Hiroaki Yanagida	
ZnO/La ₂ CuO ₄ Heterocontacts as Humidity Sensors	375
Enrico Traversa, Alessandra Bianco, Giampiero Montesperelli, Gualtiero Gusmano, Andrea Bearzotti, Masaru Miyayama, and Hiroaki Yanagida	

Piezoelectric Actuator Responsive to Environmental Humidity	385
Yuji Isogai, Masaru Miyayama, and Hiroaki Yanagida	
Piezoresistive Ceramic Sensor Based on PTCR Barium Titanate	393
Joseph S. Capurso, Aldo B. Alles, and Walter A. Schulze	
Effect of Top Metallization on the Dielectric and Ferroelectric Properties of Sol-Gel-Derived PZT Thin Films	401
G. Teowee, C.D. Baertlein, E.A. Kneer, J.M. Boulton, and D.R. Uhlmann	
Electrical and Mechanical Properties in CaF_2/SiC -Whisker Composites	413
Atsumu Ishida, Masaru Miyayama, and Hiroaki Yanagida	
Index	425

Preface

Ferroic materials have found application in both sensing and actuating devices such as detectors, high-and low-frequency transducers, capacitors, optical modulators, shutters, and photorestrictive and electrostrictive devices. The application areas of ferroics in single-crystal, bulk ceramics, thin-film, and composite forms have been expanding quite rapidly in recent years. As a result, new materials design and fabrication techniques are needed to satisfy the new emerging applications of these "smart" materials and structures.

With the drive of new national and international initiatives in the areas of advanced materials and technology, smart structures and systems, environmental beneficiation programs, etc., it is highly desirable to review and project the direction in materials design, preparation, and sensing properties. The decision of the American Ceramic Society to organize the first PAC RIM meeting, held in Honolulu, HI, November 7-10, 1993, gave an opportunity to review these topics in depth by bringing together leading researchers and device engineers from universities, national laboratories, and industry.

This volume is a collection of selected papers from three closely related symposia on ferroelectric thin films, materials for intelligent/smart systems and adaptive structures, and processing of thin films. The papers have been organized into three broad categories: *Thin Films: Preparation and Characteristics*, *Design and Properties of Materials*, and *Sensor Characteristics*. All the papers were reviewed through a peer review process. We, the editors, acknowledge and appreciate the contributions of the speakers, session chairs, manuscript reviewers, and Society officials for making this endeavor a successful one.

A.S. Bhalla
K.M. Nair
I.K. Lloyd
H. Yanagida
D.A. Payne

Thin Films: Preparation and Characteristics

PREPARATION AND EVALUATION OF FERROELECTRIC THIN FILMS

Toshio Ogawa
Shizuoka Institute of Science and Technology
2200-2, Toyosawa, Fukuroi, Shizuoka, Japan

Abstract

The stoichiometry of film compositions prepared by RF magnetron sputtering and laser ablation is discussed. Control of the crystal orientation of the films was determined from the relation between the films and substrates. In addition, a new bottom electrode material in place of platinum was developed for use with ferroelectric thin films. The ferroelectric properties and fatigue behavior of the films were evaluated with the new electrodes.

INTRODUCTION

Most of the development of ferroelectric thin films has focused on films with good ferroelectric properties. Basically three key issues involved in getting these properties have been investigated. The first issue is film preparation and the second issue is film evaluation. On film preparation, we must control the stoichiometry of film compositions and the crystal orientation of the films. Moreover, we must apply a bottom electrode to the films to allow evaluation of ferroelectric properties. The third issue is the substrate. Since films are deposited on substrates, the effect of substrates on film properties is significant.

EXPERIMENTAL

We investigated the film preparation dependence of film composition. Ferroelectric films were prepared by two methods, namely, by RF magnetron sputtering and ArF excimer laser ablation. We used sintered ceramic targets as the film materials. In the RF sputtering, two kinds of La modified PbTiO_3 ceramic targets were used. One was a high Curie point ($T_c=430^\circ\text{C}$) material and the other was a low $T_c(320^\circ\text{C})$ material. The tetragonality

To the extent authorized under the laws of the United States of America, all copyright interests in this publication are the property of The American Ceramic Society. Any duplication, reproduction, or republication of this publication or any part thereof, without the express written consent of The American Ceramic Society or fee paid to the Copyright Clearance Center, is prohibited.

(c/a) of the targets were 1.048 and 1.032 respectively¹¹. $\text{Pb}(\text{Zr}_{0.52}\text{Ti}_{0.48})\text{O}_3$ ($T_c=330^\circ\text{C}$) with 1wt% Nb_2O_5 films were prepared by laser ablation²¹. In the case of sputtering we analyzed the sputtering plasma by optical emission spectroscopy (OES) to control film composition^{11,22}.

For film evaluation, we used a nickel(Ni) alloy as a bottom electrode⁴⁻⁸ for the films to measure D-E hysteresis loops and switching characteristics⁹.

Finally, the effect of substrate on the crystal orientation of the films was studied^{11,23}. Single-crystal MgO, sapphire, quartz glass and surface oxidized Si wafers were used as substrates.

RESULTS AND DISCUSSION

Stoichiometry of Film Compositions

RF Magnetron Sputtering

A schematic picture of the sputtering equipment is shown in Fig. 1. The equipment has a relatively large spacing of 100mm between substrate and target^{11,24}. The substrate was not located directly over the target. Therefore, the film on the substrate was not bombarded with sputtering particles. When we used this equipment, the film composition was kept the same as the target. The relations between sputtering conditions and film properties are shown in Fig. 2^{11,25}. When the PbTiO_3 films with the high Curie point were deposited on r-plane sapphire at 600°C , yellow and transparent PbTiO_3 films were produced at lower content of O_2 gas. Further, the crystal orientations of the films were controlled by the gas pressure and Ar/O_2 gas ratio.

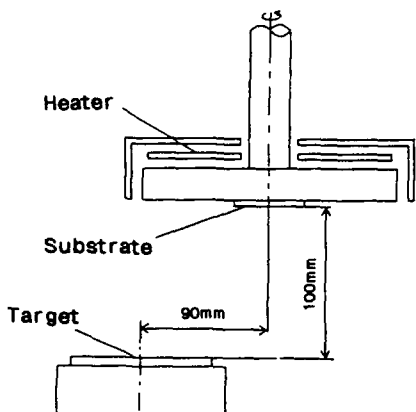


Fig. 1 Schematic picture of the sputtering equipment.

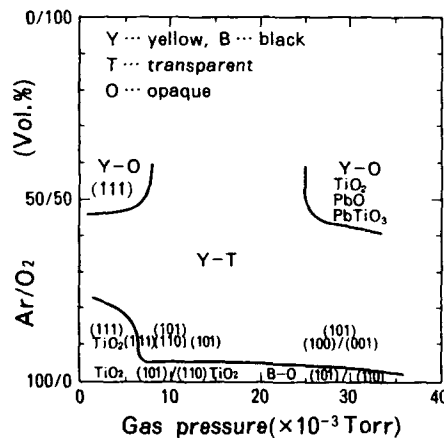


Fig. 2 The effect of sputtering conditions on film properties.

RF sputtering plasma spectra were measured by OES to analyze the deposition processes. The plasma spectra of PbTiO_3 ceramics, Ti metal and Pb metal are shown in Fig. 3²¹. We monitor peak intensities of Pb 406nm, Ar 750nm and OH 306nm. Figure 4 shows the dependence of the peak intensities on substrate temperature (T_s). Above 520°C, the intensity of Pb increases with increasing T_s . We believe this increase in Pb intensity was due to PbO vaporization from the deposited film.

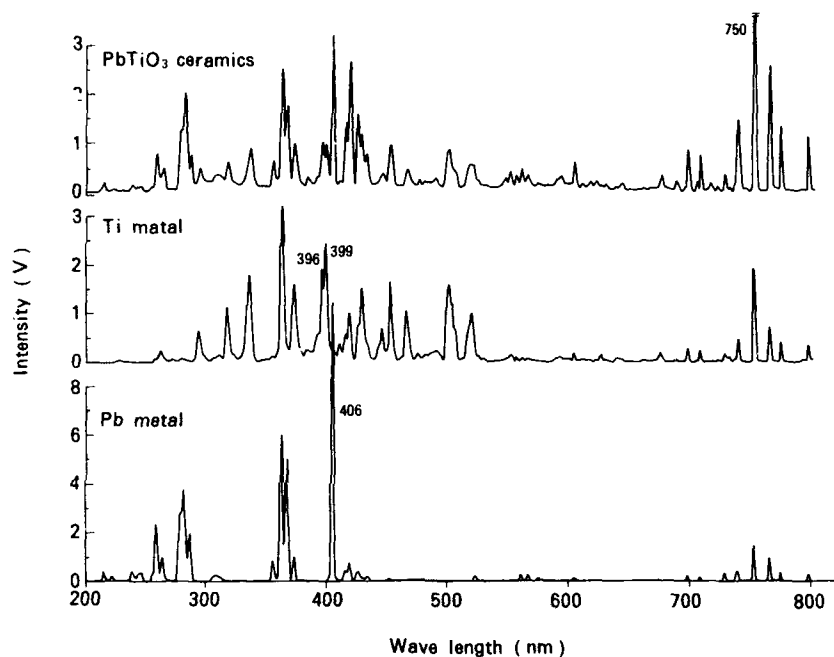


Fig. 3 RF sputtering plasma spectra of PbTiO_3 ceramics, Ti metal and Pb metal measured by OES.

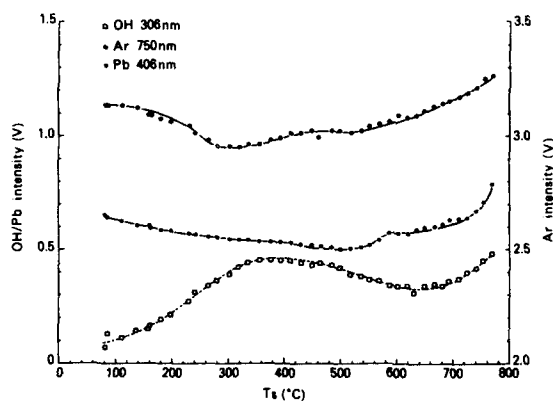


Fig. 4 The dependence of the intensities of OH, Ar and Pb spectra on temperature.

Laser Ablation

Figure 5 shows a schematic picture of the laser ablation equipment²¹. The ArF excimer laser of 193nm wavelength was led to the ceramic target. The substrate was heated up by an infrared lamp. The ablation gas was pure O₂ at 0.1 to 1 Torr. These values are 10 to 100 times larger than those in sputtering. We studied the dependence of film composition on laser fluence (Fig. 6). A lack of PbO was observed in a small laser fluence^{1,2}. We believe the film deposition resulted from thermal vaporization rather than ablation in this range. Therefore, the film had a different composition than the ceramic target. At a higher laser fluence of 6J/cm²·shot, the film compositions were the same as the target at Ts of 300 to 600°C as shown in Fig. 7. Laser ablation was suitable for oxide film preparation because the higher O₂ gas pressure in ablation suppressed the vaporization of PbO from the deposited film at a Ts of 600°C.

We compared the compositions and phase assemblages of films prepared by sputtering and by laser ablation (Fig. 8)^{1,23}. The substrate temperature had a great influence on the deposited phases for both the methods. In the case of sputtering, film compositions were affected by the substrate temperature and gas pressure. Even though sputtered particles are the same as the target composition and reach the substrate, PbO vaporization occurs from the deposited film because of lower gas pressures.

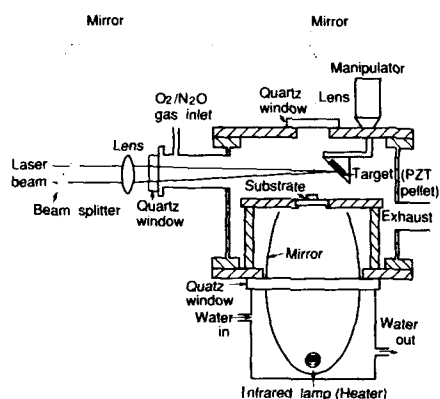


Fig. 5 Schematic picture of the laser ablation equipment.

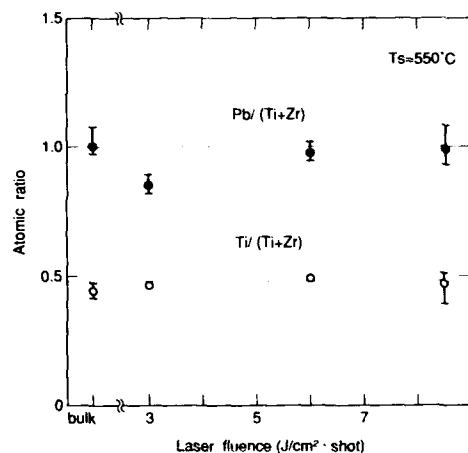


Fig. 6 Laser fluence dependence of PZT film compositions. Dashed lines show the target composition.

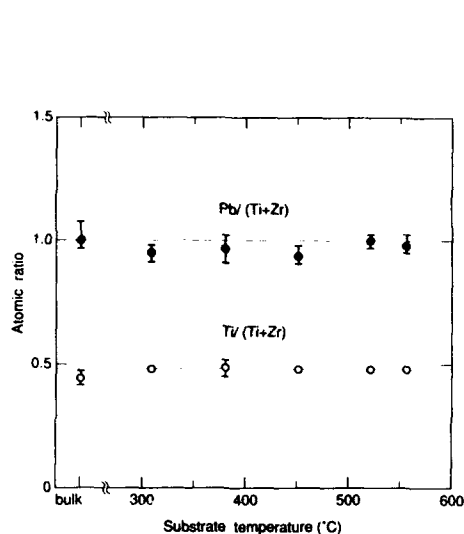
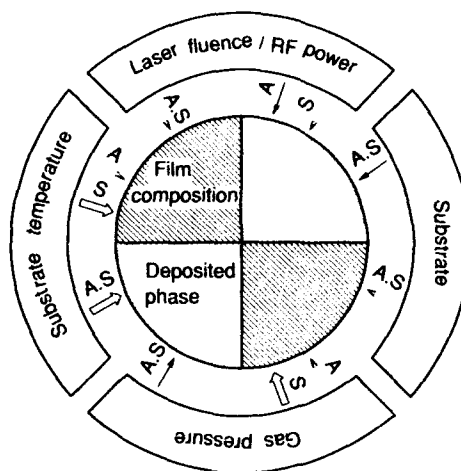


Fig. 7 Substrate temperature dependence of PZT film compositions. Dashed lines show the target composition.



A: Laser ablation, S: RF sputtering
 → great influence, → small influence
 - - - little influence

Fig. 8 Comparison between RF magnetron sputtering and laser ablation in preparation.

Crystal Orientation of Films

We studied the effect of substrates on crystal orientations in the films¹⁰⁾. The ceramic target of PbTiO_3 with c/a of 1.032 was sputtered on single-crystal MgO at $T_s=600^\circ\text{C}$. Although Ar/O_2 gas ratio and gas pressure were varied, the films on MgO preferred to orient in the direction of c -axis (c -axis \perp to substrate plane). In the case of quartz glass substrates, the films had an a -axis orientation (c -axis \parallel to substrate plane) below gas pressures of 1 mTorr (Fig. 9). Finally, in the case of sapphire substrates, we could get (111) and (101) orientations. The RHEED patterns of PbTiO_3 film surfaces with c -axis, a -axis, and (111)-direction orientations are shown in Fig. 10. Epitaxial films were fabricated on single-crystal MgO, and nearly epitaxial films on sapphire ($r\&c$). In the case of a film surface on quartz glass, however, a ring pattern was observed.

We tried to explain the effect of substrates on crystal orientations of the films by the mechanical stress added to the films. The stress was caused by the difference in the thermal expansion coefficients between the films and substrates.

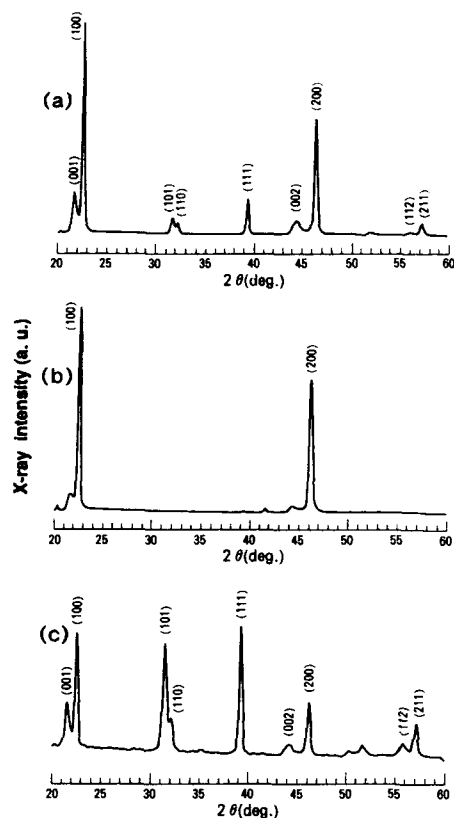


Fig. 9 X-ray diffraction patterns of PbTiO_3 ($c/a=1.048$) films on quartz glass. $\text{Ar}/\text{O}_2=90/10$ Vol.%; sputtering gas pressure, (a) 8.8×10^{-3} Torr, (b) 9.2×10^{-3} Torr, (c) 1.3×10^{-2} Torr.

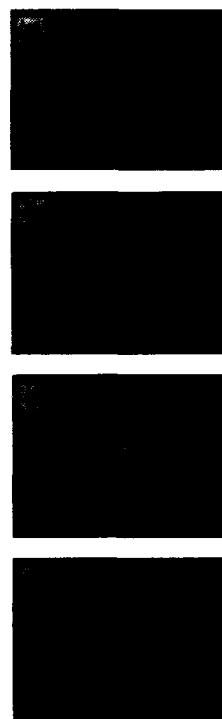


Fig. 10 RHEED patterns of crystal oriented PbTiO_3 films: c-axis oriented film on MgO(a), a-axis oriented film on quartz glass(b), (111)-direction oriented films on r-plane sapphire(c) and c-plane sapphire(d).

Figure 11 shows the thermal expansion characteristics of the substrates and PbTiO_3 ceramics. The thermal expansion coefficient of MgO is larger than the ones of sapphire and PbTiO_3 ceramics. On the other hand, quartz glass hardly expands at room temperature to 800°C . From the thermal expansion characteristics the films deposited on MgO suffered a horizontal compressive stress along the plane of the film when the films were cooled from 600°C to room temperature. A tensile stress, however, acted on the films on quartz glass(Fig. 12). We believe these mechanical stresses transformed the crystallized films into c-axis and a-axis oriented films at the Curie points. The crystal orientation of PbTiO_3 films must be aligned in the c-axis direction for the films to possess high remanent polarizations. We looked for new substrates with a large thermal expansion coefficient.

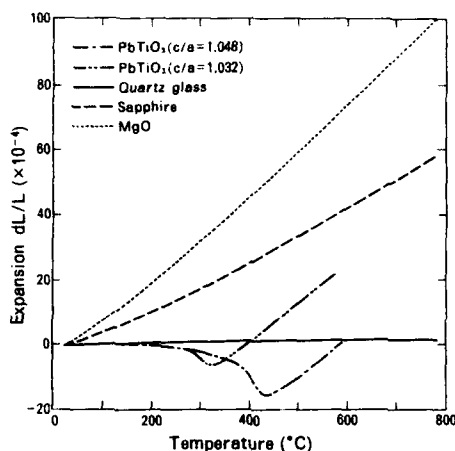


Fig. 11 Thermal expansion characteristics of various substrates and PbTiO_3 ceramics.

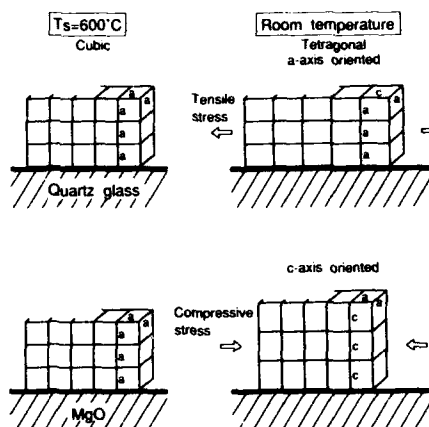


Fig. 12 The effect of mechanical stresses on crystal orientations during cooling through a film's Curie point.

We found glass ceramics composed mainly of α -quartz or cristobalite in place of MgO as shown in Fig. 13. When PbTiO_3 films were deposited on these glass ceramic substrates, the films were strongly oriented in the c-axis direction (Fig. 14).

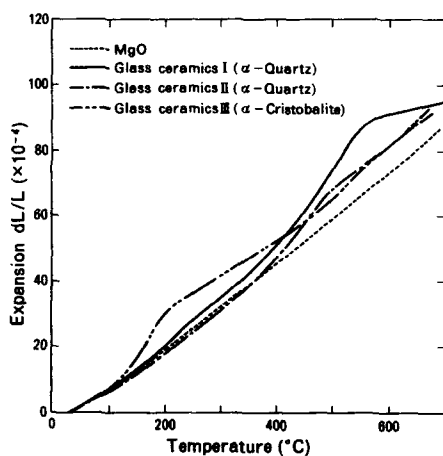


Fig. 13 Thermal expansion characteristics of glass ceramic substrates.

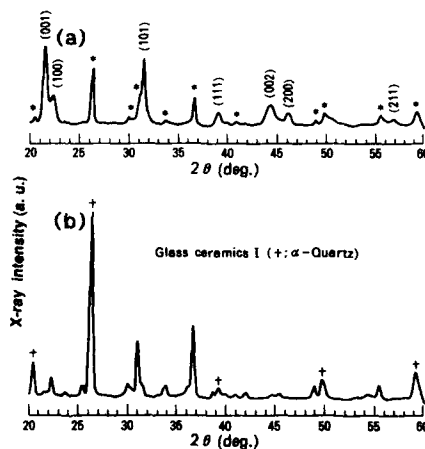


Fig. 14 X-ray diffraction patterns of PbTiO_3 ($c/a=1.048$) film on glass ceramics I (a), and the substrate (b). Diffraction lines from the substrate are shown by *'s.

Electrode for Ferroelectric Thin Films

Ni Alloy Electrode

We tested the metal electrodes deposited on a substrate for their resistance to oxidation and reactivity with PbO at a Ts of 600°C and a sputtering gas pressure of 3 to 20mTorr in the presence of 10 volume% O₂ gas (Table 1)²¹. We determined the degree of oxidation and reactivity with PbO on the electrodes from the surface color and shape deformation of the electrodes, and by the PbTiO₃ film color and the electric resistance of the films on the electrodes. They all reacted easily with PbO except for Pt and the Ni alloy. The special Ni alloy possesses excellent thermal stability and oxidation-resisting properties compared to inconel 601.

Figure 15 shows a fracture surface of the PbTiO₃ film on the Ni alloy electrode with a substrate of MgO. We found no evidence of a reaction layer between the Ni alloy electrode and the PbTiO₃ film. A 20nm-thick layer was found between the PbTiO₃ film and the Ni alloy electrode by TEM (Fig. 16).

Table 1 Evaluation of the use of high melting point metals as bottom electrodes with ferroelectric thin films.

Metal	Melting point (°C)	Oxidation at 600°C (3-20mTorr)	Reactivity with PbO at 600°C (3-20mTorr)
Ta	2996	low	high
Ti	1668	low	high
Pt	1769	stable	low
Ni alloy	1365	low	low

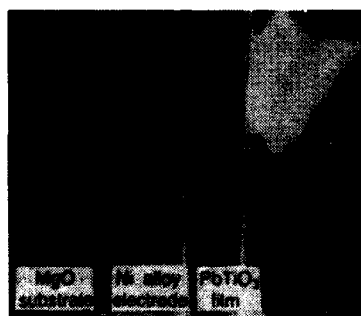


Fig. 15 Fracture surface of PbTiO₃ film on MgO with Ni alloy electrode (bar=1 μm).



Fig. 16 TEM photo of the fracture surface of PbTiO₃ film on Ni alloy electrode.

The SAM depth profile (Fig. 17) showed that a thin layer of alumina below 20nm existed on the alloy electrode. The important points of this figure are that aluminium in the alloy bulk was precipitated on the surface of the alloy electrode and oxidized into a thin layer of alumina^{1,4)}. This layer prevents PbO from diffusing into the alloy electrode. Figure 18 shows a schematic drawing of the layer structure. The structure fabricated as follows. After sputtering the Ni alloy target on a substrate in pure Ar gas at T_s of 400°C, the PbTiO_3 film was prepared in 10 volume% of O_2 gas at 600°C. In the beginning of this process, the surface of the alloy electrode was oxidized and a dense alumina film was produced on the surface of the alloy electrode. The alumina thin layer gives good thermal stability, oxidation-resistance, PbO reaction-resistance and also a high breakdown strength.

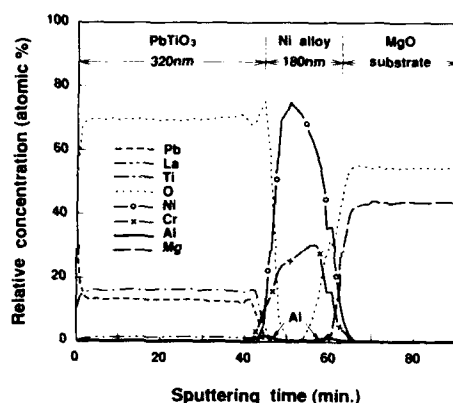


Fig. 17 SAM depth profile of the fracture surface on PbTiO_3 film/ Ni alloy electrode/ MgO substrate.

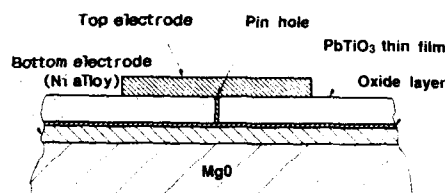


Fig. 18 Schematic drawing of the layer structure: substrate/ bottom electrode/ PbTiO_3 film/ top electrode.

Film Properties on Ni Alloy Electrode

We studied the crystal orientation of the sputtered Ni alloy films. The orientation of Ni alloy films was in a (200) orientation on MgO and a (111) orientation on sapphire. PbTiO_3 films showed a tendency to orient in the (111) direction on the alloy electrodes as shown in Fig. 19, although Ni alloy films were oriented differently on different kinds of substrates. We believe this phenomenon was probably due to a grain growth orientation.

Figure 20 shows the T_s dependence of the film compositions on the Ni alloy and Pt electrodes. We could get a stoichiometric film compositions on the Ni alloy electrode, while a notable lack of PbO was observed on the Pt electrode.

We confirmed the alumina layer on the Ni alloy electrode makes it easier to produce a perovskite phase⁹⁾.

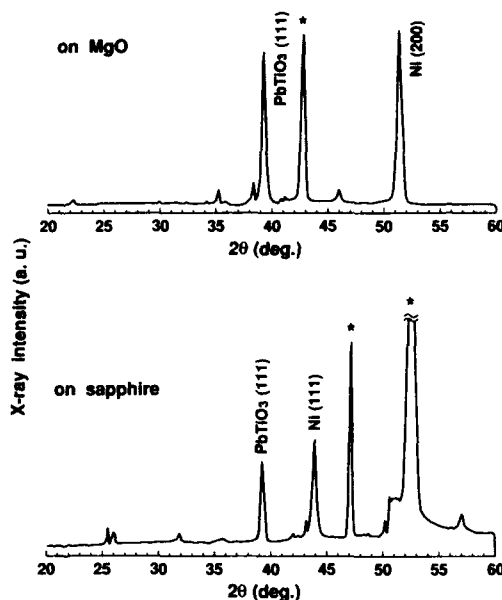


Fig. 19 Crystal orientations of PbTiO₃ films on Ni alloy electrodes. Diffraction lines from the substrates are shown by *'s.

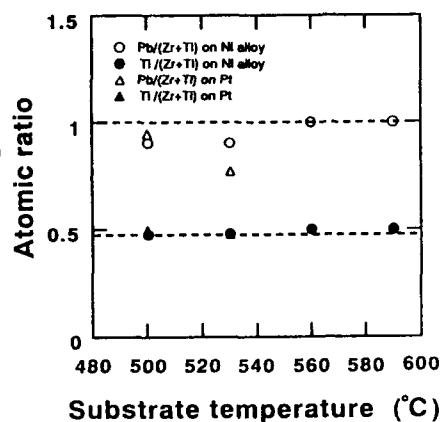


Fig. 20 Substrate temperature dependence of the PZT film compositions. Dashed lines show the target composition.

Ferroelectric Properties of Films

Hysteresis Loops

The hysteresis loops of the PbTiO₃ films on various kinds of substrates by sputtering are shown in Fig. 21. A loop of the PbTiO₃ bulk ceramics was also shown here. We could divide hysteresis loops into two groups. One is the loops of the films on MgO and on Si with MgO film, the other is the loop of the film on sapphire. The same two groups of hysteresis loops were obtained on the PZT films by laser ablation (Fig. 22). We believe the dependence of hysteresis loops on substrates was due to the crystallinity of the deposited films. When we develop FRAM devices, the applied voltage of the films should be below 5V. Therefore, we investigated thinner PZT films to reduce the applied voltage. Figure 23 shows the applied voltage dependence of remanent polarizations (Pr's) for PZT films with various thicknesses. The 0.15 μm-thick films showed Pr=15 μC/cm² even at an applied voltage of 5V.

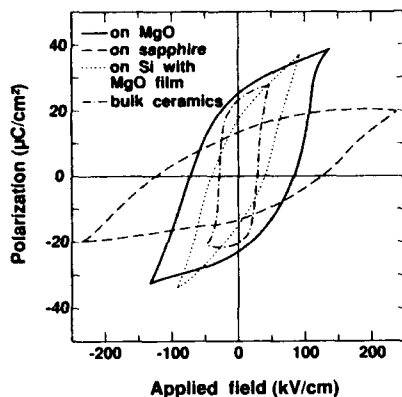


Fig. 21 D-E hysteresis loops of PbTiO_3 films prepared by sputtering on various substrates and PbTiO_3 bulk ceramics.

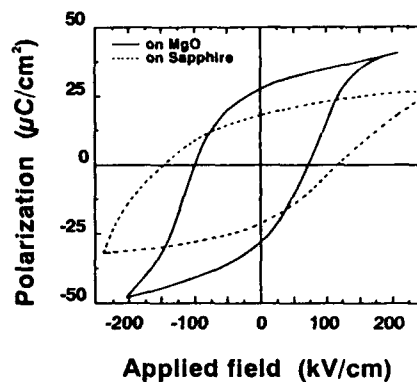


Fig. 22 D-E hysteresis loops of PZT films prepared by laser ablation.

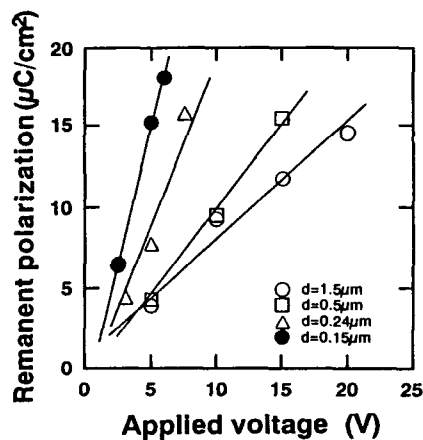


Fig. 23 Applied voltage dependence of P_r for PZT films with various thicknesses.

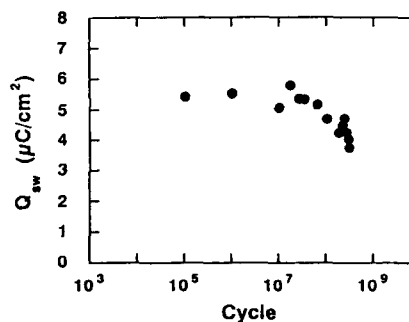


Fig. 24 Fatigue behavior for PZT films composed of Au top electrode/ PZT film/ Ni alloy bottom electrode/ surface oxidized Si(100) substrate structure.

Fatigue Behavior

We measured fatigue behavior by applying a bipolar pulse sequence ($\pm 10\text{V}$ pulse height) to the PZT films on Si with Ni alloy electrodes; the film area was 0.002 cm^2 (Fig. 24). From this figure, a decrease in switched charge (Q_{sw}) is observed around 10^8 cycles. This value is almost the same as that of a sputtered PZT film on Pt electrode¹⁵⁾.

SUMMARY

Ferroelectric thin films with a stoichiometric composition were obtained by laser ablation. While the films prepared by RF magnetron sputtering were PbO deficient, the crystal orientation of the films were sensitively affected by the gas pressure and Ar/O₂ gas ratio. We found the crystal orientations of the films could be controlled by the difference of thermal expansion coefficients between films and substrates. The new Ni alloy electrodes were suitable as bottom electrodes for ferroelectric thin films. We could get good ferroelectric properties utilizing the Ni alloy electrodes.

REFERENCES

- 1) T.Ogawa, A.Senda and T. Kasanami, Jpn. J. Appl. Phys., 28(1989) Suppl. 28-2, p.11.
- 2) H.Kidoh, T.Ogawa, A.Morimoto and T.Shimizu, Appl. Phys. Lett., 58, 2910 (1991).
- 3) T.Ogawa and A.Senda, J. Vacuum Soc. of Japan, 33, 210 (1990)(in Jpn.).
- 4) T.Ogawa, Integrated Ferroelectrics, 1, 99 (1992).
- 5) T.Ogawa, U.S. Patent No.5088002 (Feb.11,1992).
- 6) T.Ogawa S.Shindou A.Senda and T.Kasanami, Mat.Res.Soc.Symp. Proc., 243, 93 (1992).
- 7) T.Ogawa,H.Kidoh,H.Yashima,A.Morimoto and T.Shimizu, Mat.Res. Soc. Symp.Proc., 243, 501 (1992).
- 8) H.Kidoh, T.Ogawa, H.Yashima, A.Morimoto and T.Shimizu, Jpn. J. Appl. Phys., 31, 2965 (1992).
- 9) T.Ogawa, H.Kidoh, H.Yashima, A.Morimoto and T.Shimizu, To be published in Ferroelectrics (IMF-8).
- 10) T.Ogawa, A.Senda and T.Kasanami, Jpn. J. Appl. Phys., 30, 2145 (1991).
- 11) T.Ogawa, K.Inoue, K.Morita, A.Senda and T.Kasanami, Physica C 185-189, 1961 (1991).
- 12) H.Kidoh, T.Ogawa, H.Yashima, A.Morimoto and T.Shimizu, Jpn. J. Appl. Phys., 30, 2167 (1991).
- 13) T.Ogawa and H.kidoh, Proc. of 3rd Symp. on Beam Engineering of Advanced Material Syntheses, (1992) p.283 (in Jpn.).
- 14) R.B.Herchenroeder, U.S. Patent No.4312682 (Jan.26,1982).
- 15) T.Hase and T.Shiosaki, Jpn. J. Appl. Phys., 30, 2159 (1991).

PREPARATION OF (Pb,La)TiO₃ THIN FILMS BY MULTIPLE CATHODE SPUTTERING

Kiyoshi Okazaki, Hiroshi Maiwa and Noboru Ichinose*

Shonan Institute of Technology

Tsujido-Nishikaigan, Fujisawa 251, Japan

*Waseda University

Ohkubo 3-4-1, Shinjuku-ku, Tokyo 169, Japan

Abstract

Using a multiple cathode RF sputtering apparatus with four targets, (Pb,La)TiO₃ thin films are prepared on platinum and ruthenium oxide lower electrodes based on the sputtering conditions of PbTiO₃ thin films. The ferroelectric properties are measured with D-E hysteresis loops, dielectric properties and voltage-current characteristics. The thickness dependences of dielectric permittivity were measured with the depth profile and the surface analysis using a XPS. The shape changes of D-E loops of ferroelectric ceramics and thin films are also reviewed with discussion of the effects of lower fatigue substrates, internal stresses, internal bias field, surface layer effects, the interface behavior and others.

1. INTRODUCTION

Compared to BaTiO₃, PbTiO₃ is a ferroelectric material with a higher Curie point, (500 °C vs 120 °C) and a larger tetragonality of c/a (1.06 vs 1.01). PbTiO₃ ceramics are very difficult to sinter because of their large tetragonality. When La is doped into the PbTiO₃, the tetragonality, the Curie point and the internal stress induced at the Cub-Tet phase transition decrease. In this paper, (Pb,La)TiO₃ thin films are prepared using a multiple cathode RF magnetron sputtering apparatus and the ferroelectric properties are measured and discussed in comparison with bulk ceramic properties.

To the extent authorized under the laws of the United States of America, all copyright interests in this publication are the property of The American Ceramic Society. Any duplication, reproduction, or republication of this publication or any part thereof, without the express written consent of The American Ceramic Society or fee paid to the Copyright Clearance Center, is prohibited.

2. EXPERIMENTAL

The apparatus used in this experiment is a four target cathode RF sputtering (ANELVA, SPC-350) as shown in Fig.1. Sputtering targets are 3 inch disks of PbO(99.99%), La(99.9%) and Ti(99.99%) metals. Compared to a sputtering apparatus using a single compound target, multiple cathode sputtering can easily control the sputtering rate of each target in a larger input power region.

The chemical composition of sputtered thin films were characterized using a Inductively coupled plasma spectroscopy(ICP, SHIMAZU, ICPS-5000), an electron probe microanalysis (EPMA, SHIMAZU, EPMA-CI) and a X-ray photoemission spectroscopy (XPS, RIGAKU, X-7000). The crystallinity was analyzed by a XRD. A depth profile was examined using the XPS. Film thickness was measured using a surface profilometer.

For electrical measurements, Au thin films were deposited at room temperature as the upper electrode with a diameter of 0.9 mm. The dielectric properties were measured at 100 kHz using an impedance analyzer (YHP 4192A) at room temperature. D-E loops were measured with a Sawyer Tower circuit. The voltage vs current was measured using an electrometer (Advantest TR8652).

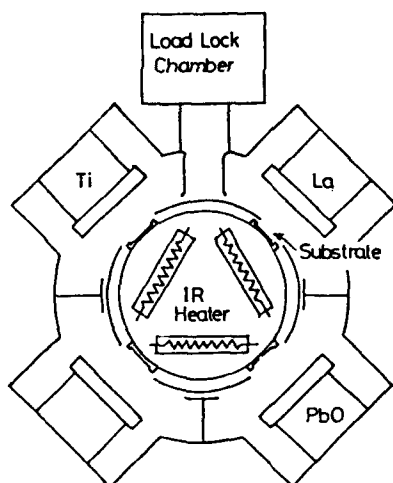


Fig. 1
Four target cathode R-F
magnetron sputtering apparatus

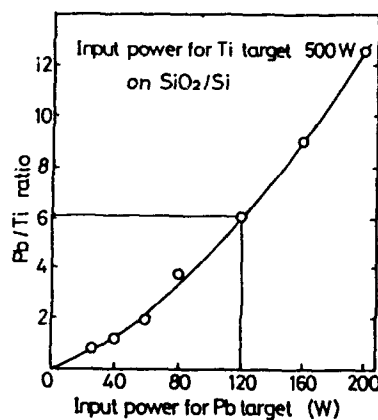


Fig. 2
Sputtered Pb/Ti ratio
determined by ICP as a function
of the input power for Pb target
at room temperature under
constant conditions

3 PREPARATION OF PbTiO_3 THIN FILMS

Adachi et al.⁽¹⁾ investigated the phase diagram of sputtered PbTiO_3 films as a function of substrate temperature. The results indicate that below 500 °C, it is amorphous, above 500 °C, it is crystalline pyrochlore and above 600 °C, it is crystalline perovskite. Maiwa et al. investigated⁽²⁾ the crystalline structure of PbTiO_3 thin films using the multiple cathode sputtering.

Figure 2 is the sputtered Pb/Ti ratio determined by ICP as a function of the input power for the Pb target at room temperature under a constant input power condition for the Ti target of 500 W on a substrate of $\text{SiO}_2(1 \mu\text{m})/\text{Si}$. From these results, if we wish get a thin film with an incident ratio of Pb/Ti = 6.1, the input power for the Pb target should be 120 W.

Figure 3 shows the X-ray diffraction patterns of PbTiO_3 thin films deposited on various substrates at an incident Pb/Ti ratio of 6.1 at a constant substrate temperature of 620 °C. Substrates are Si(100), Pt/Ti/SiO₂/Si, SiO₂/Si, c-sapphire(0001), MgO(100), SrTiO₃(100). Crystalline perovskite can be observed except on Si (100).

Figure 4 shows the crystalline structures of deposited thin films on several substrates at a substrate temperature range of 420-620 °C as a function of the incident Pb/Ti ratio. The black circle indicates the crystalline perovskite region. It is noticed that perovskite PbTiO_3 films can be formed at substrate temperature of 460-500 °C on Si substrate without a buffer layer.

To clarify the nature of the interface between Si and thin films, XPS depth profiles of thin films deposited on Si (a) at incident Pb/Ti ratio of 1.2 at 500 °C and (b) at an incident Pb/Ti ratio of 6.1 at 620 °C were measured using the XPS, as shown in Fig. 5. Their thickness was about 10 nm. The etching time corresponds to the distance from the thin film surface on Si substrate toward the bulk.

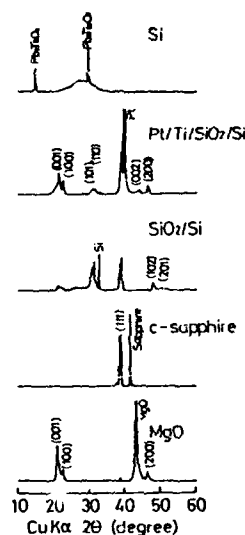


Fig. 3
X-ray diffraction patterns of PbTiO_3 thin films deposited on various substrates at a incident Pb/Ti ratio of 6.1 at a constant substrate temperature of 620 °C.

In both samples, the peaks are observed with lower binding energy relative to that of the main Si peak after 900 seconds of etching time. These peaks, from their binding energy, correspond to a metallic Si species, indicating that the substrate Si was exposed as a result of Ar ion etching.

In sample (a), Si photoemission spectra were not observed from the film surface, while the atomic percent of Si was about 20 % on the film surface in sample (b). Furthermore, Si photoemission spectra were also observed at the surface of the thin films (180 nm thick) deposited on Si under the same conditions as sample (b).

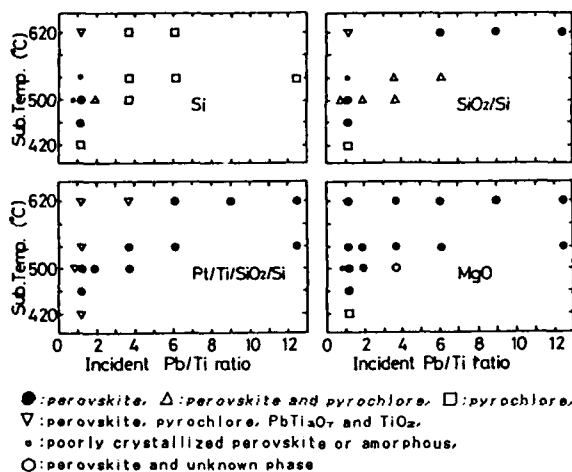


Fig. 4 Crystalline structures of deposited thin films on several substrates at a substrate temperature range of 420-620 °C as a function of the incident Pb/Ti ratio.

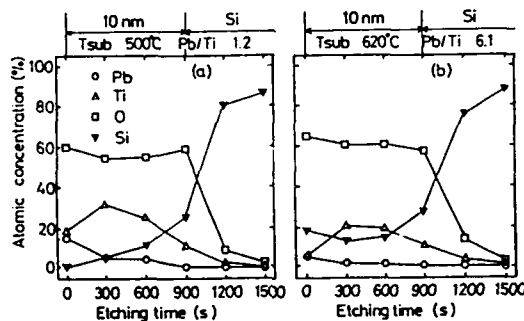


Fig. 5 XPS depth profiles of PbTiO_3 thin films deposited on Si substrate. The etching time corresponds to the distance from the thin film surface on Si substrate.

Silicon diffusion from the Si substrate and the chemical reaction with the thin films takes place with the formation of an amorphous phase which prevents the formation of the perovskite phase. Therefore, to suppress the reaction of the thin films with Si, deposition at a lower substrate temperature is critical to obtain perovskite PbTiO_3 on Si in situ.

4 REPARATION OF $(\text{Pb},\text{La})\text{TiO}_3$ THIN FILMS AND FERROELECTRIC PROPERTIES

Figure 6 shows X-ray diffraction patterns of $(\text{Pb},\text{La})\text{TiO}_3$ thin films deposited on Si, MgO , Pt/MgO , $\text{Pt}/\text{SiO}_2/\text{Si}$, $\text{RuO}_2/\text{Ru}/\text{MgO}$, $\text{RuO}_2/\text{Ru}/\text{SiO}_2/\text{Si}$ at a substrate temperature of 540 °C under RF input power conditions of 55 W for PbO, 450 W for Ti and 70 W for the La target, respectively. La content was estimated to be about 20 % by ICP. The sputtering gas ratio of Ar/O_2 was 1:1. Compared to the XRD patterns of PbTiO_3 of Fig. 3, a decrease of tetragonality was observed.

Typical ferroelectric D-E hysteresis loops are shown in Fig. 7. Figure 7(a) is the D-E loop of a 270 nm $(\text{Pb},\text{La})\text{TiO}_3$ thin film

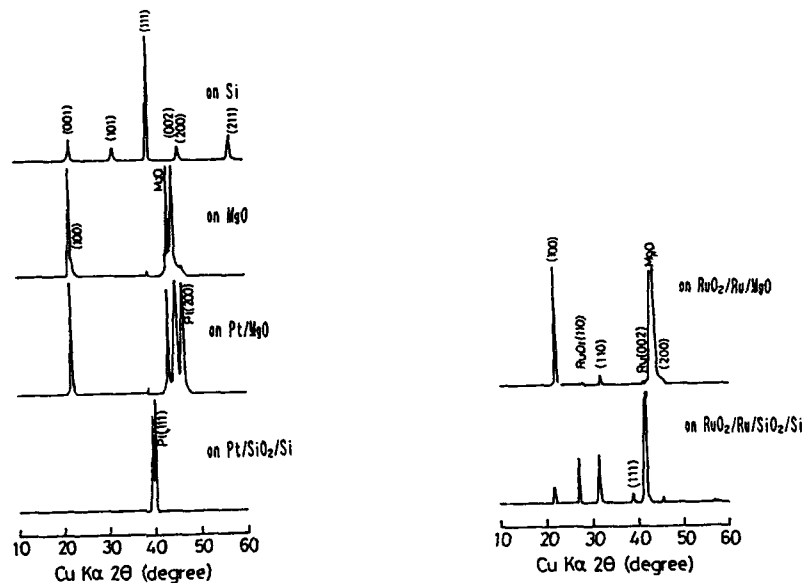


Fig. 6 X-ray diffraction patterns of $(\text{Pb},\text{La})\text{TiO}_3$ thin films deposited on various substrates at a temperature of 540 °C.

on a Pt/MgO substrate. It is noticed that this loop is somewhat asymmetric. Figure 7(b) is the loop of a 270 nm thin film on a Pt/SiO₂/Si substrate and Fig. 7(c) is the loop of a 270 nm film on a RuO₂/Ru/SiO₂/Si. These results indicate that the samples are ferroelectric films with a Curie point above room temperature. The decrease of the tetragonality has the advantage of the elimination of internal stress caused by the Cub-Tet phase transition.

Table 1 illustrates the dielectric permittivity, ϵ , loss tangent, $\tan \delta$, coercive field, E_c , and remanent polarization, P_r , of a 270 nm-thick (Pb,Lu)TiO₃ thin films deposited on various substrates. Among the samples, the highest ϵ , of 226 was obtained for the film on a Pt/SiO₂/Si. The highest P_r was obtained on a Pt/MgO, which attributed to the best crystallinity. The lower ϵ , of films on a Pt/MgO may be due to the difference of the film orientation on substrate compared to the films on Pt/SiO₂/Si.

Figure 8 shows the leakage current-applied voltage characteristic of a 270 nm thick (Pb,Lu)TiO₃ thin film deposited on a Pt/MgO substrate. As can be seen, the V-I relation has a non Ohmic saturation region. In BaTiO₃ ceramics, the V-I relation has a saturation region below the Curie point and it shows an ohmic relation in the paraelectric state above the Curie point⁽³⁾.

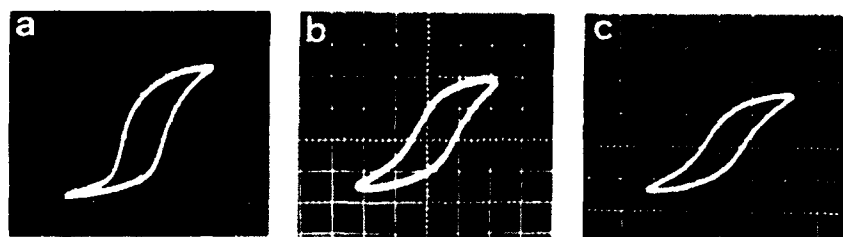


Fig. 7 Typical ferroelectric D-E hysteresis loops of 270 nm (Pb,Lu)TiO₃ thin film on (a) Pt/MgO substrate (b) Pt/SiO₂/Si, and (c) RuO₂/Ru/SiO₂/Si
X: 185 kV/cm/div, Y : 15.7 μ C/cm²/div.

Table 1. Electrical Properties of 270nm Thick (Pb,Lu)TiO₃ Thin Films

Substrate	Pt/SiO ₂ /Si	RuO ₂ /Ru/SiO ₂ /Si	Pt/MgO	RuO ₂ /Ru/MgO
orientation	(111)	random	(001)	(001)
ϵ (100KHz)	226	132	189	159
$\tan \delta$	0.04	0.08	0.05	0.05
E_c (kV/cm)	92.5	92.5	111	-
P_r (μ C/cm ²)	12.6	10.2	18.8	-

The ferroelectric I-V behaviors of both ferroelectric ceramics and thin films are very similar.

Also, it is noticed that asymmetric V-I curves are observed when a dc electric field is applied plus or minus on the top of electrode of thin film based on the electrode of the surface of substrate.

5 THICKNESS DEPENDENCES

Figure 9 shows the dielectric permittivity as a function of the film thickness of $(\text{Pb},\text{La})\text{TiO}_3$ thin film. As can be seen, the permittivity decreases with decreasing of film thickness and especially, in a small thickness region of 130 nm. This result suggests that an importance of the surface effect of ferroelectric particles and ferroelectric thin film.

Depth profile by the XPS of the $(\text{Pb},\text{La})\text{TiO}_3$ thin films deposited on $\text{RuO}_2/\text{Ru}/\text{SiO}_2(1000 \text{ nm})/\text{Si}$ substrate is shown in Fig. 10. As can be seen, each element concentration at the interface between the films and substrate is almost clear and the inter-diffusion of elements or the formation of reaction layers seems to be very small. A lead enrichment near the surface region is observed, which may be attributed to oxygen-chemisorbed lead.

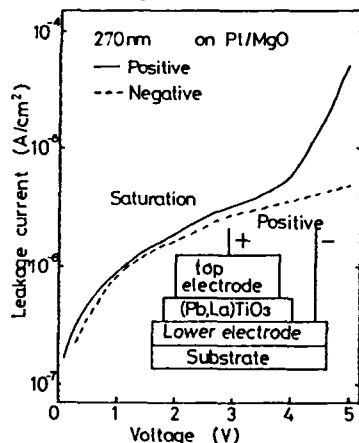


Fig. 8
Leakage current-applied voltage characteristic of 270 nm $(\text{Pb},\text{La})\text{TiO}_3$ thin film deposited on Pt/MgO substrate.

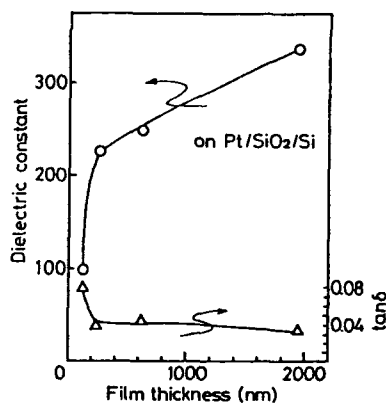


Fig. 9
Dielectric permittivity as a function of the thin film thickness of $(\text{Pb},\text{La})\text{TiO}_3$ thin film.

The surface analysis was also made using the XPS for (Pb,La)TiO₃ thin film deposited on Pt/SiO₂/Si substrate is shown in Fig. 11. It is noticed in this figure that a small thickness region less than 2nm,

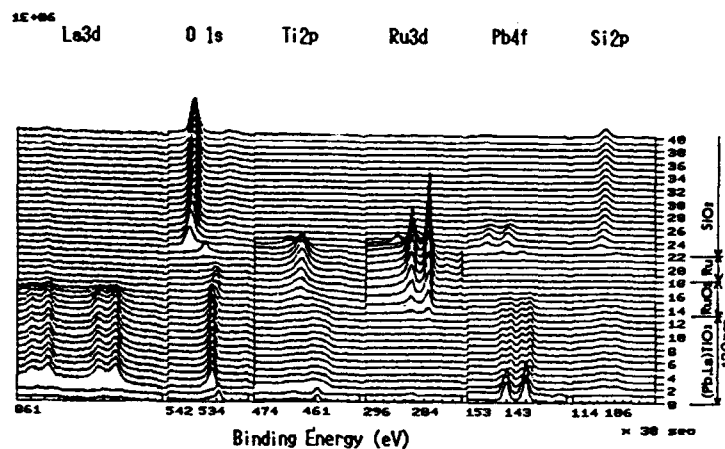


Fig. 10 XPS depth profiles for (Pb,La)TiO₃ thin film deposited on RuO₂/Ru/SiO₂/Si substrate

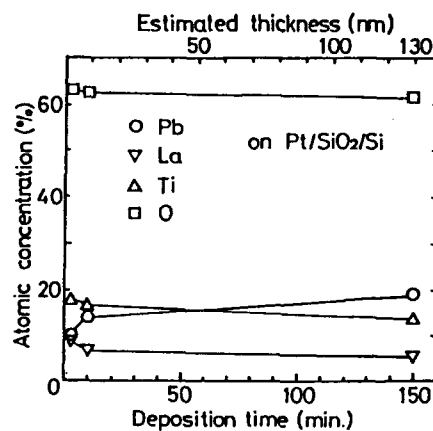


Fig. 11 Surface analysis for (Pb,La)TiO₃ thin film deposited on Pt/SiO₂/Si substrate

a Pb deficiency is observed. Pb deficiency in perovskite lattice might bring a oxygen vacancy as expressed in the form of $Pb_{1-x}TiO_{3-x}$. The oxygen vacancy seems to be a origin of the non-ferroelectric semiconductor and it may be induce the thickness dependence of the thin films.

Figure 12 is a X-ray diffraction patterns of $PbTiO_3$ thin films when the deposited thickness were changed⁽⁵⁾. As can be seen, the tetragonality is decreased with decreasing of the film thickness and the crystal structure of the 10 nm thick thin film is almost cubic. This result strongly supports that the existence of Kaenzig's surface layer with a non-ferroelectric with cubic structure⁽⁴⁾.

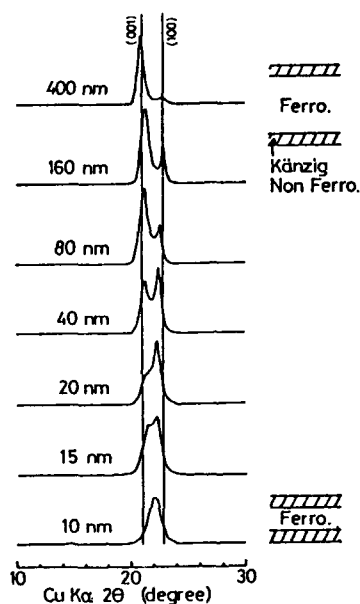


Fig. 12 X-ray diffraction patterns of $PbTiO_3$ thin films as a function of film thickness

6 FATIGUE AND INTERNAL STRESSES

Using a micro-indentation technology for transparent pore free PLZT ceramics, Yamamoto et al investigated⁽⁶⁾ the field induced anisotropic internal stress and they revealed that after dc field application, a tensile internal stress is induced in the direction of dc applied field and a compressive internal stress is induced in the direction perpendicular to the applied field. The

anisotropic internal stress was calculated from the anisotropic crack lengths.

As far as the isotropic internal stresses induced at the Cub-Tet phase transition at the Curie point after firing or heat treatment for electroding, the anisotropic internal stress mentioned before and the aging effects of ferroelectric ceramics and the aging effects were reviewed by Okazaki ⁽⁷⁾.

The isotropic internal stress of pore free $(\text{Pb}_{1-x}\text{La}_x)\text{TiO}_3$ decreases with increasing x and with decreasing the tetragonality, c/a and the Curie point, T_c . The internal stress of the sample of $x > 0.3$ and the T_c of below room temperature is zero. This fact strongly suggest that the internal stress is induced by Cub-Tet phase transition through the Curie point.

A less fatigue is also important for a less residual internal stress thin ferroelectric film. For this purpose, $\text{RuO}_2(70\text{nm})/\text{Ru}(70\text{nm})/\text{SiO}_2(1000\text{nm})/\text{Si}$ and $\text{RuO}_2/\text{Ru}/\text{MgO}$ substrates were prepared. The idea is to eliminate the lattice mismatch between the thin film and the substrate. The RuO_2 has lattice constants of $a = 0.4500\text{ nm}$ and $c = 0.3107\text{ nm}$, and the $\sqrt{2}a = 0.6364\text{ nm}$ and $1.5 a = 0.6320\text{ nm}$, and the $1.5 \times 2c = 0.9321\text{ nm}$ and $2\sqrt{3} = 0.9373\text{ nm}$.

Since 1953, Okazaki proposed ⁽³⁾ a Space Charge Model in BaTiO_3 ceramics and the related phenomena were reviewed with two kinds of the internal bias fields, E_i and E_{-i} ⁽⁸⁾. In 1982, Takahashi ascertained ⁽⁹⁾ the space charge internal field, E_i , in PZT ceramics with various dopants and revealed the linear relation between the internal bias field and mechanical quality factor, Q_m .

Ichinose et al ⁽¹⁰⁾ first found the space charge (E_i) stabilized effect for $\text{Pb}(\text{Ni}, \text{Te})_{1/2}\text{-PbZrO}_3\text{-PbTiO}_3$ ceramic ignitors. The E_i in the same direction to the remanent polarization generates during the aging process after poling and it stabilizes the piezoelectric properties against mechanical compression ⁽¹¹⁾.

Okazaki et al investigated ⁽¹²⁾ the space charge stabilized effects against static mechanical compression and repeated mechanical fatigue tests for the piezoelectric PZT ignitors. Samples with the E_i have a higher static mechanical strength and a longer repeated mechanical compression life.

It is noticed that the static mechanical compression strength of high- Q_m PZT is higher about three times compared to that of Low- Q_m PZT. Why is it so much different about three times? The difference of the E_i of about three times between the high- Q_m and low- Q_m PZT corresponds to the difference of about three times in mechanical compression modulus. This suggest the importance of the space-charge stabilized effect on electromechanical strength.

Okazaki et al investigated ⁽¹³⁾ the loop shape changes of PZT

ceramics at various electrical conditions. When an ac electric field is applied for a long time to ferroelectric ceramics, the P_r of the normal poled ceramics decreases with ac applying time. This corresponds to the decrease of the E_c . In the ceramic samples with the E_c , the coercive field, E_c , increases with ac applying time. The electrical fatigue patterns belong to "increasing E_c type". Yamamoto reported the similar result in PZT thin films⁽¹⁴⁾.

In the case of non poled ferroelectric ceramics of $Q_m = 0$, the remanent polarization, P_r , decreases and the coercive field, E_c , does not change at about constant value with ac applying time. The electrical fatigue pattern belongs to "constant E_c type". Amanuma reported⁽¹⁵⁾ a similar result in PZT thin films.

As far as the origin of the E_c , space charge diffusion model is proposed for ferroelectric ceramics^{(16) (17) (18)}. This model may be used to explain the very complicated behaviors of ferroelectric thin films combined with the internal stresses, the internal bias fields, the interface behaviors and others.

7 CONCLUSION

(Pb,La)TiO₃ thin films were prepared using a four target cathode RF sputtering apparatus and the ferroelectric properties were measured with microstructure analysis. The thickness dependences, the fatigue and internal stresses and the shape changes of D-E loops were also discussed in the comparison to ferroelectric ceramics.

8 SUMMARY

The ferroelectric properties of thin films are very complicated because of the surface layer effects, the interface between substrates and thin films, the internal bias field effects and others. The developments of substrates with less fatigue and small mismatch of lattice constants. The asymmetric polarization reversal should be also solved for the practical applications.

ACKNOWLEDGEMENT

This work supported by a Grant-in-Aid for Scientific Research from the Ministry of Education, Science and Culture of Japan and the Kanagawa Academy of Science and Technology Foundation.

REFERENCES

- 1 H. Adachi et al. Proc. of 1990 IEEE 7th ISAF, pp. 273-278.
- 2 H. Maiwa et al.: Jpn. J. Appl. Phys. Vol. 31 (1992) pp. 3029-3032 Part 1, No. 9B, Sept. 1992
- 3 K. Okazaki; Ceramic Engineering for Dielectrics(4th Edition), Gakkensha, Tokyo, 1992, in Japanese, translated into Russian [Energy Publishing Office in Moscow (1976)]
- 4 W. Keanzig : Phys. Rev. 98(1955) 549.
- 5 T. Yamamoto, et al., "Stress anisotropy of PLZT Ceramics Induced by Polarization," Jap. J. Appl. Phys., 22, S22-2, pp. 70-72 (1983)
- 6 K. Okazaki and H. Maiwa; Jpn. J. Appl. Phys., Vol. 31 (1992) pp. 3113-3116, Part 1, No. 9B, Sept. 1992. Proc. of FMA, pp. 3113-3116.
- 7 K. Okazaki: Mechanical Behavior of ferroelectric ceramics, Amer. Ceram. Soc. Bull., 68, 9 (1984) pp. 1150-1153.
- 8 K. Okazaki: "Normal Poling and High Poling and Space-Charge Effects", Jpn. J. Appl. Phys., Vol. 32(1993) pp. 4241-4244, Part 1, No 9B, Sept. 1993.
- 9 S. Takahashi: Jpn. J. Appl. Phys. 20 (1981) 95.
- 10 Ichinose et al: presented at Ann. Meet. of Inst. Elet. Comm. Eng. Japan, (1973) S-13-4.
- 12 K. Okazaki; Proc. the Workshop on Sonar Transducer Materials, Nav. Res. Lab., Washington, DC, Nov. 13-14, (1976) pp. 239-255.
- 13 K. Okazaki et al. ; Electro-Mechanical Strength of Ferroelectric Ceramics, Ferroelectrics, 1992, Vol. 131. pp. 25-40.
- 14 K. Okazaki, H. Igarashi and S. Miura: "Properties of $\text{Pb}(\text{Zr}, \text{Ti})\text{O}_3$ Ceramics under High Electric Field, "Energy and Ceramics" 1980, Elsevier Scientific Publisshing Co., Amsterdam-Oxford-New York, pp. 1085-1095.
- 15 T. Yamamoto: presented at 1993 PAC RIM, to be published in Jpn. J. Inst. Electronics, Information and Communication Eng.
- 16 K. Amanuma: presented at 1993 PAC RIM, (1993) SVP-3-93P.
- 17 K. W. Wagner: Arch. Electrotech., 2 (1908) 371, 374, 383.
- 18 K. Okazaki and H. Maiwa; Proc. of 9th Korea-Japan Ceramic Seminar, 1992. Dec. pp. 82-86.
- 19 K. Okazaki and H. Maiwa; ISAF 1992, Proc. of 8th IEEE Int'l Symp. on Appl. of Ferroelectrics, in Greenville, SC, USA, Aug. 30-Sept. 2, 1992, pp. 103-106.

GROWTH AND PROPERTIES OF PZT THIN FILMS ON A 6-8 INCH WAFER BY MOCVD

Tadashi Shiosaki, C. S. Kang*, Masaru Shimizu, Mitsuru Fukagawa**, Kenichi Nakaya** and Eiki Tanikawa***

Department of Electronics, Kyoto University, Sakyo-ku, Kyoto 606, Japan

*Samusung Electronics Co., Ltd., Yongin-Gun, Kyungi-Do, Korea.

**Amaya Co., Ltd., Koshigaya City, Saitama 343, Japan

***CAT K.K., Bunkyo-ku, Tokyo 112, Japan

ABSTRACT

Large area growths of PZT thin films were performed by a 6-8 inch single wafer type MOCVD system, using Pb(DPM)_2 (solid), $(\text{C}_2\text{H}_5)_3\text{Pb}[\text{OCH}_2\text{C}(\text{CH}_3)_3]$ (liquid), $\text{Zr}(\text{O}-t-\text{C}_4\text{H}_9)_4$ (liquid), $\text{Ti}(\text{O}-i-\text{C}_3\text{H}_7)_4$ (liquid) and O_2 . When Pb(DPM)_2 was used, highly uniform PZT films with a variation in film thickness of less than $\pm 5\%$ were grown on 6 and 8 inch Si wafers. However, the reproducibility of the film composition and electrical properties was quite poor. On the other hand, when $(\text{C}_2\text{H}_5)_3\text{Pb}[\text{OCH}_2\text{C}(\text{CH}_3)_3]$ was used, the reproducibility of the film composition was quite good. Uniform films with a variation in the Pb, Zr and Ti components of less than $\pm 1.5\%$ and in the film thickness, refractive index and dielectric constant of less than $\pm 5\%$ were successfully obtained on a 6 inch Si wafer.

To the extent authorized under the laws of the United States of America, all copyright interests in this publication are the property of The American Ceramic Society. Any duplication, reproduction, or republication of this publication or any part thereof, without the express written consent of The American Ceramic Society or fee paid to the Copyright Clearance Center, is prohibited.

1. INTRODUCTION

In the past several years, interest in the use of ferroelectric thin films, such as PbTiO_3 , $\text{Pb}(\text{Zr},\text{Ti})\text{O}_3$ [PZT], $(\text{Pb},\text{La})(\text{Zr},\text{Ti})\text{O}_3$ [PLZT], SrTiO_3 , BaTiO_3 and $(\text{Ba},\text{Sr})\text{TiO}_3$, for memory device applications including high density dynamic random access memory (DRAM) and nonvolatile memory has increased greatly. Many thin film techniques, such as evaporation, sputtering, laser ablation, chemical vapor deposition (CVD), metalorganic chemical vapor deposition (MOCVD), metallorganic decomposition (MOD) and sol-gel methods, have been reported to obtain a variety of ferroelectric thin films as mentioned above. Among these techniques, in the past several years the MOCVD technique has been attracting much attention due to the recent development of new source materials, the high controllability of the film composition and crystalline structure, a high growth rate and good step coverage. Furthermore, the MOCVD technique provides the possibility for scaling up the process from the laboratory to commercial based production. Therefore, these practicalities provide the impetus for the development of the large scale film growth technique for ferroelectrics [1-5].

In this paper, we describe the development of a 6-8 inch single wafer type MOCVD system and the properties of PZT thin films obtained using this system.

2. EXPERIMENTAL PROCEDURE

An MOCVD system was developed for commercial-based production. Figure 1 shows the MOCVD system used in our experiments. This system consisted of a gas supply system, a reaction chamber and a evacuation system. The gas supply system had five temperature controlled ovens for controlling the temperature of the source precursor vessels. The gas flow rates were precisely controlled using mass flow controllers (MFC). The reactor chamber was a vertical type and a 6-8 inch wafer could be loaded.

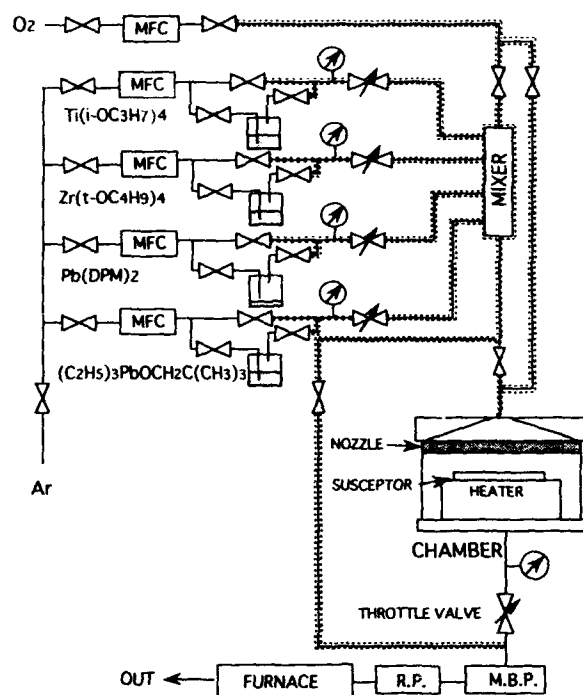


Fig.1. Schematic diagram of the MOCVD system.

In the evacuation system, a mechanical booster pump (M.B.P.) and rotary pump (R.P.) were used. The exhaust gas was decomposed in a furnace and released to the air.

In our experiments, $\text{Pb}(\text{DPM})_2$ (lead bisdipivaloymethan ; Nippon Sanso Co. or Tri Chemical Lab. Ltd., purity : 99.9%), $(\text{C}_2\text{H}_5)_3\text{Pb}[\text{OCH}_2\text{C}(\text{CH}_3)_3]$ (triethyl 2,2 dimethyl propoxy lead [TEDMPL] ; Tri Chemical Lab. Ltd., purity : 99.99%), $\text{Zr}(\text{O}-t-\text{C}_4\text{H}_9)_4$ (zirconium tetra-tert-arybutoxide ; Tri Chemical Lab. Ltd., purity : 99.9999%), $\text{Ti}(\text{O}-i-\text{C}_3\text{H}_7)_4$ (titanium tetraisopropoxide ; Tri Chemical Lab., purity : 99.9999%) and O_2 (purity : 99.995%) were used as source materials. The carrier gas used was Ar (purity : 99.9999%). $\text{Pb}(\text{DPM})_2$ was the solid source. Other

metalorganic sources were liquid. In particular, TEDMPL was used for the first time. The substrates used were Si(100) and Pt(111)/SiO₂/Si(100).

The film composition was analyzed using Electron Probe Micro Analysis (EPMA). The film thickness and refractive index were measured by the ellipsometric method.

3.RESULTS AND DISCUSSION

In the first set of experiments, Pb(DPM)₂ was used as a Pb source material. When PZT films were prepared on a 6 inch wafer using the funnel-shaped nozzle, the uniformity of film thickness and film composition were very poor, although the films were deposited over the entire substrate. Even if the growth parameters such as the gas flow rates and reaction pressures were changed, an improvement in this uniformity was not observed. However, when a nozzle with a diameter of 20 cm perforated with small holes was used, highly uniform crystalline films with a variation in film thickness of less than $\pm 5\%$ were successfully obtained on 6 and 8 inch wafers [4,5].

From these experimental aspects, it was found that there were some problems. Firstly, the reproducibility of the film composition and electrical properties was quite poor. Figure 2 shows the variation of the Pb component in the films and the deposition rate in each experiment, in which film deposition was carried out for 3 hours at a substrate temperature of 590°C and at a reaction pressure of 5Torr. in each growth run. The Pb composition in the films decreased each time the experiment was performed. The change in the Pb content, V_{Pb} , which was defined as (maximum Pb content - minimum Pb content)/(average Pb content), was 63.6% when the Pb source temperature was 125°C. These changes in the Pb content and deposition rate were caused by an instability in the supplying Pb source, because the Pb source used was a solid which had a low vapor pressure and therefore stabilization of the Pb supply over a long period was difficult compared with using a bubbling method with a liquid source. When the Pb source

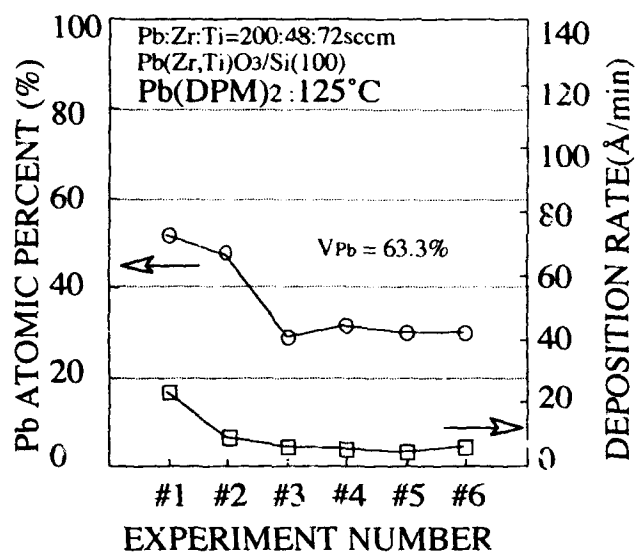


Fig.2. Variations of the Pb content in the films and deposition rate with each performance of the experiment when a solid Pb source temperature was 125°C.

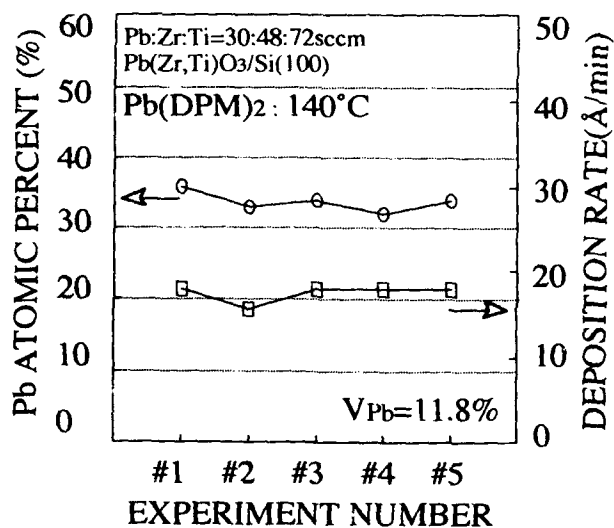


Fig.3. Variations of the Pb content in the films and deposition rate with each performance of the experiment when a solid Pb source temperature was 140°C.

temperature was set at 140°C – which was higher than its melting point (around 130°C) – an improvement in the reproducibility was observed and V_{Pb} was 11.8% as shown in Fig.3. However it was difficult to keep the temperature of all lines from the vessels containing the Pb source to the reaction chamber at a high temperature. Secondly, the growth rate was quite slow due to the low vapor pressure of the Pb solid source.

Therefore, in the second set of experiments we used TEDMPL as a new liquid Pb source. The films obtained were also crystalline. In the first stage, as with the first set of experiments, we observed the variation of the Pb content and the deposition rate of the films with each performance of the experiment. The Pb source was kept at 60°C and film deposition was carried out for 1 hour at a substrate temperature of 590°C, and at a reaction pressure of 5Torr. in each growth run. The result obtained is shown in

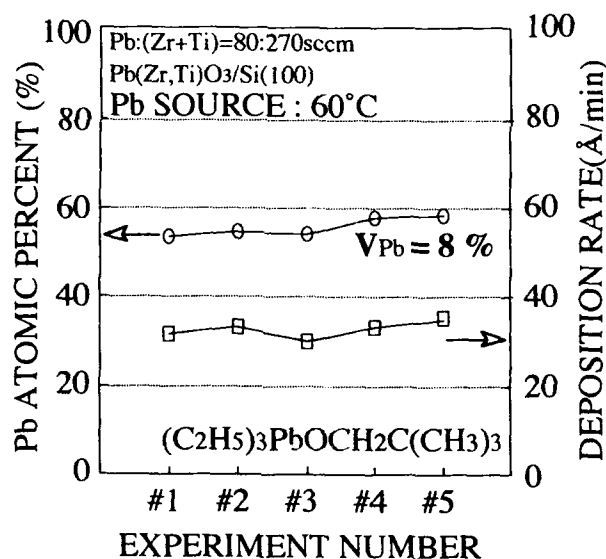


Fig.4. Variations of the Pb content in the films and deposition rate with each performance of the experiment when a liquid Pb source temperature was 60°C.

Fig.4. A dramatic improvement was seen in the variation of the Pb content and the deposition rate, compared with the results when using a $\text{Pb}(\text{DPM})_2$ source. V_{pb} was a mere 8% as shown in Fig.4.

The uniformity of the film composition, film thickness, refractive index and dielectric constant was also investigated. Uniform films with a variation in the Pb, Zr and Ti components of less than $\pm 1.5\%$ were successfully obtained on a 6 inch Si wafer, as shown in Fig.5. As well, the same films showed a narrow variation in the film thickness and refractive index of less than $\pm 5\%$ as shown in Fig.6. Figure 7 shows a variation in the relative dielectric constants of the film. The average value of the dielectric constants of the films (250nm in thickness) was around 400, and a variation in the dielectric constants of around $\pm 5\%$ was obtained. The obtained films had $\tan\delta$ of 0.03–0.07 and resistivities of 10^9 – $10^{11}\Omega\cdot\text{cm}$, respectively.

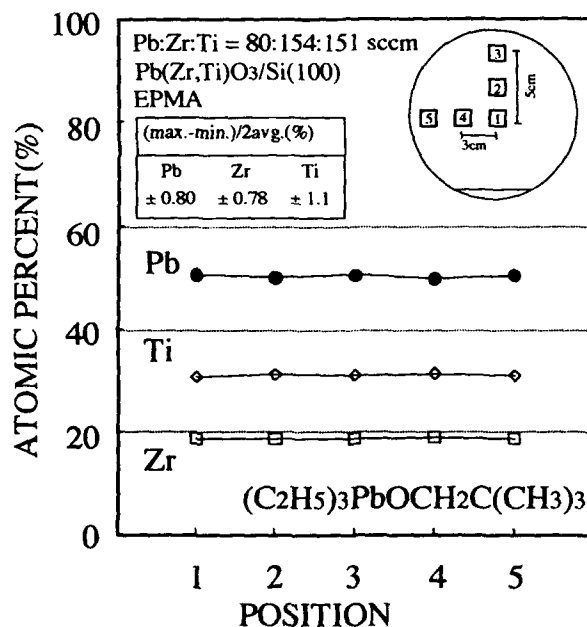


Fig.5. Variations in the Pb, Zr and Ti contents for a PZT film on a 6 inch Si wafer.

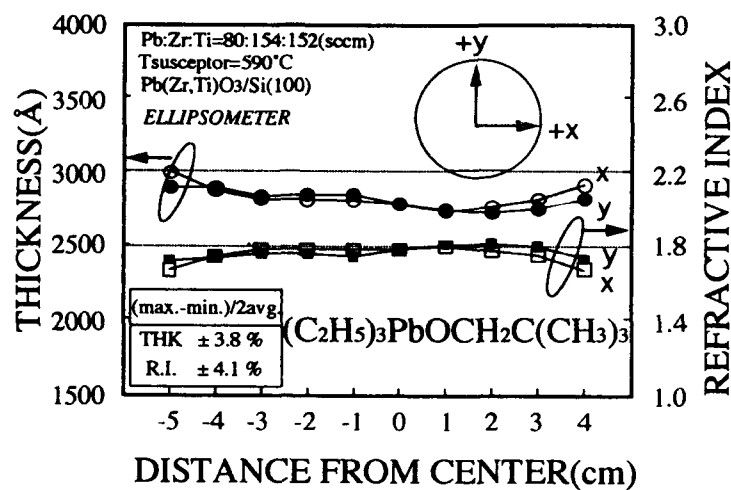


Fig.6. Variations in the film thickness and refractive index of the PZT film on a 6 inch Si wafer.

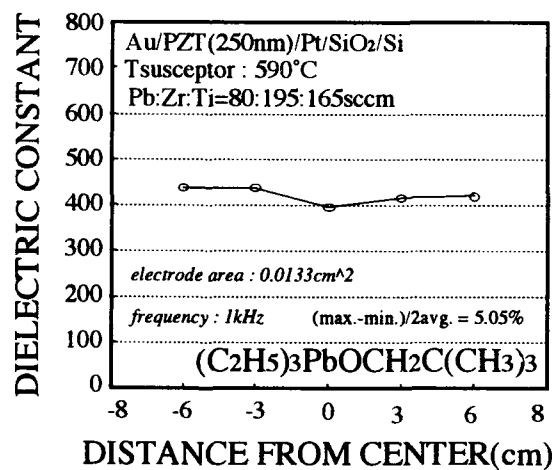


Fig.7. Variation in the dielectric constant of the PZT film on a 6 inch Si wafer.

D-E hysteresis loops were also observed. The remanent polarizations (P_r) and coercive fields (E_c) were 5.4–9.3 $\mu\text{C}/\text{cm}^2$ and 87–107 kV/cm, respectively.

4. CONCLUSIONS

A 6–8 inch single wafer type MOCVD system for growing ferroelectric thin films was developed. Large area growths of PZT thin films were performed by this MOCVD system, using $\text{Pb}(\text{DPM})_2$ (solid), $\text{Zr}(\text{O}-t-\text{C}_4\text{H}_9)_4$ (liquid), $\text{Ti}(\text{O}-i-\text{C}_3\text{H}_7)_4$ (liquid) and O_2 . $(\text{C}_2\text{H}_5)_3\text{Pb}[\text{OCH}_2\text{C}(\text{CH}_3)_3]$ (TEDMPL) was also used as a new liquid Pb source. When a solid $\text{Pb}(\text{DPM})_2$ source was used, highly uniform PZT films with a variation in film thickness of less than $\pm 5\%$ were successfully grown on 6 and 8 inch wafers. However, the reproducibility of the film composition, in particular the Pb content, and the electrical properties was poor. On the other hand, when a liquid Pb source (TEDMPL) was used, the reproducibility of the film composition with each performance of the experiment was quite good and the variation of the Pb content, V_{pb} , was 8%. The PZT films obtained on a 6 inch wafer showed variations in the Pb, Zr and Ti components of less than $\pm 1.5\%$. Variations in the film thickness, refractive index and dielectric constant of less than $\pm 5\%$ were also successfully achieved.

ACKNOWLEDGEMENTS

This work was partly supported by Grant-in Aid for scientific research (B)(No.04452176) from the Ministry of Education, Science Culture, and by research grants from the Mazda Foundation research Grant and the Foundation for the Promotion of Material Science and Technology of Japan.

REFERENCES

- [1] A. C. Greenwald, J. T. Daly and N. M. Kalkhoran : Mater. Res. Soc. Symp. Proc. 243(1992)229.
- [2] P. C. Van Buskirk, R. Gardiner, P. S. Kirlin and S. B. Krupanidhi : Proc. 7th IEEE Int. Symp. Application of Ferroelectrics (1992)p.340.
- [3] M. De Keijser, P. J. Van Veldhoven and G. J. M. Dormans : Mater. Res. Soc. Proc. 310(1993)223.
- [4] M. Shimizu, M. Fujimoto, T. Katayama, T. Shiosaki, K. Nakaya, M. Fukagawa and E. Tanikawa : Mater. Res. Soc. Proc. 310 (1993)255.
- [5] T. Shiosaki, M. Fujimoto, M. Shimizu, M. Fukagawa, K. Nakaya and E. Tanikawa : to be published in Proc. 5th Int. Symp. Integrated Ferroelectrics.

SPUTTER DEPOSITION OF FERROELECTRIC PbTiO_3 THIN FILMS ON $\text{MgO}(100)$ SUBSTRATES.

Sangsub Kim, Youngmin Kang, and Sunggi Baik
Department of Materials Science and Engineering, Pohang University of
Science and Technology, P. O. Box 125, Pohang, 790-600, Korea

ABSTRACT

Effects of surface structures of $\text{MgO}(100)$ single crystal substrates on the growth of PbTiO_3 thin films have been analyzed. The film on the cleaved substrate was not uniform and its crystallinity was inferior to those on polished or annealed substrates due to the presence of large cleavage steps. Whereas, better epitaxiality was found on the annealed substrate than on the polished substrate. Favorable effects of thermal annealing after polishing has been explained based on damage relieving mechanisms, surface step rearrangement, and surface flatness by thermal annealing.

1. INTRODUCTION

$\text{MgO}(100)$ single crystals have been widely used as a substrate for the preparation of ferroelectric thin films including PbTiO_3 ¹, PZT ² and PLZT ³ mainly due to good lattice matching, similar crystal symmetry and low chemical reactivity. Such ferroelectric thin films have been receiving great interests for several applications in nonvolatile memories, infrared detectors, optoelectronic devices, etc. It is

To the extent authorized under the laws of the United States of America, all copyright interests in this publication are the property of The American Ceramic Society. Any duplication, reproduction, or republication of this publication or any part thereof, without the express written consent of The American Ceramic Society or fee paid to the Copyright Clearance Center, is prohibited.

advantageous to grow highly epitaxial ferroelectric thin films for such applications.

A number of techniques have been employed for the film preparation. Depending on the techniques various deposition parameters have to be monitored and controlled in order to obtain highly epitaxial thin films. In case of sputter deposition, the important controlling parameters are substrate temperature, input power, gas pressure, gas composition, etc. However, the crystallinity and properties of thin films may be significantly affected by the surface conditions of substrates. Careful selections and preparation of substrates often determine the quality of films.

Three types of MgO(100) single crystal substrates(cleaved, polished and annealed) have been used for the studies of thin film formation and epitaxial growth. The cleaved MgO(100) substrates seems to be cleaner and less defective than any other types of substrates. Many studies have been carried out on the deposition of metallic thin films, especially, on the early stages of metallic film formation on the cleaved MgO(100) substrate^{4,5}. However, few works have been performed on the growth of ferroelectric thin films.

Ferroelectric thin films have been grown usually on the mechanically polished substrates^{1,3}. In spite of possible presence of disorder at the surface after polishing, highly epitaxial ferroelectric thin films have occasionally been prepared on the substrate. Nevertheless, it must be taken into consideration that the polished surface is atomically rough and contains structural disorders.

Recently, it has been reported that thermally annealed substrates are beneficial for the epitaxial growth of various oxide thin films.

Moockly et al.⁶ reported that the thermal annealing of MgO substrates at 1100 - 1200°C for 12 - 24 h in air or oxygen atmosphere were highly effective for producing epitaxial, c-axis oriented $\text{YBa}_2\text{Cu}_3\text{O}_{7-x}$ films with good superconductive properties. Awaji et al.⁷ reported that the good superconductivity could be obtained in a ultra-thin $\text{YBa}_2\text{Cu}_3\text{O}_{7-x}$ film prepared on annealed MgO(100) substrates. Similar results have been reported in other systems^{8,9}. However, it is still unclear how the surface conditions of substrates are changed by thermal annealing treatments, and why annealed substrates are more favorable for the preparation of epitaxial thin films.

We have been analyzing the surface and near-surface regions of MgO(100) substrates prepared by cleaving, polishing, and annealing. In this paper, the difference in surface structures of each substrates are reviewed. Ferroelectric PbTiO_3 thin films have been prepared on the substrates by RF magnetron sputtering. Attempts have been made to correlate between the substrate surface structures and the crystallinity and microstructures of thin films.

2. EXPERIMENTAL

Samples of approximately $10 \times 10 \times 1 \text{ mm}^3$ were prepared by cleaving along (100) planes of MgO single crystals. The surfaces were polished mechanically using successively finer grades of diamond paste down to $0.25 \mu\text{m}$. Some samples were annealed within a tube furnace made of high purity alumina (McDaniel Refractory Co.) at 1200°C for 12 h in air. The as-polished and annealed samples were cleaned ultrasonically in trichloroethylene, acetone, and methyl alcohol for 10 min each, successively, followed by boiling in methyl alcohol for 10 min.

PbTiO₃ thin films have been prepared by RF magnetron sputtering. Sputtering conditions to achieve highly c-axis oriented epitaxial PbTiO₃ thin films have been optimized previously¹⁰. Table 1. summarizes the sputtering conditions used in this study.

Table 1. Summary of sputtering conditions.

Target	PbTiO ₃ powder with 5 wt% excess PbO
Gas composition	Ar/O ₂ = 100/0
Gas pressure	1.2×10^{-2} torr
RF power density	2 W/cm ²
Substrate temperature	600°C
Substrate to target distance	70 mm

The nanometer-scale surface structures of the substrates have been studied by an atomic force microscopy (AFM). Surface morphology of the films have been studied by a scanning electron microscopy (SEM). The crystallinity of the films has been studied by X-ray rocking curve measurements and Rutherford backscattering spectrometry (RBS) combined with channeling experiments. Microstructures of the films including domain structures and epitaxial relationships have been studied by cross-sectional transmission electron microscopy.

3. SURFACE STUDIES OF MgO(100) SUBSTRATES

3.1. RBS and Channeling¹¹

It is reasonable to expect that the degree of damage in the surface

region of substrates is dependent on the preparation procedures. We have studied damages in the surface and near-surface regions of MgO substrates using Rutherford backscattering spectrometry (RBS) combined with channeling technique that can measure easily the crystal quality of the upper regions of single crystalline samples.

The cleaved MgO(100) surface showed nearly ideal bulk truncation without any significant lateral ionic displacement. Subsequent mechanical polishing introduced extensive structural damage in the surface and near-surface region. The thickness of the damaged layer after polishing with 0.25 μm diamond paste was estimated to be in the order of 3000 \AA . Such damage was found to be removed effectively after thermal annealing (1200°C, 12 h in air). However, the annealing treatment enhanced surface enrichment of impurities that might be originated from internal or external sources.

3.2. Surface Sensitive X-Ray Scattering^{12, 13}

Surface steps play an important role in the nucleation stage offering preferred nucleation sites. They often control the initial stages of film growth, and significantly influence the microstructure of the film. Thus, it is essential to characterize in an atomic-scale the surface step structures including step height, step spacing and terrace area in order to understand the film growth mechanism properly. We have studied comparatively atomic-scale step structures of MgO substrates using a surface sensitive X-ray scattering technique.

The cleaved surface have been found to contain 2- and 3-atomic-spacing steps with nearly equal population. The average terrace sizes were estimated to be 105 x 79 \AA^2 and 200 x 157 \AA^2 for 2- and 3-atomic-

spacing steps, respectively. The surface prepared by final polishing before X-ray measurement using 0.25- μm diamond paste contained various steps with step heights of 1.67-, 2-, 3-, and 5-atomic-spacing. The results of fine scans showed that the average terrace sizes were $97 \times 4 \text{ \AA}^2$ and $110 \times 7 \text{ \AA}^2$ for 2- and 3-atomic-spacing steps, respectively. On the other hand, the annealed surface contained the steps with step heights of 2- and 3-atomic-spacing and their populations decreased. In addition, their terrace sizes were increased significantly and their average sizes were estimated to be $110 \times 7 \text{ \AA}^2$ and $334 \times 10 \text{ \AA}^2$ for 2- and 3-atomic-spacing steps, respectively. Such step rearrangements of the annealed surface seem to be beneficial for the preparation of epitaxial thin films.

3.3. Atomic Force Microscopy (AFM)

Fig. 1(A) shows an AFM scan on the cleaved $\text{MgO}(100)$ surface. The large cleavage steps are clearly seen. The step heights are about 200 - 500 \AA , and their distances are about 5000 \AA . Individual terraces are not entirely flat, but show a hill-and-valley structures with an average hill-to-hill distance of 500 \AA . The finer step structures within the terraces have been described in the above section.

The surface structure have been modified significantly by mechanical polishing as shown in Fig. 1(B). The large cleavage steps have been disappeared. Preferentially oriented string-like structures are dominant. The average distance between each string is about 50 \AA . Even though its amplitude has been decreased drastically, the hill-and-valley structure is persistent. On the other hand, as shown in Fig. 1(C), for annealed substrate, string-like structures are also evident. However, the undulation has been disappeared; the surface flatness

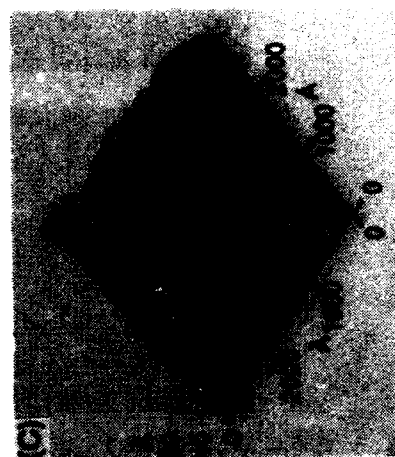
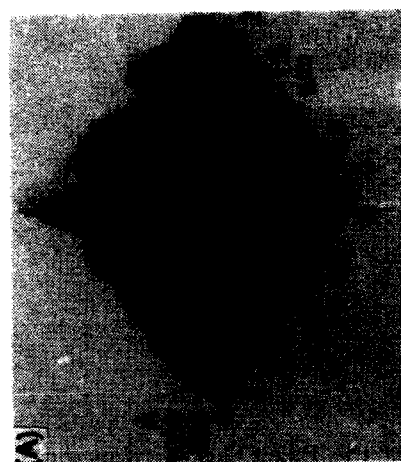
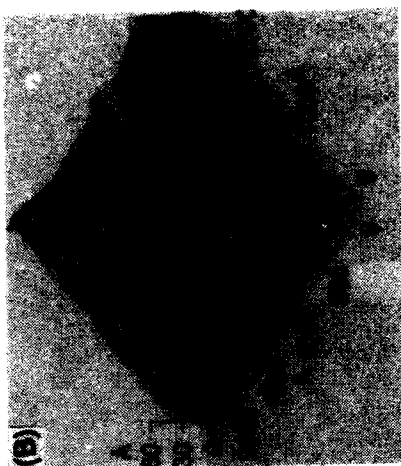


Fig. 1. Atomic force microscopy images of cleaved (A), polished (B), and annealed (C) $\text{MgO}(100)$ surfaces.

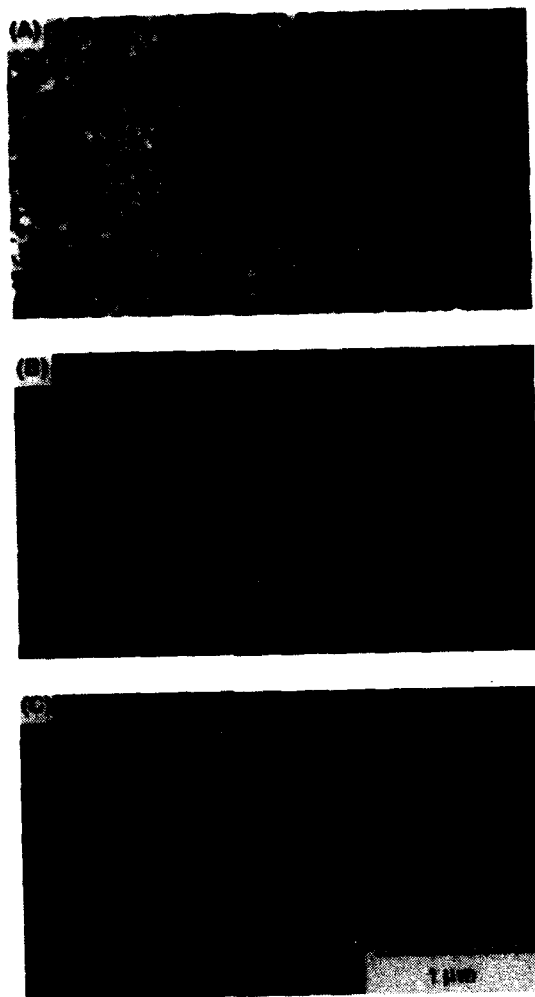


Fig. 2. Scanning electron micrograph of the PbTiO₃ thin films on cleaved (A), polished (B), and annealed (C) MgO(100) substrates.

has been improved greatly in comparison with the polished surface.

4. PbTiO_3 THIN FILMS

4.1 Thin Films Morphology

Fig. 2 shows SEM micrographs of PbTiO_3 thin films grown by RF magnetron sputtering on cleaved(A), polished(B) and annealed(C) substrates. As shown in Fig. 2(A), the PbTiO_3 thin film on the cleaved substrate is composed of fine crystallites of about 800 Å. The line indicated by an arrow in the figure reveals a cleavage step. Also not shown in the figure, the film was very non-uniform, that is, some parts of the substrate were not deposited with the film. It is interesting to note that the cleaved surface was not desirable for the preparation of smooth PbTiO_3 thin films even though the surface seems to be relatively free from defects except cleavage steps. On the other hand, the morphology of PbTiO_3 thin films on polished and annealed substrates was much smoother. As shown in Fig. 2(B), the surface of the film on the polished substrate is featureless except a few grain boundaries. The film on annealed substrate, as shown in Fig. 2(C), is perfectly flat and mirror-like.

4.2 Crystallinity of Thin Films

The crystallographic orientation of the PbTiO_3 thin films have been determined by X-ray diffraction. θ - 2θ scans were performed perpendicular to the surface plane of the PbTiO_3 thin films. The results are shown in Fig. 3, which reveal only perovskite PbTiO_3 peaks due to the reflections from the PbTiO_3 (001) and (h00) planes.

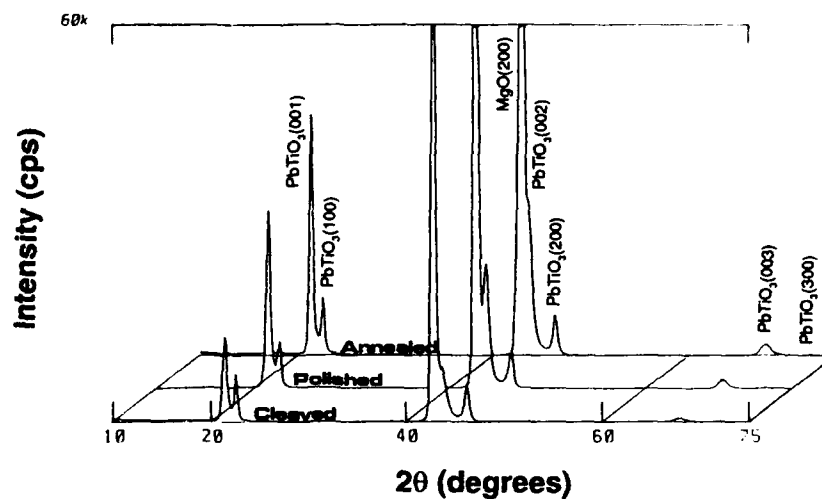


Fig. 3. X-ray θ - 2θ diffraction patterns from the PbTiO_3 thin films on cleaved , polished , and annealed $\text{MgO}(100)$ substrates.

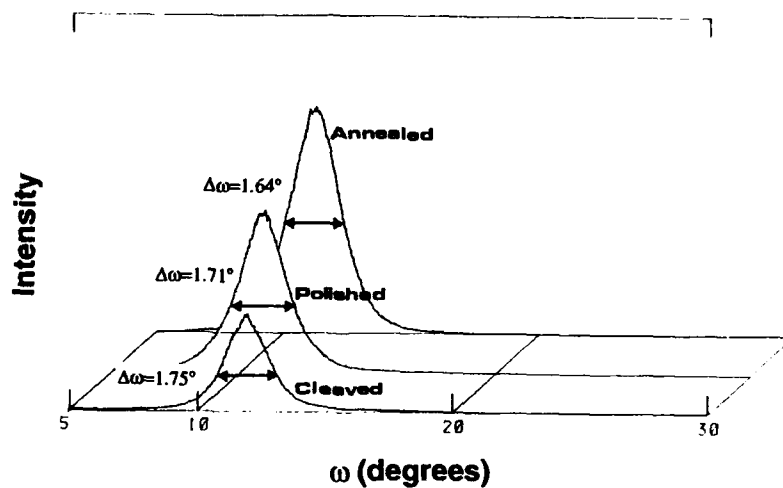


Fig. 4. X-ray rocking curves of the (001) reflections from the PbTiO_3 thin films on cleaved , polished , and annealed $\text{MgO}(100)$ substrates.

Note that the peak intensities of the film on the cleaved substrate are significantly lower. The intensity ratio of the (001) peak of the film on the cleaved substrate to the (001) peak on the polished substrate is 1:2.9, and that with respect to (001) peak on the annealed substrate is 1:3.1. The results suggest that the net volume of the thin film exposed to the X-ray beam was relatively small since the film has been grown non-uniformly on the cleaved substrate.

The crystalline quality of the PbTiO_3 thin films has been characterized by RBS combined with channeling measurement. The minimum backscattering yields in the [100] direction were measured using the lead signal and amounted to approximately 96%, 74% and 69% for cleaved, polished and annealed substrates, respectively. It indicates that the crystallinity of the film on the cleaved substrate was the worst, and those on the annealed substrate was better than that on the polished substrate. The results are consistent with the X-ray measurements. However, taking into account that single crystals or perfectly matched epitaxial thin films exhibit typically 2-4% minimum yield in RBS channeling experiments, it is reasonable to conclude that all the films contain a high density of scattering defects. The nature of scattering defects could be found in the cross-sectional TEM studies, and will be discussed in the next section.

Fig. 4 shows the results of X-ray rocking curve measurements which give informations on the crystalline perfection of the films. The half-peak widths of the rocking curves of (001) peaks of the films were determined to be 1.75° , 1.71° , and 1.64° for the films on cleaved, polished and annealed substrates, respectively. But they are still much larger than a typical single crystalline value, 0.3° .

4.3 Microstructure Analysis by TEM

Cross-sectional TEM experiments have been performed in order to investigate the microstructure of the films. Since the PbTiO_3 thin films on the cleaved $\text{MgO}(100)$ substrates have been found to be non-uniform, TEM specimens only for the films on the polished and annealed substrates have been prepared and studied comparatively.

A cross-sectional TEM micrograph of the PbTiO_3 thin film prepared on the polished $\text{MgO}(100)$ substrate is shown in Fig. 5(A). There is no evidence of a second-phase interfacial layer between the substrate and the film. It also reveals that the film is uniform, dense, and very smooth on the surface. It also shows columnar grains extending across the entire film. Randomly oriented grains are often observed in the PbTiO_3 - MgO interface region. The most significant microstructural feature is the presence of 90° -domains with width about 140 \AA , as indicated by arrows in the figure. Such domains are always oriented about 45° to the interface. These characteristics are expected for the 90° -domain structure of simple perovskite ferroelectrics of tetragonal symmetry, for which 90° -domain walls are coincident with (101) planes. Selected area diffraction(SAD) patterns were taken as a $[001]$ zone axis. The epitaxial relationship deduced from the patterns is $\text{PbTiO}_3[100] // \text{MgO}(100)$ and $\text{PbTiO}_3\langle 100 \rangle // \text{MgO}[100]$, indicating no evidence of in-plane rotation between the film and the substrate. In spite of the small tetragonality ($c/a = 1.06$) of the PbTiO_3 thin film, we could distinguish the spots from c - and a -domains as indicated by an arrow in Fig. 5(B), the SAD pattern. The corresponding reciprocal lattice is shown in Fig. 5(C).

Fig. 6 shows a TEM micrograph of the PbTiO_3 thin film prepared on the annealed $\text{MgO}(100)$ substrate. No evidence of grain boundaries

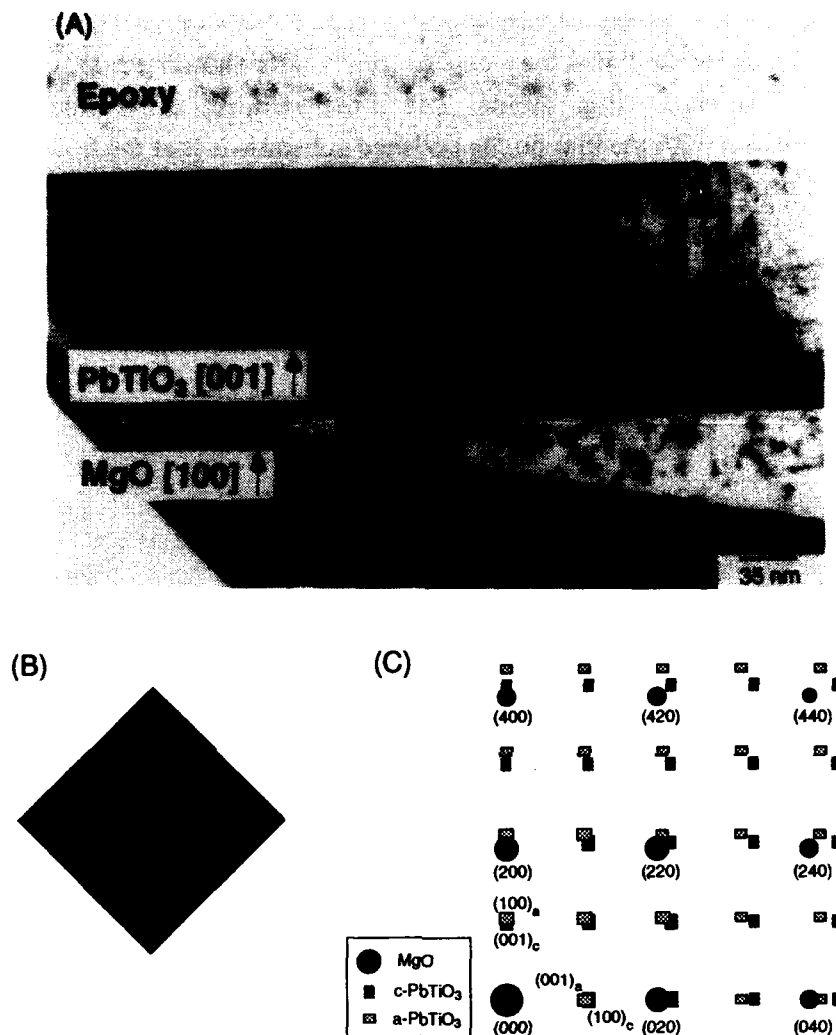


Fig. 5. (A) Cross-sectional transmission electron micrograph of the PbTiO_3 thin film grown on the polished $\text{MgO}(100)$ substrate, (B) selected area diffraction pattern, and (C) the corresponding reciprocal lattice space.

or any other defects can be found except 90° -domains. The high density of 90° -domains may explain the results showing relatively high RBS channeling yields. The most striking difference in comparison with the film on the polished substrate is that the film on the annealed substrate shows no evidence of columnar structures. It is thus reasonable to conclude that the film on the annealed substrate is less defective and structurally more homogeneous.

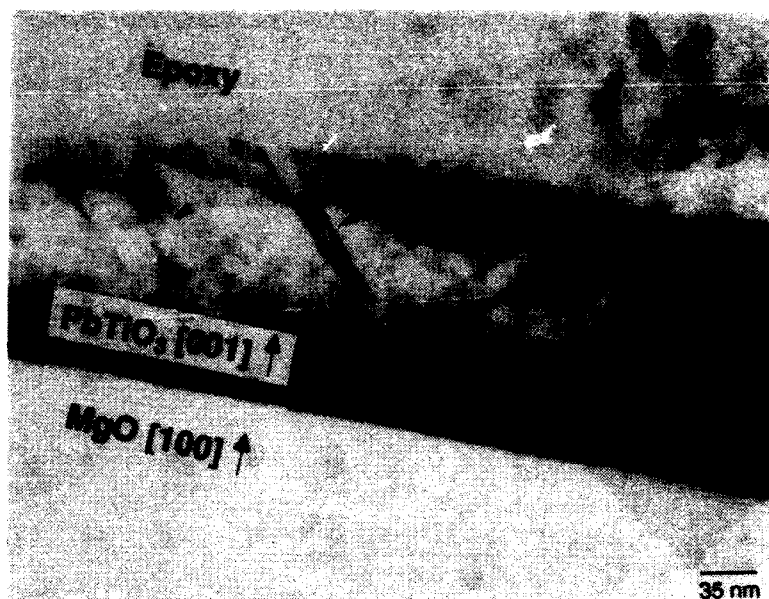


Fig. 6. Cross-sectional transmission electron micrograph of the PbTiO_3 thin film grown on the polished $\text{MgO}(100)$ substrate.

5. DISCUSSION

It is interesting to observe that the PbTiO_3 thin film on the cleaved

substrate was not uniform and its crystallinity was relatively poor, even though the surface is considered to be relatively clean and less structurally defective. Moreover, the surface and near-surface region of the cleaved surface remain highly ordered without any significant displacive defects as confirmed by RBS and channeling studies¹¹. The cleaved surface contained step structures of 2- and 3-atomic-spacing steps between large cleavage steps¹². Such fine step structures were also found on the polished and annealed surface, although their average terrace sizes were different¹³. The only remarkable difference between the cleaved surface and the polished or the annealed surfaces is presence of large cleavage steps on the cleaved surface as shown in Fig. 1(A). Except large cleavage steps, the surface must be ideal for growth of thin films. It is reasonable to consider that the surface containing large cleavage steps is particularly unfavorable for epitaxial film growth.

It has been also confirmed that the annealed MgO(100) substrate were more favorable for growth of superior crystalline PbTiO₃ thin films than the polished substrate. The beneficial effect of mechanical polishing is to remove large cleavage steps improving surface flatness. However, it disturbs finer step structures. The annealing treatment seems to rearrange the steps on the surface as well as to remove structural defects such as dislocations on and near the surface that had been created by mechanical polishing. It also improves the surface flatness further. In order to amplify the effect of surface steps on the film growth, a vicinal MgO(100) substrate inclined about 5.5° with respect to MgO(100) has been tested¹⁴. We observed that (1) the film has grown epitaxially along MgO(100) crystallographic plane and (2) slight misorientation (~1°) has been induced between PbTiO₃(001) and MgO(100). Hence, the presence of steps on the surface tends to tilt the film slightly and possibly induce

low angle grain boundaries. The observation is consistent with the TEM observations shown in Fig. 5 and 6, which confirms that the film on the polished substrate contains high populations of low angle boundaries giving a columnar structure. Removal of surface steps seems to be a key factor for the preparation of defect free epitaxial PbTiO_3 thin films.

6. SUMMARY

The microstructure and crystallinity of ferroelectric PbTiO_3 thin films on cleaved, polished and annealed $\text{MgO}(100)$ substrates have been studied comparatively. Highly c-axis oriented films could be obtained with all these types of substrates, however, in case of the cleaved substrate the film was not uniform and its crystallinity was poorest presumably due to the presence of large cleavage steps. The structural perfection of the film on the annealed substrate was better than that on the polished substrate. The beneficial effect of annealing treatment after mechanical polishing is primarily due to the reduction in surface step population as well as the rearrangement of steps and secondary due to the removal of defects on and near the surface. Surface steps tend to induce misorientation between the substrate and the film introducing low angle boundaries. Key consideration to prepare defect-free single crystalline PbTiO_3 films on $\text{MgO}(100)$ substrate is to remove finer surface steps of 2- to 3- atomic heights.

REFERENCES

- 1 I. Kanno, T. Kamada, S. Hayashi, M. Kitagawa, and T. Hirao, "Ferroelectric PbTiO_3 Thin Films Prepared by Multi-Ion-Beam Sputter and Ion-Assisted Deposition," *Jpn. J. Appl. Phys.*, **32** [7A] L950-L953 (1993).
- 2 B. A. Tuttle, J. A. Voigt, D. C. Goodnow, D. L. Lamppa, T. J. Headley, M. O. Eatough, G. Zender, R. D. Nasby, and S. M. Rodgers, "Highly Oriented, Chemically Prepared $\text{Pb}(\text{Zr}, \text{Ti})\text{O}_3$ Thin Films," *J. Am. Ceram. Soc.*, **76** [6] 1537-1544 (1993).
- 3 M. Okuyama, T. Usuki, Y. Hamakawa, and T. Nakagawa, "Epitaxial Growth of Ferroelectric PLZT Thin Film and Their Optical Properties," *Appl. Phys.*, **21**, 339-343 (1980).
- 4 J. W. He and P. J. Moller, "Epitaxial and Electronic Structure of Ultra-Thin Copper Films on MgO Crystal Surfaces," *Surf. Sci.*, **178**, 934-942 (1986).
- 5 T. Urano and T. Kanaji, "Atomic and Electronic Structure of Ultrathin Iron Film on $\text{MgO}(001)$ Surface," *J. Phys. Soc. of Jpn.*, **57** [10] 3403-3410 (1988).
- 6 B. H. Moeckly, S. E. Russek, D. K. Lathrop, R. A. Buhrman, J. Li, and J. W. Mayer, "Growth of $\text{YBa}_2\text{Cu}_3\text{O}_7$ Thin Films on MgO : The Effect of Substrate Preparation," *Appl. Phys. Lett.*, **57** [16] 1687-1689 (1990).
- 7 T. Awaji, K. Sakuta, Y. Sakaguchi, and T. Kobayashi, "Improved Surface Crystallinity of MgO Crystal Substrate through in Annealing

in Oxygen Atmosphere," Jpn. J. Appl. Phys., **31** [5B] L-642-L645 (1992).

8 D. J. Godbey, S. B. Qadri, M. E. Twigg, and E. D. Richmond, "MBE-Grown Germanium on Sapphire (1T02), Thin Solid Films, **184**, 379-386 (1990).

9 S. H. Ling, Y. S. Tang, W. S. Au, and H. K. Wong, "Epitaxial Growth of Pb(Zr, Ti)O₃ Films on MgAl₂O₄ by Pulsed Laser Deposition," Appl. Phys. Lett., **62** [15] 1757-1759 (1993).

10. Sangsub Kim, Youngmin Kang, and Sunggi Baik, "Sputter Deposition of Ferroelectric PbTiO₃ Thin Films," Ferroelectrics, (in press).

11 S. S. Kim and S. Baik, "Rutherford Backscattering and Channeling Studies of Cleaved, Polished, and Annealed MgO (100) Single Crystals" J. Am. Ceram. Soc. (in press).

12 S. S. Kim, S. Baik, H. W. Kim, and C. Y. Kim, "X-ray Study of Step Morphology on a Cleaved MgO(100) Surface," Surf. Sci. Lett., **294**, L935-L938 (1993).

13. Sangsub Kim and Sunggi Baik, "X-ray Study of Step Structures of MgO(100) Single Crystals," Appl. Surf. Sci., (in review).

14. Sangsub Kim, Youngmin Kang, and Sunggi Baik, "Growth of PbTiO₃ Thin Films on Vicinal MgO(100) Substrate," unpublished work.

DEPOSITION AND DIELECTRIC PROPERTY OF ION-BEAM ASSISTED BISMUTH TITANATE FILM

M. Azimi and P.K. Ghosh

Department of Electrical and Computer Engineering
Syracuse University,
Syracuse, NY 13244

ABSTRACT

Thin films of bismuth titanate ($\text{Bi}_4\text{Ti}_3\text{O}_{12}$) have been prepared on different substrates by ion-beam sputtering technique. These films were deposited using a Bi(bismuth)-rich $\text{Bi}_4\text{Ti}_3\text{O}_{12}$ ceramic target. Films were deposited with substrate temperatures ranging from 320°C to 550°C . We observed that the dielectric behavior of the deposited films strongly depends on the deposition parameters (such as the substrate temperature, sputter gas mixture, etc.). Results, also, indicate that films deposited at substrate temperature of about 450°C have dielectric property comparable to that of single crystal bismuth titanate.

INTRODUCTION

The interest in bismuth titanate thin films are directed towards exploiting several phenomena such as dielectric properties, polarization hysteresis and electro-optical properties of this material [1]. $\text{Bi}_4\text{Ti}_3\text{O}_{12}$ is a member of a large family of bismuth oxide layer structure ferroelectrics which exhibits switchable spontaneous polarization. Its electrical and electro-optical properties have been used for several applications [2, 3].

Various preparation techniques [4-9], including rf sputtering, have been used for the $\text{Bi}_4\text{Ti}_3\text{O}_{12}$ thin film preparation. In general it has been shown that $\text{Bi}_4\text{Ti}_3\text{O}_{12}$ target with excess Bi, over a temperature range of 400 - 700°C , can generate stoichiometric thin films. High deposition temperature or high post annealing temperature has been one of the major barriers for successful integration of these methods with integrated circuit technology. Recently laser ablation deposition technique has been employed for deposition of bismuth titanate at about

To the extent authorized under the laws of the United States of America, all copyright interests in this publication are the property of The American Ceramic Society. Any duplication, reproduction, or republication of this publication or any part thereof, without the express written consent of The American Ceramic Society or fee paid to the Copyright Clearance Center, is prohibited.

500°C, but this technique also has its drawbacks like presence of particulates and unevenness of the deposited films [10, 11].

EXPERIMENTAL

Bismuth titanate thin films were prepared by a Kaufman type ion-gun sputtering system. A schematic diagram of the sputtering system is shown in Fig. 1. In this study $\text{Bi}_4\text{Ti}_3\text{O}_{12}$ films were prepared using a 0.8 $\text{Bi}_4\text{Ti}_3\text{O}_{12}$ +0.2 $\text{Bi}_{12}\text{O}_{20}$ ceramic target with different sputtering gas mixtures. The excess Bi in target material was used to compensate for the volatile Bi during deposition. Films were deposited on various substrates at different substrate temperatures.

Samples were mounted on a substrate holder made of stainless steel and the system was pumped down to an initial background pressure of 10^{-7} torr. A pair of coil heaters was used for substrate heating. A thermocouple is mounted on the substrate holder for temperature measurement. A mixture of argon and oxygen is used as the sputtering gas. Sputter deposition was done at a chamber pressure of 10^{-4} torr.

The dielectric properties of these films have been our main focus of study. Measurements were done using a computer controlled oven in conjunction with LCR meters. In this study the dielectric measurements have been carried out in electric field less than 500 V/cm.

RESULTS AND DISCUSSION

We have investigated the effects of three deposition parameters on bismuth titanate films. These parameters are: substrate temperature, substrate type and the percentage of oxygen in the sputtering gas mixture.

Thin films of bismuth titanate were deposited at 320°C, 400°C, 450°C, 500°C, and 550°C on metallized alumina substrates, silicon wafers and ITO coated glass. Our measurements show that films deposited at temperatures between 400°C and 500°C have the highest dielectric constant and lowest loss factor at 1 kHz (fig. 2). This result is in agreement with the previous studies on bismuth titanate thin film prepared by rf sputtering technique [9]. Fig. 3 shows the variation of dielectric constant and the loss factor of bismuth titanate film on silicon substrate, as a function of temperature at different frequency. Heating and cooling cycles curves are reproducible. To observe the effect of oxygen, bismuth titanate thin films were prepared with three different percentages of oxygen in the sputtering gas mixture. Measurements show that films deposited using the gas mixture ($\text{O}_2=40\%$; $\text{Ar}=60\%$) have the higher dielectric constant and, in general, lower loss factor than films deposited using other gas mixture ($\text{O}_2=25\%$; $\text{Ar}=75\%$) (fig. 4). At first, from these results, it appears that higher oxygen content in the

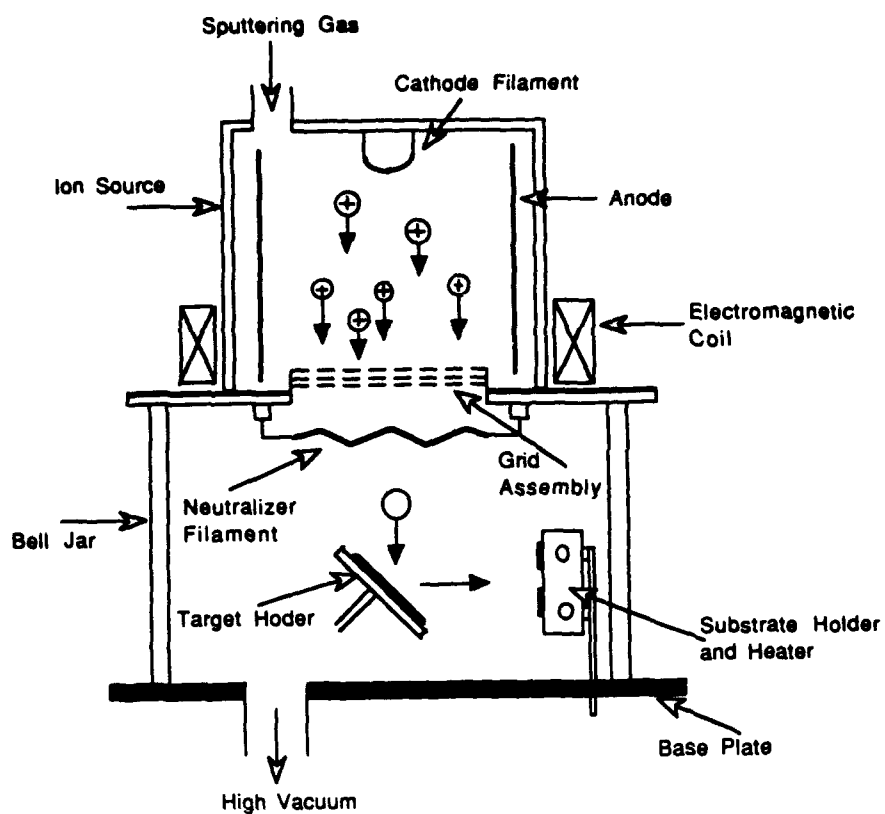
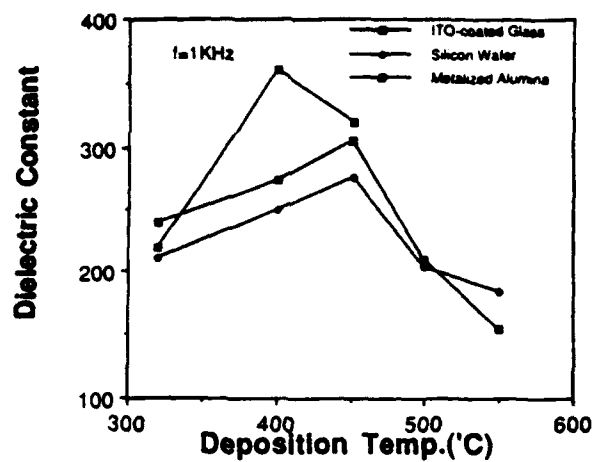
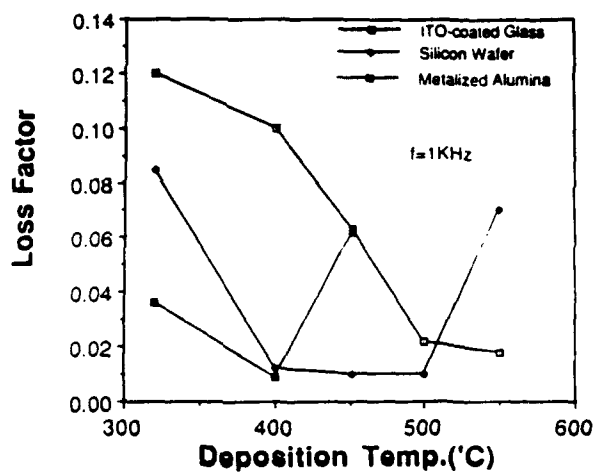


Fig. 1 Schematic diagram of the sputtering system used for $\text{Bi}_4\text{Ti}_3\text{O}_{12}$ film deposition.



(i)



(ii)

Fig. 2. Dielectric constant (i) and the loss factor (ii) of bismuth titanate thin films deposited at different temperatures on various substrates. Deposition Gas Mixture: 40% O_2 + 60% Ar

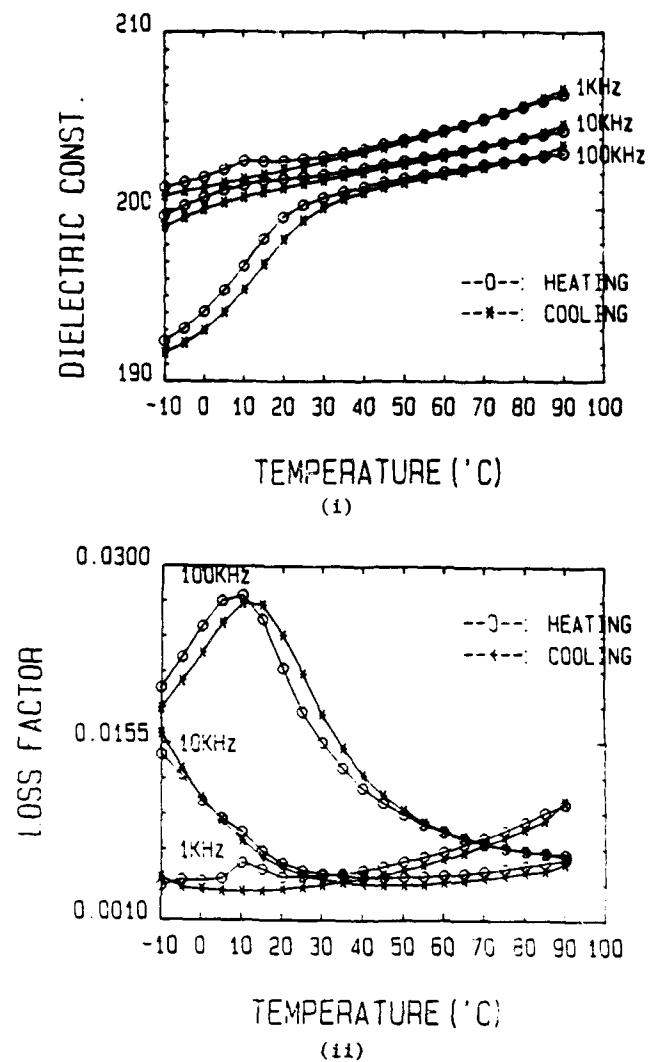


Fig. 3. Variation of the dielectric constant (i) and the loss factor (ii), of $\text{Bi}_4\text{Ti}_3\text{O}_{12}$ films on silicon, as a function of measurement temperature for both heating and cooling cycle.
 Deposition Temp.: 492°C
 Deposition Gas Mixture: 25% O_2 + 75% Ar

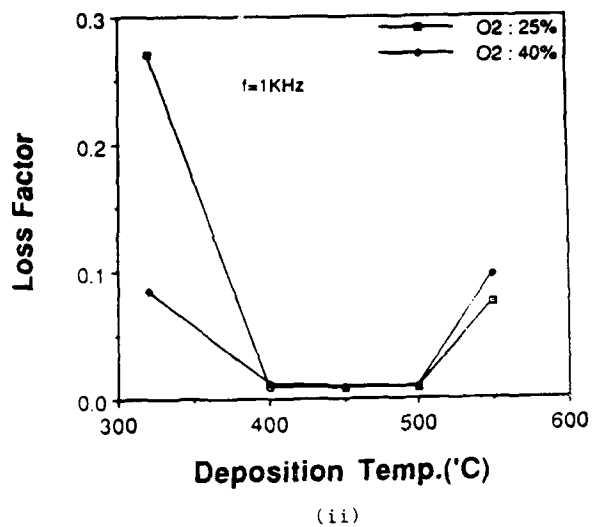
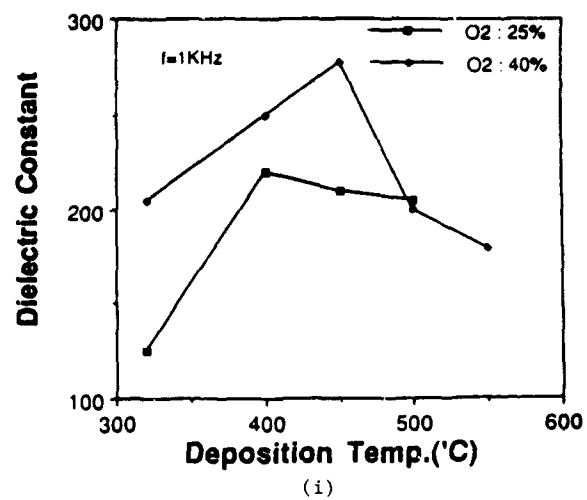


Fig. 4. Effect of sputtering gas mixture on the dielectric constant (i) and the loss factor (ii) of bismuth titanate thin films on silicon.

sputtering gas mixture results in better stoichiometric films. To examine this behavior we deposited bismuth titanate thin films using a gas mixture with higher oxygen content ($O_2=60\%$; $Ar=40\%$). Results show that films have lower dielectric constant and higher loss factor (fig. 5). Several mechanisms could be responsible for these later results. One major reason could be the oxidation of substrate material when oxygen content is high in the sputtering environment. In addition, high energy reactive oxygen atoms in the sputtering gas can change the composition of the target material during sputtering. This compositional change in the target material can result in a non-stoichiometric film. Also, oxygen atoms have much less sputtering yield than the argon atoms resulting in a non-uniform sputtering rate.

Finally, as shown in fig. 6 and 7, we observe that films deposited on ITO coated glass at temperatures above 500°C have the high dielectric constant and low loss factor compared to the films on silicon and metallized alumina. At higher temperature degradation of dielectric property of films on silicon and metallized alumina could be the result of the interaction of the substrate material with the film.

CONCLUSION

The dependence of the dielectric property of bismuth titanate thin films on deposition parameters has been examined. These films were deposited with the Ion-beam sputtering technique. The effect of various deposition parameters like the deposition temperature, gas composition, and the substrate temperature were investigated. Our results show that to achieve high dielectric constant and low loss factor, a substrate temperature of about 450° was required. Increase in oxygen content of the sputtering gas demonstrated an increase in the film quality but too much oxygen results in lower dielectric constant and higher loss factor. The effect of the substrate material was also quite noticeable. At higher deposition temperature films on ITO coated glass show better dielectric properties.

REFERENCES

1. S.E. Cummins and L.E. Cross, "Electrical and optical properties of ferroelectric $\text{Bi}_4\text{Ti}_3\text{O}_{12}$ single crystals", *J. Appl. Phys.*, Vol. 39, No. 5, pp. 2268-2274, 1968.
2. S.E. Cummins and T.E. Luke, "A new method of optically reading domains in bismuth titanate for display and memory applications", *IEEE Tran. on Elect. Devices*, Vol. ED-18, No. 9, Sept. 1971.

3. Shu-Yau Wu, "A new ferroelectric memory device, metal-ferroelectric-semiconductor transistor", IEEE Trans. on Elect. Dev., Vol. ED-21, No. 8, Aug. 1974.
4. W.J. Takei, N.P. Formigoni and M.H. Francombe, "Preparation and epitaxy of sputtered films of ferroelectric $\text{Bi}_4\text{Ti}_3\text{O}_{12}$ ", Vacuum Science & Technology, Vol. 7, No. 3, pp. 442-448, 1971.
5. S.Y. Wu., W.J. Takei, and M.H. Francombe, "Domain structures and polarization reversal in films of ferroelectric bismuth titanate", IEEE Trans. on Sonic & Ultrasonics, SU-19-S.E. Cummins, pp. 217-227, 1972.
6. W.J. Takei, S.Y. Wu and M.H. Francombe, "Optimization of epitaxial quality in sputtered films of ferroelectric bismuth titanate", J. of Crystal Growth, 28, pp. 188-197, 1975.
7. Shu-Yau Wu, "Polarization reversal and films structure in ferroelectric $\text{Bi}_4\text{Ti}_3\text{O}_{12}$ films deposited on silicon", J. of Appl. Phys., Vol. 50, No. 6, June 1979.
8. W.J. Takei, N.P. Formigoni and M.H. Francombe, "Preparation and properties of epitaxial films of ferroelectric $\text{Bi}_4\text{Ti}_3\text{O}_{12}$ ", Appl. Phys. Lett., Vol. 15, No. 8, pp. 256-258, Oct. 1969.
9. P.K. Ghosh, A.S. Bhalla and L.E. Cross, "Dielectric properties of rf sputtered bismuth titanate thin films", Sixth IEEE International Symposium on Applications of Ferroelectrics, June 1986.
10. H. Buhay, S. Sinharoy, W.H. Kasner, M.H. Francombe, D.R. Lampe, and E. Stepke, "Pulsed laser deposition and ferroelectric characterization of bismuth titanate films", Appl. Phys. Lett. 58(14), 8 April 1991.
11. R. Ramesh, K. Luther, B. Wilkens, D.L. Hart, E. Wang, J.M. Tarascon, A.I. Nam, X.D. Wu, and T. Venkatesan, "Epitaxial growth of ferroelectric bismuth titanate thin films by pulsed laser deposition", Appl. Phys. Lett. 57(15), 8 October 1990.

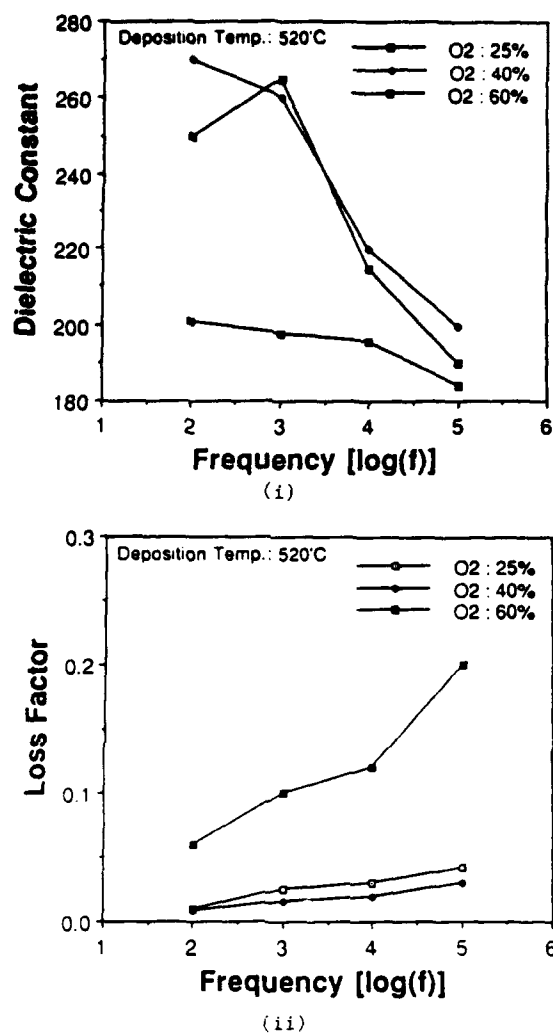
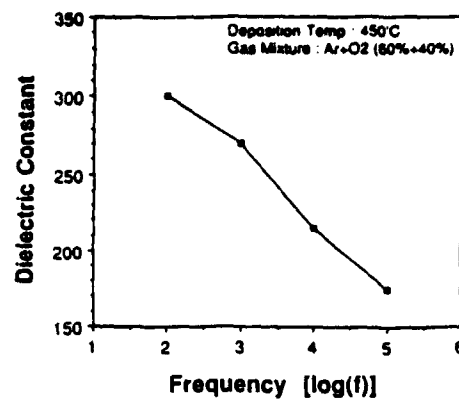
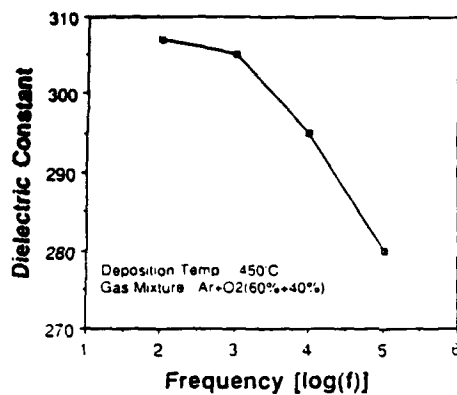


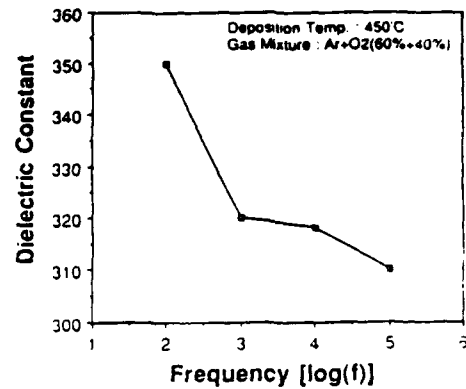
Fig. 5. Dielectric constant (i) and the loss factor (ii), of $\text{Bi}_4\text{Ti}_3\text{O}_{12}$ thin films on silicon, as a function of oxygen percentage in the sputtering gas.



(i)

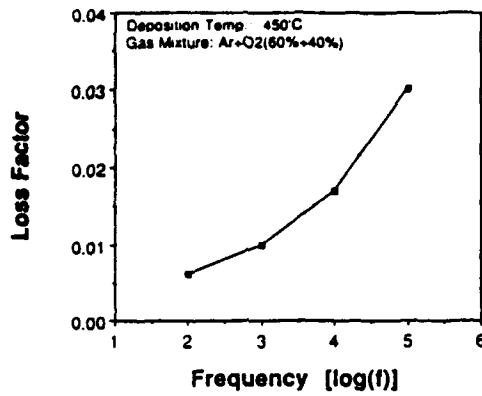


(ii)

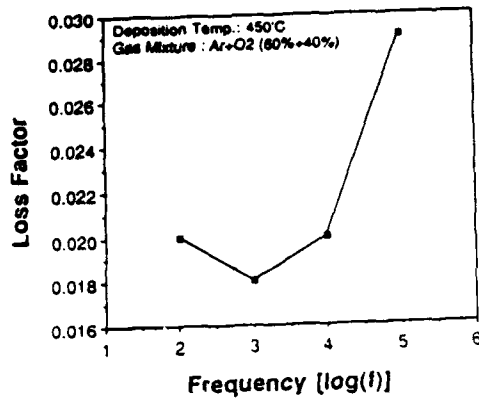


(iii)

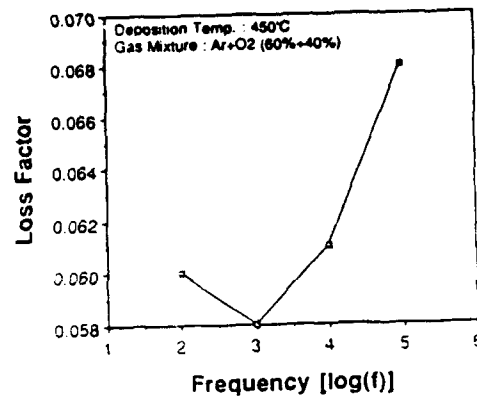
Fig. 6. Effect of the substrate type on the dielectric constant value of thin film bismuth titanate, (i) Silicon Substrate; (ii) ITO-Coated Glass Substrate and (iii) Metalized Alumina Substrate.



(i)



(ii)



(iii)

Fig. 7. Effect of the substrate type on the loss factor of Bi₄Ti₃O₁₂ thin film, (i) Silicon Substrate; (ii) ITO-Coated Glass Substrate, and (iii) Metalized Alumina Substrate.

DIELECTRIC PROPERTIES of (Ba,Sr)TiO₃ FILMS by RF SPUTTERING

N. Mikami, T. Horikawa, T. Makita, K. Sato, T. Kuroiwa, T. Honda, and H. Watarai
Mitsubishi Electric Corp. Semiconductor Research Lab., Materials & Devices Lab.
1-1 Tsukaguchi-Honmachi 8-chome Amagasaki Hyogo 661, Japan

ABSTRACT

The dielectric properties of (Ba,Sr)TiO₃(BST) thin films prepared by RF sputtering method, were investigated. Polycrystalline film structure and grain size were estimated by transmission electron microscopy (TEM) and Xray diffraction. The dielectric constant of BST films depends on their grain size rather than thickness of the film. A broad maximum in the temperature dependence of the dielectric constant of the films was observed, and Curie temperature was not clear. No hysteresis was observed in a D-E curve of the film at 77K.

INTRODUCTION

Recently, ferroelectric thin films have attracted much attention as a key material for dynamic random access memories (DRAMs), in addition to nonvolatile memories or the other applications. (Ba,Sr)TiO₃(BST) films were investigated as a first candidate for DRAM capacitor,¹⁾²⁾³⁾ because the films have high dielectric constant and no fatigue by ferroelectric domain switching at device operating temperatures, in the case of selected Ba/Sr compositions.

Miyasaka et. al.¹⁾ reported that dielectric constant of BST films is several hundreds, which is very small in comparison with that of bulk ceramics, and it decreases as the thickness of the films decreases. The decrease of dielectric constant was also observed in ferroelectric thin films such as PZT⁴⁾ and PbTiO₃⁵⁾ and in paraelectric thin films such as SrTiO₃.⁶⁾⁷⁾ On the other hand, decrease of dielectric constant with decreasing grain size was reported in BST films prepared by sol-gel method⁸⁾ and by RF sputtering.²⁾

These phenomena in thin films are often discussed in relation to size effects in ferroelectrics. Decrease of dielectric constant with grain size was found in BaTiO₃ fine particle⁹⁾¹⁰⁾ and ceramics.¹¹⁾ The Curie temperature of fine grained BaTiO₃ ceramics is shifted at several degrees from that of large grained BaTiO₃ ceramics. Ishikawa¹²⁾ reported that the Curie temperature obtained by Raman shift of soft mode of PbTiO₃ powder, is shifted to a lower temperature with decreasing powder size. Uchino¹³⁾ reported that the Cubic-tetragonal transition temperature of fine particle of BaTiO₃ is also shifted to a lower temperature with decreasing size.

Dielectric properties and ferroelectricity in thin films are not well known yet. In a

To the extent authorized under the laws of the United States of America, all copyright interests in this publication are the property of The American Ceramic Society. Any duplication, reproduction, or republication of this publication or any part thereof, without the express written consent of The American Ceramic Society or fee paid to the Copyright Clearance Center, is prohibited.

previous paper,²⁾ we reported that dielectric constant and Curie temperature supposed from temperature dependence of dielectric constant, are affected by grain size on $(\text{Ba}_{0.65}\text{Sr}_{0.35})\text{TiO}_3$ films prepared by sputtering method. In the present work, dielectric properties of $(\text{Ba}_{0.75}\text{Sr}_{0.25})\text{TiO}_3$ thin films are studied, and ferroelectricity in BST films is discussed.

EXPERIMENTAL

BST films were deposited on Pt/SiO₂/Si or Pt/Ti/SiO₂/Si substrate by RF sputtering. Pt is used as an electrode, and Ti layer is used as adhesion layer for Pt on SiO₂. A Pt top electrode with a diameter of 1mm was deposited on BST films for electrical measurement as shown in Fig.1. Sputtering conditions are shown in Table 1. The sputtering target for BST films had a composition of $(\text{Ba}_{0.75}\text{Sr}_{0.25})\text{TiO}_3$, and was purchased from Mitsubishi Materials Corp. The film structure was investigated by transmission electron microscopy and X-ray diffraction. The grain size was calculated from FWHM of the Perovskite (110) X-ray diffraction peak using SrTiO₃ powder as a standard bulk material, because its profile of the peak was clear in every case. Capacitance of the sample was measured at a frequency of 1kHz with a Hewlett-Packard 4194A impedance analyzer. The hysteresis loop was tested by Sawyer-Tower circuit where the dielectric loss was canceled by series resistors.

Table 1. Sputtering conditions of the BST films

Substrate temperature	480-750 °C
RF power	100 W
Gas pressure	1.0 Pa
Ar flow rate	9 sccm
O ₂ flow rate	1 sccm
Target-substrate distance	70 mm
Deposition rate	2.0nm/min

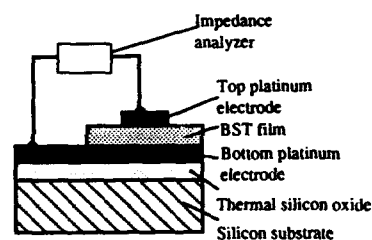


Fig.1 Sample configuration for electrical measurement

RESULTS AND DISCUSSION

Fig.2 shows a typical X-ray diffraction(XRD) pattern for a sample wafer. The wafer has a BST/Pt/SiO₂/Si configuration, and all peaks are ascribed to these layers. The Pt film is considered to be perfectly oriented in the (111) direction. Peak intensities of the BST film are changed with film deposition temperature. Fig.3 shows the relationship between diffraction peak intensities of the 90nm thick film and deposition temperature. Peak intensities of the film are weak in case of low deposition temperature, and strong in case of high deposition temperature, above 650 °C. Grains oriented in the (111) directions are predominant in the BST film deposited at 750 °C. Fig.4 shows a dark field TEM image of the film deposited at 750 °C. Bright regions indicate grains oriented (111) direction parallel to the film surface normal. The film contains columnar grains. Fig.5 shows a dark field TEM image of the film deposited at 600 °C. This film

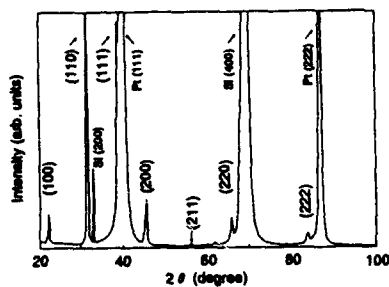


Fig.2 Typical XRD pattern of BST film.

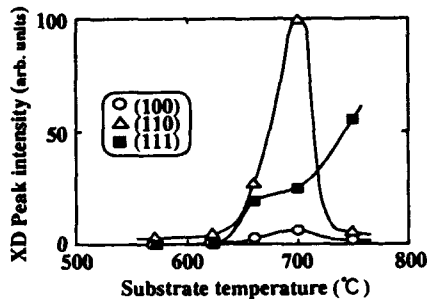


Fig.3 XRD peak intensities of BST films.

consists of small granular grains. Amorphous regions were not found in the film. These figures show how the grain structure of the BST film is changed with deposition temperature for RF sputtering. The increase of XRD peak intensities in Fig.3 is caused by the change of the grain structure. The gradual increase of the intensities suggests that the films deposited at 660 °C has a mixed structure with columnar and granular grains.



Fig.3 Dark field TEM image of BST film deposited at 750°C.

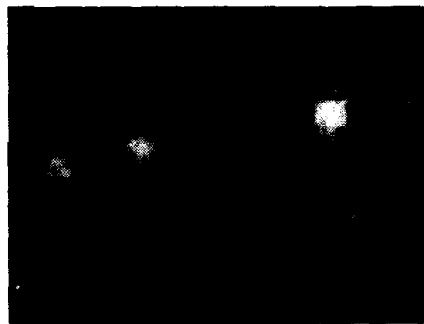


Fig.5 Dark field TEM image of BST film deposited at 600°C.

Fig.6 shows the dielectric constant of the BST films with 90nm thickness. The dielectric constant of the film is changed with film deposition temperature. the dielectric constant of granular grained films deposited below 620°C is almost the same. The dielectric constant of columnar grained film increases as the deposition temperature increase. The dielectric constant depends on the grain structure, and this can not be explained by the thickness dependence of dielectric constant. Fig.7 shows

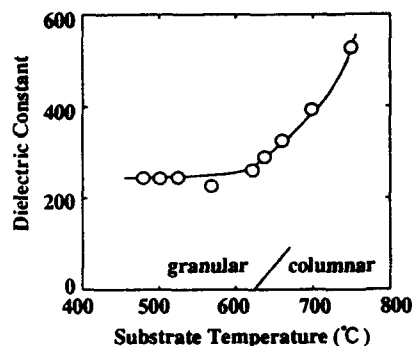


Fig.6 Dielectric constant of BST films with various deposition temperature.

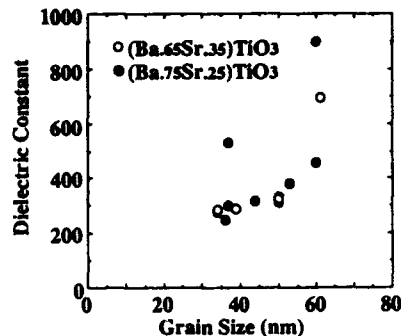


Fig.7 Dielectric constant vs. grain size calculated by Scherrer's formula

the dielectric constant dependence on grain size estimated by Scherrer's formula:

$$D = 0.9\lambda / (B \cos\theta) \quad (1),$$

where λ is the X-ray wavelength, B is the FWHM of the X-ray diffraction peak, and θ is the diffraction angle. It is considered from X-ray diffraction geometry that the grain size estimated by the formula coincides with the grain size in the direction parallel to the film thickness. Correlation between dielectric constant and grain size is good in films with comparatively small dielectric constants (below 400). On the other hand, correlation is not good in the films with dielectric constant of more than 500. The films with a high dielectric constant have a columnar structure. Grain size estimated by the formula is crystallite size in the grain, if single-crystal grain has a little tilt or other defects in it. The presence of such defects is indicated by the partial (111) electron-beam diffraction of one of the columnar grains in the dark field TEM image of Fig.4. Grain size for the granular structures coincided with that estimated by the formula in several TEM evaluations of the films.

In a columnar structured film, thickness is equal to the grain size in the direction parallel to the thickness, and the decrease of dielectric constant with thickness can be observed. The decrease with thickness does not hold in a granular structured film prepared by sol-gel method or low temperature deposition in RF sputtering. We have already reported²⁾ that column width, that is the grain size in the direction perpendicular to the thickness, is almost same in the films with different thickness and dielectric constant. Thickness dependence was also observed in epitaxially grown thin films. Therefore, it is considered that dielectric constant directly depends on grain size in the direction thickness.

Fig.8 shows the temperature dependence of dielectric constant of the BST films. The grain size of the films is shown in the figure. The dielectric constant of BST ceramics varies 1000 to 10000 and has sharp maximum in the temperature range in Fig.8. The Curie temperature of each BST composition is shown in the figure. A broad

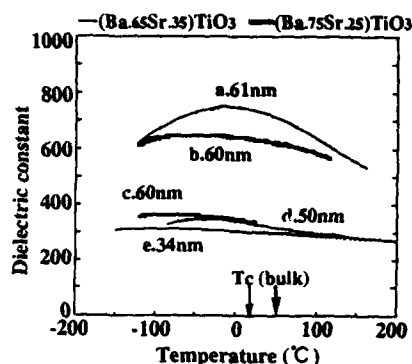


Fig.8 Temperature dependence of dielectric constant of the films. The substrate temperatures are a)750°C, b)750°C, c)750°C, d)700°C, and e)600°C.

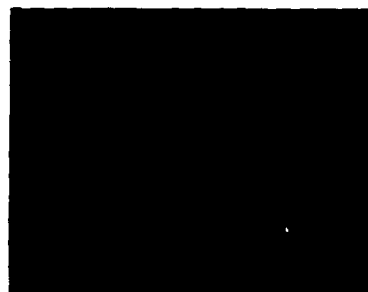


Fig.9 D-E curve of a 320nm thick BST film at 77K. Vertical axis: $3.5 \mu\text{C}/\text{cm}^2/\text{div}$. Horizontal axis: $43 \text{ kV}/\text{cm}/\text{div}$.

maximum and small temperature variation of the dielectric constant of the films in Fig.8 show they are different from bulk ceramics. Fig.9 shows D-E curve for a 320nm thick film with columnar grains at 77K. Hysteresis was not observed in the D-E curves for any films, in the temperature range between room temperature and 77K. That is over 200K lower than Curie temperature of ceramics. In previous work, we supposed that the temperature (T_{max}) where dielectric constant is maximum, is the Curie temperature, and discussed T_{max} dependence on grain size. From the hysteresis measurement, T_{max} is not the Curie temperature. Relaxor ferroelectrics have similar behavior such as a broad maximum of the dielectric constant and a slim hysteresis loop just below the Curie temperature, although Relaxor ferroelectrics have bona-fide dielectric hysteresis at the lower temperature. The present phenomenon observed in our BST films is different from the relaxor ferroelectrics, and ferroelectricity of the BST films seems to vanish.

A thin layer with low dielectric constant, or a depression layer below an electrode, was proposed to explain the origin of the thickness dependence in ferroelectric thin films. Shifts of T_{max} , suppression in temperature variation of the dielectric constant, and the absence of a hysteresis loop, can not be explained by such layer. Ferroelectricity is a cooperative phenomenon and it is thought that a certain size of cooperative region is necessary for the appearance of ferroelectricity. It is interesting that PZT films have hysteresis, and BST or BaTiO_3 does not for almost the same size films. It may suggest that size of cooperative region is different in both compounds.

CONCLUSIONS

The dielectric properties of BST films prepared by RF sputtering method were investigated. The film structure changed from a granular to a columnar as the

deposition temperature increased. The dielectric constant of the BST films depends on its grain size rather than thickness of the film. A broad maximum in the temperature dependence of the dielectric constant of the films was observed. No hysteresis was observed in the D-E curve of the film at 77K, over 200K under Curie temperature. Ferroelectricity of the film seems to vanish. High dielectric constant with no polarization in BST films is a suitable property for DRAM capacitor material.

REFERENCES

- 1)Y. Miyasaka and S.Matsubara:Proc. 7th Int. Symp. Applications of ferroelectrics, 1990(IEEE New York,1991)p.121
- 2)T. Horikawa, N. Mikami, T. Makita, J. Tanimura, M. kataoka, K. Sato, and M. Nunosita:Jpn. J. Appl. Phys. **32** No.9B (1993)p4126
- 3)T. Eimori, Y. ohno, H. kimura, J. Matufusa, S. Kishimura, A. yoshida, H. Sumitani, T. Maruyama, Y. Hayashide, K. Moriizumi, T. Katayama, M. Asakura, T. Horikawa, T. Shibano, H. Itoh, K. Sato, K. Namba, T. Nishimura, S Satoh, and H. Miyoshi:Technical Digest of IEDM (1993)631
- 4)H. Kidoh, T. Ogawa, H. Yashima:Jpn. J. Appl. Phys. **31**[9B](1992)2965
- 5)H. Funakubo, T. Hioki, M. Otsu, K. Shinozaki, and N. Mizutani:Jpn. J. Appl. Phys. **32** [9B](1993)4175
- 6)S. Yamamichi, T.Sakuma, K.Takemura, and Y. Miyasaka:Jpn. J. Appl. Phys. **30** [9B] (1991)2193
- 7)K. Abe and S. Komatsu:Jpn. J. Appl. Phys. **31** [9B](1992)2985
- 8)H. Kawano, K. Morii and Y. Nakayama:J. Appl. Phys. **73** [10] (1993)5141
- 9)C.Jaccard, W. Kanzig, and M.Peter:Helv. Phys. Acta, **26** (1954)521
- 10)M.Anliker, H.R.Brugger, and W.Kanzig:Helv. Phys. Acta, **27** (1954)99
- 11)G.Arlt, D.hennings, and D.de With:J. Appl. Phys. **58** [4](1985)1619
- 12)K.Ishikawa:Phys. Rev. B **37** [10](1988)5852
- 13)K.Uchino, E.Sadanaga, and T.Hirose:J. Am. Ceram. Soc. **72** [8] (1989)1553

PREPARATION OF A METALORGANIC DEPOSITION PRECURSOR FOR BARIUM TITANATE

Allen W. Apblett*, Galina D. Georgieva, and Isobel Raygoza-Maceda
Tulane University, Department of Chemistry, 6823 St. Charles Avenue,
New Orleans, LA 70118

ABSTRACT

A new, facile preparative route for $\text{BaTiO}(\text{Ox})_2$ has been developed (Ox=oxalate). This involves passing a solution of $\text{K}_2\text{TiO}(\text{Ox})_2$ through an ion-exchange resin to convert it to the proteo-derivative, $\text{H}_2\text{TiO}(\text{Ox})_2$. Treatment of the latter with BaCl_2 results in precipitation of $\text{BaTiO}(\text{Ox})_2$ with a ratio of barium:titanium of 1:1.009. Finally, reaction of $\text{BaTiO}(\text{Ox})_2$ with refluxing methoxyacetic acid produces an alcohol and chlorocarbon soluble ceramic precursor that may be used to prepare thin films of barium titanate by metalorganic deposition

INTRODUCTION

Metalorganic deposition (MOD) [1] is a non-vacuum, solution-based method of depositing thin films. A suitable metalorganic precursor dissolved in solution is coated on a substrate by spin-coating, screen printing, or spray- or dip-coating. The soft metalorganic film is then pyrolyzed in air, oxygen, nitrogen or other suitable atmosphere to convert the precursors to their constituent elements, oxides, or other compounds. Shrinkage generally occurs only in the vertical dimension so conformal coverage of a substrate may be realized. Metal carboxylates are often used as precursors for ceramic oxides since they tend to be air-stable, soluble in organic solvents, and decompose readily to the metal oxides. MOD processes for the generation of many oxide-based materials have already been developed: e.g. BaTiO_3 [2], ITO [3], SnO_x [4], $\text{YBa}_2\text{Cu}_3\text{O}_7$ [5] and ZrO_2 [6]. Methodology has also been developed to achieve epitaxial growth of dense, polycrystalline, zirconia thin films [7]. The usual carboxylate residue used is a long

To the extent authorized under the laws of the United States of America, all copyright interests in this publication are the property of The American Ceramic Society. Any duplication, reproduction, or republication of this publication or any part thereof, without the express written consent of The American Ceramic Society or fee paid to the Copyright Clearance Center, is prohibited.

slightly-branched alkyl chain (e.g. 2-ethylhexanoate or neodecanoate) that confers the necessary solubility in organic solvents. The synthesis of thin-films by liquid phase processing is definitely a convenient method for their preparation [8]. These methods have the possible advantages of : low-temperature processing temperatures as compared to powder processing techniques; homogeneous ceramic products; the ability to prepare composite materials and/or complex shapes; and control over the stoichiometry of the elements.

Barium titanate has been synthesized previously using a variety of metalorganic precursors [9]. These include routes based solely on metal alkoxides [9, 10] or metal carboxylates (e.g. the Pechini (or citrate) process [11]) and mixed carboxylate/alkoxide precursors [9, 12]. An example of a very successful precursor for barium titanate that is used widely by industry is $\text{BaTiO}(\text{Ox})_2$ (Ox=oxalate, $\text{C}_2\text{O}_4^{2-}$) [13]. If prepared carefully, this material comes very close to the stoichiometry of one barium to one titanium required for BaTiO_3 . Unfortunately, the synthesis of pure $\text{BaTiO}(\text{Ox})_2$ depends critically on the reaction conditions and it is quite insoluble rendering it useless for preparing BaTiO_3 thin-films. Reported herein is an improved synthesis of $\text{BaTiO}(\text{Ox})_2$ and its conversion to $\text{BaTiO}(\text{O}_2\text{CR})_4$ (HO_2R)₂, (R= CH_2OMe) a MOD precursor that is a viscous liquid that has high solubility in water and a variety of organic solvents such as methanol, ethanol, methylene chloride, and chloroform. It is also slightly soluble in acetone and tetrahydrofuran.

EXPERIMENTAL

All metal salts and carboxylic acids were commercial products and were used as supplied. CH_2Cl_2 was distilled from P_2O_5 while water was deionized and distilled before use. The ion exchange resin used was amberlite CG-120 and it was thoroughly washed with hot water, 10% HCl, and distilled water before use. Thermogravimetric analyses were obtained on a Seiko SSC 5200 TGA/DTA instrument under an air atmosphere. Barium and titanium content of the precursors were determined by X-ray fluorescence analysis on a Siemens SRS 200 XRF spectrometer. Morphology and composition of thin-films were determined on an Amray 1700 scanning electron microscope equipped with a Tracor Northern 5500 energy dispersive spectrometer. Carbon and hydrogen analyses were performed by National Chemical Consulting, Inc.

Preparation of $\text{BaTiO}(\text{Ox})_2(\text{H}_2\text{O})_4$

A solution of $\text{K}_2\text{TiO}(\text{Ox})_2(\text{H}_2\text{O})_2$ (3.54g, 10 mmol) in 150 ml of distilled water was passed through a proton-charged cation exchange column (20 g of resin). The effluent from the column was found to be very acidic (pH=2) and it was drained directly into a solution of BaCl_2 (2.44g, 10 mmol) in 100 ml of water. Immediate reaction occurred to yield a voluminous white precipitate. This was isolated by filtration, washed with water (50 ml) and dried in the air. The yield was 3.63g (81%). XRF analysis indicated a ratio of barium to titanium of 1:1.009.

Preparation of $\text{BaTiO}(\text{O}_2\text{CCH}_2\text{OMe})_4(\text{HO}_2\text{CH}_2\text{OMe})_2$

A mixture of $\text{BaTiO}(\text{Ox})_2(\text{H}_2\text{O})_4$ (1.26g, 2.8 mmol) and 20 ml of methoxyacetic acid were heated at reflux (ca. 202°C). The $\text{BaTiO}(\text{Ox})_2(\text{H}_2\text{O})_4$ dissolved gradually to give a pale yellow solution over a period of twenty hours. Removal of the excess acid in vacuo yielded a slightly-sticky pale yellow semi-solid (2.05 g, 99 %). Upon standing in humid air for several weeks, the compound forms a monohydrate, $\text{BaTiO}(\text{O}_2\text{CCH}_2\text{OMe})_4(\text{HO}_2\text{CH}_2\text{OMe})_2(\text{H}_2\text{O})$. Elemental analysis: Calculated; C 28.61%, H 4.54 Found; C 28.42%, H 4.57%.

RESULTS AND DISCUSSION

The synthesis of $\text{BaTiO}(\text{Ox})_2$ by use of an ion exchange column is a very rapid, facile, and highly-reproducible process. While one should, in principle, be able to precipitate $\text{BaTiO}(\text{Ox})_2$ by the direct reaction of solutions of $\text{K}_2\text{TiO}(\text{Ox})_2$ and barium salts, we have found in practice that the precipitate thus obtained is heavily contaminated with potassium and the barium content is low. By replacing the potassium cations with protons using a cation exchange column, this complication is removed and nearly stoichiometric $\text{BaTiO}(\text{Ox})_2(\text{H}_2\text{O})_4$ may be obtained (the Ba:Ti ratio is reproducibly 1:1.009).

While previous work on MOD has mainly concentrated on the use of long alkyl chains to solubilize the metal complexes [1], this practice is detrimental to the overall ceramic yield. This in turn leads to much larger shrinkage upon pyrolysis. The strategy adopted here is to use a methoxy group on the carboxylic residue to provide the necessary solubility characteristics. This may be due in part to favorable interactions of the methoxy group with solvent molecules and to the ability of the oxygen atom to chelate to the metal species. The substitution of methoxyacetic acid residues for oxalate is very straight-

forward since the latter is thermally-unstable above 180°C. Thus $\text{BaTiO}(\text{O}_2\text{CCH}_2\text{OMe})_4 (\text{HO}_2\text{CH}_2\text{OMe})_2$ is obtained by heating $\text{BaTiO}(\text{Ox})_2(\text{H}_2\text{O})$ in an excess of methoxyacetic acid. This material is very soluble in organic solvents, especially chlorocarbons. Pyrolysis at 700°C produces crystalline BaTiO_3 in 31.6 weight-percent ceramic yield.

The extra equivalents of coordinated acid play an important role in stabilizing the compound and attempts to remove them result in decomposition to an insoluble material. Clear evidence for the coordinated acid is provided by both infrared and proton NMR spectroscopy. The former shows a very broad absorption at 3200 cm^{-1} due to the hydroxyl stretch of the carboxylic acid. The ^1H NMR spectrum shows a broad resonance at 7.66 ppm which may also be assigned to this moiety. As well, three equal intensity methylene resonances are observed at 4.6, 4.1, and 4.0 ppm. The latter signal is very close to that of the free acid but its assignment to the coordinated acid is tenuous at best. The other two resonances could be assigned to carboxylate anions associated with either barium or titanium but, again, there is no convincing evidence this is true. It should also be noted that the three methoxy resonances are not resolved ($\delta=3.4\text{ ppm}$).

Prolonged exposure of $\text{BaTiO}(\text{O}_2\text{CCH}_2\text{OMe})_4 (\text{HO}_2\text{CH}_2\text{OMe})_2$ to humid air results in absorption of water to form a monohydrate which has much more limited solubility. Therefore, the compound should be stored in a dessicator.

Dilute solutions of the MOD precursor were prepared by dissolving 0.25g of it in 10 ml of methylene chloride. Glass slides and n-type silicon wafers were dip-coated in this solution (alternatively, films of the precursor could be spin-coated from methanol solutions) and then heated to 700°C in a muffle furnace using a ramp-rate of 5°C per minute. In this manner, coherent thin films of BaTiO_3 were obtained that exhibited the typical rainbow pattern of interference fringes. Scanning electron microscopy showed the films to be featureless and smooth.

In conclusion, the process outlined provides a convenient route for the preparation of barium titanate thin-films. We are currently applying this method to the preparation of other titanate materials.

REFERENCES

1. J. V. Mantese, A. L. Micheli, A. H. Hamdi, and R. W. Vest, M.R.S. Bull, 1989 (XIV), 1173.
2. J.J. Xu, A. S. Shaikh, and R. W Vest, IEEE Trans UFFC 36, 307 (1989).
3. J.J. Xu, A. S. Shaikh, and R. W Vest, Thin Solid Films 161, 273 (1988).
4. T. Maruyama and K. Kitamura, Jpn. J. Appl. Phys. 28, L312 (1989).
5. A. H. Hamdi, J. V. Mantese, A. L. Micheli, R.C.O. Laugal, D.F. Dungan, Z.H. Zhang, and K.R. Padmanabhan, Appl. Phys. Lett. 51, 2152 (1987).
6. V. Hebert, C. His, J. Guille, and S. Vilminot, J. Mat. Sci. 26, 5184 (1991).
7. K. T. Miller, F.F. Lange, and D.B.Marshall, J. Mat. Res. 5, 151 (1990).
8. J. Livage, in *Transformation of Organometallics into Common and Exotic Materials: Design and Activation*; NATO ASI Series E, No. 141, R.M. Laine ed. (Martinus, Nijhoff, Dordrecht, 1988).
9. P.P. Phule and S.H. Risbud, J. Mater. Sci. 25, 1169 (1990) and references therein.
10. Z. Xu, H.K. Chae, M.H. Frey, and D.A. Payne, Mat. Res. Soc. Symp. Proc. 271, 339 (1992).
11. M.P. Pechini, US Patent 3,330,697 (1967).
12. C.D. Chandler, M.J. Hampden-Smith, and C.J. Brinker, Mat. Res. Soc. Symp. Proc. 271, 89 (1992).
13. Y. Enomoto and A Yamaji, Am. Ceram. Soc. Bull. 60, 566 (1981).

SYNTHESIS AND CHARACTERIZATION OF GROUP IV METAL ADAMANTANOL ALKOXIDES AS POTENTIAL PZT PRECURSORS.

Timothy J. Boyle*, Aaron T. Pearson, and Robert W. Schwartz
Sandia National Laboratories, Advanced Materials Laboratory, 1001 University
Blvd. S.E., Albuquerque, NM 87106

ABSTRACT

The size and morphology of adamantanol (AdamO-H) make it an interesting ligand to investigate as a possible starting reagent for the generation of lead zirconate titanate (PZT) thin films. It was believed that hydrolysis, due to ambient humidity, would be reduced as the steric bulk around the metal center was increased. Group IV (Ti, Zr) metal alkoxides were reacted, in sundry stoichiometries, with adamantanol and the resulting compounds were used for film generation. Surprisingly, most of these compounds crystallized when their solutions were spin-cast deposited onto silicon substrates. The one exception was the (AdamO)Zr(OCHMe₂)₃ compound, which apparently gelled. Ellipsometric data obtained on this film showed that typical densification occurred.

INTRODUCTION

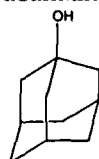
Commercially available alkoxide and acetate reagents such as Ti(OCHMe₂)₄, Zr(O(CH₂)₃Me)₄•HO(CH₂)₃Me, and Pb(O₂CMe)₂•3H₂O have been used to form complex ceramic precursors. Solution deposition of these metallo-organic carboxylates and alkoxide precursors, generally called the "sol-gel process", has been shown to be advantageous in generating high quality ferroelectric lead zirconate titanate (PZT) thin films.¹⁻³ These films are of technological interest for such diverse uses as nonvolatile memories, optical storage media, and decoupling capacitors.² However, control of the film densification and crystallization is required to prepare films with optimized dielectric, ferroelectric and electrooptic properties for these various applications. Therefore, development of an understanding of the relationships between chemical precursors, solution processing, film fabrication conditions, and film properties is essential for successful thin film device production.

One way to generate property-controlled PZT films is to utilize well characterized starting materials with the desired properties internalized. Once these novel precursors are obtained, their effects on film densification and

To the extent authorized under the laws of the United States of America, all copyright interests in this publication are the property of The American Ceramic Society. Any duplication, reproduction, or republication of this publication or any part thereof, without the express written consent of The American Ceramic Society or fee paid to the Copyright Clearance Center, is prohibited.

crystallization behavior can be studied. Subsequent modifications can then be undertaken so that property-optimized films for specific applications can be produced. Typically, metal alkyl alkoxide precursors have been used to produce PZT films, since they possess the following desirable characteristics: the organic fraction (carbon and hydrogen atoms) can be easily removed at relatively low temperatures,⁴ the compounds are stable over time (both in the solid and solution state), they are easily obtained or synthesized, and soluble in standard organic solvents.⁵ Therefore, any new compounds that are to be synthesized should possess similar characteristics to the standard starting reagents. Our approach to this problem has been to use alkyl alkoxides ligands with different sizes and shapes. It is essential to determine the structure of these new compounds both in the solid and solution state to determine the effect these changes have on the films generated.

Of the large variety of alkoxide ligands available we chose to concentrate on adamantan-1-ol [1-hydroxy adamantane or 1-hydroxy tricyclo 3,3,1,1³,1⁷.decane = AdamO-H, (*vide portus*)], for isolation of these new precursors. AdamO-H was chosen since it is a large, sterically hindering alkyl alkoxide that allows for the flexibility of judiciously adding bulk around the metal center. This ligand was used in hopes of selectively reducing hydrolysis susceptibility of these metallo-organic precursors. The methods for synthesizing these compounds and their corresponding thin film and material characteristics are reported.



= AdamO-H

EXPERIMENTAL SECTION

All compounds [(AdamO)₄M, (AdamO)₃M(OCHMe₂), (AdamO)₂M(OCHMe₂)₂, (AdamO)M(OCHMe₂)₃; M = Ti, Zr] were synthesized using standard Schlenk and glove box techniques and following the general synthetic pathway previously reported.^{6,7} All solvents were dried and freshly distilled from sodium benzophenone ketyl.⁸ Adamantan-1-ol (Aldrich^{9a}) and Zr(OCHMe₂)₄•HOCHMe₂ (Alfa^{9b}) were used as received. Ti(OCHMe₂)₄ (Aldrich^{9a}) was vacuum distilled before use.

To identify the reaction products, ¹H and ¹³C NMR spectra for each compound were obtained on a 250 MHz Bruker NMR spectrometer. The compounds were referenced against the residual impurity in C₆D₆ (CIL^{9c}). Also, TGA/DTA studies were undertaken using an STA 1500 Pl Thermal Sciences TGA/DTA (version V4.30). All samples were loaded in air and run under UHP oxygen or argon. Sample size ranged from 8 - 15 mg.

Thin films were deposited by syringe (0.15M solutions of freshly prepared starting materials dissolved in dried toluene) onto a silicon wafer (17mm X 17mm, freshly cleaned with MeOH and dried). These wafers were spun at 1500 rpm in air for 10 secs. or until gelation occurred. The changes in film thickness and refractive index at room temperature as a function of drying time were measured by ellipsometry (Gaertner L116-C). A topological surface picture (1000 X) was then obtained by optical microscopy. From the same solution, two

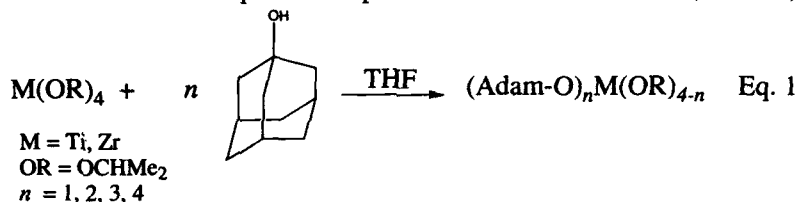
more films were generated under identical conditions. Film thickness and refractive index were obtained on these films and they were then fired under different circumjacent gases (O_2 or Ar). These films were heated at $10^\circ C$ per min to $550^\circ C$ and then fired at this temperature for 10 min. Thickness and refractive index data were once again obtained to determine densification. A photomicrograph (1000 X) was also acquired to record any visual alterations in the surface microstructure.

RESULTS AND DISCUSSION

Synthesis

We decided to initially synthesize the metallo-organic precursors independently, after which the mixed metal compounds would then be investigated. This was done since the chemical identity of the products of any binary or ternary alkoxide system consisting of Pb, Zr, and/or Ti would be more difficult to characterize than the single component systems. The initial studies therefore focused on production of titanium and zirconium adamantanoxy derivatives. Formation of the lead alkoxides was initially omitted due to two reasons: (1) lead alkoxides have a tendency to polymerize and thereby produce poorly soluble compounds;¹⁰ and (2) the carcinogenic nature of metallo-organic lead compounds predicated postponing preparation of this precursor till the other reactions had been optimized.

A series of reactions with varying stoichiometries ($n = 1, 2, 3, 4$) was undertaken (Eq. 1) to generate a systematic series of increasing sterically bulky metal alkoxides. The procedure followed for synthesis of these compounds was a slight modification of a published procedure for formation of $(AdamO)_4Ti$.^{6,7}



The metal alkoxide was dissolved in THF, adamantanol was slowly added, and if required, the mixture was heated until a clear solution resulted. The reaction mixture was allowed to cool with continued stirring for 12 hours. The solvent was then partially removed by rotary evaporation until crystalline material was observed. After warming to redissolve any precipitate, the concentrated solution was then allowed to sit at ambient temperature. When n is equal to one (Eq. 1) and $M = Ti$, the product $(AdamO)Ti(OCHMe_2)_3$ is isolated as a clear oil. When n is greater than or equal to two and $M = Ti$ or Zr , white solids or colorless crystals of the following empirical formula are isolated: $(AdamO)_{4-n}M(O-i-Pr)_n$. All the compounds isolated could be redissolved in ambient or hot toluene at 0.2M concentration or less.

Solution State

^1H and ^{13}C NMR spectra of the isolated compounds indicated that the desired alcoholysis reactions, shown in Eq. 1, had taken place cleanly. In the NMR spectra, as n is increased (Eq. 1) there is an increase in resonances associated with the adamantanoxy ligands, coupled with a decrease of *iso*-propoxide resonances. This is clearly shown in the ^{13}C NMR spectra of the titanium compounds as the reaction stoichiometry (n) was increased from 1 to 4 (see Figure 1). Based on the integration of the peaks, in the ^1H NMR spectrum, stoichiometric substitution was again proven to have occurred. When $\text{M} = \text{Ti}$ and $n = 4$, there appears to be a small impurity. This was identified by ^1H NMR spectroscopy as $(\text{AdamO})_3\text{Ti}(\text{O-}i\text{-Pr})$, the 1:3 derivative. It was also observed that with increased ligand substitution there was a significant decrease in solubility. This may be due to decreased solvation as a result of increased steric bulk around the metal center. The ^1H NMR spectra of titanium compounds are quite sharp; however, the zirconium adducts tend to exhibit broader peaks that would indicate some fluctuation in the solution state structure. Since the majority of these compounds precipitate out of solution at slightly reduced temperatures, variable temperature NMR studies, which could have helped elucidate any dynamic behavior and therefore structural information, were not undertaken. Currently, molecular weight studies are under way to determine the nuclearity of these compounds in solution.

Solid State

Pyrolysis. A series of TGA/DTA experiments on the $(\text{AdamO})_n\text{M}(\text{OCHMe}_2)_{4-n}$ ($\text{M} = \text{Ti, Zr}$) compounds were run under two ambient gases (O_2 and Ar, figure 2 shows $\text{M} = \text{Zr}$, $n = 1, 4$ spectra). It is clearly evident in the TGA that as the adamantanoxy ligation increases, the weight loss steps associated with this ligand systematically increase. This is coupled with a uniform decrease in the *iso*-propoxide steps. When correlated with the NMR data, this information further details that systematic substitution of adamantanoxides for *iso*-propoxides has occurred. The TGA/DTA spectra change dramatically based on the choice of circumjacent gas used. In the TGA, the orderly exchange of adamantanoxide for *iso*-propoxide ligands is clearly observed for both set of powders under argon; however, under oxygen, due to a large exotherm (recoalescence peak) in the DTA, a retracing is observed in the TGA spectrum.

In the DTA, under argon, all the titanium powders loose their organic fractions with small endothermic events (occurring around 425°C); however, under an atmosphere of O_2 , there appears in the DTA, an unusually large exothermic event around 300°C , associated with a relatively small weight loss in the TGA. The zirconium powders also show this behavior. Under an argon atmosphere, for all the zirconium powders, two small endothermic events occurring around 100 and 200°C in the DTA can be observed. Under O_2 , however, large exothermic events are recorded in the DTA around 300°C .

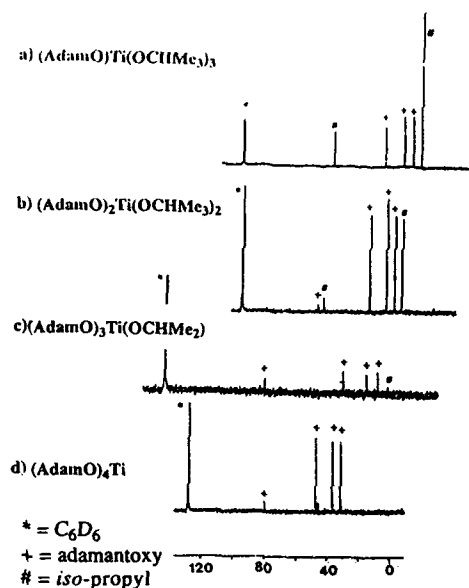
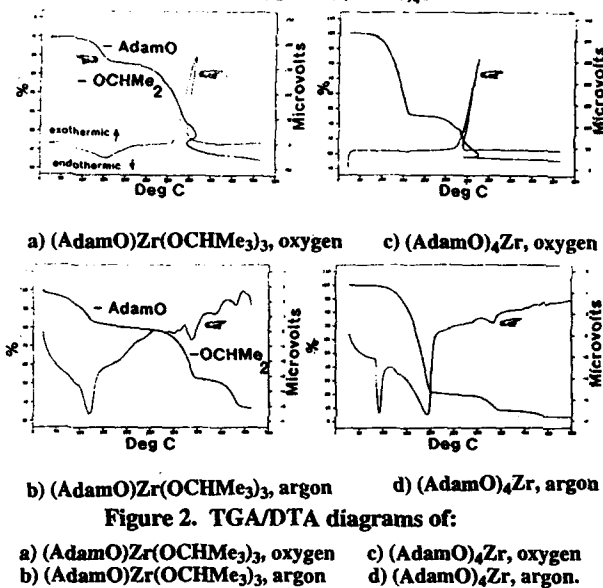


Figure 1. ^{13}C NMR Spectra (62.5 MHz, C_6D_6) of:

a) $(\text{AdamO})\text{Ti}(\text{OCHMe}_3)_3$ c) $(\text{AdamO})_3\text{Ti}(\text{OCHMe}_2)$
 b) $(\text{AdamO})_2\text{Ti}(\text{OCHMe}_3)_2$ d) $(\text{AdamO})_4\text{Ti}$



Structure. X-ray crystallographic studies of the solid state structures of selected $(\text{AdamO})_n\text{M}(\text{OR})_{4-n}$ ($\text{M} = \text{Ti}, \text{Zr}$; $\text{R} = \text{CHMe}_2$) compounds are under investigation. Drawings in Figure 3 show the basic substitution processes undergone in Eq. 1 to produce the theoretical $(\text{AdamO})_n\text{M}(\text{OR})_{4-n}$ products.

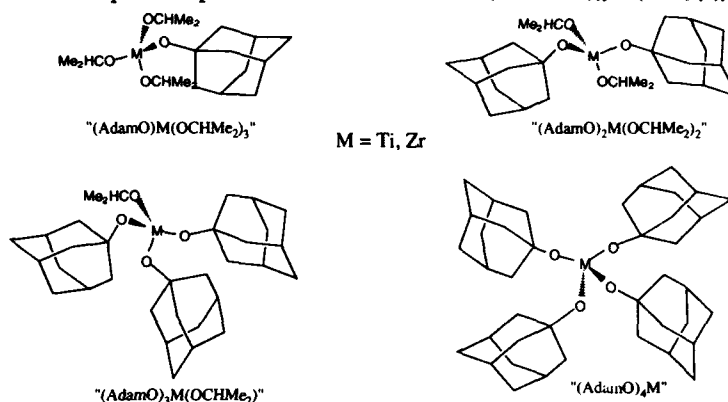
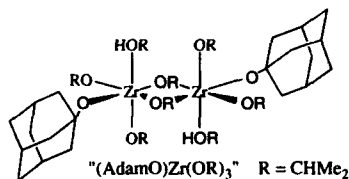


Figure 3. Substitution pattern of adamantanoxy for *iso*-propoxide ligands.

There are only two reports of transition metal adamantanoxy structures in the literature, $(\text{AdamO})_4\text{Mo}(\text{NHMe}_2)_6$ and $[(\text{AdamO})\text{Zn}(\text{CH}_2\text{SiMe}_3)]_4$ ¹¹. At this time, we assume the higher substituted titanium and zirconium compounds ($n = 3$ or 4) are mononuclear as reported for the molybdenum complex. This assumption is based on Wilkinson's adamantanoxy work,⁶ literature reports on monomeric titanium compounds which possess large aryl alkoxide coligands,¹² and simple molecular models that indicate a large steric interaction between adamantanoxy ligands occurs if the nuclearity is greater than one.

The lower substituted titanium compounds are probably oligomeric based on previous structural information found in the literature for titanium alkyl alkoxides.¹³ Furthermore, titanium has a tendency to coordinately saturate its binding sphere,¹³⁻¹⁵ unless a large number of sterically hindering ligands are used.¹² Therefore, the probability is that the central core consists of inter-linked titanium *iso*-propoxide moiety that is protected by an outer sphere of adamantanoxy ligands. This type of arrangement would not allow for attack by ambient humidity.

The reason the lower substituted zirconium complexes gel during deposition may also be deduced from the structure of zirconium *iso*-propoxide. This compound is known to be the dimeric compound $[\text{Zr}(\text{OCHMe}_2)_4 \cdot \text{HOCHMe}_2]_2$.¹⁶



In Eq. 1 with $n = 1$, a simple substitution could occur to form the empirical compound $(\text{AdamO})\text{Zr}(\text{OCHMe}_2)_3$ without disruption of the dimer (*vide portus*). Therefore, this

compound would retain the easily exchanged free alcohols associated with the starting material and therefore would still be susceptible to hydrolysis.

Film Data

The films deposited from these metal alkoxides do not produce either physical or chemical gels during spinning but tend to form crystalline clusters. This was observed by both optical microscopy and the varied ellipsometry data obtained. For a solution droplet deposited onto a glass substrate, actual crystal growth can be observed as the solvent evaporates. The non-uniformity of these films, caused by the isolated crystalline environments, does not make these films amenable to detailed ellipsometric investigations of densification. We believe that the introduction of the adamantanoxy ligand has effectively suppressed hydrolysis. The lack of any gelation (physical or chemical) is quite surprising and may be explained by the structural aspects of these precursors (*vide supra*). Furthermore, the fired films showed little change in the topological features, except for the appearance of macroscopic porosity in the crystalline regions of the films. Figure 4 is the spin cast deposited film of 0.15M (AdamO)Ti(OCHMe₂)₃ in toluene that was then fired to 550°C under an atmosphere of argon. This figure illustrates the crystalline characteristics associated with these types of compounds. The dark clusters are crystalline material; whereas, the light colored background is the silicon substrate.

The mono-adamantanoxo substituted zirconium compound, (AdamO)Zr(OCHMe₂)₃, appears to gel during spin casting, which is probably related to the structure of this compound (*vide supra*). The films generated at room temperature look uniform when compared to the other precursor films (Figure 5). The film has small variations in thickness. The darker areas are slightly thinner than the lighter areas. Ellipsometry data on this film indicates that approximately 30% consolidation occurs at room temperature. This is comparable to zirconia thin films prepared from acetyl acetone or acetic acid modified zirconium *n*-propoxide sols.¹⁷ The fired films appear granular in nature, with significant interconnected porosity.

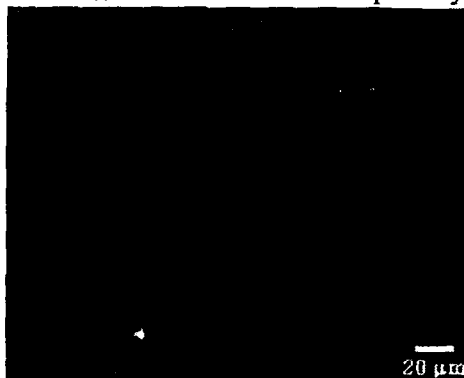


Figure 4. Film of 0.15M (AdamO)₂Ti(OCHMe₂)₃ in toluene, spin-cast deposited on a silicon wafer and then heat treated under argon.

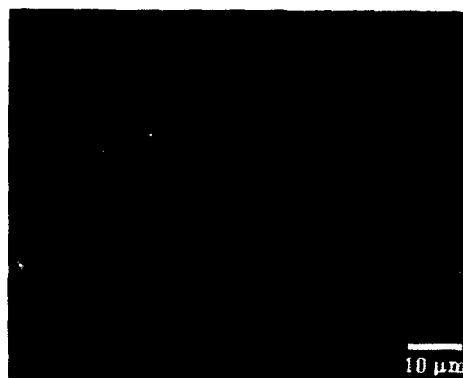


Figure 5. Film of 0.15M (AdamO)Zr(OCHMe₂)₃ in toluene spin-cast deposited on a silicon wafer.

CONCLUSIONS

It has been demonstrated that the systematic replacement of OCHMe_2 ligands with AdamO ligands for titanium and zirconium alkoxides is easily accomplished. The systematic substitution is clearly observed in the TGA/DTA as well as the ^1H and ^{13}C NMR data. Single crystal X-ray crystallography as well as molecular weight studies are underway to determine the extent of oligomerization of a number of these compounds. All the titanium adamantanoxy precursors crystallize during spin deposition instead of gelling, indicating significantly reduced reactivity with ambient humidity. The less substituted zirconium adamantanoxy complexes appear to demonstrate more of the classical gelation characteristics during spin casting. Structural information should elucidate the reasons for the observed properties of these compounds.

The higher substituted titanium and zirconium complexes are postulated to be monomeric and the steric bulk inhibits hydrolysis, as predicted. It is assumed that the lower adamantanoxy substituted titanium compounds are more oligomeric in nature with the adamantanoxy ligands surrounding and protecting the central core. This would account for the reduced hydrolysis observed for the titanium compounds. We also believe that the zirconium compounds are not as clustered as the titanium compounds and are therefore more susceptible to hydrolysis.

We have demonstrated that ligand substitution can have a large impact on the resulting characteristics of the thin films. Optimization of this technique should lead to novel routes for generation of property controlled thin films.

ACKNOWLEDGMENTS

This work was supported by the United States Department of Energy under contract DE-AC04-76DP00789. The authors would also like to thank Catherine D. Buchheit for her technical assistance.

REFERENCES

1. This work was presented in part at the 5th Annual Joint Meeting of the New Mexico Sections of the American Ceramic Society and Materials Research Society, Albuquerque, NM, October, 1993; Boyle, T.J.; Pearson, A.T.; Schwartz, R.W. (Poster Session II, #31)
2. Schwartz, R.W.; Assink, R.A.; Headley, T.J. *Mat. Res. Soc. Symp. Proc.* **1992**, 243, 245.
3. a) Yi, G.; Wu, Z.; Sayer, M. *J. Appl. Phys.* **1988**, 64, 2717. b) Budd, K.D.; Dey, S.K.; Payne, D.A. *Brit. Ceram. Soc. Proc.* **1985**, 36, 107.
4. Mazdidasni, K.S.; Lynch, C.T.; Smith II, J.S. *J. Am. Ceram. Soc.* **1965**, 48, 372.
5. Caulton, K.G. and Hubert-Pfalzgraf, L.G. *Chem. Rev.* **1990**, 90, 969.
6. Bochmann, M.; Wilkinson, G.; Young, G.B.; Hursthouse, M.B.; Malik, K.M.A. *J. C. S. Dalton* **1980**, 901.
7. A general synthesis went as follows:
 $(\text{AdamO})_3\text{Zr}(\text{OCHMe}_2)_4 \cdot \text{Zr}(\text{OCHMe}_2)_4 \cdot \text{HOCHMe}_2$ (0.30 g, 0.77 mmol) was dissolved in THF (7 mL) and to this stirred mixture, adamantanol

(0.35 g, 2.31 mmol) was slowly added. The reaction mixture was heated until a clear solution was present (this typically requires the mixture to be brought to a boil). The reaction mixture was cooled to ambient temperature and stirred for 12 hours. The solvent was partially removed by rotary evaporation until crystals appeared on the edge of the reaction vessel. The container was removed from the rotary evaporator, warmed till re-dissolution had occurred and allowed to sit at ambient temperature for 12 hours. Crystals formed from this solution.

8. Perrin, D.D. and Armarego, W.L.F. In *Purification of Laboratory Chemicals* 3rd ed. Pergamon Press: New York, 1988; Chapter 2.
9. a) Aldrich, 1001 West Saint Paul Avenue, Milwaukee, WI 53233, USA. b) Alfa Research Chemicals and Accessories, Johnson Matthey P.O. Box 8247, Ward Hill, MA 01835-0747, USA. c) Cambridge Isotope Laboratories, 20 Commerce Way, Woburn, MA 01801, USA.
10. Goel, S.C.; Chiang, M.Y.; Buhro, W.E. *Inorg. Chem.* **1990**, 29, 4640.
11. Olmstead, M.M.; Power, P.P.; Shoner, S.C. *J. Am. Chem. Soc.* **1991**, 113, 3379.
12. a) Svetich, G.W. and Voge, A.A. *Acta Cryst.*, **1972**, B28, 1760. b) Toth, R.T. and Stephan, D.W. *Can. J. Chem.* **1991**, 69, 172. c) Latesky, S.L.; Keddington, J.; McMullen, A.K.; Rothwell, I.P.; Huffman, J.C. *Inorg. Chem.* **1985**, 24, 995. d) Durfee, L.D.; Latesky, S.L.; Rothwell, I.P.; Huffman, J.C.; Folting, K. *Inorg. Chem.* **1985**, 24, 4569.
13. a) Wright, D.A. and Williams, D.A. *Acta Cryst.* **1968**, B24, 1107. b) Ibers, J.A. *Nature* **1963**, 197, 686.
14. a) Sharpless, K.B. *Chem. Scr.* **1987**, 27, 521. b) Sharpless, K.B.; Pedersen, S.F.; Dewan, J.C.; Exkman, R.R. *J. Am. Chem. Soc.* **1987**, 109, 1279. c) Williams, I.D.; Pedersen, S.F.; Sharpless, K.B.; Lippard, S.J. *J. Am. Chem. Soc.* **1984**, 106, 6430.
15. Boyle, T.J.; Barnes, D.L.; Heppert, J.A.; Morales, L.; Takusagawa, F. *Organomet.* **1992**, 11, 1112.
16. Vaartstra, B.A.; Huffman, J.C.; Gradeff, P.S.; Hubert-Pfalzgraf, L.G.; Daran, J.-C.; Parraud, S.; Yunlu, K.; Caulton, K.G. *Inorg. Chem.* **1990**, 29, 3126.
17. Presented in part at the 1993 Pac Rim Meeting of The American Ceramic Society, Honolulu, HI, November 1993, Schwartz, R.W.; Boyle, T.J.; Voigt, J.A.; Buchheit, C.D.; Mendoza, M.M. (SXVI-3-93P).

CRYSTALLIZATION BEHAVIOR AND IMPROVED PROPERTIES FOR SOL-GEL DERIVED PZT AND PLZT THIN LAYERS PROCESSED WITH A LEAD OXIDE COVER COATING

Toshihiko Tani, Toyota Central Research and Development Laboratories, Inc., Nagakute, Aichi, 480-11, Japan,
Charles D. E. Lakeman, Jie-Fang Li, Zhengkui Xu and David A. Payne, Department of Materials Science and Engineering, Materials Research Laboratory and Beckman Institute, University of Illinois at Urbana-Champaign, Urbana, IL 61801

ABSTRACT

Improved dielectric and ferroelectric properties are reported for the sol-gel preparation of lead-based perovskite-structure thin layers by a novel processing technique. The method uses a PbO cover coat to avoid the formation of additional phases on the surface. The deleterious effect of a "pyrochlore-type" phase, which is not present when a PbO cover coat is used, is attributed to PbO loss from the surface during thermal processing. Examples are given for PZT and PLZT thin layers integrated on Si with and without a PbO cover coat. Crystallization temperatures and times were reduced for the attainment of single-phase perovskite material. The dielectric, ferroelectric, and piezoelectric properties were always found to be superior for coated structures.

INTRODUCTION

Lead-containing ferroelectric thin layers have potential applications in non-volatile memory elements,^{1,2} infrared sensors,³ microactuators,⁴ and electro-optic devices^{5,6}—if they can be prepared in the perovskite structure. Materials of interest include, lead titanate (PbTiO_3 , i.e., PT), lead zirconate titanate ($\text{Pb}(\text{Zr,Ti})\text{O}_3$, i.e., PZT) and lanthanum (La)-modified PZT (i.e., PLZT). The coexistence of additional phases has, however, restricted many applications. Ishida et al. reported a cubic (i.e., non-ferroelectric) pyrochlore structure to be more stable than perovskite for sputtered materials at lower processing temperatures and

To the extent authorized under the laws of the United States of America, all copyright interests in this publication are the property of The American Ceramic Society. Any duplication, reproduction, or republication of this publication or any part thereof, without the express written consent of The American Ceramic Society or fee paid to the Copyright Clearance Center, is prohibited.

under Pb-deficient conditions.⁷ In sol-gel processing, the formation of a second phase on the surface has been a serious problem for ferroelectric properties. Several reports identified perovskite "rosette"-like grains in a fine-grain pyrochlore surface structure.⁸ Analysis indicated the pyrochlore to be richer in Zr and more deficient in Pb than the perovskite structure.⁹ Pb-based perovskite layers crystallize from either the amorphous state or transform from the aforementioned pyrochlore structure, depending upon the thermal processing conditions. Crystallization is reported to proceed at a lower temperature for Ti-rich PZT compositions and therefore at higher temperatures for Zr-rich PZT coatings.¹⁰ Higher processing temperatures can lead to an additional Pb-deficient $\text{Pb}(\text{Ti,Zr})_3\text{O}_7$ phase and interfacial reactions with silicon-based substrates.^{9,11} It is especially difficult to obtain single phase perovskite material for Zr-rich PLZT compositions since $\text{La}_2\text{Zr}_2\text{O}_7$ is a stable pyrochlore phase.¹²

Perovskite phase development in sol-gel derived thin layers has also been reported to depend upon solution chemistry.^{13,14} Lakeman and Payne noted that solutions prepared without a final stage vacuum distillation gave rosette structures, whereas properly prepared solutions (i.e., without ester present) yielded a fine-grain perovskite structure.¹³ Aging of properly processed solutions could also lead to pyrochlore formation.¹⁵ Similarly, Schwartz et al. prepared two types of solutions with acetic acid as a solvent, and found that the solution with the higher ester content formed thin layers with the greater pyrochlore content on the surface.¹⁴ In both cases, ester formation in the precursor solutions was shown to be detrimental to the formation of single phase perovskite material. Tuttle et al. proposed that phase separation occurred as hydrolysis and condensation reactions proceeded to form the gel.¹⁶

In addition to careful control of solution chemistry, three processing techniques have been proposed to reduce the pyrochlore problem for the lead-based ferroelectric thin layers:

- (i) Additions of excess Pb in solution.
- (ii) Seeding for perovskite crystallization.
- (iii) Rapid thermal processing (RTP).

It is well known that excess PbO is added to powders in conventional processing to compensate for lead-loss on heat treatment.^{17,18} This technique is also used in sputtering methods at reduced pressures.¹⁹ In sol-gel processing, it is claimed that excess PbO leads to crystallization of dense perovskite microstructures at reduced temperatures.²⁰ Tuttle et al. reported an optimum amount of 5 mol% PbO content for PZT (53/47) thin layers,⁹ while Francis and Payne found that 15 mol% gave the best properties for lead magnesium niobate (PMN)-based compositions.²¹ Crystallization at reduced temperatures was also

promoted through the use of seeded layers. Swartz et al. deposited PLZT precursor solutions on a PT interlayer and obtained perovskite PLZT.²² Hirano et al. reported on the preparation of perovskite PMN-PT layers over a seeded PZT base layer.²³ In addition, RTP has been used to maximize the perovskite content by avoiding extended time in the temperature range in which the pyrochlore phase is stable.²⁴ This kinetic approach has been used successfully for a variety of compositions and substrate materials. RTP also has a role of minimizing both PbO loss due to evaporation, and interdiffusion between the substrate and the layer.²⁵

It is also well known that for conventional mixed-oxide powder processing of lead-based ceramics, the atmosphere containing PbO vapor around the part during firing has a significant effect on defect structure, density, microstructure development, and therefore properties.^{26,27} PZT ceramics are usually sintered in O₂ atmospheres with powders containing PbO + PbZrO₃ to prevent Pb and O loss during firing.²⁸ However, no study has been reported for the use of an "atmosphere powder" technique²⁶ for lead-based thin layers. The vapor pressures of Pb and PbO are not significant at the lower temperatures (e.g., 650 °C) used for the processing of sol-gel derived thin layers,²⁹ compared with the higher temperatures (e.g., 1300 °C) used for the conventional firing of bulk ceramics. The surface area to volume ratio is, however, significantly greater for thin layer-structures, typically 10³ to 10⁴ times greater than for bulk ceramics. Furthermore, in sol-gel processing, the firing atmosphere may be different from conventional processing due to pyrolysis of residual organic species.

In this paper, we mimic the "atmosphere powder" technique and develop a novel method to prevent lead (Pb) loss in the preparation of lead-based thin layers. Initial results have been reported elsewhere for PLZT thin layers.²⁹ We now report additional information, including data for PZT. The novel method leads to complete crystallization of the perovskite structure without any additional phases on the surface of thin layer ferroelectrics.

EXPERIMENTAL PROCEDURE

Figure 1 illustrates the processing cycle for sol-gel derived PZT and PLZT thin layers. Precursor solutions for PZT and PLZT were prepared from lead acetate Pb(CH₃COO)₂, lanthanum isopropoxide La(O-iC₃H₇)₃, zirconium n-propoxide Zr(O-C₃H₇)₄, titanium isopropoxide Ti(O-iC₃H₇)₄, and 2-methoxyethanol CH₃OC₂H₄OH. The process was a modification of Budd's original method.³⁰ Compositions chosen were close to morphotropic boundaries; PZT 53/47 and, PLZT 7.5-8/70/30 and 8/65/35. An additional batch of a PbO containing "coating solution" was

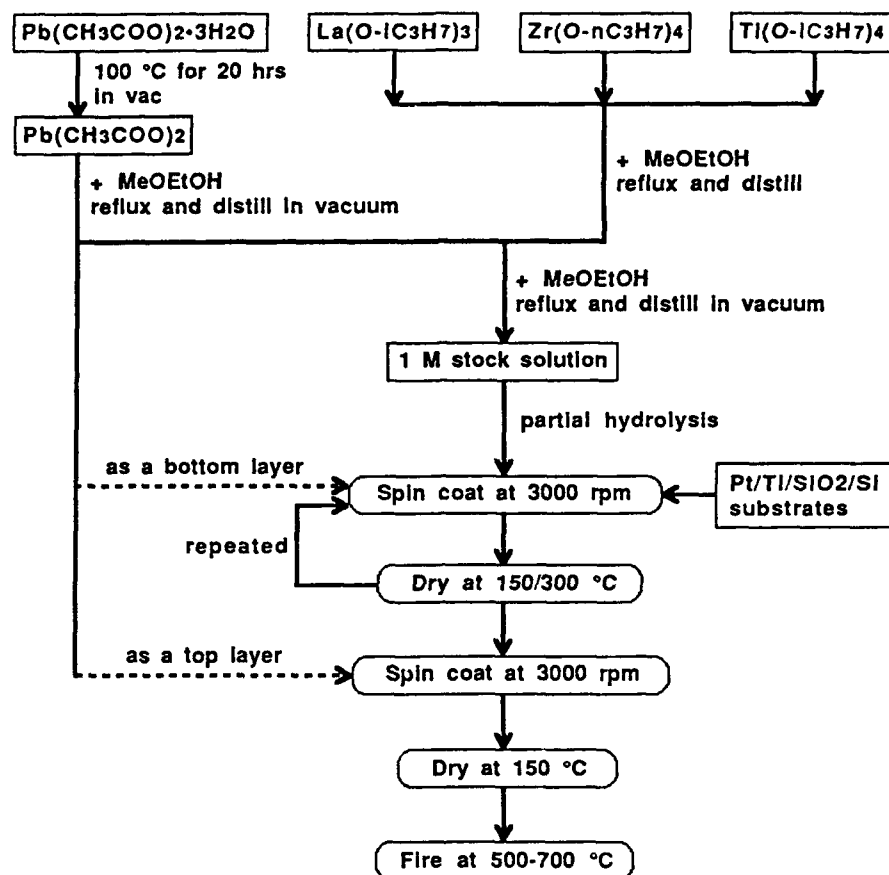


Fig. 1 Processing route for sol-gel derived PZT and PLZT thin layers

prepared separately, in a manner similar to the way the solution was prepared for PZT and PLZT. That is, anhydrous lead acetate was dissolved in 2-methoxyethanol and refluxed, followed by distillation and dilution to 1M.

Partially-hydrolyzed PZT and PLZT solutions were deposited on $\text{Pt/Ti/SiO}_2/\text{Si}$ substrates by spin-casting at 3000 rpm. After each layer was deposited, the specimen was dried at 150°C for 15 seconds and pyrolyzed at 300°C for 1 minute. After 5 to 10 depositions, the multilayer was crystallized at 500 to 700°C for 1 to 30 min in air in an electrically heated box furnace. The PbO precursor solution was deposited before (i.e., under coat) and/or after (i.e., cover coat) the spin-casting of PZT or PLZT. A typical thickness for a fired layer was 0.3 to $0.4\ \mu\text{m}$.

Crystallization behavior was examined after heat treatment by X-ray diffraction (XRD, Rigaku D/Max IIIA), and microstructures were determined by scanning electron microscopy (SEM, Hitachi S800) and transmission electron microscopy (TEM, Philips EM420). Gold electrodes were sputter-deposited through a shadow mask and dielectric and ferroelectric properties were measured on an impedance analyzer (HP4192A) and a Sawyer-Tower bridge at room temperature. The piezoelectric response behavior was determined as a function of DC electric field at an AC oscillation level of 1 V, by interferometric measurements.³¹ The instrumental details and experimental method are described elsewhere.³²

RESULTS AND DISCUSSION

PbO remained as particles on the surface of the layers which had been heat treated at 650 °C (or below) for 5 min, or at 700 °C for 1 min. By heating at 650°C for 30 min or at 700 °C for 5 min, the PbO particles disappeared from the surface. Figure 2 gives XRD data for specimens heat treated at 500 to 650 °C for 5 min with and without a PbO cover coat. There was little difference in the XRD patterns for specimens heated below 600 °C, i.e., for (111) perovskite and (222) pyrochlore. The diffraction peak for pyrochlore was broad, reflecting the nanocrystalline nature of the phase. Above 625 °C, however, there was a significant difference between specimens which had been prepared with and without a top PbO layer. PbO-covered PLZT layers gave no evidence of a pyrochlore phase when heat treated above 625 °C. On the other hand, specimens without a PbO cover coat retained the pyrochlore phase at higher temperatures (e.g., 650 °C). Although XRD data for uncovered PLZT layers heated at 700 °C for 5 min hardly detected a trace of pyrochlore, the nanocrystalline nature was clearly revealed by SEM, as indicated in Fig. 3b. In addition, an uncovered PLZT layer seeded with a PbO base layer also had a nanocrystalline surface layer (< 20 nm). By comparison, the grain size for a PbO-covered PLZT layer was somewhat greater, between 0.1 and 0.2 μm (Fig. 3a). Figure 4 gives a TEM photomicrograph for an uncovered PLZT layer in cross section, which indicates that the layer was comprised of columnar perovskite grains at the base and with nanocrystalline grains at the top surface. Lattice spacings for the surface layer, as determined by selected area electron diffraction (SAED) in the TEM, were similar to spacings previously reported for an oxygen-deficient pyrochlore phase, $\text{Pb}_2\text{Ti}_2\text{O}_6$.³³ The EDAX analysis indicated the surface layer was Zr-rich, and relatively Pb- and Ti-deficient, in agreement with the results of Tuttle et al.⁹ Nanocrystalline surface layers were not observed on any of the PbO-covered PLZT layers heat treated above 625 °C. Single phase perovskite material was always formed without any additional phases on

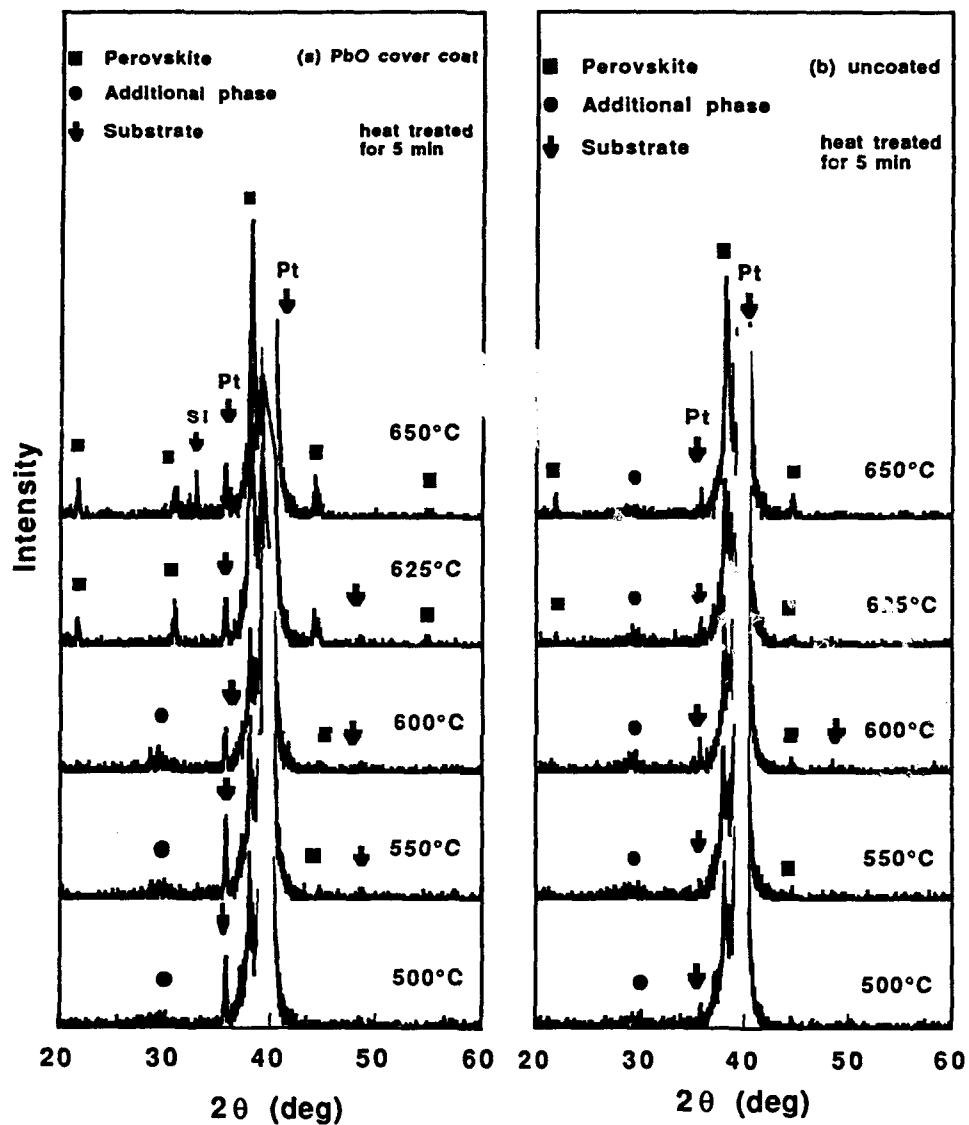


Fig. 2 XRD data for PLZT 6/65/35 thin layers heat treated at 500 to 650 °C for 5 min (a) and (b) without a PbO-precursor cover coat.

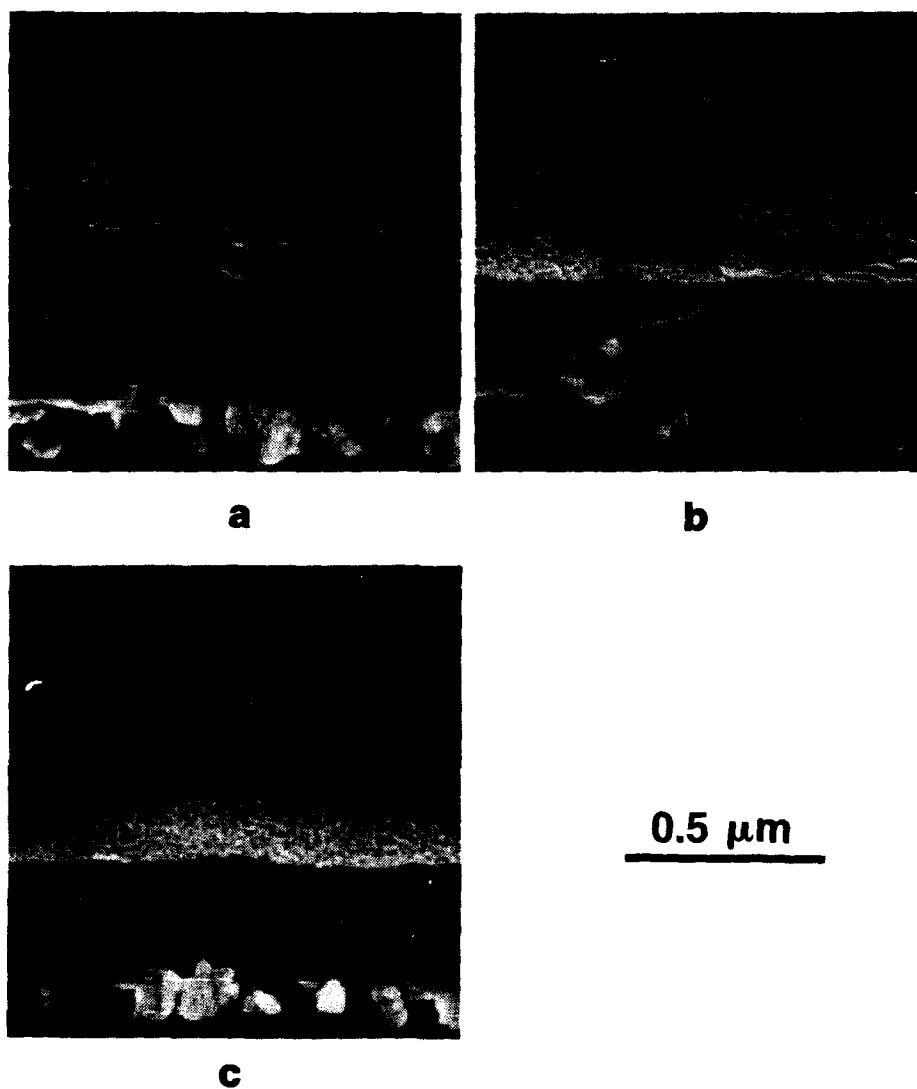
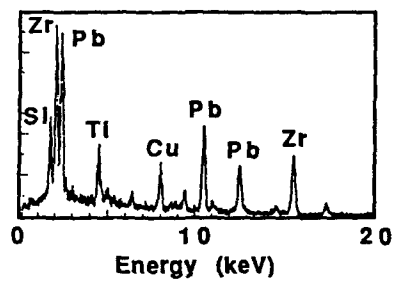
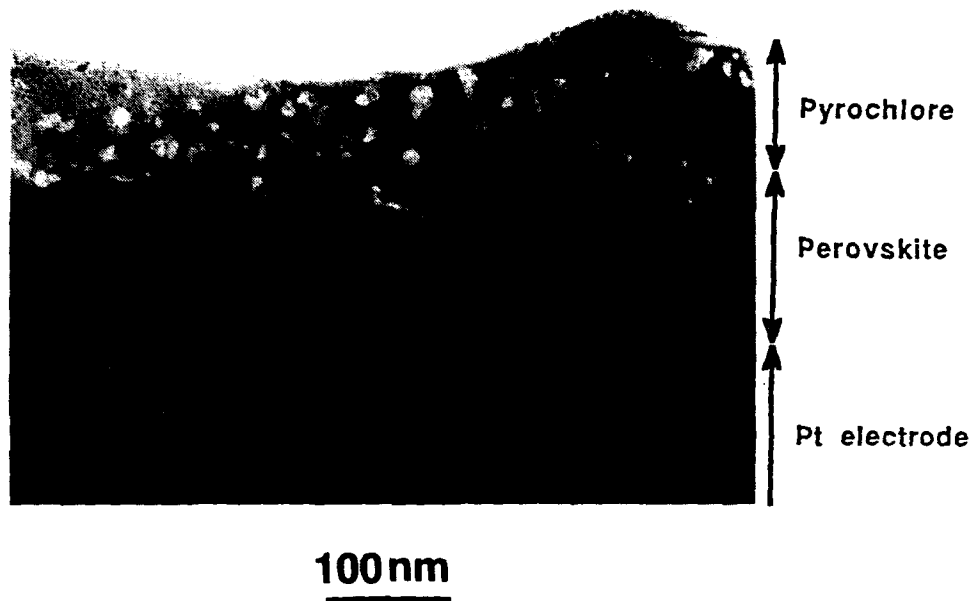
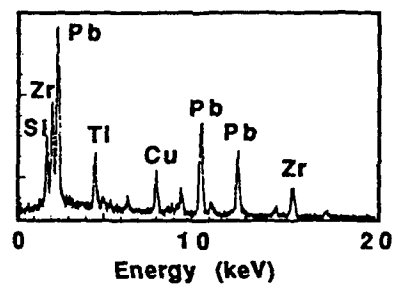


Fig. 3 SEM Photomicrographs of PLZT 7.5/70/30 thin layers fired at 700 °C for 5 min (a) with and (b) without a PbO-precursor cover coat, and (c) with a PbO-precursor undercoat.



a



b

Fig. 4 TEM photomicrograph for the cross section of uncovered PLZT thin layer heat treated at 700 °C for 30 min, with EDAX data for (a) fine-grain "pyrochlore-type" layer and (b) columnar perovskite grain.

the surface. A reduced time for complete crystallization was also observed for perovskite PLZT thin layers.²⁹ Similar behavior was seen for PZT thin layers. Figure 5 illustrates the difference in microstructures for layers heat-treated at 700 °C for 30 min with and without a PbO cover coat. It is evident that without a PbO-precursor coating, a *nanocrystalline* structure was formed on the surface, and EDAX analysis in the TEM indicated again this was an off-stoichiometric (Zr-rich and Pb-deficient) pyrochlore-type phase. In contrast, a dense, larger-grain *microstructure* was obtained for thin layers fired with a PbO cover coating.

Residual PbO particles on the surface of thin layers could be removed physically (by rubbing gently) or chemically (by dissolving in

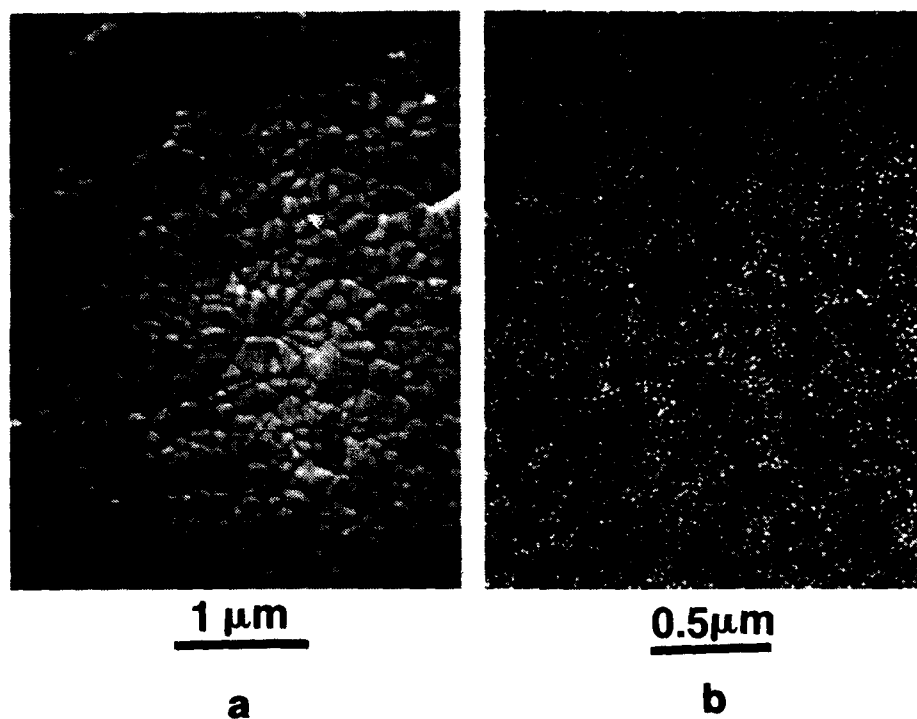


Fig. 5 SEM photomicrographs of PZT 53/47 thin layers heat treated at 700 C for 30 min (a) with and (b) without a PbO-precursor cover coat.

acetic acid). Figure 6 gives the dielectric properties as a function of frequency for PLZT 7.5/70/30 which was heat treated at 700 °C for 5 min. PbO-covered layers had the highest value of dielectric constant ($K = 615$) and lowest loss ($\tan\delta = 1.3\%$) compared with uncovered layers ($K = 239$, $\tan\delta = 5.2\%$) when measured at 1 kHz, 50 mV ac and 25°C. The deposition of an under coat had no effect on properties for un-covered PLZT layers. K values are given in Figure 7 for PbO-covered PLZT 8/65/35 layers prepared under different conditions. For example, after heat treatment at 650 °C for 1 min, single phase perovskite material was formed with a K value of 575. The maximum value for K was 714 after heat treatment at 700 °C for 5 min. The standard deviation for average K values was 2.0 to 2.5 %, which indicated good structural and compositional control for the improved processing of PLZT layers. Figure 8 gives the dielectric properties for PZT thin layers heat treated at 700 °C for 1 min. PbO-covered layers had higher values of dielectric constant ($K = 818$) and lower loss ($\tan\delta = 0.9\%$) than uncovered layers ($K = 433$, $\tan\delta = 2.4\%$).

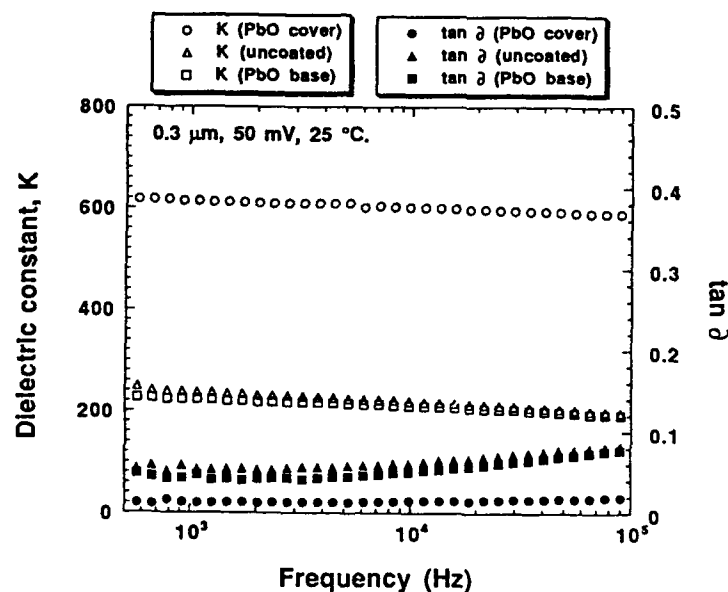


Fig. 6 Frequency dependence of dielectric constant and tangent δ for PLZT 7.5/70/30 thin layers heat treated at 700 °C for 5 min.

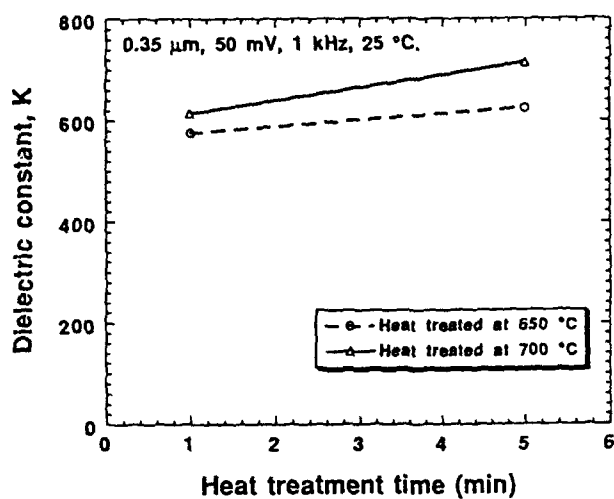


Fig. 7 Effect of thermal processing conditions on the dielectric constant of PLZT 8/65/35 thin layers with a PbO cover coat.

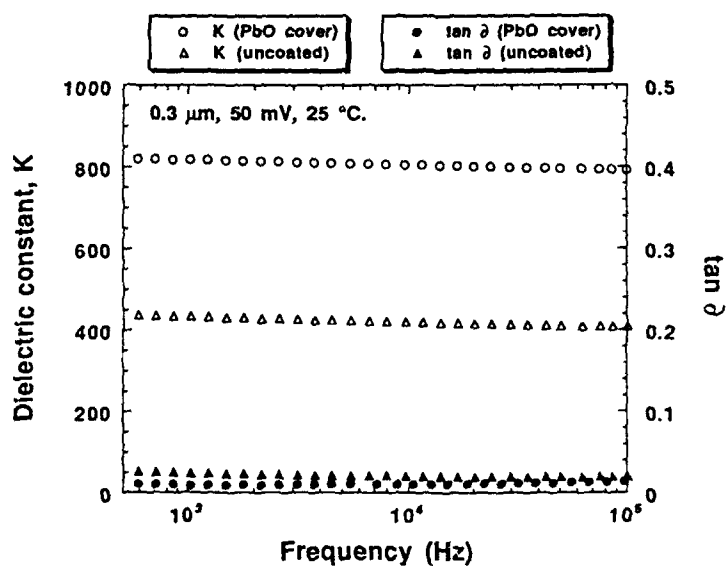


Fig. 8 Frequency dependence of dielectric constant and tangent δ for PZT 53/47 thin layers heat treated at 700 °C for 1 min.

Figure 9 illustrates the ferroelectric properties. PbO-covered PLZT exhibited slim-loop behavior with polarization saturation, whereas uncovered layers were lossy. Figure 10 compares P-E hysteresis loops of the two types of PZT thin layers. Layers prepared without a PbO-cover coat had lossy characteristics with average values of $P_r \sim 9.4 \mu\text{C}/\text{cm}^2$, $E_c \sim 104 \text{ kV}/\text{cm}$. For PbO-coated layers, the loops saturated, had higher values of remanent polarization, and with lower coercive fields. The average values for coated layers were $P_s \sim 28 \mu\text{C}/\text{cm}^2$, $P_r \sim 14.7 \mu\text{C}/\text{cm}^2$, and $E_c \sim 76 \text{ kV}/\text{cm}$.

Finally, Figure 11 indicates the piezoelectric properties for PZT thin layers prepared by the two methods as a function of applied bias at 1 kHz. Higher values of d_{33} coefficients (180 pC/N) were measured for PbO coated layers, which are close to values that have been measured for bulk ceramics (223 pC/N).²⁸ Asymmetry in the strain-field 'butterfly' loops was observed in both types of layers. It may be attributed to interfacial substrate effects and differences in physical constraints between the top and bottom surfaces of the thin-layers.³⁴

It is clear that the deposition of a PbO cover coat over a PZT and PLZT-precursor thin layer has a beneficial effect on perovskite phase development on heat-treatment. Elimination of a Pb-deficient pyrochlore-type phase on the top surface leads to a significant improvement in dielectric and ferroelectric properties and consistency. However,

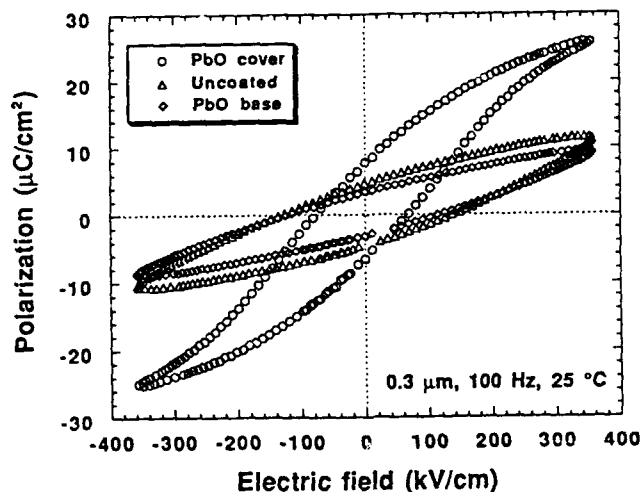


Fig. 9 Ferroelectric hysteresis for PLZT 7.5/70/30 thin layers heat treated at 700 °C for 5 min.

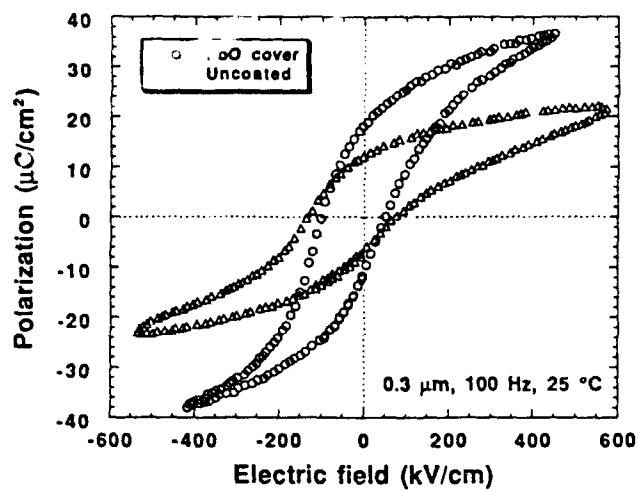


Fig. 10 Ferroelectric hysteresis for PLZT 7.5/70/30 thin layers heat treated at 700 °C for 5 min.

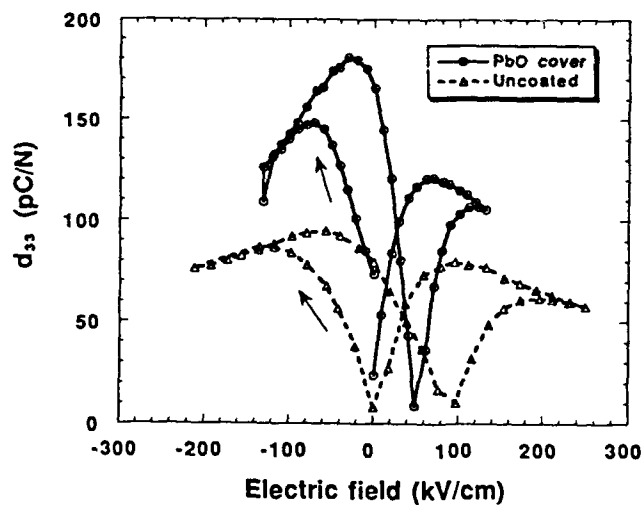


Fig. 11 Piezoelectric coefficient for PZT 53/47 thin layers heat treated at 700 °C for 1 min.

deposition of a PbO-base layer did not give any improvement in either the microstructure or the dielectric properties for the PLZT layers. These results suggest that Pb loss into the atmosphere is the major contributing factor to the formation of undesirable surface phases, rather than reaction of PbO with the base electrode materials. This novel method could be applicable to other lead-containing materials such as PMN and lead scandium tantalate (PST) which have a strong tendency to form a pyrochlore-type phase at higher processing temperatures. Furthermore, the method may be extended to other systems containing volatile species (e.g., KNbO_3 , LiTaO_3 , NaNbO_3 , etc.) to prevent alkali loss during firing of thin layers.

CONCLUSION

The results demonstrate that pyrochlore formation on the surface of PZT and PLZT thin layers is attributable to evaporative loss of PbO, and that an additional deposition of a PbO cover coat effectively prevents this problem and enhances complete crystallization of the perovskite structure. Any remaining PbO particles on the surface can readily be removed after firing and do not degrade dielectric properties. Thin layers processed with a PbO cover coat reproducibly form uniform microstructures of single phase perovskite material with improved dielectric, ferroelectric and piezoelectric properties when compared with uncoated layers. This novel method can be applied to other Pb-containing systems and extended to materials which contain other volatile species.

ACKNOWLEDGMENTS

The research was supported by DOE BES DEFG02-91ER45439 and by a grant from Toyota CRDL. The use of facilities in the Center for Microanalysis of Materials in the Materials Research Laboratory at the University of Illinois is gratefully acknowledged. We thank Professor Dwight Viehland and Mr. Paul Moses for experimental facilities for property measurements. The technical assistance of Mr. Robert Prigge and Ms. Fang Li are also gratefully appreciated.

REFERENCES

- 1 S. K. Dey, D. A. Payne, and K. D. Budd, "Thin Film Ferroelectrics of PZT by Sol-Gel Processing," *IEEE UFFC*, 35 80-81 (1988).

- 2 D. Bondurant and F. Gnadinger, "Ferroelectrics for Nonvolatile RAMs," *IEEE Spectrum*, 30 30-33 (1989).
- 3 A. Patel, N. M. Shorrocks, and R. W. Whatmore, "Lead Scandium Tantalate Thin Films for Thermal Detectors" in *Ferroelectric Thin Films II*; A. I. Kingon, E. R. Myers, and B. Tuttle, Ed.; Materials Research Society: Pittsburgh, PA, 1992; pp. 67-72.
- 4 K. R. Udayakumar, S. F. Bart, A. M. Flynn, J. Chen, L. S. Tavrow, L. E. Cross, K. G. Brooks, and D. J. Ehrlich, "Ferroelectric Thin Film Ultrasonic Micromotors" in *Proceedings of 4th IEEE Workshop on Micro Electro Mechanical Systems*, ; H. Fujita and M. Esashi, Ed.; 1991; pp. 109-13.
- 5 K. Wasa, O. Yamazaki, H. Adachi, T. Kawaguchi, and K. Setsune, "Optical TIR Switches Using PLZT Thin Film Waveguides on Sapphire," *IEEE J. Lightwave Technology*, LT-2 [5] 710-14 (1984).
- 6 K. D. Budd and D. A. Payne, "Sol-Gel Processing of Thin Layer Ferroelectrics in Lead Titanate-Based Systems," *Inst. Phys. Conf. Ser. (U. K.)*, 103 13-22 (1989).
- 7 M. Ishida, H. Matsunami, and T. Tanaka, "Preparation and Properties of Ferroelectric PLZT Thin Films by RF Sputtering," *J. Appl. Phys.*, 48 [3] 951-53 (1977).
- 8 L. N. Chapin and S. A. Myers, "Microstructure Characterization of Ferroelectric Thin Films Used in Non-Volatile Memories — Optical and Scanning Electron Microscopy" in *Ferroelectric Thin Films*; E. R. Myers and A. I. Kingon, Ed.; Materials Research Society: Pittsburgh, PA, *Mat. Res. Soc. Symp. Proc.*, **200**, 1990; pp. 153-58.
- 9 B. Tuttle, R. W. Schwartz, D. H. Doughty, and J. A. Voigt, "Characterization of Chemically Prepared PZT Thin Films" in *Ferroelectric Thin Films*; E. R. Myers and A. I. Kingon, Ed.; Materials Research Society: Pittsburgh, PA, *Mat. Res. Soc. Symp. Proc.*, **200**, 1990; pp. 159-65.
- 10 C. K. Kwok and S. B. Desu, "Low Temperature Perovskite Formation of Lead Zirconate Titanate Thin Films by a Seeding Process," *J. Mater. Res.*, 8 [2] 339-44 (1993).
- 11 T. Tani, Z. Xu, and D. A. Payne, "Preferred Orientations for Sol-Gel Derived PLZT Thin Layers" in *Ferroelectric Thin Films III*; E. R.

Myers, B. A. Tuttle, S. D. Desu, and P. K. Larsen, Ed.; Materials Research Society : Pittsburgh, PA, *Mat. Res. Soc. Symp. Proc.*, **310**, 1993; pp. 269-74.

- 12 G. H. Haertling and C. E. Land, "Hot-Pressed (Pb,La)(Zr,Ti)O₃ Ferroelectric Ceramics for Electrooptic Applications," *J. Am. Ceram. Soc.*, **54** [1] 1-11 (1971).
- 13 C. D. E. Lakeman and D. A. Payne, "Processing Effects in the Sol-gel Preparation of PZT Dried Gels, Powders, and Ferroelectric Thin Layers," *J. Am. Ceram. Soc.*, **75** [11] 3091-96 (1992).
- 14 R. W. Schwartz, R. A. Assink, and T. J. Headley, "Spectroscopic and Microstructural Characterization of Solution Chemistry Effects in PZT Thin Film Processing" in *Ferroelectric Thin Films II*; A. I. Kingon, E. R. Myers, and B. Tuttle, Eds.; Materials Research Society: Pittsburgh, PA, *Mat. Res. Soc. Symp. Proc.*, **243**, 1992; pp. 245-54.
- 15 C. D. E. Lakeman, "An Investigation into Factors affecting the Sol-Gel Processing of PZT Thin Layers," M.S. Thesis, University of Illinois at Urbana-Champaign, 1991.
- 16 B. A. Tuttle, T. J. Headley, B. C. Bunker, R. W. Schwartz, T. J. Zender, C. L. Hernabdez, D. C. Goodnow, R. J. Tissot, and J. Michael, "Microstructural Evolution of Pb(Zr,Ti)O₃ Thin Films Prepared by Hybrid Metallo-organic Decomposition," *J. Mater. Res.*, **7** [7] 1876-82 (1992).
- 17 A. I. Kingon and J. B. Clark, "Sintering of PZT Ceramics: II, Effect of PbO Content on Densification Kinetics," *J. Am. Ceram. Soc.*, **66** [4] 256-60 (1983).
- 18 B. Song, D. Kim, S. Shirasaki, and H. Yamamura, "Effect of Excess PbO on the Densification of PLZT Ceramics," *J. Am. Ceram. Soc.*, **72** [5] 833-36 (1989).
- 19 M. Ishida, S. Tsuji, K. Kimura, H. Matsunami, and T. Tanaka, "Epitaxial Growth of Ferroelectric PLZT [(Pb,La)(Zr,Ti)O₃] Thin Films," *J. Crystal Growth*, **45** 393-98 (1978).
- 20 S. D. Bernstein, Y. Kisler, J. M. Wahl, S. E. Bernacki, and S. R. Collins, "Effects of Stoichiometry on PZT Thin Film Capacitor Properties" in *Ferroelectric Thin Films II*; A. I. Kingon, E. R. Myers,

and B. Tuttle, Ed.; Materials Research Society: Pittsburgh, PA, *Mat. Res. Soc. Symp. Proc.*, **243**, 1992; pp. 373-78.

- 21 L. F. Francis and D. A. Payne, "Thin-layer Dielectrics in the $\text{Pb}[(\text{Mg}_{1/3}\text{Nb}_{2/3})_{1-x}\text{Ti}_x]\text{O}_3$ System," *J. Am. Ceram. Soc.*, **74** [12] 3000-10 (1991).
- 22 S. L. Swartz, S. J. Brigh, P. J. Melling, and T. R. Shrout, "Sol-gel Processing of Composite PbTiO_3 /PLZT Thin Films," *Ferroelectrics*, **108** 71-76 (1990).
- 23 S. Hirano, T. Yogo, K. Kikuta, K. Kato, W. Sakamoto, and S. Ogasahara, "Sol-gel Processing and Characterization of Ferroelectric Thin Films" in *Ferroelectric Films*; A. S. Bhalla and K. M. Nair, Ed.; American Ceramic Society: Westerville, OH, *Ceramic Transactions*, **25**, 1992; pp. 19-32.
- 24 L. F. Francis, Y.-J. Oh, and D. A. Payne, "Sol-gel Processing and Properties of Lead Magnesium Niobate Powders and Thin Layers," *J. Mat. Sci.*, **25** 5007-13 (1990).
- 25 R. W. Schwartz, Z. Xu, D. A. Payne, T. A. DeTemple, and M. A. Bradley, "Preparation and Characterization of Sol-Gel Derived PbTiO_3 Layers on GaAs" in *Ferroelectric Thin Films*; E. R. Myers and A. I. Kingon, Ed.; Materials Research Society: Pittsburgh, PA, *Mat. Res. Soc. Symp. Proc.*, **200**, 1990; pp. 167-72.
- 26 G. S. Snow, "Fabrication of Transparent Electrooptic PLZT Ceramics by Atmosphere Sintering," *J. Am. Ceram. Soc.*, **56** [2] 91-96 (1973).
- 27 G. H. Haertling, "Electro-optic Ceramics and Devices" in *Electronic Ceramics*; L. M. Levinson, Ed.; Marcel Dekker: New York, 1988; pp. 371-492.
- 28 B. Jaffe, W. R. Cook, and H. Jaffe, *Piezoelectric Ceramics*; Academic Press: London, 1971; Vol. 3.
- 29 T. Tani and D. A. Payne, "Lead Oxide Coatings on Sol-gel Derived Lead Lanthanum Zirconium Titanate Thin Layers for Enhanced Crystallization into the Perovskite Structure," *J. Am. Ceram. Soc.*, (1994).

- 30 K. D. Budd, S. K. Dey, and D. A. Payne, "Sol-gel Processing of PbTiO_3 , PbZrO_3 , $\text{Pb}(\text{ZrTi})\text{O}_3$ and $\text{PbLa}(\text{ZrTi})\text{O}_3$," *Brit. Ceram. Soc. Proc.*, 36 107-21 (1985).
- 31 J.-F. Li, D. D. Viehland, T. Tani, C. D. E. Lakeman, and D. A. Payne, "Piezoelectric Properties of Sol-gel Derived Ferroelectric and Antiferroelectric Thin Layers," *J. Appl. Phys.*, 75 [1] (1994).
- 32 J.-F. Li, P. Moses, and D. D. Viehland, "The Piezoelectric Spectrometer," *Review of Scientific Instruments*, (June, 1994).
- 33 F. W. Martin, "A Metastable Cubic Form of Lead Titanate Observed in Titania Nucleated Glass Ceramics," *Physics and Chemistry of Glasses*, 6 [4] 143-46 (1965).
- 34 T. Tani, J.-F. Li, D. D. Viehland, and D. A. Payne, "Antiferroelectric-Ferroelectric Switching and Induced Strains for Sol-Gel Derived Lead Zirconate Thin Layers," *J. Appl. Phys.*, 75 (6) (1994).

METAL ALKOXIDE DERIVED ORIENTED AND EPITAXIAL FERROELECTRIC THIN FILMS

Keiichi Nashimoto

Materials Research Laboratory, Fuji Xerox Co., Ltd.

1600 Takematsu, Minamiashigara, Kanagawa, 250-1, Japan

ABSTRACT

Ferroelectric thin films including LiNbO_3 , LiTaO_3 , KNbO_3 , and PZT were prepared by a process utilizing non-hydrolyzed metal methoxyethoxide precursors, spin coating, and rapid thermal annealing. Epitaxial and dense LiNbO_3 and LiTaO_3 films without any misoriented planes on sapphire (110) and (001) substrates were obtained with the present process. The LiNbO_3 started to crystallize at 400°C and the refractive indices of LiNbO_3 annealed over 600°C were close to those of bulk single crystals. Rocking curve full widths at half maximum (FWHM) for (110) of epitaxial LiNbO_3 and LiTaO_3 films on sapphire (110) less than 0.4° were observed. Epitaxial or highly oriented KNbO_3 and PZT thin films with rocking curve FWHMs for (100) of 2.5° and 1.5° , respectively, were successfully grown on MgO (100) substrates.

INTRODUCTION

Ferroelectric thin films have been prepared by a number of processes for fabricating non-volatile memories, opto-electronic devices, and surface acoustic wave devices. Among these applications, opto-electronic waveguide devices, such as, acousto-optic deflectors, electro-optic switches, and frequency doublers, require diffused ferroelectric single crystal wafers or epitaxial ferroelectric thin films. The single crystal

To the extent authorized under the laws of the United States of America, all copyright interests in this publication are the property of The American Ceramic Society. Any duplication, reproduction, or republication of this publication or any part thereof, without the express written consent of The American Ceramic Society or fee paid to the Copyright Clearance Center, is prohibited.

wafers or epitaxial thin films are essential because of low optical propagation loss, due to the absence of high angle grain boundaries, and their near single crystal properties, due to their oriented domain structures. For the optical waveguide structures, LiNbO_3 single crystals usually serve as the substrates into which the diffused optical waveguides are fabricated. However, thin film waveguide devices are desirable because the single crystal devices are expensive, quite complicated, and incompatible with integration to semiconductor lasers.

Current major epitaxial growth processes are vapor phase processes which are generally costly and complicated for the preparation of stoichiometric epitaxial ferroelectric thin films. Epitaxial ferroelectric thin films produced by these vapor phase processes include LiNbO_3 on sapphire by rf-sputtering [1], $\text{Pb}_{1-x}\text{La}_x(\text{Zr}_{1-y}\text{Ti}_y)_{1-x/4}\text{O}_3$ on sapphire by rf-magnetron sputtering [2], KNbO_3 on MgO by ion beam sputtering [3], BaTiO_3 on MgO encapsulated GaAs by pulsed laser deposition [4], and PbTiO_3 on SrTiO_3 by MOCVD [5], for instance. These thin films were prepared through manipulation of target composition and/or precise control of deposition conditions in order to obtain stoichiometric ferroelectric thin films.

As a thin film process, the sol-gel process is advantageous in reducing processing cost, stoichiometric composition control, and large area fabrication, although it has been primarily used as a process to prepare polycrystalline ferroelectric thin films. Partlow and Gregg observed a partial homoepitaxy when they prepared LiNbO_3 thin films on LiNbO_3 single crystals by the sol-gel process using hydrolyzed metal ethoxides [6]. Afterwards, LiNbO_3 thin films with preferred orientation on sapphire substrates were prepared from partially hydrolyzed metal ethoxides [7].

With respect to the growth of single crystal epitaxial ferroelectric thin films by the sol-gel process, Nashimoto *et al.* reported the solid state heteroepitaxial crystallization of LiNbO_3 thin films with single orientations on sapphire substrates from non-hydrolyzed metal ethoxide precursors [8-11]. The in-plane epitaxial crystallography and microstructure of the LiNbO_3 were also identified by pole-figure measurement and high resolution transmission electron microscopy. Examples of chemically derived oriented or epitaxial ferroelectric thin films, such as LiNbO_3 , LiTaO_3 , PbTiO_3 , PZT , $\text{Pb}(\text{Nb,Zr,Ti})\text{O}_3$, SrTiO_3 , and $\text{Pb}(\text{Mg}_{1/3}\text{Nb}_{2/3})\text{O}_3$, are listed in Table I.

In this paper, the critical effects of precursor chemistry and annealing conditions on the orientation and quality of sol-gel derived (or metal alkoxide derived) epitaxial or oriented ferroelectric thin films of LiNbO_3 , LiTaO_3 , KNbO_3 , and PZT are described.

Table I. Chemically derived oriented and epitaxial thin films.

Thin films	Year	Reference
Partially homoepitaxial LiNbO_3	1987	[6]
Oriented LiNbO_3 on sapphire	1988	[7]
Oriented PbTiO_3 on MgO	1989	[12]
Oriented PZT on SrTiO_3	1989	[13]
Oriented $\text{Pb}(\text{Mg}_{1/3}\text{Nb}_{2/3})\text{O}_3$ on MgO	1989	[14]
Epitaxial LiNbO_3 on sapphire	1990	[8, 9]
Epitaxial $\text{Pb}(\text{Nb,Zr,Ti})\text{O}_3$ on sapphire	1992	[15]
Homoepitaxial SrTiO_3	1992	[16]
Epitaxial LiTaO_3 on sapphire	1993	[17]

EXPERIMENTAL

0.6 M ethanol based precursor solutions for LiNbO_3 thin films were prepared from stoichiometric metal ethoxides in absolute ethanol as reported before [9]. The crystal structure of the double lithium niobium ethoxide was reported [18]. Methoxyethanol based precursors for LiNbO_3 , LiTaO_3 , and KNbO_3 were also prepared from ethoxides with stoichiometric composition using alcohol exchange reactions in 2-methoxyethanol in a dry nitrogen atmosphere, in order to examine the effect of chemical modification on the quality of derived films [17]. The methoxyethanol based LiNbO_3 thin film process is illustrated in Figure 1. To form 0.6 M metal methoxyethoxide solutions, equal molar amounts of each ethoxide were dissolved in absolute 2-methoxyethanol. The solutions were stirred and distilled for 2 hours. Within one hour, the boiling point of the solutions increased to 125°C indicating progress of

the alcohol exchange reaction. The distillation was followed by refluxing for 22 hours for complete alcohol exchange reaction and complexing. The formation of metal methoxyethoxides was confirmed by ^1H NMR spectroscopy of dried precursors.

$\text{Pb}(\text{Zr}_{0.52}\text{Ti}_{0.48})\text{O}_3$ thin films were prepared from methoxyethanol based precursors. The stoichiometric methoxyethanol based precursors were prepared from lead acetate, zirconium iso-propoxide and titanium iso-propoxide, as starting materials. Through distillation and refluxing of these materials in 2-methoxyethanol under dry nitrogen, polymeric methoxyethoxide complexes were synthesized. By modifying the distillation and refluxing procedure reported by Budd *et al.* [19], residual lead acetate, identified by ^1H NMR, was reduced to less than 10%.

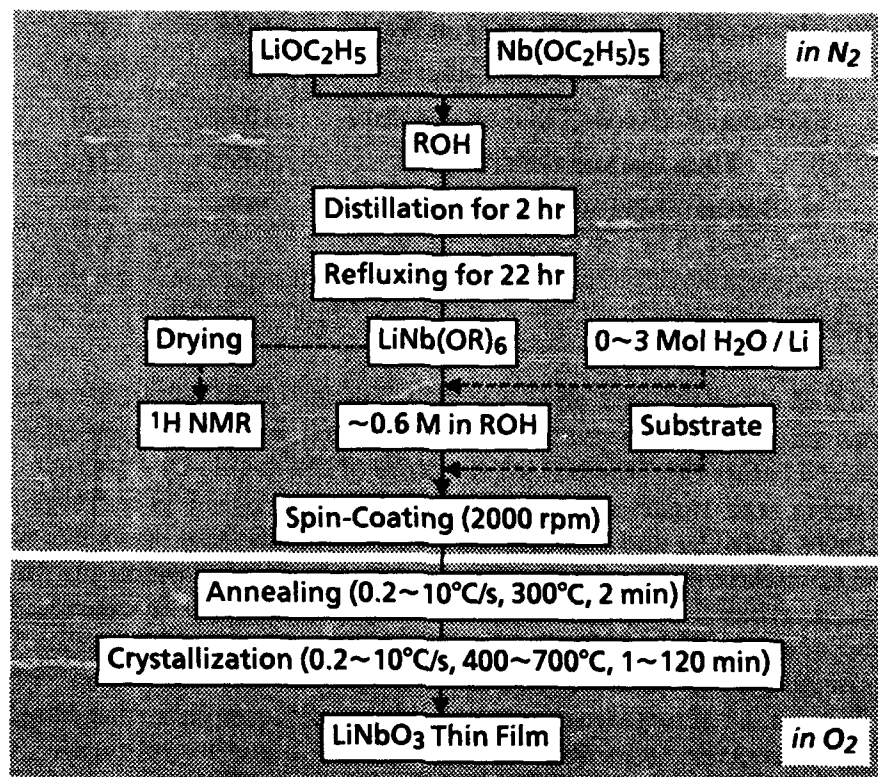


Figure 1. Sol-gel processing for epitaxial LiNbO_3 thin films.

Optically polished single crystal substrates were cleaned in organic solvents, etched, and rinsed in deionized water. The cleaned substrates were ethanol spin-dried followed by spin-coating with the prepared precursors at 2000 rpm in a dry nitrogen environment. The coated substrates were heated in oxygen at 300°C for 2 min in order to oxidize and pyrolyze the coated films. The derived amorphous films were further heated for crystallization at a specified temperature by a conventional annealing (10°C/min) or by a rapid thermal annealing (RTA, 10°C/sec). The thickness of crystallized films were around 100 nm.

Texture and quality of the films were analyzed by θ -2 θ x-ray diffraction (XRD), and XRD pole figures or XRD phi scans, with Cu K α radiation. Their morphology and structure were observed by transmission electron microscopy (TEM), scanning electron microscopy (SEM), and atomic force microscopy (AFM). Refractive indices and thickness of them were measured by ellipsometry with a He-Ne laser.

RESULTS AND DISCUSSION

LiNbO₃ Thin Films

Previous experiments [8-11] revealed a change in orientation of LiNbO₃ from epitaxial to random with an increase in amount of water added to hydrolyze metal ethoxide precursors as summarized in Table II. All LiNbO₃ thin films, prepared from non-prehydrolyzed ethoxide and methoxyethoxide precursors, crystallized epitaxially on sapphire (110) and (001) substrates at temperature over 400°C. XRD patterns of LiNbO₃ prepared from a methoxyethoxide solution and crystallized on sapphire (110) and (001) substrates at 450°C by an RTA process are shown in Fig. 2. XRD patterns of these thin films indicated no Li-deficient phase and single orientation of LiNbO₃ (110) // sapphire (110) or LiNbO₃ (001) // sapphire (001). XRD pole figures for the (012) plane of these LiNbO₃ thin films showed symmetric spot patterns with the same rotation angles as those of the (012) plane of sapphire substrates. The results indicate in-plane orientations of LiNbO₃ [001] // sapphire [001] for LiNbO₃ (110) // sapphire (110) and LiNbO₃ [100] // sapphire [100] for LiNbO₃ (001) // sapphire (001). Fig. 3 shows a typical pole figure for the (012) plane of LiNbO₃ on sapphire (001) crystallized at 700°C.

Table II. Effect of hydrolysis on orientation of LiNbO_3 thin films on sapphire (110) and (001) prepared from $\text{LiNb}(\text{OC}_2\text{H}_5)_6$.

Annealing Temp. ($^{\circ}\text{C}$)	3 mol $\text{H}_2\text{O}/\text{Li}$		1 mol $\text{H}_2\text{O}/\text{Li}$		0 mol $\text{H}_2\text{O}/\text{Li}$	
	(110)	(001)	(110)	(001)	(110)	(001)
400	R	R	O	O	E	E
500	R	R	O	O	E	E
600	R	R	O	O	E	E
700	R	R	R	O	E	E

R = Random, O = Oriented, E = Epitaxial

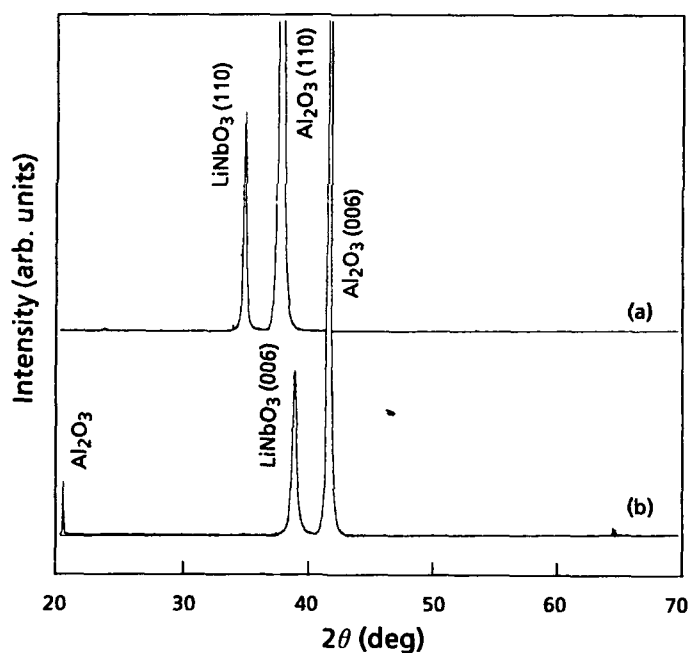


Figure 2. XRD patterns of LiNbO_3 thin films prepared from $\text{LiNb}(\text{OC}_2\text{H}_4\text{OCH}_3)_6$ at 450°C , on sapphire (a) (110) and (b) (001).

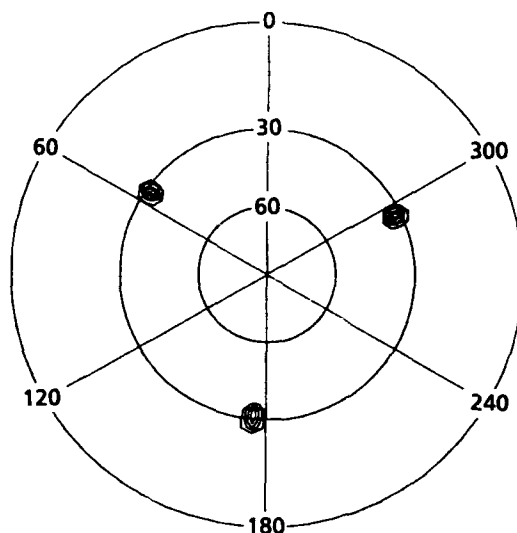


Figure 3. Typical XRD pole figure for (012) plane of LiNbO_3 thin film crystallized on sapphire (001) at 700°C .

As reported before [9-11], epitaxial LiNbO_3 thin films prepared from an ethanol based precursor and annealed at 400°C looked dense and smooth, although they had micro porosity of 10 nm in diameter when they were observed by TEM. Pores of up to 100 nm in diameter were observable by SEM when these epitaxial LiNbO_3 thin films were annealed at 700°C , although they still showed better quality than oriented or polycrystalline LiNbO_3 thin films in terms of density and refractive index. Fig. 4(a) is a SEM image of an epitaxial LiNbO_3 thin film prepared on sapphire (110) from an ethanol based precursor and annealed at 700°C . In contrast, epitaxial LiNbO_3 thin films prepared on sapphire (110) from a methoxyethanol based precursor and annealed at 700°C were fully transparent and denser than the above LiNbO_3 as shown in Fig. 4(b). In addition to the precursor chemistry, the rapid heating rate, as fast as $10^\circ\text{C}/\text{sec}$, reduced the number and size of pores. The effect of heating rate on the porosity of LiNbO_3 thin films is in agreement with the report by Eichorst and Payne when they prepared polycrystalline LiNbO_3 on silicon [20].

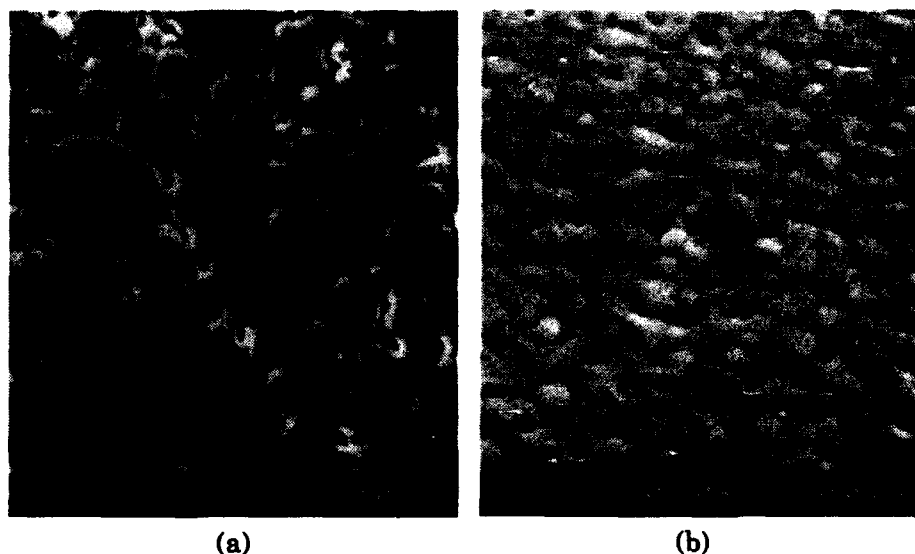


Figure 4. SEM of epitaxial LiNbO_3 prepared from (a) $\text{LiNb}(\text{OC}_2\text{H}_5)_6$ and (b) $\text{LiNb}(\text{OC}_2\text{H}_4\text{OCH}_3)_6$, on sapphire (110) at 700°C .

XRD data and refractive indices of epitaxial LiNbO_3 thin films prepared on sapphire substrates are summarized in Table III. As suggested by the SEM of LiNbO_3 thin films, porous LiNbO_3 prepared from the ethanol based precursor showed lower refractive indices than dense LiNbO_3 prepared from the methoxyethanol based precursor. RTA processed LiNbO_3 had relatively higher refractive indices than LiNbO_3 annealed at a conventional slow heating rate of $10^\circ\text{C}/\text{min}$. The slightly higher refractive indices of the RTA processed LiNbO_3 than single crystal values may be caused by residual stress in LiNbO_3 . In contrast, RTA processed LiNbO_3 had relatively large XRD rocking curve full width at half maxima (FWHM) compared with those of LiNbO_3 annealed at a slow heating rate. LiNbO_3 thin films on sapphire (110) derived from the methoxyethanol based precursors and annealed at 700°C with RTA had rocking curve FWHMs for (110) less than 0.4° . LiNbO_3 grown on sapphire (001) showed larger rocking curve FWHMs than those of LiNbO_3 on sapphire (110). RTA processed LiNbO_3 derived from the

methoxyethanol based precursor started to crystallize epitaxially at 400°C, as mentioned above, and showed almost similar refractive indices above 600°C. These LiNbO₃ thin films were epitaxial, even with the short annealing time of 1 min at 700°C, although these LiNbO₃ required more than 5 min for the densification to show high refractive indices close to single crystal values.

Table III. XRD data and refractive indices of LiNbO₃ thin films crystallized on sapphire at 700°C for 30 min.

Precursor	Orientation	Heating rate (°C/sec)	Rocking curve FWHM for (110) or (006) (deg) ¹⁾	Refractive index ²⁾
LiNb(OC ₂ H ₅) ₆	(110)	0.17	0.17	2.175
LiNb(OC ₂ H ₄ OCH ₃) ₆	(110)	0.17	0.22	2.270
LiNb(OC ₂ H ₅) ₆	(110)	10	0.50	2.183
LiNb(OC ₂ H ₄ OCH ₃) ₆	(110)	10	0.39	2.294
LiNb(OC ₂ H ₄ OCH ₃) ₆	(001)	10	1.57	2.264

¹⁾ On sapphire (110) = 0.072 deg, ²⁾ Bulk LiNbO₃ = 2.201~2.289

In differential scanning calorimetry (DSC) of dried precursors shown in Fig. 5, the peak of the exotherm around 270°C, due to oxidation and pyrolysis of organic groups of the ethanol based precursor, was very sharp (1.94×10^3 J/s·mol), while that of the methoxyethanol based precursor was mild (0.83×10^3 J/s·mol). This fact suggests that the formation of pores could be affected by the formation of gases during the oxidation and pyrolysis of organic groups, and could be suppressed by the chemical modification of the precursors as examined in the present study.

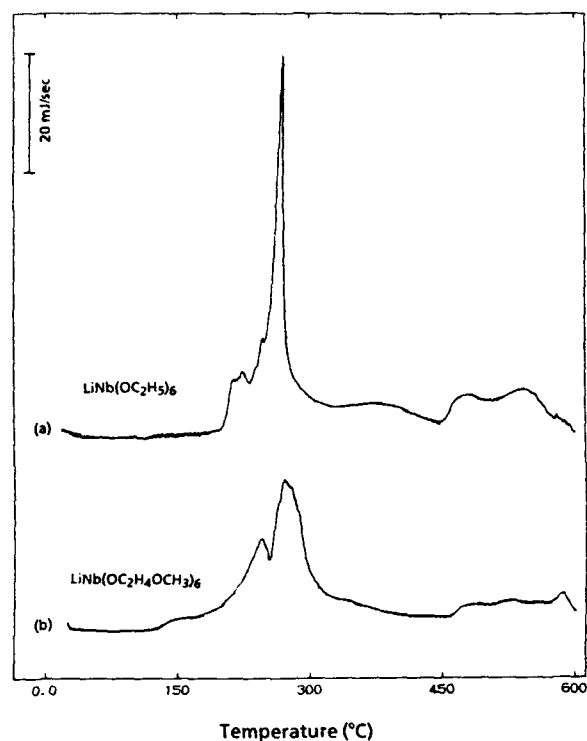


Figure 5. DSC curves of (a) dried $\text{LiNb}(\text{OC}_2\text{H}_5)_6$ powder and (b) dried $\text{LiNb}(\text{OC}_2\text{H}_4\text{OCH}_3)_6$ powder in O_2 .

LiTaO_3 and KNbO_3 Thin Films

With the present process using methoxyethanol based precursors and RTA, transparent and epitaxial LiTaO_3 thin films were successfully crystallized on sapphire (110) and (001) at 700°C [17]. No misoriented planes were observed in XRD patterns. In-plane orientations identified by XRD phi scans were LiTaO_3 [001] // sapphire [001] for LiTaO_3 (110) on sapphire (110), and LiTaO_3 [100] // sapphire [100] for LiTaO_3 (001) on sapphire (001). Rocking curve FWHMs of LiTaO_3 thin films on sapphire (110) and (001) were 0.34° for (110) plane and 1.12° for (006) plane, respectively. The films looked smooth and crack-free when they were observed by SEM. LiTaO_3 thin films, which have higher melting

temperature by about 400°C than LiNbO₃, showed relatively lower refractive indices than that of single crystal LiTaO₃ ($n_o=2.176$, $n_e=2.180$) as compared with LiNbO₃ thin films. Refractive indices of epitaxial LiTaO₃ thin films on sapphire (110) and (001) were 2.098 and 1.982, respectively. Highly oriented KNbO₃ thin films using methoxyethanol based precursors and RTA were also obtained on MgO (100) at 700°C as shown in Fig. 6. Rocking curve FWHM of KNbO₃ (100) were 2.5°.

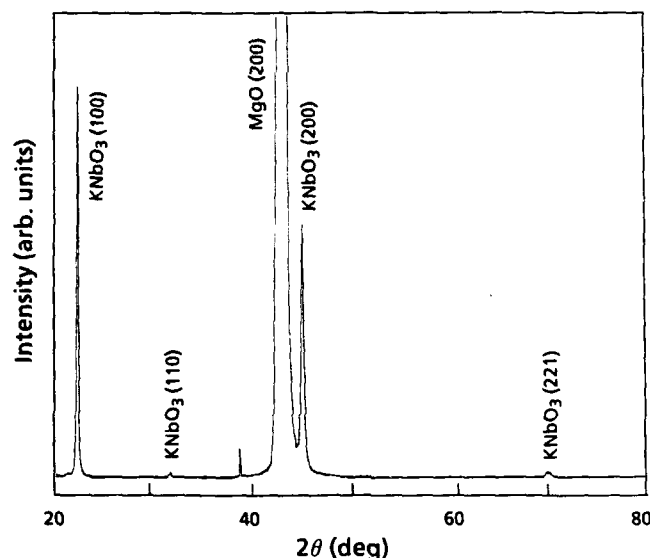


Figure 6. XRD pattern of KNbO₃ thin film crystallized on MgO (100) at 700°C.

PZT Thin Films

Pb(Zr_{0.52}Ti_{0.48})O₃ (PZT) thin films prepared from a non-prehydrolyzed methoxyethoxides and crystallized by RTA process had (001) or (100) orientation to SrTiO₃ (100) and MgO (100) substrates as shown in XRD patterns of Fig. 7. XRD patterns and phi scans of these thin films indicated epitaxial orientations of PZT (100) // SrTiO₃ (100) with PZT [001] // SrTiO₃ [001] and PZT (100) // MgO (100) with PZT [001]

// MgO [001]. PZT thin films prepared on sapphire(001) showed major (111) and minor (110) reflections in XRD patterns. The preferred (111) orientation may result from the similar oxygen packing symmetry between the sapphire (001) ((0001)) plane and the PZT (111) plane. The PZT thin films on SrTiO₃(100) started to crystallize epitaxially even at 425°C. The perovskite phase PZT thin films on MgO (100) were observed after 575°C heat treatment.

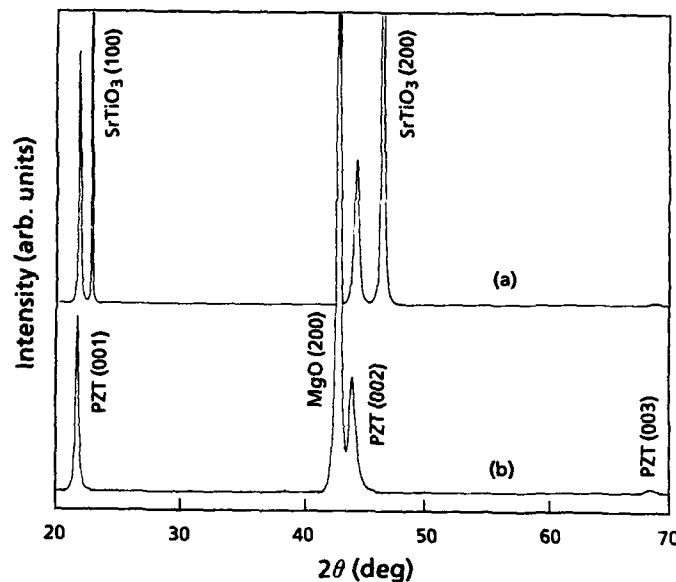


Figure 7. XRD patterns of PZT thin films crystallized at 650°C, on (a) SrTiO₃ (100) and (b) MgO (100).

XRD data and refractive indices for epitaxial PZT thin films crystallized at 650°C are summarized in Table IV. PZT prepared from partially hydrolyzed precursors showed larger XRD rocking curve FWHMs and weaker peak intensities than those of PZT films prepared from non-hydrolyzed precursors, although PZT films prepared from partially hydrolyzed precursors still had single orientation unlike the previous LiNbO₃ thin films. PZT prepared on SrTiO₃ (100) showed quite smaller XRD rocking curve FWHM (0.10° for (100) plane) than PZT prepared on MgO (100). PZT prepared from partially hydrolyzed

precursors also showed relatively lower refractive indices than PZT prepared from non-hydrolyzed precursors. PZT on MgO (100) started to crystallize epitaxially at 575°C, as mentioned above, and PZT films were epitaxial even with a short annealing time of 1 min at 650°C.

Table IV. XRD data and refractive indices of PZT thin films crystallized at 650°C.

H ₂ O (mol/Pb)	Substrate	Orientation	Intensity (k cps)	Rocking curve FWHM for (100) (deg) ²⁾	Refractive index
1 + HNO ₃ ¹⁾	MgO (100)	(100)	40	2.75	2.595
1 + NH ₄ OH ¹⁾	MgO (100)	(100)	40	2.65	2.635
0	MgO (100)	(100)	120	1.48	2.641
0	SrTiO ₃ (100)	(100)	455	0.10	2.631
0	Al ₂ O ₃ (0001)	(111)+(110)	5	—	2.531

1) Partial hydrolysis, 2) Resolution on sapphire(110) = 0.072 deg

Fig. 8 is a SEM image of an epitaxial PZT thin film prepared on SrTiO₃ (100) and annealed at 650°C. The epitaxial PZT thin film showed no obvious contrast, such as, grains, pores, and cracks from SEM observation. Observation by AFM presented surface roughness of PZT smaller than 10 nm. The quite flat surface of the PZT is promising for optical waveguide applications. In addition to the surface morphology of the PZT, the combination of PZT thin films with substrates of lower refractive indices is a crucial issue since this combination reduces the required thickness of PZT for optical waveguiding. The refractive index of SrTiO₃ is 2.399, that of MgO is 1.735, and that of PZT thin film on MgO observed in this study was around 2.64. According to our theoretical calculation, using these refractive indices, the critical thickness of PZT on SrTiO₃ is 400 nm, whereas, that of PZT on MgO is 190 nm for TE₁ mode prism coupling. Actually, Wood *et al.* observed only TE₀ mode optical coupling in a sol-gel derived PZT on SrTiO₃ of 280 nm in thickness, although refractive indices of their PZT were relatively smaller than the values in the present study [21].

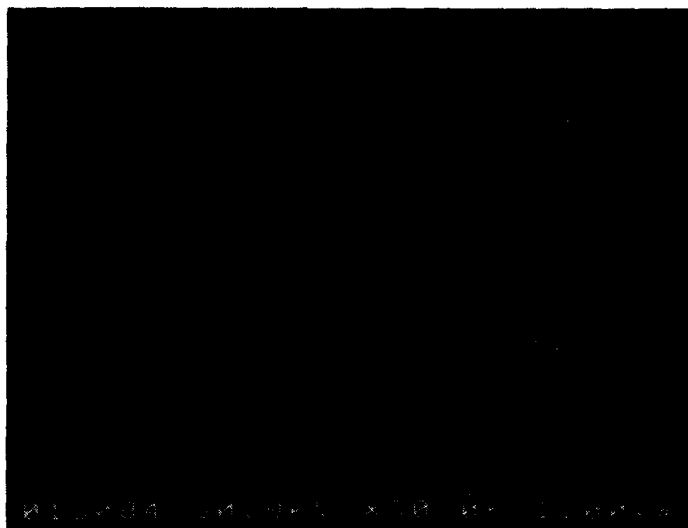


Figure 8. SEM of epitaxial PZT on $\text{SrTiO}_3(100)$ crystallized at 650°C .

CONCLUSIONS

The metal alkoxide based chemical solution process seems to be an attractive approach for preparing a variety of epitaxial and oriented ferroelectric thin films. Precursor chemistry and annealing condition were identified as critical points to obtain high quality epitaxial and oriented ferroelectric thin films. The process of utilizing chemical modification of non-hydrolyzed metal alkoxide precursors and rapid thermal annealing improved the quality of epitaxial LiNbO_3 thin films. Rocking curve FWHMs for (110) plane were less than 0.4° and refractive indices were similar to single crystal values for epitaxial LiNbO_3 crystallized on sapphire (110) at 700°C . The present process also gave crack free epitaxial or oriented LiTaO_3 , KNbO_3 , and PZT thin films. Non-hydrolyzed precursors gave epitaxial PZT with better quality than partially hydrolyzed precursors. Rocking curve FWHMs for (100) plane were as small as 0.10° for PZT (100) on $\text{SrTiO}_3(100)$ and 1.48° for PZT (100) on $\text{MgO}(100)$. The demonstrated structure of PZT on MgO is one of promising structures for optical waveguides in practice.

ACKNOWLEDGMENTS

The author is thankful to Prof. M. J. Cima and Dr. W. E. Rhine of MIT for their valuable comments. The author also would like to thank Dr. D. K. Fork of Xerox Palo Alto Research Center for XRD phi scan measurement, and Mr. S. Nakamura and Mr. H. Moriyama for their technical assistance and Dr. A. Inoue for his helpful encouragement.

REFERENCES

1. S. Takada, M. Ohnishi, H. Hayakawa, and N. Mikoshiba, "Optical Waveguides of Single Crystal LiNbO_3 Film Deposited by RF Sputtering," *Appl. Phys. Lett.*, **24**, 490-492 (1974).
2. H. Adachi, T. Kawaguchi, M. Kitabatake, and K. Wasa, "Dielectric Properties of PLZT Epitaxial Thin Films," *Jpn. J. Appl. Phys.*, **22**, suppl. 22-2, 11-13 (1983).
3. M. S. Ameen, T. M. Graettinger, S. H. Rou, H. N. Al-Shareef, K. D. Gfford, O. Auchello, and A. I. Kingon, "Processing and Structural Characterization of Ferroelectric Thin Films Deposited by Ion Beam Sputtering," *Mat. Res. Soc. Symp. Proc.*, **200**, 65-76 (1990).
4. K. Nashimoto, D. K. Fork and T. H. Geballe, "Epitaxial Growth of MgO on GaAs (001) for Growing Epitaxial BaTiO_3 Thin Films by Pulsed Laser Deposition," *Appl. Phys. Lett.*, **60**, 1199-1201 (1992).
5. M. de Keijser, G. J. Dormans, J. F. Cillessen, D. M. de Leeuw, and H. W. Zandbergen, "Epitaxial PbTiO_3 Thin Films Grown by Organometallic Chemical Vapor Deposition," *Appl. Phys. Lett.*, **58**, 2636-2638 (1991).
6. D. P. Partlow and J. Gregg, "Properties and Microstructure of Thin LiNbO_3 Films Prepared by a Sol-Gel Process," *J. Mat. Res.*, **2**, 595-605 (1987).
7. S. Hirano and K. Kato, "Preparation of Crystalline LiNbO_3 Films with Preferred Orientation by Hydrolysis of Metal Alkoxides," *Adv. Ceram. Mat.*, **3**, 503-506 (1988).
8. K. Nashimoto, M. J. Cima, and W. E. Rhine, "Effect of Water to Alkoxide Ratio on Crystallization of LiNbO_3 Powders and Thin Films," The Am. Ceram. Soc's Electron. Div. Mtg., Orlando, (1990).
9. K. Nashimoto and M. J. Cima, "Epitaxial LiNbO_3 Thin Films Prepared by a Sol-Gel Process," *Mater. Lett.*, **10**, 348-354 (1991).

10. K. Nashimoto, M. J. Cima, and W. E. Rhine, "Microstructural Evolution of Epitaxial LiNbO_3 Thin Films Derived from Metal Alkoxide Solutions," *Mat. Res. Soc. Symp. Proc.*, **202**, 439-444 (1991).
11. K. Nashimoto, M. J. Cima, and W. E. Rhine, "Structure and Optical Properties of Polycrystalline and Epitaxial LiNbO_3 Thin Films Derived by a Sol-Gel Method," *Ceramic Transactions*, **25**, 371-383 (1992).
12. C. Chen, D. F. Ryder, Jr., and W. A. Spurgeon, "Synthesis and Microstructure of Highly Oriented Lead Titanate thin Films Prepared by a Sol-Gel Method," *J. Am. Ceram. Soc.*, **72**, 1495-1498 (1989).
13. S. L. Swartz, P. J. Melling, and C. S. Grant, "Ferroelectric Thin Films by a Sol-Gel Processing," *Mat. Res. Soc. Proc.*, **152**, 227-232 (1989).
14. K. Okuwada, M. Imai, and K. Kakuno, "Preparation of $\text{Pb}(\text{Mg}_{1/3}\text{Nb}_{2/3})\text{O}_3$ Thin Films by Sol-Gel Method," *Jpn. J. Appl. Phys.*, **28**, L1271-1273 (1989).
15. C. K. Barlingay and S. K. Dey, "Observation of Sol-Gel Solid Phase Epitaxial Growth of Ferroelectric $\text{Pb}(\text{Nb,Zr,Ti})\text{O}_3$ Thin Films on Sapphire," *Appl. Phys. Lett.*, **61**, 1278-1280 (1992).
16. G. Braunstein and R. Paz-Pujalt, "Single-crystal SrTiO_3 Produced by the Method of Metallo-organic Decomposition," *Thin Solid Films*, **216**, 1-3 (1992).
17. K. Nashimoto, "Preparation and Characterization of Sol-Gel Derived Heteroepitaxial LiNbO_3 and LiTaO_3 Thin Films," *Mat. Res. Soc. Symp. Proc.*, **310**, 293-298 (1993).
18. D. J. Eichorst, D. A. Payne, S. R. Wilson, and K. E. Howard, "Crystal Structure of $\text{LiNb}(\text{OCH}_2\text{CH}_3)_6$: A Precursor for Lithium Niobate Ceramics," *Inorg. Chem.* **29**, 1458-1459 (1990).
19. K. D. Budd, S. K. Dey, and D. A. Payne, "Sol-gel Processing of PbTiO_3 , PbZrO_3 , PZT, and PLZT Thin Films," *Brit. Cer. Soc. Proc.*, **36**, 107-121 (1985).
20. D. J. Eichost and D. A. Payne, "Sol-Gel Processing of Lithium Niobate Thin-Layers for Optical Applications," *SPIE Proc.*, **1328**, 456-465 (1990).
21. V. E. Wood, J. R. Busch, S. D. Ramamurthi, and S. L. Swartz, "Guided-wave Optical Properties of Sol-Gel Ferroelectric Films," *J. Appl. Phys.*, **71**, 4557-4566 (1992).

Sol-gel Technology for Ferroelectric Thin Films

You Song Kim(*) and Hyun M. Jang(**)

(*) Research Institute of Industrial Science and Technology (RIST),
Pohang 790-600, Republic of Korea

(**) Department of Materials Science and Engineering,
Pohang University of Science and Technology (POSTECH),
Pohang 790-600, Republic of Korea

Sol-gel-derived ferroelectric thin films can offer particular promise for various microelectronic applications, including FRAM, DRAM elements, thin-film capacitors and pyroelectric IR sensors. In this article, recent progress in the sol-gel processing of two typical ferroelectric thin-film systems is briefly reviewed. These are lead zirconate titanate (PZT) solid solution and $\text{Pb}(\text{Mg}_{1/3}\text{Nb}_{2/3})\text{O}_3$ -based relaxor ferroelectrics. Several examples of the sol chemistry-structures/ferroelectric properties relationships are illustrated using various recent data, including results from the authors' laboratory.

1. Introduction

Materials scientists and engineers pursue new processing methods for the preparation of materials for specific requirements. It has recently been evidenced that sol-gel processing methods have been extensively utilized in preparing the precursor materials for the development of sophisticated and advanced electronic devices [1, 2]. The sol-gel process is particularly beneficial to manufacturing miniaturized components where accurate control of microchemistry is required.

Recently, sol-gel-derived thin films are receiving increased attention for their electrical and optical properties. Among such films, those of ferroelectric ceramics appear to offer particular promise for various microelectronic applications, including ferroelectric random access memories (FRAM), dynamic random access memory (DRAM) elements, optical waveguide devices, thin-film capacitors, and pyroelectric sensors [1, 3]. In view of these applications, this article briefly reviews some of the recent developments in the fabrication of ferroelectric thin films by the sol-gel process. The present discussion will be restricted to two typical Pb-based ferroelectric systems. They are, $\text{Pb}(\text{Zr,Ti})\text{O}_3$ (referred to as PZT) solid solution, and $\text{Pb}(\text{Mg}_{1/3}\text{Nb}_{2/3})\text{O}_3$ -based relaxor ferroelectrics. At the end of the review, we will present recent data from our laboratory and discuss briefly on the processing of $\text{PbMg}_{1/3}\text{Nb}_{2/3}\text{O}_3$ - $\text{PbZn}_{1/3}\text{Nb}_{2/3}\text{O}_3$ (referred to as PMN-PZN) pseudobinary thin film. This system is a promising candidate for the development of IR sensing elements that utilize dielectric bolometer (DB)

To the extent authorized under the laws of the United States of America, all copyright interests in this publication are the property of The American Ceramic Society. Any duplication, reproduction, or republication of this publication or any part thereof, without the express written consent of The American Ceramic Society or fee paid to the Copyright Clearance Center, is prohibited.

mode[4].

2. PZT-based thin films

Recently, sol-gel-derived PZT has been widely used to form thin-film ferroelectrics for nonvolatile memories, electrooptic components, SAW devices and pyroelectric detectors[1]. The first sol-gel PZT thin film was prepared by Fukushima and his co-workers in 1984[5]. They used a solution of lead ethylhexanoate, zirconium acetylacetonate, and titanium butoxide in a butanol solution. The film ($\text{PbZr}_{0.5}\text{Ti}_{0.5}\text{O}_3$) was deposited on fused silica and platinum plates. Only the films deposited on Pt substrates showed a hysteresis loop. A spontaneous polarization of $35.65 \mu\text{C}/\text{cm}^2$, remanent polarization of $30.56 \mu\text{C}/\text{cm}^2$ and a coercive field of $45 \text{ kV}/\text{cm}$ were measured.

In 1985 D. A. Payne and his co-workers at the University of Illinois published a paper on sol-gel PbTiO_3 , PbZrO_3 , PZT, and PLZT[6]. Their process consisted of using lead acetate and both zirconium and titanium alkoxides (n-propoxide and isopropoxide) in a methoxyethanol base. $0.2 \sim 0.7$ molar solutions were spin-cast onto substrates of silicon and fused silica. Perovskite PZT was obtained only after annealing at temperatures greater than 500°C , but not until a thicker layer had been put down. An addition of water to the precursor solution helped reduce the problem associated with microcracking of films thicker than $0.1 \mu\text{m}$. In a later paper by the same authors, PZT (53/47) was spun onto Pt substrates and fired in air for 10 minutes at 650°C [7]. They reported a coercive field of $40 \text{ kV}/\text{cm}$ and a remanent polarization of $36 \mu\text{C}/\text{cm}^2$.

Several papers on sol-gel PZT have been published by J. D. Mackenzie and his co-workers at UCLA[8, 9]. Sol-gel PZT was prepared using lead 2-ethylhexanoate, titanium isopropoxide, and zirconium n-propoxide. PZT thin films were applied to various substrates using a multiple dip coating process. The study on the ferroelectric hysteresis loop of the films using metal-ferroelectric-semiconductor configuration yielded a remanent polarization of $2.2 \mu\text{C}/\text{cm}^2$ and a coercive field of $7.5 \text{ kV}/\text{cm}$. The observed low remanent polarization and high coercive field of the PZT film compared to the bulk PZT was attributed to the small grain size[9]. Asymmetric hysteresis loops were observed. The mechanism associated with this asymmetry was attributed to the space charge compensating the contact potential difference at the interface of ferroelectric-semiconductor (PZT-Si)[9].

More recently, PZT thin films on Pt-coated Si were prepared by a modified sol-gel process using acetylacetonate as the lead source[10]. The metal (Pb) chelate complex with β -diketone seemed to be more stable towards hydrolysis than the widely used lead acetate hydrate precursor.

Sol-gel-derived PZT films typically have microstructures consisting of micrometer-sized perovskite 'rosettes' (single-crystalline radial arm emanating from a central nucleation site), surrounded by fine grained ($< 200 \text{ \AA}$) pyrochlore phase, especially in films with high Zr/Ti ratios[11, 12]. No such crystallites are observed in sputtered films. Sol-gel PZT films generally exhibit a finer perovskite grain size excluding rosettes. Such finely grained microstructures, coupled with better control of stoichiometry and enhanced

homogeneity, are responsible for superior dielectric behavior compared with sputtered films[13].

The degree of preferred orientation and its direction are important in determining the final film properties since the spontaneous polarization is directed along the direction of the preferred orientation. Thus, considerable efforts have been directed towards tailoring the orientation of PZT films to optimize ferroelectric properties. It is easier to obtain epitaxial effects with tetragonal PZT films than rhombohedral films. (111) oriented, tetragonal-rich PZT 40/60 films have been reported on (111) oriented Pt[14], whereas rhombohedral-rich PZT 60/40 films on (111) Pt did not exhibit preferred orientation[15]. More recently, Tuttle et al.[16] have fabricated highly oriented pseudocubic (100) PZT 40/60 thin films on both insulating (100) MgO and (100) Pt-coated conducting MgO substrates with (100) : (111) intensity ratios of 1000 : 1. It was shown that highly (001) oriented PZT 40/60 films had higher remanent polarization ($61 \mu\text{C}/\text{cm}^2$ compared to $0.41 \mu\text{C}/\text{cm}^2$) and lower relative dielectric permittivity (368 compared to 466) than PZT 40/60 films that were randomly oriented[16]. However, it was reported that the magnitude of the coercive field was not affected by the degree of preferred orientation[11].

3. PMN-based relaxor thin films

Relaxor ferroelectrics undergo a diffused phase transition (DPT) and have a broad Curie maximum rather than the sharp and distinct T_c of normal ferroelectrics. This effect arises from the distribution of the short-range ordered, chemically inhomogeneous microregions[17]. Each microregion (Känzig) has its own T_c . Lattice and cation disorder is known to be responsible for the compositional heterogeneity. Among the relaxor ferroelectrics, PMN is most widely studied. Its high peak value of relative permittivity of $> 15,000$ near room temperature make it one of the most attractive materials for multilayer capacitors and electrostrictive actuators.

PMN thin films were prepared from alkoxide-based solutions by sol-gel methods[18, 19, 20]. In the all-alkoxide route[18, 19], pure perovskite phase was formed at 800°C on single crystal MgO. However, a small amount of pyrochlore phase remained on Pt/Si wafer. Oriented films could be prepared on Pt/Si, with high initial heating rates ($\sim 1 \times 10^5^\circ\text{C}/\text{h}$) favoring (100) over (111) perovskite orientations[19].

In the 2-methoxyethanol route[20] for the preparation of PMN sol, the lead alkoxide precursor was first synthesized by the reflux-distillation of lead acetate hydrate in 2-methoxyethanol. The lead alkoxide precursor was subsequently combined with the presynthesized Mg-Nb double alkoxide solution. The mixed precursor solution was then reacted at $\sim 130^\circ\text{C}$ to form the Pb-Mg-Nb triple alkoxide solution. For the PMN film prepared by the 2-methoxyethanol route, (100) oriented films were obtained by fast-firing at 800°C for 5 min[20]. However, small amounts of pyrochlore phase ($\sim 5\%$) were observed. The relative dielectric permittivity of the thin film was estimated to be 1,000 to 1,250 at room temperature, which is considerably less than the value for bulk polycrystalline PMN at room temperature. The

presence of residual pyrochlore as well as other factors such as grain size, stress and interfacial effects seem to be responsible for the observed low dielectric permittivity.

The peak dielectric permittivity of PMN occurs approximately at -15°C . It can be shifted to higher temperature by the formation of a solid solution with the normal perovskite ferroelectrics, PbTiO_3 (PT). The addition of PT also increases the spontaneous polarization, P_s [21]. PMN-PT thin films were prepared by spin casting partially hydrolyzed alkoxide-based solutions (in the 2-methoxyethanol route) on Pt/Si substrates[21, 22]. Rapid heat treatment after each solution deposition step was found to be the most effective method for the stabilization of perovskite phase[22]. The highest relative permittivities ($\epsilon_r > 2,000$ with $\tan\delta < 0.03$) were obtained for thin layers having the composition 0.9PMN-0.1PT[22]. The maximum value of 2,200 is one of the highest reported ϵ_r of any sol-gel-derived ferroelectric thin film.

4. PMN-PZN pseudobinary system

Lead zinc niobate, $\text{PbZn}_{1/3}\text{Nb}_{2/3}\text{O}_3$ (abbreviated as PZN hereafter), is also a relaxor type ferroelectric material with a maximum ϵ_r around 140°C . The single crystal of perovskite PZN (prepared by the nonequilibrium flux method) exhibits anomalously large relative dielectric permittivity, together with excellent electrostrictive and optical properties[23]. Therefore, the addition of ~ 20 mol% PZN to PMN is expected to adjust the Curie temperature for $\epsilon_{r(\text{max})}$ to room temperature without deteriorating dielectric and electrostrictive properties of PMN provided that the perovskite phase is stabilized in the resulting solid solution. Examination of dielectric properties of 0.85PMN-0.15PZN pseudobinary system (high ϵ_r , large $(\partial\epsilon_r/\partial T)$, low $\tan\delta$, and $T_c \leq T_{\text{ambient}}$) suggests that the PMN-PZN thin film can be used for the fabrication of the DB (dielectric bolometer) mode IR sensing device. It is also a possible candidate for DRAM and capacitor applications.

The preparation of microchemically homogeneous perovskite PMN-PZN (abbreviated as PMZN) thin film is difficult since one of the metal alkoxides tends to precipitate preferentially due to their mutually different hydrolysis/condensation rates, in addition to the thermodynamic instability of perovskite PZN[24]. Therefore, we have prepared a stable multiple precursor sol which eliminates the problems associated with the differential rates of hydrolysis. A schematic flow diagram for the preparation of PMZN (0.85PMN-0.15PZN) thin films is shown in Fig. 1.

The XRD patterns of PMZN bulk gel and thin film deposited on Pt-coated MgO (100) type planes are shown in Fig. 2. The bulk gel heat-treated at 900°C shows a small amount of remnant pyrochlore phase. On the other hand, perovskite phase was fully stabilized in the thin layer. A strong preferential orientation of (100) type planes of the perovskite phase was observed in the PMZN thin film deposited on (111) plane of Pt (Fig. 2). As shown in Fig. 3, a full densification of the PMZN thin film was achieved within 10 min at 950°C (rapid heat-treatment). The microstructure of the thin film is characterized by uniformly sized perovskite grains, with the average grain size slightly less than $0.5\text{ }\mu\text{m}$.

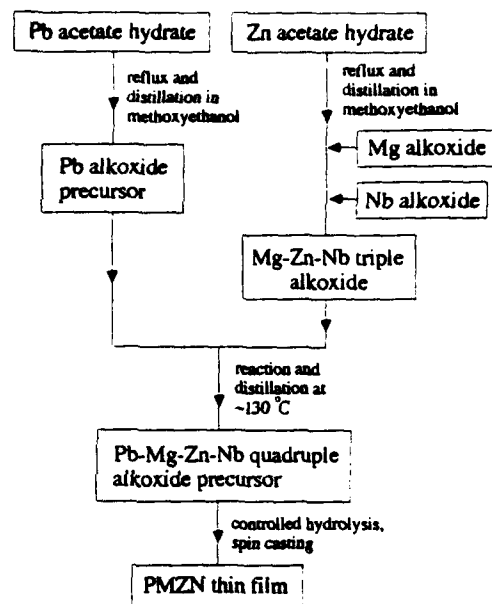


Fig. 1. Flow diagram for the preparation of PMZN thin film.

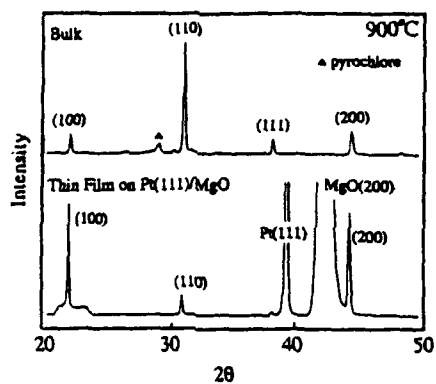


Fig. 2. XRD patterns of PMZN bulk gel and thin film deposited on (111) Pt-coated MgO (100) type planes.



Fig. 3. Scanning electron micrograph of PMZN thin film heat-treated at 950 °C for 10 min.

Aging the PMZN sol significantly affected the orientation of perovskite grains in the thin film on MgO substrate. This was attributed to changes in the gel structure which was evolved from aged solutions. As shown in Fig. 4 (a), the Pb-Mg-Zn-Nb multiple sol undergoes a transition in the rheological behavior from pseudoplastic to thixotropic after 40 days of aging. The extent of preferential orientation of (100) type planes was significantly reduced for the PMZN thin film prepared from the thixotropic sol, as indicated in Fig. 4 (b). The result indicates that the change in the network structure induced by the aging of the sol influences the orientation of perovskite grains after thin-film formation.

5. Conclusions

Sol-gel-derived ferroelectric thin films generally exhibit superior electrical properties in many aspects compared with physically deposited films. In PZT-based films, sol-gel process is advantageous in terms of improved microchemical homogeneity, ease of fabrication, and the ability to obtain films with small perovskite-grain sizes and uniform microstructures. On the other hand, thin films of PMN-based relaxor ferroelectrics generally exhibit inferior electrical properties compared with those of bulk ceramics. The main cause of this observation seems to be related with the well-known difficulty in the stabilization of perovskite phase.

PMN-PZN pseudobinary thin films were fabricated by spin casting partially hydrolyzed quadruple alkoxides-based solution on platinized MgO substrates. The perovskite phase was successfully stabilized by rapid heat treatment above 900 °C. A strong preferential orientation of (100) type planes of the perovskite phase was observed. It was also observed that aging the sol significantly influenced the orientation of perovskite grains after thin-film formation.

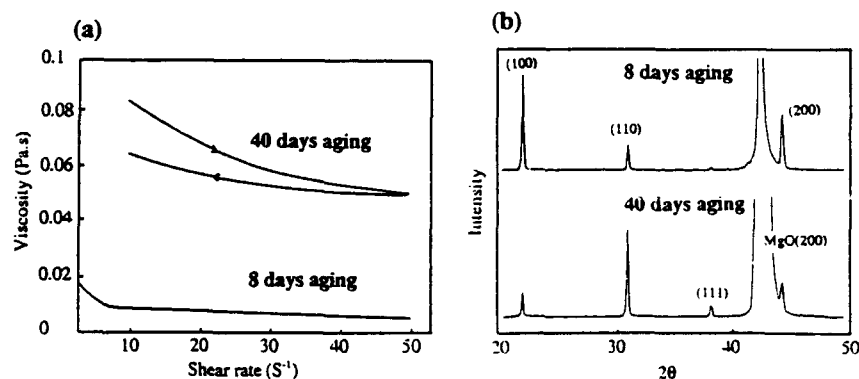


Fig. 4. (a) Viscosity versus shear rate for two PMZN sols aged for 8 and 40 days, showing a transition in rheological behavior. (b) XRD patterns of PMZN thin films derived from the sols aged for 8 and 40 days.

References

- [1] L. M. Sheppard, *Ceram. Bull.* 71 (1992) 85.
- [2] G. Yi and M. Sayer, *Ceram. Bull.* 70 (1991) 1173.
- [3] D. R. Uhlmann, G. Teowee, J. M. Boulton and B. J. J. Zelinski, *Mater. Res. Soc. Symp. Proc.* 180 (1990) 645.
- [4] R. W. Whatmore, P. C. Osbond and N. M. Shorrocks, *Ferroelectrics* 76 (1987) 351.
- [5] J. Fukushima, K. Kodaira and T. Matsushita, *J. Mater. Sci.* 19 (1984) 595.
- [6] K. D. Budd, S. K. Dey, and D. A. Payne, *British Ceram. Proc.* 36 (1985) 107.
- [7] S. K. Dey, K. D. Budd and D. A. Payne, *IEEE Transactions on Ultrasonics, Ferroelectrics and Frequency Control*, 35 (1988) 80.
- [8] C. J. Chen, E. T. Wu, Y. H. Xu, K. C. Chen, and J. D. Mackenzie, *Proc. of the First Symp. on Integrated Ferroelectrics CMC-89* (1989) 185.
- [9] C. J. Chen, E. T. Wu, Y. H. Xu, K. C. Chen, and J. D. Mackenzie, *Ferroelectrics* 112 (1990) 321.
- [10] U. Selvaraj, K. Brooks, A. V. Prasadaraio, S. Komarneni, R. Roy, and L. E. Cross, *J. Am. Ceram. Soc.* 76 (1993) 1441.
- [11] G. A. C. M. Spieringo, M. J. E. Ulenaers, G. L. M. Kampschöer, H. A. M. Van Mal, and P. K. Larsen, *J. Appl. Phys.* 70 (1991) 2290.
- [12] A. H. Carino, B. A. Tuttle, D. H. Doughty, and S. L. Martin, *J. Am. Ceram. Soc.* 74 (1991) 1455.
- [13] D. R. Uhlmann, G. Teowee, J. M. Boulton, S. Motakef, and S. C. Lee, *J. Non-cryst. Solids* 147 & 148 (1992) 409.
- [14] B. M. Melnick, J. D. Cuchiaro, L. D. McMillian, C. A. Paz de Araujo, and J. F. Scott, *Ferroelectrics* 112 (1990) 329.
- [15] R. W. Vest and W. Zhu, *Ferroelectrics* 119 (1991) 61.
- [16] B. A. Tuttle, J. A. Voigt, D. C. Goodnow, D. L. Lamppa, T. J. Headley, M. O. Eatough, G. Zender, R. D. Nasby, and S. M. Rodgers, *J. Am. Ceram. Soc.* 76 (1993) 1537.
- [17] C. A. Randall, A. S. Bhalla, T. R. Shrout, and L. E. Cross, *J. Mater. Res.* 5 (1990) 829.
- [18] K. Okuwada, M. Imai and K. Kakuno, *Jpn. J. Appl. Phys.* 28 (1989) L1271.
- [19] K. Okuwada, S. Nakamura, M. Imai and K. Kakuno, *Jpn. J. Appl. Phys.* 29 (1990) 1153.
- [20] L. F. Francis, Y. J. Oh and D. A. Payne, *J. Mater. Sci.* 25 (1990) 5007.
- [21] L. F. Francis and D. A. Payne, *Mater. Res. Soc. Symp. Proc.* 200 (1990) 173.
- [22] L. F. Francis and D. A. Payne, *J. Am. Ceram. Soc.* 74 (1991) 3000.
- [23] S. Nomura and J. Kuwata, *Mater. Res. Bull.* 14 (1979) 769.
- [24] H. M. Jang, S. H. Oh, and J. H. Moon, *J. Am. Ceram. Soc.* 75 (1992) 82.

DECREASE OF DEFECTS OF SOL-GEL DERIVED PbTiO_3 THIN FILM AND ITS GRAIN SIZE EFFECT ON FERROELECTRIC PROPERTIES

K. Saegusa and Y. Suzuki.
Sumitomo Chemical Co., Tsukuba, Ibaraki 300-32, Japan

ABSTRACT

A model was proposed that the pore interconnection within thin films during firing is responsible to the shorts of the films. According to this model, shorts can be significantly decreased by the suppression of the pore growth. This could be achieved by optimizing the hydrolysis condition of the coating solution and the rapid thermal annealing (RTA) of the film. The effect of the grain size on the dielectric properties was investigated. Grain size less than 50 nm showed to cause a decrease of the dielectric constant of PbTiO_3 thin film.

INTRODUCTION

Sol-gel derived thin films^{1,2} are often found to have defects that cause shorts, which make various applications difficult. One of the solutions is to suppress the growth and the interconnection of pores. The final sintered film is known to be affected by the gel structure of the precursor. When the particles and pores in a gel are very fine, there is a significant grain growth because of the high surface energy of fine particles leaving larger pores. We can expect that the larger particles in a precursor gel will result in finer grains (pores) in the sintered body. In the firing process, RTA is known to give smaller grain size than the conventional firing. We tried to avoid shorts utilizing the both methods. The effect of the preparation condition of the spinning solution (pH and water to alkoxide ratio), and that of the heating condition on the microstructure and the occurrence of shorts of the thin film was examined.

Another object of this paper is to understand the grain size effect on the electrical properties. Ferroelectric materials are known to have the grain size effects. Finer grains than a certain critical size would not show ferroelectricity. There are many papers that reported the grain size effect in ferroelectric systems.³⁻⁵ The absence of ferroelectric domains in grains smaller than 0.5 μm and a minimum domain width of 0.07 μm for $\sim 0.5\text{-}\mu\text{m}$ grains are also reported⁶. The critical particle size of BaTiO_3 as 0.12 μm and that of PbTiO_3 at 400°C as 0.02 μm is reported⁷⁻⁸. There is another paper that reports the critical

To the extent authorized under the laws of the United States of America, all copyright interests in this publication are the property of The American Ceramic Society. Any duplication, reproduction, or republication of this publication or any part thereof, without the express written consent of The American Ceramic Society or fee paid to the Copyright Clearance Center, is prohibited.

size of PbTiO_3 as $0.005 \mu\text{m}^9$. One of the authors also reported the grain size effect in the $\text{Pb}_{1-x}\text{Ba}_x\text{TiO}_3$ system¹⁰. But there are still a disagreement on critical crystallite size partly because there are not sufficient number of experimental data.

EXPERIMENT

Sample preparation

One mole of lead acetate trihydrate was dissolved in methoxyethanol and heated and distilled at 125°C for the dehydration and the reaction with the alcohol. One mole of titanium tetraisopropoxide was added to the solution and heated at 120°C to form the lead titanium alkoxide complex. Then 1.1 to 1.5 mole of water dissolved in methoxyethanol with catalyst (either 0.1 mole of nitric acid or 0.1 mole of ammonia) was added to the solution to do the partially hydrolysis. The concentration of the solution was adjusted to 1 M by the reduced pressure distillation. The solution were spin-coated on $\text{Pt/Ti/SiO}_2/\text{Si}$ substrate, baked at 300°C and fired at $500\text{--}900^\circ\text{C}$ at different ramp rates from $10^\circ\text{C}/\text{min}$ to $600^\circ\text{C}/\text{min}$. The powders were prepared by calcining the gel which was obtained by drying the solution at 130°C for the XRD and B.E.T. measurements.

Characterization

Dielectric constant and $\tan\delta$ were measured by precision LCR meter (HP-4275A). The remanent polarization and the coercive field was measured using the Sawyer Tower circuit. The crystallinity was evaluated by XRD measurement. The microstructure of the thin film were observed by SEM. The crystallization behavior was observed by XRD and DTA-TGA. The grain size was determined by either SEM or B.E.T. specific surface area measurement under the assumption that each primary particle was essentially a crystallite so that we could regard the calculated particle size from the BET measurement as the crystallite size. In the B.E.T. method, a powder was prepared from the stock solution by being dried and fired under the same heating condition of the film. The particle size was calculated on the basis of PbTiO_3 density of $7.96 \text{ g}/\text{cm}^3$. In the SEM method, the grain size was determined by averaging 10-20 grains which could be observed by SEM photos of thin films. Shorts were evaluated by the number of Unshorted electrodes out of 40 electrodes in most of the samples.

RESULTS AND DISCUSSIONS

Measurement and control of particle size

The results of the surface area measurement of PbTiO_3 calcined at a different temperature are shown in Table 3; corresponding spherical particle sizes calculated from

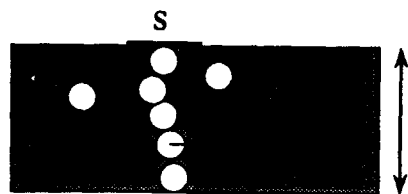


Figure 1 Model of shorts through the association of pores.

these were very small (in the range 0.06-1.4 μ m).

The effect of the firing temperature is apparently critical: the higher the firing temperature used, the larger the particles became. This tendency became prominent at 900°C.

Figure 2 shows scanning electron micrographs of PbTiO₃ thin films fired at 650°C processed with a different catalysts.

The grain size closely agree with the

particle diameter obtained from the BET analysis.

Figure 4 shows X-ray diffraction (XRD) patterns obtained from a thin film fired at temperatures in the 600-800°C range. A firing temperature of 600°C was high enough to crystallize the sample.

Model of shorts

We made a model in which the shorts occur through the interconnection of micro-pores in thin films in the sintering (Fig. 1.). When we define Nh as number of through holes per electrode, P as porosity, l as thickness of the thin film, r as the radius of pores, S as the geometrical area of the electrode, K as a coordination number by which how many pores in the next layer are adjacent to the pore under consideration, and k as an adjusting parameter for the number of the layers (l/r) because the pores do not necessarily touch each other by a point contact, then we get

$$N_h = S \cdot r^{-2} \cdot (KP)^{k \cdot l/r} / K\pi.$$

This model seems to describe the behavior of the shorts as a function of the firing temperature as shown in Fig. 2 a-b. It is obvious that Nh is strongly dependent on the change of l and r. For example, when S=0.3*0.3mm², l=400nm, P=0.05, k=1, K=3, and r=60nm, then Nh=34. But when r=20nm leaving other parameters the same value, Nh=3*10⁻⁹. When we want to avoid the shorts, the pore size must be kept as small as possible, and the film thickness as high as possible.

We tried to achieve the small pore size in two different methods. One is to control the precursor gel structure. When the particle size in a precursor gel is very small, particles tend to agglomerate, sinter and form coarse structure because of the extreme high surface energy of fine particles. We tried to control precursor gel structure through the hydrolysis condition (water to alkoxide ratio (Rw) and the pH of the catalyst). It is clear that the thin film that had the finest grains was the one obtained at the highest Rw in ammonia



(a) (b)
Figure 2 FE-SEMs of PbTiO_3 thin films fired at 650°C obtained under different hydrolysis conditions with NH_3 catalyst; (a) $R_w=1.2$, (b) $R_w=1.5$.

catalyst(Fig. 2). When $R_w > 1.5$ in ammonia solution, the casting solution was unstable and easily gelled before use. In case of the acidic solution, the highest R_w was 1.3. The other method to keep the pore size small is to use RTA technique.

It is well known that the sintered film fired by RTA technique has finer grain size than the conventionally sintered one. The heating rate of $600^\circ\text{C}/\text{min}$ decreased the pore size significantly compared with those fired under 10°C heating rate, thus reducing the shorts(Fig. 3).

Crystal phase, grain size, and their effect on the dielectric properties

The PbTiO_3 phase was not observed at 500°C but observed at 600°C and the XRD peaks became sharper and more intense at a higher sintering temperature as shown in Figure 4. The grain size of PbTiO_3 was from 50nm at 500°C to 160nm at 800°C at normal sintering condition. The smaller grain size was obtained at the same firing temperature when the RTA technique was employed.

The dielectric properties obtained are; $\epsilon=149$, $\tan\delta=19\%$, $\text{Pr}=1.1\ \mu\text{C}/\text{cm}^2$ and $E_c=50\text{kV}/\text{cm}$ when fired at 600°C and $\epsilon=198$, $\tan\delta=4.8\%$, $\text{Pr}=7.4\ \mu\text{C}/\text{cm}^2$ and $E_c=89\text{kV}/\text{cm}$ at 700°C . The dielectric constant was plotted against the grain size of PT thin films (Fig. 5). There

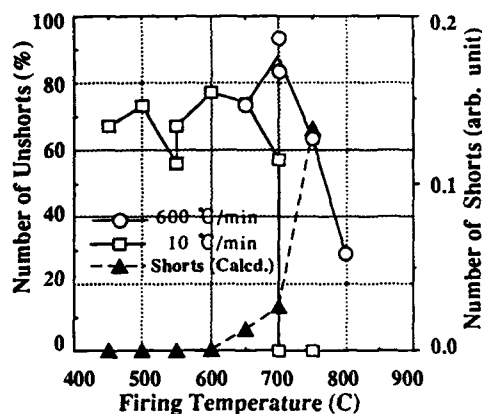


Figure 3 Effect of the firing temperature on the number of unshorts for the heating rate of $10^\circ\text{C}/\text{min}$ (\square), $600^\circ\text{C}/\text{min}$ (\circ), and the number of shorts (\blacktriangle) calculated by the proposed equation. (Film Thickness = 200nm)

seemed to be the change when the grain size is less than 50 nm. The thin film that has the grain size smaller than 40nm showed relatively high dielectric constant.

We can express the difference of the free energy of the tetragonal and the cubic state as follows;

$$\Delta G_T^\circ = G_{\text{tet},T}^\circ - G_{\text{cubic},T}^\circ$$

ΔG_T° of PbTiO_3 is 4543 J/mol¹⁰. $\Delta G_{\text{surface}}^\circ$ the excess surface energy which causes the cubic phase more stable than the tetragonal phase, can be expressed as follows where $\Delta\gamma$ is an excess surface energy per unit area, d ; a diameter of particle and n ; the number of particles, then,

$$\Delta G_{\text{surface}}^\circ = \Delta\gamma \cdot n \cdot \pi d^2/4.$$

This $\Delta\gamma$ can be estimated by putting ΔG_T° equal to $\Delta G_{\text{surface}}^\circ$ and assuming critical crystallite size, d_c . The suggested critical crystallite size, d_c , obtained by this work is 0.04 μm at 298K and the corresponding $\Delta\gamma$ of PbTiO_3 to be 3.8 J/m² which is much higher than $\Delta\gamma$ of 0.2-0.4 J/m² obtained in the earlier work.¹⁰ This difference of the surface energy seems to imply the existence of a stress in the thin film caused by the difference of the thermal expansion between the thin film and the substrate.

CONCLUSION

1. The higher the firing temperature, the larger the resultant particles.

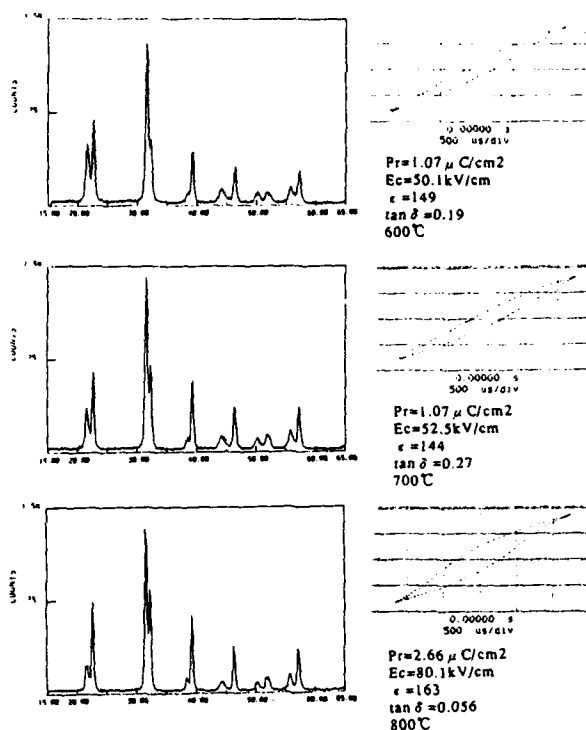


Figure 4 XRD Patterns and Electrical Properties of PbTiO_3 Thin Films Fired at 600, 700, 800 °C.

2. High R_w with ammonia as a catalyst in a partial hydrolysis step of the coating solution was effective to keep the grain small and reduce the shorts.
3. RTA technique was also effective to reduce the shorts.
4. A model which consists of pores interconnecting each other and creating a through hole in a film matrix seemed to be suitable to describe the short circuits possibility.
5. The critical crystallite size that shows the ferroelectric behavior was smaller than 50nm in the PbTiO_3 thin film system.

REFERENCES

- ¹K. D. Budd, S. K. Dey and D. A. Payne, "Sol-Gel Processing of PbTiO_3 , PbZrO_3 , PZT, and PLZT Thin Films", *Br. Ceram. Proc.*, **36** 107-21 (1985)
- ²R.W.Vest and Jiejie Xu, " PbTiO_3 films from metalloorganic precursors", *IEEE Transactions on Ultrasonics, Ferroelectrics, and Frequency Control*, **35** [6] 711-17 (1988)
- ³W. R. Buessem, L. E. Cross, and A. K. Goswami, "Phenomenological theory of high permittivity in fine-grained barium titanate", *J. Am. Ceram. Soc.*, **49** [1] 33-36 (1966)
- ⁴K. Kinoshita and A. Yamaji, "Grain-size effects on dielectric properties in barium titanate Ceramics", *J. Appl. Phys.*, **47** 371 (1976)
- ⁵A. J. Bell, A. J. Moulson and L. E. Cross, "The effect of grain size on the permittivity of BaTiO_3 ", *Ferroelectrics*, **55** 147-150 (1984).
- ⁶G. Art, D. Hennings and G. de With, "Dielectric properties of fine grained barium titanate ceramics", *J. Appl. Phys.* **58** [4] 1619-1625 (1985)
- ⁷T. Yamakawa and K. Uchino, "Particle Size Dependence of Ferro- and Antiferroelectricity", *IEEE, Proc. ISAF* 610-612 (1991)
- ⁸K. Ishikawa, K. Yoshikawa, and N. Okada, "Size effect on the ferroelectric phase transformation in PbTiO_3 ultrafine particles", *Phys. Rev. B*, **37** [10] 5852-5855 (1988)
- ⁹M. de Keijser et al., "Effects of Crystallite Size in PbTiO_3 Thin Films", *Appl. Phys. Lett.* **59** [27] 3556-3558 (1991)
- ¹⁰K. Saegusa, W. E. Rhine, and H. K. Bowen, "Effect of composition and size of crystallite on crystal phase in lead barium titanate", *J. Am. Ceram. Soc.*, **76** [6] 1505-1512 (1993)

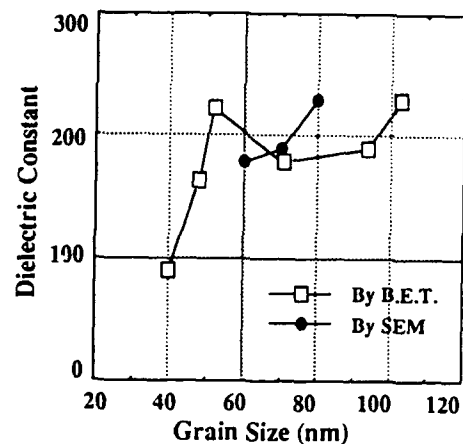


Figure 5 Dielectric constant as a function of the grain size of PbTiO_3 thin films.

PROCESSING AND CHARACTERISTICS OF SPIN-CAST FERROELECTRIC $\text{Bi}_4\text{Ti}_3\text{O}_{12}$ THIN FILMS

Relva C. Buchanan and Peir-Yung Chu, Department of Materials Science and Engineering, University of Cincinnati, Cincinnati, OH 45221-0012

$\text{Bi}_4\text{Ti}_3\text{O}_{12}$ thin films were successfully prepared on Si(100) substrates from solution precursors by spin-coating. The precursor solution consisted of a mixture of bismuth nitrate and titanium sec-butoxide, in stoichiometric ratio, dissolved in a carboxylic acid/amine solvent system. Most organics in the precursors were removed by 350 °C and crystallization occurred below 500 °C. A mechanism for molecular complex formation in the mixed alkoxide/carboxylate system is proposed. Heating rate, temperature, and film thickness showed significant effects on film (001) preferred orientation and grain growth. To limit film/substrate interfacial reactions, heat treatment was carried out at or below 850 °C. Measured remanent polarization in fired $\text{Bi}_4\text{Ti}_3\text{O}_{12}$ varied between 8-20 $\mu\text{C}/\text{cm}^2$ with a coercive field of 100-180 kV/cm, depending on processing temperature.

I. INTRODUCTION

Much interest exists in the use of ferroelectric thin films for memory and microelectronics device applications. High quality ferroelectric films, prepared on Si substrates are needed for integration with current device technologies. Most such thin films are prepared by rf-sputtering, laser ablation, chemical vapor deposition, and recently by solution deposition.

Alkoxides (sol-gel) have been successfully used as precursors for ferroelectric thin film fabrication [1,2], since a network structure can be developed in the solution stage and leads to film formation after heat treatment. When two metal alkoxides are involved in the processing, a double alkoxide molecular structure has been shown to exist in the solution [3]. This improves homogeneity and reduces the crystallization temperature. Due to the hydrolysis and polycondensation reactions within the alkoxide system, however, solution

To the extent authorized under the laws of the United States of America, all copyright interests in this publication are the property of The American Ceramic Society. Any duplication, reproduction, or republication of this publication or any part thereof, without the express written consent of The American Ceramic Society or fee paid to the Copyright Clearance Center, is prohibited.

properties, especially viscosity, change with time, which can result in variability in coating applications.

Carboxylates, on the other hand, do not normally exhibit hydrolysis and polycondensation reactions at room temperature, leading to very stable solution properties [4,5]. In this work, mixed carboxylate/alkoxide precursors were used for preparing ferroelectric ($\text{Bi}_4\text{Ti}_3\text{O}_{12}$) and oxide thin films. Precursor solutions were tailored so that a molecular complex structure can be formed and at the same time solution properties remained stable for a long shelf-life.

The symmetry of $\text{Bi}_4\text{Ti}_3\text{O}_{12}$ is monoclinic point group m [6]. It is, however, usually indexed as a pseudo-orthorhombic phase with $a=5.4489$, $b=5.4100$, and $c=32.815$. Early work on single crystal $\text{Bi}_4\text{Ti}_3\text{O}_{12}$ [6,7] showed the spontaneous polarization has components along both the a and c directions. The smaller component ($\sim 4 \mu\text{C}/\text{cm}^2$) lies along the c direction and the larger component ($\sim 50 \mu\text{C}/\text{cm}^2$) along the a direction. Strong dielectric dispersion and dielectric relaxation maxima were observed at low frequencies ($<100 \text{ Hz}$) and higher temperatures ($>100^\circ\text{C}$), attributed to the space charge generated by the inhomogeneity in the conductivity. The Curie temperature was reported at 675°C , but was highly dependent on the impurity level in the crystal [8]. Bismuth titanate also exhibits interesting optical switching properties since the orientation of the optical indicatrix can be controlled by an appropriate field. It can be, therefore, potentially used for electro-optical device applications.

Bismuth titanate films have mostly been prepared by rf-sputtering with Bi-rich targets [9]. In order to prevent the formation of pyrochlore and other impurity phases, accurate control of the target composition and substrate temperature is required. Thin films are deposited on various single crystal substrates, including MgO , spinel (MgAl_2O_4), TiO_2 , and sapphire. Cracks and the presence of twins and multi-domains have been reported due to lattice mismatch. More recently, $\text{Bi}_4\text{Ti}_3\text{O}_{12}$ films were prepared by pulsed excimer laser deposition on Si and Pt/Si substrates at temperatures as low as 500°C [10]. The films showed a saturation polarization of $28 \mu\text{C}/\text{cm}^2$ and a coercive force of $200 \text{ kV}/\text{cm}$.

II. EXPERIMENTAL

Bismuth nitrate ($\text{Bi}(\text{NO}_3)_3 \cdot 5\text{H}_2\text{O}$) and titanium sec-butoxide ($\text{Ti}(\text{OC}_4\text{H}_9)_4$) were used for preparing $\text{Bi}_4\text{Ti}_3\text{O}_{12}$ solutions. The precursors, in the desired stoichiometric ratio, were dissolved in carboxylic acid/amine mixed solvent. The solutions were then filtered with a $0.22\text{-}\mu\text{m}$ filter paper and diluted to 60-80% with xylene or alcohol [11].

The films were deposited onto Si(100) or Pt/Si(100) substrates by spin-coating at 3500-4000 rpm and were dried at 400-450 °C. This process was repeated several times to increase wet film thickness up to 1.5 μm. Final heat treatments were conducted at 500-850 °C for 2-20 min. The films were either fired with a heating rate of 10-20 °C/min or directly introduced into a furnace at a desired temperature (heating rate >100 °C/min). Fired film thickness was typically about 0.5 μm, except for property measurement, 1.4-μm thick films were used.

Thermal pyrolysis and crystallization of the precursor solutions was studied with thermogravimetric/differential thermal analysis (TG/DTA). Phase development and film orientation in the films was characterized with X-ray diffractometry (XRD). Scanning electron microscopy (SEM) was used to monitor the microstructural evolution during heat treatment and film/substrate interfacial reactions were investigated with secondary ion mass spectroscopy (SIMS). The ferroelectric properties of the films were measured with a Sawyer-Tower circuit with sputtered Au films as top electrodes.

III. RESULTS AND DISCUSSIONS

When mixed carboxylate/alkoxide precursors are used for preparing coating solutions, molecular clusters, based on FT-IR and NMR studies [11], can be formed. The formation of a molecular complex improves solution homogeneity and it functions as a building block for nucleation and crystallization upon heat treatment. When other salts (instead of carboxylates) are dissolved in carboxylic acid with alkoxides, due to ligand exchange, the metal ion also has a tendency to bond to the carboxylate ion forming a carboxylate salt. Solutions prepared by mixed carboxylate/alkoxide precursors are stable with a long shelf-life (> 1 year) under ambient atmosphere. Figure 1 shows possible molecular complex formation in calcium carboxylate and titanium alkoxide precursor system.

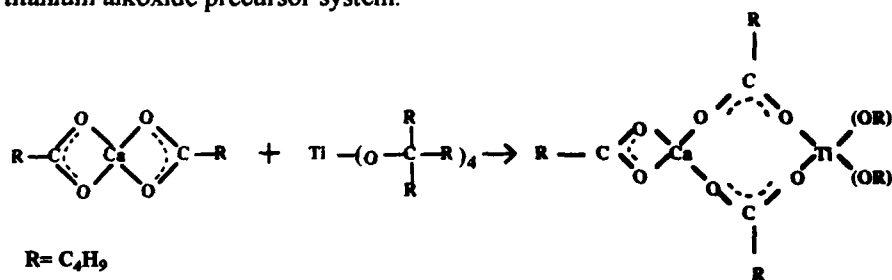


Figure 1. Molecular complex formation in the mixed calcium carboxylate and titanium alkoxide precursor.

Figure 2 shows thermal analysis data for the bismuth titanate solution. Most organics are removed below 350 °C (Figure 2a) and the crystallization temperature is below 500 °C (Figure 2b). Since films fired for only a short time exhibited sharp, well-defined XRD peaks, rapid crystallization and grain growth are indicated for this system.

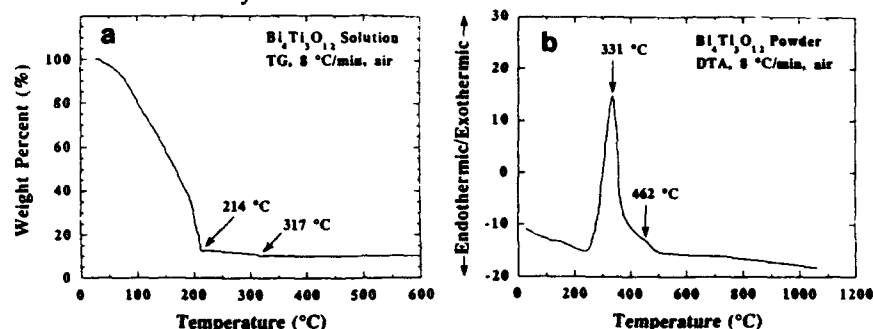


Figure 2. (a) Thermogravimetric analysis of $\text{Bi}_4\text{Ti}_3\text{O}_{12}$ precursor solution (b) Differential thermal analysis of solution-derived $\text{Bi}_4\text{Ti}_3\text{O}_{12}$ powders.

Figure 3 shows the grain growth with processing temperature. The maximum grain size increased from less than 0.1 μm at 550 °C to $\sim 1 \mu\text{m}$ at 900 °C with 10 min soak time. The grain size distribution also increased at higher temperatures. The films were crack-free and very smooth. Based on surface profilometer measurement, the average roughness was 1.8 nm and the maximum step height was 8.3 nm within a 400- μm trace distance.

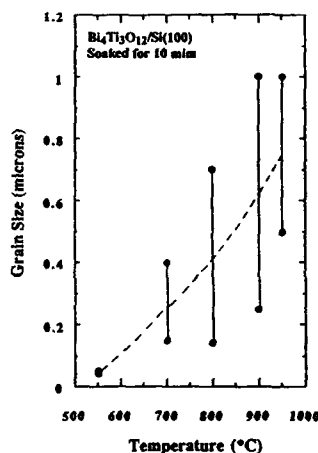


Figure 3. Grain growth with heat treatment in $\text{Bi}_4\text{Ti}_3\text{O}_{12}$ thin films.

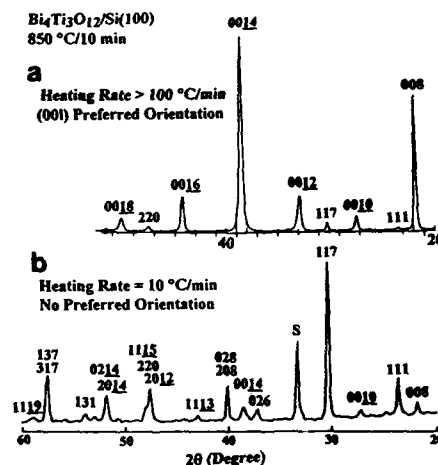
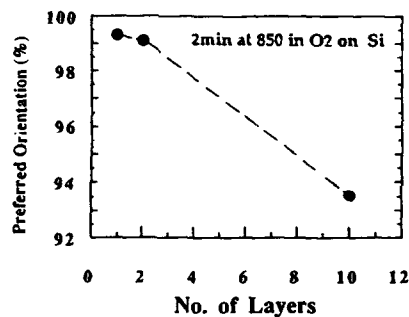


Figure 4. (a,b) Heating rate effect on film orientation.

Heat treatment significantly affected film orientation. When the film was directly introduced into the furnace at 850 °C/10 min, a strong (00l) preferred orientation was observed, as indicated in Figure 4a. However, films fired at 10-20 °C/min to 850 °C showed no preferred orientation (Figure 4b). With rapid heating, less nuclei would be generated from the precursor solution and preferred orientation or epitaxial growth is expected to be higher. With a greater thickness, although still highly oriented, lower degree of preferred orientation was observed in the rapidly heated films (Figure 5).

Thin films deposited on Pt/Si substrates generally had a lower degree of preferred orientation. Figure 6 shows the temperature effect on film orientation. Below 800 °C, little orientation was detected on Pt/Si substrate. Above 800 °C, sharp increase on the (00l) preferred orientation was observed, which is likely related with liquid phase formation in the system at this temperature. Since Si diffusion becomes significant above 850 °C, based on SIMS analysis, higher firing temperatures degrade film properties.



*Percentage of preferred orientation, based on (117) and (0014) peak intensity = $[1 - (I_{117}/I_{0014})] \times 100\%$

Figure 5. Thickness effect on film orientation.

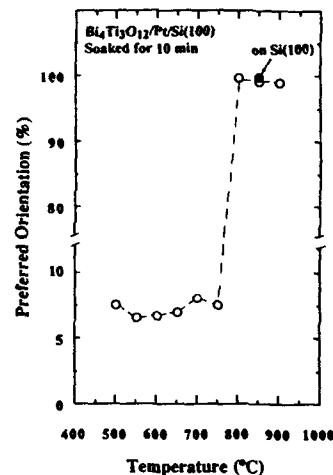


Figure 6. Effect of processing temperature on film orientation.

Figure 7 (a to d) shows the microstructure of $\text{Bi}_4\text{Ti}_3\text{O}_{12}$ films deposited on Pt/Si and Si substrates. The grains exhibit spherical morphology at 700 °C, gradually acquiring an elongated shape at higher temperatures. Higher film porosity was also observed for the films deposited on Pt/Si.

Measured ferroelectric properties for the $\text{Bi}_4\text{Ti}_3\text{O}_{12}$ films are presented in Figures 8 (a&b). The $\text{Bi}_4\text{Ti}_3\text{O}_{12}$ films, $\sim 1.4 \mu\text{m}$ thick, were deposited onto Pt/Si(100) substrates and sputtered Au was used as top electrodes. All the

measurements were performed perpendicular to the film surface. Figure 8(a) shows the remanent polarization increases from 8 to 20 $\mu\text{C}/\text{cm}^2$ with firing temperature up to 800 °C and then decreases at higher temperatures. The large remanent polarizations indicated the films were randomly oriented, apparently due to a large thickness. The coercive field shows a maximum value (180 kV/cm) at 750 °C and then drops to 100 kV/cm at 850 °C. These numbers are comparable with the films prepared by pulsed laser deposition technique [10].

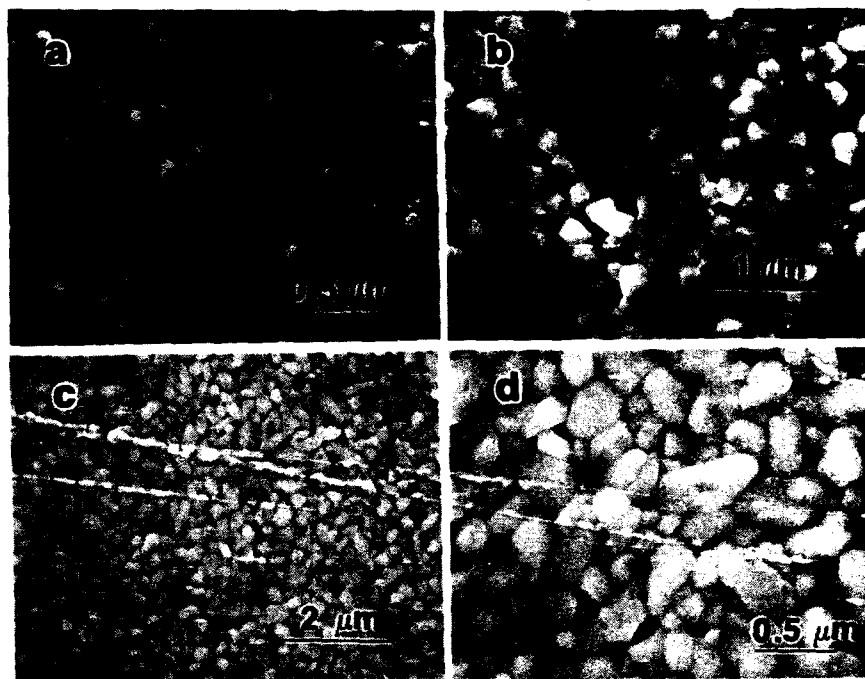


Figure 7. SEM micrograph showing microstructure of $\text{Bi}_4\text{Ti}_3\text{O}_{12}$ films (a) on Pt/Si(100), at 700 °C/2 min, (b) on Pt/Si(100), at 850 °C/10 min, (c) and (d) on Si(100), at 850 °C/10 min.

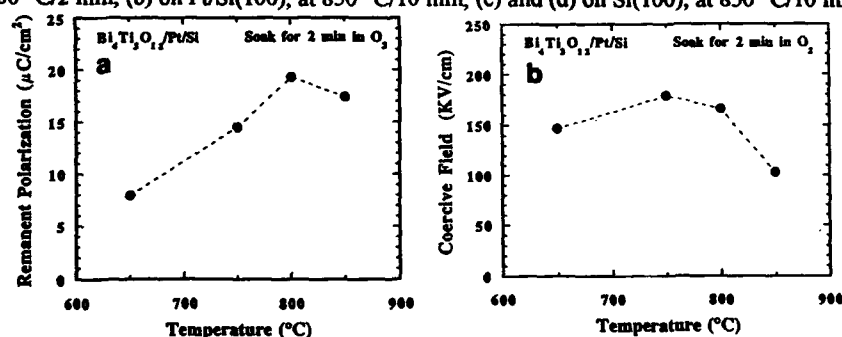


Figure 8. Effect of processing temperature on (a) remanent polarization and (b) coercive field.

IV. SUMMARY

Smooth, crack-free $\text{Bi}_4\text{Ti}_3\text{O}_{12}$ thin films were successfully deposited on Si substrates from solution precursors by spin-coating. Most organics were removed below 350 °C in the $\text{Bi}_4\text{Ti}_3\text{O}_{12}$ system and a crystalline phase developed below 500 °C with fast grain growth. The films showed strong (00l) preferred orientation depending on heating rate, temperature, and film thickness. Film properties degraded somewhat at temperatures above 850 °C, due to Si diffusion. Depending on processing conditions, $\text{Bi}_4\text{Ti}_3\text{O}_{12}$ films exhibited a remanent polarization of 8-20 $\mu\text{C}/\text{cm}^2$ and a coercive field between 100-180 kV/cm. Experimental results indicated that solution deposition to be very competitive with other techniques.

V. ACKNOWLEDGMENT

The authors would like to acknowledge Dr. Isabelle Campion for her pioneer work in this project while as a post-doctoral research associate at the University of Illinois (1989-1991). Financial support from both the University of Illinois and the University of Cincinnati is also acknowledged.

VI. REFERENCE

1. K.D. Budd, S.K. Dey, and D.A. Payne, "Sol-Gel Processing of PbTiO_3 , PbZrO_3 , $\text{Pb}(\text{Zr,Ti})\text{O}_3$ and $\text{PbLa}(\text{Zr,Ti})\text{O}_3$," *Brit. Ceram. Proc.*, 36, 107(1985).
2. S. Hirano and K. Kato, "Processing of Crystalline $\text{Li}(\text{Nb,Ta})\text{O}_3$ Films with Preferred Orientation Through Metal Alkoxides," *Mat. Res. Soc. Symp. Proc.*, 155, 181(1989).
3. L.F. Francis, Ph.D. Thesis, U. of Illinois at Urbana-Champaign, 1991.
4. R.W. Vest, Final Technical Report for Naval Avionic Center under Contract No. 16J-79-C-0352, Nov. 1980.
5. P.-Y. Chu, I. Campion, and R.C. Buchanan, "Processing Effects on High T_c Properties of $\text{YBa}_2\text{Cu}_3\text{O}_{7-x}$ Films from Carboxylate Solution Precursors," *J. Mater. Res.*, 8[2], 261(1993).
6. S.E. Cummins and L.E. Cross, "Electrical and Optical Properties of Ferroelectric $\text{Bi}_4\text{Ti}_3\text{O}_{12}$ Single Crystals," *J. Appl. Phys.*, 39[5], 2268(1968).
7. A. Fouskova and L.E. Cross, "Dielectric Properties of Bismuth Titanate," *J. Appl. Phys.*, 41[7], 2834(1970).
8. T.E. Luke, "Impurity Control of Domain Switching in Ferroelectric Bismuth Titanate," *J. Appl. Phys.*, 45[4], 1605(1974).
9. W.J. Takei, S.Y. Wu, and M.H. Francombe, "Optimization of Epitaxial Quality in Sputtered Films of Ferroelectric Bismuth Titanate," *J. Cryst. Grow.*, 28, 188(1975).
10. H. Buhay, S. Sinharoy, W.H. Kasner, M.H. Francombe, D.R. Lampe, and E. Stepke, "Pulsed Laser Deposition of Ferroelectric Bismuth Titanate," p. 139 in 1990 IEEE 7th International Symposium on Applications of Ferroelectrics, IEEE, 1990.
11. P.-Y. Chu and R.C. Buchanan, "Characteristics of Oxide Thin Films from Carboxylate Precursors," *J. Mater. Res.*, 6[8], 1737(1991).

DENSIFICATION AND CRYSTALLIZATION OF ZIRCONIA THIN FILMS PREPARED BY SOL-GEL PROCESSING

R. W. Schwartz, J. A. Voigt, C. D. Buchheit and T. J. Boyle
Sandia National Laboratories
The Advanced Materials Laboratory
Albuquerque, NM 87185-5800

ABSTRACT

We have investigated the effects of precursor nature and heat-treatment schedule on the densification and crystallization behavior of sol-gel derived zirconia thin films. Precursor solutions were prepared from *n*-propanol, zirconium (IV) *n*-propoxide, and either acetic acid, or 2,4-pentanedione (acac) and water additions. By controlling the ligand type and ligand-to-metal ratio, we were able to prepare films which displayed significant differences in densification behavior. We attribute the dissimilarity in densification to variations in the nature of the as-deposited films, as influenced by ligand type and concentration. While the acac-derived film was a physical gel, (i.e., a physical aggregation of the oligomeric species), the acetic acid-derived film, which exhibited less consolidation, was a chemical gel that could not be redissolved in the parent solvent. Films prepared with large acac/metal ratios and small water additions exhibited minimal crosslinking at 25°C, displayed the greatest consolidation (~ 86% shrinkage) and the highest refractive index ($n = 2.071$) when heat-treated. These results indicate the importance that M-O-M bonds (crosslinks) formed at low temperature can have on densification behavior. We also report on the effects of heat-treatment schedules and ramp rates on densification behavior. All of the films of the present study crystallized into the cubic phase, at temperatures ranging from ~ 400°C to greater than 700°C, depending on the heating rate.

To the extent authorized under the laws of the United States of America, all copyright interests in this publication are the property of The American Ceramic Society. Any duplication, reproduction, or republication of this publication or any part thereof, without the express written consent of The American Ceramic Society or fee paid to the Copyright Clearance Center, is prohibited.

INTRODUCTION

Sol-gel derived ceramic thin films are under investigation for a variety of different applications. Multicomponent systems, such as lead zirconate titanate (PZT), are being studied for uses ranging from decoupling capacitors¹ to optical storage discs,² while single component systems are being investigated for use as porous³ and dense membranes.⁴ The successful development of ceramic thin films for many of these applications requires that the as-deposited amorphous film be transformed into the desired crystalline phase, and for certain applications, completely densified.

In the preparation of ceramic thin films by sol-gel processing, effects of solution chemistry variations (i.e., differences in precursor type, reaction conditions, solution aging, etc.) on material properties have been noted by many authors⁵⁻⁸. Unfortunately, to date, the pathways by which these effects are manifested are poorly understood. While thin films with properties acceptable for several of the applications discussed above have been prepared, a true understanding of the ability to use controlled solution chemistry variations to influence final ceramic properties has yet to be realized. For example, for the fabrication of electronic ceramic thin films, it would be desirable to utilize precursors that produce films which display a tendency toward consolidation, rather than low temperature crystallization. By selecting appropriate precursors, it should be possible to completely densify the thin film prior to the onset of crystallization, producing films with minimal porosity. Since pores can act as light scattering centers, the ability to completely densify the film could lead to the fabrication of non-porous crystalline films suitable for optical storage devices. Alternatively, for the fabrication of porous membranes, chemical precursors and/or fabrication conditions which result in residual porosity should be employed. One strategy for inducing porosity is to use precursors which undergo hydrolysis during deposition.⁹ A second approach is to prepare films which tend to crystallize at low temperatures during firing. This leads to crystalline inclusions within the film which can significantly hinder shrinkage, even when present in small quantities.¹⁰

In the present study, we have attempted to develop an understanding of the pathways by which solution chemistry variations impact ceramic thin film properties. The technical approach we employed was to generate known differences in oligomeric precursor

structure, and then relate these structural variations to observed differences in film densification and crystallization behavior. Our precursors were synthesized by reacting metal alkoxide compounds with different chelating ligands. We also studied the effects of varying the chelating ligand/metal ratio.¹¹⁻¹⁴ We have selected zirconia as a model system for this investigation for a variety of reasons. First, in doped form, it is being studied for use as a dense oxygen separation membrane;⁴ and second, it is an end-member of the technologically significant electronic material, lead zirconate titanate.

EXPERIMENTAL

Zirconium (IV) *n*-propoxide•*n*-propanol* was used as the starting compound for synthesis of the 0.4 M *n*-propanol solutions of the present study. Two chelating ligands, acetic acid* and 2,4-pentanedione[§] (acac; CH₃COCH₂COCH₃) were used to generate different oligomeric solution species which were used for film fabrication.

The acetic acid based solution was prepared by reacting neat zirconium (IV) *n*-propoxide•*n*-propanol with purified acetic acid¹⁵ in a molar ratio of 1:1.5, in a glove box. The reaction mixture was then removed from the glove box, and after approximately five minutes, sufficient dry *n*-propanol[§] was added to yield a 0.4 M (zirconium) solution. The solution was allowed to age for three days at 25°C under argon prior to use in film fabrication. This precursor system will be referred to as the HOAc system.

The acac-based precursor solutions were prepared by reacting zirconium (IV) *n*-propoxide•*n*-propanol with an *n*-propanol solution containing the acac ligand. After allowing thirty minutes for the chelation reaction, a solution of water in *n*-propanol of equal volume was added to the zirconium-acac reaction mixture. Solutions were stirred during both phases of the preparation. Final solution concentration was 0.25 M or 0.4 M in zirconium. To generate different oligomers, solutions with two different *r* (moles acac/mole Zr) and *h* (moles H₂O/mole Zr) ratios were employed.¹⁶ For the first solution,

* Aldrich Chemical Company; Milwaukee, WI

§ Fisher Scientific, Pittsburgh, PA

acac and water additions were used so that $r = 2.0$, $h = 0.5$; and for the second solution, $r = 0.5$, $h = 4.0$. These solutions will henceforth be referred to as acac-H and acac-L, respectively, for high and low acac/metal ratios. The acac-H solution was aged for 4 days prior to use while the acac-L solution was aged for one day prior to use. Longer aging times for this solution resulted in gelation. As for the HOAc precursor, reactions and aging were again carried out at room temperature under an argon atmosphere. Further details of the preparation procedures are given in Reference 17. Solution viscosities, as a function of concentration, were measured at 30.0°C using a Koehler K-23300 kinematic viscosity bath and calibrated Size 1 Ubbelodhe viscometer tubes.

A similar acac-based solution chemistry was used to prepare films for low temperature pyrolysis heat-treatment studies. For these studies, zirconium (IV) *n*-butoxide•*n*-butanol⁷ was used as the starting compound and *n*-butanol⁸ was used as the solvent. Identical reaction procedures to those discussed above were used. Reactant ratios were: $r = 0.5$, $h = 2.0$. Solutions were aged 2 days prior to use.

Films were fabricated onto silicon wafers by spin-casting at 3000 rpm, unless otherwise noted. Continuous uniform films were prepared for each of the precursor solutions. As deposited, film thicknesses ranged from ~2200 Å to ~3200 Å, depending on the precursor solution. Fired film thicknesses ranged from ~450 Å to ~550 Å. Gelation times of the depositing films (i.e., the time required for stabilization of the interference colors during spinning) varied from 5 to 6 seconds. Ellipsometry (Gaertner L116-C; $\lambda = 6328$ Å) was used to monitor changes in film thickness and refractive index as a function of time, or heat-treatment conditions. Measured ψ and Δ values were converted to thickness and refractive index values using Gaertner GC4A software for single layer non-absorbing films. Typically, refractive indices and thicknesses of three different films were measured and then averaged. In general, ellipsometry measurements were very reproducible from sample to sample.

Redissolution experiments were conducted to determine the nature of the gel that was formed during deposition. These experiments consisted of spinning a film under standard conditions, waiting for ten seconds, and then immersing the film in *n*-propanol (the parent solvent) to determine film solubility. Redissolution was also evaluated after the film was dried for 18 hours at 25°C; and after heat-treatment at 200°C for 5 minutes. The ability to redissolve a film was taken as an indication that primarily a physical aggregation process

had occurred during gelation.¹⁸ Alternatively, when as-deposited films did not redissolve, it was assumed that extensive chemical gelation (i.e., the formation of M-O-M bonds between the oligomers) had occurred during deposition.¹⁸

Three different firing strategies were used for heat-treatment of the films. Low temperature isothermal consolidation was studied by placing the films on a hot plate held at the desired temperature, and measuring the changes in thickness and refractive index for different heat-treatment times. The effects of ramp rate on shrinkage and densification at higher temperatures were determined by heating the films to 700°C at three different rates: 5°C/min, 50°C/min and ~ 100°C/min (i.e., simply inserting the film into the furnace at T). A hold time of ten minutes was employed. Finally, an AET Addax RMV-04 rapid thermal processing (RTP) furnace was used to heat films to various temperatures at 300°C/min and 3000°C/min. Once the desired temperature was attained, samples were rapidly quenched to < 150°C. This last procedure allowed for determination of the non-isothermal shrinkage and crystallization behavior of the films.¹⁹

RESULTS AND DISCUSSION

Solution Characteristics and Precursor Nature

From the dependence of solution viscosity on concentration, kinematic viscosity measurements may be used to determine the relative extent of oligomer interaction.²⁰ We have measured the viscosities of the three precursor systems at concentrations ranging from 0.05 M to 0.4 M, and the results are shown in Figure 1. The acac-L solution showed a strong dependence of viscosity on concentration, indicating that as concentration was increased, this precursor system exhibited a much stronger interaction between solution oligomeric species than the other two systems. This result implies that the oligomers formed in this process are either larger, or more ramified (or both), than the oligomers generated in the other two chemical systems.²¹ Based on the known reactions of acac and water with alkoxide compounds, this result is expected.¹⁶ For small additions of acac, the alkoxy ligands of the starting compound that are not replaced by acac are free to react with the water added in the subsequent reaction step. Hydrolysis and condensation occur, leading to M-O-M bond

formation. Under these reaction conditions, i.e., small acac/metal and large water/metal ratios, the extensive hydrolysis and condensation reactions of the remaining alkoxy groups lead to the generation of comparatively large oligomeric species, as has previously been determined by small angle X-ray scattering.^{13, 14, 16}

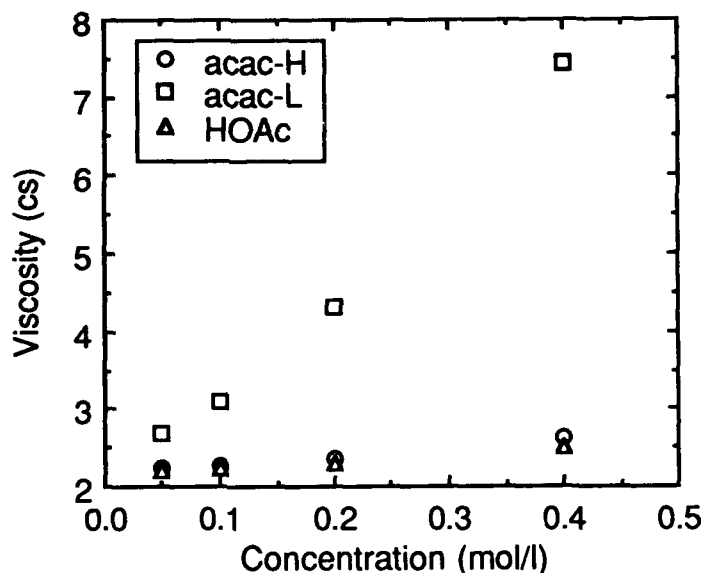


Figure 1. Kinematic viscosity measurements as a function of concentration for the three precursor systems of the present study. Test conditions: 30.0 ± 0.1 °C.

In contrast, the acac-H precursor solution displayed only a minor dependence of viscosity on solution concentration, indicating the presence of relatively non-interacting species. Again, this is an expected result. With large acac additions, the original alkoxide compounds become highly chelated. Since the acac ligand is stable toward hydrolysis, the number of remaining (alkoxy) ligands available for subsequent hydrolysis and condensation reactions is greatly reduced. Therefore, there are fewer reaction sites for M-O-M bond formation, and smaller oligomeric species are produced.^{13, 14, 16}

From the minimal dependence of viscosity on concentration, kinematic viscosity measurements of the oligomers formed from the HOAc system imply that these species are also relatively non-interacting.

Nature of the As-Deposited Film

To investigate the effects of precursor nature on the characteristics of the deposited films, the solubilities of selected films in the parent solvent were characterized. These experiments were conducted to determine whether a chemical or physical gel was formed during deposition. Results are presented in Table I. Films prepared from both acac systems formed only physical gels. This indicates that primarily a physical aggregation process was responsible for gelation, rather than extensive crosslinking between oligomers. This may be due to the stability of the acac ligand to hydrolysis,²² the relative extent of alkoxy replacement by acac, and/or to the role that acac plays in sterically limiting the accessibility to any remaining alkoxy ligands. In contrast, it was not possible to redissolve the film formed from the HOAc precursor, implying that true chemical gelation, or M-O-M bond formation via hydrolysis and condensation between the oligomeric solution species, had occurred during deposition. Evidently, either the acetate ligands are less stable toward hydrolysis during deposition,²² or the accessibility of remaining alkoxy (or hydroxy) ligands is not as diminished as for the acac-based precursors. Results for films prepared

Table I.
Results of redissolution experiments for acac and acetic acid derived thin films.

<u>Precursor</u>	<u>Temp.</u> (°C)	<u>Time</u>	<u>Dissolution Behavior</u>	<u>Gel Nature</u>
acac-H	25	10 sec.	Dissolved	Physical
acac-H	25	18 hrs.	Partially Dissolved	Intermediate
acac-H	200	5 min.	Insoluble	Chemical
acac-L	25	10 sec.	Dissolved	Physical
acac-L	25	18 hrs.	Insoluble	Chemical
acac-L	200	5 min.	Insoluble	Chemical
HOAc	25	10 sec.	Insoluble	Chemical
HOAc	25	18 hrs.	Insoluble	Chemical
HOAc	200	5 min.	Insoluble	Chemical

from precursor solutions synthesized with alkoxide compounds modified by sterically large ligands (1-adamantanol) seem to indicate that the accessibility of remaining alkoxy ligands to ambient moisture initiated hydrolysis and condensation is very important in defining the nature of the as-deposited film.²³ These results indicate the importance that ligand type can have in defining precursor reactivity, and consequently, the nature of the as-deposited film.

With extended hold times at room temperature, the dissolution behavior of the acac-derived films changes; the acac-L film no longer dissolves and the acac-H film only partially dissolves. This change in dissolution behavior indicates that the films are transforming to chemical gels through continued condensation reactions. With heat-treatment at 200°C, it becomes no longer possible to dissolve any of the films. We believe this is an indication of still more extensive condensation reactions. As discussed below, the extent of chemical crosslinking between oligomeric species in the as-deposited films is key in defining film densification behavior.

Film Shrinkage and Densification Behavior

Our initial investigations of film shrinkage (consolidation) and densification focused on the effects of precursor nature on room temperature consolidation following deposition. Results presented in Figure 2 illustrate the variation in normalized film thickness as a function of time after t_g . Consolidation at room temperature is most likely due to the capillary contraction associated with removal of residual solvent,²⁴ and continued condensation reactions.²⁴ We feel that the change in dissolution behavior of the films with long hold times at 25°C provides strong evidence for the occurrence of continued condensation reactions.

It is evident that while all of the films exhibit significant shrinkage at room temperature, the film prepared from the acac-H precursor consolidates to the greatest extent. After three hours, its thickness has decreased by about 40%, compared to approximately 25% for the acac-L and HOAc-based films. We feel that the greater shrinkage of the acac-H film is due to the initial absence of M-O-M bonds between oligomeric clusters, as discussed above. Since the interaction of the oligomers in this film may best be described as occurring via a simple physical aggregation process, the oligomers are less constrained to rearrange during drying at 25°C, resulting in extensive film consolidation. As the redissolution data indicate,

however, M-O-M bond formation does occur with time. On the other hand, the HOAc derived film is already chemically crosslinked immediately after deposition. Because of this, the oligomers are less free to rearrange through capillary contraction, and the film consolidates less at this temperature.

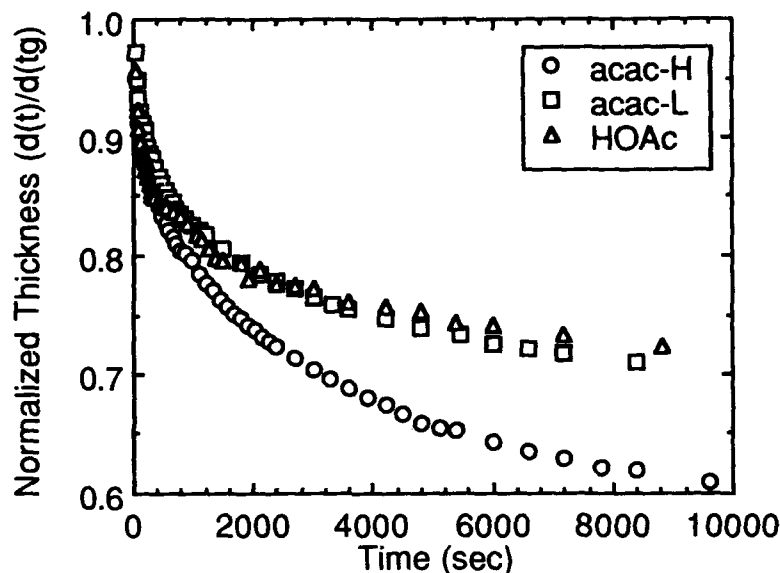


Figure 2. Effect of precursor type on room temperature consolidation of sol-gel derived zirconia thin films.

Based on this explanation, we might expect the acac-L film, which also displays little crosslinking in the as-deposited state, to behave more like the acac-H film than the HOAc film. The observed behavior may be due to the greater tendency of this system to exhibit more extensive condensation reactions at 25°C than the acac-H system, thus inhibiting densification. An indication of this tendency may be noted in Table I, where after 18 hours at room temperature, the acac-H film still partially dissolved, while the acac-L film did not dissolve. Refractive indices for the films at this point of the fabrication process ranged from 1.55 to 1.58.

To obtain information regarding the importance of the processes which can contribute to densification and/or consolidation, i.e., capillary contraction, continued condensation reactions, structural relaxation and crystallization,²⁴ we have studied the isothermal

consolidation of the thin films at three different temperatures. Figure 3 shows typical results for film consolidation at 25°C, 200°C, and 400°C, for the acetic acid derived films. The films were heat-treated by placing on a hot plate held at the desired temperature. As expected, as the heat-treatment temperature is increased and more of the physical processes described above become active, consolidation of the film increases. For this precursor, at 400°C, the film thickness has decreased to approximately 20% of its thickness at t_g .

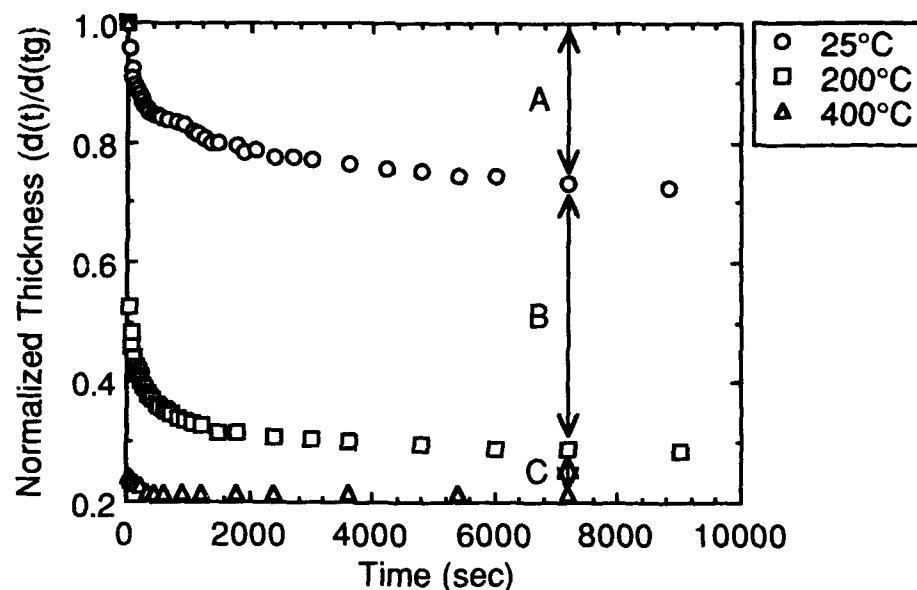


Figure 3. Effect of heat-treatment temperature on the consolidation of acetic acid derived zirconia thin films. Heat-treatments at 200 and 400°C were performed by placing the sample onto a hot plate pre-set at the desired temperature. A: consolidation at 25°C; B: relative consolidation between 25 and 200°C; C: relative consolidation between 200 and 400°C.

To further analyze the contributions of the various physical processes to overall consolidation, we have calculated the relative consolidation which occurred after heat-treatment for two hours in three different temperature regimes, as shown by the arrows in Figure 3. Results of this analysis are presented in Figure 4 for the three different precursor systems. It can be seen that significant

consolidation occurs at very low temperatures for each of the three precursors. Since it is expected that the only active processes at low temperature (25°C) would be capillary contraction and continued condensation reactions,²⁴ we may state that these two processes contribute significantly to the overall consolidation of the thin films. In the temperature regime from 25 to 200°C, still greater shrinkage (~40-50%) occurs. We again believe that the primary active mechanism in this regime is continued condensation, although potentially, structural relaxation may also play a role. Between 200 and 400°C, we would expect still further condensation reactions, as organic pyrolysis is completed, as well as structural relaxation. Also, by 400°C, all of the films crystallized into the cubic zirconia phase, as determined by X-ray diffraction experiments. Thus, crystallization also contributes to consolidation in this temperature regime. While we have yet to determine whether organic pyrolysis is completed prior to the onset of crystallization, we plan to evaluate this by using TGA and FT-IR reflectance spectroscopy to study organic pyrolysis, as well as hot stage X-ray diffraction, to determine crystallization onset.

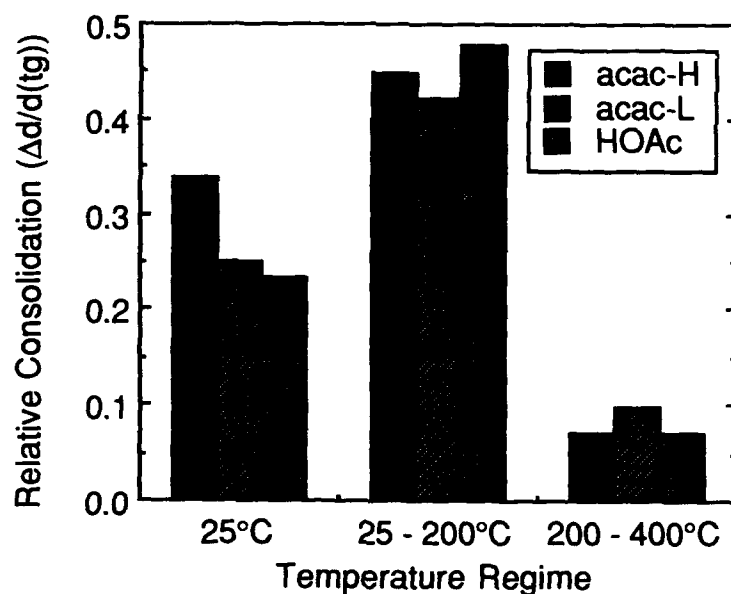


Figure 4. Relative consolidation of the zirconia thin films in three different temperature regimes: 25°C; 25 to 200°C; and 200 to 400°C (see arrows in Figure 3).

The variation in "total" film shrinkage for the three precursors as a function of temperature is further illustrated in Figure 5. As observed for room temperature consolidation, the film prepared from the acac-H precursor exhibited the greatest total shrinkage, consolidating to ~14% of its original thickness. Again, we attribute the greater consolidation of this film, which persists to high process temperatures, to the physical gel nature of the as-deposited film and the initial absence of chemical crosslinks between oligomers.

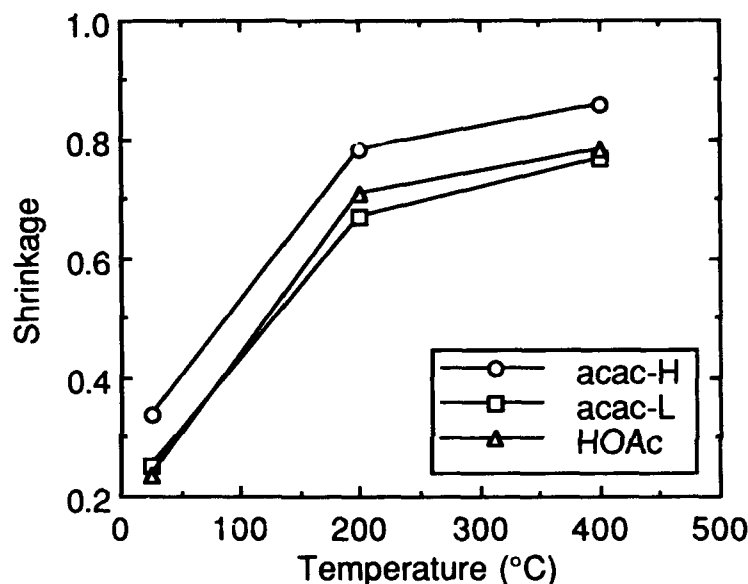


Figure 5. Effects of precursor nature and heat-treatment temperature on the "cumulative" shrinkage of zirconia thin films. Data at 200 and 400°C is for samples heat-treated on a hot plate held at the appropriate temperature. Shrinkage measured after two hours at each temperature.

The observed differences in film consolidation were paralleled by variations in film density (refractive index) for films heat-treated to 700°C at ~ 100°C/min. The acac-H precursor yielded the film with the highest refractive index, 1.948. The film prepared from the acac-L precursor solution displayed a refractive index of 1.897 and the HOAc derived film displayed a refractive index of 1.908. Since all of the films of the present study crystallized in the same phase, cubic zirconia, we can use refractive index as an indicator of material density. The

refractive index value for the acac-H film corresponds to a density of ~88%, as determined from the Lorentz-Lorentz equation,²⁵ assuming a refractive index of 2.150 for theoretically dense cubic zirconia.^{26,27} Using this same approach, the acac-L and the HOAc derived films are ~85% dense. Higher film densities were obtained for both acac and acetic acid precursors by utilizing the faster heating rates accessible with the AET Addax furnace (see below).

While crystallization of the films into the non-stable cubic phase may at first seem surprising, similar behavior has been noted previously for other sol-gel derived materials.²⁸ Typical X-ray diffraction patterns for films heated to 700°C are shown in Figure 6. As mentioned, all of the films, regardless of the chemical precursor system, crystallized in the cubic phase. There were, however, minor differences in the crystallite sizes of the films prepared from the different precursors. The acac-H precursor system yielded a grain size of ~130Å, while the HOAc derived films exhibited a grain size of only ~100Å, as determined by X-ray line broadening analysis using the Scherrer equation. For the conventionally fired materials, all of the films were highly microstrained, as determined by line broadening analysis using the Gauss squared technique. We observed no apparent effects of heating rate, or low temperature pyrolysis hold, on the crystalline nature of the films fired to 700°C using a tube furnace. Films prepared by rapid thermal processing with the AET Addax furnace displayed delayed crystallization onsets, as expected.²⁹ For example, when using a heating rate of 3000°C/min, the acac-H film crystallized at ~700°C, compared with ~400°C for isothermal heat-treatment.

Effect of Ramp Rate and Heat-Treatment Conditions on Densification

As a final area of investigation, we have studied the effects of low temperature pyrolysis holds and ramp rates on film densification. Results for the effects of ramp rate are shown in Figure 7. As expected, greater consolidation and higher refractive indices (i.e., higher densities) are obtained for higher heating rates. This result is believed to arise from the retention of a lower viscosity structure to higher temperatures as condensation reactions are delayed because of kinetic considerations.³⁰ Because the lower viscosity structure is retained, greater consolidation and densification occurs prior to the onset of crystallization.

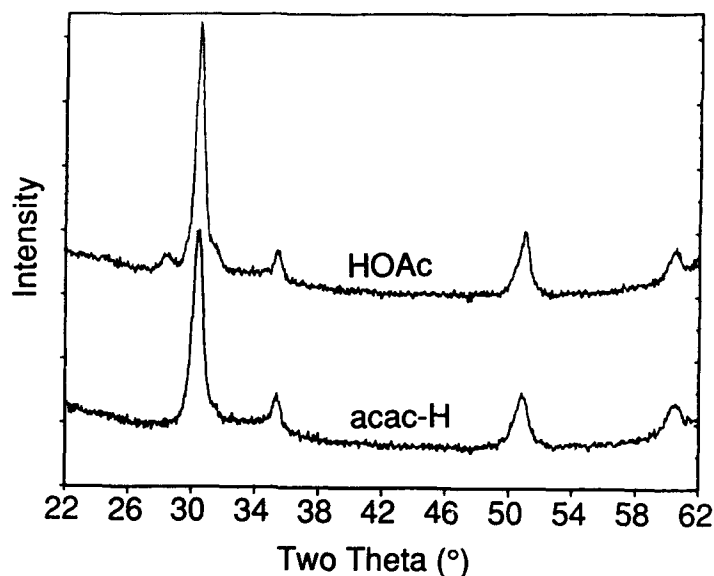


Figure 6. X-ray diffraction patterns for acac-H and HOAc derived zirconia thin films heated to 700°C at 5°C/min. No pyrolysis heat-treatment; heat-treatment initiated two minutes after deposition.

The effect of heating rate on densification is most significant for the acac-H film. This film should be most amenable to densification due to the comparative absence of chemical crosslinks at room temperature. By simply inserting this film into the furnace at temperature, a film with density of ~88% was obtained. Films prepared from the other precursor systems also displayed higher densities for faster heating rates, although, as seen in this figure, the effect was not as pronounced as for the acac-H precursor.

We have also investigated the effects of faster ramp rates on the densification behavior of the acac-H and the HOAc derived films using the AET furnace. At a heating rate of 300°C/min, films prepared from both precursors exhibited higher densities than those prepared by conventional firing strategies. Using this higher ramp rate to heat the films to 700°C, it was possible to prepare an HOAc derived film with a refractive index of 1.943 (ρ ~88%) and an acac-H film with an index of 2.064 (ρ ~95%). The greater densification of the films at the faster heating rates is again attributable to retention of the high free energy, low viscosity material structure to higher process temperatures.³⁰ The highest density obtained was for an acac-H film heated to 800°C at

3000°C/min. Under these conditions, we were able to prepare a film with a refractive index of 2.071 (ρ ~96% of theoretical). Higher density acetic acid derived films were also produced at the higher heating rates, but for similar heat-treatment conditions the densities of these films were always lower than those of the acac-H derived films. The highest density HOAc-based film, prepared by firing to 700°C at 3000°C/min, was ~89% dense.

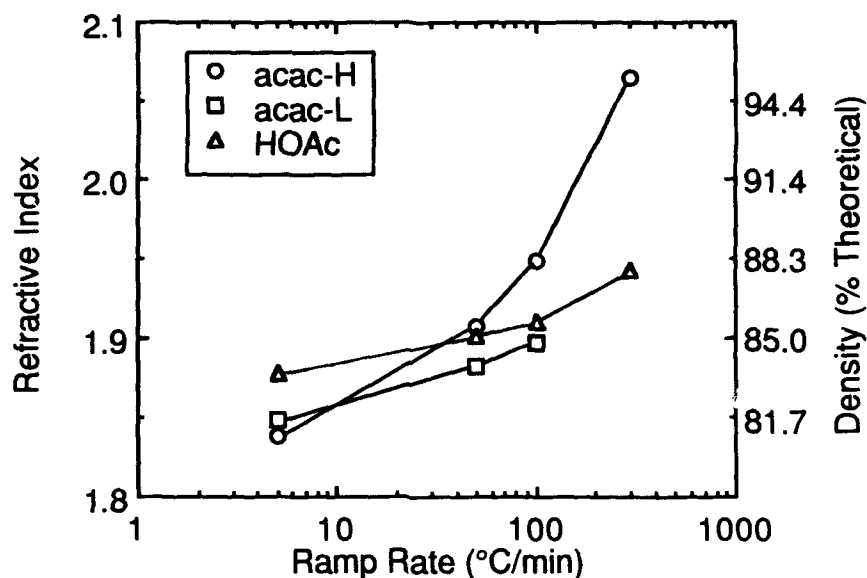


Figure 7. Effect of ramp rate on the refractive index and relative density of sol-gel derived zirconia thin films. Lower ramp rates (5, 50 and ~100°C) were obtained by firing in a tube furnace; highest ramp rate (3000°C/min, 5°C/sec) obtained by firing with AET Addax RTP furnace.

The use of low temperature pyrolysis holds also affected the densification behavior of zirconium (IV) *n*-butoxide, acac-based films. Prior to ramping the films to 700°C for crystallization, these films were subjected to low temperature holds for pyrolysis of organic species. In Figure 8 it may be seen that, in general, as the pyrolysis temperature is increased, the refractive index of the film decreases. The magnitude of the variation is also significant, with film densities decreasing by about 3 to 5%, for the higher temperature pyrolysis heat-treatments. As the pyrolysis temperature is increased, it is expected that more

condensation reactions would take place as organic pyrolysis is more extensive. As these reactions occur to greater and greater extents, subsequent densification with heat-treatment to higher temperatures is inhibited, as is evident in the data.

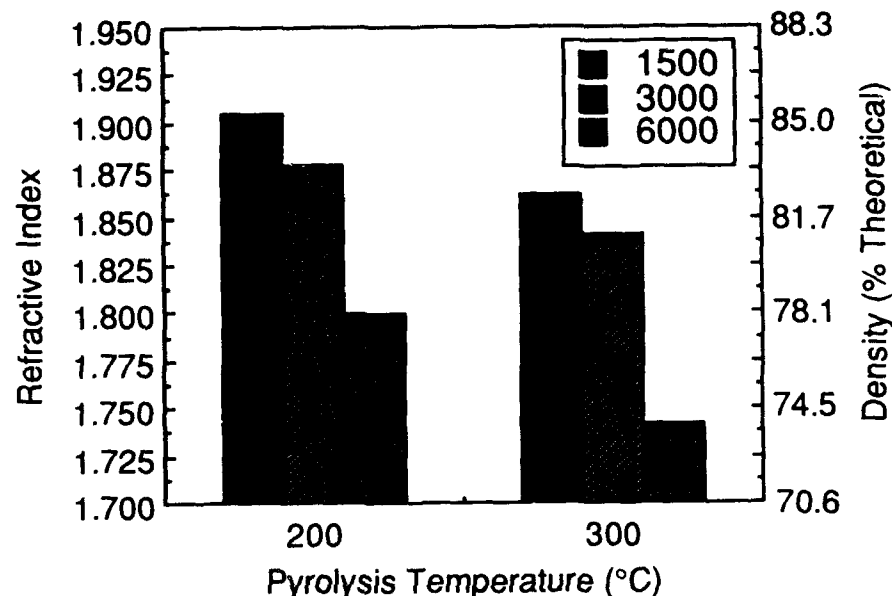


Figure 8. Effect of spinning speed and low temperature pyrolysis heat-treatment on the refractive index of zirconia thin films fired at 700°C for 10 minutes, using a ramp rate of ~ 100°C/min.

CONCLUSIONS

Zirconia thin films were prepared from three different chemical precursor systems. The general nature of the films, as well as the film consolidation and densification behavior, were highly dependent on the ligand used to modify the alkoxide starting compound, and on the modifying ligand/metal ratio. Films prepared from precursors using more hydrolytically stable chelating agents or high chelate/metal ratios densified to the greatest extent. This presumably occurs because the gelled film that was formed was more the result of a simple physical aggregation of oligomeric species, rather than chemical crosslinking. Because of this characteristic, these films were able to consolidate to a

greater extent; not only at room temperature, but also as the heat-treatment temperature was increased.

Films prepared from precursors which underwent more extensive chemical crosslinking during deposition, i.e., the HOAc-based sols, consolidated to a lesser extent, presumably because of the existence of the M-O-M bonds between the oligomeric clusters. The results of low temperature pyrolysis experiments would also seem to support this conclusion. Films prepared with higher temperature pyrolysis holds, i.e., conditions expected to lead to more extensive condensation reactions and M-O-M crosslink formation, densified to a lesser extent on subsequent heating.

Heating rate also impacted densification behavior and crystallization temperature. As heating rate was increased, higher density films were obtained. Very rapid heating rates, attained using the rapid thermal processor, produced films of the highest density, ~96%. All of the films prepared from the three precursors crystallized into the cubic phase, at temperatures as low as 400°C.

ACKNOWLEDGEMENTS

We would like to acknowledge M. M. Mendoza and D. L. Lamppa for excellent technical support. We also thank M. Gonzales for providing the X-ray diffraction results. This research was funded by the U. S. Department of Energy under contract DE-AC04-94AL85000.

REFERENCES

1. R. W. Schwartz, D. Dimos, S. J. Lockwood, and V. M. Torres, "Electrical Properties of Sol-Gel PZT Thin Films for Decoupling Capacitor Applications," in Ferroelectric Thin Films III, Eds., E. R. Myers, B. A. Tuttle, S. B. Desu, and P. K. Larsen, (*Mat. Res. Soc. Symp. Proc.*, Pittsburgh, PA, 310, 1993) pp. 59-64.
2. C. E. Land, "Optical Information Storage in PLZT Thin Films," *Ceramic Trans.*, 11, 343 (1990).
3. C. J. Brinker, T. L. Ward, R. Sehgal, N. K. Raman, S. L. Hietala, D. M. Smith, D.-W. Hua, and T. J. Headley, "'Ultramicroporous' Silica-based Supported Inorganic Membranes," *J. Membrane Sci.*, 77, 165 (1993).

4. E. A. Hazbun, "Ceramic Membrane for Hydrocarbon Conversion," U. S. Patent 4,791,079 (1988).
5. R. W. Schwartz, B. C. Bunker, D. B. Dimos, R. A. Assink, B. A. Tuttle, D. R. Tallant, and I. A. Weinstock, "Solution Chemistry Effects in $\text{Pb}(\text{Zr,Ti})\text{O}_3$ Thin Film Processing," *Integrated Ferroelectrics*, **2**, 243 (1992).
6. R. A. Assink and R. W. Schwartz, " ^1H and ^{13}C NMR Investigations of $\text{Pb}(\text{Zr,Ti})\text{O}_3$ Thin-Film Precursor Solutions," *Chem. of Mater.*, **5** (4), 511 (1993).
7. S. J. Lockwood, R. W. Schwartz, B. A. Tuttle, and E. V. Thomas, "Solution Chemistry Optimization of Sol-Gel Processed PZT Thin Films," in *Ferroelectric Thin Films III*, Eds., E. R. Myers, B. A. Tuttle, S. B. Desu, and P. K. Larsen, (*Mat. Res. Soc. Symp. Proc.*, Pittsburgh, PA, **310**, 1993) pp. 275-280.
8. C. D. E. Lakeman, J.-F. Campion, and D. A. Payne, "Factors Affecting the Sol-Gel Processing of PZT Thin Layers," in *Ceramic Trans.*, **25**, 411 (1992).
9. Y.-J. Kim and L. F. Francis, "Processing and Characterization of Porous TiO_2 Coatings," *J. Am. Ceram. Soc.*, **76** (3), 737 (1993).
10. G. W. Scherer, "Effect of Inclusions on Shrinkage," in *Better Ceramics Through Chemistry IV*, Eds., B. J. Zelinski, C. J. Brinker, D. E. Clark, and D. R. Ulrich, (*Mat. Res. Soc. Symp. Proc.*, Pittsburgh, PA, **180**, 1990) pp. 503-514.
11. D. Chaumont, A. Craievich, and J. Zarzycki, "A SAXS Study of the Formation of ZrO_2 Sols and Gels," *J. Non-Cryst. Sol.*, **147 & 148**, 127 (1992).
12. A. Larbot, J. A. Alary, C. Guizard, L. Cot, and J. Gillot, "Hydrolysis of Zirconium *n*-Propoxide," *J. Non-Cryst. Sol.*, **104**, 161 (1988).
13. R. Guinebretiere, A. Dager, A. Lecomte, and H. Vesteghem, "Tetragonal Zirconia Powders from the Zirconium *n*-Propoxide-Acetylacetone-Water-Isopropanol System," *J. Non-Cryst. Sol.*, **147 & 148**, 542 (1992).
14. G. De, A. Chatterjee, and D. Ganguli, "Zirconia Fibres from the Zirconium *n*-Propoxide- Acetylacetone- Water- Isopropanol System," *J. Mat. Sci. Lett.*, **9**, 845 (1990).
15. D. D. Perrin and W. L. F. Armarego, *Purification of Laboratory Chemicals 3rd Edition* (Pergamon Press, New York, 1988) Chapter 2.
16. P. Toledano, M. In, and C. Sanchez, "Synthese et Structure du Compose:
[$\text{Ti}_{18}(\mu_5\text{-O})_2(\mu_4\text{-O})_2(\mu_3\text{-O})_{10}(\mu_2\text{-O})_8(\mu_2\text{-OBU}^n)_{14}(\text{OBU}^n)_{12}(\text{acac})_2$," *C. R. Acad. Sci. Paris*, t. **313**, Serie II, 1247 (1991).

17. R. W. Schwartz, T. J. Boyle, J. A. Voigt, and C. D. Buchheit, to be submitted to *J. Am. Ceram. Soc.*
18. C. J. Brinker, private communication (1993).
19. J. L. Keddie, P. V. Braun, and E. P. Giannelis, "Interrelationships Between Densification, Crystallization, and Chemical Evolution in Sol-Gel Titania Thin Films," *J. Am. Ceram. Soc.* (1993).
20. R. J. Young, Introduction to Polymers (Chapman Hall, New York, 1981) pp. 123 - 128.
21. S. Sakka, "Gel Method for Making Glass," in Treatise on Materials Science and Technology, Vol. 22 (Academic Press, New York, 1982).
22. C. Sanchez, F. Babonneau, S. Doeuff, and A. Leautic, "Chemical Modifications of Titanium Alkoxide Precursors," in Ultrastructure Processing of Advanced Ceramics, Eds., J. D. Mackenzie, D. R. Ulrich (Wiley Interscience, New York, 1988) pp. 77 - 87.
23. T. J. Boyle, A. T. Pearson, and R. W. Schwartz, "Synthesis of Novel Titanium and Zirconium Alkoxides as Precursors for Lead Zirconate Titanate (PZT) Thin Films, presented at the 1993 American Ceramic Society PAC RIM meeting, Honolulu Hawaii, November, 1993.
24. C. J. Brinker and G. W. Scherer, Sol-Gel Science (Academic Press, Boston, 1990) Chapters 8 and 9.
25. M. Born and E. Wolf, in Principles of Optics (Pergamon Press, New York, 1975) p. 87.
26. R. Rujkorakam and J. R. Sites, "Crystallization of Zirconia Thin Films by Thermal Annealing," *J. Vac. Sci. Technol. A*, 4 (3), 568, (1986).
27. A. K. Chin, A. Satyanarayan, J. H. Zarrabi, and W. Vetterling, "Cubic Zirconia as a High-Quality Facet Coating for Semiconductor Lasers," *J. Appl. Phys.*, 64 (3), 994 (1988).
28. Ph. Colomban and E. Bruneton, *J. Non-Cryst. Sol.*, 147 & 148, 201 (1992).
29. J. L. Keddie and E. P. Giannelis, "Effect of Heating Rate on the Sintering of TiO_2 Thin Films: Competition between Densification and Crystallization," *J. Am. Ceram. Soc.*, 74, 2669 (1991).
30. C. J. Brinker, W. D. Drotning, and G. S. Scherer, "A Comparison Between the Densification Kinetics of Colloidal and Polymeric Silica Gels," in Better Ceramics Through Chemistry, Eds., C. J. Brinker, D. E. Clark, and D. R. Ulrich, (*Mat. Res. Soc. Symp. Proc.*, Pittsburgh, PA, 32, 1984) pp. 25-32.

MICROSTRUCTURE OF EPITAXIAL FERROELECTRIC/METAL OXIDE ELECTRODE THIN FILM HETEROSTRUCTURES ON LaAlO_3 AND SILICON

Subodh G. Ghonge and Edward Goo
Department of Materials Science and Engineering, University of Southern California, Los Angeles, California 90089

R. Ramesh
Bellcore, Red Bank, New Jersey 07701

R. Haakenaasen and D. K. Fork
Xerox Palo Alto Research Center, Palo Alto, CA 94305

ABSTRACT

TEM and X-ray diffraction studies of PZT, PLZT, lead titanate and bismuth titanate ferroelectric thin films and $\text{YBa}_2\text{Cu}_3\text{O}_{7-x}$ (YBCO), $\text{Bi}_2\text{Sr}_2\text{CaCu}_2\text{O}_8$ (BSCCO) and $\text{La}_{0.5}\text{Sr}_{0.5}\text{CoO}_3$ (LSCO) electrically conductive oxide thin films, that are sequentially deposited by pulsed laser ablation, show that these films may be deposited epitaxially onto LaAlO_3 (LAO) or Si substrates. The conductive oxides are promising candidates for use as electrodes in place of metal electrodes in integrated ferroelectric device applications. The oxide electrodes are more chemically compatible with the ferroelectric films. High resolution electron microscopy has been used to investigate the interface between the ferroelectric and metal oxide thin films and no reaction was detected. Epitaxial growth is possible due to the similar crystal structures and the small lattice mismatch. The lattice mismatch that is present causes the domains in the ferroelectric films to be preferentially oriented and in the case of lead titanate, the film is single domain. These films may also have potential applications in integrated optical devices.

To the extent authorized under the laws of the United States of America, all copyright interests in this publication are the property of The American Ceramic Society. Any duplication, reproduction, or republication of this publication or any part thereof, without the express written consent of The American Ceramic Society or fee paid to the Copyright Clearance Center, is prohibited.

INTRODUCTION

Pulsed laser ablation is a technique which has been successfully used to grow thin films of high T_c superconducting oxides.¹ This technique has been recently extended to growth of high quality ferroelectric thin films which are being investigated for applications such as electro-optic devices, nonvolatile RAMs etc.² These ferroelectric films are being grown as part of an electrode/ferroelectric/electrode/substrate heterostructure. Initial work has been done on growing these heterostructures on oxide substrates such as LaAlO_3 , MgO and SrTiO_3 with the ultimate aim of trying to integrate these heterostructures on Si substrates for potential integrated device applications. The electrodes which have been used are YBCO and LSCO which are perovskite-type oxides exhibiting metallic behavior at room temperature. The advantage here is the close lattice matching between the substrate, electrode and the ferroelectric which can result in the growth of an epitaxial ferroelectric film on a single crystal substrate. Also, the similar chemistry (all the components of the heterostructure are oxide perovskites) between the different components of the heterostructure reduces the chances of interfacial reaction between the ferroelectric film and the electrode which results in degradation of dielectric properties when metal electrodes are used.

EXPERIMENTAL PROCEDURE

All the films were deposited by laser ablation. A 248-nm KrF pulsed excimer laser was directed at a rotating, sintered polycrystalline target of the required material and the resulting plume was caught on a heated substrate. The targets are mounted on a four-target rotating carousel, thus enabling in situ deposition of the multi-layered structure. The thicknesses of the layers were controlled by controlling the number of laser pulses. Film deposition rates were between 0.5 and 1 Å/s. The yttria stabilized zirconia (YSZ) layers on Si were deposited at Xerox. The other films were deposited at Bellcore.

Cross-sectional and planar samples of the material were prepared by standard techniques.³ 3 mm discs were cut with an ultrasonic disc cutter. The samples were mechanically polished to 100 μm , dimpled to 20 μm followed by argon ion milling at 3 kV to obtain electron transparency. Conventional TEM work was carried out on a Philips 420 transmission electron microscope at 120 kV and high resolution on a Akashi 002B transmission electron microscope at 200 kV.

RESULTS AND DISCUSSION

Initial work was done on bismuth titanate (BT) ferroelectric films. BT has been shown to be suitable for memory and electro-optic switching applications.⁴ Figure 1 shows a TEM micrograph of the heterostructure. Film growth is epitaxial as confirmed by the selected area diffraction pattern shown in the inset. The lattice parameters for $\text{PrBa}_2\text{Cu}_3\text{O}_{7-x}$ (PBCO) are 3.87 Å, 3.93 Å and 11.71 Å. BT is also orthorhombic with lattice parameters of 5.41 Å, 5.43 Å and 32.82 Å. This provides a suitable lattice match for epitaxial growth along a [001] oriented substrate such as LaAlO_3 which has a pseudo-cubic lattice constant of 3.78 Å. The crystallographic relationship between the three layers in this case is $[100]_{\text{LaAlO}_3} \parallel [100]_{\text{PBCO}} \parallel [110]_{\text{BT}}$. Figure 2 shows a high resolution image of the interface between the PBCO and the BT ferroelectric film. The interface is seen to have a high density of structural defects.

Next, a PT/YBCO/LAO heterostructure was investigated. Lead titanate is a perovskite-type ferroelectric with a Curie-point of 490°C and a relatively large tetragonal distortion (c/a ratio ~ 1.064).⁵ Its large spontaneous polarization ($P_s = 75 \mu\text{C}/\text{cm}^2$) and small dielectric constant ($\epsilon_r \sim 100$)⁶ along the c -axis make it an excellent candidate for applications such as infrared detectors and piezoelectric transducers. Highly c -axis oriented PbTiO_3 thin films on MgO single crystals and on epitaxial Pt films have been obtained.⁷ T. Imai et al. have attempted at depositing PbTiO_3 thin films on Si wafers and Pt sheets by laser ablation.⁸ However, they could not achieve c -axis oriented growth due to the polycrystalline nature of the substrate.

Figure 3 shows an X-ray diffractometer scan for the heterostructure. Only the (00 l) peaks can be seen with a complete absence of the (h 00) peaks which indicates that the film is c -axis oriented or epitaxial. No 90° domains can be seen in bright field and dark field images of the sample. Dark field images from a planar sample taken under a multi-beam condition do not show the presence of 180° domains. Cross-sectional TEM showed a single domain film. This is attributed to the compressive stresses induced in the film by the lattice mismatch between PT and the underlying YBCO and LAO substrate which can be relieved by a c -axis orientation which occurs due to the large tetragonal distortion of PT⁹.

Another system which has shown considerable promise is the lanthanum-modified lead zirconate titanate (PLZT) perovskite system. PLZT films have been fabricated by various techniques such as sol-gel processing¹⁰ and rf-planar magnetron sputtering.¹¹ It has also been shown that the fatigue and retention characteristics of ferroelectric lead zirconate titanate (PZT) thin films grown with YBCO thin film top and bottom electrodes are far superior to those obtained with conventional platinum top electrodes.¹² Also, in the

case of the PZT and PLZT ferroelectric thin films, since the smaller *a*-axis lattice parameter has a better lattice match with the underlying YBCO film than the *c*-axis lattice parameter (due to the relatively large *c/a* ratio of PLZT), a preferential *c*-axis orientation of the ferroelectric film is expected and can improve ferroelectric properties. Here the PLZT composition we have looked at is $\text{Pb}_{0.9}\text{La}_{0.1}(\text{Zr}_{0.2}\text{Ti}_{0.8})_{0.975}\text{O}_3$ (PLZT) grown with $\text{YBa}_2\text{Cu}_3\text{O}_{7-x}$ (YBCO) as the bottom electrode. These PLZT/YBCO heterostructures have also been grown on a [001] single crystal LaAlO_3 substrate. The lattice parameters of tetragonal PLZT are $a=3.90\text{\AA}$ and $c=4.06\text{\AA}$ while those of orthorhombic YBCO are $a=3.82\text{\AA}$, $b=3.89\text{\AA}$, and $c=11.68\text{\AA}$. LAO has rhombohedral symmetry with $a=3.78\text{\AA}$ and $\alpha=90.83^\circ$. Figure 4 shows an X-ray diffractometer scan for the heterostructure. The absence of peaks other than from the (100), (010) and (001) families of planes implies that the films are highly textured. The absence of any (100)_{PLZT} peak and the very strong (001)_{PLZT} peak imply that the ferroelectric film is *c*-axis oriented. Figure 5 shows a high resolution micrograph of the PLZT/YBCO interface region viewed along the [100] zone axis of the PLZT. The epitaxy and *c*-axis orientation in PLZT is maintained across 90° domains in *b*-axis YBCO.

Most earlier investigations of such heterostructures have used the high- T_c superconducting oxides such as $\text{YBa}_2\text{Cu}_3\text{O}_{7-x}$ and $\text{Bi}_2\text{Sr}_2\text{CaCu}_2\text{O}_{8+x}$ as electrodes utilizing their high electrical conductivity at room temperature. Another electrode which has shown superior fatigue properties for ferroelectric capacitors is $\text{La}_{0.5}\text{Sr}_{0.5}\text{CoO}_3$ (LSCO), which has the perovskite crystal structure, good electrical conductivity^{13,14} and a good lattice matching with LAO and PLZT. LSCO is pseudo-cubic with $a=3.83\text{\AA}$. These LSCO/PLZT/LSCO heterostructures were grown on a [001] single crystal LaAlO_3 substrate. From the X-ray diffractometer scan for this heterostructure (Figure 6) it may be concluded that the PLZT film has a strong *c*-axis orientation with a small degree of *a*-axis orientation. Figure 7 is a bright field TEM micrograph showing all the layers of the heterostructure. Although defects are seen in the film, the films are single crystal. No domains were observed in the PLZT film. The LSCO electrode shows a large density of defects especially at the LSCO/PLZT interface due to the lattice mismatch between a_{PLZT} and a_{LSCO} (~1.8%). Figure 8 shows a high resolution micrograph of the PLZT/LSCO interface region viewed along the [100] zone axis. No second phase is seen at the interface which implies that there is no interfacial reaction. Even though the interface is rough, the PLZT/LSCO growth is epitaxial as expected since PLZT has a good lattice match with the underlying LSCO. It is predominantly *c*-axis oriented which is expected since the a_{LSCO} (3.83Å) has a better lattice match with a_{PLZT} (3.90Å) than with c_{PLZT} (4.06Å). With the silicon substrate samples, two different types of

heterostructure were investigated. One with a buffer layer of yttria stabilized zirconia and another with a buffer layer of SiO_2 . A schematic of one of these heterostructures is shown in Figure 9. A thin film of $\text{Bi}_4\text{Ti}_3\text{O}_{12}$ was deposited between the buffer layer and the LSCO/PLZT/LSCO heterostructure. Bismuth titanate with its large c lattice parameter can be easily deposited with a preferred c -axis orientation. This can result in growth of subsequent layers with a preferred orientation. X-ray diffraction scans show a preferred orientation for both these heterostructures. However, pole figure scans reveal a high degree of epitaxy only for the sample with the YSZ buffer layer and not for the one with the SiO_2 layer as can be seen from Figures 10 and 11. More work is being done to characterize the microstructure of these samples by TEM.

CONCLUSION

Epitaxial growth of single domain PT thin films has been achieved. YBCO and LSCO are suitable oxides for use as conducting electrodes. Epitaxial growth of PLZT on silicon has been demonstrated.

REFERENCES

1. A. Inam, M. S. Hegde, X. D. Wu, T. Venkatesan, P. England, P. F. Miceli, E. W. Chase, C. C. Chang, J. M. Tarascon, and J. B. Wachtman, *Appl. Phys. Lett.* **53**, 908 (1988).
2. J. F. Scott and C. A. Paz de Araujo, *Science*, **246**, 1400 (1989); G. H. Haertling and C. E. Land, *J. Amer. Ceram Soc.* **54**, 1 (1971).
3. J. C. Bravman and R. Sinclair, *J. Electron Microsc. Tech.* **1**, 53 (1984).
4. L. H. Parker and A. F. Tausch, *IEEE Circuits Devices Magazine* **6**, 17 (1990).
5. G. Shirane, R. Pepinsky, and B. Frazer, *Acta Cryst.* **9**, 131 (1956).
6. V. G. Gavrilachenko, R. I. Spinko, M. A. Martynenko, and E. G. Fesenko, *Sov. Phys. Solid State* **12**, 1203 (1970).
7. K. Iijima, Y. Tomita, R. Takayama, and I. Ueda, *J. Appl. Phys.* **60**, 361 (1986).
8. T. Imai, M. Okuyama, and Y. Hamakawa, *Jpn. J. Appl. Phys.* **30**, 2163 (1991).
9. S. G. Ghonge, E. Goo, and R. Ramesh, *Appl. Phys. Lett.* **62**, 1742 (1993).
10. T. Kawano, T. Sei, and T. Tsuchiya, *Jap. J. Appl. Phys.* **30B**, 2178, 1991.
11. H. Adachi, T. Mitsuyu, O. Yamazaki, and K. Wasa, *J. Appl. Phys.*, **60**, 736 (1986).
12. R. Ramesh, A. Inam, W. K. Chan, B. Wilkens, K. Myers, K. Remschnig,

- D. L. Hart, and J. M. Tarascon, *Science* **252**, 944 (1991).
13. G. H. Jonker and J. H. Van Santen, *Physica* **19**, 120 (1953).
14. J. T. Cheung, P. E. D. Morgan, D. H. Lowndes, X. Y. Zheng, and J. Breen, *Appl. Phys. Lett.* **62**, 2045 (1993).

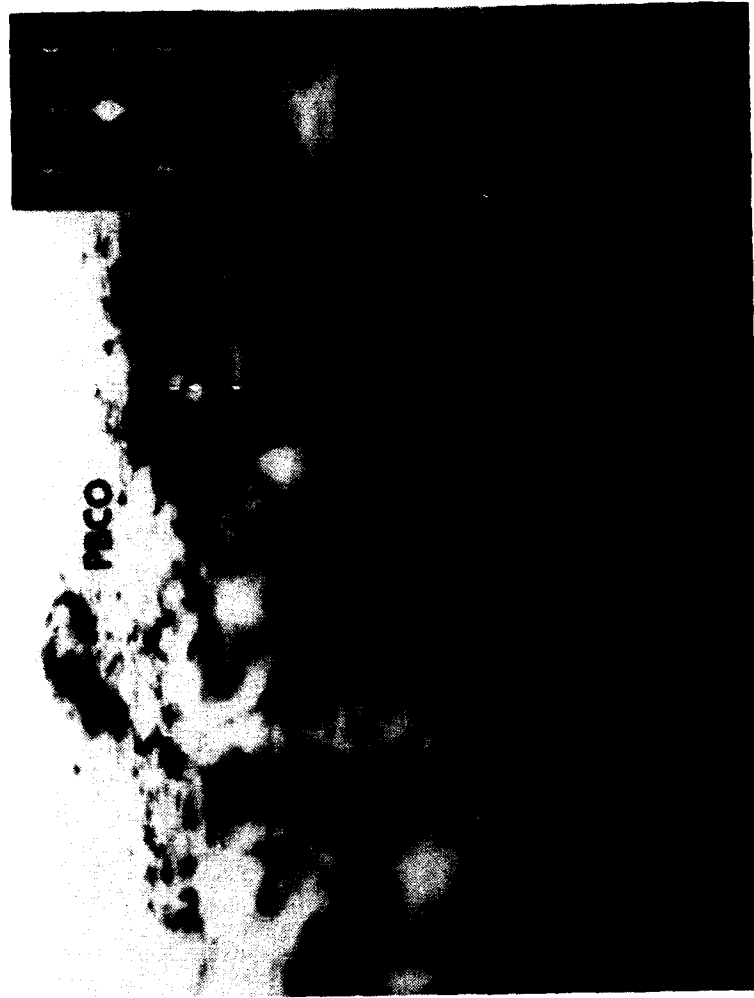


Figure 1. Cross-sectional TEM micrograph of the PBCO/BT/LAO heterostructure along the BT [110] zone axis



Figure 2. High resolution image of the PBCO/BT interface.

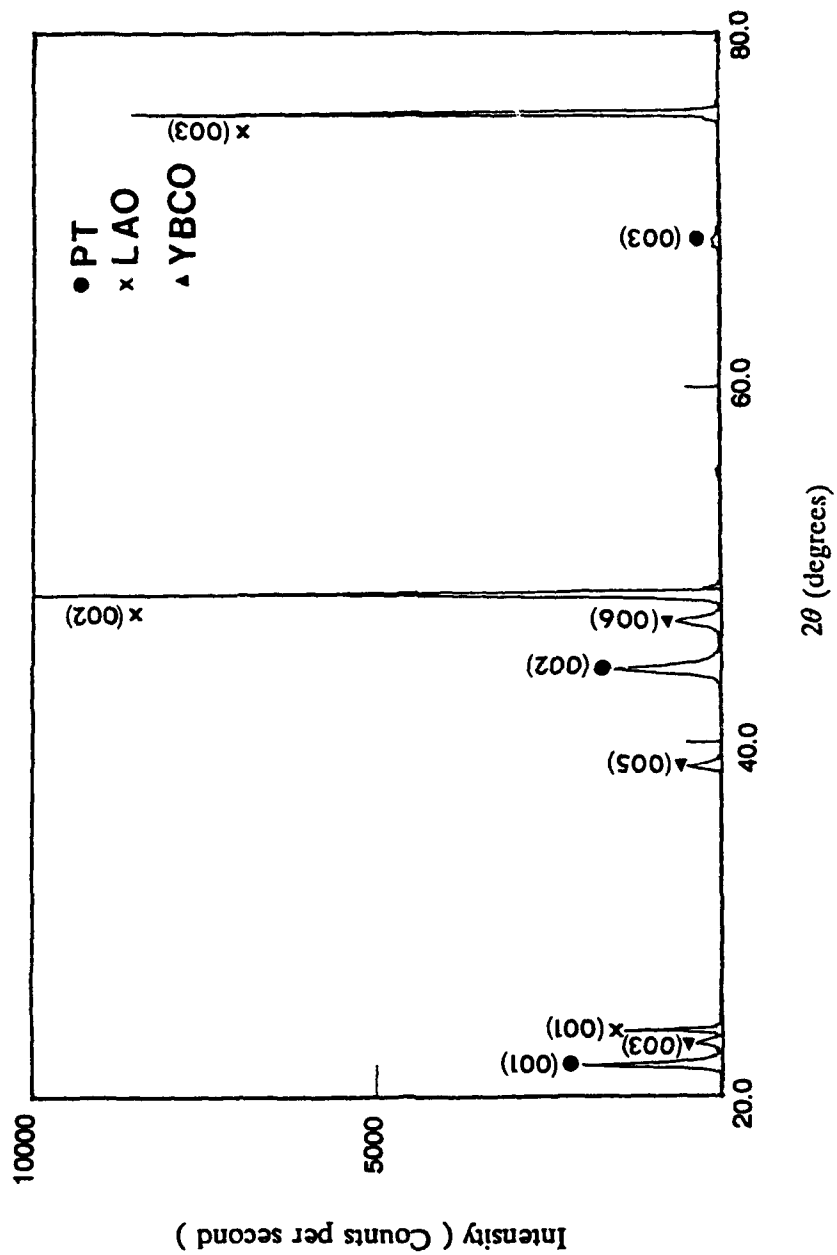


Figure 3. X-ray diffraction pattern from the PT/YBCO/LAO heterostructure.

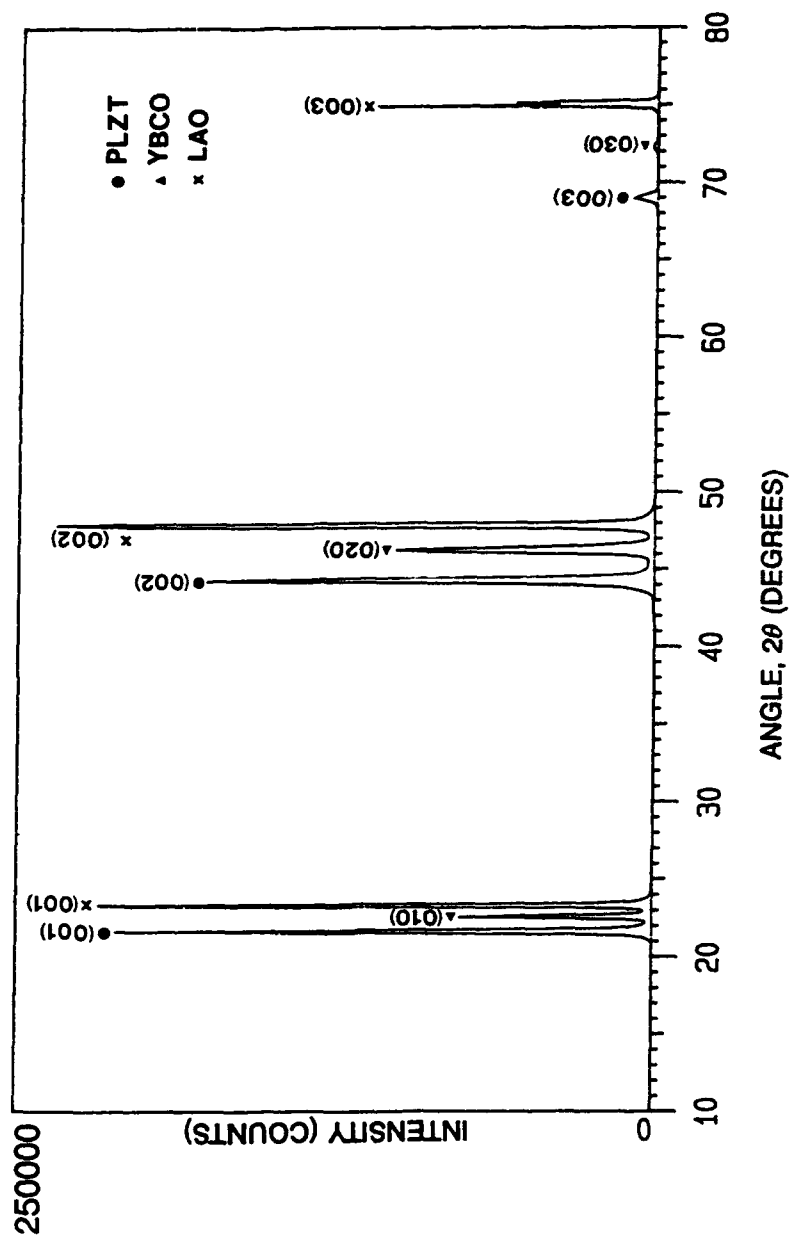


Figure 4. X-ray diffraction pattern from the PLZT/YBCO/LAO heterostructure.



Figure 5. High resolution image of the PLZT/YBCO interface along the [100] zone axis of PLZT.

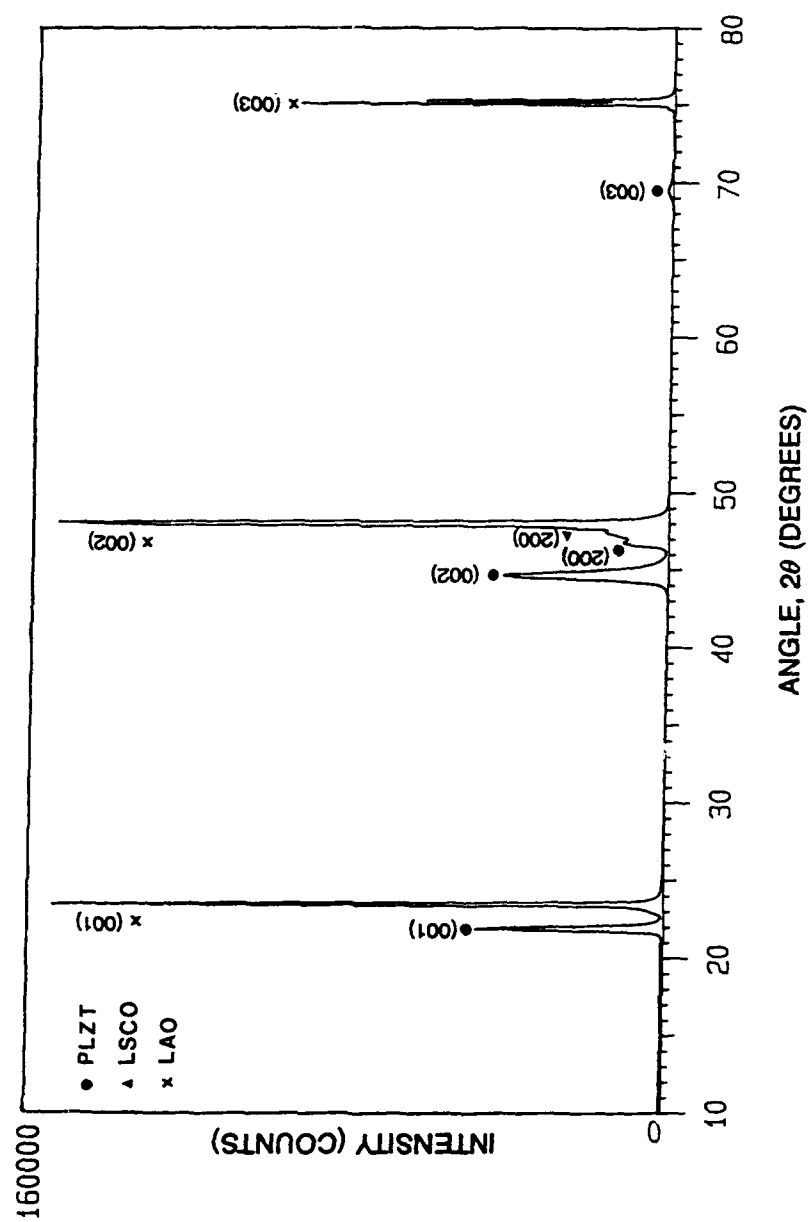


Figure 6. X-ray diffraction pattern from the PLZT/LSCO/LAO heterostructure.



Figure 7. Bright field image of LSCO/PLZT/LAO heterostructure along the [110] zone axis of PLZT.



Figure 8. High resolution image of the PLZT/LSCO interface along the $[100]$ zone axis of PLZT.

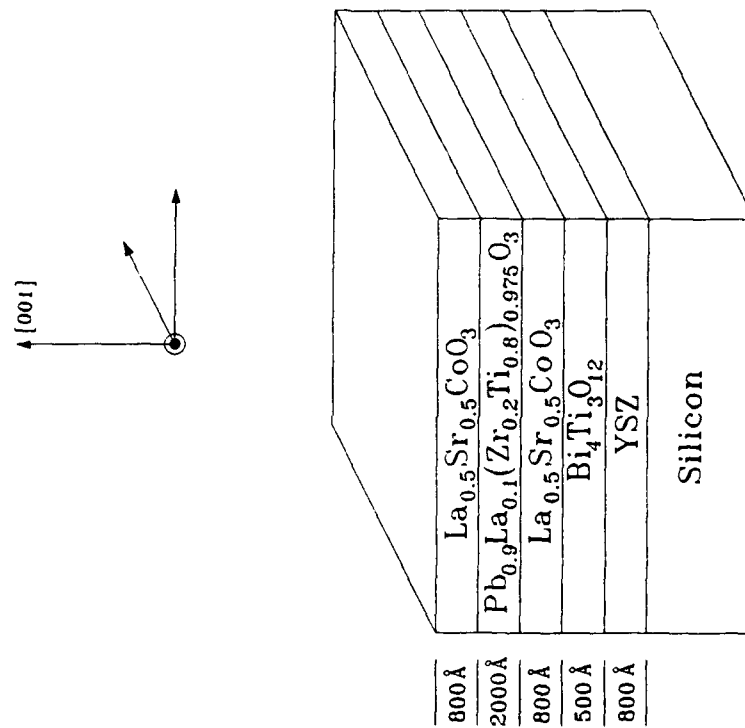


Figure 9. Schematic of the LSCO/PLZT/LSCO/BT/YSZ/Si heterostructure.

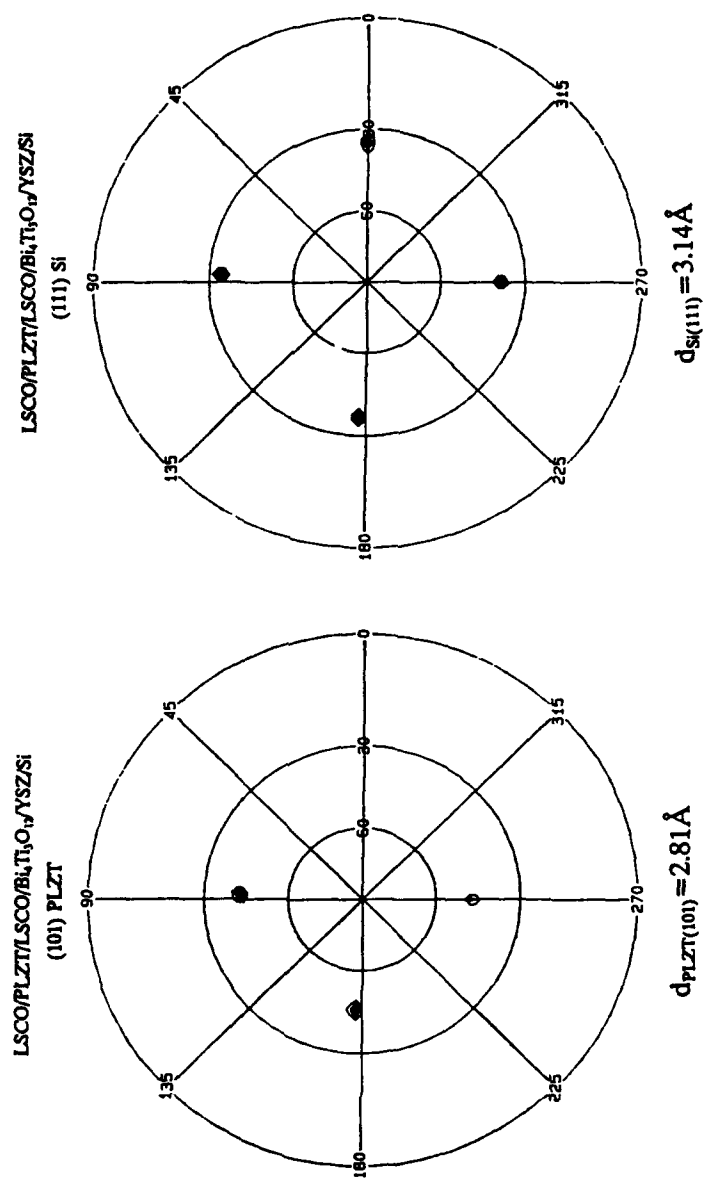


Figure 10. (101)PLZT and (111)Si Wulff projection pole figures from the LSCO/PLZT/LSCO/BT/YSZ/Si heterostructure.

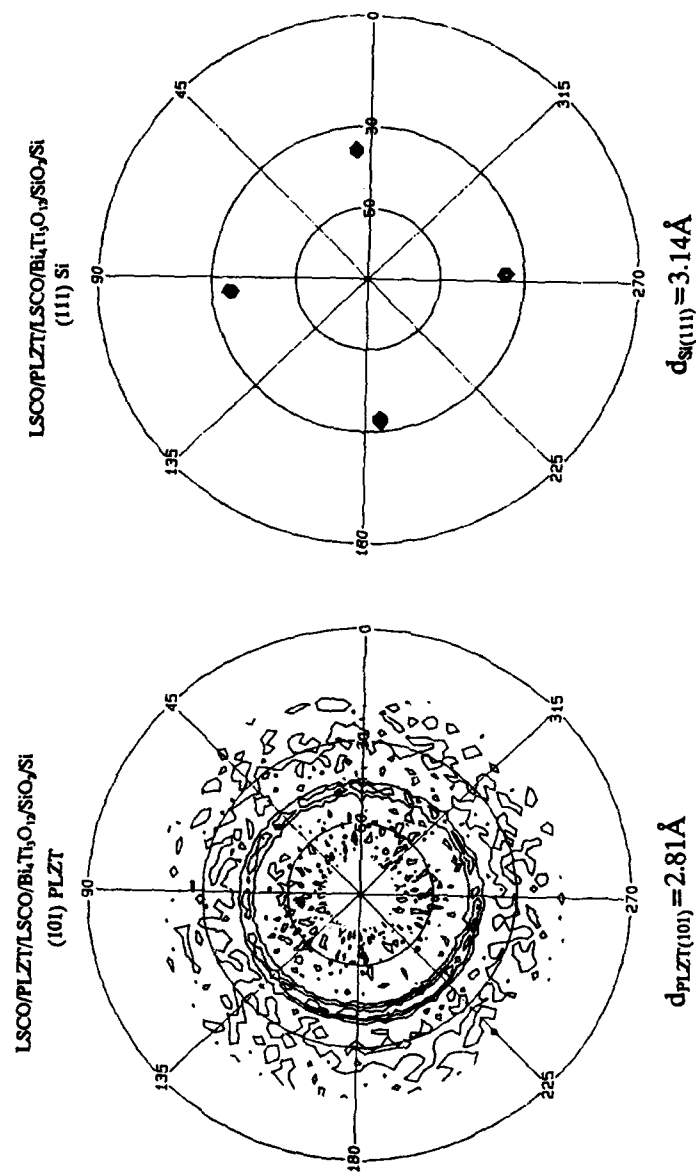


Figure 11. (101)PLZT and (111)Si Wulff projection pole figures from the LSCO/PLZT/LSCO/BT/SiO₂/Si heterostructure.

MICROSTRUCTURE DEVELOPMENT IN PARTICULATE CERAMIC COATINGS

Y.J. Kim, N. M. Wara, B. V. Velamakanni* and L. F. Francis
Department of Chemical Engineering and Materials Science
University of Minnesota, Minneapolis, MN 55455
*3M Company, St Paul, MN 55144

ABSTRACT

Microstructure development in particulate coatings is influenced by the particle-particle interactions and additional mechanisms, such as reaction and phase separation, which are driven by compositional changes in a coating during deposition and drying. The effect of agglomeration rate on microstructure uniformity and pore content is demonstrated using coatings produced from aqueous alumina dispersions. The addition of cellulose acetate and acetone to the alumina dispersion leads to phase separation and a coating with large cylindrical pores. The formation of particles by reactions during deposition is also discussed. The pore content of particulate titania coatings prepared in this way can be varied from 30 to 60% by changing the coating conditions.

INTRODUCTION

Ceramic coatings are often prepared from dispersions containing ceramic particles, a liquid, and sometimes binders or additives. These dispersions are coated using a variety of methods, including spraying, spin coating, dip coating and blade coating. Particulate-based processes have several advantages for the preparation of porous coatings. Particulate coatings typically have relatively large pores and thus lower capillary stresses on drying. Thus, thick ($>100\mu\text{m}$) or thin coatings can be prepared without cracking. If crystalline particles are used, less shrinkage and residual stress develops with heating as compared with sol-gel coatings which shrink considerably during drying and densification. However, the principle advantage of particulate routes is tailoring of pore size and content through changes in particle size, size distribution and dispersion stability.

Microstructure in particulate-based coatings is affected by the characteristics of the particles and the particle-particle interactions or dispersion behavior. The particle characteristics (i.e., particle shape, size and size distribution) directly influence the pore space characteristics (i.e., pore content, shape, size and size distribution) of the coating. Equally important are the attractive and repulsive particle-particle interactions which determine the rate at

To the extent authorized under the laws of the United States of America, all copyright interests in this publication are the property of The American Ceramic Society. Any duplication, reproduction, or republication of this publication or any part thereof, without the express written consent of The American Ceramic Society or fee paid to the Copyright Clearance Center, is prohibited.

which particles aggregate or agglomerate. A process that controls the particle characteristics and agglomeration can be used to tailor microstructure. For example, Xu and Anderson [1] used ceramic dispersions with controlled agglomerate size to develop porosity in ceramic membranes. Analogous controls are used to establish the green density and pore characteristics in ceramic bodies formed by methods such as colloidal consolidation [2] and slip casting [3]. Particle-particle interactions will affect the packing and agglomeration process and thus the pore size in and between agglomerates. Particles dispersed in a liquid are attracted to each other by van der Waals forces. Electrostatic repulsive forces are generated between particles that have surface charge of the same sign. Steric repulsion arises from adsorbed polymer layers on particle surfaces. Short range repulsive forces, hydration forces, become important as particles become closer in later stages of processing.[4] To prevent agglomeration and form a well-packed microstructure, repulsive forces must dominate.

Processes that occur during deposition (e.g., reaction, evaporation, aggregation) influence microstructure development. For example, coatings prepared from silicon alkoxide sols undergo simultaneous polymerization reactions and drying; the combination of these two processes causes the sol-to-gel transformation and affects gel structure.[5] With rapid reactions, the layer gels before much solvent is removed by drying and a porous coating results. The composition of the coated layer changes continually as volatile components are removed and as species from the atmosphere are adsorbed. Compositional changes can serve as a driving force for microstructure changes in the developing layer. In this paper, we describe several methods of microstructure control for particulate-based coatings. Coatings prepared from dispersions of alumina in water serve as an example of the influence of particle-particle interactions on microstructure and multicomponent dispersions containing alumina, water, cellulose acetate and acetone show the added influence of phase separation. The use of in situ particle formation and stabilizing additives to tailor pore content and structure is discussed for titania coatings.

ALUMINA COATINGS

Experimental Procedure

Alumina coatings were prepared by spin coating aqueous alumina dispersions onto glass substrates. Dispersions containing 50 weight% alumina with pH values of 4, 6.5, 9, and 11.5 were prepared by combining alumina (Alcoa A16, average particle diameter = 0.34 μm) with deionized water. The pH was adjusted by titrating with hydrochloric acid or tetramethyl ammonium hydroxide. After acid or base addition, the dispersions were stirred and sonicated for 10 minutes using an ultrasonic horn (Heat Systems, 20 kHz horn with 3/4" tip). The pH adjustment and ultrasonic treatment were carried out a second time and repeated again after 24 hours. Immediately after the final ultrasonic treatment, the dispersions were spin coated onto glass cover slips using a spinning rate of 1500 rpm for 60 seconds. After room temperature drying, the microstructures were examined using scanning electron microscopy (SEM; JEOL Model 840).

Dispersions containing varying amounts of alumina and cellulose acetate were prepared by combining a 50 weight% alumina dispersion (pH=4) with a 10 weight% solution of cellulose acetate (molecular weight of 30,000) in acetone. A range of compositions were investigated. (See Table I.) To prevent phase separation of the polymer in the coating solution, the weight ratio of cellulose acetate:acetone:water was fixed at 5:25:70. Some dispersions required that additional acetone and water be added to the 10 weight% cellulose acetate solution before combination with the alumina-water dispersion. The combined alumina-cellulose acetate dispersions were stirred for 1 hour and placed in an ultrasonic bath for 1 hour, with stirring at 10 minute intervals. Coatings were prepared on glass slides using manual drawdown (0.75 in/sec) of a rigid doctor blade set at a fixed gap (0.02 in.). Immediately after deposition, the coatings were immersed in a water bath for 5 minutes. As described later, this procedure affects the phase separation process and consequently the final microstructure. The microstructures of the resulting composite coatings were investigated by SEM.

Table I Dispersion and Coating Compositions for Alumina-Cellulose Coatings

Samp. No.	Alumina (g)	Water (g)	Cellulose Acetate (g)	Acetone (g)	Dry Coating Composition
1	25.0	25	5	70	62 vol% Alumina 38 vol% Cell. Acet.
2	17.7	25	5	70	54 vol% Alumina 46 vol% Cell. Acet.
3	11.1	25	5	70	42 vol% Alumina 58 vol% Cell. Acet.
4	5.3	25	5	70	26 vol% Alumina 74 vol% Cell. Acet.

Effect of Colloidal Stability

Figure 1 shows the change in microstructure for coatings prepared using alumina dispersions having a range of pH values. Near the isoelectric point (pH=9), electrostatic repulsion between particles is low, attractive forces dominate and the agglomeration rate is high. Consequently, the microstructure contains large agglomerates and is poorly packed. As the pH is shifted away from the isoelectric point, surface charges develop and electrostatic repulsion increases; the microstructures show better particle packing and a decreased number of large agglomerates. Coatings prepared from well stabilized dispersions (pH=4) have a uniform, packed microstructure, presumably with a minimum of pore space. These results demonstrate a simple method to control microstructure (i.e., increasing repulsive interactions changes the microstructure from agglomerated and porous to well-packed and dense. Similar strategies are used in other ceramic forming methods. For coatings, variables such as coating rate and thickness also affect the microstructure and are part of on going investigations.

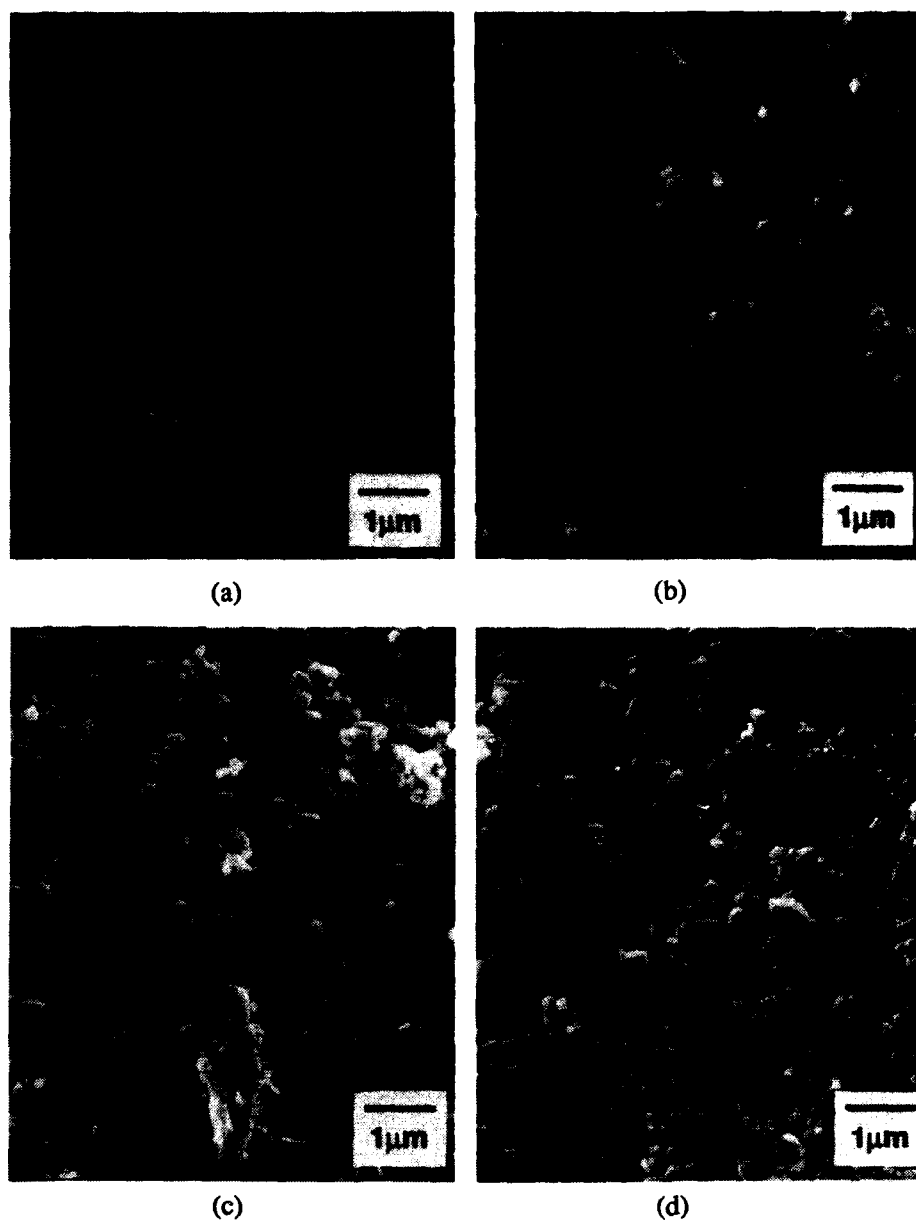


Fig. 1 SEM micrographs of alumina coatings prepared from dispersions with pH values of (a) 4, (b) 6.5, (c) 9, and (d) 11.5.

Effect of Cellulose Acetate Addition

Figure 2 shows the changes in microstructure of alumina coatings with increasing cellulose acetate content. The combined alumina-cellulose acetate dispersions used to prepare these coatings were stabilized at a pH of 4 so as to prevent agglomeration of alumina particles. The presence of acetone tended to decrease the effectiveness of electrostatic repulsion, but the cellulose acetate provided some steric stabilization to the dispersions. Zeta potential, viscosity and polymer adsorption studies on this system will be reported elsewhere.[6] As the polymer content is increased, the coatings change from an open particulate structure to a continuous polymer network with dispersed alumina particles. A new type of cylindrical pore structure is introduced with higher polymer content. At approximately 58 volume % cellulose acetate, the microstructure is characterized by evenly distributed and symmetrical large pores. The origin of microstructural features can be understood in terms of the polymer phase separation behavior.

Phase separation occurs over a large compositional region in the ternary system of cellulose acetate, acetone and water.[7] The separation arises because acetone is a solvent and water a nonsolvent for cellulose acetate. At the cellulose acetate:acetone:water weight ratio of 5:25:70 used in this research, the cellulose acetate dissolves completely in the acetone/water mixture. As a deposited layer of the solution dries, its composition is driven into the two phase region because the solvent (acetone) evaporates at a faster rate than the nonsolvent (water). This process is encouraged by immersion into a water bath; acetone diffuses out of the coating and water diffuses in. The phase separated system consists of a continuous polymer-solvent phase and a discontinuous water droplet (polymer lean) phase. Due to polar interactions between the cellulose acetate and the water droplets, the polymer collects on the surface of the water droplets. As the diffusion of acetone and water continues, the polymer chains begin to entangle and eventually the coating gels with the pore structure determined by the water droplet configuration. The resulting coating microstructure is asymmetric with a thin dense polymer layer at the coating-nonsolvent bath interface and a thick porous underlayer. Cellulose acetate layers find application as asymmetric desalination membranes.[8] The pore structure can be altered by changing variables, such as the initial composition, the relative humidity in the coating atmosphere, and the time delay before water immersion. [7,8]

The addition of the cellulose acetate and acetone to the aqueous alumina dispersion has a significant effect on the coating microstructure. The coatings prepared with minor amounts of polymer (Fig 2a) have a uniform pore size and a more open structure as compared to those prepared without the polymer (Fig. 1). At low polymer contents, the alumina particles appear to interfere with the phase separation mechanism. However, with greater amounts of polymer (Fig 2c, d), cylindrical pores form due to the segregation of the water rich phase. Backscattering electron images show that alumina particles are uniformly distributed in the composite.[6] A variety of microstructures can be generated by varying the dispersion composition or the processing variables; thus, the combination of ceramics and polymers in phase separating systems has great potential for developing new composites and for microstructural tailoring.

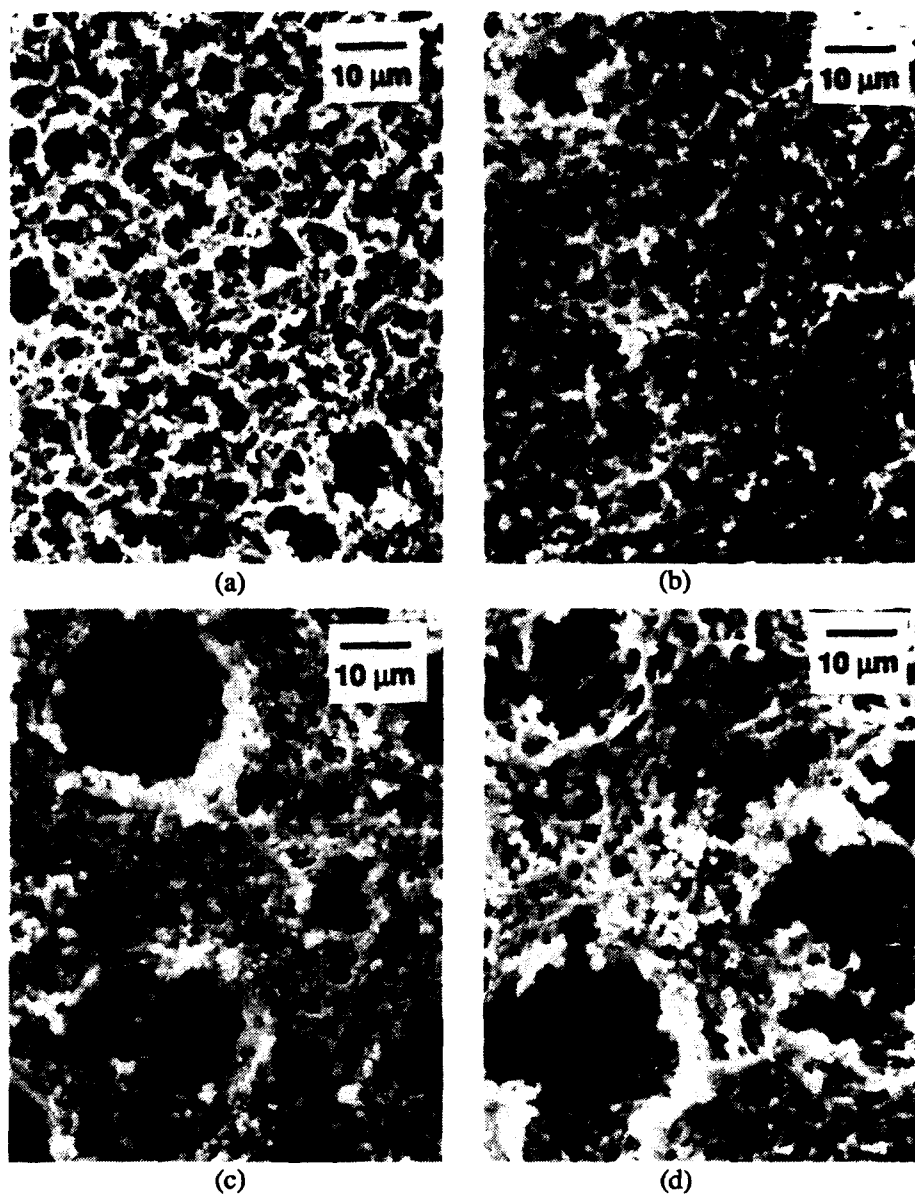


Fig. 2 SEM micrographs of alumina-cellulose acetate coatings containing (a) 38, (b) 46, (c) 58, and (d) 74 volume % cellulose acetate. The bottom surface of the coating (the coating separates from the glass substrate) is shown.

TITANIA COATINGS

Experimental Procedure

Titania coatings were prepared by depositing anhydrous titanium ethoxide/ethanol solutions onto silicon substrates. Spin coating was carried out in controlled relative humidity (~45% for most experiments). The details of solution and coating preparation are reported elsewhere.[9] Reaction during spin coating leads to the formation of a coating of particles and particle clusters; thicker coatings were prepared by repeated depositions. To control particle agglomeration, additions of hydroxypropyl cellulose (HPC, molecular weight of 100,000) and hydrochloric acid to the solutions were investigated. Coatings were heat treated in a box furnace to remove residual organics and develop porous crystalline microstructures. Firing temperatures up to 1000°C were investigated, using a heating rate of 10°C/min and dwell time of 20 minutes.

The effects of processing variables on the coating microstructure were characterized after deposition and at stages during thermal treatment. Structural features, such as particle size, pore size and thickness, were evaluated by SEM (JEOL 840, Hitachi S-900) and transmission electron microscopy (TEM; Phillips CM30). For a semiquantitative comparison of the pore content in the coatings, a thermogravimetric desorption of liquids (TDL) method was used. Unfortunately, conventional techniques for measuring porosity, such as mercury porosimetry and gas adsorption, can not be used on thin coatings and more sophisticated methods based on a SAW device [10] are not available for our research. TDL is a simple alternative and has been successfully used to characterize the porosity of silica gels.[11] In our procedure, the pore space of a coating (still on the Si substrate) is filled with ethylene glycol by first holding the coating in vacuum for 20 minutes and then soaking in ethylene glycol for 5 minutes. After carefully removing excess liquid, the sample is loaded into a thermogravimetric analyzer (TGA; model TGA7, Perkin Elmer) and heated at 10°C/min to 800°C. The relative amount of porosity is determined from the weight loss data and the coating dimensions. The volume percent of the coating that was filled with the liquid is determined and used as a measure of percent porosity in the coating.

Control of Coating Porosity

Figure 3 shows a typical as-deposited and dried coating. The microstructure consists of particles (~200 nm) and agglomerates of particles with a range of pore sizes. Particles form during deposition as atmospheric moisture diffusing into the coating reacts with Ti ethoxide.[9] The microstructural features strongly depend on the processing variables (i.e., Ti concentration, spinning rate, relative humidity). The use of solutions with higher Ti concentration and slower spinning rates results in a larger particle size and thicker coating. In general, the coating contains a large pore content, including pores between agglomerates and within agglomerates. Additionally, TEM results shows small pores within individual particles.[12] This result is consistent with the research on the precipitated particles prepared in bulk solution.[13]

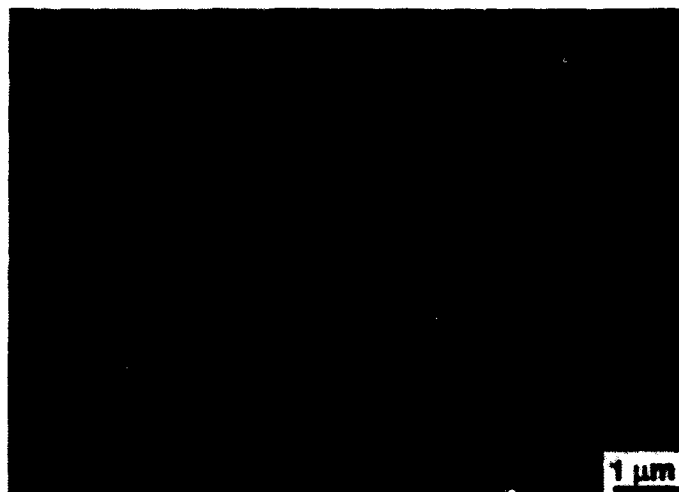
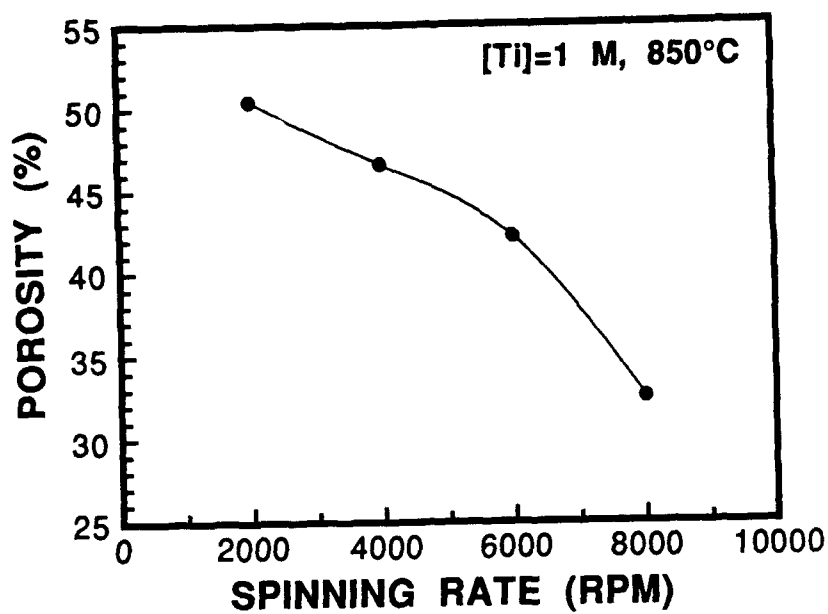


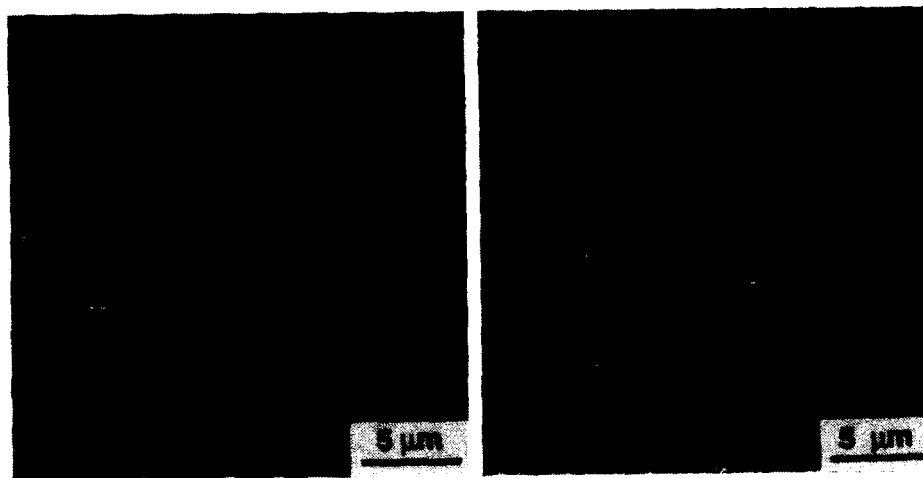
Fig. 3 SEM micrograph of a coating prepared using a 0.5M Ti ethoxide solution spin coated at 2000 rpm. Five layers were deposited with 100°C heat treatments between depositions.

Results from TDL experiments are shown in Figure 4 for coatings prepared using a 1.0M Ti ethoxide solution and several spinning rates. The percent porosity in the coatings decreases from 50 to 32% as the spinning rate increases. At faster spinning rates, particles are smaller and less time is available for agglomeration. The TDL data are consistent with SEM results. For coatings prepared using a 0.5M Ti solution, a larger percent porosity is measured, but the measurements were not as repeatable on these coatings due to their smaller thickness. In principle, TDL can be used to evaluate pore size distribution by measuring desorption isotherms; however, these experiments were not successful with our samples, perhaps due to the small quantity of material or the relatively large pore size. TDL does provide a good semiquantitative means of comparing pore contents in thin coatings; more research is underway on this method.

Coating porosity is also affected by the number of depositions and the firing temperature, as shown in Figure 5. As more layers are deposited, the porosity of the coatings decreases from 61 to 44%. This result is expected since newly formed particles can fill some of the pores in subsequent layers. TEM results show that, in addition to particles, a residual thin gel layer deposits.[12] This gel layer also builds up in the pore space of the coating and tends to decrease the porosity. The effect of thermal treatment on the microstructure is also shown in Figure 5. When a heating rate of 10°C/min is used, coatings heated at 1000°C show about 4% lower porosity than those at heated 850°C and microstructures do not show significant sintering. With faster heating rates and longer dwell time, more densification occurs; however, full density is difficult to achieve due to the constraint of the substrate.



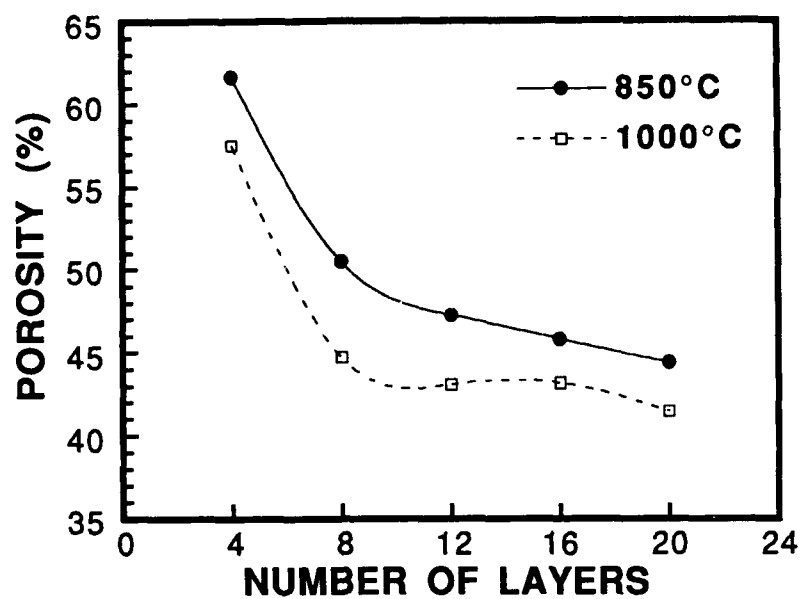
(a)



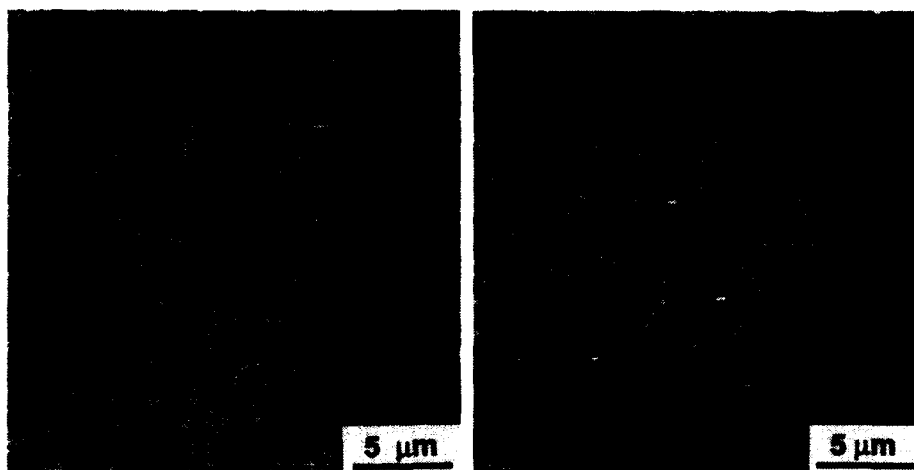
(b)

(c)

Fig. 4 (a) TDL data for coatings prepared using a 1.0M Ti solution and SEM micrographs of two of the coatings: (b) 2000 rpm and (c) 8000 rpm. All coatings were prepared with 8 depositions and a final firing at 850°C.



(a)



(b)

(c)

Fig. 5 (a) TDL data for coatings prepared using a 1.0M Ti solution and spin coated at 2000 rpm and SEM micrographs: (b) 4 layers (thickness = 2.25 μm) heated at 850°C and (c) 20 layers (thickness = 7.20 μm) heated at 850°C.

Control of Particle Agglomeration

Titania particles formed during deposition agglomerate easily due to strong attractive forces. To prevent agglomeration of particles in bulk precipitation of titania from Ti ethoxide solutions, hydrochloric acid [14] and hydroxypropyl cellulose (HPC) [15] have been used as electrostatic and steric stabilizers, respectively. For coatings which are formed by in situ particle formation, these stabilizers are added to the precursor solution before deposition. A series of experiments was carried out to find the optimum amount of additive. Hydrochloric acid gives the particles positive surface charge for electrostatic repulsion, but when the acid content is above a critical level particle formation is inhibited. HPC prevents agglomeration by creating a protective polymer layer on the particle surface; a wide range of polymer content could be used, but too much polymer led to bridging flocculation of the particles. Figure 6 compares the effectiveness of the steric and electrostatic stabilizers on single layer coatings prepared with optimal amounts of the additives. Without additives, the coating contains large particle agglomerates. By contrast, the use of stabilizing additives, especially HPC, results in separated particles and small agglomerates. Electrostatic stabilization proved less effective than steric because of the limitation on the amount of acid that could be added and the ineffectiveness of electrostatic repulsion in low dielectric constant liquids. For both additives, the optimum concentration depends on Ti concentration in the solution and other processing variables, such as spinning rate. Coatings with a uniform pore size were prepared using HPC and multiple depositions, as illustrated in Figure 7. Particles have a uniform size and are packed well into a denser coating.

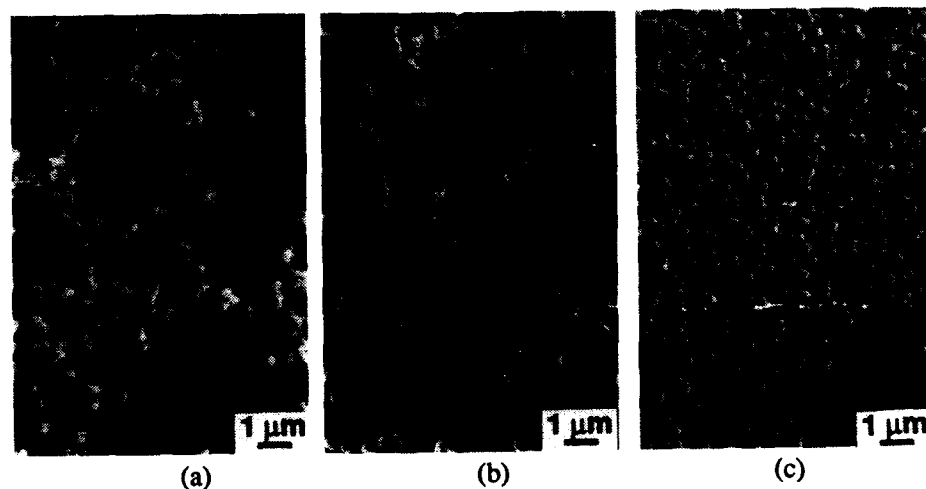


Fig. 6 SEM micrographs of coatings prepared from 0.2M Ti ethoxide solution (a) w/o additives, (b) w/ HCl (8.5×10^{-4} M) and (c) w/ HPC (1.7×10^{-3} g/cm³).

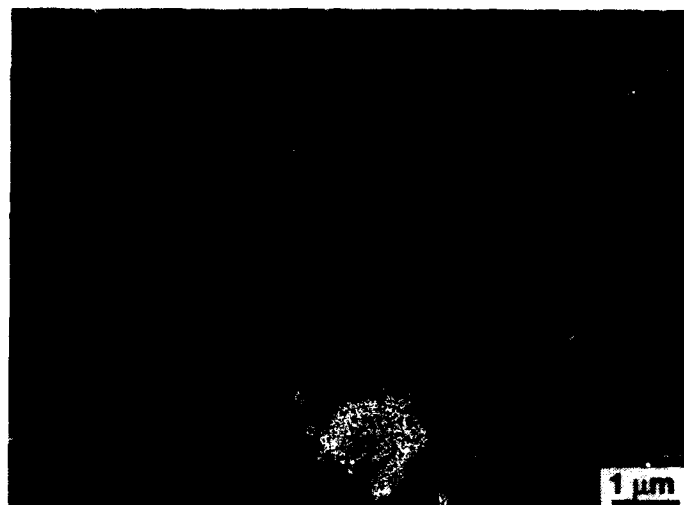


Fig. 7 SEM photomicrograph of the coating prepared from 0.2M Ti solution at 2000 rpm and heat-treated at 1000°C with HPC additive. Heatings at 550°C between depositions were used.

SUMMARY

Particulate ceramic coatings were prepared using dispersions of particles in a liquid, mixed ceramic-polymer dispersions and solutions that form particles during deposition. Microstructure development in all cases is affected by the particle-particle interactions in the coating during deposition. As expected, increasing repulsive forces between particles leads to less agglomeration and a more densely packed microstructure. Compositional changes occurring during deposition and drying can be used to create more complex microstructures. An alumina-cellulose acetate system was formulated to undergo phase separation during deposition and drying. The composite microstructure has additional assymetric porosity. Titania coatings were prepared through particle formation by reaction during spin coating. This route allows the fabrication of ceramic coatings with a large range in pore contents. In summary, this research has shown that microstructure development in coatings can be driven by compositional changes that are not usually accessible in processing of bulk ceramics.

ACKNOWLEDGEMENTS

The authors gratefully acknowledge research support from the U. S. Army Research Office and the 3M Company. We also acknowledge the use of facilities at the High-Resolution Electron Microscopy Center at the University of Minnesota.

REFERENCES

1. Q. Xu and M. A. Anderson, "Synthesis of Porosity Controlled Ceramic Membranes," *J. Mater. Res.*, **6**[5], 1073-1081 (1991).
2. I. A. Aksay, "Microstructure Control Through Colloidal Consolidation," pp. 94-103 in Forming of Ceramics, Advances in Ceramics, **9**, Ed. J. A. Mangels and G. L. Messing (The American Ceramic Soc., Columbus, 1984).
3. A. K. Nikumbh, H. Schmidt, K. Martin, F. Ponz and F. Thummler, "Influence of pH on the Rheological Properties of Al₂O₃ Slips," *J. Mater. Science*, **25**, 15-21 (1990).
4. B. V. Velamakanni, J. C. Chaing, F. F. Lange and D. S. Pearson, "New Method for Efficient Colloidal Particle Packing via Modulation of Repulsive Lubricating Hydration Forces," *Langmuir*, **6**[7], 1323-5 (1990)
5. R. A. Cairncross, L. F. Francis, and L. E. Scriven, "Competing Drying and Reaction Mechanisms in the Formation of Sol-to-Gel Films, Fibers, and Spheres," *Drying Technology*, **10**[4], 893-923 (1992).
6. N. M. Wara, B. V. Velamakanni and L. F. Francis, to be submitted.
7. H. Strathmann, P. Scheible and R. W. Baker, "A Rationale for the Preparation of Loeb-Sourirajan-Type Cellulose Acetate Membranes," *J. of Appl. Polymer Science*, **15**, 811-826 (1971).
8. R. E. Kesting, Synthetic Polymeric Membranes: A Structural Perspective, (John Wiley & Sons, New York, 1985).
9. Y. J. Kim and L. F. Francis, "Processing and Characterization of Porous Titania Coatings," *J. Amer. Ceram. Soc.*, **76** [3], 737-42 (1993).
10. G. C. Frye, A. J. Ricco, S. J. Martin, and C. J. Brinker, "Characterization of the Surface Area and Porosity of Sol-Gel Films Using SAW Devices," pp. 349-354 in Better Ceramics Through Chemistry III, Edited by C. J. Brinker, D. E. Clark, and D. R. Ulrich. *Mat. Res. Soc. Symp. Proc.*, **121**, (North-Holland, New York, 1988).
11. J. Goworek and W. Stefaniak, "Characteristics of the Pore Structure of Silica Gels by Thermogravimetric Desorption of Liquids," *Colloids and Surfaces*, **55**, 359-364 (1991).
12. Y. J. Kim and L. F. Francis, to be submitted.
13. L. H. Edelson and A. M. Glaeser, "Role of Particle Substructure in the Sintering of Monosized Titania," *J. Amer. Ceram. Soc.*, **71** [4], 225-235 (1988).
14. J. L. Look and C. F. Zukoski, "Alkoxide-Derived Titania Particles: Use of Electrolytes to Control Size and Agglomeration Levels," *J. Amer. Ceram. Soc.*, **75** [6], 1587-1595 (1992).
15. J. H. Jean and T. A. Ring, "Processing Monosized TiO₂ Powders Generated with HPC Dispersant," *Am. Ceram. Soc. Bull.*, **65**[12] 1574-77 (1986).

ROLE OF MACRODEFECTS IN PZT THIN FILMS FOR MICROELECTROMECHANICAL SYSTEMS

T. G. Cooney, E. A. Hachfeld and L. F. Francis
Department of Chemical Engineering and Materials Science,
University of Minnesota, Minneapolis, MN 55455-0132

ABSTRACT

Sol-gel derived lead zirconate titanate thin films were deposited on Si/SiO₂/Ti/Pt substrates which had varying surface roughness (~40-100 Å RMS) and contained larger features with varying vertical relief (0.1 - 0.6 μm). The incidence of cracking increased as the surface roughness increased. Cracks initiated at the corners of rectangular surface features; macrodefects were more severe on narrow surface features and those with larger height and when more sol layers were deposited. To avoid defects, changes in the sol composition and device design are suggested.

INTRODUCTION

Microelectromechanical systems (MEMS) are comprised of small (10's of microns) mechanical and electromechanical devices fabricated on the surface of semiconductor-based integrated circuits. Major components of the technology include microactuators and microsensors. MEMS has commercial applications spanning biomedical (e.g., blood pressure sensors), manufacturing (e.g., microflow controllers), information processing (e.g., imagers and displays) and automotive (e.g., accelerometers for air bags) industries.[1-3] While MEMS devices have been fabricated using common materials in microelectronics, such as polycrystalline silicon, silicon nitride, silica and some metals, the use of piezoelectric ceramic thin films in these devices holds promise for improving their performance. Ceramics in the Pb(Zr_{1-x}Ti_x)O₃ (PZT) system have outstanding electromechanical properties that are useful for both sensing and actuating functions. However, integration of ceramics into complex MEMS devices, such as the pressure sensor shown in Figure 1, poses processing challenges. The ceramic layer must have the appropriate composition and crystal structure; it should be uniform and free of macrodefects, such as cracks and delamination. Film quality is especially critical for MEMS as the thin films are often subjected to mechanical deformation during use.

The sol-gel method is well suited to the preparation of ferroelectric thin films and currently is a popular processing route.[4] Advantages of the sol-gel

To the extent authorized under the laws of the United States of America, all copyright interests in this publication are the property of The American Ceramic Society. Any duplication, reproduction, or republication of this publication or any part thereof, without the express written consent of The American Ceramic Society or fee paid to the Copyright Clearance Center, is prohibited.

route over other fabrication methods include better stoichiometric control and compositional variety, low level doping capability, simplicity and low cost.[5] Disadvantages include difficulties with coverage of surface features and forming uniform layers, free of macrodefects such as cracks. Stresses that develop during processing are responsible for many of the defects. Garino and Harrington [6] found tensile stress levels of 100 - 400 MPa in sol-gel derived PZT films. Stress singularities at edges and concentration of stresses at microscopic flaws or surface features magnify stress and lead to defects.

Considerable progress has been made in understanding processing issues for ferroelectric thin films deposited on flat, uniform substrates. High quality layers with the perovskite structure and good ferroelectric properties have been fabricated by many groups. However, for more wide-spread application of ferroelectric thin films in the microelectronics industry and specifically for MEMS applications, a better understanding of the formation and control of macrodefects is needed. In this paper, we investigate the effects of surface topology on macrodefect formation in sol-gel derived PZT thin films. Fine scale surface roughness and larger scale vertical relief features are intentionally introduced and their effects on film structure studied by microscopy methods.

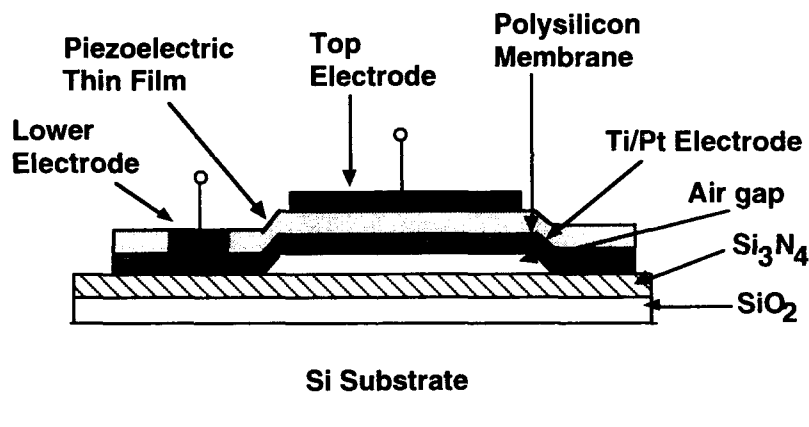


Fig. 1 Schematic diagram of an integrated pressure sensor with a sol-gel derived PZT layer acting as a force sensor. [7]

EXPERIMENTAL PROCEDURE

Alkoxide solutions based on the 2-methoxyethanol system were prepared using the method developed by Budd *et al.*[8] The precursor solution had the composition of $\text{Pb}(\text{Zr}_{0.54}\text{Ti}_{0.46})\text{O}_3$ and had a concentration of 1M in Pb. The alkoxide solution was partially hydrolysed by combining equal volumes of

precursor and a solution of 2-methoxyethanol, water and NH_4OH such that the hydrolysis ratio ($[\text{H}_2\text{O}]/[\text{Pb}]$) was 1 and 0.12 moles of NH_4OH were added per mole of Pb. After 24 hours, the partially hydrolysed solutions were deposited onto Si/SiO₂/Ti/Pt substrates by spin coating at 2000 rpm for 60 seconds. Each layer was dried at 200°C for one minute on a hot plate. After four layers were deposited and dried, the samples were heated at 400°C for 10 minutes and then 700°C for 15 minutes. The process was repeated to prepare thicker films. This heating schedule was chosen based on TGA results (Fig. 2) that showed organic pyrolysis in the range of 400-550°C and XRD results that showed complete perovskite formation after the 700°C treatment.

Varying surface roughness and larger regions of vertical relief were built into the Si/SiO₂/Ti/Pt substrates so that surface coverage and film integrity could be systematically investigated. The basic substrate had 1000 Å of thermally grown SiO₂ with layers of Ti (400 Å) and Pt (1000 Å) deposited by sputtering. Substrates with surface roughnesses varying from 40 to 100 Å root mean square (RMS) were prepared by altering the sputtering conditions. Vertical relief structures had two features: large flat areas (50 x 100 μm) to simulate the raised membranes for pressure sensors or the larger area surfaces of actuators, and narrow projections (~3 μm wide) to represent conduits into micropumps or electrode pads. These features were fabricated by depositing a layer of phosphosilicate glass (PSG) by CVD (2700 - 7000 Å), patterning and etching the pattern in the PSG layer, reflowing to smooth edges, growing 1000 Å of thermal oxide on exposed Si, and lastly sputtering Ti (400 Å) and Pt (1000 Å).

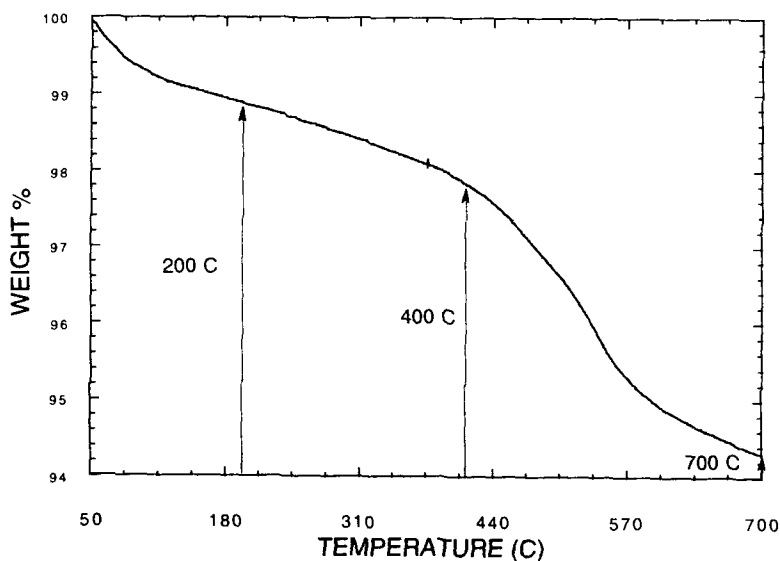


Fig. 2 Thermogravimetric analysis of a PZT thin film (10 layers, 0.8 μm).

Optical microscopy and scanning electron microscopy (SEM; JEOL 840) were used to characterize thin film macro and microstructures, and macrodefect evolution. Surface roughness was monitored by phase measurement interferometric microscopy (PMIM; Zygo Maxim 3D).

RESULTS AND DISCUSSION

Figure 3 shows the variation in surface roughness with increasing film thickness for films crystallized at 700°C and for those heated only to 200°C. The substrate was initially at 38 Å RMS roughness. With one deposition, the crystalline film roughness is similar to that of the substrate while the amorphous film is smoother. The crystallization treatment enhances the roughness, perhaps due to the morphology of the grains or the differences in densification around surface features. As more layers are deposited, the roughness increases. This result indicates that the surface features affect the uniformity of the sol-gel coating; surface protrusions may trap sol during the spin off stage of the deposition in which the centrifugal forces drive the liquid off. As the layers become thicker and surfaces become rougher, the incidence of cracking also increases. Cracking develops in the amorphous films at a lower level of surface roughness and at lower overall film thicknesses as compared with the crystalline films. The level of stress in the thin film depends on the thermal treatment; Garino and Harrington reported that the room temperature residual stress after

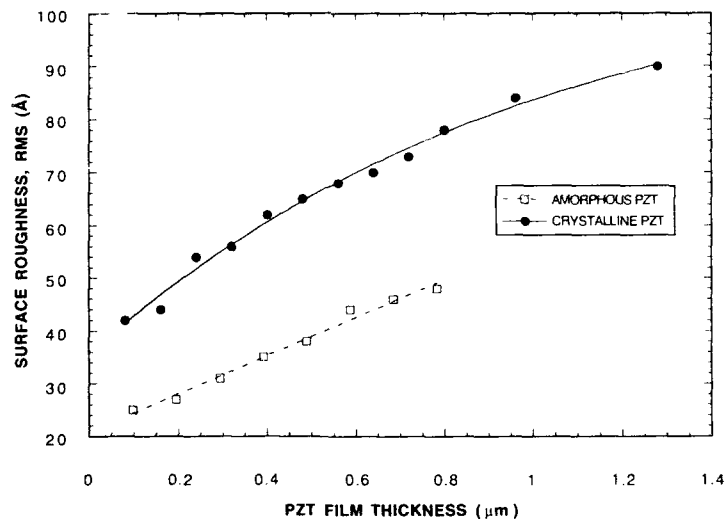


Fig. 3 Surface roughness measured from PMIM on PZT layers deposited on a Pt/Ti/SiO₂/Si substrate with 38 Å RMS roughness.

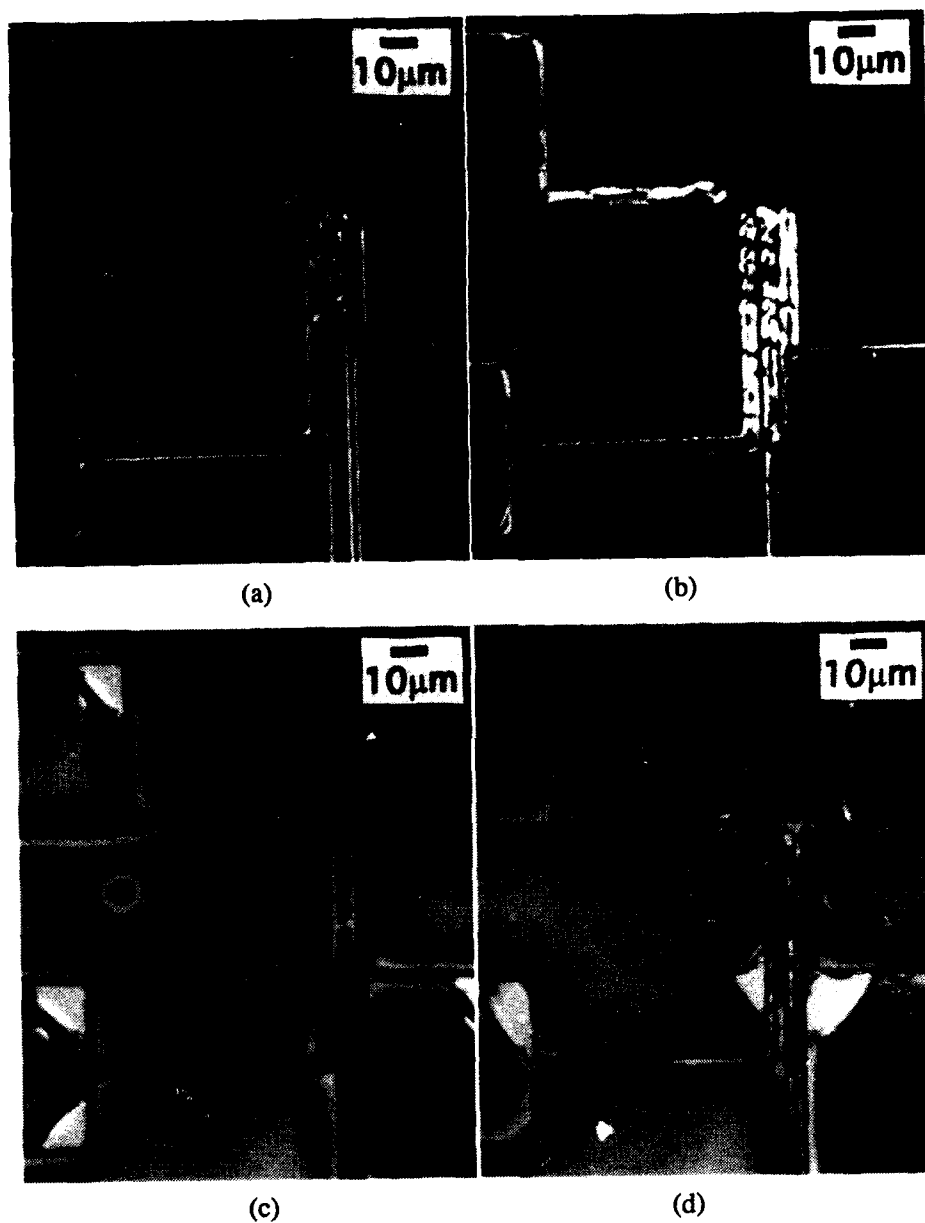


Fig. 4 Optical micrographs of one layer (0.08 μm) of PZT sol deposited and heat-treated (to 700°C) on features with (a) 0.4 μm and (b) 0.6 μm vertical relief, and two layers deposited and heat-treated on features with (c) 0.4 μm and (d) 0.6 μm vertical relief.

pyrolysis was slightly greater than that after crystallization of perovskite. [6] Complete film cracking and delamination for crystalline films occurs after 16 layers (or 1.28 μm final thickness), corresponding to a surface roughness of 90 Å RMS. In another set of experiments, substrates with a range of surface roughnesses were prepared and a single sol layer deposited on each and heated to 700 °C. Interestingly, as the roughness of the substrate increased, the incidence of cracking increased and complete film failure was observed for a single crystallized layer deposited a substrate with 90 Å RMS roughness.

The effect of step height and number of layers on the defect formation is illustrated in Figure 4. With a single layer deposited and heat-treated (Fig 4b), cracks begin to form at corners. The cracking becomes severe first on the narrow areas of the steps and particularly where several narrow areas are close to one another. The incidence of cracking increases with step height (Fig 4b) and with multiple depositions the macrodefect formation is more widespread with delamination across the large raised areas (Fig 4c). Irregularities in coverage [9] and stress concentration are the most likely cause of this behavior. Our future research plans include quantifying these effects.

To avoid the defects due to surface topology, two approaches can be taken. First, the microfabrication routes can be carefully chosen to provide surfaces that are very smooth and MEMS devices can be designed such that the sol-gel layer is deposited on flat surfaces. Recessed membranes in pressure sensors, for example, have been cleverly developed so that a PZT sol-gel layer is easily incorporated.[10] The second option is to design tolerance to topological variation into the solution chemistry and processing conditions; that is, develop a sol-gel process that creates a layer that is less susceptible to stress induced macrodefects. This approach involves recognizing the critical stages in the process (when the stress is great) and using changes in sol composition and process conditions to relieve stress. Recent work on drying control chemical additives and other additives, such as polyethylene glycol, suggests that the chemical route has promise. The best approach is most likely a combination of improvements in design of MEMS structures to accommodate ceramic films and improvements in thin film processing to make the films more tolerant of surface topology.

ACKNOWLEDGEMENTS

This research was supported by the National Science Foundation. Support from the ISHM educational foundation is also acknowledged. We thank Mr. P. Schiller and Mr. D. Glumac for preparing substrates, and Prof. D. L. Polla for helpful conversations.

REFERENCES

1. See for example: R. T. Howe, R. S. Muller, K. J. Gabriel and W. S. N. Trimmer, *IEEE Spectrum*, July 1990, pg 29; L. O'Connor, "MEMS: Microelectromechanical Systems," *Mech. Engineering*, Feb. 1992. pg. 40-47

2. L. O'Connor, "Tiny Devices Take on Tough Tasks in Biomedicine," *Mech. Engineering*, May 1993, pg. 62-67
3. Miniturization Technologies, Congress of the United States, Office of Technology Assessment, 1991.
4. G. H. Haerling, "Current Status of Thin/Thick Film Ferroelectrics," pg. 1-18 in Ferroelectric Films, edited by A. S. Bhalla and K. M. Nair, *Ceramic Transactions*, **25** (American Ceramic Society, 1992).
5. C. J. Brinker and G. W. Scherer, Sol-Gel Science: The Physics and Chemistry of Sol-Gel Processing, (Academic Press, New York, 1990)
6. T. J. Garino and M. Harrington, "Residual Stress in PZT Thin Films and Its Effect on Ferroelectric Properties," pg. 341-347 in Ferroelectric Thin Films II, *Materials Research Society Symposium Proceedings*, **243**, edited by A. I. Kingon, E. R. Myers, and B. A. Tuttle. (Materials Research Society, Pittsburgh, PA, 1990).
7. C.-C. Hsueh, C. Ye, A. Helgeson, and D. L. Polla, "Sol-gel Derived Ferroelectric Thin Films in Silicon Micromachining," pg. 231-244 in *ISIF-91 3rd International Symposium on Integrated Ferroelectrics*, 1991.
8. K. D. Budd, S.K. Dey, and D. A. Payne, "Sol-gel Processing of PbTiO_3 , PbZrO_3 , $\text{Pb}(\text{ZrTi})\text{O}_3$ and $\text{PbLa}(\text{ZrTi})\text{O}_3$," *Brit. Ceram. Proc.*, **36**, 107-21 (1985).
9. D. E. Bornside, "Mechanism for the Local Planarization of Microscopically Rough Surfaces by Drying Thin Films of Spin-Coated Polymer/Solvent Solutions," *J. Electrochem. Soc.*, **137** [8], 2589-2595 (1990).
10. P. Schiller and D. L. Polla, "Integrated Piezoelectric Microactuators Based on PZT Thin Films," *7th International Conference on Solid State Sensors and Actuators*. Yokohama, Japan, June 1993.

Design and Properties of Materials

NONLINEAR CONDUCTION MECHANISM IN PEROVSKITE TYPE CERAMICS

N. ICHINOSE, Waseda University
Tokyo 169, Japan

ABSTRACT

Intelligent functions such as PTCR (Positive Temperature Coefficient Resistor) and VDR (Voltage Dependent Resistor) effects in perovskite type ceramics may be generated by the formation of potential barrier at the grain boundary. Of the various conduction mechanisms reported for the origin of the nonlinearity, the most prominent one is due to electron tunneling and/or hole transport induced by impact ionization, explained by a double Schottky type potential barriers model. Thus grain boundaries have a significant role in determining the flow of electronic current. It is well known that these effects depend upon oxygen partial pressure. Energy barriers are closely related to adsorbed oxygen on grain surfaces. The interfacial energy levels are thought to be caused by the chemisorbed oxygen onto the interfaces of the grains. In the present study, the relation between the type of the chemisorbed oxygen and these effects has been investigated.

1. INTRODUCTION

Perovskite type ceramics such as BaTiO_3 and SrTiO_3 based ceramics have been widely used for electronic applications as resistors and capacitors. It is well known that PTCR (Positive Temperature Coefficient Resistor) and VDR (Voltage Dependent Resistor) effects in the perovskite type ceramics may be generated by the formation of potential barrier at the grain boundary. It has been reported that the energy barriers are closely related to adsorbed oxygen on grain surfaces, because these effects are degraded by heating in reducing atmosphere and restored by reoxidation.¹⁻²⁾ The interfacial energy levels are thought to be caused by the chemisorbed oxygen onto the interfaces of the grains.

The physical origin of these interface states is not an intrinsic one due to lattice mismatch at grain boundaries, but an extrinsic one due to lattice defects such as point, line, or planar defects. When oxygen in air is chemisorbed at such defects on the grain surfaces, electrons become localized at the surfaces and give rise to positive surface potential. To maintain the electrical neutrality, ionized shallow donors and bulk electron traps compensate excess charges. As a result, electron depletion layers are formed and act as conduction barriers. These interface states are thought to correspond to acceptor type energy levels formed by the chemisorbed oxygen as

To the extent authorized under the laws of the United States of America, all copyright interests in this publication are the property of The American Ceramic Society. Any duplication, reproduction, or republication of this publication or any part thereof, without the express written consent of The American Ceramic Society or fee paid to the Copyright Clearance Center is prohibited.

shown in Fig. 1. It is important to study the electronic states at the grain boundaries in view of the oxygen adsorption, including oxygen chemisorption and oxidation. However, the type of the chemisorbed oxygen has rarely been reported.

In the present study, the relation between the type of chemisorbed oxygen and these effects in the perovskite type ceramics has been investigated.

2. PTCR EFFECT IN BaTiO₃ BASED CERAMICS³⁾

BaTiO₃ based ceramics were prepared by the conventional ceramic processing as shown in Fig. 2. The mixture was calcined at 1000°C for 2h in air, pelletized, pressed into disks of 18mm diameter under 0.5ton/cm², and then fired at 1300°C for 2h in air. The sintered samples were reduced at 1100°C for 2h in a 50% H₂-Ar flowing atmosphere. Annealing conditions are shown in Table 1.

The In-Ga alloy was pasted on both surfaces of the samples to provide ohmic contact for the electrodes. The voltage-current characteristics were measured by a 2-terminal method using a dc power supply. The behaviour of the chemisorbed oxygen was examined by means of ESR. ESR spectra at X-band frequency were obtained at room temperature (the field modulation : 100kHz, the applied magnetic field : 3250±500 Oe, the microwave power : 5mW).

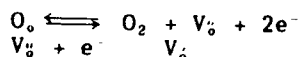
Figure 3 shows the temperature dependence of the resistivity in undoped BaTiO₃ annealed for 1h at various temperature in air.

Figure 4 represents Arrhenius plots of the resistivity in undoped BaTiO₃ annealed for 1h at various temperature in air. Above Curie temperature, they are shown in Fig. 5. It is found from Fig. 4 that the barrier height ϕ may be calculated by using the following equation.

$$R = R_0 \exp (e\phi / kT)$$

Figure 6 gives the calculated barrier height ϕ as a function of annealing temperature. This curve shows a similar tendency to PTCR effect in Fig. 7. It may be said from this fact that the chemisorbed oxygen plays an important role for forming the barrier height at grain boundary.

Figures 8-10 show ESR spectra at room temperature of undoped BaTiO₃ as sintered, as reduced and reoxidized at various conditions. A strong signal with symmetrical line shape was detected around $g=2$ in all samples. The signal (■) at around $g=1.99$ is identified as F-center⁴⁾, i.e., a signal electron trapped at an oxygen vacancy surround by two Ti⁴⁺ and/or Ti³⁺, which is represented as V_o. This V_o may be generated by the following equation.



The hyperfine sextet (Δ) observed in all samples in Figs. 8-10 is interpreted as a Ti^{3+} center, arising from the hyperfine interaction with Ti^{47} nuclei ($I=5/2$) surrounding the oxygen vacancy. Ti^{3+} created by the $\text{Ti}-\text{V}_0-\text{Ti}$ interaction is considered to be related to semiconducting properties.

In Figs. 8-10, ESR spectra indicate that the chemisorbed oxygen exists only as O_2^- with anisotropic signal (\circ); $g_{\parallel}=2.019$, $g_{\perp}=2.034$, $g_{\text{iso}}=2.077$.⁵⁾ The intensity of the O_2^- peak increase with increasing reoxidizing temperature. On the other hand, for samples as sintered and as reoxidized above 650°C , ESR spectra indicate that chemisorbed oxygen exists as O_2^- and O^- with anisotropic signals (\circ); $g_{\parallel}=g_{\perp}$, $g_{\text{iso}}=2.058$. Above 650°C of reoxidizing temperature, chemisorbed oxygen O_2^- is stable and the amount of O_2^- is increasing with increasing reoxidizing temperature. It is found from these facts that the chemisorbed oxygen O_2^- may play an important role in PTCR effect of BaTiO_3 based ceramics.

3. VDR EFFECT IN SrTiO_3 BASED CERAMICS⁶⁾

SrTiO_3 based ceramics are also prepared by the conventional ceramic processing as shown in Fig. 11. Their compositions are described in Table 2. The mixture was calcined at 1000°C for 3h in air, pelletized, pressed into disks of 18mm diameter and 3mm thickness under a pressure of $1\text{ton}/\text{cm}^2$, and then fired at 1450°C for 3h in air. The sintered samples were reduced in a 50mol.% H_2 -Ar flowing atmosphere at 1300°C for 5h. The samples obtained were polished on both sides into 1mm thickness. In order to compose the boundary layer structure, the samples were partially reoxidized in air at 800 - 1300°C for 1h.

The In-Ga alloy was also pasted on both surfaces of the samples to provide ohmic contact for the electrode. ESR spectra at X-band frequency were obtained at same conditions for previous samples. Isothermal capacitance transient spectroscopy (ICTS) measurements were performed by means of an impedance analyzer at room temperature.

Figure 12 shows dc voltage-current characteristics for sample B reoxidized at 800 - 1300°C for 1h in air. The non-linearity increases with increasing reoxidizing temperature. Sample C gave a similar tendency to sample B with reoxidizing temperature in the voltage-current characteristics. But for sample A, slightly non-ohmic properties were observed and did not change much with reoxidizing temperature.

Figures 13-15 show the nonlinear coefficient α and donor concentration N_d of samples A-C reoxidized at 800 - 1300°C for 1h in air. For all samples A-C, the barrier height ϕ_n shows a

similar reoxidizing temperature dependence to that of the α , which means that the α increases with increasing the ϕ_N . Consequently, the VDR effect of SrTiO_3 based ceramics is concluded to be caused by the increase of the barrier height ϕ_N by the oxygen chemisorption on grain surfaces.

Figure 16 represents ESR spectra of sample A as sintered, as reduced and as reoxidized at 800-1300°C for 1h in air. The signals assigned to O^- are clearly detected in sample A reoxidized above 1000°C. The ESR signal assigned to O^{2-} was not observed, because O^{2-} has no unpaired spin.

Figure 17 shows the biased voltage dependence of ICTS spectra for the sample reoxidized at 900°C for 1h in air. The ICTS spectra obtained under a biased voltage of -35V have a negative peak, while the zero biased spectra have a positive peak. This indicates the existence of the acceptor type trap level below the equilibrium Fermi level, i.e., interface states.

Figures 18 and 19 show ICTS spectra normalized by the background capacitance for the samples reoxidized below 1050°C and above 1100°C, respectively. It is seen that a discrete deep level is detected in the samples reoxidized below 1050°C. On the other hand, two deep levels are detected in the samples reoxidized above 1100°C, which are denoted T_1 and T_2 for convenience. As the time constant of the peak in Fig. 18 is close to that of the peak T_1 in Fig. 19, these peaks are considered to originate from the same interface states. Figure 20 gives DLTS spectra for the sample reoxidized at 1200°C for 1h in air. Three deep levels corresponding to the oxygen chemisorption levels as $\text{O}^{2-}(\text{P}_1)$, $\text{O}^-(\text{P}_2)$ and $\text{O}_2^-(\text{P}_3)$ were detected. The ICTS peaks T_1 and T_2 for the sample reoxidized at 1200°C in Fig. 19 are in good agreement with the DLTS peaks P_1 and P_2 in Fig. 20, respectively. Therefore, it seems that the peak in Fig. 18 and the T_1 peak in Fig. 19 originate from O^- chemisorption level, and that the T_2 peak is caused by O^{2-} chemisorption level. But a peak attributed to O^{2-} chemisorption states cannot be detected in the ICTS spectra, because the time constant of the O^{2-} peak is very short.

The intensity of the O^{2-} peak(T_2) increase remarkably with increasing reoxidizing temperature. It is considered that O^{2-} chemisorption level is newly generated by the reoxidation above the oxidation temperature. Its energy level becomes deeper and its trap density increases due to the increase in the amount of O^{2-} chemisorption with increasing reoxidizing temperature.

4. CONCLUSION

The conclusions are as follows

- (1) The chemisorbed oxygen O_2^- may play an important role in PTCR effect of BaTiO_3 based ceramics.

- (2) The O^- and O^{2-} chemisorption levels may contribute to the non-ohmic conduction in $SrTiO_3$ based ceramics

REFERENCES

- 1) E. Sonder, M. M. Austin and D. L. Kinser ; J. Appl. Phys. 54 (1983) 3566
- 2) F. A. Selim, T. K. Gupta, P. L. Hower and W. G. Carlson ; J. Appl. Phys. 51 (1980) 765
- 3) T. Takahashi, Y. Nakano and N. Ichinose ; J. Cerm. Soc. Japan 98 (1990) 879 (In Japanese)
- 4) T. Takeda and A. Watanabe ; J. Phys. Soc. Jpn. 21 (1966) 267
- 5) M. Che and A. J. Tench ; in Advanced in Catalysis, edited by D. D. Eley, H. Pines and P. B. Weisz (Academic Press, 1982) vol. 31 p.77
- 6) Y. Nakano and N. Ichinose ; J. Mater. Res. 5 (1990) 2910

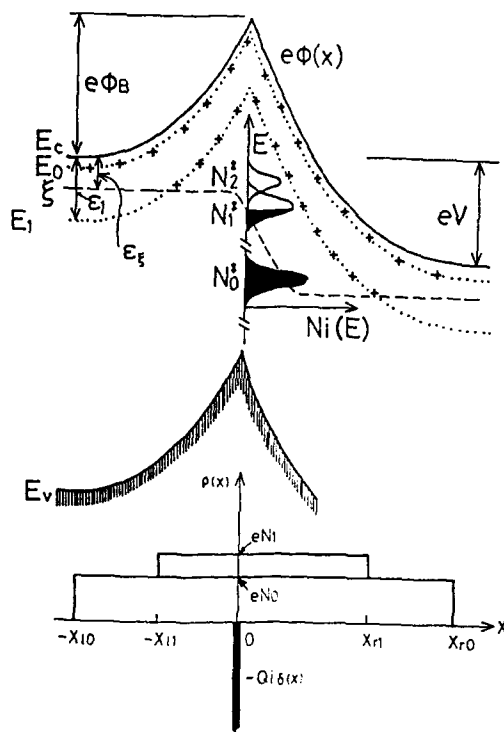


Fig. 1 Proposed DSB Model for charged grain boundary

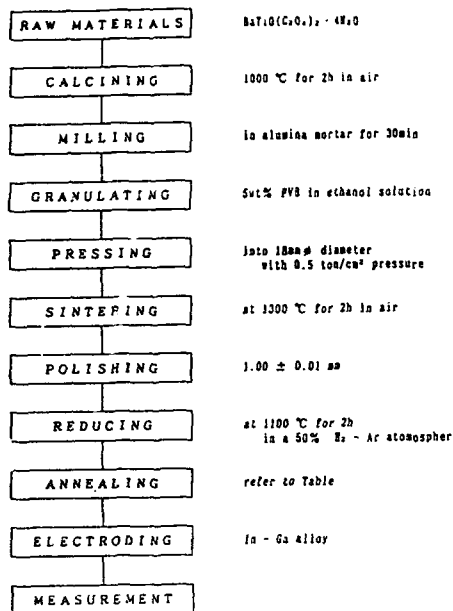


Fig. 2 Simplified flow diagram for the fabrication of nonstoichiometric undoped BaTiO_{3-x} thermistors

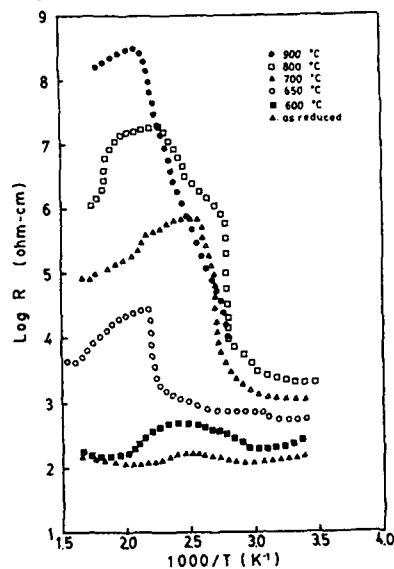


Fig. 4 Arrhenius plots of the resistivity in undoped BaTiO_3

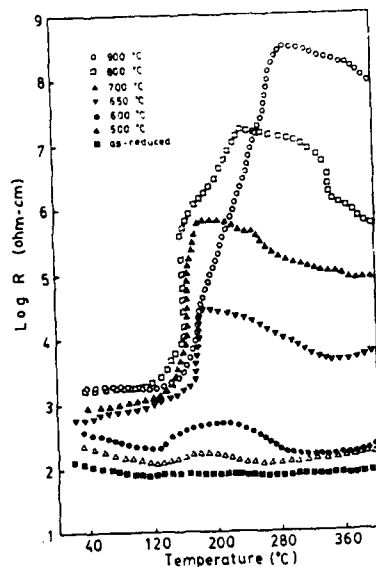


Fig. 3 Temperature dependence of the resistivity in undoped BaTiO_3 annealed for 1h at various temperatures in air

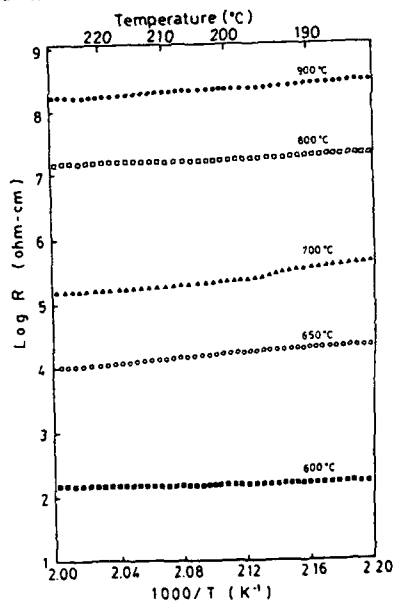


Fig. 5 Arrhenius plots of the resistivity above Curie-temperature of undoped BaTiO_3 annealed for 1h at various temperatures in air

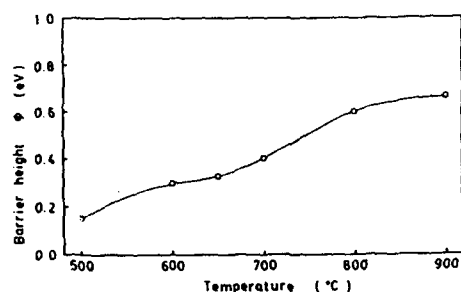


Fig. 6 Relation between the barrier height estimated by Arrhenius plots and the annealing temperature for 1h in air

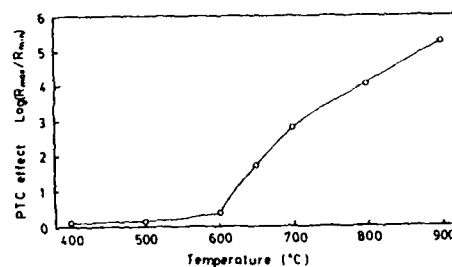


Fig. 7 Magnitude of PTC effect as a function of annealing temperature for 1h in air

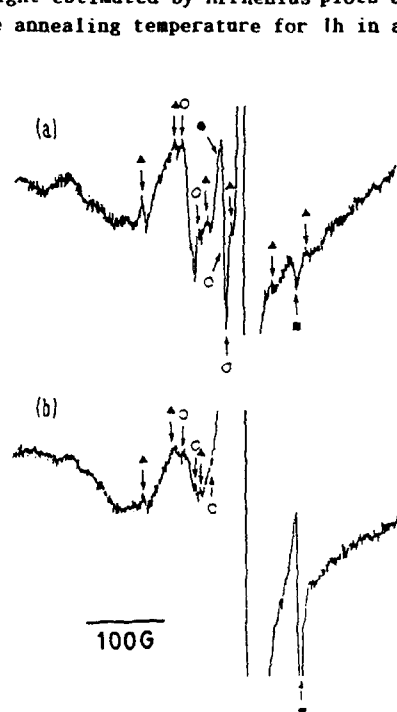


Fig. 8 ESR spectra at room temperature of undoped BaTiO₃

(a) as sintered at 1300°C in air for 2h
(b) as reduced at 1100°C in H₂-Ar for 2h
○:O₂⁻, ●:O⁻, ▲:Ti³⁺ (h.f.s.), ■:V.

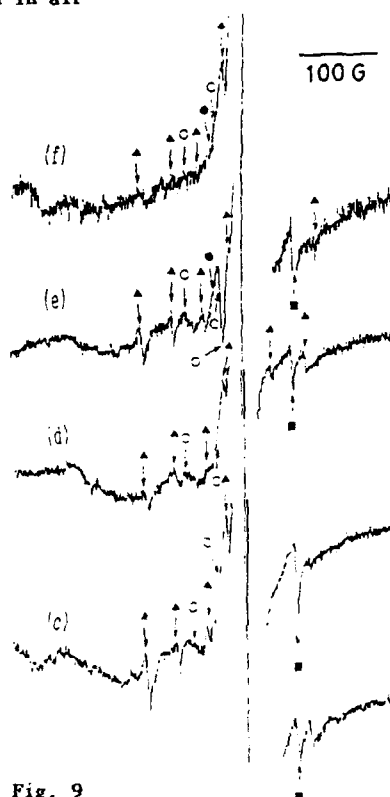


Fig. 9

ESR spectra at room temperature of undoped BaTiO₃ annealed for 1h at various temperatures in air

(c) 500°C, (d) 600°C, (e) 650°C, (f) 700°C
○:O₂⁻, ●:O⁻, ▲:Ti³⁺ (h.f.s.), ■:V.

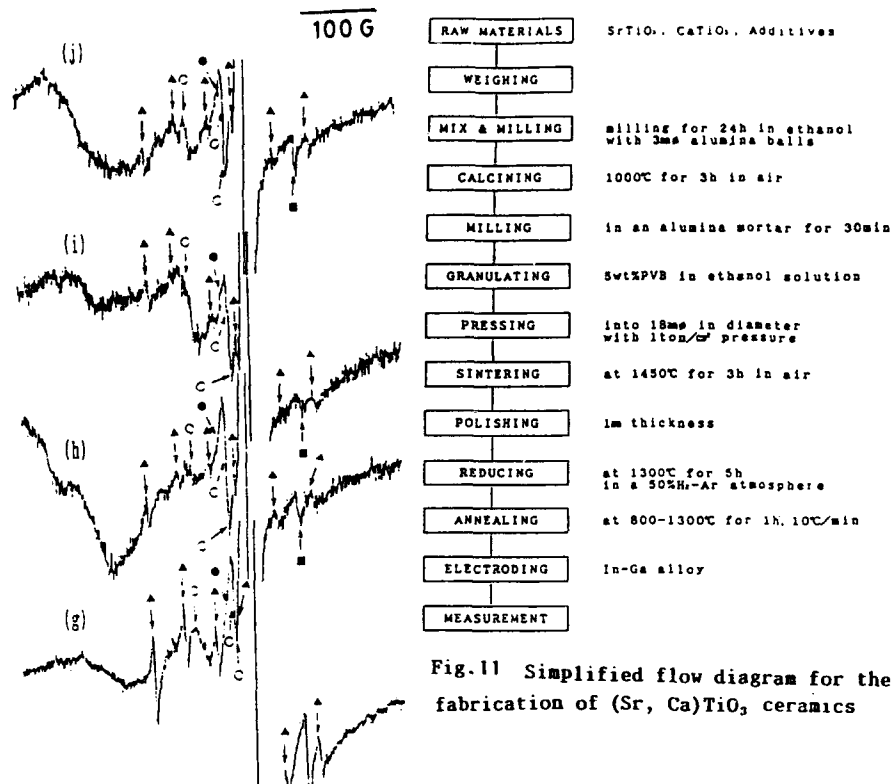


Fig. 10

ESR spectra at room temperature of undoped BaTiO₃ annealed for 1h at various temperatures in air

(g) 800°C, (h) 900°C (i) 950°C (j) 1000°C
 ○: O₂⁻, ●: O⁻, ▲: Ti³⁺ (h.f.s.), ■: V.

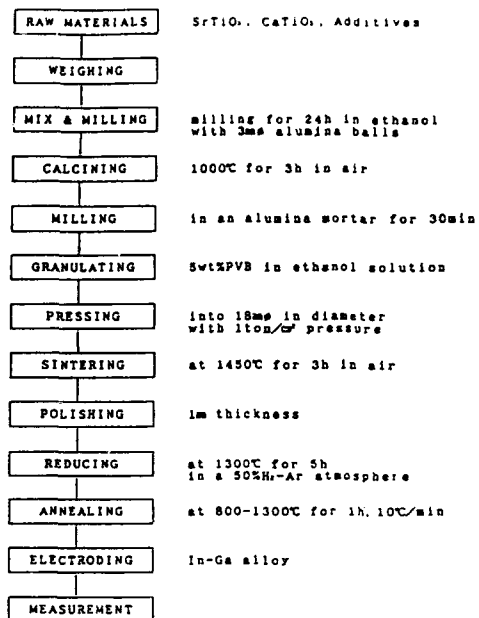


Fig. 11 Simplified flow diagram for the fabrication of (Sr, Ca)TiO₃ ceramics

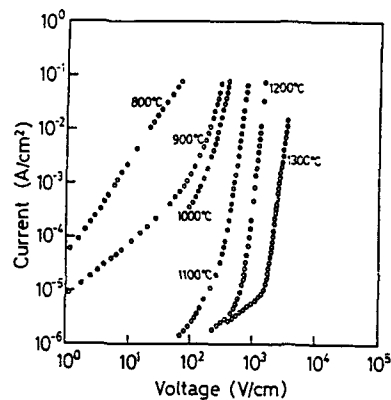


Fig. 12

DC current-voltage characteristics of sample B annealed at various temperature in air

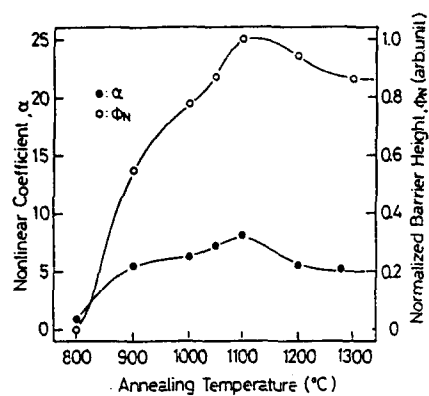


Fig. 13 sample A

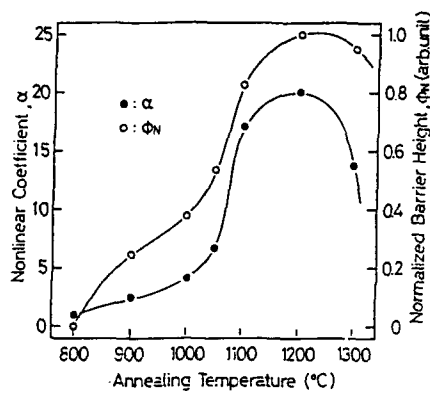


Fig. 14 sample B

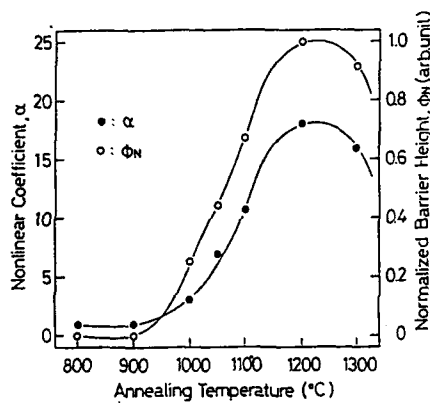


Fig. 15 Nonlinear coefficient and normalized barrier height as a function of annealing temperature in air for sample C

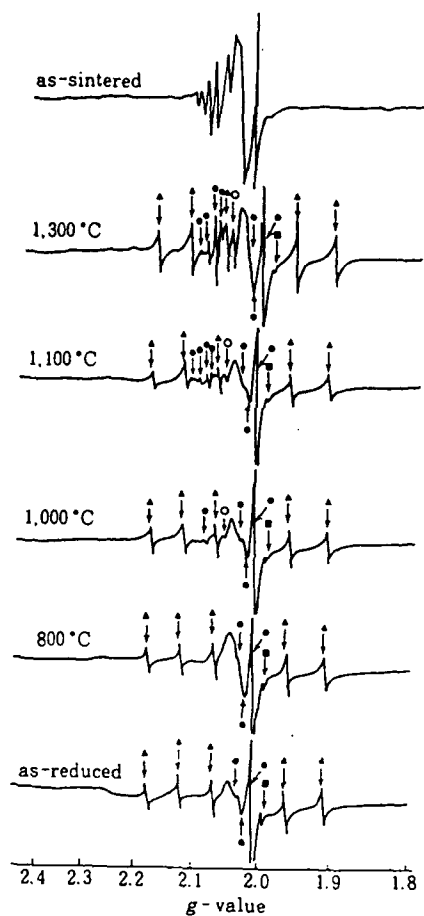


Fig. 16 ESR spectra of sample A as reduced and reoxidized at 800-1300°C for 1h in air

(○) free electron, O⁻ (g_{\parallel}), Ti³⁺ ($h.f.s.$),
 (○) O⁻ (g_{\perp}), (●) O₂⁻ (g_{xx} , g_{yy} , g_{zz}),
 (▲) Ti³⁺ ($h.f.s.$), (■) V₀

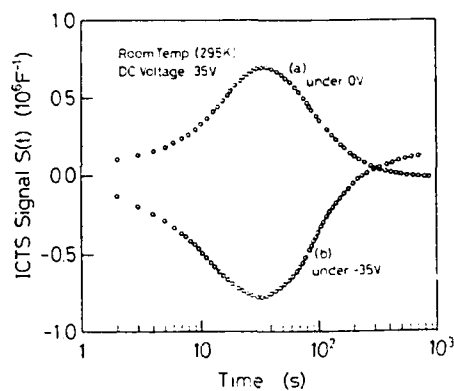


Fig. 17 Bias voltage dependence of ICTS spectra for the sample reoxidized at 900°C for 1h in air

- (a) under a zero biased voltage and
- (b) under a biased voltage of - 35V

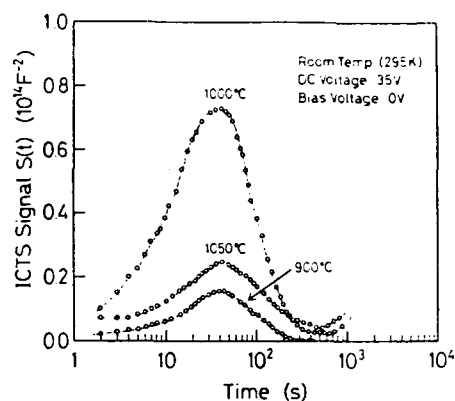


Fig. 18 ICTS spectra normalized by the background capacitance for the samples reoxidized at 900-1050°C for 1h in air

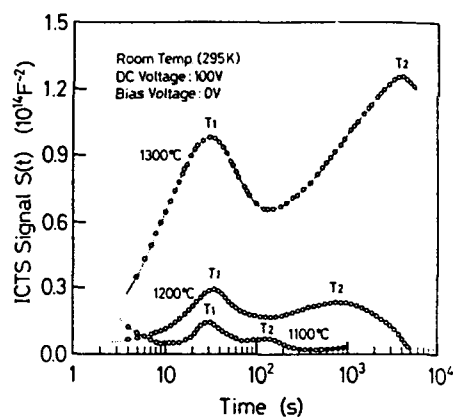


Fig. 19 ICTS spectra normalized by the background capacitance for the samples reoxidized at 1100-1300°C for 1h in air

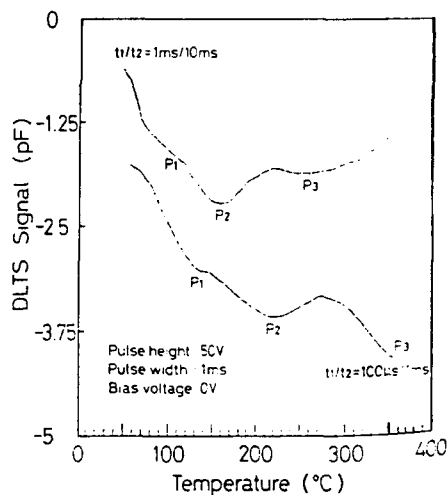


Fig. 20 DLTS spectra for the sample reoxidized at 1200°C for 1h in air

Table 1 Experimental condition of annealing temperature and time

Experimental Condition	Temperature (°C)	Time (h)	Atmosphere
ANNEALING 1	400, 500, 600, 650.	0.5	Air
ANNEALING 2	650.	0.17, 0.5, 0.75, 1.0, 1.3, 1.7, 2.0, 2.5,	Air
ANNEALING 3	400, 500, 600, 650, 700, 800, 900,	1.0	Air

Table 2 Sample compositions of starting materials

Sample	Powder Composition (mol)			
	SrTiO ₃	CaTiO ₃	La ₂ O ₃	Nb ₂ O ₅
A	1.00	0	0.003	-----
B	0.90	0.10	0.003	-----
C	0.90	0.10	-----	0.003

* Al₂O₃ 0.25(wt%)
TiO₂ 0.50(wt%)
SiO₂ 0.25(wt%)
CuO 0.02(wt%)

CONDUCTION MECHANISM OF SrTiO_3 THIN FILMS BY RF-SPUTTERING

T.Kuroiwa, T.Honda*, H.Watarai*, N.Mikami, T.Horikawa, T.Makita and K.Sato

Mitsubishi Electric Corp. Semiconductor Research Lab. :

1-1, Tsukaguti Honmachi 8-chome, Amagasaki, Hyogo 661, Japan

**Mitsubishi Electric Corp. Materials & Electronic Devices Lab. :*

1-57, Miyashimo 1-chome, Sagami-hara, Kanagawa 229, Japan

ABSTRACT

Conduction mechanism of SrTiO_3 thin films have been demonstrated. The SrTiO_3 films were prepared on $\text{Pt/SiO}_2/\text{Si}$ -wafer by means of a conventional RF-magnetron sputtering technique. Electrical properties of SrTiO_3 films were measured with $\text{Pt/SrTiO}_3/\text{Pt}$ structure. Leakage current characteristics were examined on as-deposited and annealed films. Leakage current conduction mechanism in a low electric field was different from that in a high electric field. In the low electric field, it was suggested that leakage current was caused by electrical traps at and/or near the interface between a top electrode and the SrTiO_3 film. In the high electric field, leakage current conduction mechanism was interpreted in terms of Pool-Frenkel conduction due to oxygen vacancies.

INTRODUCTION

Thin films with high dielectric constant have been highly attractive with respect to application to Dynamic Random Access Memory (DRAM) capacitors⁽¹⁾⁽²⁾. Because high dielectric constant capacitors would enable the realization of simpler processes and lower cost in DRAM fabrication. In recent years, electrical properties of $\text{Pb}(\text{Zr},\text{Ti})\text{O}_3$ ⁽³⁾⁻⁽⁵⁾, $(\text{Pb},\text{La})(\text{Zr},\text{Ti})\text{O}_3$ ⁽⁶⁾, SrTiO_3 ⁽⁷⁾⁻⁽¹⁰⁾, $(\text{Ba},\text{Sr})\text{TiO}_3$ ⁽¹¹⁾⁽¹²⁾ thin films were studied intensively, but leakage current conduction mechanism has been one of the unresolved issues.

In the present work we report the conduction mechanism of the SrTiO_3 thin films. The SrTiO_3 films were prepared by means of a Radio-Frequency (RF) magnetron sputtering technique on $\text{Pt/SiO}_2/\text{Si}$ -wafer substrates. We

To the extent authorized under the laws of the United States of America, all copyright interests in this publication are the property of The American Ceramic Society. Any duplication, reproduction, or republication of this publication or any part thereof, without the express written consent of The American Ceramic Society or fee paid to the Copyright Clearance Center, is prohibited.

suggest that leakage current conduction mechanism in a low electric field is different from that in a high electric field.

EXPERIMENTS

SrTiO₃ thin films were prepared by a conventional RF-magnetron sputtering technique under O₂ atmosphere with a ceramic single-target. Typical sputtering conditions of the SrTiO₃ films were shown in table 1. The deposition rate was determined from the film thickness measured with a surface profiler (DEKTAK3030). Substrates used (100)silicon wafers with a thermally oxidized layer 300nm in thickness. Platinum films with a thickness of 100nm were deposited as a bottom electrode on the SiO₂/Si -wafers at the substrate temperature of 600°C using a RF sputtering method. The SrTiO₃ films were cooled under O₂ atmosphere in a sputtering chamber immediately after the deposition was finished. For electrical measurements, Pt films with a diameter of 0.5mm were deposited on the SrTiO₃ films as a top electrode through a shadow mask at room temperature. Post annealing was performed with a tubular furnace made of quartz. Capacitance and leakage current were measured with an LCR meter (YHP4274A) and an electrometer with a built-in DC voltage source (YHP4140B), respectively.

Table 1. Typical sputtering conditions of SrTiO₃.

Substrate temperature	600 °C
Gas pressure	26.6 Pa
Sputtering gas (Ar/O ₂)	0/10
Input RFpower	250 W
Target diameter	80 mm
Target-substrate distance	35 mm
Deposition rate	4.5 nm/min.

RESULTS AND DISCUSSION

Leakage Current in Low Electric Field

Figure 1 shows leakage current density versus voltage for SrTiO₃ films annealed without a Pt top electrode at 450°C and at 700°C in O₂. Figure 2 exhibits leakage current characteristics for SrTiO₃ films annealed with a Pt top electrode at the same annealing conditions as the films shown in fig.1. As regards the leakage current of the films annealed without the top electrode, no remarkable difference in leakage current characteristics was found between the as-deposited film and the 450°C-annealed film. However, when the annealing was performed without the top electrode at 700°C, the leakage current enlarged abruptly with voltage, as shown in fig.1. In contrast, as shown in fig.2, the leakage current of the film annealed at 700°C with the top electrode was not increased so much in comparison with the as-deposited

film. These results indicate that the leakage current characteristics in the film annealed with the Pt top electrode are different from these in the film annealed without the top electrode. It is implied that the leakage current may be affected by the interface state between the SrTiO_3 film and the Pt top electrode. Figure 2 also shows that the leakage current becomes low after the annealing in the low electric field below 1.5V. It is suggested that the leakage current in the low electric field are concerned with the factors which could be recovered by thermal treatment. Electrical traps due to stress, strain, damage and/or defects are considerable as the factors. If these traps are localized at and/or near the interface between a SrTiO_3 film and a Pt top electrode, internal field would be formed at and/or near the interface. Furthermore the internal field based on such traps may be faded by thermal treatment.

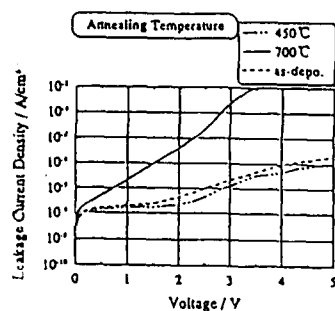


Fig. 1. Leakage current-voltage characteristics for as-deposited and annealed (at 450°C and at 700°C in O_2 , without Pt top electrode) SrTiO_3 films.

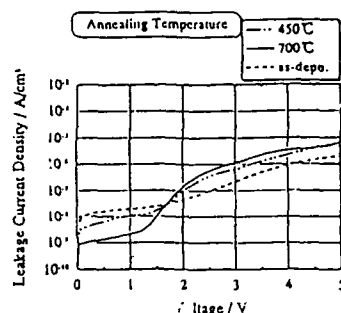


Fig. 2. Leakage current-voltage characteristics for as-deposited and annealed (at 450°C and at 700°C in O_2 , with Pt top electrode) SrTiO_3 films.

Capacitance-bias voltage characteristics for the films of as-deposited and annealed SrTiO_3 are shown in fig.3, where annealing was performed at 700°C in O_2 after deposited a Pt top electrode.

The maximum capacitance was obtained at the bias voltage of 1V for the as-deposited film but at 0V for the annealed film. This result denoted that internal field exists in the as-deposited SrTiO_3 film but is vanished by the annealing. Therefore, it is suggested that leakage current caused by the traps at and/or the interface between the SrTiO_3 film and the Pt top electrode is dominant in the low electric field.

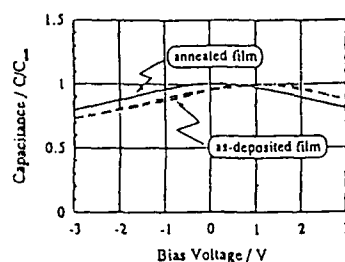


Fig. 3. Capacitance-bias voltage characteristics for as-deposited and annealed (at 700°C in O_2 , with Pt top electrode) SrTiO_3 films.

Leakage Current in High Electric Field

Figure 4 shows leakage current characteristics for SrTiO₃ films annealed with a Pt top electrode at 700°C into N₂ and O₂. The leakage current was much larger when the film was annealed in N₂ at 700°C. It is speculated that oxygen may be given off from the SrTiO₃ film owing to annealing in N₂ at 700°C, and oxygen vacancies are induced. Leakage current would not increase if the generation of the oxygen vacancies could be prevented in the film. The Pt top electrode was capped with a TiN film for the purpose of suppressing the generation of oxygen vacancies in the SrTiO₃ film in case of annealing in N₂ above 700°C. Figure 5 shows leakage current characteristics for the SrTiO₃ films which were annealed with the Pt and with the TiN/Pt top electrode in N₂ at 775°C. The leakage current for the film annealed with the Pt top electrode is significantly large. However, the leakage current of the film annealed with the TiN/Pt top electrode is not changed in comparison with the film annealed with the Pt top electrode in O₂ at 700°C, which was shown in Fig.4 and Fig.5. Therefore, oxygen vacancies in the SrTiO₃ films play important role in leakage current conduction mechanism. The oxygen vacancies form a donor level in a SrTiO₃. Carriers trapped at the donor level are emitted due to Schottky effect at the electric field higher than that required for exciting the carriers to conduction band. This suggests Pool-Frenkel conduction. Current density, J , for the Pool-Frenkel conduction is described as

$$J = C_0 E \exp \left[\frac{-q (\phi - \sqrt{q E / \pi \epsilon})}{k T} \right]$$

C_0 : Constant
 E : Electric Field
 q : Electrical Charge
 k : Boltzmann's Constant

T : Absolute Temperature
 ϕ : Barrier Height
 ϵ : Dielectric Constant

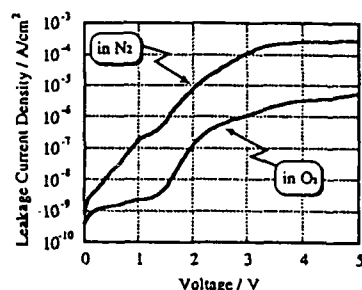


Fig.4. Leakage current-voltage characteristics for SrTiO₃ films 80nm in thickness annealed in N₂ or O₂ with Pt top electrode.

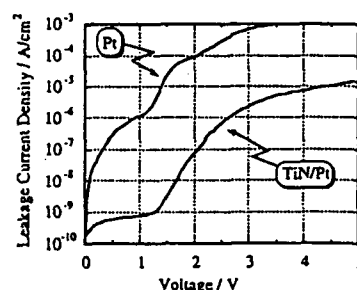


Fig.5. Leakage current-voltage characteristics for SrTiO₃ films 80nm in thickness annealed in N₂ with Pt or TiN/Pt top electrode.

Figure 6 shows a Pool-Frenkel plot for the SrTiO₃ film 100nm in thickness. Ohmic behavior is found in the low electric field, the region (a) in fig.6, because electric conductivity is constant. Good linearity is given in the high electric field of the region (c), which suggested Pool-Frenkel conduction. The intermediate region (b) has not been understood well. Refractive index was calculated as 1.7 from the slope of the line according with the Pool-Frenkel conduction. The value is slightly small as compared with the bulk's value of 2.3-2.6 but would be acceptable. Hence, in the high electric field, it is considered that leakage current caused by oxygen vacancies is dominant.

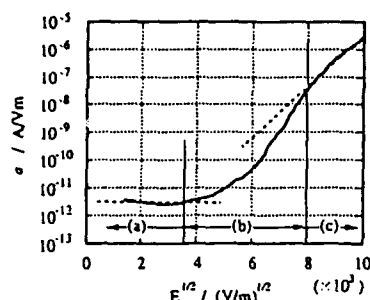


Fig.6. Pool-Frenkel plot for SrTiO₃ film 100nm in thickness.

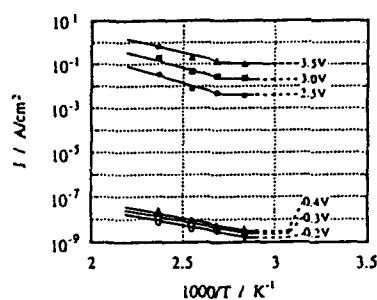


Fig.7. Arrhenius plot on leakage current at various applied voltage. SrTiO₃ film 60nm in thickness are used for this plot.

Conduction Mechanism

It was mentioned above that leakage current in low electric field is caused by electrical traps due to imperfections at and/or near the interface between a SrTiO₃ film and a Pt top electrode. In this case, carriers for electrical conduction have to be excited to conduction band from the trap level in low electric field. Leakage current density versus reciprocal absolute temperature is shown in fig.7. Activation energy in the low electric field, $E^{1/2}(\text{V/m})^{1/2} < 3.0 \times 10^3$ in fig.6, is evaluated as 0.19eV, which corresponds to a level due to the traps at and/or near the interface. The activation energy 0.19eV is suggested that the carriers in the trap level are easily excited to conduction band in such low electric field. On the other hand, it was also mentioned above, leakage current in high electric field is caused by oxygen vacancies into a SrTiO₃ film. Activation energy in the high electric field, $E^{1/2}(\text{V/m})^{1/2} > 8.0 \times 10^3$ in fig.6, is evaluated as 0.79eV, which corresponds to a level due to the oxygen vacancies. The value of 0.79eV implied that the carriers become to be excited to conduction band in such high electric field. Hence, leakage current conduction mechanism in the film may be considered that carriers for electrical conduction is excited to conduction band from the level which was formed by the traps or the oxygen vacancies. Consequently, it is considered that leakage current is caused by the traps at and/or near the

interface in the low electric field. In the high electric field, it is suggested that leakage current corresponds to Pool-Frenkel emission current caused by the oxygen vacancies.

CONCLUSIONS

The conduction mechanism of SrTiO_3 thin films was demonstrated. The SrTiO_3 films were prepared on $\text{Pt/SiO}_2/\text{Si}$ -wafer by means of a conventional RF-sputtering technique. The leakage current conduction mechanism in a low electric field is different from that in a high electric field. In the low electric field, it is considered that the leakage current is caused by electrical traps at and/or near the interface between a SrTiO_3 film and a Pt top electrode. It is suggested that the leakage current corresponds to the Pool-Frenkel emission current caused by the oxygen vacancies in the high electric field.

REFERENCES

- (1) K.Koyama, T.Sakuma, S.Yamamichi, H.Watanabe, H.Aoki, S Ohya, Y.Miyasaka and T.Kikkawa : Technical Digest of IEDM, (1991) 823.
- (2) T.Eimori, Y.Ohno, H.Kimura, J.Matsufusa, S.Kishimura, A.Yoshida, H.Sumitani, T.Maruyama, Y.Hayashide, K.Moriizumi, T.Katayama, M.Asakura, T.Horikawa, T.Shibano, H.Itoh, K.Sato, K.Namba, T.Nishimura, S.Sato and H.Miyoshi : Technical Digest of IEDM, (1993) 631.
- (3) J.F.Scott, C.A.Araujo, B.M.Melnic, L.D.Mcmillan and R.Zuleeg : J. Appl. Phys. 70(1991) 382.
- (4) K.Kashihara, H.Itoh, K.Tsukamoto and Y.Akasaka : Extended Abstracts of SSDM (1991) 192.
- (5) S.E.Bernacki : Ferroelectric Thin Films II, edited by A.I.Kingon, E.R.Myers and B.Tuttle (Mat. Res. Soc. Symp. Proc. Vol.243, Pittsburgh, 1992) p135.
- (6) T.Okudaira, A.Hachisuka, N.Soyama, K.Ogi, H.Arima, T.Matsukawa and K.Horie : Extended Abstracts of SSDM (1991) 204.
- (7) W.B.Pennebaker : IBM J. Res. Develop. (1969) 686.
- (8) S.Yamamichi, T.Sakuma, K.Takemura and Y.Miyasaka : Jpn. J. Appl. Phys. 30(1991) 2193.
- (9) T.Kuroiwa, T.Honda, H.Watarai and K.Sato : Jpn. J. Appl. Phys. 31(1992) 3025.
- (10) K.Abe and S.Komatsu : Jpn. J. Appl. Phys. 32(1993) 4186.
- (11) Y.Miyasaka and S.Matsubara : Proc. 7th Int. Symp. the Applications of Ferroelectrics, Illinois, 1990 (IEEE, New York, 1991) p121.
- (12) T.Horikawa, N.Mikami, T.Makita, J.Tanimura, M.Kataoka, K.Sato and M.Nunoshita : Jpn. J. Appl. Phys. 32(1993) 4126.

DIELECTRIC, STRUCTURAL AND MICROSTRUCTURAL CHARACTERISTICS OF TETRAGONAL-STRUCTURED PLZT RELAXORS

Xunhu Dai, Z. Xu, and Dwight Viehland
Department of Materials Science and Engineering, and the Materials Research
Laboratory
University of Illinois, Urbana, Illinois 61801

Tetragonal PLZT ceramics ($\text{Zr/Ti} = 40/60$) with lanthanum contents of approximately 12 atomic% possess a unique transformation. Dielectric constant measurements have revealed a spontaneous switching between relaxor and normal ferroelectric behaviors, in addition significant thermal hysteresis effects were observed near the switching temperature. Temperature dependent x-ray line broadening above the switching temperature was observed which revealed the development of significant internal strain indicating the presence of local cubic-tetragonal structural transformations which preserve the average cubic symmetry, while line splitting was observed below the switching temperature indicating the formation of a macroscopic tetragonal structure. Micropolar domain coarsening and a subsequent transformation to a normal micron-sized domain configuration was observed by hot-stage transmission electron microscopy.

I. INTRODUCTION

There exists a particular class of ferroelectrics known as relaxors which exhibit a diffuse phase transition. These materials are characterized by a shift of the dielectric permittivity maximum with frequency and the absence of any macro-symmetry changes at a structural transformation. Relaxor behavior is believed to arise due to a compositional and/or structural heterogeneity which acts to break the translational invariance of the polarization. Viehland and Li¹ have recently attributed the breaking of the translational symmetry in the mixed B-site cation relaxor family to the formation of a locally charge non-neutral phase. As a consequence polar nanodomains form which are inhibited from undergoing a normal long-range ordered ferroelectric transformation. At lower temperatures, these polar nanodomains have been shown to undergo a Vogel-Fulcher-like slowing down of the polarization fluctuations²⁻⁴. These glass-like characteristics were attributed to correlations between the polar nanodomains.

Short-range ordered regions have been observed in many mixed B-site cation relaxors such as $\text{Pb}(\text{Sc}_{1/2}\text{Ta}_{1/2})\text{O}_3$ (PST)⁵ and $\text{Pb}(\text{Mg}_{1/3}\text{Nb}_{2/3})\text{O}_3$ (PMN)^{6,7}. The scale of the polar nanodomains was seen to be approximately 5-10 nm. Similar sized polar nanodomains have also been found in La-modified lead zirconate titanate (PLZT)⁸. Coarsening of polar nanodomains with reducing temperature has been observed in PLZT 8.2/70/30 ceramics,⁹ in which the number and size of stable polar nanodomains increased at the expense of the paraelectric matrix. Decreasing temperature may result in enhanced tendencies towards long-range ordering (LRO), however the system did not transform the mixture of polar nanodomains and the paraelectric matrix into a completely LRO ferroelectric state. The application of an electric field is known to align the polar nanodomains transforming the relaxor to a LRO state. This transition is often referred to in the literature as the field induced micro- to macro-domain transition. A number of experiments have been performed on this field-induced transition¹⁰⁻¹², however this

To the extent authorized under the laws of the United States of America, all copyright interests in this publication are the property of The American Ceramic Society. Any duplication, reproduction, or republication of this publication or any part thereof, without the express written consent of The American Ceramic Society or fee paid to the Copyright Clearance Center, is prohibited.

transformation has never been observed without the assistance of an applied DC electrical bias.

It is the aim of the present paper to report the findings of a spontaneous (thermally driven) relaxor to normal ferroelectric transformation in tetragonal PLZT ceramics. Investigations have been performed by electric property measurements (dielectric spectroscopy), structural analysis (X-ray diffraction) and micro-morphology observations (transmission electron microscopy).

II. EXPERIMENTAL PROCEDURES

$(\text{Pb}_{1-x}\text{La}_x)(\text{Zr}_y\text{Ti}_{1-y})\text{O}_3$ (denoted as PLZT $x/y/1-y$) ceramics were prepared by a conventional mixed oxide method followed by hot-press sintering, as well as a post-sintering annealment. The processing details are presented in a previous publication.¹³ PLZT ceramics with a composition 12/40/60 were chosen for study.

The dielectric permittivity of the specimens was measured using a Hewlett-Packard 4284A inductance-capacitance-resistance (LCR) meter which can cover a frequency range from 20 to 10^6 Hz. The dielectric data were obtained by putting the samples in a small tube furnace specifically equipped for such measurements. Data were taken by cooling the samples from high temperature at a rate of $4^\circ\text{C}/\text{min}$. X-ray diffraction data were taken using a Scintag X-ray diffractometer equipped with a hot-stage. Samples were carefully polished and followed by a heat treatment at 650°C for a half hour in air. The heat treatment cleaned the samples and reduced the residual surface stress left from polishing. The diffractometer was operated at 40 kV and 20 mA. The θ - 2θ scanning rate was $4^\circ/\text{min}$, using incremental steps of 0.02° .

Transmission electron microscopy (TEM) studies were carried out in a Phillips EM-420 electron microscope (120kV) using a normal double tilt hot-stage. Bright-field images of the samples were obtained as a function of temperature. Accurate values of temperature were difficult to obtain since the samples tended to heat under the electron beam. Reported values of temperature can only be regarded as relative indications.

III. RESULTS AND DISCUSSION

III.1 DIELECTRIC BEHAVIOR

Figure 1 illustrates the dielectric response of PLZT 12/40/60 over a wide temperature range. Arrows are used in the figure to indicate heating and cooling measurements. This composition possessed a unique dielectric response, which seemingly revealed different types of ferroelectric behavior in the high and low temperature regimes. On cooling from high temperatures, the dielectric constant initially reached a maxima which was frequency dependent and of a broad and dispersive character, the dielectric constant then exhibited a frequency independent discontinuity which was much like a first-order transition into a normal ferroelectric state. The dielectric permittivity on heating underwent a similar discontinuity at a temperature approximately 20°C higher than that in the cooling mode. At higher temperatures the dielectric response again exhibited typical relaxor-type characteristics.

La-doping in ferroelectric perovskites is believed to disturb the long-range Coulomb interaction which drives the formation of spontaneous polarization below T_c . Consequently, the formation of micron-sized domains is strongly inhibited as La-content increases. At high temperatures normal micron-sized domains may not be able to form, rather instead favoring the establishment of polar nanodomains. With decreasing temperature, strong correlations between polar nanodomains may develop which would

tend to drive the system towards a long-range ferroelectric state. However, thermal energy would oppose this ordering tendency. If correlations could develop rapidly enough on cooling, interactions may be able to overcome the thermal energy and a transformation to a long-range ferroelectric state could proceed. However, if correlations can not develop rapidly enough, the system would become kinetically trapped in the polar nanodomain state. A Vogel-Fulcher analysis was performed on the 12/40/60, however no correlation with the relaxor to normal ferroelectric transformation temperature was found. This is probably a reflection of the critical nature of the establishment of long-range order from the polar nanodomain state.

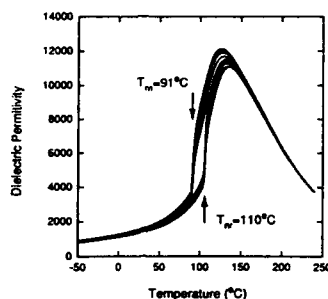


Figure 1. Dielectric constant as a function of temperature of PLZT 12/40/60. Arrows represent the heating and cooling measurements.

III.2 X-RAY LINE BROADENING MEASUREMENTS

On cooling the composition 12/40/60 exhibited a continual increase in the degree of line broadening between 300 and 90°C, as shown in Figure 2(a). This broadening suggests the development of nonuniform internal strains associated with the tetragonality of the polar nanodomains. The local tetragonal distortions are small and randomly axed with respect to each other along equivalent crystallographic directions, yielding an average cubic symmetry. As the temperature is decreased the volume fraction of the polar nanodomains increases, resulting in an increase of the internal strain energy which scales to the volume of the inclusion¹⁴. The large internal strain energy can be relieved in the long-range ordered state through twin-related micron-sized domain formation. At 90°C line splitting in the (200) reflection became evident. This splitting suggests that the nonuniform internal strain has transformed to a macroscopic tetragonal deformation. Data from heating measurements (see Figure 2(b)) revealed reverse structural changes relative to the cooling mode, exhibiting a change from macroscopic to local tetragonal symmetries. Pronounced thermal hysteresis was also observed in the temperature of the normal to relaxor transformation. It was evident that on cooling the splitting in the (200) reflection did not occur until ~90°C, where as on heating the splitting became evident near ~105°C. This hysteresis is consistent with that observed from the dielectric measurements.

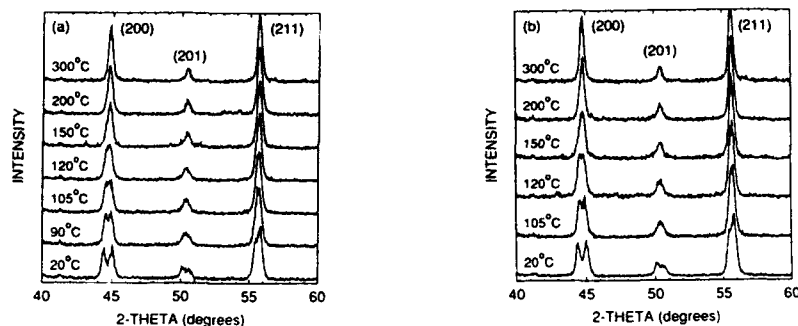


Figure 2. X-ray diffraction of PLZT 12/40/60 under (a) cooling and (b) heating measurement.

The spontaneous relaxor to normal ferroelectric transformation is visible from both the line splitting and the sudden drop in the dielectric permittivity, which occurred at identical temperatures. The abruptness of this transformation resembled that expected of a first-order phase transition, however quite unexpectedly the transformational temperature ($\sim 90^\circ\text{C}$) did not agree with that of the dielectric maximum ($\sim 150^\circ\text{C}$). This indicates that the dielectric maximum has nothing to do with the establishment of long-range order, but rather the slow dynamics of interacting polar clusters. In addition, strong thermal hysteresis effects in the transformational temperature were observed ($\sim 20^\circ\text{C}$), similar to that anticipated for a strongly martensitic transition. Thermal hysteresis effects in many martensitic materials are related to the magnitude of the transformational strain: the larger the strain, the larger the degree of thermal hysteresis. The thermal hysteresis effects observed in the relaxor to normal ferroelectric transformation may be related to the relatively large internal strain in the micropolar domain state. This internal strain will make a significant positive contribution to the total free energy, effectively decreasing the thermodynamic stability of the system. Consequently, on cooling from the polar nanodomain state, the thermodynamic stability of the system will be decreased relative to that on heating from the normal ferroelectric state. As a result, the observed transformational temperature on cooling will be lower than that on heating.

III.3 HOT-STAGE TRANSMISSION ELECTRON MICROSCOPY STUDIES

Figures 3(a)-(f) illustrate the temperature dependence of the TEM micrographs for the composition 12/40/60 on heating and subsequent cooling. Various types of domain structures can readily be seen in these micrographs (as will be discussed in more detail below). In addition, strong coarsening effects are also evident on cooling. Figure 3(a) shows the room temperature bright-field image. Fine domain striations can readily be seen to exist inside the normal micron-sized domains. This subdomain structure may provide partial stress-relief of internal electrostrictive strains associated with polarization nonuniformity, and may be the first stage of relaxation of the traditional micron-sized domain structure to a polar nanodomain state. Upon heating to 90°C , the micron-sized domains gradually decreased in size, leaving only the tweed-like pattern, as shown in Figure 3(b). The tweed-like structure then persisted to $\sim 105^\circ\text{C}$, as shown in Figure 3(c). It is relevant to note that similar tweed-like structures are commonly observed in ferroelastic and martensitic materials. Tweed-like structures are believed to be observed

when ordering processes have not completely occurred due in part to sample nonuniformity.^{15,16} At higher temperatures polar nanodomains typical of a relaxor state were clearly seen. The scale of the polar nanodomains then decreased within increasing temperature. Near 350°C all contrast due to polar nanodomains had disappeared, as shown in Figure 3(d). On subsequent cooling from 350°C, the scale of the polar nanodomains can be seen to coarsen gradually with decreasing temperature, as shown in Figure 3(e). Near the temperature of the tetragonal line splitting in the bragg reflections, a mixture of fine parallel domains and a tweed-like structure formed. This morphology remained unchanged to room temperature, as shown in Figure 3(f). The room temperature domain structure after cooling was different than that before heating. This difference may relate to size effects due to the thinness of the TEM specimens. The micron-sized domain structure observed before heating formed within a bulk sample. On cooling TEM specimen from high temperatures, accumulated elastic strains may be partially released through free surfaces reducing the tendency to establish normal micron-sized domains. However, tweed-like structures may form, as shown in Figure 3(f) (region A).

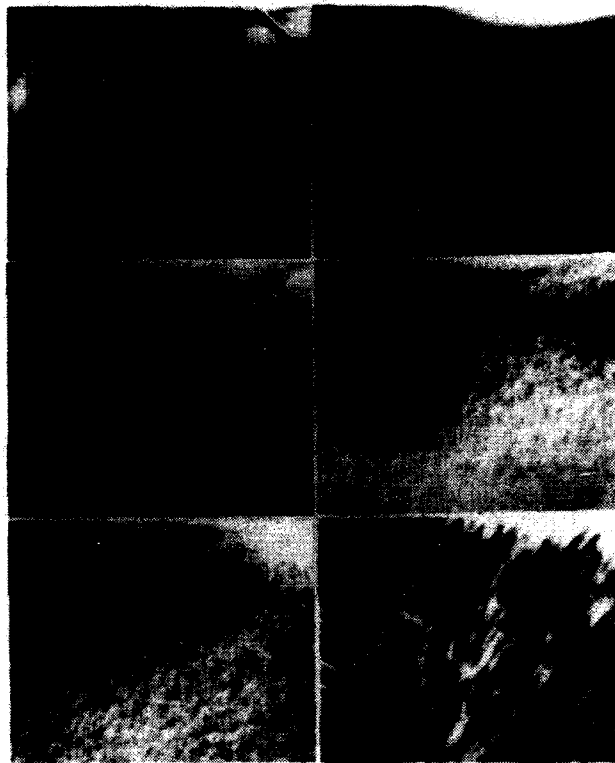


Figure 3. Temperature dependence of domain configuration of PLZT 12/40/60 on heating (a) - (d) and cooling (d) - (f). (a) 25°C, (b) 90°C, (c) 105°C, (d) 350°C, (e) 105°C, (f) 25°C.

IV. CONCLUSIONS

A relaxor to normal ferroelectric transformation, which is structurally a local to global tetragonal symmetry transition, was observed using dielectric spectroscopy and x-ray line splitting. In-situ hot-stage TEM observations confirmed the formation of micron-sized domains from polar nanodomains. In addition, the morphology of the structure sequences which the material passes through on cooling from the polar nanodomain state to the long-range ferroelectric state was identified.

ACKNOWLEDGEMENTS

This research was supported in fully by the Office of Naval Research (ONR) under contract No. N00014-92-J-1522. The use of facilities in the Center for Microanalysis of Materials Research Laboratory at the University of Illinois at Urbana-Champaign is gratefully acknowledged.

REFERENCES

1. D. Viehland and J.F. Li, J. Appl. Phys. 74, 4121 (1993).
2. D. Viehland, S. J. Jang, and L. E. Cross, Phys. Rev. B 46, 8003 (1992).
3. D. Viehland, J. F. Li, S. J. Jang, L. E. Cross, and M. Wuttig, Phys. Rev. B 46, 8013 (1992).
4. D. Viehland, S. J. Jang, L. E. Cross, and M. Wuttig, Phil. Mag. A 64, 835 (1991).
5. C. A. Randall, D. J. Barber, R. W. Whatmore, and P. Groves, J. Mat. Sci. 21, 4456 (1986).
6. E. Husson, M. Chubb, and A. Morell, Mat. Res. Bull. 23, 357 (1988).
7. J. Chen, H. M. Chan, and M. P. Harmer, J. Am. Ceram. Soc. 72, 593 (1989).
8. C. A. Randall, D. J. Barber, and R. W. Whatmore, J. of Microscopy 45, 275 (1987).
9. C. A. Randall, D.J. Barber, R. W. Whatmore, and P. Groves, Ferroelectrics 76, 311 (1987).
10. E. T. Keve and A. D Annis, Ferroelectrics 5, 77 (1973).
11. X. Yao, Z. L. Chen, and L. E. Cross, J. Appl. Phys. 54, 3399(1983).
12. S. M. Fan, J. W. He, and X. Yao, Ferroelectrics 77, 181 (1988).
13. Xunhu Dai, A. DiGiovanni, and Dwight Viehland, J. Appl. Phys. 74, 3399 (1993).
14. P. A. Porter and K. E. Easterling, in *Phase Transformations in Metals and Alloys* (Chapman and Hall, New York, 1981).
15. E. Sajle, Phase Transition 34, 25 (1991).
16. S. Marais, V. Heine, C. Nex, and E. Salje, Phys. Rev. Lett. 66, 2480 (1991).

HYDROACOUSTIC EVALUATION OF 1-3 PIEZOCOMPOSITE PLATE AND RING STRUCTURES

Robert Y. Ting, Thomas R. Howarth and Kurt M. Rittenmyer
U.S. Naval Research Laboratory
Underwater Sound Reference Detachment
P.O. Box 568337
Orlando, Florida 32856-8337

INTRODUCTION

Piezoelectric composites with a 1-3 connectivity pattern have been investigated for potential underwater sonar transducer applications [1]. Recently, with increasing interest in the development of intelligent systems and adaptive structures, emphasis on using 1-3 piezocomposites in actuator applications has become more noticeable. This class of composite materials consists of aligned thin ceramic rods imbedded in a polymeric resin. The high content of a polymeric phase offers the advantage of providing large area coverage for the fabrication of flexible and/or conformal actuator arrays. These materials exhibit excellent piezoelectric properties so that they deliver adequate displacement under moderate electric drives. These good properties can be obtained at fairly low ceramic volume fractions, hence the 1-3 piezocomposites provide an additional benefit of a good acoustic impedance match to water [2]. In addition, compared with the conventional actuators of the magnetostrictive or piezoceramic type, the 1-3 piezocomposite structures can be fabricated for array designs of much reduced profile and low standoff. In this paper, we discuss some recent results on the evaluations of 1-3 piezocomposite plate and ring structures both in air and in water.

PIEZOCOMPOSITE PLATES

Efforts to improve the performance of 1-3 piezocomposites are constantly sought. A recent theoretical analysis by Hossack and Auld [3] suggested that the inclusion of gas-filled holes aligned vertically with the thin ceramic rods in a 1-3 composite will improve the electromechanical efficiency of the material. It recognized the significant antiphase cross-coupled strains in the material due to the Poisson's stress effect in both the ceramic and the polymer phases. The proposed concept was to form gas-filled holes in the polymer matrix to relieve some of this cross-coupling and thus enhance the uniformity of the thickness-mode displacement. It was expected that this modification in effectively creating a 1-3-1

To the extent authorized under the laws of the United States of America, all copyright interests in this publication are the property of The American Ceramic Society. Any duplication, reproduction, or republication of this publication or any part thereof, without the express written consent of The American Ceramic Society or fee paid to the Copyright Clearance Center, is prohibited.

composite would improve the electromechanical efficiency of the material. We set out to take some initial steps in validating this new concept.

Piezoelectric 1-3 composite samples were prepared by Fiber Materials Inc. (Biddeford, Maine). Square plates of $50.8 \times 50.8 \times 6.35 \text{ mm}^3$ were fabricated by using nominally $1 \times 1 \text{ mm}^2$ square rods of PZT-5H ceramics. The volume fraction of the ceramic content was about 10%. An epoxy resin having a hardness of HD-68 was used as the matrix material. A silver epoxy resin was applied to both the top and the bottom sides of the sample as electrodes. The typical sample showed a thickness coupling coefficient of about 60%, and a dielectric constant of 200.

Vertically aligned holes, 0.5 mm or 1 mm in diameter, were drilled into the polymer matrix. The position of the drilled holes was determined based on the design proposed in Ref. [3]. In one case, the holes were placed in the center of four ceramic rods, termed the "diagonal" configuration. In another case, the holes were positioned in between every two individual ceramic rods, the so-called "parallel" configuration. Lastly, a combined case of these two configurations to create a maximum number of holes in the polymer matrix.

The dielectric and piezoelectric properties of these samples were examined in an acoustic coupler [4]. The complex dielectric constants and the piezoelectric d_{3h} and g_{3h} coefficients (hydrostatic mode) were determined as a function of temperature and pressure by using the acoustic reciprocity technique [5].

Figure 1 shows the d_{3h} coefficient of the samples as a function of pressure up to 14 MPa. Curve 1 is for a "control" 1-3 sample with no holes. Its d_{3h} coefficient of 40.5 pC/N was found to be constant over the pressure range tested, and no pressure hysteresis effect was observed. Compared with this "control", the composite samples containing various amounts of vertically aligned holes showed a somewhat reduced d_{3h} , and considerably increased pressure dependence of the property. For clarity, the result from the sample having a "diagonal" configuration is not presented in Fig. 1, but would be only slightly lower than that of the "control". Curve 2 gives the result from a "parallel" configuration sample, and Curve 3 for the "combined" configuration. The hydrostatic piezoelectric voltage constants (g_{3h}) of these samples exhibit a similar trend.

The analysis of Ref. [3] predicted that the piezoelectric d_{3h} coefficient of the 1-3 composite would improve two to four folds by introducing the different hole patterns in the polymer phase. The calculation was based on the finite element ANSYS code [6]. The reason for the discrepancy between the analytical prediction and the experimental result is not clear at this time. A careful re-examination of the theory is necessary in order to define the optimum hole configurations and the extent of improvements in terms of the ceramic and polymer parameters. The boundary effect of a finite-size sample on the expected property improvement will also have to be investigated.

PIEZOCOMPOSITE RINGS

In order to assess the feasibility of using 1-3 piezocomposite in cylindrical structures, the hydroacoustic behavior of 1-3 rings was investigated. Composite rings having an inner diameter of 338.5 mm and a thickness of 3.175 mm were fabricated. Each ring was 101.6 mm long, containing only 5% volume fraction of PZT-5H piezoceramic rods that were nominally $1 \times 1 \text{ mm}^2$ in size. This low ceramic volume fraction was for the ease of fabrication, and, as it was found out later, was too low for actively driving the sample to obtain adequate displacement and sound pressure above the noise floor of the testing facility. A 10% volume fraction of S-2 roving fiber was also loaded in the ring for structural integrity. Silver epoxy resin paste was also used as electrodes, approximately 0.1 mm thick.

Dielectric characterization carried out in air showed that the 1-3 piezocomposite ring exhibited a thickness resonance at 2 kHz and a length resonance at 10 kHz. In-air displacement measurement by using a laser Doppler vibrometer [7] was also performed at different positions on the ring with a drive level of approximately 0.3 kV/cm. This measurement confirmed the 2 kHz resonance of the ring, as shown in Figure 2.

In order to successfully achieve the desired control of the dynamic behavior of a certain structure, multiple actuators containing discrete PZT ceramic elements are commonly employed [8]. However, the 1-3 composite can be fabricated as an integrated part of the structure, and the formation of multiple elements may be realized by simply applying a desired electrode pattern over the monolithic composite layer. The high volume content of the polymeric phase not only serves the purpose of relieving the ceramic d_{31} and d_{32} effects to increase the net d_{3h} value, but also decouples the cross-talk between individually electroded elements. This simplified technique for array formation has been demonstrated in ultrasonic medical imaging application [2]. For the 1-3 piezocomposite rings with continuous silver-epoxy electrodes, we striped the outside electrode layer and formed a small 3×3 array pattern with each element being approximately $17.8 \times 26.9 \text{ mm}^2$ in size. The inter-element coupling in such an array was investigated by driving one element and measuring the response of its neighboring elements. Figure 3 presents the normalized measurement result, showing that above the 2 kHz resonance frequency the inter-element coupling is generally -15 to -20 dB over the frequency band. This coupling begins to increase slightly as the frequency approaches the 10 kHz length resonance. But, in general, the decoupled behavior suggests that the electrode-patterned array can be adequately addressed as independent elements.

The composite rings were also evaluated for their transmitting and receiving characteristics as a function of frequency. Because the ceramic loading (at 5%) was too low to produce an adequate sound pressure in water above the system background noise level, transmitting voltage response (TVR) evaluation was not successful. However, the free field receiving sensitivity (FFVS) was obtained over the frequency range of 2 to 80 kHz. This response, determined to be -166 dB re 1 V/ μPa , was relatively constant over the frequency band, as shown in Figure 4 (note that each of the three responses also has an in-line 40 dB preamplifier gain). In

comparison, a similar cylindrical array containing discrete lead titanate solid ceramic elements exhibited a much irregular receiving response, indicating the existence of many different vibrational modes in that structure. For a similar cylindrical array of the 0-3 piezorubber composite (NTK-307) elements, the FFVS characteristic closely fashioned that of the 1-3 ring, except for a deep "hole" at about 6 kHz, which is a very undesirable feature for a receiving array. It is believed that this loss of sensitivity in the 0-3 composite ring is related to an extensional mode in that material due to the d_{31} and d_{32} effects [9].

SUMMARY

An effort to improve the electromechanical property of 1-3 piezocomposite by introducing a gas-filled phase was shown experimentally to be unsuccessful, contrary to the finite-element prediction from a recent theory. Additional analysis is needed to resolve this discrepancy. The dynamic behavior of 1-3 piezocomposite rings was investigated and thickness and length resonances were found as expected. Electrode-patterned array elements in the ring exhibit adequate decoupling so that they can be addressed as independent elements mounted on a monolithic structure. The broad-band receiving response of the 1-3 piezocomposite ring was also found to be superior to that of a similar cylindrical structure consisting of either discrete piezoceramic transducers or 0-3 piezocomposite elements.

REFERENCES

- [1] R. Y. Ting, *Ferroelectrics*, 67, 143 (1986).
- [2] W. A. Smith, A. A. Shaulov and B. M. Singer, *Proc. 1984 IEEE Ultrasonics Symp.* p. 539 (1984).
- [3] J. A. Hossack and B. A. Auld, presented at the 1992 IEEE Ultrasonics Symp. Tucson, AZ, Nov 1992.
- [4] C. C. Sims and T. A. Henriquez, *J. Acoust. Soc. Amer.* 36, 1705 (1964).
- [5] *Ibid*
- [6] ANSYS, Swanson Analysis Systems Inc. Houston, PA.
- [7] K. M. Rittenmyer and P. S. Dubbelday, *J. Acoust. Soc. Amer.* 91, 2254 (1992).
- [8] R. L. Clark, C. R. Fuller and A. Wicks, *J. Acoust. Soc. Amer.* 90, 346 (1991).
- [9] M. L. Pecoraro, in *Proc. Transducers for Sonics and Ultrasonics*, eds. McCollum, Hamonic and Wilson, Technomic Publ. Lancaster, PA, p. 383 (1993).

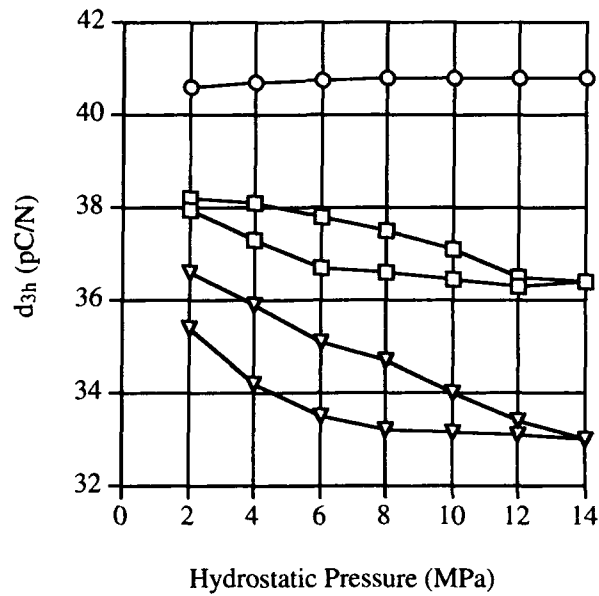


Figure 1: Comparison of measured hydrostatic piezoelectric charge constant versus hydrostatic pressure. Response O is for the control sample (without holes), response \square is for a parallel hole configuration and response \blacktriangledown is for a combined hole configuration.

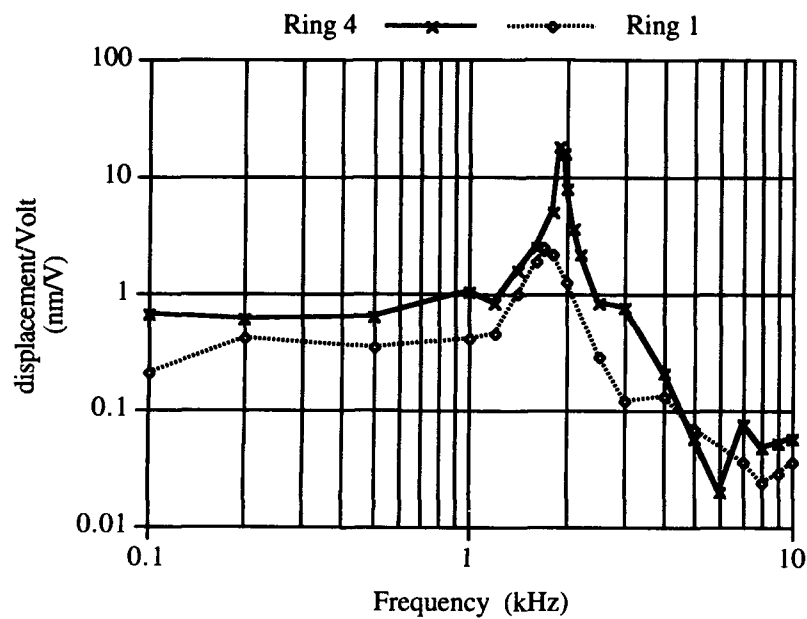


Figure 2: Comparison of in-air displacement per volt of two 1-3 piezocomposite ring structures as measured using laser Doppler vibrometry.

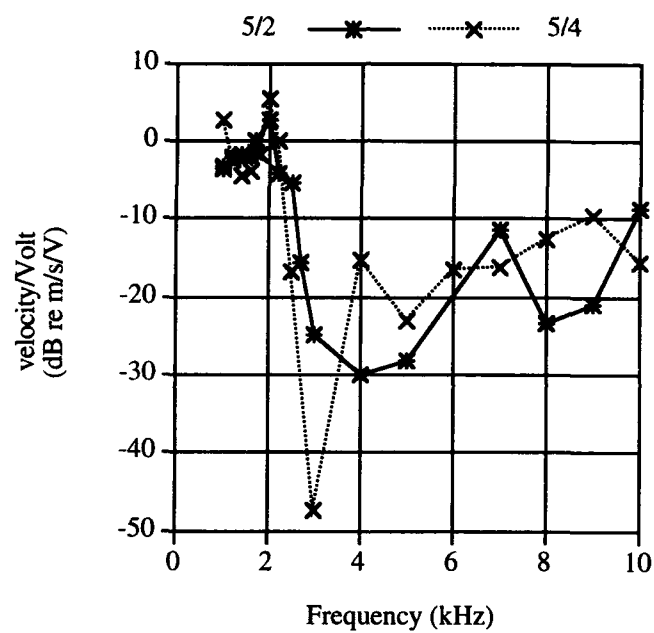
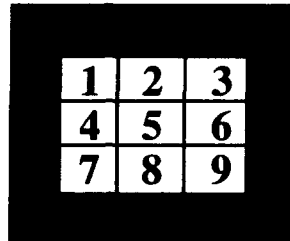


Figure 3: Inter-element coupling between adjacent elements mounted on a 1-3 monolithic ring structure as measured using laser Doppler vibrometry.

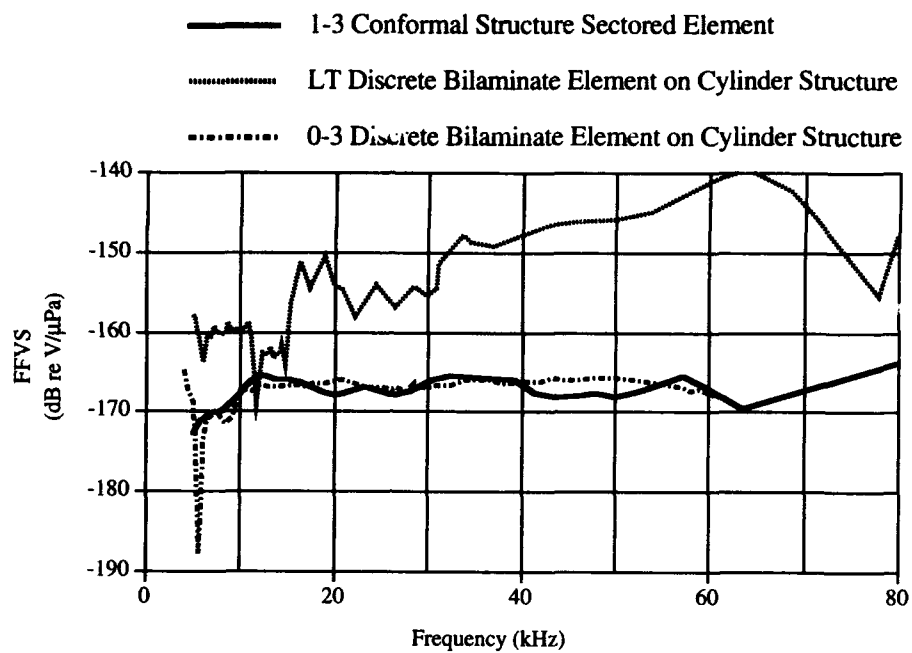


Figure 4: Free field voltage sensitivities of PbTiO_3 , 1-3 and 0-3 elements in a cylindrical structural configuration.

FABRICATION AND PROPERTIES OF 1-3 PZT-POLYMER COMPOSITES

R. J. Gentilman, D.F. Fiore, H.T. Pham, K.W. French, and L.J. Bowen

Materials Systems Inc.
521 Great Road
Littleton, MA 01460

ABSTRACT

Cost effective manufacturing processes have been demonstrated for 1-3 PZT-polymer composite transducers which can be scaled to large areas. PZT ceramic preforms containing uniform rods aligned in a precise array are produced by injection molding. The PZT preforms contain 361 rods which are 1.1 mm diameter and 8 mm long. The preforms are sintered, poled, laid up to make composites of arbitrarily large size, and then encapsulated into a polymer matrix. Composites have been produced with both flexible and rigid polymers. The composites are machined flat and parallel and then electroded. Several 100 mm square transducers with a composite thickness of 6.3 mm have been fabricated and evaluated. These have shown good performance both as projectors and hydrophones. Transducer fabrication has been scaled to 250 mm square panels. Ultrafine scale 1-3 PZT composites have also been produced by injection molding. Uniform arrays of 120 μm diameter, 1000 μm long PZT fibers in an epoxy matrix have been produced. PZT 1-3 composite arrays with fibers as small as 70 μm diameter and an aspect ratio of 10 have also been fabricated.

INTRODUCTION

Piezoelectric 1-3 ceramic/polymer composites offer fabrication and performance advantages over monolithic ceramic and polymer piezoelectric materials in both sensing and actuating applications. The most common 1-3 composites contain arrays of lead zirconate titanate (PZT) ceramic rods separated by a relatively compliant polymer second phase (Figure 1).

Transducers made from 1-3 composite material have several advantages over monolithic ceramic, piezoelectric polymer, or 0-3 composite devices. Depending upon the specific application, these advantages may include: high receiving sensitivity and transmitting response, minimal lateral mode response, acoustic impedance match to water, high capacitance, and low mass.

To the extent authorized under the laws of the United States of America, all copyright interests in this publication are the property of The American Ceramic Society. Any duplication, reproduction, or republication of this publication or any part thereof, without the express written consent of The American Ceramic Society or fee paid to the Copyright Clearance Center, is prohibited.

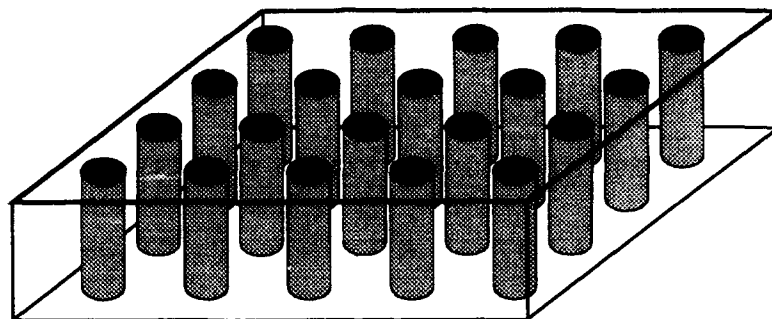


Figure 1. Schematic description of the 1-3 PZT-polymer composite configuration, showing aligned PZT rods in a polymer matrix

Underwater Navy applications exist for high performance, cost effective, large area transducers operating at frequencies well below resonance. On the other hand, medical ultrasound and underwater acoustic imaging systems require efficient high frequency transducers to achieve sufficient image resolution.

Piezoelectric transducers are most efficient if they operate at or near the thickness mode resonance frequency, which is equal to:

$$f_{\text{res}} = c / 2 L$$

where:

f_{res}	=	thickness mode resonance frequency (kHz)
c	=	sonic velocity of the material (m/s)
L	=	thickness (mm)

The sonic velocities of piezoelectric ceramics and composites fall in the range of 2000-4000 m/s. In addition, composite transducers show optimum performance for rod aspect ratios equal to or greater than 4. Therefore, extremely fine scale 1-3 composites with PZT rod diameters of 100 μm or less are required for high frequency ($\gg 1$ MHz) resonance applications.

In the present work, a ceramic injection molding manufacturing process for low cost fabrication of composite transducers has been developed. This process has been used to fabricate arrays of net-shape PZT ceramic rods attached to a common ceramic base. This allows easy handling of hundreds or thousands of precisely aligned piezoelectric elements during the subsequent steps of composite assembly. Coarse scale (~ 1 mm diameter elements) as well as extremely fine scale ($< 100 \mu\text{m}$ diameter elements) ceramic preforms have been produced and assembled into

finished 1-3 transducers. Coarse scale composite transducers as large as 250 mm square have been produced, with no inherent limit to much larger areas. Fine scale composite transducers having element diameters below 120 μm have also been produced for high frequency resonant applications. Tooling has been developed that extends the process capability to much finer dimensions. In the present work, the goal for 1-3 composites is 25 μm element diameter which would allow transducer operating frequencies to be extended well above 10 MHz.

TRANSDUCER FABRICATION

The process steps used to fabricate PZT composite transducers are shown in Figure 2. The PZT ceramic powder is first thoroughly mixed with a wax binder which acts as a carrier during molding, allowing transfer as a viscous fluid under heat and pressure. During injection molding, shown schematically in Figure 3, the heated thermoplastic mixture of ceramic powder and organic binder is forced into a cooled mold creating a net shape green part. The molded part is subsequently heated slowly in air to remove the organic binder. The PZT shape is then sintered at 1250°C for 1 hr, under controlled atmosphere conditions to prevent excessive lead oxide vaporization and consequent degradation of the piezoelectric properties.

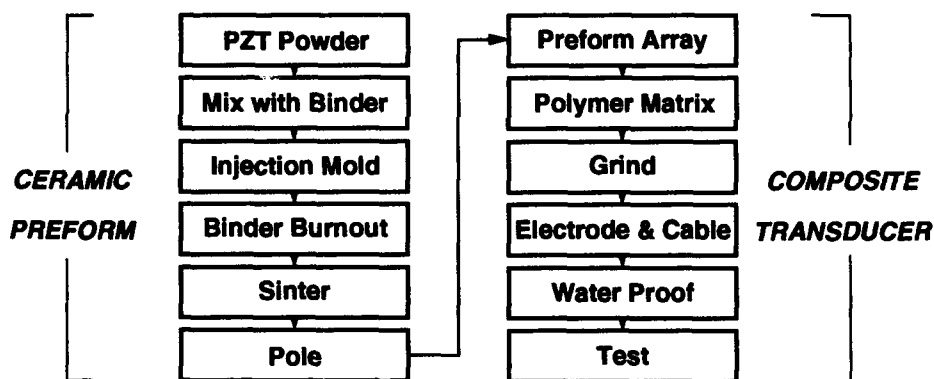


Figure 2. The 1-3 composite transducer fabrication process, consisting of ceramic preform fabrication (left) and composite transducer assembly (right).

For 1-3 piezoelectric composites, the sintered net shape preform contains the active PZT elements already formed into the required configuration and arranged on a ceramic baseplate. The preform can be contact poled under high electric field, or alternatively the composite can be contact or corona poled after encapsulation in the polymer matrix. The matrix is a castable resin, infiltrated into the PZT preforms without the aid of applied pressure. After the matrix has been cured, the ceramic baseplate is removed by grinding and the composite is finished flat and parallel. Permanent electrodes are applied and wires attached to complete the transducer.

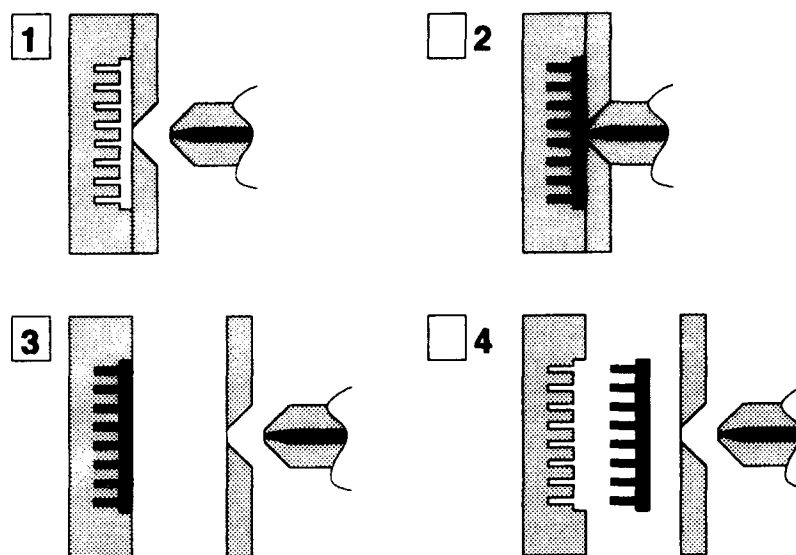


Figure 3. Schematic description of the injection molding process for 1-3 PZT preforms. (1) Hot wax-ceramic mixture in nozzle. (2) Injection of mix into mold. (3) Mix cools and forms solid part. (4) Net shape 1-3 preform is ejected from mold.

In this study, the piezoelectric ceramic was PZT-5H (Morgan Matroc Inc.). When sintered, the injection molded ceramic exhibited excellent and highly reproducible piezoelectric and dielectric characteristics (Table 1). Several polymers were utilized as the matrix material, including: soft polyurethane, voided polyurethane containing 40 volume percent of 50 μm hollow polymer microspheres, and hard Spurr epoxy.

Table 1. Properties of sintered PZT-5H formed by injection molding.

d_{33}	=	$700 \pm 50 \text{ pC/N}$
Dielectric constant	=	3200
Density	=	7.5 g/cm^3

RESULTS AND DISCUSSION

Transducers for undersea applications require 1-3 PZT/polymer composites having relatively low PZT volume fraction (0.15) to facilitate acoustic impedance matching to water. Coarse scale composites for large area projection have been produced with PZT rods measuring 1.1 mm diameter and 6.3 mm long. The sintered 1-3 preform, consisting of a 19 x 19 array of PZT rods on an integral 50 mm square base plate, is shown in Figure 4.



Figure 4. Injection molded and sintered PZT 1-3 preform with 361 identical 1.1 mm diameter rods.

The preforms are easily aligned for assembly into large area composites, as seen in Figure 5. To produce a composite, the polymer matrix is poured into the array of PZT rods and allowed to set. The PZT bases plates are then removed by surface grinding. Copper-plated glass fiber reinforced circuit boards are attached to the major faces to act as electrodes and as acoustic impedance transformers. Figure 6 shows a finished 100 mm square transducer assembled from four 50 mm PZT preforms.

Composite transducers with active material measuring 100 x 100 x 6.3 mm have been extensively tested underwater in both receive and transmit modes. Figure 7 shows representative data from these tests. The 1-3 composites demonstrate good response linearity in both operational modes at frequencies from the lowest measured, 1 kHz, up to the thickness mode resonance at 250 kHz. Lateral modes have not been observed. The receiving response is very high at approximately -187 dB re: 1 V/ μ Pa over this frequency range. Most importantly, the material is an excellent underwater actuator, coupling efficiently into water without the need of matching layers due to its close acoustic impedance match. The composites have been driven at applied rms fields from 0 to 200 V/mm without breakdowns and show linear amplitude response over this entire voltage range.

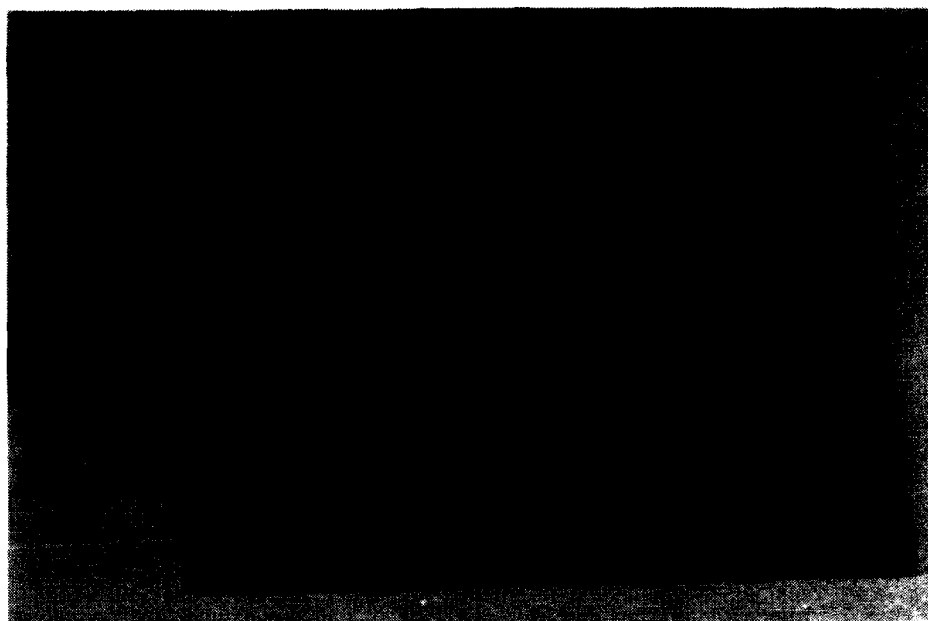


Figure 5. Preform lay-up to form large area 1-3 composite arrays (250 mm x 250 mm).

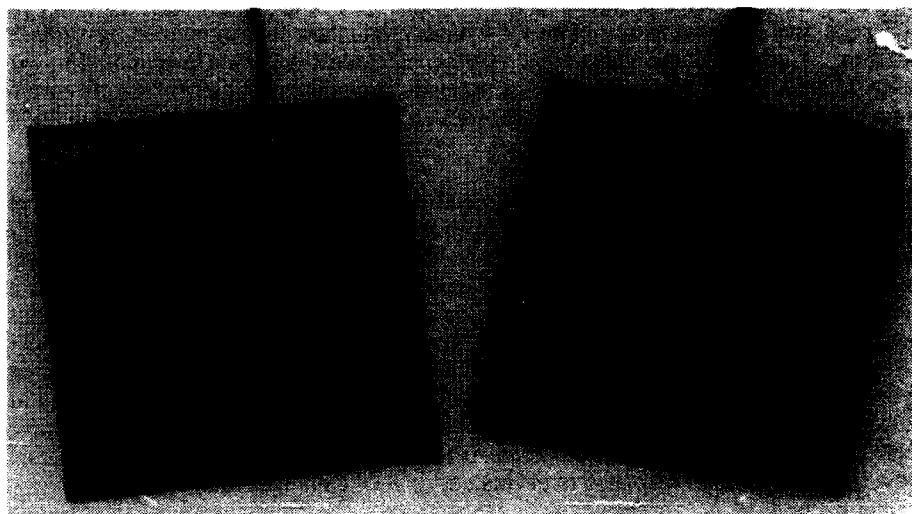


Figure 6. Finished 100 mm 1-3 transducers, with cable and waterproofed, ready for testing.

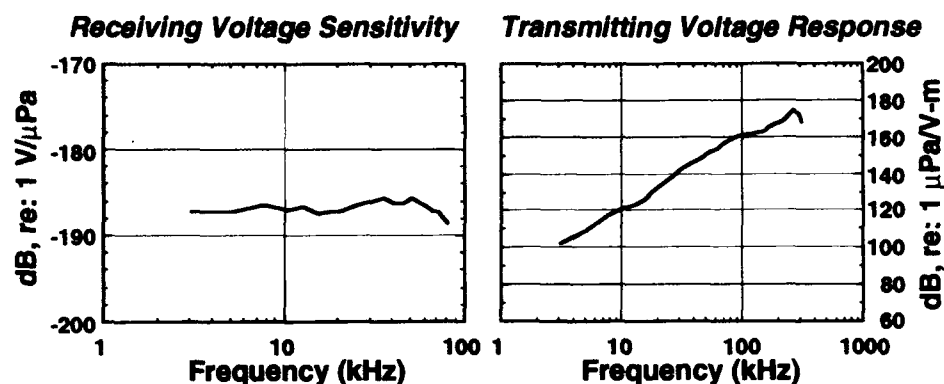


Figure 7. Response of 1-3 composite transducers in receive and transmit modes. The active material is 6.3 mm thick and has an area of 100 x 100 mm, with 1.1 mm diameter PZT rods in a matrix of voided polyurethane.

Similar injection molding processes have also been used to form ultrafine scale 1-3 PZT elements for high frequency resonant applications. Development of tooling to allow intact separation of the green PZT part from the tool has been a major focus of effort in the fabrication of ultrafine scale 1-3 preforms with fibers as small as 70 μm diameter. The degree of taper and the smoothness of the tool cavities are important for successful removal of the molded part from the tool. Figure 8 shows a scanning electron micrograph of an as-molded PZT preform with 0.25 volume fraction of 70 μm mid-point diameter fibers. The PZT elements have significant taper and an aspect ratio of approximately 10.

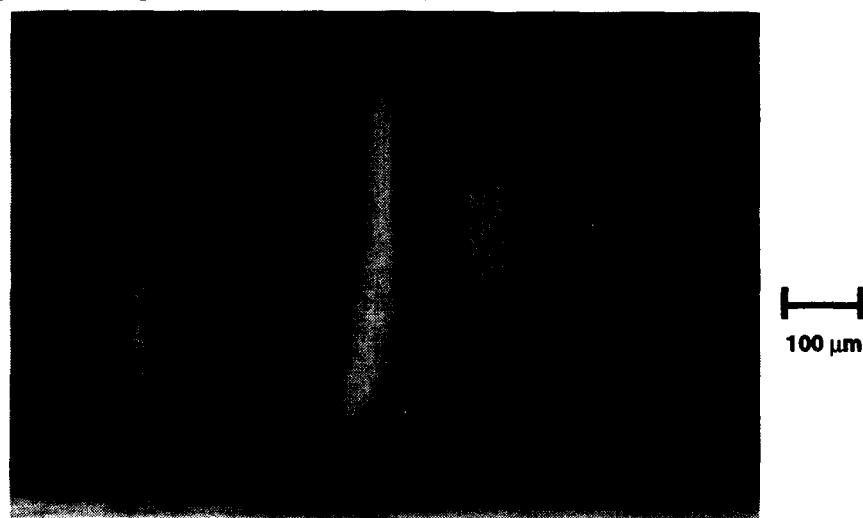


Figure 8. As-molded 1-3 fiber array with 70 μm midpoint diameter PZT fibers.

The as-sintered surface of a 70 μm midpoint diameter fiber is shown at high magnification in Figure 9. The grain size is in the range of 2 to 5 μm , typical for PZT-5H. The material appears dense and pore-free even though the fiber diameter is only 40 μm at this point along its length. The injection molding process is thus capable of producing very fine dimensions. Although most resonant applications require aspect ratios of only 4 to 5 to gain the performance benefits of the 1-3 composite configuration, the aspect ratio achieved for these fibers is approximately 10. The objective of the ultrafine scale research is to push the limitations of the technique with a goal of achieving 25 μm diameter fibers.



Figure 9. As-sintered surface of injection molded fiber, showing the PZT microstructure and grain size.

SUMMARY

Ceramic injection molding has been shown to be a viable and cost effective process for fabricating both PZT ceramics and piezoelectric ceramic/polymer transducers. The process tooling is capable of producing a large number of identical parts and is versatile in terms of the variety of formable PZT composite element shapes. The electrical properties of injection molded PZT ceramics are comparable with those prepared by conventional powder pressing. By using ceramic injection molding to fabricate composite preforms and then laying up the preforms to form larger composite arrays, piezoelectric composite transducers can be manufactured cost-effectively in large quantities. These have been manufactured in large area arrays for Navy projector applications and show excellent performance in both receiving and projection operation.

Ultrafine scale 1-3 composite structures suitable for high frequency acoustic imaging applications have also been net-shape formed by this method. The process capability has been extended to 1-3 fiber arrays containing PZT volume fractions up to 0.4 and PZT elements as small as 70 μm in diameter and 750 μm long. Smaller diameters appear feasible based on the current work.

ACKNOWLEDGEMENTS

This work was funded by the Office of Naval Research. The authors wish to thank Dr. F. Geil of Westinghouse Corporation and A. Medeiros of Raytheon Company for measurements on 1-3 transducer samples.

APPLICABILITY OF CERAMICS FOR CRYOGENIC USE

S. Nishijima, A. Nakahira, K. Niihara and T. Okada,
ISIR Osaka Univ., Ibaraki Osaka 567 Japan

Ceramic thermal shield support used at cryogenic temperatures had been developed for superconducting magnet system. The ceramic materials were screened, based on thermal conductivity down to cryogenic temperature, mechanical properties and machinability, and zirconia was chosen as the candidate for the thermal shield support. The thermal conductivity down to 10 K was measured, the thermal penetration through the support was calculated and compared with the stainless steel support. It was found that with approximately 1/5 of heat penetration to 80K, with 1/4 of that to 4.2 K, a shield can be made with zirconia support. The machinability of the zirconia was also examined. The bolt shaped shield support was successfully developed. The other possible applications of ceramic materials for cryogenic use were also discussed.

INTRODUCTION

The organic matrix composites have been used as insulating and/or structural materials of superconducting magnet (SCM). Several severe requests for the materials have arisen: thermal shield support, coil bobbin of Nb₃Sn for AC application, spacer for cooling channel in large scale SCM. To answer these requests, the research and development of the material based on a new concept, are important. In this work, the applicability of ceramics to cryogenic temperature range was examined.

THERMAL SHIELD SUPPORT

Thermal shield support is important for the stable operation of SCM to reduce the heat penetration to the cryogenic area. According to the thermal design of Large Helical Device (LHD), ^[1] it has been clarified that the heat penetration through the stainless steel (S.S.) supports of the thermal radiation shield was one of the most effective paths. The heat penetration to the 80K stage was markedly larger than expected. As the thermal shield supports were located near or on the plasma vessel (Fig.1), particular problems to be considered

To the extent authorized under the laws of the United States of America, all copyright interests in this publication are the property of The American Ceramic Society. Any duplication, reproduction, or republication of this publication or any part thereof, without the express written consent of The American Ceramic Society or fee paid to the Copyright Clearance Center, is prohibited.

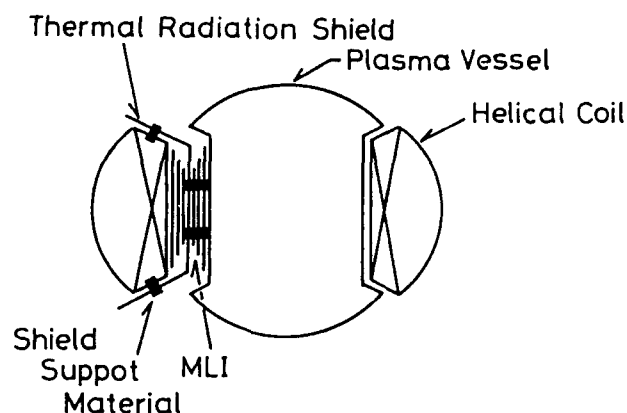


Fig.1 Schematic illustration of plasma vessel, superconducting magnets, thermal radiation shield and shield supports.

included radiation resistance, durability, heat resistance and low thermal conductivity [2]. The support made by S.S. was not suitable because of high thermal conductivity. The support could not be replaced after the construction of LHD and therefore durability up to 10 years and radiation resistance up to 10MGy was needed. The plasma vessel was heated up to a temperature near 400K for evacuation and hence the organic composites were not advisable considering the outgassing and the dissociation. To solve the problems the ceramic supports were developed and the performance was estimated.

Table 1 lists the considered ceramics. The characteristics of S.S. were also tabulated for the comparison. The HIP processed alumina was presented as (2) in the table. It was clear that zirconia was the most promising because it shows the lowest thermal conductivity, high strength and similar thermal expansion coefficient to metals which makes it compatible with metals at cryogenic temperatures.

CRYOGENIC CHARACTERISTICS OF ZIRCONIA

The mechanical strength and thermal conductivity of zirconia were measured at cryogenic temperatures to estimate the applicability of the zirconia shield support.

Table 1 Comparison of characteristics of several ceramics and S.S.

	Al ₂ O ₃ (1)	Al ₂ O ₃ (2)	Al ₂ O ₃ /TiC	Si ₃ N ₄	ZrO ₂	18-8 S.S.
Flexural strength (MPa)	392	588	833	1180	1470	617
Thermal conductivity (W/m/K)	21.5	24.7	28.1	21.4	3.1	14.8
Thermal expansion coefficient (x10 ⁻⁶ /K)	5.25	6.00	5.52	1.00	9.00	14.7

The 3 point flexural tests were performed based on JIS-R1601. The rectangular shaped specimen of 4x3x50 mm was used setting the span to 40mm. The flexural speed was 0.5mm/min. The number tested was 3 at each condition. It was known that the stress induced martensitic transformation (transformation from tetragonal to monoclinic phase transition) toughened the zirconia [3]. It was necessary to confirm the possible mechanism even at cryogenic temperature. The temperature dependence of the flexural strength was shown in Fig.2. The partially stabilized zirconia with yttria was chosen. The amount of yttria was varied. The zirconia with 3 mole % yttria (3Y-ZrO₂) showed the highest strength even at cryogenic temperatures. It was also confirmed that even at cryogenic temperature the strength of zirconia did not show a decrease.

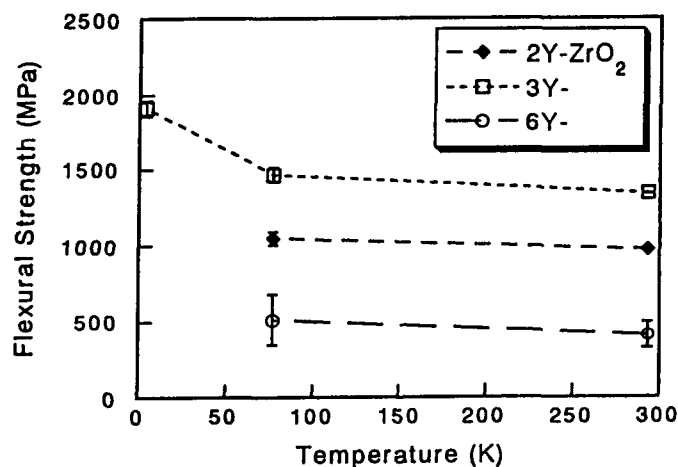


Fig.2 Flexural Strength of zirconia.

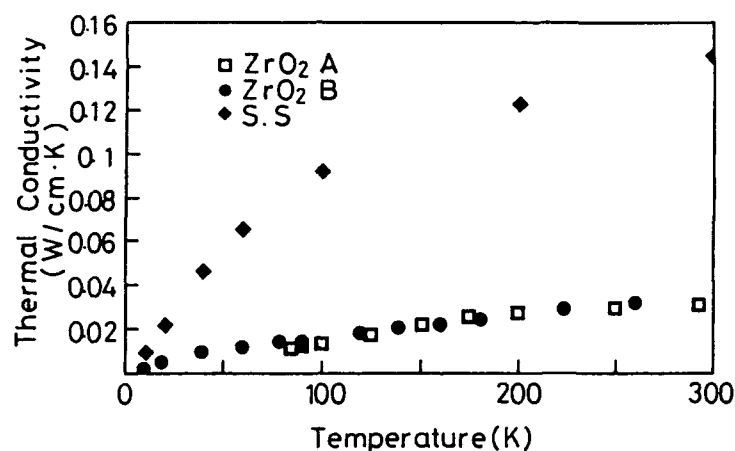


Fig.3 Temperature dependence of thermal conductivity of zirconia and Stainless Steel (S.S.)

The thermal conductivity was also measured in steady state conditions setting the temperature difference at 1K. The shape of the specimen for thermal conductivity measurement was cylindrical (17mm in diameter, 10mm in height). The measured temperature range was from 10K to room temperature (RT). In this experiment, 3Y-ZrO₂ was used because it showed the highest strength at cryogenic temperatures. In Fig.3 the temperature dependence of thermal conductivity was presented. The thermal conductivity of S.S. was also presented and was confirmed that the zirconia was more profitable than S.S. in the sense of thermal penetration.

APPLICABILITY OF ZIRCONIA SHIELD SUPPORT

The feasibility study of the zirconia supports was made using the cryogenic data. Table.2 shows the thermal conductivity integral for each material. The integration was made from 4.2 to 77K or 77 to 300K considering the two

Table 2 Thermal conductivity integral for each support material

	Th(K)	Tl(K)	$\int KdT$ (W/M)
ZrO ₂	300	77	5.59
	77	4.2	0.5
18-8 S.S	300	77	27.4
	77	4.2	3.17
GFRP	300	77	0.94
	77	4.2	0.09

Table.3 Heat penetration through shield supports in LHD system

	300K	70K	77k	4.2K
ZrO ₂		2600W		270W
18-8 S.S.		12600W		1400W

cases that the support was located on either the superconducting vessel or plasma vessel. When the zirconia supports were employed, the heat penetration through the supports could be reduced to one-fifth as compared with S.S. supports in both cases.

The heat penetration through the supports in actual LHD was estimated using the thermal conductivity integral. The calculation was made considering that 10 supports are needed for 1 m² of thermal radiation shield; that is, the supports were installed every 30cm on the shield. By this assumption, an approximate total of 3100 supports were needed for LHD. The diameter and the length of the supports was assumed as 6 and 20 mm, respectively. The estimation was presented in Table.3. When the supports were set on the plasma vessel, the heat penetration to the radiation shield through zirconia supports was calculated as 2600W and 12600W through S.S. supports. The large improvement was expected.

The machinability of the zirconia was also examined, finding that screw shaped supports were fabricable. A set of screws was manufactured successfully. Concerning radiation damage, it was confirmed that the mechanical degradation was not induced at the dose level [4].

OTHER APPLICATION

Other than the shield support the ceramic materials could also be applicable to the spacer in the large scaled SCM or coil bobbin. The spacer is needed to show small thermal contraction down to cryogenic temperatures, high compressive modulus, high compressive strength and electric insulating properties. The electric insulating properties and high temperature (approximately 700K) resistance for coil bobbin of Nb₃Sn AC coils. In such application ceramics are ought to be needed. The mechanical strength of zirconia was confirmed to be increased with decreasing temperature and hence the application of ceramic materials is ought to be possible.

CONCLUSION

The zirconia shield support was successfully developed. The shield support can reduced the heat penetration to the shield by approximately one-fifth

when compared with S.S. support. The results suggest that the cryogenic application of ceramics to cryogenic temperature should be possible.

ACKNOWLEDGEMENT

This work was partly supported by the cooperative work "Advanced Materials Creation and Their Limit State Protection for Environmental Preservation" between the Institute of Scientific and Industrial Research and the Welding Research Institute at Osaka University.

REFERENCES

1. Yamamoto, J. ed., Thermal Loading in the LHD Coil System, Reports on Cooling System and Cryogenic Technology for LHD (1992)
2. Okada, T., Nishijima, S., Takahata, K. and Yamamoto, J., Research and Development of Insulating Materials for Large Helical Device, *Cryogenics* (1991) 31 307-311
3. Heuer, A.H. and Ruhle, M., On the Nucleation of the Martensitic Transformation in Zirconia, *Acta. Metall.* (1985) 33 2101-2112
4. Miyata, K. and Atobe, K., Evaluation of Mechanical Properties in Reactor Irradiated Oxide Ceramics and Non-Oxide Ceramics, KURRI-TR-313 (1989)

MODELLING OF THE METAL-FERROELECTRIC-METAL CAPACITOR: PART 1 - THEORETICAL CONSIDERATIONS

G. TEOWEE

Donnelly Corp., 4545 E. Fort Lowell Road, Tucson, AZ 85712

D.R. UHLMANN

Arizona Materials Laboratories, Department of Materials Science and Engineering, University of Arizona, Tucson, AZ 85721

ABSTRACT

Metal-Ferroelectric-Metal structures, typified by Pt-PZT-Pt capacitors, are the basic building blocks for ferroelectric devices with applications in ferroelectric memory and high density DRAM'S. A model of a Pt-PZT-Pt capacitor is herein proposed which is based on totally depleted back-to-back Schottky barriers rather than partially-depleted Schottky barriers within the PZT films. Poisson's equation was solved under this assumption, resulting in expressions for space charge, field and potential in the capacitors. The contacts/metals used are not limited to Pt; and the effects of various other electrodes vis-a-vis differences in work function are also discussed.

INTRODUCTION

Lead zirconate titanate (PZT) is a widely explored ferroelectric (FE) material utilized in a wide range of applications [1]. It is a solid solution containing lead titanate (PT) and lead zirconate (PZ) in various stoichiometric ratios. PZT x/y refers to $\text{Pb}(\text{Zr}_{x/100}\text{Ti}_{y/100})\text{O}_3$ where $x, y \leq 100$ and $x+y=100$. In the PZ-PT phase diagram, the rhombohedral-tetragonal boundary is the most important feature, termed the morphotropic phase boundary (MPB). It is located at about 53 atom % Zr, 47 atom % Ti (PZT

To the extent authorized under the laws of the United States of America, all copyright interests in this publication are the property of The American Ceramic Society. Any duplication, reproduction, or republication of this publication or any part thereof, without the express written consent of The American Ceramic Society or fee paid to the Copyright Clearance Center, is prohibited.

53/47). The dielectric constant, electromechanical coupling factor and piezoelectric coefficients have their maximum values here [1].

Previous modeling of PZT capacitors was based on the assumption of partially depleted PZT films, i.e., depletion widths smaller than the film thickness [2]. Adsorbed oxygen at the surfaces of titanate ceramics has often been suggested to give rise to trapping surface states [3] or device-like acceptor states [4]. The presence of such surface states and polarization states at the interfaces can lead to band bending, which in turn affects the type of contact formed, viz., ohmic or rectifying. Rectifying contacts result in uneven field and potential distributions in the PZT films, which affect the final device characteristics.

II. MODEL OF THE PT-PZT-PT CAPACITOR

Metal-FE-metal structures, typified by Pt-PZT-Pt capacitors, are the basic building blocks for active and passive FE devices. It is recognized that the capacitors are not simple metal-insulator-metal devices with ohmic contacts, but rather back-to-back Schottky barriers. These Schottky barriers are themselves fairly complicated due to the presence of surface states at the interfaces, the polycrystallinity of the PZT films which can significantly affect surface states at the Pt-PZT interfaces, and domain structures which affect the states of polarization in the PZT films. Additionally, the depletion width may be comparable to or even larger than the film thickness resulting in wholly depleted films between the electrodes.

The work function of Pt metal, ϕ_{Pt} , is 5.5 eV. The typical band gap, E_g , and electron affinity, X_{PZT} , for a PZT film are about 3.5 eV and 1.75 eV respectively. For a p-type PZT film (the conductivity in PZT ceramics [1] has been determined to be p-type), the Fermi level, E_f , lies closer to the valence band, E_v , than to the conduction band, E_c . Since the work function of Pt is higher than that of PZT, the contact should be ohmic.

The maximum work function of p-type PZT is estimated to be ~4.25eV; and metals with work functions higher than this value - such as Cu (4.64eV), Ag (4.54eV), Au (5.31eV) and Pd (5.35eV) - are expected to yield ohmic contacts, while metals with lower work functions - such as Al (4.20eV) and In (4.12eV) - should yield rectifying contacts. These assumptions are based on considering only the difference of the work functions; and it is recognized that the nature (especially interdiffusion and interfacial surface

states) of the metal-PZT interface can also affect significantly the junction characteristics.

I-V leakage characteristics of these capacitors indicate, however, that the contact is not ohmic (or linear); rather, the current depends logarithmically on the applied voltage. In most cases, the current dependence is not a simple Schottky emission or space-charge limited conduction. More often than not, the specific I-V characteristics are dependent not only on the deposition method but also on the post-deposition and post-metallization procedures adopted. To complicate matters further, there may exist different regimes of leakage current and its dependence on voltage. The only case where the contacts can be rectifying is in the presence of surface states (arising, e.g., from absorbed oxygen at the PZT surface and/or termination of the PZT crystalline lattice at the metal contacts). These surface states with a density of D_0 and a neutral energy level at E_0 result in band bending near the contacts and barrier heights of ϕ_b at the interfaces. It is further assumed (at least initially) that these barrier heights are similar at both interfaces, i.e., the capacitor should behave electrically symmetrically independent of the polarity of the applied voltage.

Conduction across any insulator including FE films can involve several mechanisms such as Schottky emission, Frenkel-Poole emission, tunneling emission, space-charge, ohmic and ionic conductions. Usually (but not necessarily), one process dominates at one temperature or field regime. For example, at low fields, ohmic conduction usually takes place; while at high fields an exponential dependence is observed.

Ferroelectrics are non-linear dielectric materials having high values of dielectric constant, and the domain structure plays an important role in determining its ultimate conductivity. The presence of light or radiation can lead to carrier photogeneration (due to photovoltaic effects); and this can affect the leakage current. In bulk FE's, a slowly decreasing current is almost always detected. The situation is made more complicated by the fact that at any applied field, the ferroelectric will switch eventually, which leads to a sudden current increase. It has been reported in sol-gel derived PZT films [5] that the current was ohmic at low fields, but evolved into an exponential dependence upon the application of higher fields; while another study indicated that Frenkel emission was dominant as characterized by a dependence on the square root of the field [6].

Equilibrium

At equilibrium (no applied bias), it is assumed that the width of the depletion region, w , is larger than the thickness, t , of the PZT film, i.e., the film is totally depleted. This assumption is based on the fact that the dielectric constant of PZT films is very high ($\sim 1000-3000$) compared to the values of conventional oxides such as SiO_2 (~ 3.8). Poisson's equation may be used to calculate the field and potential distribution in the totally depleted film, i.e.,

$$\frac{-d^2\phi}{dx^2} = \frac{dE}{dx} = \frac{\rho(x)}{\epsilon_{\text{PZT}}} \quad (1)$$

where ϕ = potential
 E = electric field
 ρ = charge density
 ϵ_{PZT} = dielectric constant of PZT

The solutions to Poisson's equation are shown in Fig. 1. Note that t and the acceptor concentration, N_a , are constant throughout the film. The effects of the polycrystalline nature of the PZT film (e.g. termination of flux at grain boundaries) are neglected for now. By applying Gauss' Law at the Pt-PZT interface, the maximum field E_0 is:

$$E_0 = \frac{qN_a t}{2\epsilon_{\text{PZT}}} \quad (2)$$

The built-in potential, ϕ_i , at the center of the film is obtained from the negative of the area under the field:

$$\phi_i = \frac{1}{2} \left(\frac{qN_a t}{2\epsilon_{\text{PZT}}} \right) \cdot \frac{t}{2} = \frac{qN_a t^2}{8\epsilon_{\text{PZT}}} \quad (3)$$

The density of electrons, n_e , at the center of the film (with the highest barrier height of $\phi_b + \phi_i$) is:

$$n_s = N_c e^{\frac{-q(\phi_b + \phi_i)}{kT}} \quad (4)$$

where N_c is the effective density of states at the conduction band. The currents are proportional to the electron density; and at equilibrium with no external bias

$$J_I = J_{II} = KN_c e^{\frac{-q(\phi_b + \phi_i)}{kT}} \quad (5)$$

where J_I and J_{II} are the thermally induced current densities at interfaces I and II respectively; and K is a proportionality constant. Since $J_I = J_{II}$, there is no net current flow, as expected.

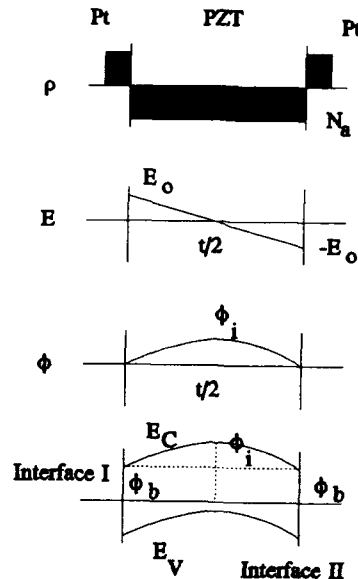


Figure 1. Solutions to Poisson's equation for a wholly depleted PZT film, showing the charge distribution (ρ), electric field (E), potential (ϕ) and energy band diagram at equilibrium.

Current-Voltage Characteristics

Upon application of an external voltage, V_a (or field, V_a/t), the charge remains essentially constant since N_a and t are fixed. The field is, however,

shifted by V_a/t , as indicated in Fig. 2. The distance, y (denoting zero field or maximum potential) is given by:

$$y = \frac{1}{2} \left[t - \frac{V_a}{E_o} \right] \quad (6)$$

(where $V_a < E_o t$)

The new built-in voltage $\phi'_i(V_a)$ as a function of applied bias, V_a , is:

$$\phi'_i(V_a) = \frac{E_o t}{4} - V_a \left[\frac{1}{2} - \frac{V_a}{4E_o t} \right] \quad (7)$$

From Fig. 1:

$$\phi_i = \frac{E_o t}{4} \quad (\text{at } V_a = 0) \quad (8)$$

$$\therefore \phi'_i(V_a) = \phi_i - V_a \left[\frac{1}{2} - \frac{V_a}{4E_o t} \right] \quad (9)$$

The current consists predominantly of a net electron flow across the depleted film even though the film was initially assumed to be p-type. Note, however, that by the depletion approximation, no majority free carriers are present throughout the wholly depleted films. The current results from injection of electrons at the interfaces. The effective barrier heights seen at interface I and II are $\phi_b + \phi'_i(V_a) + V_a$ and:

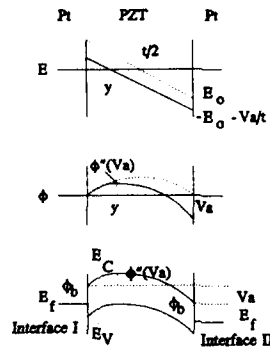


Figure 2. Solutions to Poisson's equation for a wholly depleted PZT film showing the electric field (E), potential (ϕ) and energy band diagram at an applied bias $V_a < E_{ot}$

$$\phi_b + \phi'_i(V_a) = \phi_b + \phi_i - V_a \left[\frac{1}{2} - \frac{V_a}{4E_o t} \right] \quad (10)$$

and

$$\phi_b + \phi'_i(V_a) + V_a = \phi_b + \phi_i + V_a \left[\frac{1}{2} + \frac{V_a}{4E_o t} \right] \quad (11)$$

The current flows at both interfaces due to the applied voltage, V_a , are then:

$$J_I = KN_c e^{-q \left[\phi_b + \phi_i - V_a \left(\frac{1}{2} - \frac{V_a}{4E_o t} \right) \right] / kT} \quad (12)$$

$$J_{II} = KN_c e^{-q \left[\phi_b + \phi_i - V_a \left(\frac{1}{2} + \frac{V_a}{4E_o t} \right) \right] / kT} \quad (13)$$

The net current due to electron flow is:

$$J_T = J_I - J_{II}$$

$$= 2KN_c e^{-q(\phi_b + \phi_i)/kT} e^{-\frac{qV_a^2}{16\phi_i kT}} \left[\sinh \frac{qV_a}{2kT} \right] \quad (14)$$

Moazzami et.al. have reported that $J \propto \sinh V$, where J and V are the current density and voltage respectively, based on leakage current data for their sol-gel derived PZT films [5].

Consider now an applied bias, $V_a > E_o t$. The effective barrier heights at interfaces I and II are ϕ_b and $\phi_b + V_a$, respectively as shown in Fig. 3.

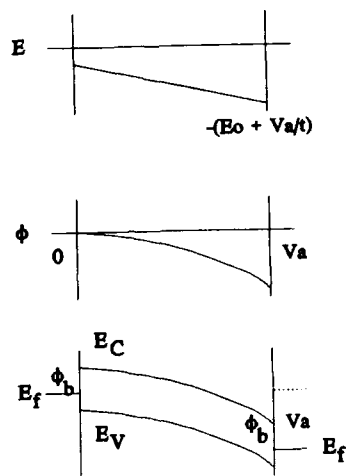


Figure 3. Solutions to Poisson's equation for a wholly depleted film showing the electric field (E), potential (ϕ) and energy band diagram at an applied bias $V_a > E_o t$.

Hence the current flow is

$$\begin{aligned}
 J_T &= J_I - J_{II} \\
 &= KN_c e^{-q\phi_b/kT} (1 - e^{-qV_d/kT})
 \end{aligned} \tag{15}$$

Since $V_A > E_o t$ (or $4\phi_i$), the term in the bracket ~ 1 , and

$$J_T = KN_c e^{-q\phi_b/kT} \tag{16}$$

The current is limited only by interface I; and for constant ϕ_b (assumed independent of applied voltage), the current is constant with increasing voltage above $E_o t$. Note that in contrast to the case of a partially depleted semiconductor film - metal contact, the current here is limited by the built-in voltage, ϕ_i , rather than by the barrier height. A general plot of the I-V behavior of the back-to-back Schottky barriers according to the present model is shown in Fig. 4. Also shown is the plot for a conventional, partially depleted Pt-PZT-Pt capacitor which is dominated by the reverse bias current (Eq. 16) of a Schottky barrier and is fairly independent of applied bias.

By rearranging the voltage and thickness terms in Eq. 14, the current is proportional to e^{-kt^2} where t = thickness of the film and k = constant. Hence it is predicted that the current should increase with decreasing thickness.

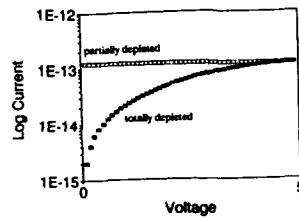


Figure 4. The predicted totally depleted and partially depleted I-V characteristics of a Pt-PZT-Pt capacitor with similar barrier heights at both interfaces.

Non-Symmetrical Electrodes

Consider now the case where the barrier heights are different at the two interfaces, i.e., $\phi_{b1} \neq \phi_{b2}$, as shown in Figure 5. Such a situation would

arise when the top and bottom electrodes are of different metals (hence different work functions) or undergo different firing conditions. The difference between these barrier heights is: $\phi_{b1} - \phi_{b2} = \Delta\phi$. With an applied bias of $+V_a$, the effective barrier heights seen by interface I and interface II are $\phi_i^1(V_a) + \phi_{b2}$ and $\phi_i^1(V_a) + \phi_{b1} - \Delta\phi + V_a$, respectively. The total current is then:

$$J_T(+V_a) = KN_c e^{-q(\phi_i^1(V_a) + \phi_{b2})/kT} - KN_c e^{-q(\phi_{b1} + \phi_i^1(V_a) - \Delta\phi + V_a)/kT} \quad (17)$$

$$\text{but } \phi_{b2} - \phi_{b1} = \Delta\phi$$

$$\text{Hence } J_T(+V_a) = KN_c e^{\frac{-q(\phi_i^1(V_a) + \phi_{b1})}{kT}} e^{-q\Delta\phi/kT} [1 - e^{-qV_a/kT}] \quad (18)$$

Due to the built-in voltage, $\Delta\phi$, there is no current flow until $V_a > \Delta\phi$.

With a negative applied voltage of $-V_a$, the effective barrier heights seen at interfaces I and II are $\phi_i'(V_a) + \phi_{b1}$ and $\phi_i'(V_a) + \phi_{b2} + \Delta\phi + V_a$ respectively. The total current is:

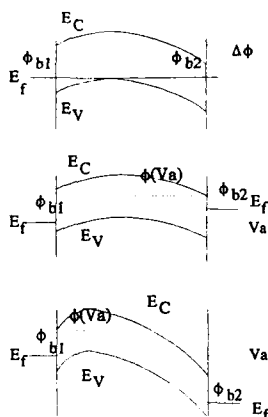


Figure 5. Energy band diagram of the asymmetric Pt-PZT-Pt capacitor with different barrier heights at positive and negative applied biases

$$\begin{aligned}
J_T(-V_a) &= KN_c e^{-q(\phi_i(V_a) + \phi_{bi})/kT} \\
&- KN_c e^{-q(\phi_i(V_a) + \phi_{bi} + V_a)/kT} \\
&= KN_c e^{-q(\phi_i(V_a) + \phi_{bi})/kT} \left[1 - e^{-q \frac{V_a}{kT}} \right] \quad (19)
\end{aligned}$$

Note that $J_T(-V_a) \neq J_T(+V_a)$ unless $\Delta\phi = 0$ (identical barrier heights). Thus depending on the difference between the barrier heights at the two interfaces, the current can be higher or lower by $e^{q\Delta/kT}$ when the polarity is reversed.

Thus, in a Pt-PZT-Pt capacitor with dissimilar barrier heights (e.g., in capacitors which have not been post-metallization annealed), the currents are expected to be polarity-dependent.

III. CONCLUSIONS

A model of the Pt-PZT-Pt capacitor has been proposed which is based on totally depleted back-to-back Schottky barriers rather than partially depleted Schottky barriers. The model predicts the existence of a built-in field within the films which can impact the dielectric and FE behaviors of the capacitors, as well as the saturation leakage current beyond a threshold field (or voltage) after an initial exponential increment.

ACKNOWLEDGMENTS

The financial support of the Air Force Office of Scientific Research and Donnelly Corporation is gratefully acknowledged.

REFERENCES

- [1] B. Jaffe, W.R. Cook and M. Jaffe, Piezoelectric Ceramics, Academic Press, 1971.
- [2] C.J. Brennan, Proc. of 3rd Intl. Symp. Integ. Ferroelectrics (1991), 354.
- [3] H.A. Sauer and S.S. Flaschen, Bulletin of the Amer. Ceram. Soc. 39, 304 (1960).

- [4] Ohmic Contacts to Semiconductors (Ed. B. Schwartz, Electrochemical Society, New York 1969)
- [5] R. Moazzami, C. Hu and W.M. Shepherd, 28th Ann. Proc. Rel. Phys. 21, 23 (1990).
- [6] S.K. Dey and R. Zuleeg, 14, 189.

MODELLING OF THE METAL-FERROELECTRIC METAL CAPACITOR: PART II - EXPERIMENTAL VERIFICATIONS

G. TEOWEE

Donnelly Corp., 4545 E. Fort Lowell Road, Tucson, AZ 85712

D.R. UHLMANN

Arizona Materials Laboratories, Department of Materials Science and
Engineering, University of Arizona, Tucson, AZ 85721

ABSTRACT

Metal-Ferroelectric-Metal structures, typified by Pt-PZT-Pt capacitors, are the basic building blocks for ferroelectric devices. The present paper offers experimental verification for PZT films of a proposed model based on totally depleted back-to-back Schottky barriers rather than partially depleted films. The presence of a built-in field within the PZT films can explain the ubiquitous higher values of coercive field in FE films compared with bulk ceramics, the asymmetry of hysteresis loops found in some FE films (due to uneven field distributions), the diffuse transition of dielectric constant with temperature near T_c , and the much lower values of dielectric constant for relaxor FE films compared with values for bulk ceramics.

INTRODUCTION

Ferroelectric (FE) films, especially lead zirconate titanate (PZT) films, have received increasing attention for microelectronic applications, in the areas of non-volatile ferroelectric memory and high dielectric constant materials for high density DRAMs. PZT is a widely explored FE material utilized for its FE, dielectric, electro-optic, acousto-optic, pyroelectric and piezoelectric properties in both bulk and thin film forms [1]. There has been significant progress in the preparation of high quality PZT films involving wet

To the extent authorized under the laws of the United States of America, all copyright interests in this publication are the property of The American Ceramic Society. Any duplication, reproduction, or republication of this publication or any part thereof, without the express written consent of The American Ceramic Society or fee paid to the Copyright Clearance Center, is prohibited.

chemical methods [e.g., 2] and physical vapor deposition techniques such as sputtering [e.g., 3], laser ablation [e.g., 4] and MOCVD [e.g., 5]. For comparison with the predictions of the model presented in a companion paper, actual device characteristics, including the leakage current vs. voltage relations, were obtained on sol-gel derived PZT 53/47 films prepared in our laboratories. The details of film preparation and leakage characterization have been published elsewhere [e.g., 6].

Metal-FE-metal structures, typified by Pt-PZT-Pt capacitors, are the basic building blocks for active and passive FE devices. It is recognized that the capacitors are not simple metal-insulator-metal devices with ohmic contacts, but rather back-to-back Schottky barriers.

Previous modelling of PZT capacitors was based on the assumption of partially depleted PZT films, i.e., depletion widths smaller than the film thickness [7]. In contrast to previous models, the proposed paper offers experimental verification to a model based on totally depleted back-to-back Schottky barriers. The theoretical background has been presented in an accompanying paper [8].

EXPERIMENTAL

The precursor solution corresponding to the MPB composition namely PZT 53/47 was prepared using Pb acetate and Ti/Zr alkoxides. Fifteen mole % excess PbO was incorporated in the precursor to compensate for PbO loss during post-deposition annealing. The substrates were Si(100) wafers which had been thermally oxidized before being sputtered with Pt to yield Pt(2000Å)/SiO₂(1500Å)/Si. Spincoating was performed in a Class 100 clean room using a Headway Spinner at 2000 rpm for 30s. The precursor solution was filtered using a syringe filter (0.2 μm) to minimize particle contamination. The green films were fired at 400C to burn off the organics, yielding films ~1700Å thick per coating. To obtain thicker films, multiple coatings were performed. Typically three coatings were used to obtain films about 0.54 μm thick. Finally, the films were fired at 700C to crystallize them to single-phase perovskite.

Top Pt electrodes with thickness of 1500Å and diameter of 1.0 mm were rf-sputtered through a shadow mask. The monolithic Pt-PZT-Pt capacitors were completed by obtaining back-contact by acid-etching exposed portions of the films which had been coated with an acid resist. The acid resist was removed by rinsing with toluene. Prior to characterization, the

capacitors were post metallization annealed at temperatures between 100C and 700C for 30 mins under O₂.

The phase assembly in the films was monitored by X-ray diffraction (XRD) using a Scintag Diffractometer; the dielectric properties were obtained using a HP 4192A LF Impedance Analyzer; the FE properties were measured using a Radiant Technologies RT-66A Ferroelectric Tester; and the I-V leakage characteristics were obtained using a Keithley 617 electrometer at both polarities with 0.1V step and 1024s delay time.

RESULTS AND DISCUSSION

The solutions to Poisson's equation based on the assumption of total depletion within the FE PZT film are illustrated in Fig. 1 for the equilibrium case with no applied external voltage. The maximum field, E_o, and built-in potential, ϕ , at the center of the film are given by:

$$E_o = \frac{qN_a t}{2\epsilon_{PZT}} \quad (1)$$

$$\phi_i = \frac{qN_a t^2}{8\epsilon_{PZT}} \quad (2)$$

where q = electronic charge, N_a = acceptor concentration, t = film thickness and ϵ_{PZT} = dielectric constant of the PZT film.

The magnitude of this built-in field (see Fig. 1) depends on the distance within the film. The field is zero at the center and is of different signs at the electrode interfaces. The maximum field is found at the interfaces. The presence of this field can affect significantly the FE properties of the film. For example, assuming N_a = 10¹⁸/cm³, film thickness t = 0.5 μ m and ϵ_{PZT} = 1000, it is estimated from Eq. 1 that E_c = 45.2 kV/cm. The magnitude of this field is comparable to the coercive fields, E_c, (~20-60 kV/cm) measured for typical sol-gel or sputtered PZT films (see Table I). The E_c for similar bulk ceramics is about 1-10 kV/cm. Thus the higher values of E_c found in FE films can be attributed to this built-in field which must be overcome to switch the domains.

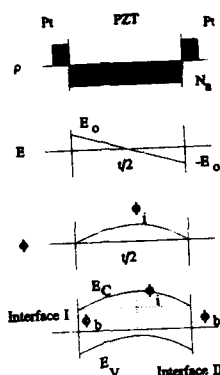


Fig. 1 Solutions to Poisson's equations for a wholly depleted PZT film, showing the charge distribution (ρ), electric field (E), potential (ϕ) and energy band diagram at equilibrium.

Table I. Typical Values of Coercive Field in PZT Films and Bulk Ceramics.

PZT Composition	E_c (kV/cm) of Film	E_c (kV/cm) of Bulk Ceramics
50/50	35-60	6.5
90/10	35	11
0/100	100	6.7
53/47 (AML)	20-60	

Since E_0 is linearly dependent on N_a , a high purity PZT film with low value of N_a (hence low level of defects or non-stoichiometry) is expected to yield low value of E_c . Note, too, that if the acceptor concentration, N_a , is not uniform throughout the film (resulting perhaps from Pb non-stoichiometries or insufficient thermal annealing of the two PZT-electrode interfaces) the uneven field distribution can lead to asymmetric values of E_c , frequently encountered in FE films.

Such an uneven built-in field also gives rise to different regions within the film with different Curie temperatures, which in turn leads to a broad transition in FE properties over a range of temperature, an expectation which

is well documented for the dielectric constants of FE thin films as a function of temperature.

Additionally, the presence of such a built-in field can smear out the FE properties of films of relaxor ferroelectrics (e.g., lead magnesium niobate or PMN: $\text{PbMg}_{1/3}\text{Nb}_{2/3}\text{O}_3$) which are much more sensitive to electric fields than are films of normal FE's such as PZT. The presence of the built-in field leads to a prediction that the dielectric constants of thin films of relaxor FE's should be much lower than their bulk counterparts.

Prior to the present modelling, the observation of substantially smaller dielectric constants for relaxor thin films (typically $\epsilon \sim 1000$) compared with bulk samples (typically $\epsilon \sim 10,000$) had remained a puzzle (e.g., see Table II); and significant research effort had been (mis)directed to processing films of relaxor FE's with properties closer to those of bulk specimens.

Table II. Typical (Literature) ϵ_r Values of Relaxor Films and Bulk Ceramics.

Material	Typical ϵ_r of Films	Typical ϵ_r of Bulk Ceramics
$\text{Pb}(\text{Mg}_{1/3}\text{Nb}_{2/3})\text{O}_3$	1000-1800	> 15000
$\text{Pb}[(\text{Mg}_{1/3}\text{Nb}_{2/3})_{0.9}\text{Ti}_{0.1}]\text{O}_3$	2200	19500
$\text{Pb}(\text{Fe}_{1/2}\text{Nb}_{1/2})\text{O}_3$	< 100	~12000

For 1 μm thick relaxor films, control of N_a down to $10^{16}/\text{cm}^3$ is necessary to achieve an E_c of 1 kV/cm. Since N_a is closely related to Pb vacancies, this calculation illustrates the critical need to control precisely the PbO content in PbO-containing relaxor films. Control to the indicated level is not presently possible.

For FE films thicker than the depletion width, the overall capacitance (and hence dielectric constant) will be dominated by the depletion capacitance unless the films are thick enough that the majority of the voltage drop takes place in the bulk or neutral portion of the film rather than in the depletion zones. As a first approximation, assume that the bulk capacitance will dominate when the film thickness is ~ 10 times the depletion width (typically 0.5-1 μm), i.e., 5-10 μm . The transition to bulk behavior for FE films is thus

not expected unless the films are thicker than 5-10 μm . Hence the use of relaxor films for high density DRAM applications does not appear feasible.

A general plot of the I-V behavior of the back-to-back Schottky barriers according to the proposed model is shown in Fig. 2a. The predictions agree quite well with the observed I-V characteristics (Fig. 2b) of Pt-PZT-Pt capacitors. Also shown in Fig. 2a are the I-V characteristics of a conventional partially depleted Pt-PZT-Pt capacitor which is dominated by the reverse bias current of a Schottky barrier and is fairly independent of applied bias. The behavior predicted by such a conventional model is seen to be in poor agreement with the experimental results.

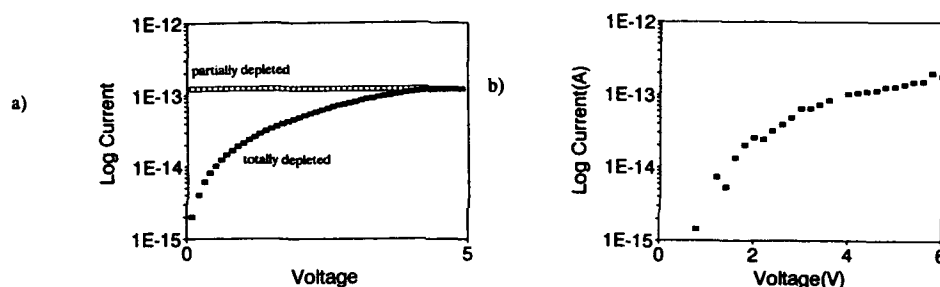


Figure 2 The a) predicted totally depleted and partially depleted and b) measured I-V characteristics of a Pt-PZT-Pt capacitor with similar barrier heights at both interfaces.

The leakage current of FE films is dependent on a variety of intrinsic and extrinsic factors such as type of charge carriers, temperature, thickness, dielectric-metal interfaces, electric field, band gap, phase assemblages (for multicomponent films), degree of preferred orientation, presence of grain boundaries, other microstructural features and the electrical history. The typical leakage characteristics of PZT capacitors do not follow any simple behavior such as that observed for conventional bulk insulators, such as

Schottky, Frenkel Poole, tunnelling, space-charge limited or ionic mechanisms. The present model predicts well the saturation of the leakage currents at high voltages, whereas other treatments must assume image lowering force or series resistance at high fields in order to explain such saturation or deviation from linear extrapolations.

Also predicted by the model is the increase of current in thinner films, viz. $J \propto \exp(-kt^2)$ where k =constant and t^2 =film thickness, at fixed applied field. Shown in Fig. 3 is the logarithm of current measured for PZT capacitors as a function of thickness square at fixed field of 60 kV/cm. Unlike in the case for conventional ohmic capacitors where the current density at fixed field is independent of thickness, for fully depleted FE capacitors, the logarithm of current density is expected to decrease linearly with square of film thickness. It is clearly seen that the current decreases exponentially with increasing square of thickness of the PZT films as expected according to the model. The increase of leakage current in thinner PZT films has important implications considerable for the use of such films in DRAM applications where the increasing miniaturization of device features (viz. film thickness) can lead to undesirable leakage characteristics.

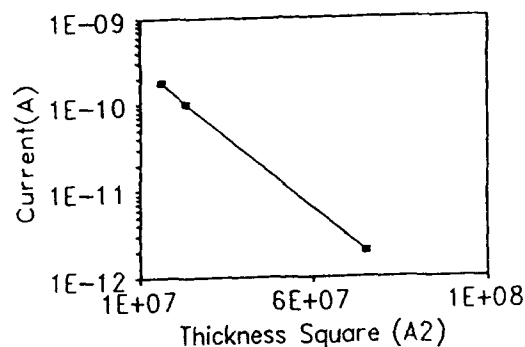


Figure 3. Log of Current vs. thickness square at 60 kV/cm field for PZT capacitors fired at 700C.

The I-V characteristics of Pt-PZT-Pt capacitors where the PZT film was fired to 700C for 30 min. with and without post-metallization annealing (PMA) are shown in Figs. 4a and b respectively. Note that the magnitude of

the leakage current is dependent on the polarity of the applied voltages for the unannealed capacitor, but is symmetrical upon post-metallization annealing at 700C (as predicted by the present model).

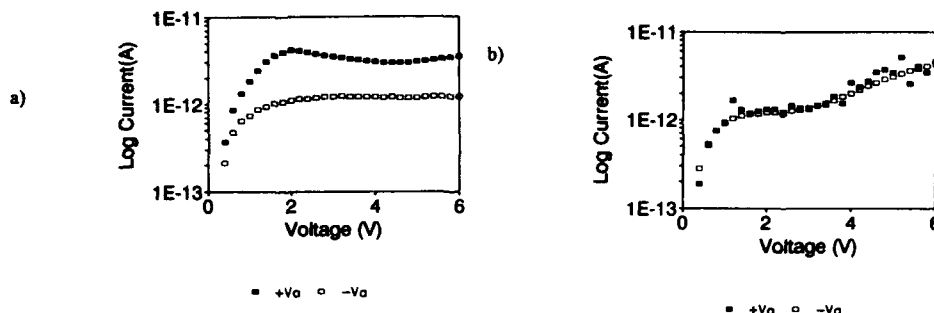


Figure 4 The I-V characteristics with positive and negative voltages in Pt-PZT-Pt capacitors which a) have not been, and b) have been post-metallization annealed at 700C. The PZT film was fired at 700C for 30 min.

In an earlier systematic study of the effects of PMA Pt-PZT-Pt capacitors, it was reported that with increasing PMA temperature, the apparent bulk resistivity increased but the leakage current, dielectric constant, remanent polarization and spontaneous polarization decreased [9].

Within the context of the present model, the observations in that study can be explained. With higher PMA temperatures, more PbO diffused into the substrate and top electrodes. Preliminary EDAX studies have indicated the presence of Pb in the Pt substrates after firing. These PbO losses lead to the inferior dielectric and FE properties. The increasing "bulk ρ " and decreasing leakage current with increasing PMA temperature can be correlated with increased PbO diffusion into the substrate and top electrodes, giving rise to higher barrier heights at the interfaces. With higher PMA temperatures, the barrier heights at the two interfaces tend to be similar but

higher; and hence the capacitors were more symmetric electrically with much smaller leakage currents.

CONCLUSIONS

A model of the Pt-PZT-Pt capacitor has been proposed which is based on totally depleted back-to-back Schottky barriers rather than partially depleted barriers. The predictions of the model agree closely with measured device characteristics obtained in our laboratories and elsewhere.

The model appears to have far-reaching consequences for understanding PZT (or other FE) films. It predicts that there exists a large built-in field (about 20 kV/cm) within the films. The presence of such built-in fields can explain the elevated values of E_c compared to those of corresponding bulk ceramics, the asymmetry of hysteresis loops found in some FE films (due to uneven field distributions), the diffuse transition of ϵ_r values with temperature near T_c and the much lower values of ϵ_r in relaxor films (about 1000-2000) compared with values for bulk ceramics (up to 25,000). Aging behaviors of the films can be influenced by the fields. Leakage currents can be minimized by resorting to thicker PZT films. The deleterious effects of aging (viz., the monotonic decrease of ϵ_r with time due to gradual domain reorientation) can be mitigated by tailoring the N_A profile across the film to achieve a constant field along the polarization direction.

ACKNOWLEDGMENTS

The financial support of the Air Force Office of Scientific Research is gratefully acknowledged.

REFERENCES

- [1] B. Jaffe, W.R. Cook and M. Jaffe, Piezoelectric Ceramics, Academic Press, 1971.
- [2] G. Teowee, J.M. Boulton and D.R. Uhlmann, Mat. Res. Soc. Symp. Proc., Vol. 243, 255 (1992).
- [3] K. Hirata, N. Hosokawa, T. Hase, T. Sakuma and Y. Miyasaku, Jpn. J. Appl. Physics, 31, 3021 (1992).
- [4] D. Roy and S.B. Krupanidhi, J. Mater. Res., 7, 2521 (1992).

- [5] T. Tomonari, T. Ishiu, R. Sakata and T. Takenaka, *Jpn. J. Appl. Phys.*, **31**, 2998 (1992).
- [6] G. Teowee, J.M. Boulton, E.A. Kneer, M.N. Orr, D.P. Birnie II, D.R. Uhlmann, S.C. Lee, K.F. Galloway and R.D. Schrimpf, to be published in *Proc. 8th ISAF* (1992).
- [7] C.J. Brennan, *Proc. 3rd Int'l Symp. Integ. Ferroelectrics* (1991), 354.
- [8] G. Teowee and D.R. Uhlmann, companion paper presented at the Nov. 1993 Pac Rim Ceramic Congress, Ferroelectric Films Symposium.
- [9] G. Teowee, J.M. Boulton, C.D. Baertlein, R.K. Wade and D.R. Uhlmann, to be published in *J. Non-Cryst. Solids*, 1993.

PIEZOELECTRIC CERAMICS AND CERAMIC COMPOSITES FOR INTELLIGENT MECHANICAL BEHAVIORS

Hongyu Wang* and Raj N. Singh* †

Department of Materials Science and Engineering, University of Cincinnati,
Cincinnati, OH 45221-0012

ABSTRACT

Crack propagation in piezoelectric PZT ceramics under applied static electric fields has been studied using the Vickers indentation technique in an effort to develop the intelligent mechanical responses of ferroelectric ceramics and ceramic composites. It was observed that crack lengths decreased under a positive applied field (the polarity of the applied electric field was the same as that for poling) and increased under a negative applied field. Such an effect became more profound with increasing field strength. These observations were in contrary to the expectation based on the piezoelectric characteristics of PZT ceramics. The direction of surface polishing had little effect on the crack extension behavior. More work is being done to further investigate the mechanisms for the observed behavior, including the possibility of a 180° domain switching in the surface layer because of the surface polishing.

I. INTRODUCTION

Piezoelectric ceramics show functional electromechanical responses which can be used for sensing stresses and producing strains/displacements. These functional responses can also be used in imparting intelligent mechanical behavior in ceramics and ceramic composites in such a way that the overall reliability of ceramics is enhanced. In addition, piezoelectric ceramics normally have rather low fracture toughness [1-5] while they are often subjected to high electric fields as well as high mechanical stresses in many of the potential smart applications [6-8]. Therefore, the study of the effect of electromechanical interaction on the crack propagation behavior of piezoelectric materials and improvement in their reliability are of great interests.

* Member, American Ceramic Society

† Fellow, American Ceramic Society

To the extent authorized under the laws of the United States of America, all copyright interests in this publication are the property of The American Ceramic Society. Any duplication, reproduction, or republication of this publication or any part thereof, without the express written consent of The American Ceramic Society or fee paid to the Copyright Clearance Center, is prohibited.

It is known that the ferroelectric phase of piezoelectric ceramics has a significantly higher resistance to fracture than the paraelectric phase. Mehta and Virkar [5] reported that the K_{IC} of an unpoled commercial lead zirconate titanate (PZT) material decreased with increasing temperature up to its Curie point (T_C) and remained constant thereafter. Cook *et al.* [9] examined the flexural strength of an unpoled BaTiO₃ sample as a function of temperature and found that the strength decreased from room temperature to T_C and remained constant above T_C . Several mechanisms have been suggested for the toughening of the ferroelectric phase, including microcracking and crack/twin interaction [10-12], and domain switching (the c-axes become perpendicular to the crack surface.) in the near stress field of a crack tip, which absorbs energy for the crack propagation [4,5,10,11].

Poled piezoelectric ceramics exhibit an anisotropy in fracture toughness [4,5,13,14]: the fracture toughness along the poling direction is higher than that in the perpendicular direction. Okazaki and co-workers [13,14] attributed this anisotropy to the residual internal stresses induced by the electric field during poling. Other researchers suggested that the operation of domain reorientation at the tips of cracks propagating parallel, but not perpendicular, to the poling direction is responsible for the anisotropy [4,5].

Although in most of the applications, piezoelectric materials are subjected to electric fields, the study of their mechanical behavior under the influence of applied electric fields has been scarce. McHenry and Koepke [15] examined the electric field effect on subcritical crack growth in PZT materials using a double torsion technique. They found that high electric fields (a.c. and d.c.) applied perpendicular to the crack front enhanced crack propagation in unpoled PZT; in poled PZT, the application of electric fields perpendicular to the crack plane always "turned" the crack in a direction opposite to the poling direction. Furuta and Uchino [16] have reported a dynamic observation of crack initiation and propagation in a piezoelectric multilayer actuator which was driven by a bipolar electric field. They found that cracks were initiated at the internal electrode edge and could only be observed under an electric field.

In the present study, the influence of externally applied electric fields on crack extension was studied using the Vickers indentation technique which has the advantage of revealing the anisotropy of fracture resistance in two orthogonal directions. Correlation between field strength and crack length measurement enabled a quantitative analysis of the influence, and the results of this study are expected to provide new insights into the behavior of piezoelectric ceramics under applied electric fields in various applications. Some of these results can then be incorporated into "smart" applications of ferroelectric ceramics such as stress sensing and crack inhibition using the generation and application of electric fields.

II. EXPERIMENTAL PROCEDURE

Two types of PZT materials, hard (EC-64) and soft (EC-65), produced by the Acoustic Division of EDO Corporation, Salt Lake City, UT, were tested in the present study. Some selected properties of the materials, according to manufacturer's literature, are listed in Table 1.

Table 1. Selected Properties of Materials Tested in Present Study

Properties	EC-64	EC-65
Young's Modulus (GPa)	78	66
Curie Temperature (°C)	320	350
Mechanical Q factor	400	100
Dielectric Constant @ 1 kHz	1300	1725
Coupling factor k_{33}	0.71	0.72
Piezoelectric constant ($\times 10^{-12}$ m/V)		
d_{33}	295	380
d_{31}	-127	-173
d_{15}	506	584

Specimens for indentation tests were cut using a diamond saw from 6.35 mm thick plates (EC-64) or discs (EC-65) that were electroded and poled by the manufacturer. The surfaces for indentation were parallel to the poling direction as shown in Fig. 1. The surfaces for indentation were hand-polished first using 600 mesh SiC paper and then diamond pastes from 15 μm down to 0.25 μm .

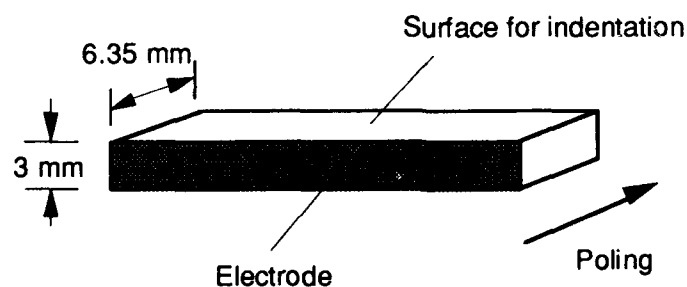


Fig. 1. Schematic showing the poling direction, electrode and indentation surfaces of the specimen used in this study.

A special set-up, schematically shown in Fig. 2, was made for holding the specimen as well as providing insulation between the specimen and the indentation instrument.

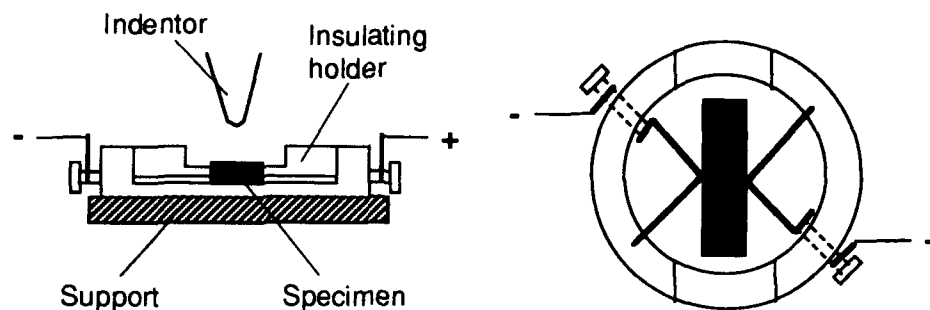


Fig. 2. Experimental set-up for the indentation test with applied electric fields.

Static electric fields were applied across the electroded specimen in either the same or opposite directions to that for poling using a high voltage power supply unit (Model 610C, Trek Inc., Medina, NY). The field strengths were determined according to the coercive fields of the materials. Indentation tests were conducted with a Vickers indenter at a load of 1.2 kg for 20 sec. Crack lengths in all four directions were measured.

III. RESULTS AND DISCUSSION

When a static electric field is applied to the electrodes across a poled PZT specimen, the specimen will either expand or contract depending upon the polarity of the electric field, Fig. 3. If the polarity of the electric field is the same as that for poling (positive field), Fig 3 (a), the specimen will expand in the poling direction and contract in the perpendicular direction due to the Poisson's effect. It is conceivable that, under a positive electric field, the specimen will experience a tensile force in the poling direction and a compressive force in the perpendicular direction. In addition, this externally applied electric field will help maintain the existing domains and make any domain reorientation more difficult. Therefore, in this case the cracks propagating in the directions perpendicular to the poling direction, C_1 and C_3 , are expected to grow longer than they do without the external field because of the tensile force at the crack tip; the cracks propagating parallel to the poling direction, C_2 and C_4 , will be under a combined influence of (i) a compressive force due to the Poisson's effect, which will tend to shorten the cracks and (ii) the fact that the domains are under a reinforcing electric field and difficult to reorient, which will diminish its toughening effect, if any, and elongate the cracks.

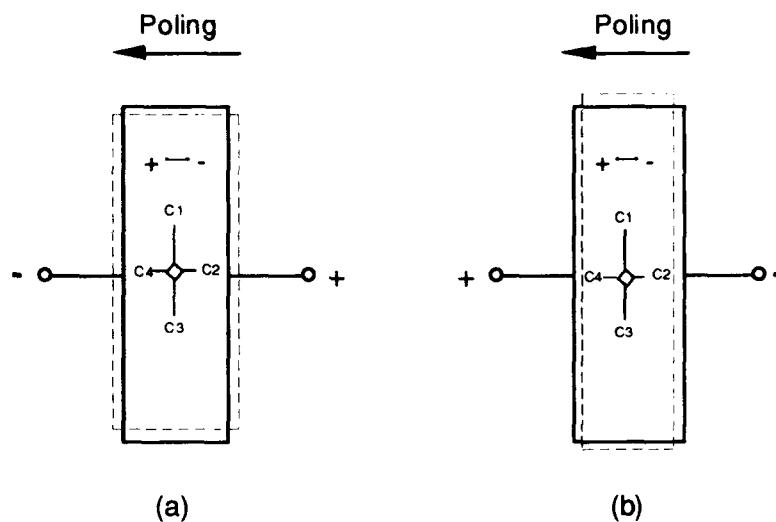


Fig. 3. Schematic showing the piezoelectric effect under applied electric fields of different polarities. Also shown are the dipole orientation and the cracks generated by Vickers indentation.



Fig. 4. Scanning electron micrograph showing the anisotropy in crack lengths in a poled PZT (EC-64) specimen without the applied electric field. Arrow indicates the poling direction.

When the polarity of the applied electric field is opposite to that of the poling field (negative field), Fig. 3 (b), a reverse effect to the above would be expected. Lengths of cracks C_1 and C_3 should be decreased because their tips now are subjected to a compressive force, and cracks C_2 and C_4 are under a combined influence of (i) a tensile force due to the Poisson's effect, which will increase the crack length, and (ii) the ease of domain reorientation as the domains are now under an opposite field to that for poling, which will tend to shorten the cracks.

As expected, an anisotropy of crack lengths was observed in the poled PZT specimens without the application of an external electric field (Fig. 4). The cracks parallel to the poling direction are shorter than those perpendicular to the poling direction. The cracks in the hard EC-64 specimen are shorter than those in the same directions in the soft EC-65 specimen, indicating that the former has a higher resistance to crack propagation.

With an applied electric field, the anisotropy in crack lengths still exists, but changes in crack lengths were somewhat surprising. The results are given in Table 2. Each data point is the mean of five measurements.

Table 2. Effect of Electric Field Polarity and Strength on Indentation Crack Lengths in PZT

Electric Field (V/mm)	C_1 (mm)	C_2 (mm)	C_3 (mm)	C_4 (mm)
EC-64 PZT (hard)				
0	121.87	88.58	123.05	85.68
+ 700	116.88	80.48	111.82	81.12
- 700	130.78	87.75	129.08	87.1
EC-65 PZT (soft)				
0	156.56	91.62	159.88	90.06
+500	156.12	83.74	158.90	77.78
-500	180.82	94.16	176.20	86.46
+1000	147.18	79.14	147.34	77.24

As can be seen from Table 2, for both soft and hard PZT ceramics, the general trend for cracks in all four orientations was that with a positive electric field, the crack lengths decreased. Such decreases became more profound with increasing field strength, as demonstrated by the EC-65 (soft) PZT sample when the field strength was increased from +500 v/mm to +1000 v/mm. On the other hand, with a negative electric field the trend was to increase the crack length.

The above observations are exactly opposite to what was expected. Several possible causes in the experimental system were first checked out. The

polarity of the poling field was marked on the samples by the manufacture and further confirmed by measuring the signs of charges released by the specimens under a unidirectional compressive stress across the electrodes. The polarity of the high voltage power supply unit was also verified. To further confirm the effects, indentation tests were conducted with the diagonals of the indentation at 45° angles with the poling direction as shown in Fig. 5, and the results are shown in Table 3.

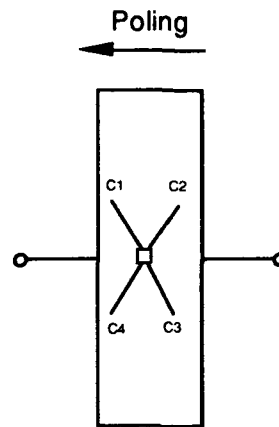


Fig. 5. Schematic showing the 45° indentation test. Note that the cracks are no longer orthogonal to each other.

Table 3. Effect of Indentor Orientation on Crack Lengths in PZT.

Electric Field (V/mm)	C ₁ (mm)	C ₂ (mm)	C ₃ (mm)	C ₄ (mm)
EC-64 PZT (hard) 45° indentation				
0	97.4	100.28	99.65	92.96
+ 700	94.98	96.26	90.88	94.82
- 700	101.13	107.20	104.02	103.54

It is noted that the trend observed in Table 2 is also seen for the 45° indentation test, that is, with a positive field the crack lengths decreased and with a negative field the crack lengths increased.

It has been reported that surface finishing process can reorient domains in thin surface layers on bulk piezoelectric ceramics [17]. Such an effect is largely attributed to the mechanical stresses produced during surface finishing, which

becomes more profound with increasing size of the polishing media [17]. The surprising observations made in this study could be explained if the domains had undergone a 180° reversal reorientation in the surface layer of the specimen during surface finishing. Further work is being conducted with some new samples from EDO acoustic division to confirm this hypothesis.

Since the domain reorientation during surface finishing process is related to the mechanical stresses applied to the domains, the effect of polishing direction has been investigated in the present study. The aforementioned specimens were polished with the polishing wheel running along the length of the specimen, i.e., perpendicular to the domains in the poled PZT ceramics (see Fig. 1), which was expected to cause more domain reorientation. Therefore, a specimen was prepared with all the polishing operation being done along the poling direction across the thickness of the specimen. The results of indentation test are shown in Table 4.

Table 4. Effect of Polishing Direction on Crack Lengths in PZT

Electric Field (V/mm)	C ₁ (mm)	C ₂ (mm)	C ₃ (mm)	C ₄ (mm)
EC-65 PZT (soft) polished along the poling direction				
0	145.28	86.80	157.82	77.24
+ 500	149.67	82.18	155.87	81.27
- 500	157.92	88.88	170.90	78.04

It is noted that the same trend, especially the increase in crack length with a negative field, was observed. Hence, it is concluded that the polishing direction has little effect on the crack extension behavior.

IV. SUMMARY

Crack extension behavior in PZT ceramics has been studied under externally applied electric fields utilizing the indentation technique. Crack lengths are observed to decrease when the polarity of the electric field is the same as that for poling and increase with an electric field having an opposite polarity. This observation is in contrary to the expectation based on the piezoelectric characteristics of PZT ceramics. Further studies are being carried out to see if such an inconsistency is caused by domain reorientation during polishing process or by some other mechanisms.

ACKNOWLEDGMENTS: The authors would like to thank Prof. Yong-Ling Wang for helpful discussions and Mr. Donald E. Bonnema of EDO Corporation for kindly providing the PZT samples. This work was supported by the National Science Foundation through a grant No. DMR-9202111.

REFERENCES

1. S. W. Freiman, K. R. McKinney, and H. L. Smith; pp. 659-76 in *Fracture Mechanics of Ceramics*, Vol. 2. Edited by R. C. Bradt, D. P. H. Hasselman, and F. F. Lange. Plenum, New York, 1974.
2. J. G. Bruce, W. W. Gerberich, and B. G. Koepke; pp. 687-709 in *Fracture Mechanics of Ceramics*, Vol. 4. Edited by R. C. Bradt, D. P. H. Hasselman, and F. F. Lange. Plenum, New York, 1978.
3. S. P. Kovalev, "Study of Ferroelectric Ceramic Fracture by Indentation," *Strength Mater. (Engl. Transl.)*, 1031-55 (April 1982).
4. G. G. Pisarenko, V. M. Chushko, and S. P. Kovalev, "Anisotropy of Fracture Toughness of Piezoelectric Ceramics," *J. Am. Ceram. Soc.*, **68** [5] 259-65 (1985).
5. K. Mehta and A. V. Virkar, "Fracture Mechanisms in Ferroelectric-Ferroelastic Lead Zirconate Titanate (Zr:Ti = 0.54:0.46) Ceramics," *J. Am. Ceram. Soc.*, **73** [3] 567-74 (1990).
6. S. Trolier-McKinstry and R. E. Newnham, "Sensors, Actuators, and Smart Materials," *MRS Bull.*, **18** [4] 27-33 (1993).
7. K. Uchino, "Ceramic Actuators: Principles and Applications," *MRS Bull.*, **18** [4] 42-48 (1993).
8. R. E. Newnham and G. R. Ruschau, "Smart Electroceramics," *J. Am. Ceram. Soc.*, **74** [3] 463-80 (1991).
9. R. F. Cook, S. W. Freiman, B. R. Lawn, and R. C. Pohanka, "Fracture of Ferroelectric Ceramics," *Ferroelectrics*, **50**, 267-72 (1983).
10. R. C. Pohanka, S. W. Freiman, K. Okazaki, and S. Tashiro; pp. 353-64 in *Fracture Mechanics of Ceramics*, Vol. 5. Edited by R. C. Bradt, A. G. Evans, D. P. H. Hasselman, and F. F. Lange. Plenum, New York, 1983.
11. R. C. Pohanka, S. W. Freiman, and R. W. Rice, "Fracture Processes in Ferroic Materials," *Ferroelectrics*, **28**, 337 (1980).
12. S. W. Freiman, L. Chuck, J. J. Mecholsky, D. L. Shelleman, and L. J. Storz; pp. 175-85 in *Fracture Mechanics of Ceramics*, Vol. 8. Edited by R. C. Bradt, A. G. Evans, D. P. H. Hasselman, and F. F. Lange. Plenum, New York, 1986.
13. K. Okazaki, "Mechanical Behavior of Ferroelectric Ceramics," *Bull. Am. Ceram. Soc.*, **63** [9] 1150-52, 57 (1984).
14. T. Yamamoto, H. Igarashi, and K. Okazaki, "Internal Stress Anisotropies Induced by Electric Field in Lanthanum Modified PbTiO₃ Ceramics," *Ferroelectrics*, **50**, 273-78 (1983).
15. K. D. McHenry and B. G. Koepke; pp. 337-52 in *Fracture Mechanics of Ceramics*, Vol. 5. Edited by R. C. Bradt, A. G. Evans, D. P. H. Hasselman, and F. F. Lange. Plenum, New York, 1983.
16. A. Furuta and K. Uchino, "Dynamic Observation of Crack Propagation in Piezoelectric Multilayer Actuators," *J. Am. Ceram. Soc.*, **76** [6] 1615-17 (1993).
17. S. Cheng and I. K. Lloyd, and M. Kahn, "Modification of Surface Texture by Grinding and Polishing Lead Zirconate Titanate Ceramics," *J. Am. Ceram. Soc.*, **75** [8] 2293-96 (1992).

PHOTOSTRICTION AND ITS APPLICATIONS

Kenji Uchino and Sheng-Yuan Chu
International Center for Actuators and Transducers
Materials Research Laboratory, The Pennsylvania State University
University Park, PA 16802

Abstract

The photostrictive effect is the superimposing of photovoltaic and piezoelectric effects. $(\text{Pb},\text{La})(\text{Zr},\text{Ti})\text{O}_3$ ceramics doped with WO_3 exhibit large photostriction under irradiation of purple-color light, and are applicable as remote control actuators. Photo-driven relays and micro walking devices which have been developed, are designed to start moving as a result from the irradiation, having neither electric lead wires nor electric circuit.

INTRODUCTION

Photostrictive effect is a phenomenon in which strain is induced in the sample when it is illuminated. This effect is focused especially in the fields of micromechanism and optical communication.

With decreasing the size of miniature robots/actuators, the weight of the electric lead wire connecting the power supply becomes significant, and remote control will definitely be required for sub-millimeter devices. A photo-driven actuator is a very promising candidate for micro-robots. On the other hand, the key components in optical communication are solid state lasers as a light source, optical fibers as a transfer line, and displays/ telephones as a visual/audible interface with the human. The former two components have been developed fairly successfully, and the photo-acoustic device (i. e. optical telephone or "photophone") will be eagerly anticipated in the next century.

Photostrictive devices which function when they receive the energy of light will be particularly suitable for use in the above-mentioned fields. In principle, the photostrictive effect is the superimposing of a photovoltaic effect, where a large voltage is generated in ferroelectrics through the irradiation of light,¹⁾ and a piezoelectric effect, where the material expands or contracts from the voltage applied. The photovoltaic effect mentioned here generates a greater-than-band-gap voltage, and is quite different from that based on the p-n junction of semiconductors (i. e. solar battery). It is generated when electrons excited by light move in a certain direction of the ferroelectric crystal due to the spontaneous polarization (i. e. crystallographic anisotropy).

To the extent authorized under the laws of the United States of America, all copyright interests in this publication are the property of The American Ceramic Society. Any duplication, reproduction, or republication of this publication or any part thereof, without the express written consent of The American Ceramic Society or fee paid to the Copyright Clearance Center, is prohibited

This paper describes the details of the fundamental photostrictive effect in $(\text{Pb,L a})(\text{Zr,Ti})\text{O}_3$ ceramics first, then introduces its applications to a photo-driven relay and a micro walking machine, which are designed to move as a result of irradiation, having neither lead wires nor electric circuit.

PHOTOSTRICTIVE PROPERTIES

Materials Research

PLZT ($x/y/z$) samples were prepared in accordance with the following composition formula: $\text{Pb}_{1-x}\text{La}_x(\text{Zr}_y\text{Ti}_{1-y})_{1-x/4}\text{O}_3$. The interrelation of photovoltaic current with remanent polarization is plotted for the PLZT family in Fig. 1. The average remanent polarization exhibiting the same magnitude of photo-current differs by 1.7 times between the tetragonal and rhombohedral phases; this suggests the photo-induced electron excitation is related to the (0 0 1) axis-oriented orbit, i. e. the hybridized orbit of p-orbit of oxygen and d-orbit of Ti/Zr. The photostrictive figure of merit is evaluated by the product of the photovoltaic voltage and the piezoelectric coefficient. Therefore, PLZT (3/52/48) was selected because the largest figure of merit is obtained with this composition.^{2,3)}

Impurity doping on PLZT also affects the photovoltaic response significantly.⁴⁾ Figure 2 shows the photovoltaic response for various dopants with the same concentration of 1 atomic % under an illumination intensity of 4 mW/cm^2 at 366 nm. The dashed line in Fig. 2 represents the constant power curve corresponding to the non-doped PLZT. Regarding the photostriction effect, it is known that as the photovoltaic voltage increases, the strain value increases, and with increasing photo-current, there is an increase in the overall response. The photovoltaic response is enhanced by donor doping onto the B-site (Nb^{5+} , Ti^{5+} , W^{6+}). On the other hand, impurity ions substituting at the A-site and/or acceptor ions substituting at the B-site, whose ionic valences are small (1 to 4), have no effect on the response. Figure 3 shows the photovoltaic response plotted as a function of atm % of WO_3 doping concentration. Note that the maximum power is obtained at 0.4 % of the dopant.

Even when the composition is fixed, the photostriction still depends on the sintering condition or the grain size.⁵⁾ Figure 4 shows the dependence of the photostrictive characteristics on the grain size. The smaller grain sample is preferable, if it is sintered to a high density.

Effect of Light Polarization Direction

Effect of the light polarization direction on the photovoltaic phenomenon was investigated on the polycrystalline PLZT, using an experimental setup shown in Fig. 5 (a). This experiment is important when the photostriction is employed to "photophones", where the sample is illuminated with the polarized light traveling through an optical fiber. The rotation angle θ was taken from the vertical spontaneous polarization direction, as shown in Fig. 5 (b). Both the photovoltaic voltage and current provided the maximum at $\theta = 0$ and 180 deg and the minimum at $\theta = 90$ deg; this also indicates that the contributing electron orbit may be the p-d hybridized orbit mentioned above.

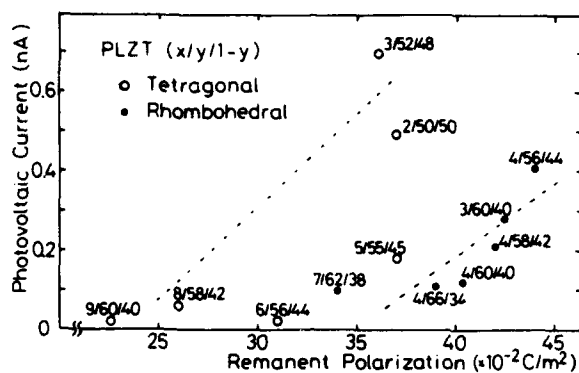


Fig.1. Interrelation of photovoltaic current with remanent polarization in PLZT family.

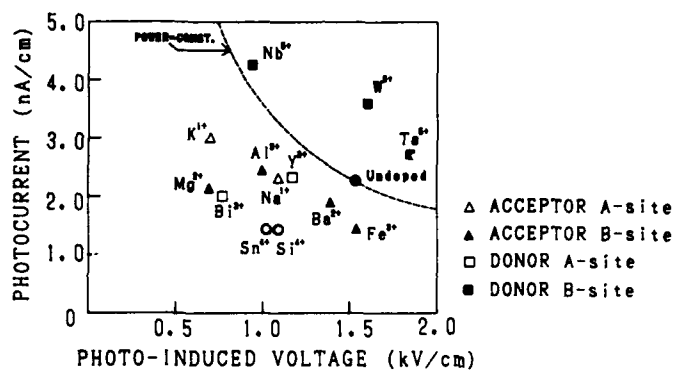


Fig.2. Photovoltaic response as a function of impurity doping.

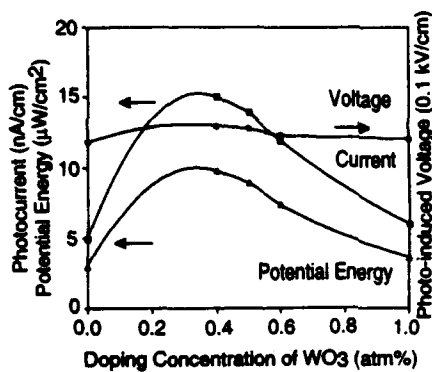


Fig.3. Photovoltaic current and voltage as a function of dopant concentration in WO₃ doped PLZT.

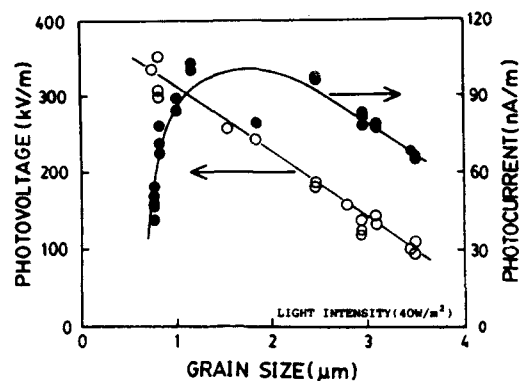


Fig.4. Grain size dependence of photostrictive characteristics in PLZT(3/52/48).

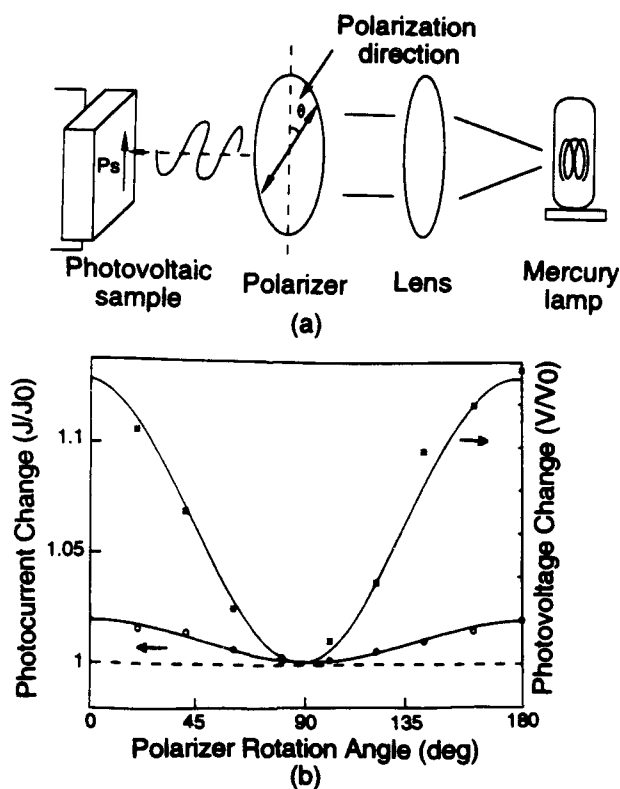


Fig.5. (a) Measuring system of the dependence of photovoltaic effect on light polarization direction, and (b) photovoltaic voltage and current as a function of the rotation angle.

PHOTOSTRICTIVE ACTUATORS

Photo-Driven Relay

A photo-driven relay was constructed using a photostrictor as the driver (Fig. 6).⁴⁾ The driving part was a bimorph which consisted of two ceramic plates (5mmx20mmx0.16mm in size) joined so that their polarization directions were opposing. A dummy plate was positioned adjacent to the bimorph to cancel the photovoltaic voltage generated on the bimorph. Utilizing a dual beam method, switching was controlled by alternately irradiating the bimorph and the dummy. The time delay of the bimorph that ordinarily occurs in the off process due to a low dark conductivity could be avoided, making use of this dual beam method. Figure 7 shows the response of a photostrictive bimorph made from PLZT doped with 0.5 at% WO_3 under an illumination intensity of 10 mW/cm^2 . The amount of displacement observed at a tip of the bimorph (2 cm long and 0.32 mm thick) was $150 \mu\text{m}$. A snap action switch was used for the relay. Switching by a displacement of several tens of micron was possible with this device.⁶⁾ The On/Off response of the photo-driven relay showed a typical delay time of 1 - 2 sec.

Micro Walking Device

A photo-driven micro walking machine has also been developed using the photostrictive bimorphs.⁷⁾ It was simple in structure, having only two ceramic legs (5mmx20mmx0.35mm) fixed to a plastic board (Fig.8). When the two legs were irradiated with purple light alternately, the device moved like an inchworm. The photostrictive bimorph as a whole was caused to bend by $150 \mu\text{m}$ as if it averted the radiation of light. The inchworm built on a trial basis exhibited rather slow walking speed (several $\mu\text{m/min}$) as shown in Fig. 9, since slip occurred between the contacting surface of its leg and the floor.

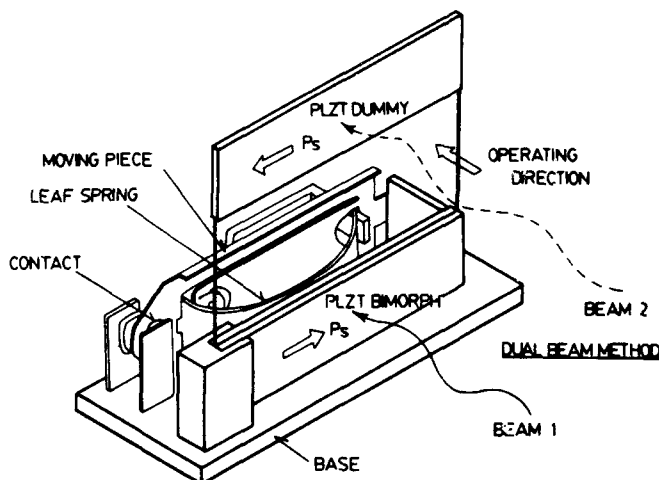


Fig.6. Structure of the photo-driven relay.

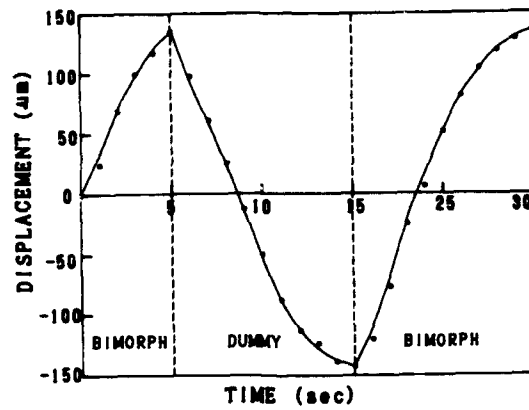


Fig.7. Bimorph deflection of the device made from WO_3 0.5 atm% doped PLZT.

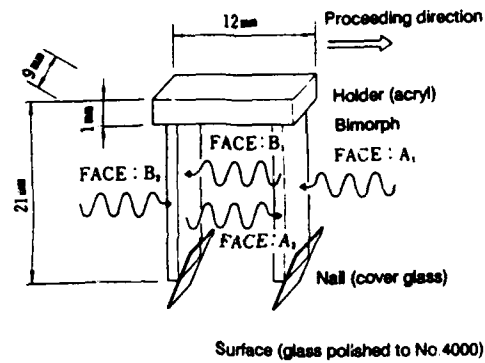


Fig.8. Structure of the photo-driven micro walking machine, and the direction of irradiation.

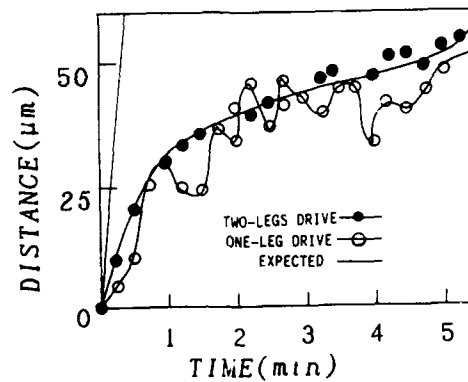


Fig.9. Position change of the photo-driven micro walking machine with time.

CONCLUSION

The photostrictive actuators can be driven by the irradiation of light alone, so that they will be suitable for use in actuators, to which lead wires can hardly be connected because of their ultra-small size or of their employed conditions such as ultra-high vacuum. New actuators of this type have considerable effects upon the future micro-mechatronics.

This work was supported by US Army Research Office through Contract No. DAAL 03-92-G-0244.

References

- 1) V. M. Fridkin, Photo-ferroelectrics, Solid-State Sciences 9, Springer-Verlag (1979).
- 2) K. Uchino, Y. Miyazawa and Late S. Nomura, "Photovoltaic Effect in Ferroelectric Ceramics and Its Applications," Jpn. J. Appl. Phys. 22, Suppl. 22-2, 102 (1983).
- 3) K. Uchino, M. Aizawa and Late S. Nomura, "Photostrictive Effect in $(\text{Pb},\text{La})(\text{Zr},\text{Ti})\text{O}_3$," Ferroelectrics 64, 199 (1985).
- 4) M. Tanimura and K. Uchino, "Effect of Impurity Doping on Photostriction in Ferroelectric Ceramics," Sensors & Mater. 1, 47 (1988).
- 5) T. Sada, M. Inoue and K. Uchino, "Photostrictive Effect in PLZT Ceramics," J. Ceram. Soc. Jpn. 5, 545 (1987).
- 6) R. Sato, T. Taniguchi and M. Oba, "Piezoelectric Relays," OMRON Technics, No. 70, 52 (1983).
- 7) K. Uchino, "Micro Walking Machines Using Piezoelectric Actuators," J. Rob. Mech. 1, 124 (1989).

EFFECTS OF HEAT TREATMENTS ON PHOTOSTRICTION IN PLZT CERAMICS

Kazuhiro NONAKA, Akira TAKASE, Tadahiko WATANABE,
and Hisayoshi YOSHIDA*
Kyushu National Industrial Research Institute, Shuku, Tosu 841,
Japan
*Industrial Technology Center of Saga, Nabeshima, Saga 849,
Japan

ABSTRACT

The photostrictive effect has been studied in PLZT(3/52/48) ceramics heat-treated at 700-1100° C for 1h in various atmospheres such as nitrogen, air, and oxygen. The photostrictive efficiency was markedly enhanced by the heat treatment in nitrogen, whereas the lower efficiency was recognized in samples heat-treated in oxygen.

1. INTRODUCTION

Accompanying the recent development in areas such as optical transmission, micromechanism, and space technology, a new-type actuator directly driven by light irradiation has received considerable amount of attention¹⁻⁶. This actuating mechanism is based on the photostrictive effect, which is explainable by the superposition of the photovoltaic effect and the piezoelectricity.

The photovoltaic phenomenon⁷ is observed in certain ferroelectrics, which generates a steady current opposite in direction to the polarization under short circuit conditions and produces very high electric field (several kV/cm) under open

To the extent authorized under the laws of the United States of America, all copyright interests in this publication are the property of The American Ceramic Society. Any duplication, reproduction, or republication of this publication or any part thereof, without the express written consent of The American Ceramic Society or fee paid to the Copyright Clearance Center, is prohibited.

circuit conditions with an application of near-ultraviolet radiation. The well known piezoelectric effect reveals a strain proportional to an applied electric field. According to several reports on the photostrictive actuator, it has been considered that one of the most significant problems for the practical usage is its slow response speed^{1,2,5}.

This paper describes the effect of heat treatments in various atmospheres on the photostriction in PLZT ceramics. We have clarified that the photostrictive efficiency can be markedly enhanced by the heat treatment in nitrogen.

2. EXPERIMENTAL

The conventional oxide-mixing method was adapted for the preparation of PLZT. PbO , La_2O_3 , ZrO_2 , and TiO_2 powders of purity above 99.6% were used as raw materials. They were mixed with proper ratio corresponding to the composition of $(\text{Pb}_{0.97}, \text{La}_{0.03})(\text{Zr}_{0.52}, \text{Ti}_{0.48})_{1-0.03/4}\text{O}_3$, which is reported to have the highest photostrictive efficiency², calcined at 900°C for 10h, and ball milled. The milled powders were CIP-treated into 18mm diameter, 4mm thick disk shapes. They were sintered at 1200°C for 2h in PbO atmosphere. The resulting ceramics had a bulk density of more than 99% of the theoretical value. The samples were polished, heat-treated at 700-1100°C for 1h in various atmospheres such as nitrogen, air, and oxygen in a magnesia crucible, and cut into $3 \times 3 \times 8\text{mm}^3$ bar shapes. The $3 \times 8\text{mm}^2$ surfaces were silver electroded. Poling was performed by applying 2kV/mm of electric field for 30min in 150°C silicon oil.

The radiation from a ultra-high-pressure mercury lamp (500W) was passed through glass filters to have the wavelength of 300-400nm with a maximum strength around 365nm ($40\text{mW}/\text{cm}^2$), and illuminated to the samples ($3 \times 8\text{mm}^2$, polished surface). The photoinduced current was measured as a function of the applied voltage from -100 to +100V by an electrometer. The photovoltaic current and voltage were determined from the intercepts of the vertical axes and the horizontal axes, respectively. The photostriction was recorded using a strain gauge attached to the bottom plane opposite to the illuminating

surface. The piezoelectric parameters were determined by the resonance-antiresonance method with a vector impedance analyzer.

3. RESULTS AND DISCUSSION

Figure 1 shows the photocurrent as a function of heat treatment temperature. Samples heat-treated in nitrogen gave more than twice values of photocurrent generated in the pretreated sample. On the contrary, the photocurrent was decreased by the heat treatments in oxygen. In the samples heat-treated in the air, the photocurrent increased somewhat with increasing heat treatment temperature.

Figure 2 shows photovoltage as a function of heat treatment temperature. We found the tendency for the photovoltage to be changed by the heat treatments in different atmospheres in similar manner to the relation between the photocurrent and the heat treatment atmospheres (Fig.1); the photovoltage was enhanced by the heat treatment in nitrogen.

Figure 3 shows electro-mechanical coupling factor (K_{33}) and piezoelectric strain constant (d_{33}) as a function of heat treatment temperature. The K_{33} was found to be discernibly increased by the heat treatments in nitrogen. The samples heat-treated in the

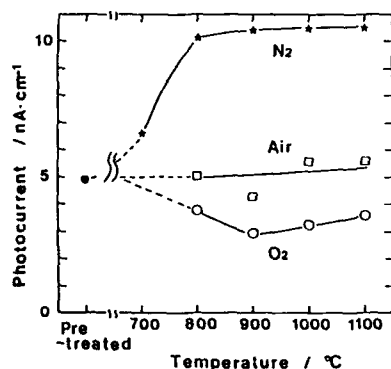


Fig.1 Photocurrent generated in the samples heat-treated for 1h in various atmospheres as a function of heat treatment temperature.

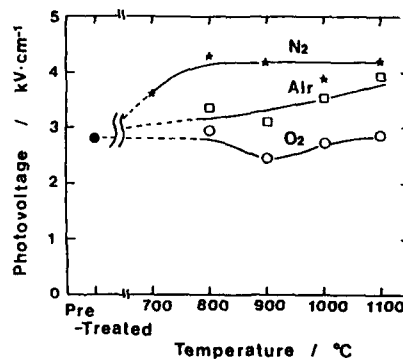


Fig.2 Photovoltage generated in the samples heat-treated for 1h in various atmospheres as a function of heat treatment temperature.

air or oxygen exhibited increased K_{33} compared with that in pretreated samples, but almost no change with the different atmospheres was recognized. The d_{33} , calculated from the product of K_{33} and the square root of the product of dielectric constant(ϵ_{33}^T) and elastic compliance(s_{33}^E), was also enlarged by the heat treatment in nitrogen. From the electrical measurements, the heat treatment in nitrogen was noticed to make both ϵ_{33}^T and s_{33}^E rather higher, and consequently, provides a large d_{33} value.

Figure 4 shows photostrictive response for the samples heat-treated in various atmospheres. The sample heat-treated in nitrogen revealed markedly enhanced photostrictive response. The maximum strain became 1.8 times that in the pretreated sample, whereas the sample heat-treated in oxygen gave a smaller strain maximum. It has been reported that the photostriction is expressed by

$$x(t) = d_{33} E_0 \{1 - \exp(-t/RC)\}$$

where $x(t)$ is the photostriction, E_0 the saturated photovoltaic field, t the time, R the resistance under illumination, and C the capacitance^{1,2,5}. When the sample is optically irradiated, the photostriction progressively occurs following the RC as the time constant to achieve the maximum strain of $d_{33} E_0$.

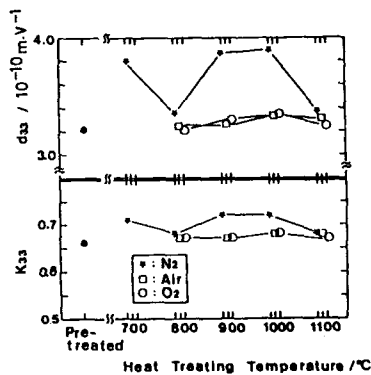


Fig. 3 Electro-mechanical coupling factor(K_{33}) and piezoelectric strain constant(d_{33}) as a function of heat treatment temperature.

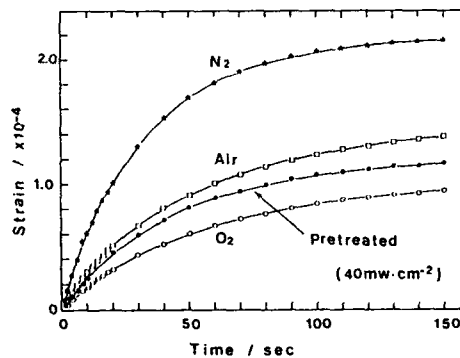


Fig.4 Photostrictive response for the samples heat-treated at 900 ° C for 1h in various atmospheres.

The time constant, RC, was measured to be 19, 30, and 34 sec for the samples heat-treated in N₂, air, and O₂, and 23 sec for the pretreated samples, respectively. The RC was found to be slightly decreased by the heat treatment in nitrogen. The maximum strains calculated from $d_{33}E_0$ are noted to be somewhat smaller than those actually observed in each samples. Considering the maximum-strain ratios among the samples, however, the ratios estimated from the measured strain data agreed closely with those calculated from the $d_{33}E_0$ values.

ACKNOWLEDGEMENT

We thank Mr. Tsuyoshi Hagio for contributions to XPS measurements.

REFERENCES

1. P. S. Brody, "Optomechanical Bimorph Actuator", *Ferroelectrics*, 50, 27-32(1983).
2. K. Uchino, M. Aizawa, and S. Nomura, "Photostrictive Effect in (Pb, La)(Zr, Ti)O₃", *ibid*, 64, 199-208(1985).
3. T. Sada, M. Inoue, and K. Uchino, "Photostriction in PLZT Ceramics", *J. Ceram. Soc. Japan*, 95[5], 545-50(1987).
4. M. Tanimura and K. Uchino, "Effect of Impurity Doping on Photostriction in Ferroelectric Ceramics", *Sensors and Materials*, 1, 47-56(1988).
5. T. Nakada, C. Dong-Hui, H. Chi-Yu, Y. Yamauchi, and T. Yamauchi, "Study on Optical Servo System (Contribution to Optical Actuator)", *Trans. Japan Soc. Mech. Eng.*, 57[542], 3228-33(1991).
6. S. Hattori, T. Fukuda, and S. Nagamori, "A Study on Optical Piezo-Electro Actuator(Response Experiments by U.V. Beam and Photo Response Model", *J. Rob. Soc. Japan*, 9[6], 692-99(1991).
7. V. M. Fridkin, "Photoferroelectrics", *Solid State Science Vol.9*, Springer-Verlag, N.Y.(1979).

TEMPERATURE MODULATION OF THE ELECTRO-OPTIC EFFECT IN BaTiO_3 AND LiNbO_3 - A THEORETICAL APPROACH

G. Zavala-Enriquez and P.K. Ghosh

Syracuse University
Syracuse, NY 13244

ABSTRACT

For many optical processing it is important to have a knowledge of the effect of external forces on the refractive indices of the crystal. In this paper we will report some preliminary results of our effort towards developing a theoretical understanding of that effect. Barium titanate (BaTiO_3) and lithium niobate (LiNbO_3) were considered first for this study. Results indicate that the birefringence induced by the electric field in lithium niobate has weak temperature dependence. But in barium titanate the electric field induced birefringence depends rather strongly on the temperature. The degree of the induced effect varies on the magnitude and/or the direction of the external forces under specific conditions. These results indicate that there may be a possibility, in a real life applications, to reduce the necessary power supply by changing the operating temperature.

INTRODUCTION

In certain types of crystals it is possible to effect a change in the index of refraction which is proportional to the applied electric field. In addition to the change in refractive index in the direction of the applied field, it is possible for the refractive index to change also in the other direction. Crystals having this anisotropic property are commonly called birefringent [1-3]. The change in the refractive index due to an applied electric field known as the electro-optic effect, has been used to develop many devices such as light deflectors, light switches, light modulators, and optical pulse generators. Electro-optic materials are generally quite temperature sensitive. In this preliminary study we tried to develop a theoretical understanding of the behavior of birefringence when both the

To the extent authorized under the laws of the United States of America, all copyright interests in this publication are the property of The American Ceramic Society. Any duplication, reproduction, or republication of this publication or any part thereof, without the express written consent of The American Ceramic Society or fee paid to the Copyright Clearance Center, is prohibited.

electric field and the temperature are varied. For our study we have selected barium titanate (BaTiO_3) and lithium niobate (LiNbO_3) crystals.

THE INDICATRIX

To understand the behavior of birefringent crystal, the concept of the indicatrix has been found useful. The indicatrix can be defined as follows

$$b_1^2 x_1^2 + b_2^2 x_2^2 + b_3^2 x_3^2 + 2b_4 x_2 x_3 + 2b_5 x_1 x_3 + 2b_6 x_1 x_2 = 1 \quad (1)$$

where each b is related to $1/n^2$ (n is the refractive index). For the uniaxial crystal the optical indicatrix is an ellipsoid of revolution and equation 1 reduced to

$$b_1 x_1^2 + b_1 x_2^2 + b_3 x_3^2 = 1 \quad (2)$$

Application of electric field will induce a change in the indicatrix by varying the refractive indices, ie. b coefficients in eq. 2: The linear change in b coefficients due to an electric field applied along an arbitrary direction can be defined as

$$\Delta b_i = r_{ij} E_j \quad (3)$$

where r_{ij} are known as the electro-optic coefficients. Some electro-optic coefficients vanish due to the crystal symmetry. In the next two sections, starting with the proper r -matrix for barium titanate and lithium niobate, we develop an intuitive solution to show the change in the birefringence of these two materials with the electric field and the temperature.

BARIUM TITANATE

The tetragonal phase (4mm), of the barium titanate crystal, is the one which we have worked with since this phase exists in the temperature range of interest (5°C to 130°C) [4]. In the tetragonal phase the crystal is uniaxial and the electro-optic tensor is [3]:

$$[r_{ij}] = \begin{bmatrix} 0 & 0 & r_{13} \\ 0 & 0 & r_{13} \\ 0 & 0 & r_{33} \\ 0 & r_{51} & 0 \\ r_{51} & 0 & 0 \\ 0 & 0 & 0 \end{bmatrix} \quad (4)$$

An external electric field will change refractive indices and the resulting indicatrix can be written as follows:

$$\begin{aligned} & (o^2 + r_{13}E_3)x_1^2 + (o^2 + r_{13}E_3)x_2^2 + (e^2 + r_{33}E_3)x_3^2 \\ & + 2r_{51}E_2x_2x_3 + 2r_{51}E_1x_1x_3 = 1 \end{aligned} \quad (5)$$

where $o = \frac{1}{n_o}$ and $e = \frac{1}{n_e}$.

Using the above equation [eq. 5] we find that no birefringence is produced when light propagates along [001] direction. In the case when light propagates along [100] or [010] directions, the resulting birefringence is the same, except the direction. Selecting [100] as the light propagation direction we observe that application of electric field E_2 in x_2 direction and E_3 in x_3 direction results in a rotation of the indicatrix about x_1 . The equation of the resulting indicatrix becomes

$$\begin{aligned} & (o^2 + r_{13}E_3)x_1^2 + (o^2 + r_{13}E_3)x_2^2 + (e^2 + r_{33}E_3)x_3^2 \\ & + 2r_{51}E_2x_2x_3 = 1 \end{aligned}$$

The new birefringence can then be approximate as [5]

$$\Delta n = (n_o - n_e) + \frac{n_e^3}{2} E_3 \left(r_{33} - \frac{n_o^3}{n_e^3} r_{13} \right) - n_o^3 \frac{r_{51}^2 E_2^2}{o^2 - e^2}$$

Fig. 1 and 2 show the variation of Δn as a function of electric field at different temperatures. To calculate this behavior we have used n_o and n_e values at 25°C [6] and for other temperatures we have used published birefringence data [7]. We have also used the published electro-optic coefficients of the crystal [8, 9]. As shown in the figures (fig. 1 and 2) that at low temperatures the effect of E_2 is comparably higher than that of E_3 . But, at high temperatures, the role reversed and the contribution of E_3 is greater than E_2 . We observe that the percentage change in Δn with the electric field depends nonlinearly on the temperature and as shown in fig. 3, at lower temperatures the amount of change is considerably higher than that at higher temperatures.

LITHIUM NIOBATE

Ferroelectric lithium niobate belongs to trigonal 3m symmetry group up to 1210°C [10]. In this phase the electro-optic tensor is given as follows [3]:

$$[r_{ij}] = \begin{bmatrix} 0 & -r_{22} & r_{13} \\ 0 & r_{22} & r_{13} \\ 0 & 0 & r_{33} \\ 0 & r_{51} & 0 \\ r_{51} & 0 & 0 \\ -r_{22} & 0 & 0 \end{bmatrix}$$

Application of an electric field will result in a new indicatrix. The equation of the new indicatrix is:

$$\begin{aligned} & (o^2 - r_{22}E_2 + r_{13}E_3)x_1^2 + (o^2 + r_{22}E_2 + r_{13}E_3)x_2^2 + (e^2 - r_{33}E_3)x_3^2 \\ & + 2r_{51}E_2x_2x_3 + 2r_{51}E_1x_1x_3 - 2r_{22}E_1x_1x_2 = 1 \end{aligned}$$

To calculate the change in birefringence with electric field and temperature we

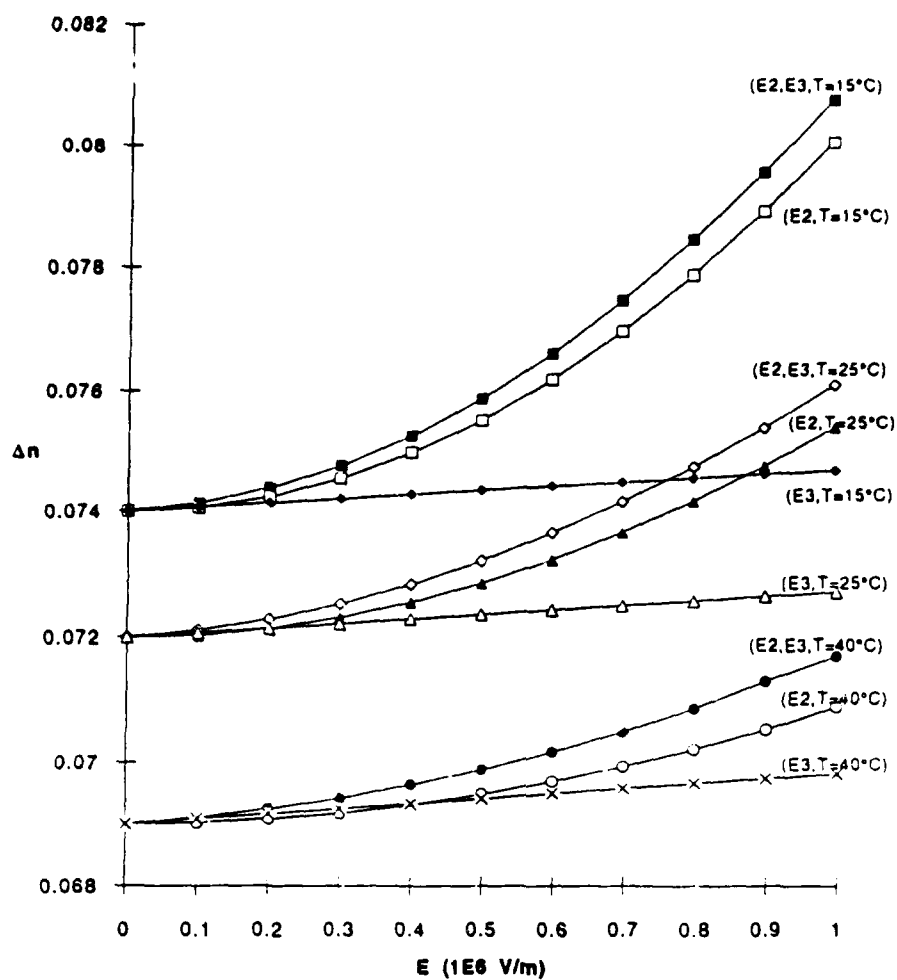


Fig. 1. Variation of birefringence with the electric field at different temperatures (15°C - 40°C) in BaTiO_3 crystal.

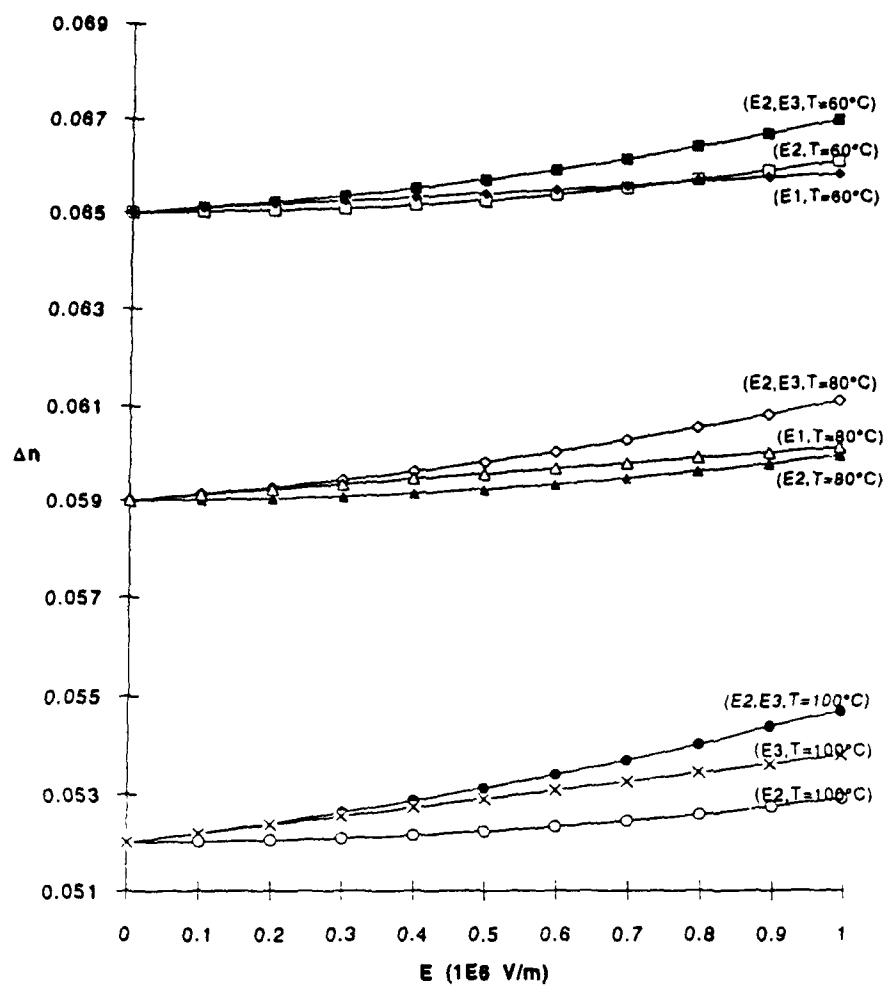


Fig. 2. Variation of birefringence with the electric field at 60°C, 80°C and 100°C temperatures in BaTiO_3 crystal.

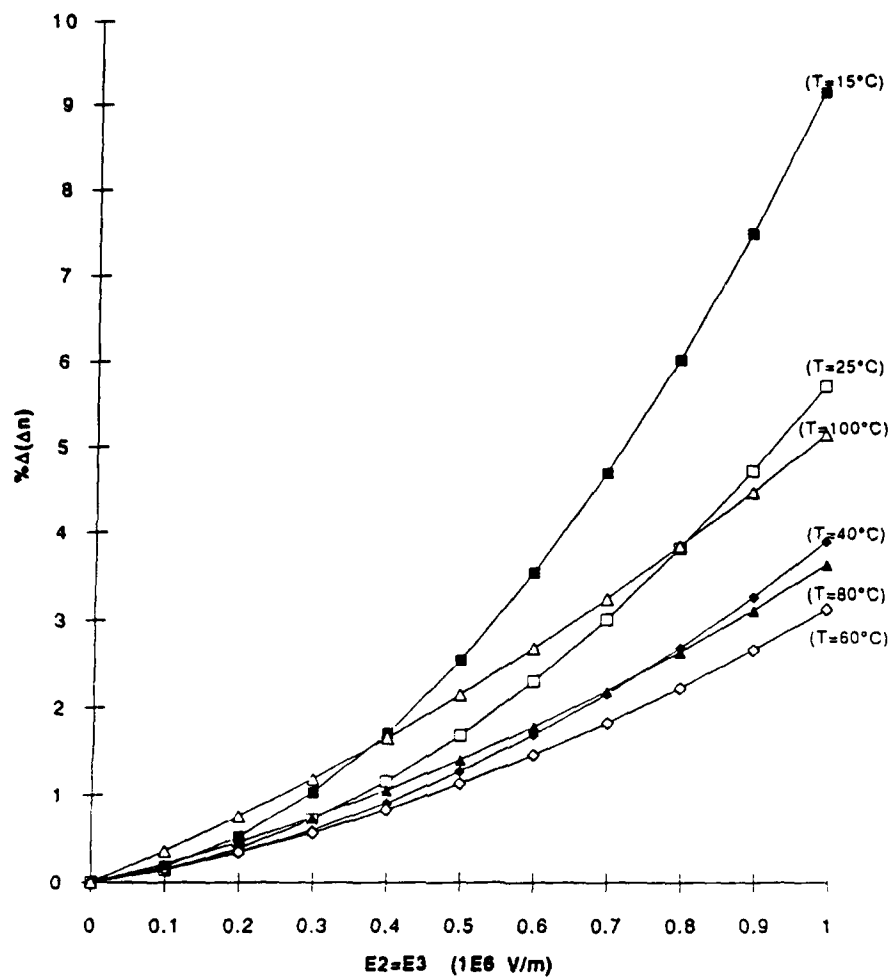


Fig. 3. The percentage change in Δn as a function of the electric field at different temperatures in BaTiO_3 crystal.

have used the published temperature dependence of the electro-optic coefficients [11] and the temperature dependence of the refractive indices found in the literature [12]. As shown in fig. 4, substantial change in birefringence occurs when the electric field is applied along x_2 and x_3 directions. As for the temperature effect (fig. 5) we observed that the birefringence induced by the electric field does not have a strong temperature dependence.

CONCLUSION

In this preliminary theoretical study we have developed an intuitive approach to understand the dependence of the birefringence on the electric field and the temperature. We studied the behavior of barium titanate and lithium niobate. Results indicate that the birefringence induced by the electric field depends strongly on the temperature in barium titanate whereas in lithium niobate temperature dependence of the birefringence is rather small. Also, in barium titanate the amount of change in birefringence is greater at lower temperature.

REFERENCES

1. J.F. Nye, "Physical Properties of Crystals", Oxford Science Publications, New York, 1985.
2. K. Iizuka, "Engineering Optics", 2nd Ed., Springer-Verlag, New York, 1983.
3. A. Yariv, "Optical Electronics", 3rd Ed., CBS College Publishing, New York, 1985.
4. H.E. Kay and P. Vansden, *Phil. Mag.* 40, 1019, 1949.
5. O.G. Vlokh and I.S. Zheludev, *Sov. Phys. Cryst.* 5, 390, 1960.
6. M.S. Shumate, *Appl. Phys. Lett.* 5, 178, 1964.
7. D. Meyerhofer, *Phys. Rev.* 112, 413, 1958.
8. I.P. Kaminow, *Appl. Phys. Lett.* 7, 123, 1965, Erratum 8, 54, 1966.
9. A.R. Johnston and J.M. Weingar, *J. Opt. Soc. Am.*, 55, 828, 1965.

10. S.C. Abrahams, H.J. Levinstein, and J.M. Reddy, *J. Phys. Chem. Solids*, 27, 1019, 1966.
11. J.D. Zook, D. Chen and N. Otto, *Appl. Phys. Lett.*, 11, 159, 1967.
12. M.V. Bobden and J. Warner, *Phys. Lett.* 22, 243, 1966.

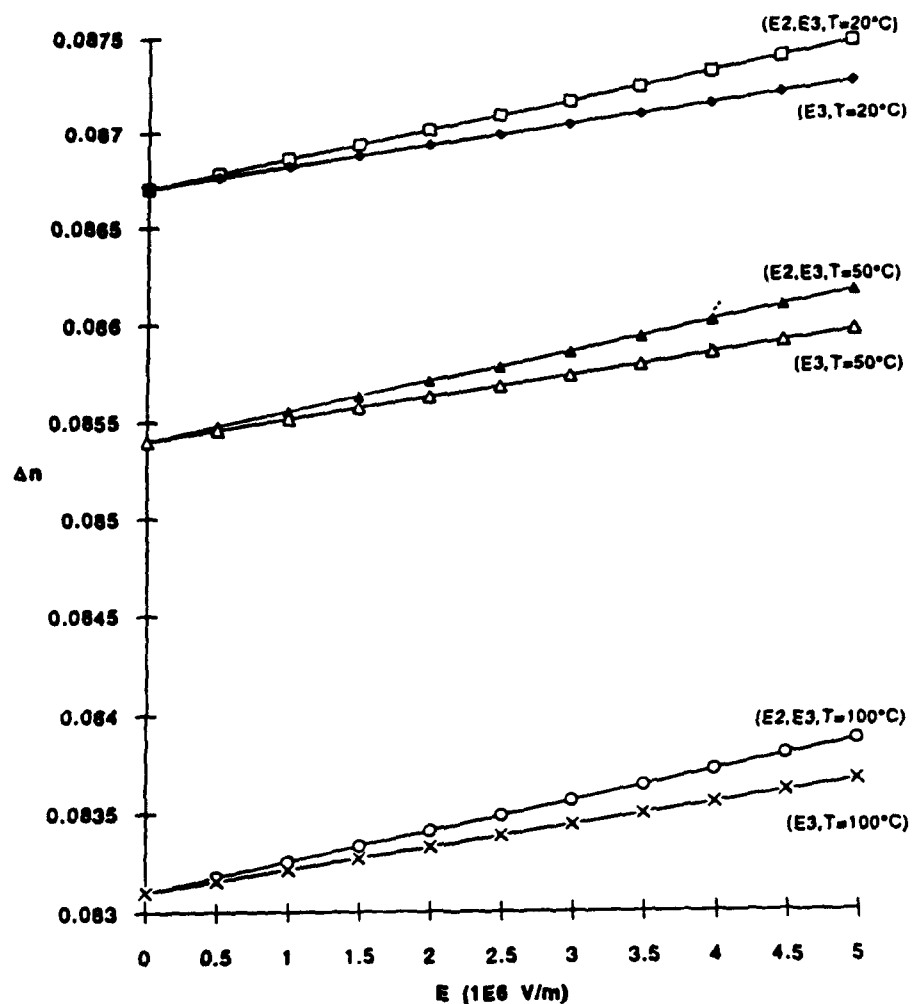


Fig. 4. Variation of birefringence with the electric field at different temperatures in LiNbO_3 crystal.

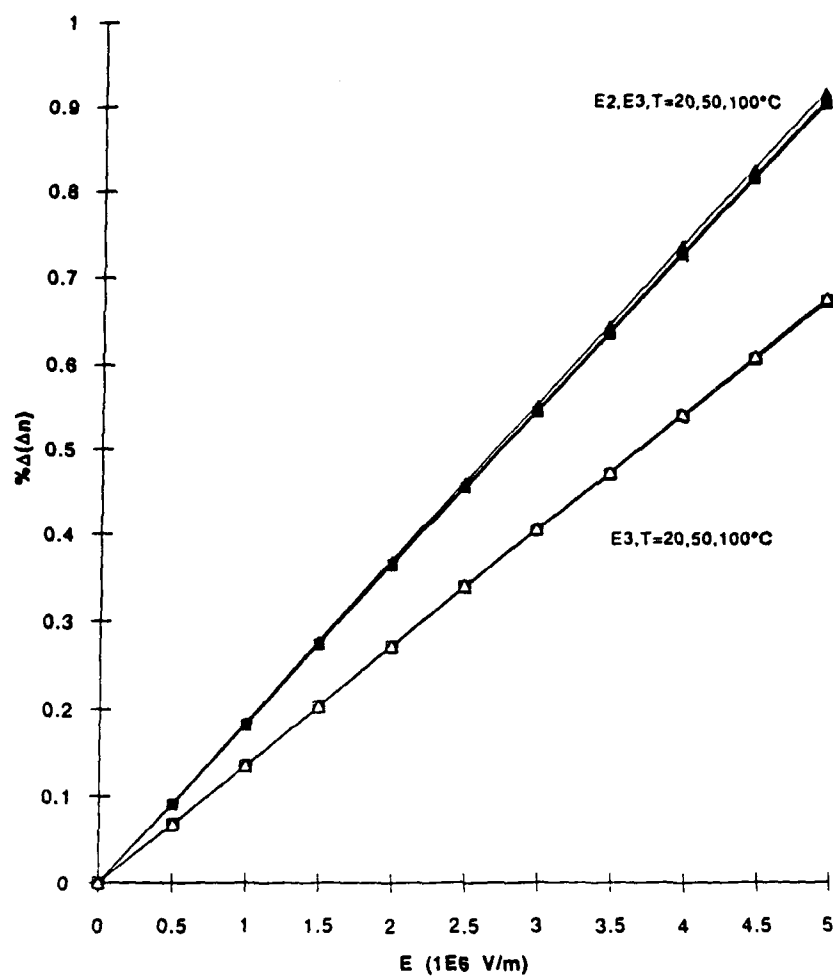


Fig. 5. The percentage change in Δn as a function of the electric field at different temperatures in LiNbO_3 crystal.

Sensor Characteristics

Smart / Intelligent Sensors

Tsuneharu Nitta and Shunichiro Kawashima
Central Research Laboratories, Matsushita Electric Industrial Co., Ltd.
Moriguchi, Osaka 570 Japan

ABSTRACT

A variety of ceramic sensors have been developed. Recently, intelligent functions are required for sensors in order to fabricate the reliable system with high performance. Many sensors are used in home appliances to obtain an easy and friendly operation. These requirements can be achieved by using sensors and micro-computers. Examples of sensors used in home appliances are reviewed. It is described that the combination of sensors and micro-computers with new software are important.

INTRODUCTION

In the ceramic industry, a variety of sensor elements have been developed. Typical ceramic sensor is a thermistor, which shows superior semiconductor-type temperature dependence of the electric resistivity around the room temperature. The thermistor have been used for semiconductor circuits due to a good matching in temperature characteristics. The thermistors are widely used in the consumer electronics by reason of their desirable characteristics at room temperature. Sensors with various function except for thermistors have been adopted in the consumer electronics. Recently sensors are used with the micro-computer, as the price of the micro-processor decreases. Therefore, sensors are easily able to get intelligences by supports of the computer. Also, new logic algorithms are introduced into the consumer electronics for human friendly operation. In this paper, the concept for the smart or intelligent sensors are discussed, especially for the application to consumer electronics.

HISTORICAL

To the extent authorized under the laws of the United States of America, all copyright interests in this publication are the property of The American Ceramic Society. Any duplication, reproduction, or republication of this publication or any part thereof, without the express written consent of The American Ceramic Society or fee paid to the Copyright Clearance Center, is prohibited.

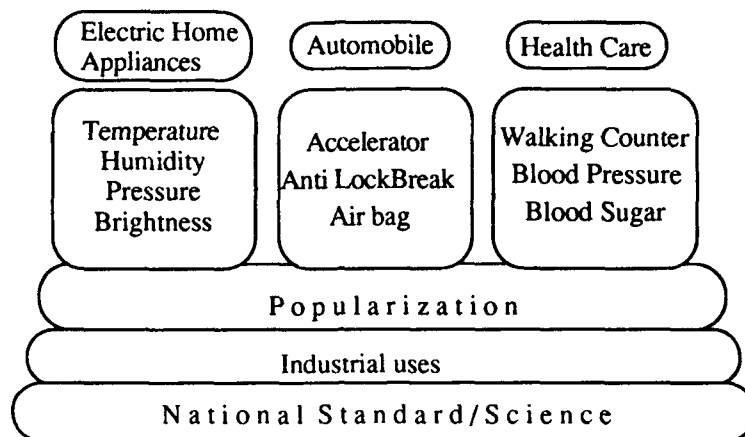


Figure 1 Popularization of sensors

The hierarchy in the market and popularization process of sensors are shown in figure 1. Many sensors are used around us in various market fields, such as the electric home appliances, the automobiles, or the health or medical cares, as many as industrial applications. Sensors has been popularized by the technology evolutions. Basically both physical and chemical constants of the national standards are measured and kept in their accuracies at the national laboratories. The number of significant figures of the standards should be almost ultimate, for example, six nines or ten nines and so on. On the contrary, the accuracy is not so important in the home appliances. Both easy operation and cheap cost are essential. In the electric home appliances these functions, such as temperature, humidity, pressure, brightness etc., are measured and are used for the control of equipments. Much more sensors are used to keep driving safe for vehicles. Sensors also have a important role in the field of health care and medical care. An example of an early home appliance in Japan can be seen for the foot warmer called Maruyama Kotatsu, used in the bed in winter. Maruyama means the round roof, and Kotatsu means the foot warmer in Japanese. In this equipment, a thermostat of bimetal switch is adopted to prevent the feet from the burn. The bimetal is the simplest and most reliable combination of sensor and actuator, where we can see an example of smart operation. However, this application is so primitive and its controllability is not so good. More reliable and sophisticated function have been realized later in the heater using PTC ceramics, which is used in hair driers. A list of the sensors in the electric and electronic home appliances are shown in figure 2. There are many

	Thermal	Weight	Gas	Humidity	Photo	Magnetic
Microwave Oven	●	●	●	●	●	●
Rice Cooker	●					
Refrigerator	●	●				
Air Conditioner	●	●	●	●	●	●
Oil Fan Heater	●	●			●	●
Washing Machine		●			●	●
Vacuum Cleaner		●			●	●
Steam Iron	●				●	
Television					●	
VCR					●	●
CD					●	●
Video Camera					●	●
Compact Cassette					●	●

Figure 2 Sensors in home appliances

kinds of sensors such as magnetic, photo, humidity, gas and so on. Most popular one among them is the thermal function. Recently data obtained from sensors are changed from a simple value to sophisticated signals for use of multi-functions. There are many sensors in the microwave-oven and the air-conditioner. Many kinds of sensors are necessary, because condition preferences of the each user are complicated for these appliances. In this paper we define the smart/intelligent sensors as fusion of sensor elements and micro-processors with heartware, where the heartware corresponds to the human friendly software such as bio-information, non-linear logic such as chaos, and neural networks, fuzzy logic etc.

EXAMPLES OF SMART/INTELLIGENT SENSORS IN HOME APPLIANCES

Housing is also one of the most important living necessities. In the advanced industrialized countries, there are many commodities, that is,

clothes, foods, and houses etc., so that peoples have a tendency to demand more mentally or heartfelt comfortable lives. In the consumer electronics industry, we should supply happy and comfortable lives in the future. One answer for the requirement in the home appliances is shown in figure 3. This will be achieved by the combination of sensors and micro-computers with a heartware, as mentioned above. In this computer new algorithms as a heartware will be adopted, such as neural networks, fuzzy logic, or non-linear control system of chaos. Fuzzy logic was proposed by professor Zadeh of U.C. Berkeley in the mathematics. In Japan his proposal was applied to many technologies, and many home appliances adopted his theory. The new control logic realizes that home appliances will works in accordance with user's preferences without troublesome operations of switches which are attached in machines. In future the home appliance equipments learns preferable conditions of each user just on site in his home. For example, four smart/intelligent sensor systems in the home appliances are described in this paper. The first is a microwave oven, in which the combination of a humidity sensor and a micro-processor can be seen. The second is a washing machine, where a photo-sensor and a neuro-fuzzy logic are used. The third a rice cooker where a thermal sensor and a neuro-fuzzy

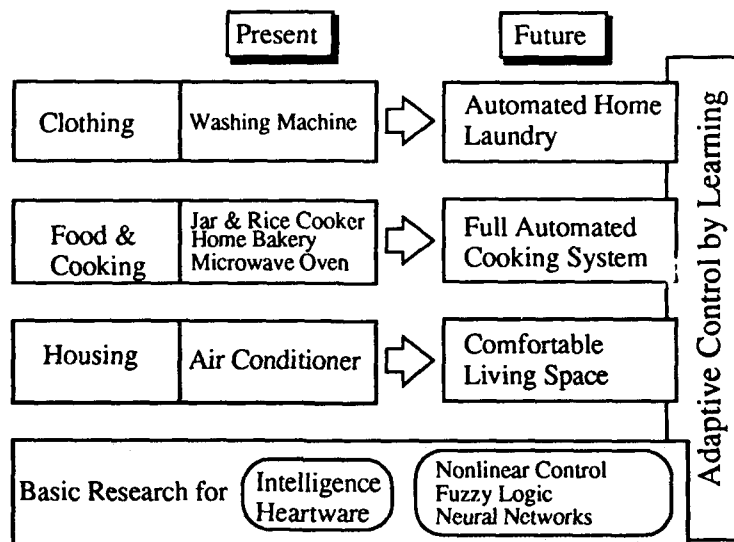


Figure 3 Scope for the applications of sensors to home appliances

logic are used. The fourth is a home air-conditioner, where an activity sensor using two-dimensional pyroelectric sensor and neural networks are used.

HUMIDITY SENSORS IN MICROWAVE OVENS

A relative humidity sensor is shown in figure 4, which was developed by Nitta in 1978¹. This sensor is called as Humiceram, and sold from Matsushita Electric (Panasonic). This was firstly introduced into the microwave oven for automatic cooking. The sensitivity to the humidity of Humiceram was obtained by the electric resistance. As the relative humidity increases, the resistance decreased exponentially. The sensor is located in the air drain of the microwave oven, and detects the water vapor from the cooking food. The time flow of microwave cooking is shown in figure 5. As the food is cooked well, the vapor will abruptly blow out after a non-vapor interval. The sensor can easily detect the boiling of the food. The idea for the control proposed is that the humiceram should detect only the point of changing humidity by the micro-computer. Next, the micro-computer predicts the time to put off the microwave power. The prediction by the

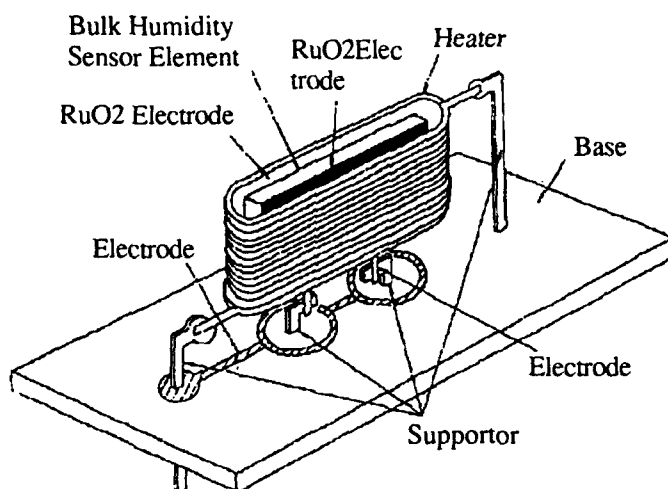


Figure 4 The structure of Humiceram, which is the humidity sensor using $\text{MgCr}_2\text{O}_4\text{-TiO}_2$

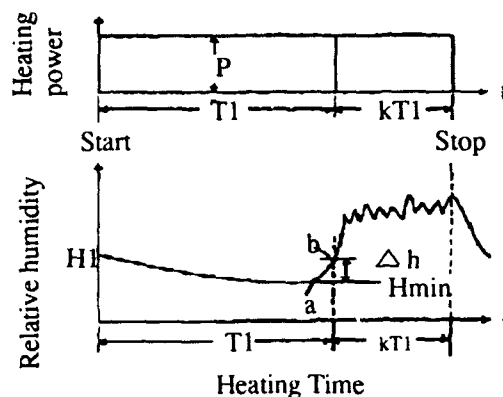


Figure 5 Time dependent humidity change at the position of air-drain

micro-computer is essential for the sensors obtaining the intelligence. It is important that it need not detect the absolute humidity, but only a slight change of humidity. Easy detection is essential for the home appliance. The sensor was used by combination of the micro-processor, however in those days its control algorithm did not designed by the concept of the heartware, but by the conventional logic.

WASHING MACHINES

As the pioneer machine for realizing the human friendly easy operation, a fuzzy logic washing machine was developed. This machine was operated by a micro-processor and a photo-sensor. The sensor catches the dirtiness or muddiness of the water during washing by detecting the transparency of the water. A fuzzy logic predicted and decided the washing time intervals, water level, and spin-drying time. More than 500 washing courses could be automatically prepared in the semiconductor memory. For more choices of washing, a neural-network concept was added to the fuzzy logic. This concept is called as neuro-fuzzy logic. More than 4000 washing courses became preferred by this system. At every washing, the machine chose the only one setting by sensing the dirtiness of the water and by accepting the users wills. Figure 6 shows the washing curve determined by many experiments for washing. These two graphs show the transparency data of the water during washing. Characteristics of dirtiness/muddiness of the water are shown in the left figure. If the dirtiness was almost caused by mud,

the transparency is shown by a bottom curve. When the dirtiness was caused by fat, transparency change vs. time is expressed by the top curve. The difference between two curves can be detected by sensors. Then the time to stop the machine is determined. The saturation value of transparency shown in the right figure were different for each dirtiness. When the dirtiness was due to fat, the saturation time is shorter than the other. Thus we could recognize the time to stop. Two simple fuzzy rules which was determined by the above experiments were applied for this washing machine. The first rule is that if transparency is high and saturation time is short, then washing time must be very short. The second rule is that if transparency is low and saturation time is long, then the washing time must be very long. These two simple fuzzy rules realized a human friendly washing machines. The washing machines were widely used in Japan, and they became best sellers.

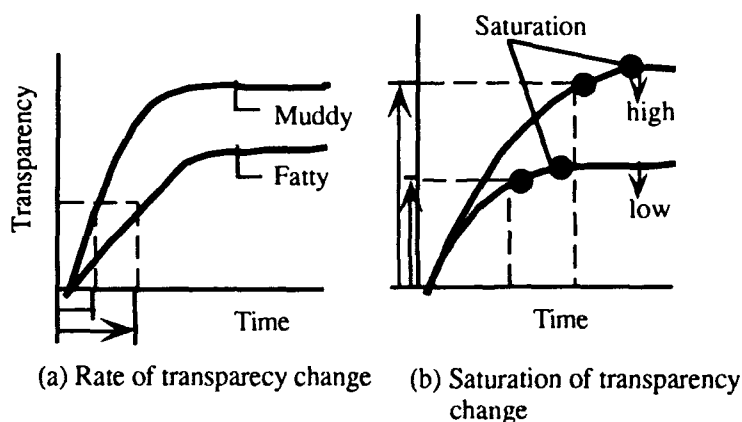


Figure 6 Transparency change against washing time. The rate and the saturation of transparency change is different between for mud and fat.

RICE COOKERS

The smart/intelligent sensors have been applied to the rice cooker. Figure 7 shows the market of the rice cooker in Japan, and also shows the technology innovations. Rice have been a main food for more than two thousand years in Japan. Rice cooking is a typical cuisine culture. Therefore the rice cooker have been required to satisfy the consumers' delicate taste.

Some successive technologies have been developed. At first the heater was made of a simple resistor, and controlled by thermal switch of bimetals or a thermo-magnetic effect. Then the micro-computer were introduced in order to control the electric power and time intervals. Recently micro-computer with fuzzy logic were introduced in the rice cooker. Induction heating(IH) were also adopted to obtain the high power heating, which overcame the fuel gas heating. Neural-networks algorithm was also introduced into the control of rice cooking. The know-how of rice cooking have been traditionally transferred as a heritage in Japan. It has been required to realize this know-how by the electronic control system. The rice cooking curve is shown in figure 8, which is a presentation of the know-how of rice cooking. There were two specific temperatures in the heat diagram. One was 70°C and the other was boiling temperature of 100°C. Starch in rice granule transformed from beta type to alpha type at 70°C. This temperature was called as gelatinization temperature. The most important know-how was that the heating must pass through this temperature as fast as possible.

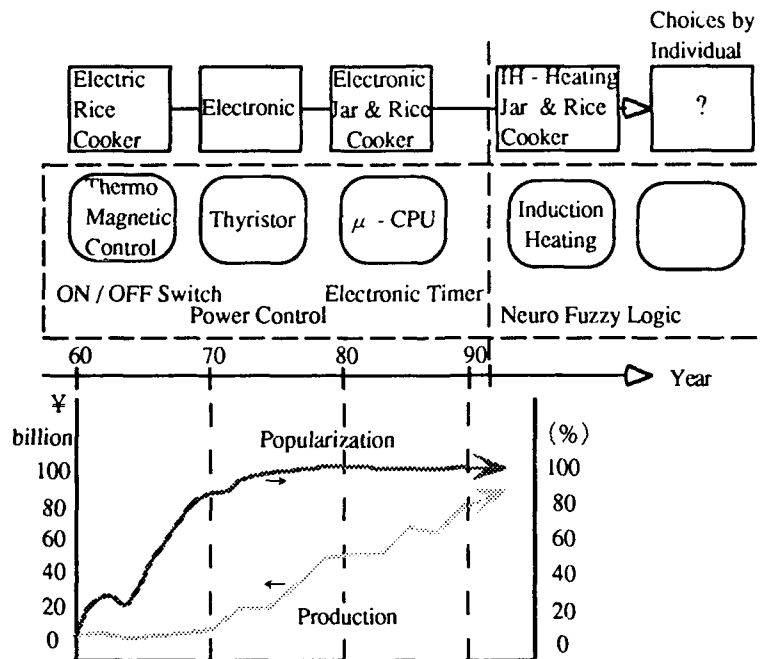


Figure 7 Technology innovation and market growth for rice cooker in Japan

If the rice kept around this temperature, the shape of each rice granule is degenerated and the taste was degraded. Then it was desired that the rice should be heated around 100 °C as boiling period, where the beta starch changed to alpha as the granule kept its shape. The cooking curve mentioned above has been realized by a combination of a thermistor and induction heater controlled with neural-networks algorithm.

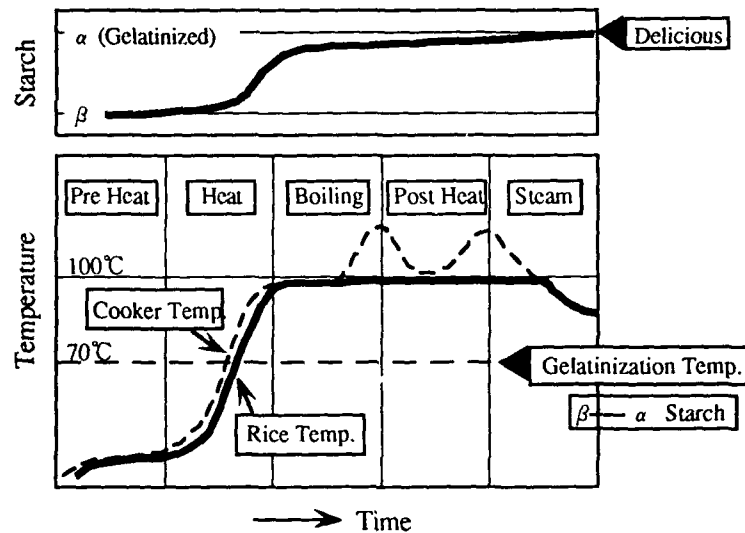


Figure 8 Heating diagram for rice cooker

AIR-CONDITIONERS

The evolution of the air-conditioner in Japan is noteworthy. In 1970s the air-conditioner called as a cooler, because the function was only cooling. In 1980s the name was changed to the air-conditioner. Both cooling and heating function were provided. In 1990s control software was improved by the new logic mentioned before. Both the sensor and the micro-computer with new control logic have important roles for this room air-conditioner. The compressor was evolved mechanically from reciprocal or rotary types to a small scroll type, and the mechanical noises from motors were much reduced. Sensors also evolved from a bimetal switch to a thermistor. At present two dimensional infrared imaging sensor are adopted in order to recognize the number and position of the persons in the room. The activity of

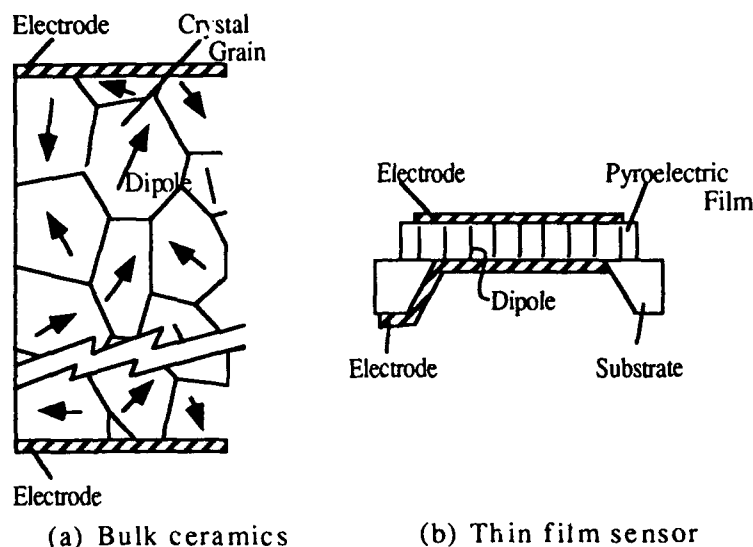


Figure 9 Structures of bulk and thin film pyroelectric sensors

each person should be taken into account for the control of air-conditioner to provide comfortable conditions. Saving of energy and resources also have been accomplished by the evolution of both mechanism and software. At first an activity sensor was introduced into the air-conditioner. This sensor detected the motion of persons by the bulk ceramic pyroelectric element. The meshed cover chopped the infrared radiation from moving persons, and motions were detected. However, this type sensor could not detect the position of the person. Then new algorithms were introduced into the control for the air-conditioner. The neural networks and fuzzy logic control were adopted in order to obtain the amenity for living spaces. Many sensing factors, such as temperature, humidity, are gathered to the neural networks in the micro-computer. The computer controlled electric power, air flow, and direction of air flow. So much sophisticated controls were accomplished by the neural networks. The fuzzy logic was applied to the electric power control in order to save energy. An advanced infrared imaging sensor was developed for higher sensitivity and discrimination of the personal motion from the background. The sensor was composed of a linear pyroelectric sensor array, which contains eight pyroelectric elements of the thin film on single chip. The dimension of each element was about 3 mm. Figure 9 shows a schemes of the pyroelectric sensor². The left figure is the bulk conventional type of ceramics, and the right figure is the newly developed thin film type. In order to obtain the quick response and the high resistivity,

the heat capacity of the pyroelectric element should be small. It was required that the elements were made of the thin film without the substrate. It was also desired that the polarization of the ferroelectric thin film was oriented. These requirements were realized by improving the production processes. Two dimensional infrared image was obtained by scanning the elements from the left to the right. The recognizing area was 70 degrees of the vertical angle and 150 degrees of horizontal angle. Total pixels were 512. These two dimensional image were composed of 512 pixels and processed by the micro-computer. The position of persons and background temperature were determined by using neural network algorithms. The air flow and temperature were controlled by these data.

OTHER SENSORS IN CONSUMER ELECTRONICS

ARM-VIBRATION SENSORS

The electronic arm vibration sensor in video movie was developed³. A CCD device was used as an optical sensor in the video movie. The area of each pixel of CCD decreased year by year, and the number of pixels on a chip

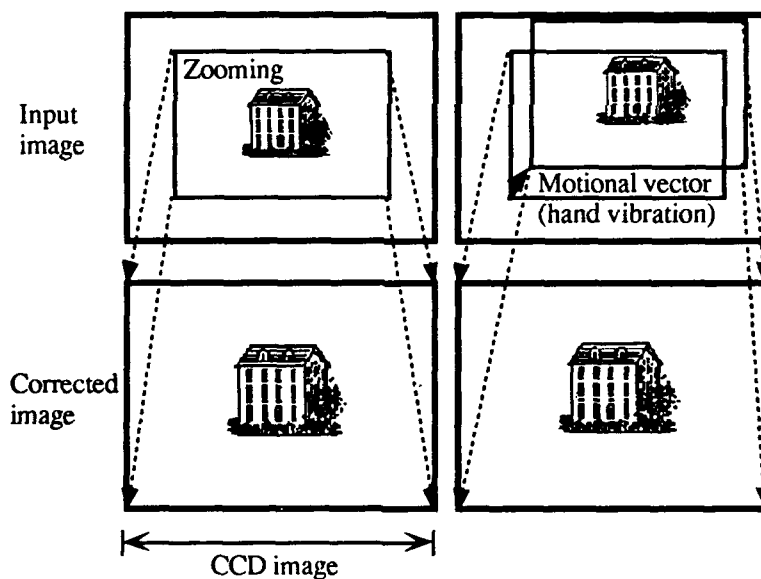


Figure 10 The scheme of correction of pictures by electronic arm vibration sensor for the video movie.

increased. Figure 10 shows the diagram of operation for the electronic arm vibration sensing in the video movie. Since both size and weight of the movie camera decreased, the arm/hand vibration influenced on the image stability. The electronic image processing was applied in order to reduce the image vibrations. Conventionally both piezoelectric gyro-sensor and actuator were used. The arm vibration during recording could be easily corrected by electronic process from the CCD image. First an image was obtained by CCD, and then zoomed. If the video camera are vibrated, the zoomed area moved electronically by using memories. Next corrected image could be obtained only by the projection of zoomed area as if the arm vibration did not happen. The correction of the arm vibration was realized electronically without any mechanical sensor and actuator by the high definition of the CCD. The fuzzy rules which was used to discriminate the motions of object from the vibration of arms are as follows. The first rule for motion of object is that if detected motional vectors are independent, and difference becomes large, then object are moving. The second rule for vibration of arms is that if detected motional vectors are almost similar and differences are small, then the image is vibrating by arm/hand motions.

IMMUNOREACTION SENSORS

Sensitivities are compared for several molecular detection in the table 1. Gas chromatography has a high sensitivity, but time for detection was too long. The specialist and skilled dog were the most sensitive, however they have a potential only for the smelled molecules, such as perfumes. Since almost all molecules were non-smell, it had been desired that those molecules could be easily detected with high sensitivity and selectivity. The typical non-smell molecule is explosives, such as of TNT(tri-nitro-toluene). Bio-sensor with high sensitivity for TNT was accomplished by using an immunoreaction in the living body. The principal of the bio-sensor is shown in figure 11. A monoclonal antibody for a special molecule was obtained by the antigen-antibody reaction in a mouse. This antibody was a fluorescent material. When the special molecule of antigen chemically attached to the antibody, the fluorescence of the antibody quenched immediately. Thus very small amount of molecules could be detected. If the antibody for any molecule would be obtained, any molecule can be detected. The advantage of this method was a molecular selectivity by the immunoreaction.

Table 1 Specifications of various sensors
for molecule detecting

Method	Sensitivity (g / ml)	Sensing Time	Working Time
Gaschro. / ECD	$10^{-7} \sim -9$	20 ~ 40 min	Full
Gaschro. / MAS	$10^{-7} \sim -9$	20 ~ 40 min	Full
Specialist	$* 10^{-13}$	~ 1 sec	30 min
Skilled Dog	$* 10^{-17}$	~ 1 sec	15 min
Immunoreaction	$10^{-10} \sim -14$	~ 60 sec	Full

* Sensing in case of perfume or smell compounds only

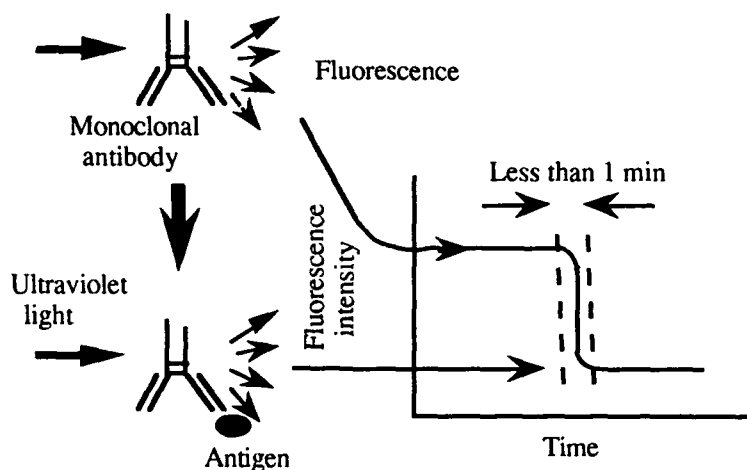


Figure 11 Principles of antibody fluorescence quenching. The intensity of fluorescence from monoclonal antibody much decreases after addition of antigen.

OPTICAL NEURON DEVICES

A optical space modulator was researched for the future optical computer. The scheme of the optical neuron-device are shown in figure 12. This was used for pattern recognition by simulating the neural networks of parallel signal processing. Using this device, incomplete character could be immediately recognized by some optical calculations. A liquid crystal and a conductive polyamide film were included as functional materials in this device. This was one of the examples of character pattern recognitions.

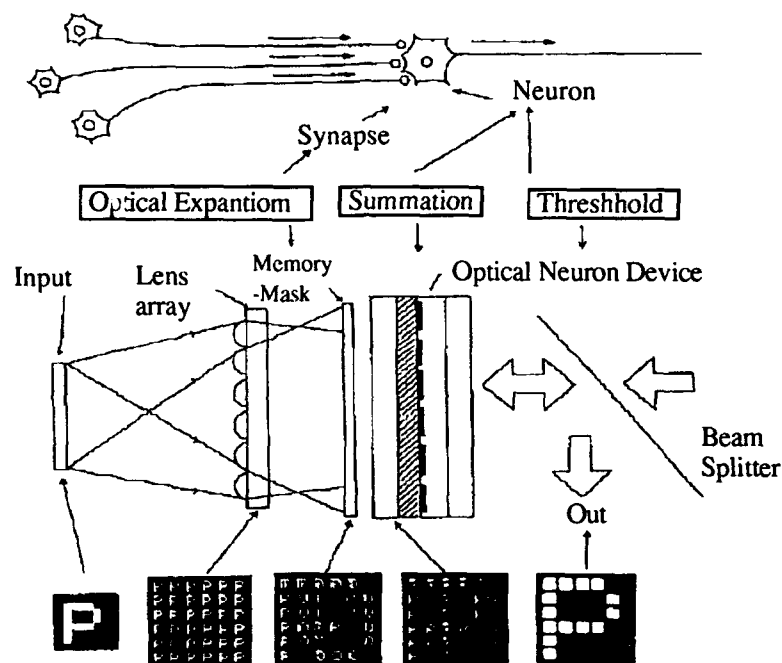


Figure 12 The scheme of the optical neuron-device for recognition of incomplete characters.

SUMMARY

The smart/intelligent sensors applied for the home appliances were summarized. It is proposed that the sensor should adopt mechanisms of the living body functions to realize the human friendly home appliances. The function of the conventional sensor was single and the corresponding

actuator was controlled by the central controller. For the smart/intelligent sensor, both sensors and actuator must be controlled by the software with hardware concepts. This situation was called as a sensor fusion. In other word, this should be named by trinity of sensors, actuators and micro-processor with new algorithms.

REFERENCES

1. K.Nitta, "Humidity sensitive electrical conduction of $\text{MgCr}_2\text{O}_4\text{-TiO}_2$ porous ceramics", J. Am. Ceram. Soc. 63, 295-300(1980).
2. K.Iijima et al., "Sputtering of lead-based ferroelectrics", Mat. Res. Soc. Symp. Proc., 310, 455-465(1993).
3. K.Uomori et al., "Automatic image stabilization system by full-digital signal processing", IEEE Trans. on Consumer Electronics, 36[3]510-519(1990).

OPTICAL HYDROGEN SENSOR USING Pd/MoO_x FILMS

Jun-ichi Hamagami, Ben Huybrechts, Yuichi Watanabe* and
Masasuke Takata

Department of Electrical Engineering, Nagaoka University of Technology,
1603-1 Kamitomioka, Nagaoka, Niigata 940-21, Japan

*Present Address;

Department of Materials Science and Technology, Faculty of Industrial
Science and Technology, Science University of Tokyo, 2641 Yamazaki,
Noda, Chiba 278, Japan

An optical hydrogen sensor which colors under an H₂-atmosphere is prepared. The sensor consists of a molybdenum oxide (MoO_x) layer (500-1300 nm) on a glass substrate covered with a very thin palladium layer of about 10 nm. Both layers are deposited by radio-frequency magnetron sputtering. The sputtering of the MoO_x films is carried out in a mixed Ar-O₂ atmosphere using a molybdenum metal plate as the target. The relationship between the hydrogen gas sensing properties and oxygen content in the MoO_x film is examined. The oxygen content in the films, estimated by X-ray photoelectron spectroscopy (XPS), increases with the oxygen concentration in the sputtering gas. For amorphous MoO_x films the initial coloration rate slightly increased with the oxygen concentration in the films. The initial coloration rate for the crystalline MoO₃ film, obtained by sputtering in an oxygen atmosphere, was 7 times higher than the one for the amorphous MoO_x films.

To the extent authorized under the laws of the United States of America, all copyright interests in this publication are the property of The American Ceramic Society. Any duplication, reproduction, or republication of this publication or any part thereof, without the express written consent of The American Ceramic Society or fee paid to the Copyright Clearance Center, is prohibited.

INTRODUCTION

Several optical sensors for the detection of inflammable and/or poisonous gas, e.g., hydrogen [1-6], carbon monoxide [7,8] have been reported. The main advantage of this type is that there is no danger for ignition and no influence of electromagnetic noise on sensing properties.

To detect hydrogen even at room temperature, the present authors have developed optical semitransparent inorganic sensors having a high sensitivity. These sensors consist of sputtered transition metal oxide films such as WO_3 [1-4], MoO_3 [5] covered with a very thin palladium layer. Recently a novel Pd thin film sensor [6] was discovered. For the above materials, the hydrogen detection is based on changes in the color of the films which occur in the visible and near-infrared regions. Although the mechanism for the Pd sensor is not yet completely understood, the coloration mechanism for the metal oxide sensors was proposed in the following way. Upon exposing these sensors to hydrogen molecules, the palladium layer acts as a catalyst for the dissociation even at room temperature [9]. The atomic hydrogens reach the palladium-metal oxides interface. The change in color of the film results from a chemical reaction of the hydrogen with the metal oxide resulting in the formation of hydrogen bronze. This coloring reaction can easily be observed with the naked eye.

In the present work, we investigated the relationship between the initial coloration rate and the oxygen content in the oxide layer.

EXPERIMENTAL PROCEDURE

Double-layered thin films consisting of molybdenum-oxide and palladium layers (Pd/MoO_x) were prepared by using a radio-frequency sputtering apparatus (Tokki, SPK-301).

At first MoO_x films were deposited on a glass substrate (Corning #7059) by using a 110 mm diameter metallic Mo (99.99%, Furuuchi) target. The rf power used was 100 W (2 W/cm^2) operating at 13.56 MHz. The substrates

were not intentionally heated. However, the substrate temperature was found to increase up to 90-110°C during MoO_x deposition. The sputtering atmosphere used was an Ar-O₂ gas mixture containing 0 to 100% O₂. The purity of the Ar and the O₂ gas was higher than 99.999% and 99.9%, respectively. The sputtering chamber was initially evacuated to 8×10^{-4} Pa and then the Ar-O₂ mixture was introduced. The total operating pressure, which was controlled by the main valve to maintain a constant value, was 0.67 Pa during deposition. The Mo target was presputtered for about 15 min, before the main sputtering. The deposition rate of the MoO_x films, which depended on the O₂ concentration in the Ar-O₂ sputtering atmosphere, was in the 9-33 nm/min range. Their thickness of the MoO_x films was 520 nm to 1300 nm, measured by using a surface texture measuring instrument (Surfcom 200C, Tokyo Precision).

Secondly, the Pd thin films were sputtered on the MoO_x films using the same rf sputtering apparatus and a Pd (99.99%, Furuuchi) target. The sputtering atmosphere used was Ar and the total operating pressure was 0.13 Pa with an rf power of 100 W. The substrate temperature was below the 40°C. The Pd thickness was about 10 nm calculated from its deposition rate, about 2.5 nm/s, which was obtained for films with thickness from 150 nm to 450 nm.

The crystal structure of the films was determined by x-ray diffraction measurements with Cu-K_α radiation (RAD-2C with work station 2050, Rigaku).

The oxygen content in the MoO_x films under various sputtering atmosphere were semiquantitatively evaluated from x-ray photoelectron spectroscopy (XPS-100SX, JEOL). Monochromatic Mg-K_α x-rays (energy=1253.6 eV) were used for the surface analysis of the MoO_x films. The pressure in the spectrometer is typically in the 10⁻⁶ Pa range. The XPS spectra of all the MoO_x films were measured in one batch. The binding energy scale was calibrated by assigning 284.6 eV to the C 1s signal as suggested by Wagner [10].

The optical transmittance spectra of the films were measured with a double-

monochromator spectrometer (UV-365, Shimadzu) at room temperature in the wavelength range 250-2500 nm.

The basic apparatus to measure the coloration is shown schematically in Fig. 1. The light from a halogen lamp passed first through a chopper then through the Pd/MoO_x film in the cell, and then through a monochromator with a wavelength of 780 nm. This measurement wavelength corresponded to that of a common semiconductor laser. After passing through the monochromator, the light was detected with a photomultiplier tube. A more detailed description of the system has been published elsewhere [6]. The detected gas was Ar containing 0.1% H₂ gas. All experiments were performed at atmospheric pressure and room temperature. Before introduction of the detected gas the cell containing the sample was filled with dry air.

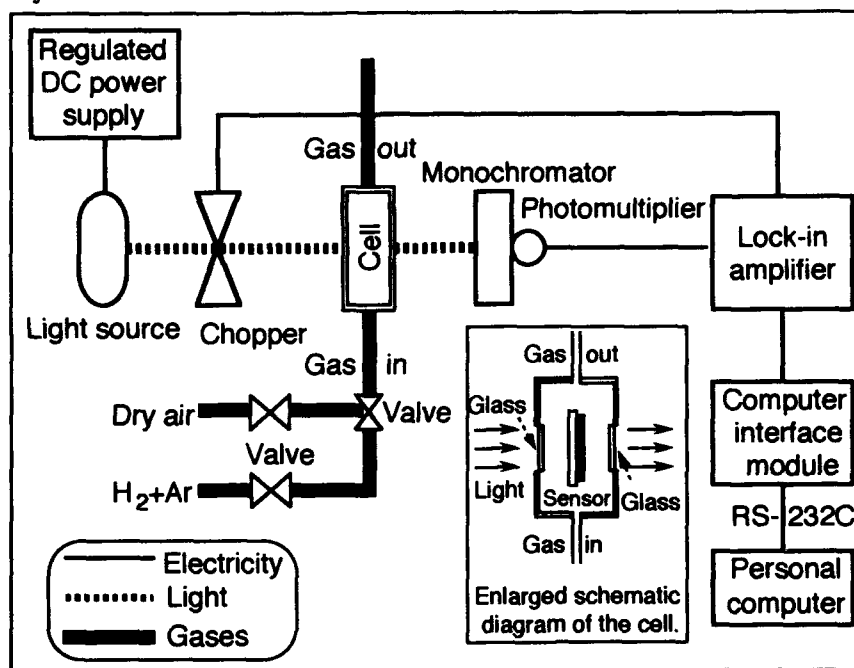


Figure 1 Experimental setup for measuring the coloration of Pd/MoO_x thin films, and an enlarged schematic diagram of the cell.

RESULTS and DISCUSSION

Figure 2 shows the x-ray diffraction patterns of the MoO_x films prepared in mixed Ar- O_2 gas atmospheres. The x-ray diffraction patterns were different from each other, indicating the dependence of the crystal structure and crystallinity on the O_2 concentration in sputtering gas atmosphere. The film deposited in Ar had one peak at $2\theta=40.4^\circ$ which corresponds to the (110) plane of cubic Mo (Joint Committee on Powder Diffraction Standards: JCPDS #4-809). Others prepared in a sputtering atmosphere with 20-40% O_2 content were confirmed to be almost completely in amorphous state. The sample sputtered in 50% O_2 showed some small amount of crystallinity. However, the diffraction pattern of the films deposited under a sputtering atmosphere of 10% and 100% O_2 showed that these films contained a mixture of amorphous and a crystalline phase. The film prepared under Ar-10% O_2 sputtering atmosphere had three peaks $2\theta=36.7^\circ$, 37.3° , and 53.4° corresponding to the (200), $(\bar{2}11)$, and $(\bar{3}12)$ planes of monoclinic MoO_2 (JCPDS #32-671). The film deposited under an O_2 sputtering atmosphere had four peaks at $2\theta=23.4^\circ$, 27.4° , 45.8° , and 49.3° which can be respectively assigned to the (110), (021), (200), and (022) planes of orthorhombic MoO_3 (JCPDS #5-508).

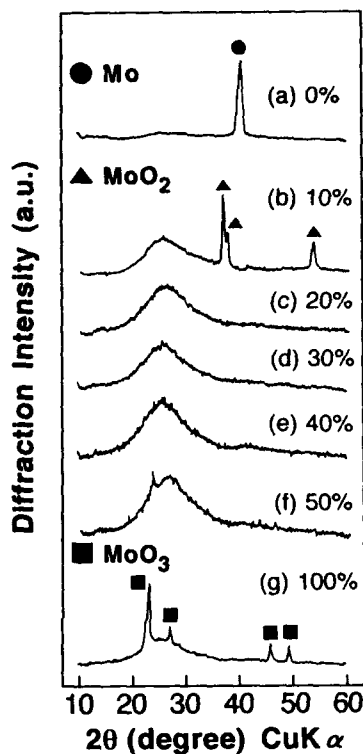


Figure 2 X-ray diffraction patterns of the MoO_x films deposited in Ar- O_2 gas atmosphere for various oxygen concentrations.

On the other hand, all the MoO_x films covered with a very thin Pd layer did not show any peaks of Pd (JCPDS #5-681) with the same x-ray measurement conditions. Since the thickness of the Pd film was only about 10 nm, the diffraction intensity of Pd in the Pd/ MoO_x films could not be detected.

Figure 3 shows typical XPS spectra of Mo 3d and O 1s level in the MoO_x films. The emission intensity of the XPS spectrum for both O 1s and Mo 3d levels decreased with increase in oxygen concentration in the sputtering atmosphere. The emission intensity rate of [O 1s] to [Mo 3d_{5/2}], which was calculated by integrating the line profiles of the XPS spectra, was different. The values of [O 1s]/[Mo 3d_{5/2}] ratio were 1.08 for the crystalline MoO_2 film and 1.36 for the crystalline MoO_3 film while the ratio for amorphous MoO_x films ranged from 1.20 to 1.30. Amorphous MoO_x thin films have intermediate values between those for MoO_2 and MoO_3 .

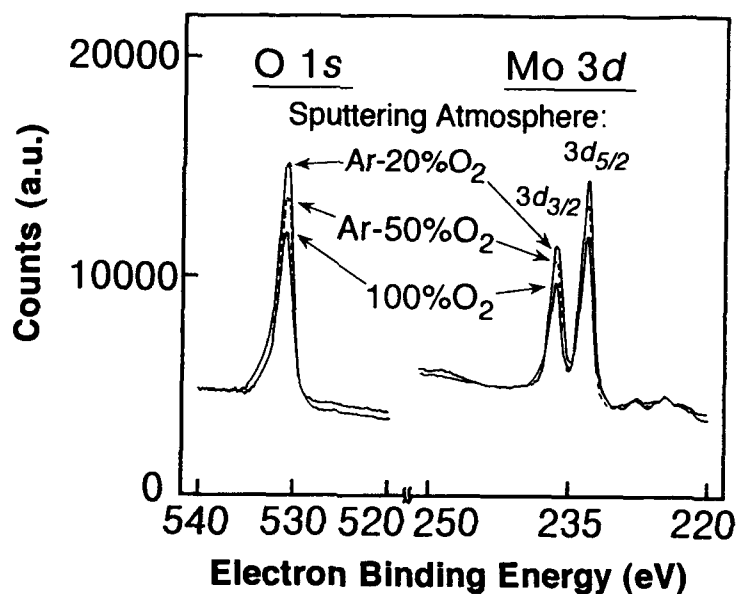


Figure 3 Typical XPS spectra of MoO_x thin films for O 1s level and Mo 3d level.

Figure 4 shows the spectral transmittance of the MoO_x films of before (a) and after (b) covering with a Pd layer of about 10 nm in the wavelength region 250-1000 nm. The thickness of the MoO_x films prepared in a sputtering atmosphere with 20-100% O_2 content ranged from 520-760 nm. As seen in the Fig. 4(a), the MoO_x films formed between 20% and 50% O_2 concentration in sputtering gas atmosphere were transparent and have an average transmittance higher than 80% in the visible and near-infrared regions. The films sputtered below 10% O_2 concentration, grew the crystals of Mo and MoO_2 , and were not transparent in this wavelength region. On the other hand, the films prepared in O_2 sputtering atmosphere were slightly white colored, resulting from scattering caused by the unevenness of the film surface. The optical transmittance of the Pd/ MoO_x films (see Fig. 4(b)) decreased in the visible and near-infrared regions, comparable with that of the MoO_x films without Pd layer.

Figure 5 shows the changes of the normalized optical transmittance T_N of the Pd/ MoO_x films deposited under Ar- O_2 sputtering atmosphere containing higher than 20% O_2 , as a function of exposure time to Ar containing 0.1% H_2 gas. The Ar gas containing 0.1% H_2 was introduced into the cell, at time $t=0$, represented the symbol "ON" in the figure. The transmittance was normalized by using the following equation:

$$T_N(t) = T_H(t) / T_A$$

where T_A and T_H are the optical transmittance in dry air and hydrogen containing gas, respectively. As seen in the figure, the normalized transmittance of the Pd/ MoO_x films formed in an oxygen sputtering atmosphere for the MoO_x film decreased rapidly with increasing time after introducing to Ar-0.1% H_2 mixture gas and almost saturated after approximately 300 s. The film was colored dark-blue, and the transmittance of this film changed from 38% to 6%. On the other hand, the transmittance of the films prepared in an Ar- O_2 mixture sputtering atmosphere (20-50% O_2) decreased very slowly with increasing exposure time and did not saturate even after 600 s. However, the optical transmittance of all Pd/ MoO_x films decreased to almost 0% after exposed to H_2 gas for 2 days. The coloration rate increased significantly with an increase in the O_2 concentration in the sputtering gas.

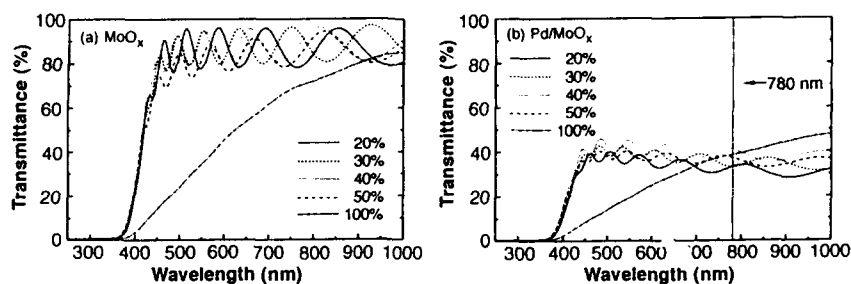


Figure 4 (a) Transmittance spectra of MoO_x films sputtered in a mixture of Ar and O_2 gas. The thickness of the samples ranged from 520 to 620 nm. Labels indicate the O_2 concentration in the sputtering gas. Samples sputtered in Ar- O_2 gas with 0% and 10% O_2 were not transparent. (b) Optical transmittance spectra of MoO_x films covered with a Pd layer of about 10 nm.

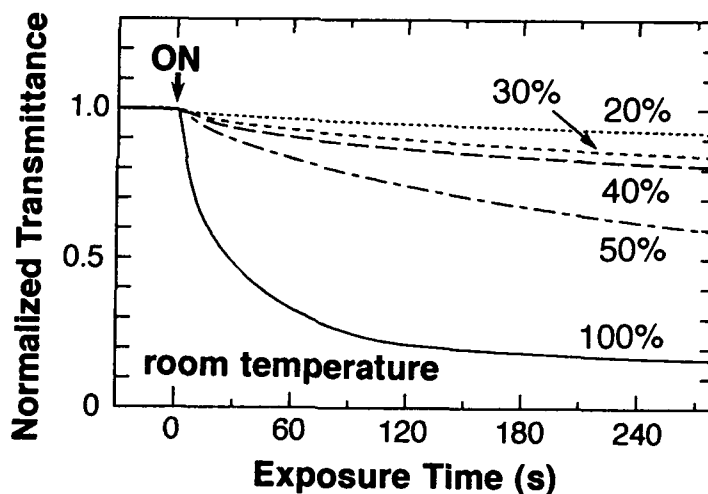


Figure 5 Changes in optical transmittance at 780 nm for Pd/MoO_x thin films under Ar-0.1% H_2 at room temperature. The MoO_x films sputtered using Ar- O_2 mixtures with different O_2 concentrations as shown in the figure.

Figure 6 shows the initial coloration rate for amorphous MoO_x thin films as a function of $[\text{O } 1s]/[\text{Mo } 3d_{5/2}]$ obtained from XPS measurement. The initial coloration rate was defined as

$$\text{Initial coloration rate} = (T_A / T_G) / 10$$

where T_A is the optical transmittance of the films in dry air, and T_G the optical transmittance after 10 s in 0.1% H_2 containing Ar gas. It is found that the oxygen content in the amorphous MoO_x films influences the initial coloration rate. This result might be explained as following. It was already shown by x-ray analysis that hydrogen molybdenum bronze (H_yMoO_x) was formed after exposure to hydrogen [11]. The coloration phenomenon was explained by the reduction of Mo^{6+} to Mo^{5+} , caused by the formation of H_yMoO_x . It was shown by electron spin resonance (ESR) of Pd/MoO_x film before and after exposing the sample to H_2 gas, that the ESR signal characteristic of Mo^{5+} at room temperature increases after exposure to H_2 gas [5]. The dominant oxidation state of Mo before and after exposure to H_2 gas was Mo^{6+} and Mo^{5+} ion, respectively. Therefore, the coloration of the film is considered to be originated from the formation of Mo^{5+} ion. Color centers of Mo^{5+} are the product of reduced Mo^{6+} sites in the MoO_x films. The high coloration rate is probably caused by an increase number of reaction sites, Mo^{6+} . This is based on the assumption that the crystal structure and surface morphology of the amorphous MoO_x films were almost the same.

On the other hand, the initial coloration rate for the crystalline MoO_3 films is equal to about 0.023 s^{-1} . This was more than 7 times faster than that one for amorphous MoO_x films. This is probably caused by the crystallinity including the orientation and/or surface conditions.

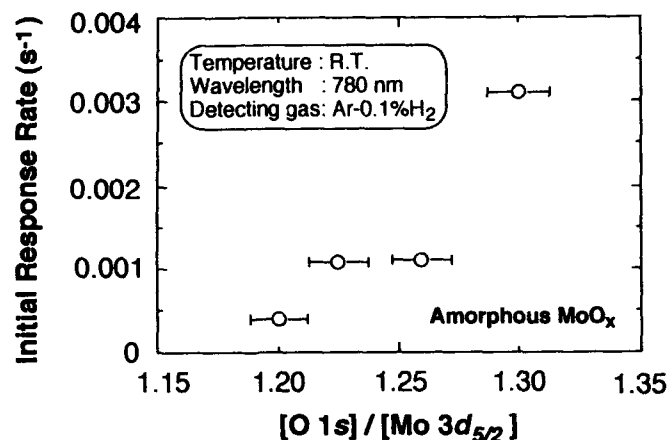


Figure 6 The initial coloration rate for amorphous MoO_x thin films as a function of $[\text{O } 1s]/[\text{Mo } 3d_{5/2}]$. The increase in initial coloration rate is believed to be due to an increase in the number of Mo^{6+} reaction sites. The initial coloration rate of the MoO_3 film sputtering in pure O_2 is 0.023 s^{-1} . This high rate is attributed to the crystallinity of the film.

CONCLUSION

The oxygen content in the MoO_x films, estimated by XPS, increases with the oxygen concentration in the Ar-O_2 sputtering mixture gas. The initial coloration rate of the amorphous MoO_x films, measured at room temperature, increased with an increase in oxygen content. This is explained by an increase in the number of Mo^{6+} sites. The Mo^{6+} ions are reduced to Mo^{5+} by the hydrogen, thereby coloring the film. The initial coloration rate for crystalline MoO_3 films, which is about 7 times higher than for amorphous MoO_x , is believed to be caused by its crystallinity.

ACKNOWLEDGEMENTS

This work has been supported in part by fellowships of the Japan Society for the Promotion of Science for Japanese Junior Scientist.

REFERENCES

1. K. Ito and T. Kubo, "Gas Detection by Hydrochromism", Proceedings of the 4th Sensor Symposium, Tsukuba, Japan, 153 (1984).
2. K. Ito and T. Ohgami, "Hydrogen detection based on coloration of anodic tungsten oxide film", *Appl. Phys. Lett.*, 60, 938 (1992).
3. K. Ito, T. Ohgami and T. Nakazawa, "Effect of water on hydrogen-sensitive tungsten oxide films", *Sensors and Actuators B*, 12, 151 (1993).
4. Y. S. Oh, J. Hamagami, Y. Watanabe, and M. Takata, "Preparation and characterization of an optically-detectable hydrogen gas sensor consisting of Pd/WO₃ thin films", *Sensors and Actuators B*, 13-14, 547 (1993).
5. J. Hamagami, Y. S. Oh, Y. Watanabe, and M. Takata, "Preparation and characterization of an optically detectable H₂ gas sensor consisting of Pd/MoO₃ thin films", *Sensors and Actuators B*, 13-14, 281 (1993).
6. Y. S. Oh, J. Hamagami, Y. Watanabe, M. Takata, and H. Yanagida, "A Novel Palladium Thin Film Hydrogen-Detector", *J. Ceram. Soc. Japan*, 101, 618 (1993).
7. T. Kobayashi, M. Haruta, S. Tsubota, and H. Sano, "Thin Films of Supported Gold Catalysts for CO Detection", *Sensors and Actuators B1*, 222 (1990).
8. T. Kobayashi, M. Ando, and M. Haruta, Enhancing effect of gold deposition in the optical detection of reducing gases in air by metal oxide thin films", *Sensors and Actuators B*, 13-14, 545 (1993).
9. Lewis F.A., *The Palladium Hydrogen System*, Academic Press, New York (1967).
10. C. D. Wagner, W. M. Riggs, L. E. Davis, J. F. Moulder, and G. E. Muilenberg, *Handbook of X-Ray Photoelectron Spectroscopy* (Perkin-Elmer, 1979).
11. J. Hamagami, "A New Optical Hydrogen Sensor using Pd/MoO_x Thin Films", Master's Thesis, Nagaoka University of Technology, 1993.

Gas Sensing by AC Impedance under DC Bias of CuO/ZnO pn Heterocontact.

Kazuyasu Hikita and Masaru Miyayama

*Research Center of Advanced Science and Technology, University of Tokyo,
Meguro, Tokyo 153, JAPAN*

Hiroaki Yanagida

Faculty of Engineering, University of Tokyo, Bunkyo, Tokyo 113, JAPAN

Abstract

Complex impedance has been studied for pn heterocontact with a couple of CuO/ZnO semiconductors by applying DC bias voltage in the atmosphere of air-balanced flammable gases of CO or H₂ (4000ppm) between 250°C and 400°C. The frequency dependence of reactance showed a minimum peak, and the size and frequency of which were changed with the kinds of gas. Additional resistance and capacitance, which were specific to the ambient gases adsorbed, were introduced to the interface of semiconductors and were measured by means of impedance. As a result, air-balanced CO gas could be distinguished from H₂ gas by use of the minimum peak of reactance at 400°C. The feasibility of identification of gas was presented by means of tuning the sensor to the minimum reactance with DC bias and AC frequency. A new method of gas identification was presented by using complex impedance characteristics of heterocontact.

To the extent authorized under the laws of the United States of America, all copyright interests in this publication are the property of The American Ceramic Society. Any duplication, reproduction, or republication of this publication or any part thereof, without the express written consent of The American Ceramic Society or fee paid to the Copyright Clearance Center, is prohibited.

I. Introduction

Recently, ceramic gas sensors have been used increasingly to monitor gases under such severe conditions as high temperature, chemically corrosive environment, and poisonous atmosphere. The importance of ensuring a safe living environment in today's world strongly necessitates improving methods of selecting for carbon monoxide (CO).

The sensing characteristics of heterocontact types of gas sensors have been studied for a variety of gases such as water vapor, flammable gases (H_2 , CO, C_3H_8), chlorine, nitrogen oxides and others.¹⁻⁵ It was reported that the selectivity for CO gas from H_2 gas was improved by using a heterocontact comprised of ZnO and CuO (prepared from basic copper carbonate).²⁻³ The best selectivity for CO was obtained when the DC bias voltage of +0.5V was applied on the heterocontact for the direction of easy flow of current. In addition, this useful method of tuning by semiconductivity cannot be applied to the usual ceramic-semiconducting types of gas sensors, because their sensitivity is changed little by applied voltage only.

The advantage of using gas sensors with pn heterocontact is that the different characteristics of gas adsorption on various semiconducting ceramic surfaces (p- and n-type) makes it possible to distinguish between gases effectively. The present study examined changes caused by CO and H_2 gas in the AC impedance of a CuO/ZnO heterocontact under a DC bias, and this paper proposes a new method of gas identification.

II. Experimental Procedure

(1) Principle and Analytical Method

Figure 1. shows a band structure supposed for the ideal pn heterojunction composed of CuO (p-type) and ZnO (n-type).^{2,4,6-7} Near the interface of heterocontact of p-type and n-type semiconductors, the transient region called "depletion layer" with little charge carrier is formed. It is expected both the

capacitance and the charge transport behavior would be changed by the adsorption of gases at the depletion layer. Such changes of electrical properties will be useful to distinguish gases.

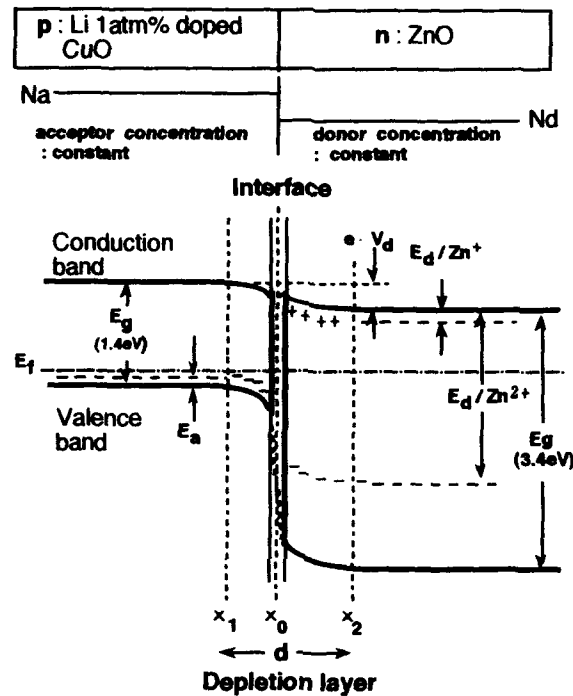


Fig.1. Ideal band structure of CuO/ZnO heterojunction.

The basic equivalent circuit of the pn heterocontact is supposed to be formed by the serial connection of the bulk resistance (R_s) and the impedance of the interface (Z_i), which is composed by the parallel connection of a resistance (R_i) and a capacitance (C_i) at the interface, as shown in Figure 2. The total impedance Z is defined by a resistance R (real part) and a reactance X (imaginary part) as follows,

$$Z = R + jX \quad (1)$$

$$= [R_s + (R_i X_i^2) / (R_i^2 + X_i^2)] + j[R_i^2 X_i / (R_i^2 + X_i^2)] \quad (2)$$

By erasing parameter X_i ,

$$[(R - (R_s + (R_i / 2)))^2 + X^2 = (R_i / 2)^2 \quad (3)$$

Eq. (3) draws a semicircle ($X < 0$) as shown in Fig. 3. Accordingly, the minimum point of X is obtained as eq. (4) and where, the relation of eq. (5) is given.

$$R = R_s + (R_i / 2) \quad (4)$$

$$\omega R_i C_i = 1 \quad (5)$$

The equivalent circuit of pn heterocontact can be obtained by analyzing Cole-Cole plot. As described later, when the relation of $R_s \ll R_i$ is obtained in actual measurement, the resistance R and the reactance X is written by use of the components (C_i and R_i) and the angular velocity ω as below.

$$R = R_i / (1 + \omega^2 C_i^2 R_i^2) \quad (6)$$

$$X = -\omega C_i R_i^2 / (1 + \omega^2 C_i^2 R_i^2) \quad (7)$$

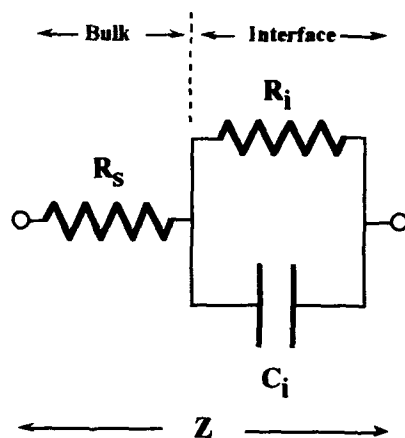


Fig.2 Equivalent circuit of heterocontact.

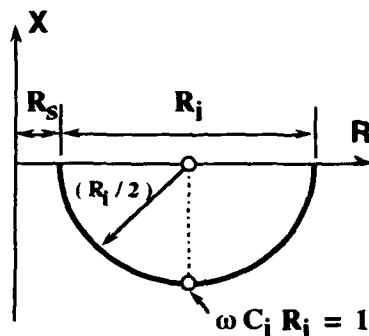


Fig.3 Theoretical impedance diagram (Cole-Cole plot) for the electrical equivalent circuit of the heterocontact (Fig.2).

(2) Samples and Equipments

The starting powder materials of ZnO (n-type semiconductor, 99.99% purity) and CuO (p-type semiconductor, 99.9% purity) were pressed into disks 10mm in diameter and sintered for 3 hours at 1000°C for ZnO and 800°C for CuO, respectively. The relative density of the ZnO was 98% of theoretical value and that of CuO 90%. Figure 4(A) shows the structure of CuO/ZnO pn heterocontact

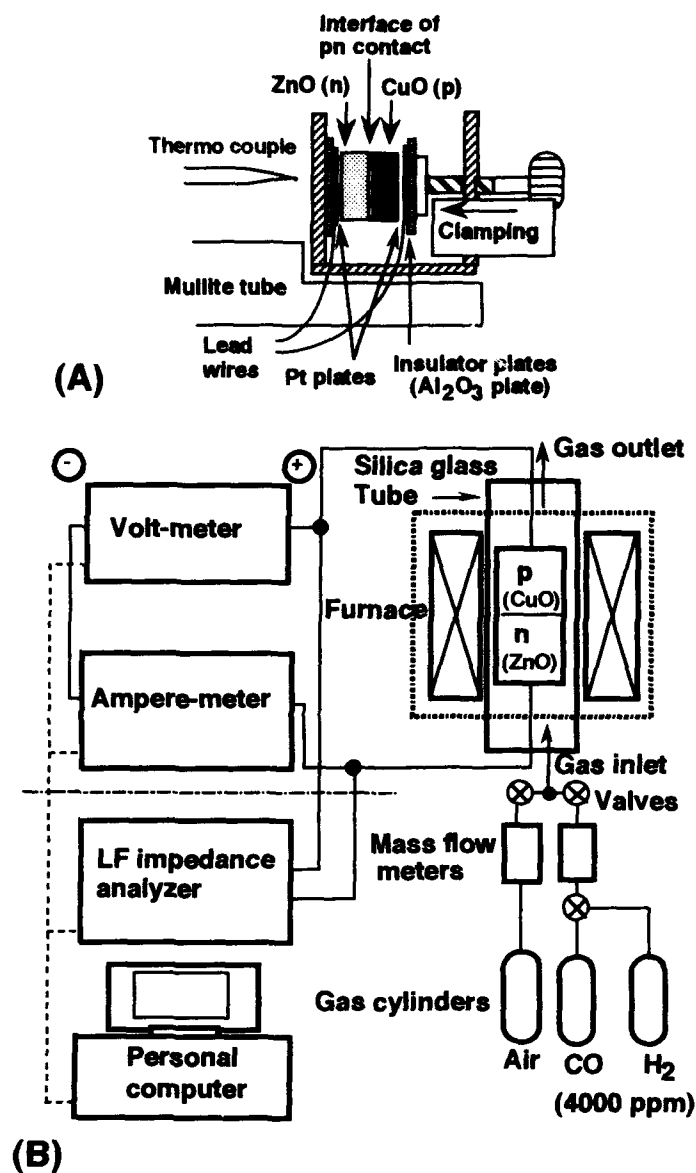


Fig.4. (A) Structure of a pn heterocontact comprising semiconducting ceramic disks of CuO and ZnO.
 (B) Block diagram of measurement system of DC current-voltage characteristics and complex impedance under controlled gas atmosphere.

and the sample holder. The CuO and ZnO ceramic disks were clamped into the stainless steel sample holder using a pair of platinum plates.

Figure 4(B) shows a block diagram of measurement system for DC voltage characteristics and complex impedance under controlled gas atmosphere and temperature. As the testing gases, air, air-balanced CO (hereinafter, CO mixture) and air-balanced H₂ gases (hereinafter, H₂ mixture) of 4000ppm were flowed at the rate of 200 ml/min. The DC voltage characteristics and complex impedance, Z, at the frequencies ranging from 10Hz to 10MHz under a DC bias voltage (-10V ~ +10V) were measured by applying AC signal (sine wave of 1V) in the controlled gas atmosphere between 250°C to 400°C.

III. Results and Discussions

(1) Influence of gases on some electrical properties

Figure 5 shows current-voltage characteristics of a CuO/ZnO pn heterocontact under a testing gas atmosphere at 400°C. In this system (using a high-purity CuO ceramic disk) H₂ gas exhibited larger current changes than did a CO gas mixture at

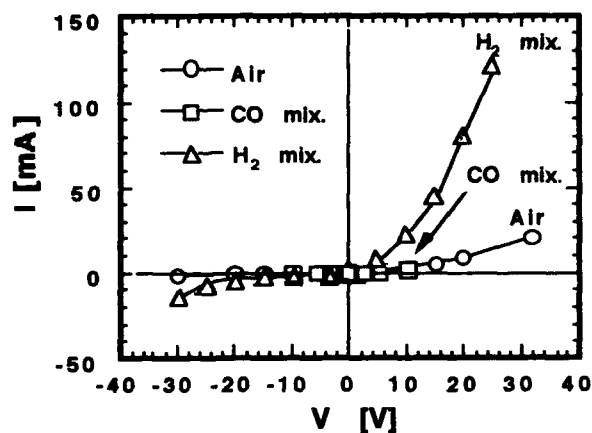
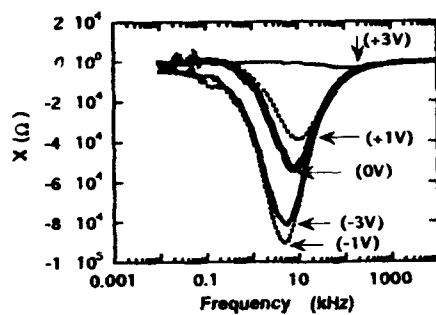
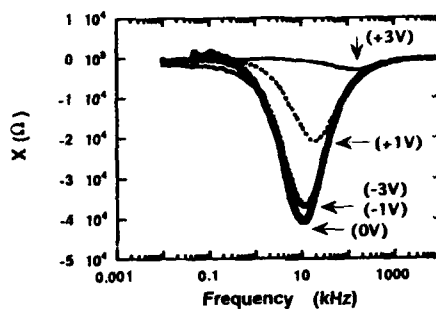


Fig.5. Rectifying characteristics of CuO/ZnO pn heterocontact in the testing gas atmospheres (Air, CO (4000ppm) and H₂ (4000ppm)), at 400°C.

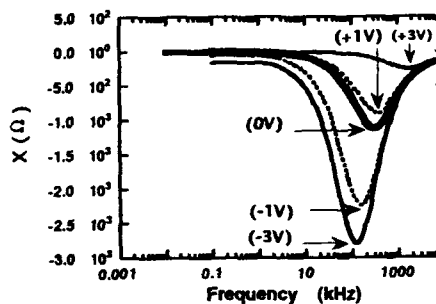
250°C to 400°C. Good selectivity for CO gas thus is considered difficult to obtain by means of only the DC voltage characteristics for this system.



(a) in air



(b) in CO mixture



(c) in H₂ mixture

Fig.6. Dependence of reactance (X) on frequency and DC bias applied on the pn heterocontact in each testing gas (Air, CO(4000ppm) and H₂(4000ppm)) at 400°C.

Figure 6 shows the dependence of reactance X (an imaginary component of impedance) on both frequency and DC bias voltage applied to the heterocontact in each testing gas at 400°C. The curve shows a peak at each characteristic frequency that depends on the ambient gases and the bias voltage. The peak in the air shifted from 7.9kHz (without a DC bias) to lower frequencies under small minus DC bias of -1 and -3V. In a CO gas mixture with air, however, the peak of reactance did not show a clear shift to lower frequency caused by CO gas and the small minus DC bias, and the maximum reactance was given when the DC bias was zero. In an H_2 gas mixture, the reactance peak for zero bias voltage shifted to high frequency over 300kHz, and the height was about 2% of that measured in air, resulting in the smallest value among the three testing gases. The reactance peak increased and shifted to lower frequencies when minus bias were applied.

Accordingly, since the mode of changing the reactance displays its own characteristics, featured by DC bias and measuring frequency, it is considered the CO gas can be distinguished from H_2 gas. The frequency and bias dependence of reactance showed little noticeable dependence on the testing atmosphere at 250°C and 300°C.

(2) Identification of CO gas from H_2 gas

Figure 7 shows the DC bias dependence of the reactance measured at 10kHz for each gas atmosphere at 400°C. In Fig. 7(A), the reactance is normalized by the reactance measured under the DC bias at 0V in the air, as the form of $X/X(\text{in Air, at 0V})$. The feature for each gas can be observed remarkably on the difference in DC bias dependence in the minus bias region. The appearance of a reducing gas can be detected by a decrease in the magnitude of reactance ratio under zero bias.

In Fig. 7(B), the reactance(measured at 10kHz) is normalized by the reactance measured under the DC bias at 0V for each gas atmosphere, as the form of $X/X(\text{at 0V})$. A decrease in reactance ratio that biases to a minus voltage (e. g. , between -1 and -3V) indicates a CO gas mixture. On the other hand, an increase in the magnitude of reactance ratio in the minus bias voltage indicates the existence of H_2 gas. Accordingly, the two gases are easily distinguishable because they exhibit opposite signs for reactance change when the DC bias moves from 0 V into the minus range.

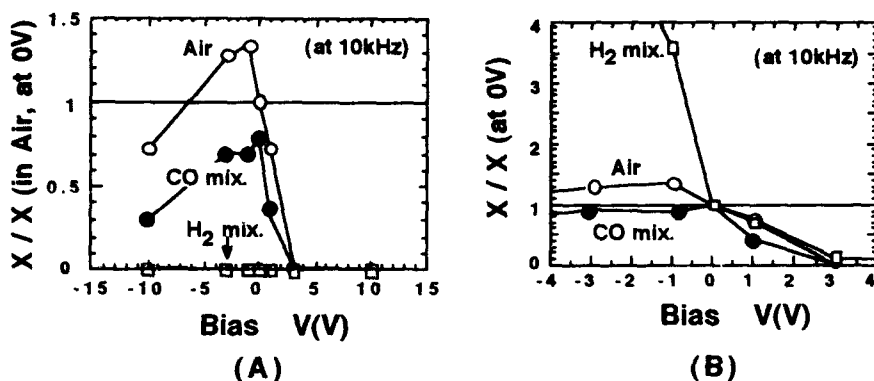


Fig.7. DC bias dependence of reactance (10kHz, 400 °C) for each testing gas (Air, CO (4000ppm) and H₂ (4000ppm)) at 400 °C. (A), normalized by the reactance under the bias of 0[V] in air. (B), normalized by the reactance under the bias of 0[V] in each testing gas.

Figure 8 shows the AC frequency dependence of the reactance (measured under the DC bias at -1V) normalized by the reactance measured at 5kHz under the same bias for each gas atmosphere, as the form of $X/X(\text{ at } 5\text{kHz})$. The features of each gas are remarkably evident in the high-frequency region, over 5kHz. A decrease in reactance ratio when the frequency changes from 10 to 100kHz under the same bias voltage (-1V) indicates a CO mixture, and a remarkable increase in reactance within the same frequency range shows an H₂ mixture. These two gases thus also can be distinguished easily because the changing directions of their reactance between 10 and 100kHz are quite opposite.

As described above, the sensitivity of the sensor can be tuned to the maximum for the intended gas by means of applying minus DC bias at a constant frequency or of scanning AC frequency under a minus DC bias. Namely, this shows the feasibility of the tuning of the electrical properties of CuO/ZnO heterocontact suitable for gas identification.

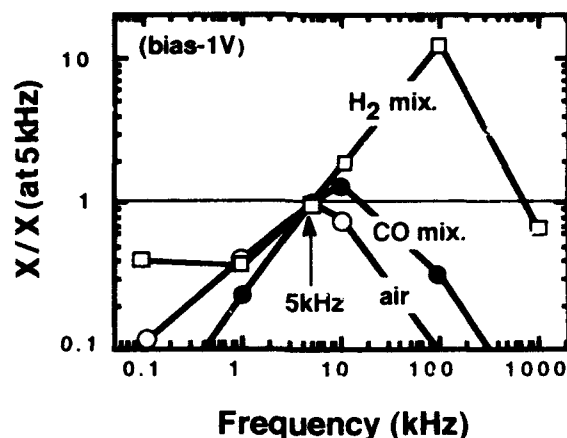


Fig.8. AC frequency dependence of reactance ratio, $X/X(5\text{kHz})$, which is normalized by the reactance at 5kHz under the DC bias of -1[V] in each testing gas at 400°C.

(3) Analysis of equivalent circuit components

Figure 9(A) shows the plot of bias dependence of resistance R_i , which is large in the bias range of minus for each gas atmosphere. The changes of R_i by CO and H₂ gases and their bias dependencies were almost same with those of reactance at 10 kHz shown in Fig. 7(A). Figure 9(B) shows the bias dependence of capacitance C_i of equivalent circuit at 400°C. At 400°C, the increase of capacitance was observed among flammable gas mixture. Especially, H₂ gas contributed to make the capacitance increased largely. It is considered that the electrical charge produced by the (chemical) adsorption of reducing gases increased the capacitance of the interface. In air, the increase of capacitance was observed with an increase of DC bias from -1V to +1V. On the other hand, in reducing gas atmosphere, the capacitance C_i increased under the minus DC bias.

This is considered to mean that the capacitance of pn heterocontact is controlled by the adsorption of gases (O₂, CO and H₂) on the interface and that the adsorbed gases also give a conduction path among the contacted interfaces. The bias dependence of those resistance and capacitance was varied with the kinds of absorbed gas. In CO gas mixture, since the capacitance was almost constant for

the DC bias range between -10V and +3V, the amount of charge produced by adsorption seemed to be almost constant and to have small independence on DC bias.

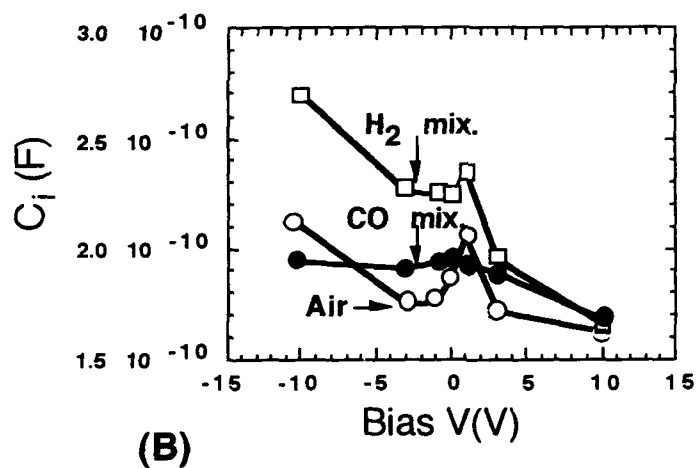
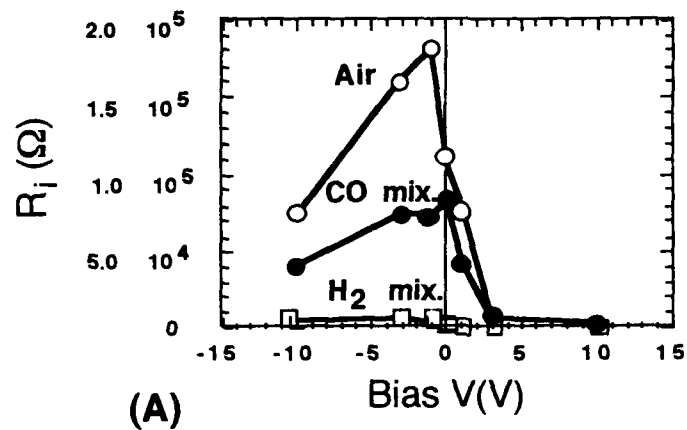


Fig.9. DC bias dependence of (A) the resistance R_i and (B) the capacitance C_i composing equivalent circuit of pn heterocontact in each testing gas at 400 °C.

Figure 10 shows a equivalent circuit for the interface of pn contact proposed on which the additional resistance R_{ads} and capacitance C_{ads} are formed by adsorption or reaction of gases. The R_{ads} means an additional path for electrical conduction produced by gases. The R_{ads} and C_{ads} are considered to be connected in parallel to the original resistance (R_{io}) and capacitance (C_{io}) present in air atmosphere. Here, R_{io} and C_{io} are treated to be constant. If the introduction of gases gives the specific capacitance C_{ads} and resistance R_{ads} , the dependence of reactance on frequency should be changed. Accordingly, the gas identification using DC bias dependence and AC frequency dependence can be expected to be feasible.

As described above, by investigating of dependence of reactance on bias and frequency in CO or H_2 gas, the gas identification, especially for CO gas, was found to be feasible by use of only a single sensor element of pn heterocontact. The function of identification was given by selecting the optimum AC frequency and DC bias for the intended gas. This can be said to be the tuning for the desired sensing characteristics by selecting optimum measuring conditions.

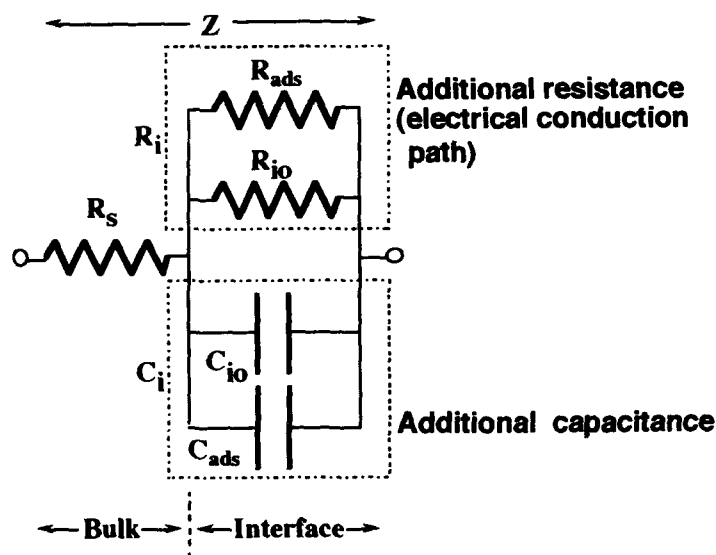


Fig.10 Equivalent circuit of heterocontact with additional circuit elements in a reducing gas atmosphere.

The use of tuning function of the pn heterocontact would give a new promising field for the sensing and identification of gas species which have been difficult by a single measurement of DC resistance or capacitance.

IV. Conclusions

A new principle and method of identification of gas was investigated by use of the impedance of heterocontact with CuO/ZnO in the atmosphere of air balanced H₂ or CO (4000ppm, respectively) at 250-400°C.

(1) In the measurements of AC impedance under DC bias, the frequency dependence of reactance showed a minimum peak. The absolute value of reactance was decreased and the frequency giving the peak of reactance were changed by CO and H₂ gases. The DC bias also gave changes on the value and the peak frequency of reactance in a different manner in CO and H₂ gases.

(2) The gas identification of CO and H₂ gases were shown to be feasible by (i) measuring reactance changes and their DC bias dependence at a fixed frequency or by (ii) measuring reactance changes and their frequency dependence at a fixed DC bias.

(3) According to the analysis of equivalent circuit of heterocontact by means of Cole-Cole plot, the changes in impedance were found to correspond to that the additional resistance and capacitance, which is specific to the ambient gases, were introduced to the interface impedance.

References

¹Y.Nakamura, M.Ikejiri, M.Miyayama, K.Koumoto and H.Yanagida, "The Current-Voltage Characteristics of CuO/ZnO Heterojunctions", *J.Chem.Soc.Jpn.*, **1985**, 1154-1159 (1985).

²Y.Nakamura, T.Tsurutani, M.Miyayama, O.Okada, K.Koumoto and H.Yanagida, "The Detection of Carbon Monoxide by the Oxide-Semiconductor Hetero-

Contacts", *J.Chem.Soc.Jpn.*, **1987**, 477-483 (1987).

³Y.Nakamura, H.Yoshioka, M.Miyayama, H.Yanagida, T.Tsurutani and Y.Nakamura, "Selective CO Gas Sensing Mechanism with CuO/ZnO Hetero-contact", *J.Electrochem.Soc.*, **137**, No.3, 940-943(1990).

⁴Y.Ushio, M.Miyayama and H.Yanagida, "Effects of Interface States on Gas Sensing Properties of a CuO/ZnO Thin Film Heterojunction", *Sensors & Actuators*, in press.

⁵H.Yanagida, "Intelligent Ceramics", *Ferroelectrics*, **102**, 251-257 (1990).

⁶E.Inoue, "Photoconduction of Electrophotographic Materials", *Chemistry and Chem.Industry*, **23**, 158(1970).

⁷F.P.Koffyberg and F.A.Benko, "A Photoelectrochemical Determination of the Position of the Conduction and Valence Band Edge of p-Type CuO", *J.Appl.Phys.*, **53**, 1173- (1982).

RELATIONSHIP BETWEEN CRYSTAL ORIENTATION AND GAS SENSING PROPERTY OF SPUTTERED SnO_2 FILMS

Masasuke Takata

Department of Electrical Engineering, Nagaoka University of Technology
Kamitomioka, Nagaoka, Niigata 940-21, JAPAN

The usage of N_2/O_2 gas mixture in the preparation of tin oxide thin films by sputtering was examined in order to clarify the relationship between the resulting crystal structure and the H_2 gas sensing properties. The formation of single phase SnO_2 and the degree of preferential orientation of the (110) plane were improved by increasing the oxygen concentration in the sputtering gas. A higher gas sensitivity was observed for films having higher degrees of the orientation of the (110) planes, and the maximum sensitivity was increased by about 1.5 times of that for the film prepared in Ar/O_2 atmosphere.

INTRODUCTION

Sintered bodies and/or thin films of tin oxide have been used for gas sensors as well as the films of well-known transparent conducting medium, because of their outstanding semiconducting nature. The sensing properties are originated from the considerable change in the electrical conductivity caused by the reaction between the material and gases to be detected.

Several models for the sensing mechanisms have already been proposed by some investigators [1-5]. Though some differences can be found in each model, all of them assume the existence of pre-adsorbed atmospheric gases

To the extent authorized under the laws of the United States of America, all copyright interests in this publication are the property of The American Ceramic Society. Any duplication, reproduction, or republication of this publication or any part thereof, without the express written consent of The American Ceramic Society or fee paid to the Copyright Clearance Center, is prohibited.

on the surface of the material. Further, the reactivity of the constituent elements in the material (mostly oxygen) with the specific gas species should be an important factor in the gas sensing mechanisms.

In the preceding papers [6], the sensitivity of SnO_2 thin film for H_2 gas was examined in terms of the effect of preferential orientations of the specific crystallographic planes. As a result, it was confirmed that the higher sensitivity was observed for the films having higher degree of the preferential orientation for (110) planes which correspond to the plane having the maximum surface atomic density in SnO_2 [6]. Since the surface atomic density determines both the number of adsorption sites and the reactive sites, the above result seems to be reasonable. It should be noted that the degree of the preferential orientation can be changed by the preparation method of thin films. In the preceding work, SnO_2 thin films were prepared by r.f. magnetron sputtering technique using Ar/O_2 gas mixture.

For the present work, the effect of usage of N_2/O_2 gas mixture on the sputtering of SnO_2 is investigated with respect to its crystal orientation and the gas sensing properties.

EXPERIMENTAL PROCEDURES

Sample Preparation

Tin oxide films were deposited on glass substrates (7mm x 17mm, Corning #7059) by sputtering from a SnO_2 powder target, using a radio-frequency magnetron sputtering apparatus (SPK-301, Tokki). The high vacuum chamber was evacuated preliminary with an oil diffusion pump up to an ultimate pressure of nearly 3×10^{-6} Torr. Then, nitrogen gas (>99.9%) and oxygen gas (>99.9%) were introduced into the chamber by controlling the mixing ratio and the total gas pressure. Target to substrate spacing is 40 mm. The applied r.f. power was fixed at 200W (3.96 W/cm^2). The target was water-cooled and the substrates were not heated intentionally. However, the substrate temperature was found to increase up to 180-200°C during the deposition. The thickness of the films was measured with a surface texture

measuring instrument (Surfcom-200B, Tokyo Precision) and was in the range of 0.5-3.0 μm .

Structural Analysis and Sensitivity Measurements

The crystal structures of the films were examined by a x-ray diffractometer measurements using $\text{Cu-K}\alpha$ radiation (40kV, 100mA ; Rint 1500 with Hitachi Work Station 2050, Rigaku). The diffraction intensity data were acquired at sampling steps of 0.020° at the scan speed of $4^\circ/\text{min}$ in the range from 20° to 60° of 2θ . The degree of preferential orientation for (hkl) plane, $F(\text{hkl})$, was calculated from the following formula,

$$F(\text{hkl}) = \frac{I(\text{hkl})}{I(110)+I(101)+I(211)} \quad (1)$$

where $I(\text{hkl})$ is the integrated diffraction intensity evaluated from the x-ray diffraction pattern. In the present work, the diffractions from (110), (101) and (211) plane were chosen for the evaluations of preferential orientation, because they correspond to the largest three peaks in the x-ray diffraction profile for SnO_2 powder (JCPDS 21-1250) ; the calculated values of $F_p(110)$, $F_p(101)$ and $F_p(211)$ for SnO_2 powder are 0.409, 0.320 and 0.272, respectively. Then, when the value of $F(\text{hkl})$ for the film exceed these values, we regard that the film has crystallographically 'orientated' structure with respect to the (hkl) plane.

The gas sensing properties were estimated by measuring the differences in the electrical conductivity between dry air and air containing 50ppm H_2 at 300°C . The sensitivity, S , was defined as

$$S = \frac{R_a}{R_g} \quad (2)$$

where R_a and R_g are the electrical resistivities in the dry air and in the air containing 50ppm H_2 gas, respectively. Before performing the sensitivity measurements, the films were annealed at 500°C for 18h in an electric furnace in order to eliminate the effect of thermal hysteresis within the films accompanied by the preparations. The conventional four probe method was applied for the resistivity measurement. Gold electrodes were formed on the

surface of the films by vacuum evaporation and electrical contacts were made by using Pt wire attached to the electrodes with silver paste. The samples were placed in a silica glass tube which was heated to 300°C with an infrared image furnace (RHL-410, Sinku-Riko). The R_a and R_g were measured during flowing the dry air and air containing 50ppm H_2 gas, respectively, into the tube by 20 ml/min. The whole measurement was conducted automatically by using a digital electrometer (TR8652, Advantest), programmable DC voltage/current generator (TR6142, Advantest), digital multimeter (TR6846 and TR6851, Advantest), and a personal computer (PC9801, NEC).

RESULTS AND DISCUSSION

Crystal Structure of SnO_2 Thin Film

In general, the crystal structure of thin films prepared by sputtering is sensitive to the sputtering conditions, such as gas species, gas pressure, and applied power, etc. Figure 1 shows x-ray diffraction profiles for the films prepared by sputtering in N_2/O_2 gas mixture. The oxygen concentration in the sputtering gas affected both the resulted crystalline species and the degrees of preferential orientation of specific crystallographic plane. For the films prepared under oxygen-free atmosphere, only three peaks were observed in the profile and were assigned to the diffractions from (101) plane of metallic tin and from (101) and (112) planes of tin mono-oxide, respectively. In spite of the usage of SnO_2 powder as the target, the reductive nature of nitrogen seems to enhance the formation of the above species during the deposition. The present observation should be compared with the preceding result [6] in which the film prepared in atmosphere consisted of SnO_2 . It is also noted that the only one peak for metallic tin and two peaks for SnO are observed in the profile. This suggests the appearance of the preferential orientation in the respective crystal structure.

The incorporation of a small amount of oxygen in the sputtering gas caused a drastic change in the resulted crystal species in the film. By mixing only 10ppm of oxygen into nitrogen gas, the new peaks appeared at around 2θ

$=26^\circ, 34^\circ, 52^\circ$, and 58° in the diffraction profile of the film prepared. These peaks could be assigned to the diffractions from (110), (101), (211), and (002) planes of SnO_2 , respectively. By increasing the oxygen concentration up to 100ppm, the diffractions from metallic tin and SnO were completely annihilated and those from SnO_2 phase became dominant in the profiles. At the same time, the preferential orientations for (101) plane began to grow apparently. When the oxygen concentration exceeded 100ppm, the preferentially orientated planes were converted from (101) to (110) plane and the degree of preferential orientation of (110) plane was increased with increasing the oxygen concentration up to 10%. Further increase in the oxygen concentration up to 100% affected neither the crystalline species nor the degrees of orientation in the film, i.e. no changes were observed in the profiles.

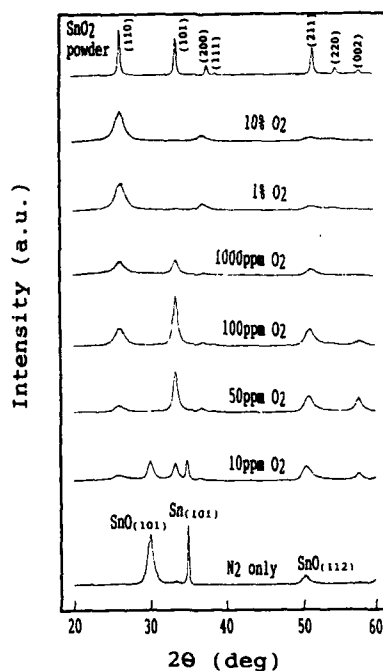


Fig. 1. The X-ray diffraction profiles of the films prepared by sputtering in N_2/O_2 atmosphere of 8×10^{-3} Torr, in which the oxygen content was changed from 0 to 10%. The X-ray diffraction profile for SnO_2 powder is also presented.

Figure 2 shows the relationship between the degree of preferential orientation of (110) planes in the film and the oxygen concentration in the gas mixture. The data for the film prepared in Ar/O₂ atmosphere [6] were also replotted in this figure. The orientations could be observed obviously in the films prepared with the gas containing more than 1% of oxygen. It should be noted that the degree of orientation was higher for the films prepared in N₂/O₂ atmosphere than those prepared in Ar/O₂ atmosphere, even for the same oxygen concentration range from 10 to 30%.

In addition, the linewidth of each peak in the x-ray diffraction profile was significantly different between the SnO₂ film prepared in N₂/O₂ atmosphere and that in Ar/O₂; the width of diffraction peaks in the former films was much broader than those in the latter films. There seems to be two major reasons for the broadening : 1. the crystalline size in the former film is smaller than that in the latter film. 2. the crystal lattice is highly distorted in the former film. At present, detailed analyzes of microstructure with a SEM apparatus are ongoing in order to clarify the origin of the broadening of diffraction peaks.

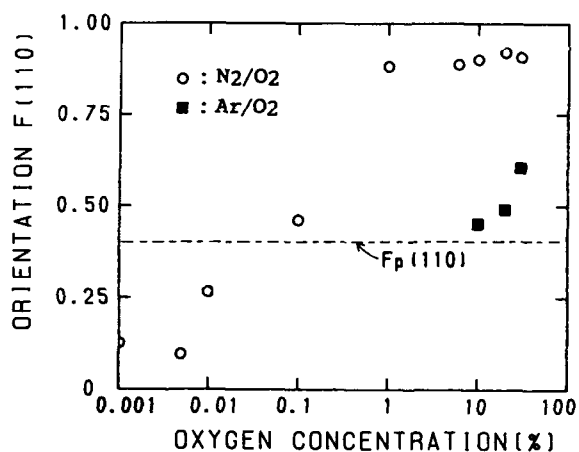


Fig. 2. The degree of preferential orientations (○) of (110) plane, $F(110)$, as a function of O₂ concentration in N₂/O₂ sputtering gas (sputtering gas pressure : 8×10^{-3} Torr, radio-frequency power : 200 W). The data (■) for the films prepared in Ar/O₂ gas mixture are also shown.

Gas Sensing Properties

As described above, the films prepared in O_2 free atmosphere consisted of metallic tin and SnO . For these films the $F(110)$ is zero by definition. Further, these films showed no changes in the electrical resistivity when they were subjected to air containing 50ppm H_2 gas (i.e., no sensitivity).

Except for the films prepared in O_2 free atmosphere, the films containing SnO_2 phase showed changes in the electrical resistivities when subjected to air containing 50ppm H_2 . Figure 3 shows the sensitivity of the films prepared in N_2/O_2 gas mixture as a function of the degree of preferential orientation of the (110) plane. The data for the films prepared in Ar/O_2 atmosphere [6] were also replotted in this figure. It can be seen that the sensitivity is higher for a film having higher degree of the preferential orientation $F(110)$, irrespective of the gas mixture.

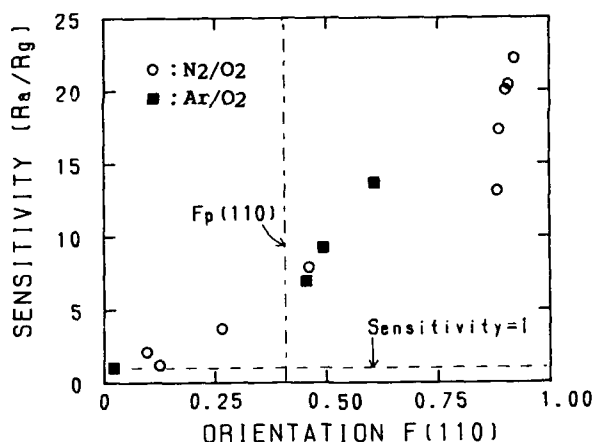


Fig. 3. The relationship (○) between the sensitivities and the degree of orientations of (110) plane, $F(110)$, of films prepared in N_2/O_2 (sputtering gas pressure : 8×10^{-3} Torr, radio-frequency power : 200 W). The data (■) for the films in Ar/O_2 atmosphere are also plotted.

CONCLUSION

The effect of the usage of N_2/O_2 gas mixture upon the crystal structure and the gas sensitivity of tin oxide films prepared by sputtering method were examined. The important results are summarized as follows:

- (1) Films prepared in oxygen-free atmosphere consisted of mixture of metallic tin and SnO, while the incorporation of oxygen in the sputtering gas resulted in the enhanced formation of SnO_2 single phase and the degree of preferential orientation of the (110) plane.
- (2) The highly orientated films were obtained at relatively low oxygen concentration in the sputtering gas in comparison with the films prepared in mixed Ar/O_2 atmosphere.
- (3) The higher gas sensitivity was observed in the films having higher degree of the orientation of (110) plane, and the maximum sensitivity was increased by about 1.5 times compared with the film prepared under Ar/O_2 atmosphere.

REFERENCES

- [1] M. Takata and H. Yanagida, "Effects of Gas Adsorption upon Electrical Conductivity of Oxide Semiconductors", *Yogyo Kyokai-shi*, 87[1], 13-21 (1979).
- [2] K. Hara, "Gas-sensing Mechanisms of Semiconducting Thin-film Gas Sensors", *Proc. of the 1st Sensor Symp.*, Japan, 109-112 (1981).
- [3] T. Seiyama, A. Kato, K. Fujiishi and M. Nagatani, "A New Detector for Gaseous Components Using Semiconductive Thin Films", *Anal. Chem.*, 34, 1502 (1962).
- [4] M. Nitta, S. Kanefusa and M. Haradome, "Propane Gas Detector Using SnO_2 Doped with Nb, V, Ti or Mo", *J. Electrochem. Soc.*, 125[10], 1676-1679 (1978).
- [5] G. N. Advani and A. G. Jordan, "Thin Films of Tin(VI) Oxide as Solid State Gas Sensors", *J. Electron. Mater.*, 9, 29-49 (1979).
- [6] J. -S. Ryu, Y. Watanabe and M. Takata, "Correlation between Gas Sensing Properties and Preferential Orientations of Sputtered Tin Oxide Films", *J. Ceram. Soc. Japan*, 100[9], 1165-68(1992).

EVALUATION OF THE GAS RESPONSE OF ZnO/La₂CuO₄ HETERO-CONTACTS WITH DIFFERENT ELECTRODE MATERIALS

Enrico TRAVERSA, Masaru MIYAYAMA* and Hiroaki YANAGIDA**

Dept. of Chemical Sciences and Technologies, Univ. of Rome "Tor Vergata", Via della Ricerca Scientifica, 00133 Rome (Italy).

*Research Center for Advanced Science and Technology (RCAST), Univ. of Tokyo, 4-6-1, Komaba, Meguro-ku, Tokyo 153 (Japan).

**Dept. of Industrial Chemistry, Faculty of Engineering, Univ. of Tokyo, 7-3-1, Hongo, Bunkyo-ku, Tokyo 113 (Japan).

ABSTRACT

This paper reports the sensitivity to CO and H₂ of hetero-contacts between p-type La₂CuO₄ and n-type ZnO semiconductors, with different electrode materials applied on ZnO pellets. Hetero-contacts were prepared by mechanically pressing sintered pellets of the two oxides. Three different electrode materials were used for ZnO pellets (Zn-containing Ag, In- and Ga-containing Ag, and Al pastes), and different resistivities were observed using different electrodes. For ZnO pellets and for hetero-contacts the gas-sensitivity was dependent on the electrode materials applied on the pellets. The greater the resistivity of the ZnO pellets, the larger the gas sensitivity of the hetero-contacts. Slight differences in the potential barrier height are induced by the different resistivities of the three ohmic contacts. The larger the band-bending at ZnO/La₂CuO₄ interface, the larger the influence of adsorbates, resulting in increased sensitivity.

To the extent authorized under the laws of the United States of America, all copyright interests in this publication are the property of The American Ceramic Society. Any duplication, reproduction, or republication of this publication or any part thereof, without the express written consent of The American Ceramic Society or fee paid to the Copyright Clearance Center, is prohibited.

INTRODUCTION

The development of new methods to monitor gaseous pollutants in air is a vital step in the measurement of environmental deterioration. Measurements of gas concentrations in air have mostly been carried out using analytical instruments, which are very precise, but also very costly, and not suitable for on-line monitoring [1]. Solid-state gas sensors, which are cheap, compact, resistant enough to be placed on-site, and fast enough for continuous monitoring, are therefore needed for the detection of hazardous gases at low concentrations. A number of chemical sensors for gases have been developed using different kinds of sensing mechanisms [2]. However, important problems, such as insufficient gas selectivity, lack of systems able to detect very low gas concentrations, and changes in the sensing properties caused by surface contamination, are still to be solved. One approach which may bring us closer to solving these problems is the investigation of novel principles of gas detection leading to advanced sensing systems [3]. The interfaces between p- and n-type semiconductors have recently been shown to possess a gas-sensing mechanism different from that of the single oxide semiconductors [4]. In a previous paper, the sensitivity to reducing gases (CO and H₂) of the hetero-contacts between p-type La₂CuO₄ and n-type ZnO was investigated [5]. It was found that they showed high sensitivity to gases, especially to H₂. In this paper, results obtained on ZnO/La₂CuO₄ hetero-contacts with different electrode materials applied on ZnO are discussed. Their reducing gas sensing properties were measured. The detection mechanism is discussed, comparing the results obtained with the different electrode materials.

EXPERIMENTAL PROCEDURE

Pellets for the ZnO/La₂CuO₄ hetero-contacts were prepared following the procedure reported elsewhere [5]. For electrical measurements, three different kinds of electrode materials, which produce ohmic contacts, were applied to the ZnO pellets: Ag paste containing Zn, Ag paste containing In and Ga, and Al paste (all Demetron). The pastes were printed on the sides of the pellets and then fired at different temperatures, following the supplier's

recommendations, i.e. 500°C, 580°C, and 640°C for the three pastes, respectively. Ag paste electrodes were used on the La_2CuO_4 pellets to give ohmic contacts. Electrical measurements were carried out on each pellet and on the hetero-contact of the two oxides, obtained by mechanically pressing two pellets of the different oxides together, using a sample holder developed by us for this purpose.

The electrical measurements were performed using a digital electrometer (Advantest, mod. TR8652) and a programmable d.c. source (Yokogawa mod. 7651), controlled by a computer. The current-voltage (I-V) characteristics were measured at different temperatures (room temperature, 200°C, 300°C, and 400°C), and at different concentrations of CO and H_2 (up to 2000 ppm) in dry air. In order to evaluate their response time, a constant d.c. voltage was applied to the specimens and changes in current upon variation of the concentration of the gases were recorded.

RESULTS AND DISCUSSION

The I-V curves for the pellets of La_2CuO_4 and of ZnO with the three different electrodes (Ag+Zn paste, Ag+In/Ga paste, and Al paste) were linear and the pellets showed ohmic behaviour. This linear behaviour was observed at all the temperatures tested. The resistivity of La_2CuO_4 decreased from 25°C to 200°C, and above 200°C increased with increasing temperature. The resistivity of ZnO increased up to about 300°C, and then decreased above 300°C. The temperature-dependence of the resistivity had the same trend for all the electrodes used, but different quantitative values were recorded with different electrodes. At 400°C, the resistivities were 10 Ω cm for La_2CuO_4 , and 400, 600, and 1200 Ω cm for ZnO with electrodes made of Ag+Zn, Ag+In/Ga, and Al, respectively.

For bulk ZnO, doping with trivalent elements, such as Al, Ga, and In, produces new donor levels [6]. The trivalent ions occupy normal Zn^{+2} sites, with conversion of a Zn^{+2} ion to a Zn^{+} ion to maintain electrical neutrality, resulting in increased electron concentration [7]. One would thus have expected that Al/ZnO/Al pellets would have had the lowest resistivity, which was not the case. For ohmic contacts on n-type semiconductors with surface states, it is necessary that the metal, or an ingredient of the

electrode system, has a high oxygen affinity to disrupt the surface layer [8]. The oxygen affinity order is: $\text{Al} \gg \text{Ga} > \text{Zn}$. Ag has very little oxygen affinity. Once again the order of resistivity is the opposite of what is expected. One possible explanation for the different resistivities, given the firing temperatures of the electrodes, may be a slight oxidation of the electrodes following the oxygen affinity order, which results in increasing resistivity. Overlong firing may have caused slight oxidation of the electrodes, after disruption of the surface layer. However, the composition of the pastes used for printing electrodes is not precisely known, and may have affected the formation of the ohmic contacts.

The gas sensitivity of the single pellets was investigated. The linear I-V curves for all the pellets continued in the presence of the gases tested. The gas sensitivity of the La_2CuO_4 single pellets is reported elsewhere [5]. The results for the ZnO pellets with Al, Ag+Zn, and Ag+In/Ga electrodes were in line with the generally accepted gas sensing mechanism for ZnO (n-type semiconductor), which is based on the decrease in resistivity caused by a decrease in adsorbed O_2 concentration due to the oxidation of reducing gases [9]. The electrode materials influenced the electrical response of the pellets to the gases tested. At $T < 400^\circ\text{C}$, ZnO did not show sensitivity to gases. At 400°C , ZnO pellets were almost insensitive to CO, except for the ZnO pellets with Ag+In/Ga electrodes, which showed a sensitivity (I/I_0 , in this case) of about 1.25. The best H_2 sensitivity, about 2, was shown by ZnO with Ag+In/Ga electrodes, while ZnO with Al electrodes showed the worst sensitivity (1.15), and intermediate sensitivity (1.4) was obtained for ZnO with Ag+Zn electrodes. The very low porosity of the ZnO pellets is responsible of these very low sensitivities. The response time to H_2 was rather long (several minutes), while the response time to CO was faster, but with unstable results. The higher the sensitivity of the pellet, the longer the response time, as shown in fig. 1, where a comparison of the response time to 2000 ppm of CO or H_2 for the three ZnO pellets is reported.

The different gas sensitivities observed for ZnO with different electrode materials may have different explanations. It seems likely that the different sensitivities of these pellets is related to trapping. ZnO with Al electrodes may have an increased trap density, favouring mutual compensation of donors and acceptors

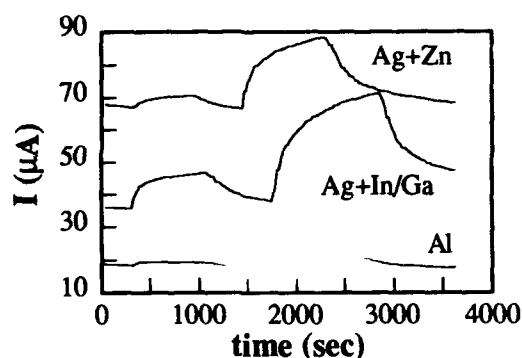


Fig. 1 Typical current response of ZnO with different electrodes, at 0.01 V and 400°C, in the presence of 2000 ppm of CO or H₂.

in the bulk, which produces a high concentration of defects and low carrier concentration [10]. These defects or traps within the space-charge layer or at the surface can bind electrons and decrease the efficiency of electron injection or extraction at the surface [11]. The influence of the thickness of the depletion layer, or a different catalytic effect on the oxidation reactions of the metal in the electrodes may also explain these results. It would seem that the gas sensitivity of ZnO pellets depends on the interface between the electrode and ZnO.

The I-V curves measured in air of the La₂CuO₄/ZnO hetero-contacts showed typical p-n diode behaviour in the temperature range from 25°C to 400°C. The measurements carried out on the hetero-contacts showed that also in this case their gas-sensitivity was dependent on the electrode materials applied on ZnO pellets. The I-V curves in the presence of reducing gases continued to show p-n diode behaviour. The sensitivity (I/I_0) increased with the temperature: CO was detected only at 400°C, H₂ at $T > 300^\circ\text{C}$. Fig. 2 shows the I-V curves, measured at 400°C in environments with different concentrations of gases, for the hetero-contacts between La₂CuO₄ and ZnO with Ag+Zn electrodes, and fig. 3 the sensitivity to gases (I/I_0) calculated from the curves in fig. 2. The same is shown in figs. 4 and 5 for contacts with Ag+In/Ga electrodes, and in figs. 6 and 7 for contacts with Al electrodes.

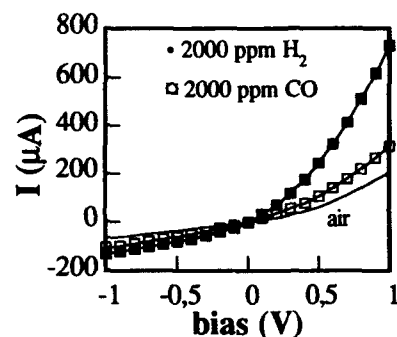


Fig. 2 Dark I-V characteristics of ZnO(Ag+Zn electrode)/La₂CuO₄ hetero-contacts at 400°C at various gas concentrations.

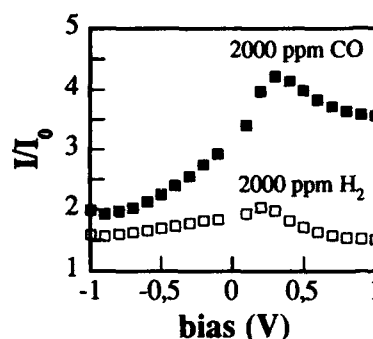


Fig. 3 The bias-dependence of the gas sensitivity (I/I_0) of ZnO(Ag+Zn)/La₂CuO₄ contacts from the data in fig.2.

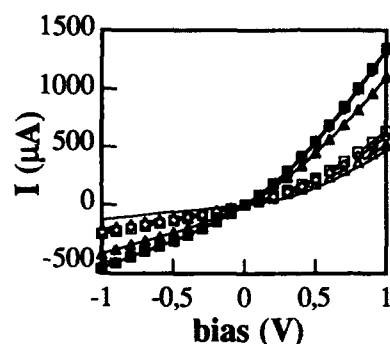


Fig. 4 Dark I-V curves of ZnO(Ag+In/Ga elecir.)/La₂CuO₄ at 400°C at various gas concentrations. (Solid and open symbols are 1000, 1500 and 2000 ppm CO and H₂).

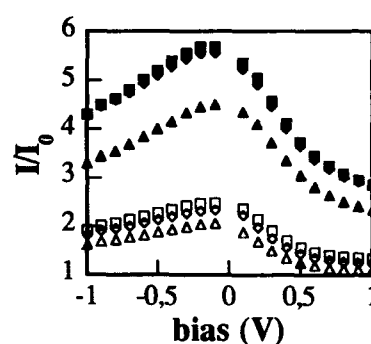


Fig. 5 The bias-dependence of the gas sensitivity (I/I_0) of ZnO(Ag+In/Ga)/La₂CuO₄ from the data in fig. 4. The symbols are the same as in fig. 4.

It was observed that the contacts' gas sensitivity was voltage dependent, and that this also depended on the materials used in the electrodes. The presence of the gases mainly affected the forward current, which increased with increasing gas concentration, and only slightly affected the reverse current. The

highest sensitivity was observed for the contact with an Al electrode, which for 2000 ppm of H_2 was above 10 at 1 V of forward bias. For CO, a different trend for sensitivity with bias was observed, with greater sensitivity at reverse bias. The CO-sensitivity was about 3.5 at 2000 ppm and 1 V (forward). The lowest sensitivity (4.2 for 2000 ppm of H_2 at 0.3 V forward) was observed for the contact with the Ag+Zn electrode, together with a different trend of bias-dependence, which showed a maximum at 0.3 V of forward bias. Contacts with the Ag+In/Ga electrode behaved differently: the maximum sensitivity was observed in reverse bias. This may be related to the steeper increase of reverse current level upon contact with hydrogen (fig. 3). Moreover, poor resolution of the electrical response was observed for different concentrations of H_2 . Fig. 8 shows the d.c. response time upon applied voltage after exposure to 2000 ppm of CO or H_2 at 400°C for all the hetero-contacts. The response to H_2 was very fast (less than 1 min), while the response to CO was much slower. Fast response to H_2 and the most stable results were again obtained by using ZnO with Al electrodes in the contacts. The contact with the Ag+In/Ga electrode showed a faster response to CO and unstable results.

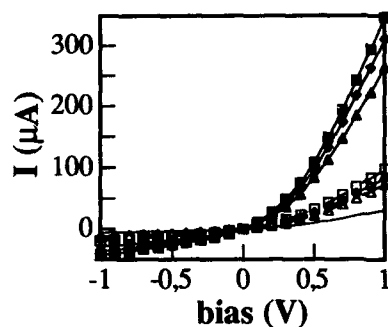


Fig. 6 Dark I-V curves of ZnO(Al electr.)/La₂CuO₄ at 400°C at various gas concentrations. (Solid and open symbols are 1000, 1500 and 2000 ppm CO and H_2 ; solid line in air).

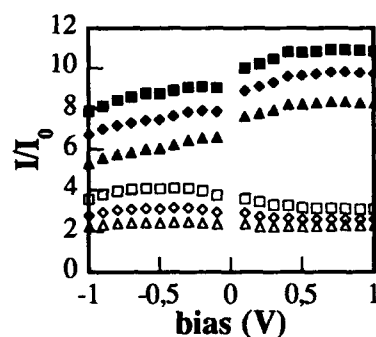


Fig. 7 The bias-dependence of the gas sensitivity (I/I_0) of ZnO(Al)/La₂CuO₄ from the data in fig. 6. The symbols are the same as in fig. 6.

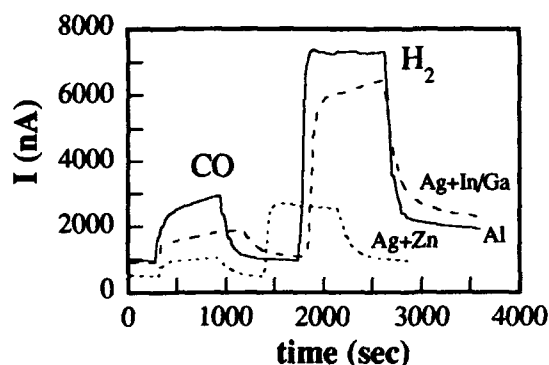


Fig. 8 The typical current response of ZnO/La₂CuO₄ hetero-contacts with different electrode materials at 0.01 V (0.1 V for Al electrodes) and 400°C, in the presence of 2000 ppm of CO or H₂.

The behaviour of the contacts therefore followed a different trend with respect to the electrode materials from that observed for the single ZnO pellets, which showed the lowest H₂ sensitivity with the Al electrodes. One can observe that the greater the resistivity of the ZnO pellets, the greater the gas sensitivity of the hetero-contacts. In a similar way it was observed that the humidity-sensitivity of Au/ZnO Schottky barrier was dependent on the materials for ohmic contact used for ZnO pellets, and the best results were obtained with Al ohmic contact (highest resistivity) and the worst with Ag+Zn contact (lowest resistivity) [12]. This can be explained in terms of slight differences in the potential barrier heights induced by the different resistivities of the three ohmic contacts, which act in the same way for the Schottky barrier and the p-n junction. The larger the band-bending at ZnO/metal or ZnO/p-type semiconductor interfaces, the greater the influence of adsorbates, resulting in increased sensitivity.

CONCLUSIONS

The sensitivity to reducing gases of ZnO pellets and of La₂CuO₄/ZnO hetero-contacts was affected by the electrode materials. This suggested a possible contribution to the sensing mechanism of the ZnO/electrode interface. The electrode materials

applied on ZnO pellets in the hetero-contacts influenced their gas sensitivity through a different mechanism. The sensitivity of the hetero-contacts was probably influenced by the resistivity of the ZnO pellets, which changes with the different electrodes. The higher the resistivity of the ZnO pellet, the higher the gas sensitivity. Slight differences in the potential barrier height may be induced by the different resistivities of the three ohmic contacts. The larger the band-bending at the ZnO/La₂CuO₄ interface, the larger the influence of adsorbates, resulting in increased sensitivity.

ACKNOWLEDGMENTS

This work was supported by the Japan Society for the Promotion of Science (JSPS) and the National Research Council of Italy (CNR), under the auspices of their agreement of scientific co-operation.

REFERENCES

- 1 N. Yamazoe and N. Miura, Environmental gas sensing; pp. 340-45 in *Transducers '93*, IEE, Tokyo, Japan, 1993.
- 2 S.R. Morrison, Semiconductor gas sensors, *Sens. Actuators*, **2**, 329-41 (1982).
- 3 H. Yanagida, Intelligent materials - A new frontier, *Angew. Chem.*, **100**, 1443-46 (1988).
- 4 Y. Nakamura, H. Yoshioka, M. Miyayama, H. Yanagida, T. Tsurutani and Y. Nakamura, Selective CO gas sensing mechanism with CuO/ZnO heterocontact, *J. Electrochem. Soc.*, **137**, 940-43 (1990).
- 5 E. Traversa, M. Miyayama and H. Yanagida, Gas sensitivity of ZnO/La₂CuO₄ hetero-contacts, *Sens. Actuators B*, **17**, 257-61 (1994).
- 6 H. Yanagida, Interstitial defects in ceramic materials, *Seramikkusu*, **8**, 331-36 (1973).
- 7 M. Takata, D. Tsubone and H. Yanagida, Dependence of electrical conductivity of ZnO on degree of sintering, *J. Am. Ceram. Soc.*, **59**, 4-8 (1976).
- 8 B.M. Kulwicki, Ceramic sensors and transducers, *J. Phys. Chem. Solids*, **45**, 1015-31 (1984).

- 9 S. Saito, M. Miyayama, K. Koumoto and H. Yanagida, Gas sensing characteristics of porous ZnO and Pt/ZnO ceramics, *J. Am. Ceram. Soc.*, **68**, 40-43 (1985).
- 10 G. Heiland and D. Kohl, Interpretation of surface phenomena on ZnO by the compensation model, *Phys. Stat. Sol. (a)*, **49**, 27-37 (1978).
- 11 G. Heiland, Homogeneous semiconducting gas sensors, *Sens. Actuators*, **2**, 343-61 (1982).
- 12 E. Traversa and A. Bearzotti, A novel humidity detection mechanism for ZnO dense pellets, submitted for publication to *Sens. Actuators B*.

ZnO/La₂CuO₄ HETERO-CONTACTS AS HUMIDITY SENSORS

Enrico TRAVERSA, Alessandra BIANCO, Giampiero MONTE-SPERELLI, Gualtiero GUSMANO, Andrea BEARZOTTI#, Masaru MIYAYAMA* and Hiroaki YANAGIDA**

Dept. of Chemical Sciences and Technologies, Univ. of Rome "Tor Vergata", Via della Ricerca Scientifica, 00133 Rome (Italy).

#Inst. of Solid State Electronics (IESS), National Research Council of Italy (CNR), Via Cineto Romano 42, 00156 Rome (Italy).

*Research Center for Adv. Science and Technology (RCAST), Univ. of Tokyo, 4-6-1, Komaba, Meguro-ku, Tokyo 153 (Japan).

**Dept. of Industrial Chemistry, Faculty of Engineering, Univ. of Tokyo, 7-3-1, Hongo, Bunkyo-ku, Tokyo 113 (Japan).

ABSTRACT

The humidity sensitivity of hetero-contacts between p-type La₂CuO₄ and n-type ZnO semiconductors, and of the single oxides, as a comparison, was studied. Hetero-contacts were prepared by mechanically pressing sintered pellets of the two oxides. The electrical analysis of the hetero-contacts was carried out using d.c. and a.c. measurements at various relative humidity (rh) values, in order to evaluate the sensing mechanism and the electrical properties of these p-n junctions. The current-voltage (I-V) curves were typical of p-n diodes at all rh values. The current versus rh sensitivity of the hetero-contacts was bias-dependent, and at 2.5 V it was as high as 4 orders of magnitude. The capacitance-voltage (C-V) curves showed the presence of a large number of interface states, responsible for the diode behavior. The rh-sensitivity was explained in terms of the variation of the barrier height at the junctions due to the saturation of the original interface states by physisorbed water, which leads to the release of trapped electrons, resulting in an increase in the forward current.

To the extent authorized under the laws of the United States of America, all copyright interests in this publication are the property of The American Ceramic Society. Any duplication, reproduction, or republication of this publication or any part thereof, without the express written consent of The American Ceramic Society or fee paid to the Copyright Clearance Center, is prohibited.

INTRODUCTION

A recent approach to improve the sensitivity of gas sensors is the use of metal/semiconductor interfaces [1]. Very high sensitivity to gases has been found in the non-linear forward-bias part of current-voltage (I-V) curves of Schottky barriers [2]. Operating in the non-linear region of I-V curves of ZnO varistors has recently been found to give very high hydrogen sensitivity [3]. Specific gas sensing characteristics have been reported for hetero-contacts between p-type and n-type semiconductors, showing rectifying I-V curves typical of p-n junctions [4].

The concept of the use of the non-linear region of I-V curves has also been applied to humidity detection. For humidity sensing, the use of diode-type sensors using perovskite-type oxides in contact with a metal needle has been reported [5]. Humidity sensitivity in the forward bias region of the rectifying I-V curves of Pd/ZnO diodes has been detected [6]. Recently, some of the authors of this paper reported that dense ZnO pellets with a Schottky barrier are sensitive to humidity, showing a mechanism which cannot be explained in terms of ionic or electronic conduction, but which may be related to the variation of the barrier height due to the presence of surface states [7]. The discovery of Kawakami and Yanagida that a hetero-contact between p-type NiO and n-type ZnO showed I-V curves which were sensitive to moisture [8] introduced a new class of ceramic humidity sensors. Thus, the humidity-sensitivity of p-n hetero-contacts between bulk sintered bodies [9,10], or of open p-n hetero-junction thin films [11], has been studied. It has been observed that increasing rh results in a substantial increase in the current flowing across the junction under forward bias. The result is a device which is highly rectifying at high levels of rh, with polarity coincident with an ordinary p-n junction, which operates at room temperature.

The conduction mechanism attributed to these sensors is different from those usually reported for other ceramic humidity sensors [12]. It is based on the electrolysis of adsorbed water taking place at p-n contact sites [13]. The amount of hydrolysis increases at higher humidities, because the higher the humidity, the higher the amount of water adsorption. In the proximity of p-n junctions, electron holes are injected from the p-type semiconductor into the adsorbed water molecules, giving rise to protons

in the adsorbed water phase. The positive charge is liberated at the surface of the n-type semiconductor, thereby resulting in electrolysis of the adsorbed water. The process of electrolysis provides a self-cleaning/self-recovery mechanism. In this respect, p-n heterojunctions can be regarded as intelligent materials [14].

In a previous paper, the sensitivity to reducing gases (CO and H₂) of La₂CuO₄/ZnO hetero-contacts was investigated [15]. This paper sets out the results of a study of the humidity-sensitivity of these hetero-contacts. We decided to use dense pellets of the two oxides to study the effect of the p-n interfaces on the moisture-sensitivity of this previously unstudied hetero-contact. In fact, the humidity-sensitive ionic-type conduction mechanism is enhanced by high porosity and high intrinsic resistance [16], and thus the use of dense, pore-free semiconductors would make the influence of ionic conduction as low as possible.

EXPERIMENTAL PROCEDURE

The description of the procedure used for the preparation of the pellets for the ZnO/La₂CuO₄ hetero-contacts is reported elsewhere [15]. The electrical response of the specimens was analyzed by taking d.c. measurements at different relative humidity (rh) values, obtained by varying the flow rates of dry and wet N₂ in a test cell where the temperature was also controlled. Monitoring of rh was carried out using a commercial sensor (Phys-chem, mod. PCRC-11). The volume of the test chamber was 150 cm³ and the total flow was 200 scm³/min. With this experimental arrangement, fairly reproducible trends were measured. Dark current-voltage (I-V) characteristics were measured at room temperature using a digital multimeter (Hewlett Packard, mod. 3458A) and a programmable d.c. source (Keithley, mod. 230), controlled by a computer. The rh-dependence of d.c. was measured by recording the current upon application of a constant bias, varying rh continuously from nearly dry conditions to about 95% rh, at a constant rate of 1% rh per minute. Stability and response time tests were performed by recording for at least 8 h the current upon a constant d.c. voltage application, during rh cycling, using a Keithley quasistatic CV-meter 595. Using the same equipment, high frequency (100 kHz) dark capacitance-voltage (C-V) characteristics were carried out at various rh values. In order to

evaluate the frequency dependence of the resistive and capacitive parameters, electrochemical impedance spectroscopy (EIS) measurements were carried out at 40°C, using a frequency response analyzer (Solartron, mod. FRA 1255), following the procedure described elsewhere [17].

RESULTS AND DISCUSSION

The I-V curves of the ZnO pellets were linear at all the rh values tested, and the pellets showed ohmic behavior, as expected for an n-type semiconductor. The electrical response of the pellets was not affected by moisture. The lack of rh-sensitivity of ZnO pellets can be explained in terms of their very low porosity, and thus specific surface area, and of their low intrinsic resistance, which hinder the ionic-type humidity-sensitive conduction mechanism. Results obtained on porous ZnO pellets showed in fact considerable rh-sensitivity. The electronic-type mechanism can occur only at high temperatures. The pellets of La_2CuO_4 also showed ohmic behaviour, but they were slightly sensitive to rh, in spite of their very low resistivity (about 10 Ω cm at room T). The sensitivity at 95% rh, evaluated as $I_{\text{wet}}/I_{\text{dry}}$, was about 2. This negligible rh-sensitivity of the La_2CuO_4 pellets is due to their porosity (about 25%), which permits water physisorption in the pores. EIS measurements confirmed the results of d.c. analysis, showing for the single pellets a merely resistive behaviour at all rh values, independent of rh for ZnO, and slightly rh-sensitive for La_2CuO_4 pellets.

For mechanically pressed hetero-contacts, qualitatively reproducible results were obtained using the same specimens in different sets of measurements, but the samples did not give reproducible quantitative results. In these terms the results may be considered significant. Fig. 1 shows the I-V curve of $\text{La}_2\text{CuO}_4/\text{ZnO}$ hetero-contacts measured in dry conditions. The curve shows typical p-n diode behaviour, with a rectifying current in the forward direction ($\text{La}_2\text{CuO}_4^+/\text{ZnO}^-$). The substantial increase in current in the forward bias region takes place above 3 V. A large hysteresis can be observed. The rectifying character is enhanced with relative humidity, as shown in fig. 2, where the I-V curves recorded at various rh values are reported. The higher the rh, the smaller the hysteresis. Very high sensitivity, expressed as $I_{\text{wet}}/I_{\text{dry}}$,

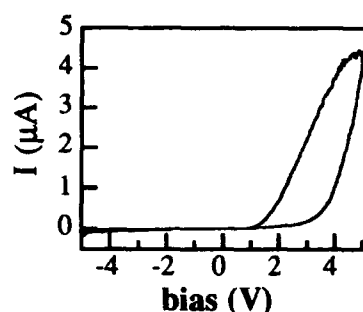


Fig. 1 Dark I-V characteristic of $\text{La}_2\text{CuO}_4/\text{ZnO}$ hetero-contacts at room temperature and 0% rh.

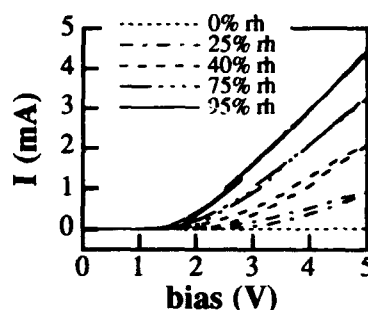


Fig. 2 Dark I-V characteristics of $\text{La}_2\text{CuO}_4/\text{ZnO}$ hetero-contacts at room temperature and at various rh values.

where I_{dry} is the current recorded in a nearly dry environment, was measured for the hetero-contacts, up to about 4 orders of magnitude at 2.5 V d.c. and 95% rh. The rh-sensitivity was bias-dependent, and very large increases in current were recorded only with forward-bias (fig. 3), whilst with reverse-bias samples were insensitive to rh. It can be observed that the sensitivity increased in the bias range where in dry conditions the forward current did not increase steeply, and that this sensitivity decreased above about 3 V. The bias-dependence of the rh-sensitivity is thus probably due to the occurrence of non-linear conduction phenomena.

The rh-dependence of the current of the hetero-contacts at room temperature and 2.5 V d.c. is reported in fig. 4. One can observe that the sensitivity of the current over the entire rh range tested is of about 4 orders of magnitude, and that the sensitivity is larger at rh lower than 30% and at the highest rh values.

Fig. 5 shows the current response of the hetero-contacts to cyclic rh variations at 2.5 V (only a part of the test is reported). For these tests, stable results were obtained applying bias in the range from 1 to 3 V. The response time of the hetero-contacts was nearly the same as that of the reference rh sensor. This fast response indicates that the rh-sensitivity relies on water physisorption. Fig. 6 shows the high frequency (100 kHz) voltage-dependence of $1/C^2$, measured in a nearly dry environment and at 95% rh, in the reverse bias region. The diffusion potential at the p-n junction interface is usually indicated by the intersection of the

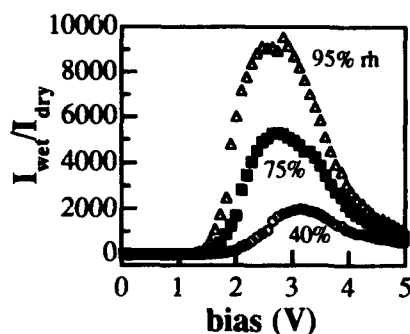


Fig. 3 The voltage-dependence of the rh-sensitivity of $\text{La}_2\text{CuO}_4/\text{ZnO}$ various rh values, evaluated from the data in fig. 2.

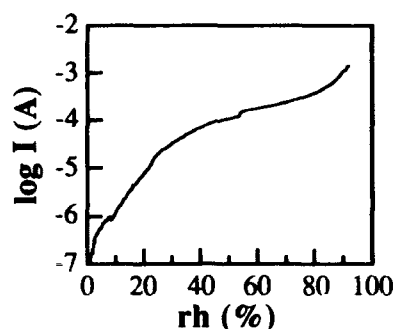


Fig. 4 The rh-dependence of dark current for $\text{La}_2\text{CuO}_4/\text{ZnO}$ hetero-contacts at 2.5 V d.c. at room temperature.

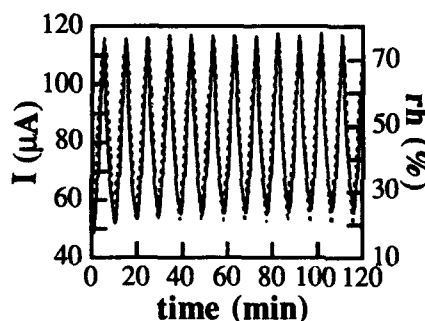


Fig. 5 Dark current response of $\text{La}_2\text{CuO}_4/\text{ZnO}$ to cycling rh, at 2.5 V at room temperature (I is the solid line, rh is the dotted line).

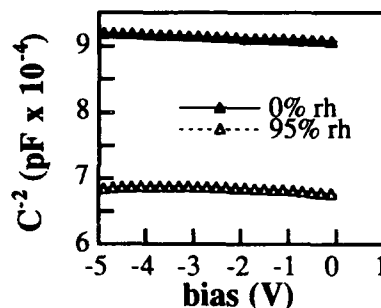


Fig. 6 The voltage-dependence of $1/C^2$ of $\text{La}_2\text{CuO}_4/\text{ZnO}$ at room T, at 0% and 95% rh in the reverse bias region.

extrapolated line of $1/C^2$, evaluated in the reverse bias region, with the bias axis [18]. However, in this case the diffusion potential value that would be obtained was unrealistically large in both the presence and the absence of humidity. Therefore, it was assumed that the interface barrier at the $\text{La}_2\text{CuO}_4/\text{ZnO}$ hetero-contacts is not a physical diffusion barrier, but a chemical-like barrier, due to the presence of a high density of interface states derived from chemical adsorbates [19]. These adsorbates are likely

to be derived from oxygen and/or water adsorption. These results are largely consistent with those obtained for CuO/ZnO thin films [20], for which it was determined that the presence of interface states is fundamental for their sensing properties. The trend of $1/C^2$ is more or less the same in dry and wet conditions, but in the presence of moisture an increase in capacitance is noticeable at all bias values. Fig. 7 shows the high frequency (100 kHz) dark capacitance-voltage (C-V) characteristics in a nearly dry environment and at 95% rh. The increase in capacitance in the forward bias region is much steeper in the presence of moisture than in the nearly dry environment.

All these results show that the charge transfer at the p-n junction sites of the hetero-contacts under forward bias is likely to be due to the pinning of the Fermi level from interface states. The high rh-sensitivity can be explained in terms of the saturation of the original interface states by physisorbed water, which, with increasing rh, leads to the release of trapped electrons, resulting in an increase in the forward current. The relaxation of trapped states may explain the large hysteresis observed in the I-V curves in dry conditions. The reduction of the hysteresis with increasing rh is thus explained by the filling of the original interface states.

The a.c. measurements confirmed these results. The complex impedance spectra of the hetero-contacts measured at 40°C under zero d.c. bias showed the presence of a depressed semicircle at all rh values, as shown in fig. 8, characteristic of a resistor and a capacitor in parallel. The higher the rh, the larger the depression of the semicircle. In comparison with d.c. measurements, little variation with rh was observed, in agreement with measurements being carried out under zero d.c. bias. It was observed that the EIS spectra were affected by the a.c. signal amplitude. The higher the signal amplitude, the lower the resistance of the specimen. This is probably due the greater influence of the a.c. bias at low frequencies. The results reported were obtained with a signal amplitude of 1 V. Given that the contributions of the semiconductors and of the semiconductor-electrode interfaces are merely resistive, as shown by the EIS measurements carried out on the single pellets, the semicircle can be attributed to the p-n junction interfaces. The strong frequency-dependence of the capacitance clearly showed the presence of interface states [21]. At high rh, the larger depression of the EIS spectra may be explained by non-

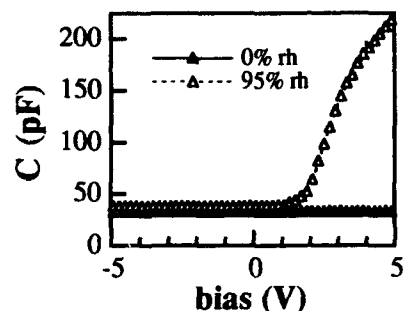


Fig. 7 High frequency (100 kHz) dark C-V characteristics of hetero-contacts at room temperature, at 0% and 95% rh.

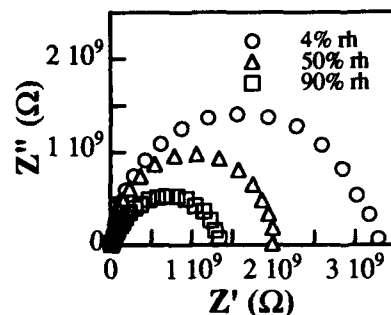


Fig. 8 Complex impedance plot for the $\text{La}_2\text{CuO}_4/\text{ZnO}$ hetero-contacts at 40°C , at various rh.

homogeneous saturation of the original interface states by physisorbed water, thereby resulting in slightly different relaxation times. The interface capacitance was calculated at the frequency where the maximum of the semicircle was found, i.e. 600 mHz at 4% rh, 400 mHz at 50% rh, and 80 mHz at 90% rh. It was affected by moisture: at 4%, 50% and 90% rh, evaluated at 0.13, 0.15, and 1.5 nF, respectively.

CONCLUSIONS

$\text{La}_2\text{CuO}_4/\text{ZnO}$ hetero-contacts are highly sensitive to rh. Their rh-sensitivity is due to phenomena occurring at the p-n oxide interface. The sensitivity is bias-dependent, with a maximum at about 2.5 V in forward bias. The diode behaviour of the hetero-contacts is to be explained in terms of pinning of the Fermi level from the interface states. The large rh-sensitivity may be explained in terms of the saturation of the original interface states by physisorbed water. With increasing rh, the forward current increases because of the release of trapped electrons caused by physisorbed water molecules. The role of electrolysis in the sensing mechanism needs further study.

The current versus rh sensitivity of the hetero-contacts can be as large as 4 orders of magnitude over the entire rh range, at 2.5 V. They show fast response, but problems in stability and

reproducibility are to be observed. In order to overcome these problems, the use of open hetero-junctions in thin-film form will be tested, together with the choice of a proper bias for the measurements.

ACKNOWLEDGMENTS

This work was supported partly by the Japan Society for the Promotion of Science (JSPS) and the National Research Council of Italy (CNR), under the auspices of their agreement of scientific co-operation, and partly by the CNR, under the auspices of the Targeted Project "Special Materials for Advanced Technologies".

REFERENCES

- 1 W. Göpel, New materials for gas sensors; pp. 14-16 in *Transducers '93*, IEE, Tokyo, Japan, 1993.
- 2 H. Kobayashi, K. Kishimoto, Y. Nakato and H. Tsubomura, Mechanism of hydrogen sensing by Pd/TiO₂ Schottky diodes, *Sens. Actuators B*, **13**, 125-27 (1993).
- 3 F.C. Lin, Y. Takao, Y. Shimizu and M. Egashira, Preparation and H₂ sensing properties of ZnO varistors gas sensors, *Denki Kagaku*, **61**, 1021-22 (1993).
- 4 Y. Nakamura, H. Yoshioka, M. Miyayama, H. Yanagida, T. Tsurutani and Y. Nakamura, Selective CO gas sensing mechanism with CuO/ZnO heterocontact, *J. Electrochem. Soc.*, **137**, 940-43 (1990).
- 5 J.P. Lukaszewicz, Diode-type humidity sensor using perovskite-type oxides operable at room temperature, *Sens. Actuators B*, **4**, 227-32 (1991).
- 6 S. Tsurumi, K. Mogi and J. Noda, Humidity sensors of Pd-ZnO diodes; pp. 661-64 in *Transducers '87*, IEE, Tokyo, Japan, 1987.
- 7 E. Traversa and A. Bearzotti, A novel humidity detection mechanism for ZnO dense pellets, submitted for publication to *Sens. Actuators B*.
- 8 K. Kawakami and H. Yanagida, Effects of water vapor on the electrical conductivity of the interface of semiconductor ceramic-ceramic contacts, *J. Ceram. Soc. Jpn.*, **87**, 112-15 (1979).

- 9 Y. Toyoshima, M. Miyayama, H. Yanagida and K. Koumoto, Effect of relative humidity on current-voltage characteristics of Li-doped CuO/ZnO junction, *Jpn. J. Appl. Phys.*, **22**, 1933 (1983).
- 10 Y. Nakamura, M. Ikejiri, M. Miyayama, K. Koumoto and H. Yanagida, The current-voltage characteristics of CuO/ZnO heterojunctions, *J. Chem. Soc. Jpn.*, 1154-59 (1985).
- 11 Y. Ushio, M. Miyayama and H. Yanagida, Fabrication of thin-film CuO/ZnO heterojunction and its humidity-sensing properties, *Sens. Actuators B*, **12**, 135-39 (1993).
- 12 J.G. Fagan and V.R.W. Amarakoon, Reliability and reproducibility of ceramic sensors: part III, humidity sensors, *Am. Ceram. Soc. Bull.*, **72** [3] 119-30 (1993).
- 13 H. Yanagida, Intelligent ceramics, *Ferroelectrics*, **102**, 251-57 (1990).
- 14 H. Yanagida, Intelligent materials - A new frontier, *Angew. Chem.*, **100**, 1443-46 (1988).
- 15 E. Traversa, M. Miyayama and H. Yanagida, Gas sensitivity of ZnO/La₂CuO₄ hetero-contacts, *Sens. Actuators B*, **17**, 257-61 (1994).
- 16 Y. Shimizu, H. Arai and T. Seiyama, Theoretical studies on the impedance-humidity characteristics of ceramic humidity sensors, *Sens. Actuators*, **7**, 11-22 (1985).
- 17 G. Gusmano, G. Montesperelli, E. Traversa and G. Mattogno, Microstructure and electrical properties of MgAl₂O₄ thin films for humidity sensing, *J. Am. Ceram. Soc.*, **76**, 743-50 (1993).
- 18 S.M. Sze, *Physics of Semiconductor Devices*; Ch. 2. Wiley, New York, 1981.
- 19 W. Platen, H.J. Schmutzler, D. Kohl, K.A. Brauchle and K. Wolter, Interface states of Ag/(110)GaAs Schottky diodes without and with interfacial layers, *J. Appl. Phys.*, **64**, 218-24 (1988).
- 20 Y. Ushio, M. Miyayama and H. Yanagida, Effects of interface states on gas sensing properties of a CuO/ZnO thin film heterojunction, *Sens. Actuators B*, **17**, 221-26 (1994).
- 21 K.K. Baek and H.L. Tuller, Electronic characterization of ZnO/CuO heterojunctions, *Sens. Actuators B*, **13**, 238-40 (1993).

PIEZOELECTRIC ACTUATOR RESPONSIVE TO ENVIRONMENTAL HUMIDITY

Yuji Isogai and Masaru Miyayama

Research Center for Advanced Science and Technology,
University of Tokyo, Tokyo, 153, Japan

Hiroaki Yanagida

Department of Industrial Chemistry,
University of Tokyo, Tokyo, 113, Japan

ABSTRACT

Bending behavior responsive to environmental humidity was investigated on a PZT actuator consisting of porous and dense PZT plates ($\text{Pb}_{0.995}\text{Nb}_{0.01}(\text{Zr}_{0.53}\text{Ti}_{0.47})_{0.99}\text{O}_3$). A dense PZT plate with a high electrical resistivity was bonded by hot-pressing with a porous PZT plate, which showed a large resistivity change from 10^{14} to $10^7 \Omega\text{cm}$ for a change of relative humidity from 5 to 85%. In such a structure, DC voltage applied to the bonded plate gives an electric field on both parts at a low humidity, but only on the dense part at a high humidity. A bending displacement responsive to a change of humidity was observed in the bonded PZT plates under DC bias. Bending mode was similar to that of an unimorph. The hot-pressing temperature affected the microstructure and humidity sensitivity of porous PZT plate, and as a result the bending behavior of the PZT actuator.

I. INTRODUCTION

Piezoelectric actuators have been used for many kinds of mechanical systems, such as VTR head actuators, dot-matrix printers and micro pumps. Should an actuator system be required to perform both the sensing and the actuating functions, a sensor and a processor element are needed in the system. It is known that the reliability of the system would be lowered by the excessive number of elements in the system. If the piezoelectric actuator itself

To the extent authorized under the laws of the United States of America, all copyright interests in this publication are the property of The American Ceramic Society. Any duplication, reproduction, or republication of this publication or any part thereof, without the express written consent of The American Ceramic Society or fee paid to the Copyright Clearance Center, is prohibited.

also had sensing function and a feed back function, the system could be simplified to a single element with higher reliability.

The objective of this study was to fabricate an atmosphere responsive actuator which would sense the change of humidity or the change of gas concentration, and respond by changing the value of deformation and displacement. In the present study, the actuator, which consists of a porous and a dense PZT plate, was prepared, and bending behaviors were observed in relation to the various relative humidities. A combination of sensing and actuating functions in the bonded PZT plates, which sense a change of environmental humidity and then induce a bending displacement, was discussed.

II. EXPERIMENTAL

(1) Specimen Preparation

PZT ceramics ($\text{Pb}_{0.995}\text{Nb}_{0.01}(\text{Zr}_{0.53}\text{Ti}_{0.47})_{0.99}\text{O}_3$) were prepared from reagent oxides (purity 99.9%) of PbO , Nb_2O_5 , ZrO_2 and TiO_2 . These powders were ball-milled and calcined in air at 850°C for 6 hours. The calcined powder was pressed into disks. Some of them were sintered in air at 1050°C for 2 hours to obtain dense samples. The dense PZT disk and the press-formed PZT disk were stacked and hot-pressed together in air at 750 – 795°C , under 8MPa. Before hot-pressing, glass frits were applied to the interface between dense PZT disk and press-formed PZT disk. The hot-pressed bulk, which has a change in density in the direction of the thickness, was cut, into test pieces, 3mm (width) x 11mm (length) x 1mm (thickness) in size, polished and electroded with silver paste at 500°C . The actuators were poled by applying a DC field of 7.5kV/cm at 25°C for 3 hour in the air. The single plates of dense and porous PZT with 5mm x 5mm x 1mm (thickness) in size were prepared in a similar manner in order to separately measure the humidity sensitivity of them.

(2) Measurement

The microstructure of the samples was observed with a scanning electron microscope (JEOL Co., LTD Model JSMT330A), and the pore size distribution of the porous sample was measured with a pore sizer (Shimadzu Co., LTD Model 9320). The single plates of dense and porous PZT were set into a chamber of 40cc. The DC electrical resistivities at 25°C under various humidities were measured using an electrometer (Advantest Co., LTD Model R8340A) which had a constant voltage supply within. The humidity at 25°C was controlled, from 5% to 85%, by mixing dry and wet air, saturated with water vapor. The total gas flow rate was 100cc/min. The humidity was checked with a humidity meter (Chino Co., LTD Model HN-K). The bending displacement induced by electric field of 0 ~ 4 kV/cm under various

humidities was measured using a photonic noncontact sensor (Ewig engineering Co., LTD Model 8500).

III. RESULTS

(1) *Structure*

Though a conventional piezoelectric actuator has nearly theoretical density, the actuator in the present study consists of porous and dense PZT plates which are both 0.5mm in thickness. The structure of the actuator is shown in Fig. 1 (a) and the microstructure at the interface is shown in Fig. 1 (b). Sharp changes in density and grain size were observed at the interface. The relative density and average grain size of porous and dense PZT plates sliced from bonded body, are shown in table 1. The distinct difference in density was observed at each PZT plate. Figure 2 shows the pore size distribution of porous PZT plate hot-pressed at 750°C. This porous PZT plate had a narrow pore-size distribution with average pore size of 0.30 μ m.

(2) *Humidity Sensitivity*

The humidity-resistivity characteristics of porous and dense PZT plates are shown in Fig. 3. These characteristics were measured under DC 50V in order to clarify the resistivity changes in the states by applying a fairly high DC voltage on the actuator in moist environments. The resistivities of porous PZT plates decreased tremendously with increasing humidity. Especially the porous PZT plate which was hot-pressed at 750°C, showed a large resistivity change from 10^{14} to $10^7 \Omega\text{cm}$, for a change of relative humidity from 5 to 85%. The resistivities of porous ceramics are generally influenced by adsorption and by the capillary condensation of water. The average pore size of the one hot-pressed at 750°C was 0.30 μ m. This suggests that this porous PZT plate could easily adsorb and condense water. The conduction mechanisms were assumed to be proton hopping between adsorbed water molecules, and ionic conduction of hydronium ions through the condensed water layer on the ceramics surface. These are quite similar many other porous ceramics.¹⁾²⁾ In contrast to the porous PZT plate, the dense PZT plate maintained a high resistivity (over $10^{13} \Omega\text{cm}$) up to R.H.70%. Under experimental conditions, the response time of resistivity to change in relative humidity was about 3 minutes. The value of resistivity generally became a little smaller with increasing applied DC field.

(3) *Displacement Characteristics*

Figure 4 shows the value of bending displacement versus applied electric field for the sample hot-pressed at 795°C at several humidities states. The displacements induced by electric field were observed, and the value of

displacement increased as relative humidity increased. Hysteresis in displacement during the change of the applied voltage, as observed in normal PZT actuators, were observed in the present study. Figure 5 shows the dependence of the displacement on relative humidity of the actuators treated at different temperatures. The sample which was hot-pressed at 750°C, exhibited a drastic change of displacement between R.H.10% and 20%, but changes at above R.H.30% were not large. However, the one hot-pressed at 795°C showed a continuous increase for an increase of relative humidity from 10 to 70%. The bending behavior was not stable over R.H.70%.

IV. DISCUSSIONS

Under DC bias, piezoelectric ceramics expanded in the direction of the applied field and shrunk in the direction perpendicular to that of the applied field. At a low humidity, both porous and dense parts of the actuator indicated high resistivity. The applied DC voltage gave an electric field on both parts. At a high humidity, most of the applied DC voltage was concentrated on the dense side because water adsorption on the porous side caused the decrease in resistivity at the porous side. Then bending behavior occurs because the amount of shrinkage in the longitudinal direction of dense part was more than that of the porous part. This bending mode was quite similar to that of an unimorph. The degree of bending displacement by applying 4kV/cm electric field at R.H.70% was nearly 5 times as much as that at R.H.10%, as shown in Figs. 5 and 6. The hot-pressing temperature was found to affect the microstructure and humidity sensitivity of porous PZT pate, and subsequently the bending behavior of the PZT actuator. The behavior of bending displacement became unstable over R.H.70%. It was assumed to be resultant from the dew at the edge of the dense plate, which due to current leakage, disturbed the constant applied electric field.

A simple model for bending in an actuator consisting of two plates with a same thickness, was introduced.³⁾

$$x_d = d_{31d} E_d / t_d \quad (1.1)$$

$$x_p = d_{31p} E_p / t_p \quad (1.2)$$

where d_{31} , E and t are the piezoelectric strain constant, the applied electric field ratio and thickness of PZT plate, respectively (in this case $t_d = t_p$). Subscripts d and p indicate dense and porous PZT plate. The degree of bending displacement (d) is given in Eq. 2.

$$d = 3L^2V(x_d - x_p)Y_p/d / (t_d + t_p)(1 + Y_p/d)^2 \quad (2)$$

$$Y_p/d = Y_p / Y_d$$

where L , V and Y are length of plate, applied voltage and young's modulus respectively.

At a high humidity, it was assumed that applied electric field concentrated only on the dense part of the PZT actuator; that is $x_p = 0$. The value of bending displacement (d) which occurred under DC 400V was calculated by substituting the following values into Eq. 2.; $E_d = 1$, $E_p = 0$, $V = 400$ (v), $L = 11 \times 10^{-3}$ (m), $t_d = t_p = 0.5 \times 10^{-3}$ (m), $d_{31d} = -130 \times 10^{-12}$ (m/v) and Y_p/d

= 0.6. The values of $d_{31}d$ and Y_p/d were estimated from the reference 4.⁴⁾ The calculated value, was about $9\mu\text{m}$, and approximately agreed with the measured value ($11\mu\text{m}$).

Equation 2 shows that the value of bending displacement (d) varied in proportion to the square length of the actuator (L^2), and inversely to the total thickness ($t_d + t_p$). If an actuator with size of $35\mu\text{m}$ length, 0.5mm total thickness were prepared, it would be assumed to show over $100\mu\text{m}$ bending displacement under 200 DC volts at a high humidity.

A piezoelectric actuator which had both of the humidity sensing function and the actuating function was developed by combination of porous and dense PZT plates. Such a device element is expected to simplify the system and to improve the reliability of the system.

V. CONCLUSIONS

- 1) The humidity responsive PZT actuator, which consisted of porous and dense PZT plates, with size of 3mm (width) \times 11mm (length) \times 1mm (thickness), showed a value of bending displacement from 2 to $11\mu\text{m}$ with increasing humidity from 10 to 70% , under 4kV/cm electric field.
- 2) The hot-pressing temperature affected the microstructure and humidity sensitivity in porous part of PZT actuator, and subsequently the bending behavior of PZT actuator.
- 3) A simple model was applied to the actuator consisting of two plates with the same thickness. The calculated bending value at a high humidity approximately agreed with the experimental value.

References

1. T. Nitta, Z. Terada and S. Hayakawa, "Humidity-Sensitive Electrical Conduction of $\text{MgCr}_2\text{O}_4\text{-TiO}_2$ Porous Ceramics" J. Am. Ceram. Soc., 63[5-6]295-300 (1979)
2. H. Arai, "Humidity Sensor" Denki Kagaku, 15[1]38-45 (1982)
3. T. Kawai, "Functionally Gradient Material for Measurement and Instrumentation" Ceramics, 24[10]975-979 (1989)
4. H. Banno, "Effects of Shape and Volume Fraction of Closed Pore on Dielectric, Elastic, and Electromechanical Properties of Dielectric and Piezoelectric Ceramics" Am. Ceram. Soc. Bull., 66[9]1332-37 (1987)

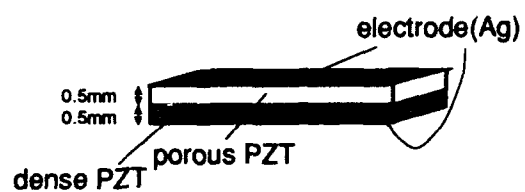


Fig. 1 (a). A schematic illustration of actuator.



Fig. 1 (b). Scanning electron micrograph of the interface between porous and dense PZT plates.

Table 1. Relative density and average grain size of porous and dense PZT plates.

Specimen	Relative density	Average grain size
Porous PZT plate (hot-pressed at 750°C)	62 %	0.6 μm
Porous PZT plate (hot-pressed at 795°C)	78 %	0.6 μm
Dense PZT plate	98 %	1.3 μm

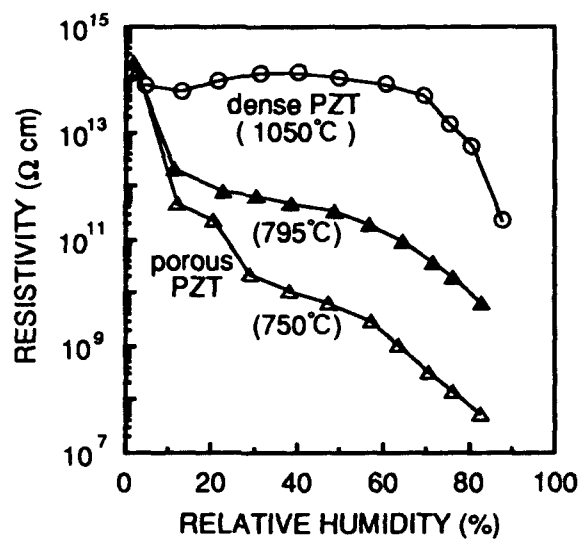


Fig. 2. Humidity sensitivity of porous and dense PZT plates under DC 50V at 25°C.

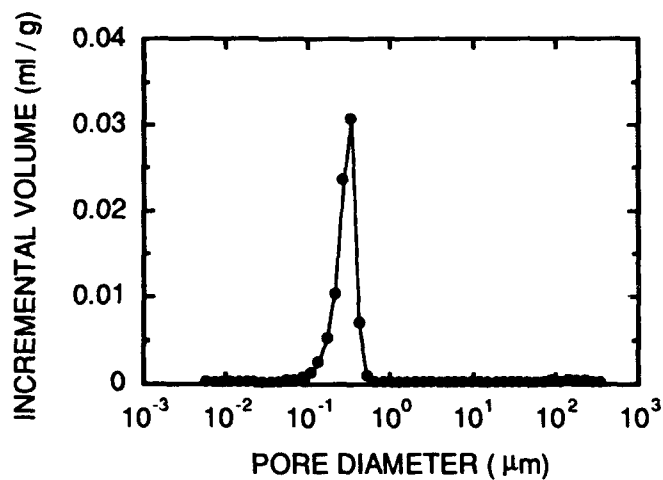


Fig. 3. Pore size distribution of porous PZT hot-pressed at 750°C.

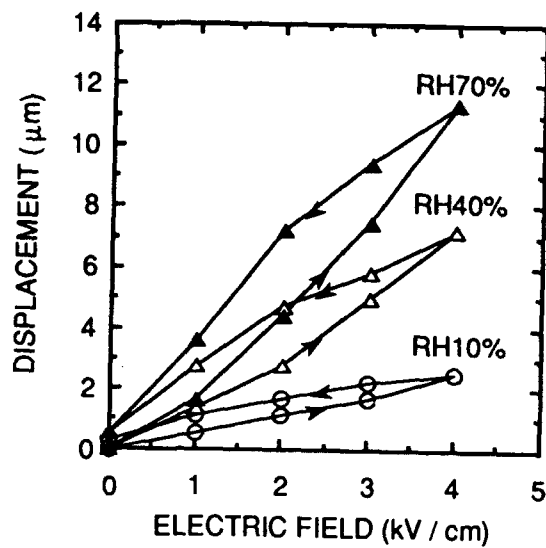


Fig. 4. Displacement versus applied electric field for actuator hot-pressed at 795°C.

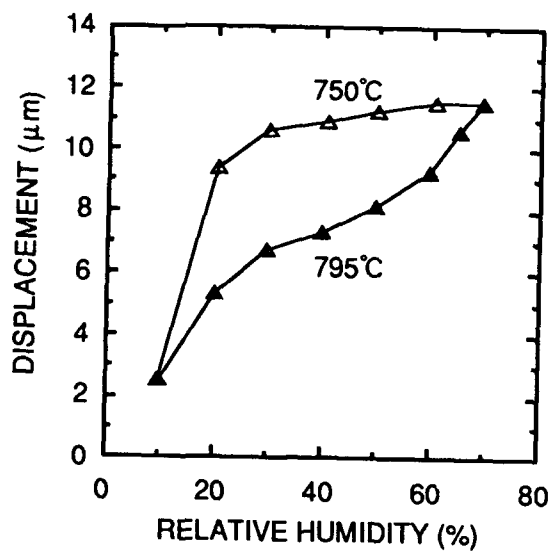


Fig. 5. Displacement as a function of relative humidity at 4kV/cm.

PIEZORESISTIVE CERAMIC SENSOR BASED ON PTCR BARIUM TITANATE

Joseph S. Capurso*, Aldo B. Alles, and Walter A. Schulze*
New York State College of Ceramics at Alfred University, Alfred, New York 14802

High purity, chemically prepared barium titanate was doped with 0.3 atom% La and 0.04 atom% Mn by precipitation. Using standard techniques, tape-cast sheets of the PTCR composition as well as the base insulating powder were made. A three-layer sensor was laminated with the upper and lower PTCR layers separated by an insulating BaTiO₃ layer. After binder burnout, the device was sintered at 1350°C in flowing N₂ followed by cooling in flowing O₂ at 300°C/hour. The sensor was loaded using a standard four-point bend test configuration. The change in resistivity with increasing load was observed to be linear, with positive and negative piezoresistive coefficients for the PTCR layers under compression and tension, respectively. These trends are in general agreement with the Heywang-Jonker model of grain boundary potential barriers.

I. INTRODUCTION

Positive temperature coefficient of resistance (PTCR) barium titanate is a well-studied material which exhibits a large increase in resistivity over a relatively small temperature range beginning at its Curie temperature (T_C). This phenomenon was first observed in the mid-1950's,¹ and was explained by Heywang in terms of a double Schottky potential barrier existing at the boundaries between semiconducting BaTiO₃ grains.² Below T_C , these barriers are partially compensated by the directional mismatch of ferroelectric domains terminating at the grain boundary, according to Jonker.³ The barrier was described as a two-sided electron depletion region of some finite thickness $2b$ (cm). The number of electrons trapped at the grain boundary per unit area, n_s (cm⁻²), is equal to the barrier thickness multiplied by the number of conduction electrons per unit volume, n_0 (cm⁻³):

$$n_s = 2bn_0$$

Supported by the Army Research Office, U.S. Department of Defense, under Grant No. DAAL03-92-G-0374.

* Member, American Ceramic Society.

To the extent authorized under the laws of the United States of America, all copyright interests in this publication are the property of The American Ceramic Society. Any duplication, reproduction, or republication of this publication or any part thereof, without the express written consent of The American Ceramic Society or fee paid to the Copyright Clearance Center, is prohibited.

When combined with Poisson's equation describing potential (V) as a function of charge density ($\rho_v = en_o$) and permittivity ($\epsilon = \epsilon_r \epsilon_o$):

$$\nabla^2 V = \frac{\rho_v}{\epsilon} = \frac{en_o}{\epsilon_r \epsilon_o}$$

an expression for barrier height (ϕ_o) is obtained:

$$\phi_o = \frac{en_o^2}{8\epsilon_r \epsilon_o n_o}$$

Relative permittivity (ϵ_r) for paraelectric BaTiO₃ (above T_c) follows the Curie-Weiss law⁴:

$$\epsilon_r = \frac{C}{T - \theta}$$

where C and θ are constants. Samara⁵ showed that an analogous hydrostatic pressure dependence exists above T_c :

$$\epsilon_r = \frac{C'}{P - P_o}$$

The resistivity of BaTiO₃ ceramic with z grains per unit length is:

$$\rho = \rho_b \left(1 + \frac{z b k T}{e \phi_o} e^{\frac{e \phi_o}{k T}} \right)$$

where ρ_b is the resistivity of the bulk ($\Omega \cdot \text{cm}$).

Relatively little attention has been focused on the piezoresistive effect in PTCR barium titanate. Early investigations of the pressure sensitivity of semiconducting BaTiO₃ disks^{6,7} indicated that piezoresistivity is maximized at temperatures near T_c in the paraelectric state under uniaxial compressive stress, although discrepancies in the direction (sign) of

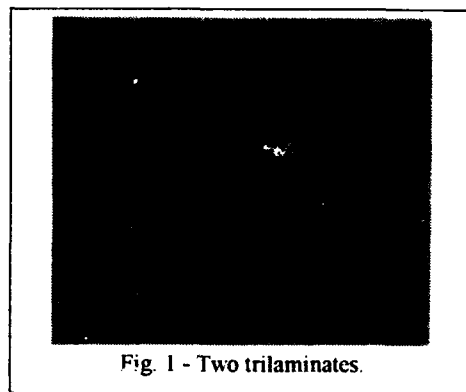


Fig. 1 - Two trilaminates.

AD-A285 937

FERROIC MATERIALS: DESIGN PREPARATION AND
CHARACTERISTICS. CERAMIC TRANSAC. (U) AMERICAN CERAMIC
SOCIETY INC WESTERVILLE OH A S BHALLA ET AL.

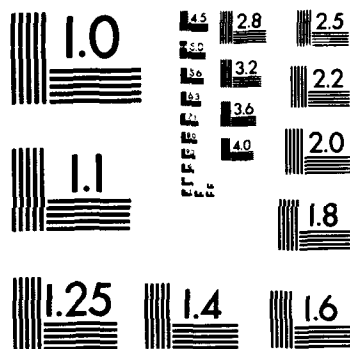
575

UNCLASSIFIED

10 NOV 93 XB-OWN N00014-93-1-0366

NL

END
FILMED
DTIC



MICROCOPY RESOLUTION TEST CHART
 NATIONAL BUREAU OF STANDARDS
 STANDARD REFERENCE MATERIAL 1010a
 (ANSI and ISO TEST CHART No. 2)

resistance change were seen. More recent work⁸⁻¹⁰ further reinforces the concept of piezoresistivity being due to the sensitivity of ϵ_r to temperature and pressure near T_c through its effect on the magnitude of grain boundary potential barriers.

In this work, four-point bending will be used to apply stress to a *trilaminate* structure¹¹, which consists of two layers of PTCR barium titanate separated by a relatively thick layer of insulating BaTiO_3 . Using this configuration, the effect of pressure on resistivity in both the compression and tension modes can be observed. A photograph of two trilaminates is shown in figure 1.

II. PROCESSING

Trilaminates are produced by laminating tape-cast sheets of barium titanate together to form a relatively thick structure which can withstand a moderate mechanical stress. The composition of the trilaminate with respect to its thickness is determined by the stacking sequence of tape layers, which are either insulating or semiconducting. Insulating tape is produced from as-received powder, while semiconducting tape consists of the same powder plus precipitated dopants.

Dopant Incorporation

The method of dopant addition is critical to the synthesis of PTCR materials, since very low levels of impurities must be extremely well-dispersed in the BaTiO_3 host material to ensure homogeneity of electrical properties and microstructure. Typical dopant levels for the PTCR material used in this work are 0.3 atom% lanthanum and 0.04 atom% manganese. Lanthanum (La^{3+}) replaces Ba^{2+} in the perovskite lattice, forcing the reduction of Ti^{4+} to Ti^{3+} and the liberation of a conduction electron, thus causing semiconductivity. The addition of manganese results in the formation of deep acceptor traps at the grain boundaries, enhancing the PTCR effect.

The dopants are added to an aqueous slurry of BaTiO_3 particles as soluble nitrates. Excess CO_3^{2-} ions in the slurry cause the La and Mn ions to be precipitated as carbonates over a 24-hour ball milling cycle. Gelation of polyvinyl alcohol (PVA) dissolved in the slurry (when the slurry is poured into an ethanol bath) causes the formation of a sponge-like mass which locks the precipitated dopant particles into position relative to the larger BaTiO_3 grains, thus preventing segregation and maintaining dispersion. The sponge-like material is drained of excess liquid, then calcined for 2 hours at 700°C to eliminate the PVA. This has proven to be an adequate measure to sufficiently bond the precipitated dopants to the BaTiO_3 grains, ensuring homogeneity throughout the remainder of the process.

Trilaminate Fabrication

The doped powder is redispersed in an ethanol/toluene-based polyvinyl buterol binder vehicle, and ball milled for 24 hours. This slurry is then de-aired, and cast onto

a Teflon[®] surface using a standard double doctor blade process. Cast velocity is 1.5 cm/s, with the final blade set at 0.5 mm. Constant air flow is maintained during drying, which takes place at room temperature. Dried tape thickness is typically 0.1 to 0.2 mm (4 to 8 mils). An identical procedure is used to produce undoped tape.

The tapes are cut to a blank size of 2"x1 1/4", then stacked to 36 layers (9 doped, 18 undoped, 9 doped). The stack is laminated at 2500 psi at 80°C for three minutes, then cut into rectangular bars with typical dimensions of 45x10x4 mm.

Burnout/Sintering

The trilaminate bars are sintered in a tube furnace, using the profile shown in figure 2. The binder burnout portion of the profile was developed from thermogravimetric analysis of the tape binder, and consists of 20°C/hour ramps to 300°C (point of maximum weight loss) and to 400°C (end of weight loss). The profile then proceeds at 3°C/minute to a one-hour hold at 1350°C. To employ liquid-phase assisted sintering, a Ti-excess powder must be used (in this case, Ba/Ti=.992), together with a sintering temperature above the 1322°C liquidus.¹² Cooling rates can be varied to adjust the amount of grain boundary oxidation required.

Oxygen is passed through the tube furnace at a rate of 1°C/minute to aid in binder removal, and also to help remove any residual carbonates left over from the powder-making process. At 1250°C, the gas is switched to nitrogen, which promotes grain growth by forming oxygen vacancies in the BaTiO₃ lattice, thus enhancing diffusional transport. The gas is switched back to oxygen after 45 minutes of the peak hold, to enhance the PTCR effect by oxidizing the grain boundaries (forming electron traps).

Trilaminate densities are in the range of 94% to 96% of theoretical (6.017 g/cc), with

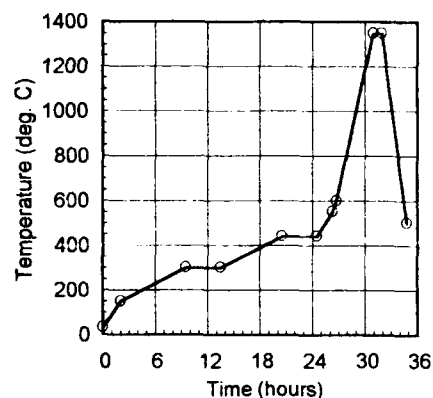


Fig. 2 - Sintering profile.

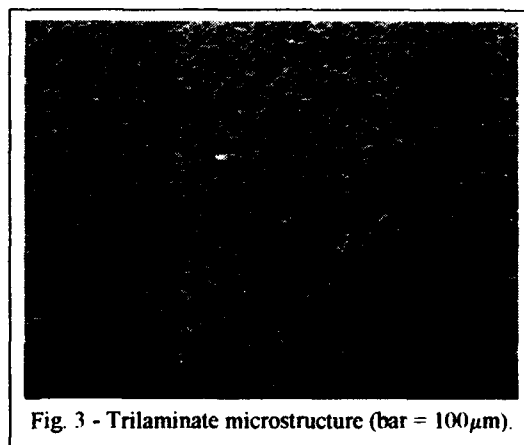


Fig. 3 - Trilaminate microstructure (bar = 100μm).

shrink factors (dimensional ratio: green/fired) of $1.20 \pm .01$. A typical trilaminate microstructure is shown in figure 3. Note that the semiconducting material has a significantly larger grain size (40 to 60 μm) than the insulating material (10 to 30 μm), and that the semiconductor/insulator interfaces are very well defined. Implantation of platinum shavings between tape layers confirms that the interface does not move significantly upon sintering.

III. TESTING

The four-point bend configuration is used to stress the trilaminate. This configuration provides a region of constant stress between the two inner contact points (see fig. 4). Electrical contact to the trilaminate is made by evaporating aluminum metal onto either side, leaving a gap on each surface which is well within the region of constant stress.

Note that the upper semiconducting layer is in compression only, since it lies completely above the plane of zero stress. This layer undergoes a volumetric decrease, resulting in an overall constriction of unit cells and thus a decrease in relative permittivity (ϵ_r). Conversely, the lower semiconductor layer is strictly in tension, experiences a volumetric increase, an expansion of unit cells and therefore an increase in ϵ_r . From Heywang's model (described earlier), one would therefore expect a resistivity increase in compression and a decrease in tension, due to the effect of ϵ_r on the barrier magnitude.

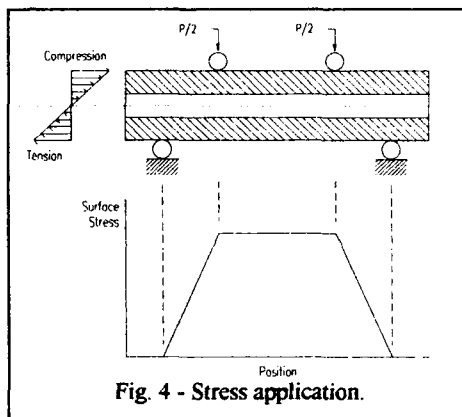


Fig. 4 - Stress application.

IV. PRELIMINARY RESULTS AND DISCUSSION

To evaluate the effectiveness of the dopant incorporation process, disks were produced and their PTCR responses measured. Figure 5 shows the effect of Mn dopant level: it can be seen that a very slight change in this level has a dramatic effect on the slope of the PTCR curve. Also, an optimum level of 0.04 atom% Mn is apparent, in terms of maximizing the resistivity jump and minimizing room temperature resistivity. Higher levels of Mn cause an excess of acceptor states at the grain boundary and thus reduce the effectiveness of domain compensation. The effect of annealing conditions is also shown (fig. 6). As the cooling ramp rate is decreased, the oxidation of grain boundaries is enhanced; providing more acceptor states and resulting in a sharper PTCR

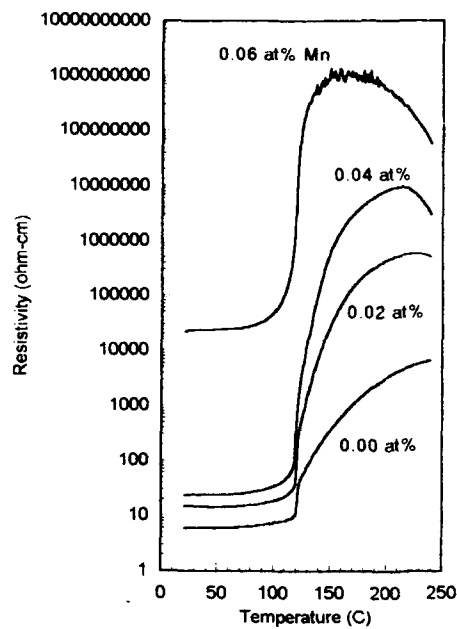


Fig. 5 - PTCR response vs. Mn level (-5° C/min.).

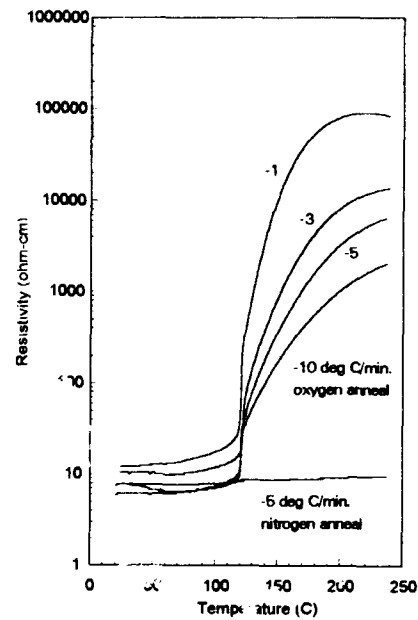


Fig. 6 - PTCR response vs. cooling rate (0.00 atom% Mn).

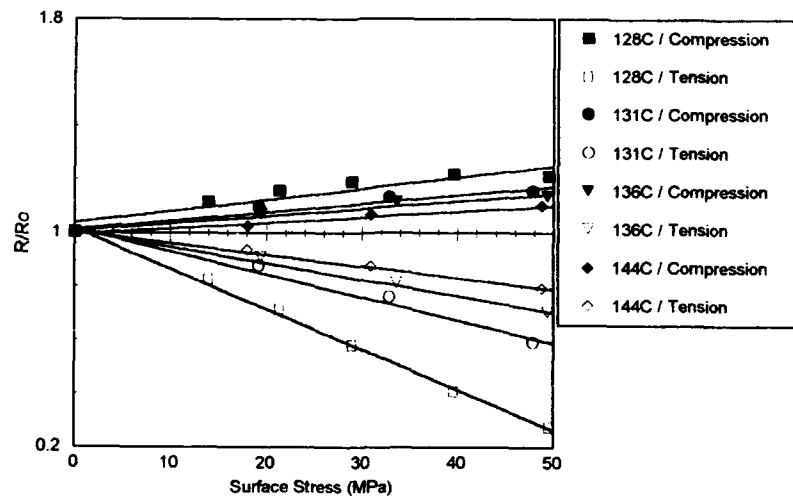


Fig. 7 - Trilaminate piezoresistive response at several temperatures.

effect. Note that PTCR behavior can be completely suppressed by cooling in reducing conditions. It can therefore be seen that the shape of the PTCR curve can be dictated by use of two processing levers: Mn dopant concentration and annealing conditions.

The piezoresistive response of the trilaminate is shown in figure 7, for several temperatures. Note that in all cases, the resistance ratio (resistance at pressure divided by unstressed resistance) is greater than one in compression and less than one in tension, substantiating the arguments stated previously. Also note that the responses are linear, and are more pronounced in tension.

It can be seen that the piezoresistive effect is reduced in magnitude as the temperature is raised further above T_C (123°C). This is yet another confirmation that piezoresistivity is a result of changing relative permittivity, since ϵ_r is most sensitive to pressure and temperature changes as T_C is approached from above, according to the Curie-Weiss dependencies. The temperature dependence of ϵ_r is illustrated in figure 8 for undoped barium titanate.

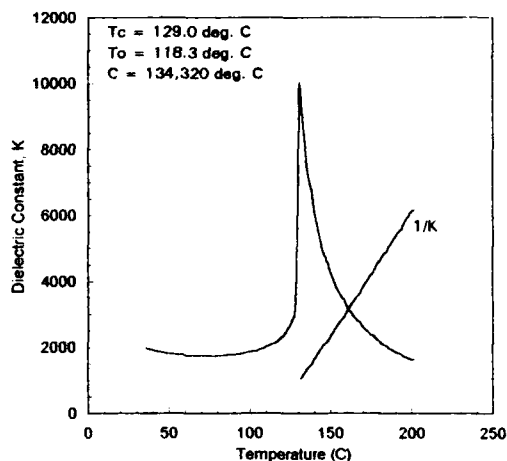


Fig. 8 - Dielectric constant vs. temperature for undoped BaTiO₃.

V. SUMMARY

A new type of pressure sensor based on barium titanate - the *trilaminate* - has been described. Trilaminate processing has been discussed in terms of dopant incorporation, tape fabrication, and sintering conditions. The piezoresistive response of the trilaminate is in sign agreement with Heywang's model, and is more pronounced at temperatures approaching the Curie point from above, indicating that the basic mechanism responsible is a change in the relative permittivity of the material in the vicinity of grain boundaries. It was also seen that the PTCR response of semiconducting BaTiO₃ can be engineered through variation of the manganese dopant level and of annealing conditions.

VI. WORK IN PROGRESS

- Investigation of pressure effects below T_C (in the ferroelectric regime).
- Modeling of the apparent linear piezoresistive response of trilaminate structures.

- Determination of the link between piezoresistivity and PTCR response, i.e. the effect of mean acceptor level (type of dopant) and density of states (annealing conditions).
- Measurement of elastic moduli vs. composition and temperature.
- Examination of microstructural development vs. sintering conditions.
- A revisitation of disk piezoresistivity under uniaxial compression.
- Investigation of grain size effects on trilaminate performance.

Acknowledgments: We wish to acknowledge the generosity of the Transelco Division of Ferro Corp. (Penn Yan, NY) for donation of BaTiO₃ powders, to Palomar-MSI (San Diego, CA) for provision of tape casting organics, and to Texas Instruments (Attleboro, MA) for information on testing. Thanks also go to J. Thiebaud, Dr. V. Amarakoon, Dr. W. Bentz, Dr. V. Burdick, Dr. W. Carlson, D. Hoelzer, Dr. J. Reed, and Dr. J. Varner for their help and advice. Finally, the efforts of A. Ormsby, D. Green, and A. Baker in constructing the various pieces of processing equipment required for this work are gratefully acknowledged.

References

1. P.W. Haayman, R.W. Dam, and H.A. Klasens, "Method of Preparation of Semiconducting Materials," West German Patent 929,350, June 23, 1955.
2. W. Heywang, "Barium Titanate as a Semiconductor with Blocking Layers," *Solid State Elec.*, **3** [1] 51-8 (1961).
3. G.H. Jonker, "Some Aspects of Semiconducting Barium Titanate," *Solid State Elec.*, **7**, 895-903 (1964).
4. B. Jaffe, W.R. Cook, Jr., and H. Jaffe, *Piezoelectric Ceramics*, p. 77, Academic Press, New York, 1971.
5. G. Samara, "Pressure and Temperature Dependences of the Dielectric Properties of the Perovskites BaTiO₃ and SrTiO₃," *Phys. Rev.*, **171** [2] 378-86 (1966).
6. H.A. Sauer, S.S. Flaschen, and D.C. Hoesterey, "Piezoresistance and Piezocapacitance Effects in Barium Strontium Titanate Ceramics," *J. Am. Ceram. Soc.*, **42** [8] 363-6 (1959).
7. O. Saburi, "Piezoresistivity in Semiconductive Barium Titanates," *J. Phys. Soc. Japan*, **15** 733-4 (1960).
8. H. Igarashi, M. Michiue, and K. Okazaki, "Anisotropic Resistivity Under Uniaxial Pressure in PTC Ceramics," *Jpn. J. Appl. Phys.*, **24** [suppl. 24-2] 305-7 (1985).
9. A. Amin and M.B. Holmes, "Pressure and Temperature Dependencies of the Direct-Current Resistance of Semiconducting (Ba,Sr)TiO₃ and (Ba,Pb)TiO₃," *J. Am. Ceram. Soc.*, **71** [12] C482-3 (1988).
10. A. Amin, "Piezoresistivity in Semiconducting Positive Temperature Coefficient Ceramics," *J. Am. Ceram. Soc.*, **72** [3] 369-76 (1989).
11. A.B. Alles and W.A. Schulze, "Piezoresistive Sensor," United States Patent 5,225,126, July 6, 1993.
12. D.E. Rase and R. Roy, "Phase Equilibria in the System BaO-TiO₂," *J. Am. Ceram. Soc.*, **38** [3] 102-13 (1955).

EFFECT OF TOP METALLIZATION ON THE DIELECTRIC AND FERROELECTRIC PROPERTIES OF SOL-GEL DERIVED PZT THIN FILMS

G. Teowee, C.D. Baertlein,
Donnelly Corp., 4545 E. Fort Lowell Rd, Tucson, AZ 85712

E.A. Kneer, J.M. Boulton and D.R. Uhlmann,
Arizona Materials Laboratories, Department of Materials Science and
Engineering, Tucson, AZ 85712

INTRODUCTION

Lead zirconate titanate (PZT) is a widely explored ferroelectric (FE) material utilized in a wide range of applications [1]. It is a solid solution containing lead titanate (PT) and lead zirconate (PZ) in various stoichiometric ratios. PZT x/y refers to $\text{Pb}(\text{Zr}_{x/100}\text{Ti}_{y/100})\text{O}_3$ where $x, y \leq 100$ and $x+y=100$. In the PZ-PT phase diagram, the rhombohedral-tetragonal boundary is the most important feature, termed the morphotropic phase boundary (MPB). It is located at about 53 atom % Zr, 47 atom % Ti (PZT 53/47). The dielectric constant, electromechanical coupling factor and piezoelectric coefficients achieve their maximum values here [1].

The PZT-substrate interface has been reported to affect significantly the FE properties and specifically the fatigue behavior [2]. The bottom electrode (or the substrate) is typically a noble metal, namely Pt and/or Au which is inert towards oxidation. Oxide electrodes, namely RuO_2 , have attracted considerable recent attention [e.g., 3]. Such electrodes were reported to yield excellent fatigue-free PZT films up to 10^{10} cycles. In an earlier study, Fraser and Maldonado [4] compared the fatigue behavior of bulk PLZT ceramics with various metal electrode and found that In offered the best fatigue performance (up to 10^9 cycles).

To the extent authorized under the laws of the United States of America, all copyright interests in this publication are the property of The American Ceramic Society. Any duplication, reproduction, or republication of this publication or any part thereof, without the express written consent of The American Ceramic Society or fee paid to the Copyright Clearance Center, is prohibited.

Different metals are characterized by different values of work function, which in turn impact the nature of the metal-PZT junction, i.e., whether it is ohmic, non-ohmic or injecting. Values of the work function of various top metal electrodes are shown in Table I.

Table I. Work Functions of Various Top Metal Electrodes [5].

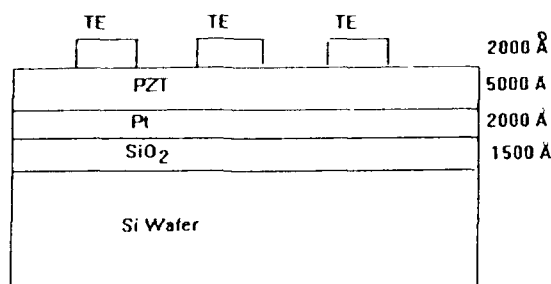
Metal	Work Function (eV)
Ag	4.54
Al	4.25
Au	5.31
Bi	4.22
Cr	4.50
Cu	4.64
In	4.12
Mg	3.66
Ni	5.19
Pb	4.25
Pd	5.36
Pt	5.50
Sn	4.42
V	4.30
Zn	4.62

The degree and extent of interdiffusion at the interface are determined by the post-metallization annealing performed (if any), which has been reported to enhance the overall FE properties [6]. There is presently a lack of studies directed to exploring systematically the effect of different metallization on thin film FE capacitors. In contrast, there have been numerous studies forming ohmic contacts to bulk FE or titanate ceramics using e.g., Ni, Ag/Zn, Cu and Co/Ag [7,8]. By varying the top metallization while maintaining the lower substrate constant (namely Pt), the nature of the top metal-PZT interface can be determined especially by charging the polarity of the applied field. The present paper presents the results of using various top metal electrodes (ranging from noble to non-noble metals) on the dielectric and FE properties of sol-gel derived PZT thin films.

EXPERIMENTAL

The precursor solutions based on the MPB composition (namely PZT 53/47) were prepared using Pb acetate and Ti/Zr alkoxides. Fifteen mole % excess PbO was incorporated in the precursor to compensate for PbO loss during post-deposition annealing. The substrates were Si(100) wafers which had been thermally oxidized before being sputtered with Pt to yield Pt(2000Å)/SiO₂(1500Å)/Si. Spin coating was performed in a Class 100 clean room using a Headway Spinner at 2000 rpm for 30s. The precursor solution was filtered using a syringe filter (0.2 μm) to minimize particle contamination. The green films were fired at 400C to burn off the organics, yielding films ~1700Å thick per coating. To obtain thicker films, multiple coatings were performed. Typically three coatings were used to obtain films about 0.47 μm thick. Finally, the films were fired at 700C to crystallize them to single-phase perovskite.

Top electrodes of Ag, Al, Au, Bi, Cr, Cu, Mg, Ni, Pb, Pd, Sn, V and Zn with thicknesses of 1500Å and diameters of 0.5-2 mm were evaporated through a shadow mask using a Varian Vacuum Evaporator VEIO. The top Pt electrodes were sputtered. The monolithic PZT capacitors were completed by obtaining back-contact by acid-etching exposed portions of the films which had been coated with an acid resist. The acid resist was removed by rinsing with toluene. The final device configuration for the capacitor arrays is shown in Figure 1. During measurement of leakage current, the Pt substrate was always maintained as reference ground and the top metal electrode positive or negative with respect to Pt.



TE= Top Electrode

Figure 1. Device Configuration of the Top Metal-PZT-Pt Capacitor

The phase assembly in the films was monitored by X-ray diffraction (XRD) using a Scintag Diffractometer; the dielectric properties were obtained using a HP 4192A LF Impedance Analyzer; the FE properties were measured using a Radiant Technologies RT-66A Ferroelectric Tester; and the I-V leakage characteristics were obtained using a Keithley 617 electrometer at both polarities with 0.2V step and 16s delay time. The fatigue and retention behaviors of these capacitors will be reported in another paper [9].

RESULTS AND DISCUSSION

XRD results indicated that the PZT 53/47 films fired at 700C for 30 min. were single-phase perovskite and hence ferroelectric in nature. The values of dielectric constant, ϵ_r , and dissipation factors, $\tan \delta$, obtained from the impedance analyzer from various capacitor pads with various diameters ranging from 0.5-2 mm indicated that the dielectric properties were independent of electrode diameter. Measured ϵ_r 's and $\tan \delta$'s at 1V 1kHz signal as a function of the top electrode metal are shown in Table II.

Table II. Dielectric Constant, ϵ_r , and Dissipation Factor, $\tan \delta$ measured at 1V and 1kHz Signal.

Metal	ϵ_r	$\tan \delta$
Ag	870	0.11
Al	300	0.14
An	840	0.11
Bi	1300	0.14
Cu	940	0.11
In	520	0.10
Mg	840	0.10
Ni	950	0.10
Pb	800	0.15
Pt	1780	0.10
Sn	770	0.10
Zn	910	0.10

Note that the data in Table II were derived from capacitors which were not subjected to any post-metallization annealing. The values of ϵ_r were dependent on the choice of top metallization, and ranged from 300-1780. On the other hand, the values of $\tan \delta$ were *relatively independent of the top metal*, averaging about 0.12. The noble metals (e.g., Au and Pt) and transition metals (e.g., Bi, Cu and Zn) tended to result in capacitors with high ϵ_r values (>800), while reactive metals (e.g., Al or In) yielded low ϵ_r values (300-500).

The typical band gap, E_g , and electron affinity, χ_{PZT} , for a PZT film are about 3.5eV and 1.75eV respectively [10]. For a p-type PZT film (as for PZT ceramics), the Fermi level, E_f , lies closer to the valence band, E_v , than to the conduction band E_c (see Fig. 2).

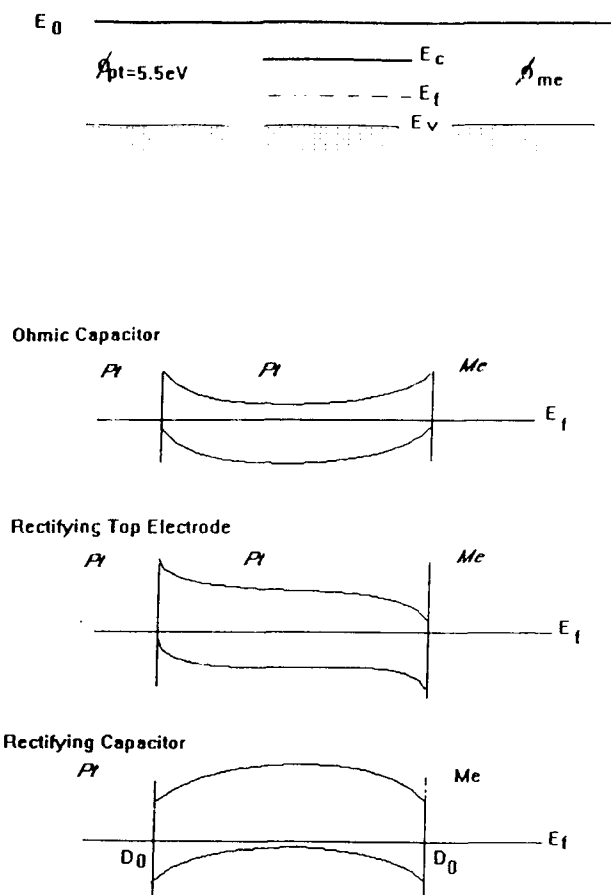


Figure 2. Energy Band Diagram of Pt, PZT and Pt-PZT-Metal Capacitor

The maximum work function of p-type PZT is then 4.25eV. Since the work function of Pt ($\phi_{Pt} = 5.5\text{eV}$) is higher than that of PZT, the Pt-PZT contact should be ohmic. In fact metals with work functions higher than that of PZT - such as Au (5.31eV), Ni (5.19eV), Pd (5.36eV) and Cu (4.64eV) - are expected to yield ohmic contacts; while metals with similar or lower work functions than 4.25eV - namely Al (4.25eV), In (4.72eV) and Mg (3.66eV) - should result in rectifying contacts. It is expected that for Pt-PZT-Pt, Pt-PZT-Au or Pt-PZT-Ni, the capacitors should be ohmic (see Fig. 2). These assumptions are based solely on the difference of the work functions; and it is recognized that the nature (e.g. interdiffusion, defects, interfacial surface states and the presence of oxide paraelectric interfacial layers) can affect significantly the junction characteristics.

The I-V characteristics were time-dependent, i.e., the currents did not decrease and saturate to stable readings until up to 1024s after application of voltages. Note that a delay time of 16s was used to measure these currents, thus the leakage currents measured did not necessarily reflect the true leakage processes involved. However, in microelectronics applications, long delay times are not practical. Hence, the leakage currents measured here are meant to compare the effect of top electrodes.

The I-V leakage characteristics at both polarities of all the capacitors with various top metallizations indicate, irrespective of top electrodes, that the contacts were not ohmic. Rather, the current varies logarithmically with the applied voltage. This current dependence is not a simple case of either Schottky emission or space - charge limited conduction. After an initial dramatic increase of current at small voltages, the current seems to saturate at higher voltages (see e.g. Figs. 3a and b).

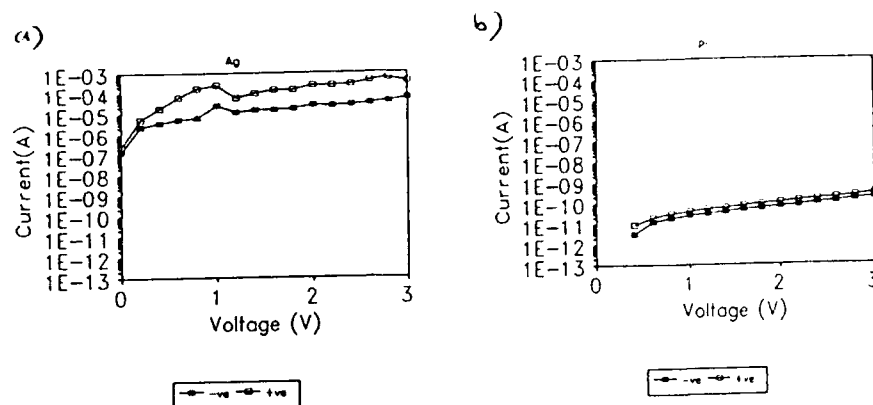


Figure 3. The Leakage Current Vs. Negative and Positive Voltage of PZT Capacitors (area = $1.96 \times 10^{-3} \text{ cm}^2$) having A) Ag, and B) Pt Top Electrodes.

The only case where the contacts can be rectifying is in the presence of surface states (arising, e.g., from adsorbed oxygen at the PZT surface and/or termination of the PZT crystalline lattice at the metal contacts). These surface states with a density of D_0 and a neutral energy level at E_0 result in band bending near the contacts and barrier heights of ϕ_b at the interfaces. The barrier heights at the two interfaces are, most often than not, different from each other. Such a situation arises when the top and bottom electrodes are of different metals (hence different work functions) or undergo different firing treatments resulting in dissimilar junction characteristics. These surface states would also depend on the top electrodes used, and in particular are affected by the affinity of the metal towards oxygen which could impact on the adsorbed oxygen at the interface.

The I-V characteristics also exhibited a strong dependence not only on the polarity but also on the top metallization used. Figs. 3a and b show the leakage currents as a function of applied voltage for PZT capacitors with Ag and Pt top electrodes, respectively, at both polarities. While the difference in the leakage currents of positively and negatively biased (with respect to the Pt substrate) PZT capacitors was only about a factor of 10, the leakage characteristics can differ by 7 orders of magnitudes depending on the top electrode. The leakage currents at an applied voltage of 3V (or an applied field of $\sim 65 \text{ kV/cm}$) of the various capacitors are shown in Table III.

Table III. Leakage Currents at an Applied Voltage of +3V and -3V of PZT Capacitors with Different Top Electrodes.

Top Metal	I (at +3V) A	I (at -3V) A
Ag	3.53×10^{-4}	5.5×10^{-5}
Al	8.45×10^{-11}	4.94×10^{-11}
Au	8.59×10^{-11}	1.56×10^{-10}
Bi	1.32×10^{-10}	1.19×10^{-10}
Cr	3.84×10^{-9}	2.43×10^{-10}
Cu	3.91×10^{-11}	1.89×10^{-10}
In	6.46×10^{-4}	1.31×10^{-6}
Mg	2.06×10^{-6}	5.81×10^{-8}
Ni	3.13×10^{-10}	6.28×10^{-10}
Pb	1.18×10^{-10}	8.31×10^{-11}
Pt	2.50×10^{-10}	1.60×10^{-10}
Sn	5.44×10^{-11}	3.63×10^{-10}
Zn	1.64×10^{-10}	1.21×10^{-10}

Mott-Schottky plots (viz. $\frac{1}{C^2}$ versus V) were not obtained for these capacitors since such plots necessitate an ohmic contact on one side (the Pt-PZT interface is clearly non-linear as evident in the I-V characteristics of Pt-PZT-Pt capacitors) while the other junction can be rectifying. Another complication is the fact that the dielectric constant of the PZT film was dependent on the applied voltage, rendering the Mott-Schottky relation a highly non-linear one and making impossible the determination of barrier height from the linear extrapolation of the plots.

Hysteresis loops were obtained from these capacitors using a 5V pulse. The results for saturation polarization, P_s , the average remanent polarization, P_r , and coercive field (obtained by averaging the magnitudes of the positive and negative values) are shown in Table IV.

Table IV. Values of Spontaneous Polarization, P_s , Average Permanent Polarization, $\overline{P_r}$, and Average Coercive Field $\overline{E_c}$ of Various PZT Capacitors.

Top Metal	$P_s(\mu\text{C}/\text{cm}^2)$	$\overline{P_r} (\mu\text{C}/\text{cm}^2)$	$\overline{E_c}(\text{kV}/\text{cm})$
Ag	19.17	5.94	20.84
Al	7.54	4.23	55.79
Au	26.21	10.32	25.98
Bi	29.56	13.56	31.26
Cu	20.17	5.45	44.25
In	12.79	7.35	46.89
Mg	14.01	6.28	34.32
Ni	23.29	8.02	26.37
Pb	22.18	9.85	32.53
Pt	38.31	19.68	47.32
Sn	20.29	9.85	38.32
Zn	29.90	20.01	47.32

Au, Bi and Zn top electrodes tend to result in capacitors having large values of permanent and spontaneous polarization; while Au and Ag top electrodes yield the lowest coercive fields ($<26\text{kV}/\text{cm}$). Pt top electrodes yield the highest remanent and spontaneous polarizations. Note that capacitors having In and Al exhibited the highest values of E_c ($\sim 50\text{kV}/\text{cm}$). These high E_c values can arise from oxide formation at the PZT-Al or PZT-In interfaces due to the high reactivities of these top metals. Higher voltage would then be needed to switch the FE domains, since a large proportion of the voltage was applied across these interfacial oxide layers due to the small dielectric constant of the layers compared to those of the FE PZT film. Additionally, in Al, In and Mg top electroded capacitors, there exist large shifts in the hysteresis loop along the coercive field axis resulting in asymmetrical loops with disparate values of the coercive fields due to the oxide layers.

CONCLUSIONS

Pt-PZT-Metal capacitors were prepared utilizing various top metallizations and PZT films which were previously fired to 700°C to convert them into single-phase perovskite films. The dielectric (e.g. dielectric constant and leakage characteristics) and FE (e.g. remanent polarization and coercive field) properties were highly dependent in the choice of metals used. The highest dielectric constants were obtained for capacitors having noble or transition metals; the lowest leakage currents were obtained using Au or Pt top electrodes; and the highest polarizations (both remanent and spontaneous) were measured for capacitors having noble metals or Bi. There was not a consistent dependence of these properties (especially leakage currents) on the work function of the metal used. The electronegativity or affinity for oxygen of the electrode plays a more important role in affecting the junction characteristics. For several reactive top metals such as In, Zn, Cu and Al, the formation of interfacial oxide layers at the Pt-metal junctions leads to high values of coercive field (~50kV/cm) compared to when noble metals or Zn are used (~20-25kV/cm). The overall best dielectric and FE behaviors are derived from capacitors having noble metals, especially Pt, as the top and bottom electrodes.

ACKNOWLEDGMENTS

The financial support of the Air Force Office of Scientific Research is gratefully acknowledged.

REFERENCES

- [1] B. Jaffe, W.R. Cook and M. Jaffe, Piezoelectric Ceramics, Academic Press, 1971.
- [2] I.K. Yoo and S.B. Desu, *Mater. Sci. & Engr.*, **B13**, 319 (1992).
- [3] C.K. Kwok, D.P. Vijary, S.B. Desu, N.R. Panikh and E.A. Mill, *Proc. 4th ISIF*, 412 (1992).
- [4] D.B. Fraser and J.R. Maldonado, *J. Appl. Phys.*, **41** 2172 (1970).
- [5] *CRC Handbook of Chemistry and Physics*, 1993.

- [6] G. Teowee, J.M. Boulton, C.D. Baertlein, R.K. Wade and D.R. Uhlmann, paper to be published in J. Non-Cryst. Solids, 1993.
- [7] S. Wada and F. Ishiguro, Jpn Kokai 75 84 896, Jul 9, 1975.
- [8] R. Ashida, R. Urahara and N. Mori, Jpn-Kokai 75 38 095, Apr 9, 1975.
- [9] G. Teowee, E.A. Kneer, C.D. Baertlein, J.M. Boulton and D.R. Uhlmann, presented at the 6th ISIF, Monterey, 1994.
- [10] G. Teowee, Ph.D. dissertation, University of Arizona, 1992.

ELECTRICAL AND MECHANICAL PROPERTIES IN CaF₂/SiC-WHISKER COMPOSITES

Atsumu Ishida and Masaru Miyayama

Research Center for Advanced Science and Technology,
University of Tokyo, Tokyo 153, Japan

Hiroaki Yanagida

Department of Industrial Chemistry,
University of Tokyo, Tokyo 113, Japan

ABSTRACT

Electrical and mechanical properties in ceramic composites were investigated in order to examine fracture prediction techniques and fatigue detection in ceramics. Composites were fabricated with calcium fluoride as the insulating matrix and silicon carbide whiskers as the conducting additive. Electrical conduction paths were formed by adding more than 3 vol% of silicon carbide whiskers. Additions of silicon carbide whiskers did not improve the fracture strength, especially of the composites with a conduction path. By applying a bending load to the composites, the electrical resistance increased up to fracture. When the load was applied repeatedly below the fracture limit, a gradual increase of electrical resistance was observed before fracture. These results suggested the possibility of predicting fracture and detecting fatigue in ceramic composites. A pull out behavior of silicon carbide whiskers which disconnect the conduction paths of the composites was confirmed from scanning electron microscopy observation.

To the extent authorized under the laws of the United States of America, all copyright interests in this publication are the property of The American Ceramic Society. Any duplication, reproduction, or republication of this publication or any part thereof, without the express written consent of The American Ceramic Society or fee paid to the Copyright Clearance Center, is prohibited.

INTRODUCTION

Ceramics used for structural and engineering purpose have particular features, such as high thermal resistance, high corrosion resistance, and hardness. On the other hand, brittleness is one of the main problem which gives limitation in putting ceramics to practical use.

In order to overcome the brittleness problem, many approaches are known, such as (1) increase of safety factor by increasing mass, (2) seek better performances such as durability, strength, and toughness, (3) detection of a local fracture or microcracks, and so on. One of the problem induced by increasing mass is a large scale in production, consumption, and waste which disrupt environment. Although, improving the performances of ceramics are widely investigated by controlling structure¹⁻³ and by composite,⁴⁻⁸ difficulties in recycling and in handling, and requirement of complicated high skill are also considered to be the limitation in promoting the use of ceramics.

In the present study, a system to predict fracture of ceramics is investigated. A method to build in a self-diagnosis mechanism in ceramics is proposed as one of the intelligent mechanism,⁹ and prediction of fatal fracture in fiber reinforced plastic has been reported.¹⁰ Prediction of fracture in structural ceramics is expected to be a promising method to increase the practical applications.

Composites consisting of an insulating matrix with electric conducting additives show a large variation in electrical resistivity with different composition and microstructure.^{11,12} Electrical resistivity of the composites decreases drastically by forming conduction paths. In this study, electrical resistivity under applying load was measured on composites with electrical conduction paths consisting of insulating calcium fluoride (CaF_2) and conducting silicon carbide (SiC). In such composites, a change of electrical resistivity is expected by microdeformation or by a change of connectivity of the conduction paths subjected to an external load before the fatal fracture.

EXPERIMENTAL

CaF_2 and SiC were chosen as insulator and conductor ceramics. Although CaF_2 is known as an ionic conductor, a high electrical resistivity is achieved around room temperature. CaF_2 powder with purity over 99.9% and particle size of under 2 μm (Kojundo Chemical Laboratory Co., Ltd. Japan)

was used in this study. For conductor ceramics, whisker morphology was chosen as the whisker has abilities to produce conduction paths at a low concentration and to enhance toughness. SiC whiskers from 0.1 to 1 μm in diameter and from 50 to 200 μm in length (Tokai Carbon Co., Ltd. Japan) were used as the starting materials.

The starting materials were mixed with ethanol in an ultrasonic bath and then dried. The mixed powder was pressed into pellets of 15 mm in diameter at 220 MPa, and sintered by hot-pressing at a pressure of 40 MPa at 900° to 1100°C for 30 min. To prevent the pellets from contacting and bonding with alumina dies during hot-pressing, hexagonal boron nitride powder was used to cover the surface of the pellets. Samples were cut and machined to a proper shape and evaluated. Relative density, scanning electron microscopy (SEM) observation, XRD, electrical resistivity and fracture strength were evaluated.

The electrical resistivity of the composites at room temperature was measured by the two-probe direct-current method using an ultrahigh-resistance meter. As electrodes, platinum (6 mm in diameter) were formed by sputtering at both sides of the disk pellets. The measurements of fracture strength were conducted on test pieces of about 15 x 2 x 1 mm with the surface and the edge of the samples polished by #2000 emery paper. Fracture strength was measured with three-point bending apparatus with a span of 10 mm and cross head speed of 0.2 mm/min.

The measurement of electrical resistivity under applied load was conducted on the test piece with platinum sputtered at both ends of the test piece as electrodes and connected to an electrical resistance meter. Two types of measurements were carried out. One is a single mode testing which applies a load until the test piece fractured. Another is a low cyclic testing, applying load below the fracture limit repeatedly.

RESULTS AND DISCUSSION

Figure 1 shows the SEM observation of the sintered CaF_2 and CaF_2/SiC -whisker composite with 10 vol% of the whiskers hot-pressed at 1000°C. Both ceramics have high relative density of 97%. It appears that the addition of SiC whiskers up to 10 vol% seems to give no effect in hindering densification by hot-pressing at 1000°C. Aggregation of the SiC whiskers was not observed in the composites. The grain growth of CaF_2 is inhibited by

addition of SiC whiskers in the composites. From XRD, no peak except CaF_2 and SiC was observed.

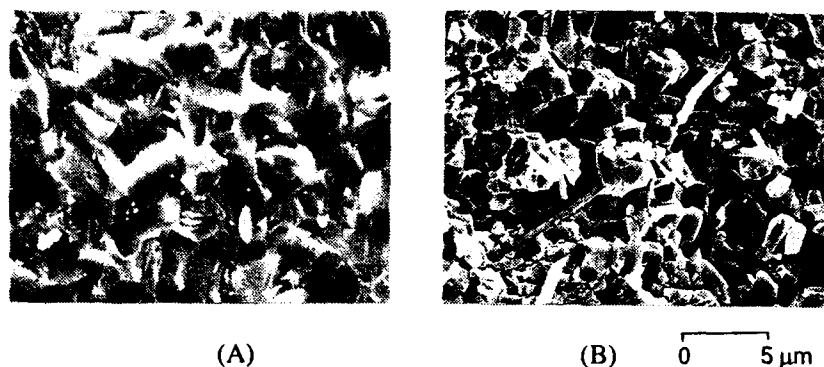


Figure 1. SEM observation of (A) CaF_2 and (B) $\text{CaF}_2/10\text{-vol\%}\text{-SiC}$ -whisker composite hot-pressed at 1000°C .

Electrical Properties

Electrical resistivity as a function of SiC-whisker content in the composites hot-pressed at 1000°C is shown in Figure 2. Electrical resistivity decreases markedly from 10^{12} to $10^5 \Omega\text{cm}$ for SiC-whisker content from 2 to 3 vol% which shows that the conduction path has been formed in this region. As the composites were fabricated with the conductive material having whisker morphology, an electrical conduction path was achieved with relatively small amounts of whiskers.

Mechanical Properties

The fracture strength as a function of SiC-whisker content of the composites is shown in Figure 3. The minimum value of the fracture strength was observed in the composites with 3 vol% of SiC whiskers which is nearly half of single-phase CaF_2 ceramics. The fracture strength decreased with SiC-whisker content from 1 to 3 vol%, which is similar to the change of electrical resistivity shown in Figure 2. As a result, additions of SiC whisker up to 10 vol% seem to give no remarkable effects on improving the fracture strength of the composites.

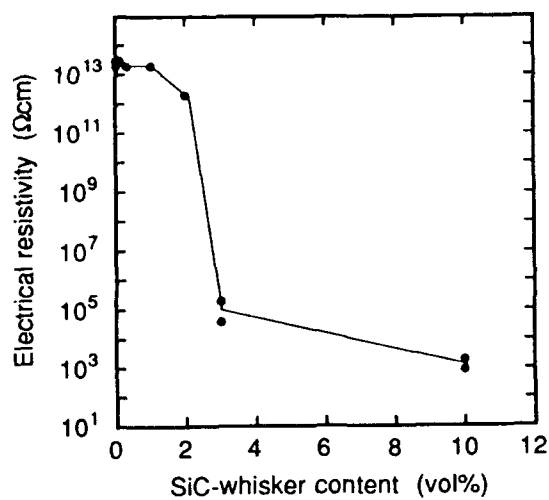


Figure 2. Electrical resistivity as a function of SiC-whisker content in CaF₂/SiC-whisker composites hot-pressed at 1000°C.

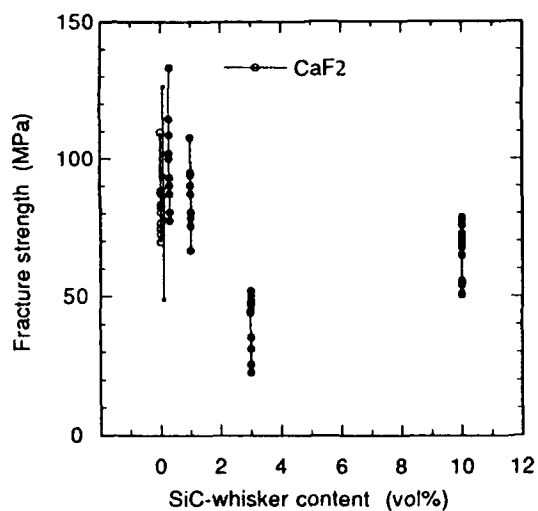


Figure 3. Fracture strength as a function of SiC-whisker content in CaF₂/SiC-whisker composites hot-pressed at 1000°C.

The reasons of lower fracture strength are not clear in this system. One of the reasons might be the high tensile matrix stress due to the thermal mismatch of two materials. Furthermore, the formation of the conduction path may have some influence on crack propagation to lower the fracture strength. The contact between the SiC whiskers in the composites is presumed to be weak, as the sintering temperature is quite low compared with the dissociation temperature of SiC. The increase in contact of the SiC whiskers in the composites appears to influence the fracture strength.

Figure 4 shows the load-deflection curves of CaF₂ and CaF₂/SiC-whisker composites sintered at 1000°C. The curves are separated into two groups. The first group includes single-phase CaF₂ and the composites without a conduction path which shows small deflections up to fracture. The second group is the composites with a conduction path which show larger deflections compare with the first one. As a gradient of load-deflection curve represents an elastic modulus of the composites, the composites with a conduction path have lower elastic moduli than single-phase CaF₂ and the composites without a conduction path. The low elastic modulus of the composites seems to be related to the increase in contact of the SiC whiskers in the composites, as in the case of decreasing fracture strength.

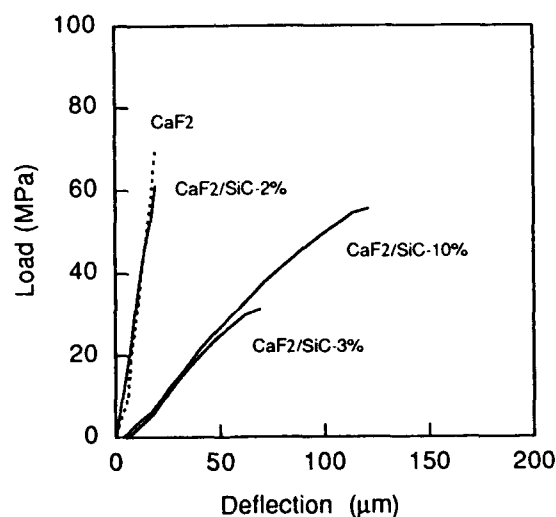


Figure 4. Load-deflection curves of CaF₂ and CaF₂/SiC-whisker composites sintered at 1000°C.

Fracture Predicting and Fatigue Detection

The relation between applied load, deflection, and electrical resistance of the $\text{CaF}_2/10\text{-vol\%}\text{-SiC}$ -whisker composite hot-pressed at 1000°C is shown in Figure 5. Electrical resistance of the composites started to increase after applying about half of the fractured load, and increased by about 7% of the initial electrical resistance at fracture. It is suggested that breaking of the conduction paths has occurred by applying the load before fracture. Thus prediction of fracture would be possible by measuring the increase of the electrical resistance of the composites.

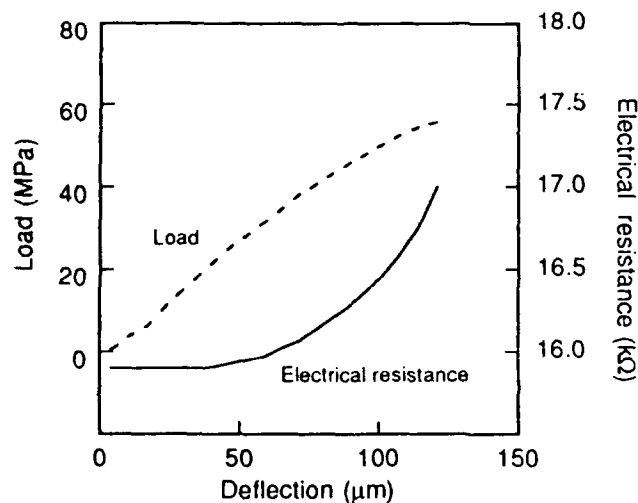


Figure 5. Load-deflection curve and change of electrical resistance by applying bending load to $\text{CaF}_2/10\text{-vol\%}\text{-SiC}$ -whisker composite hot-pressed at 1000°C with initial electrical resistivity of $1 \times 10^3 \Omega\text{cm}$.

The increase in electrical resistance by applying loads was observed in other composites with a conduction path as well. Figure 6 shows the increased ratio of electrical resistance as a function of SiC-whisker content. The ratios show no clear dependence on the SiC-whisker content or on the sintering temperature. Although the connectivity of the conduction paths expected to change drastically with the composites which is close to the critical volume fraction of forming the conduction path, a large increase of the

electrical resistance was not observed in $\text{CaF}_2/3\text{-vol\%}\text{-SiC}$ -whisker composite. An ambiguity results in adopting the bend test which gives rise to both compression and tension in the different part of the test piece by applying load.

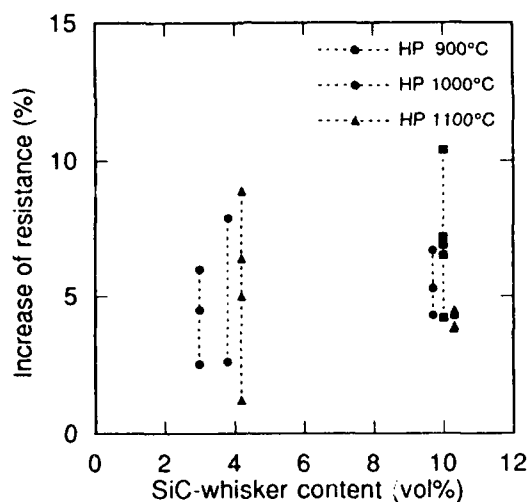


Figure 6. Ratio of increase in electrical resistance to initial electrical resistance as a function of SiC-whisker content in CaF_2/SiC -whisker composites.

Possibility of detecting the fatigue of the composites was investigated by low cyclic loads test. The relation between repeated times, deflection, and electrical resistance of the $\text{CaF}_2/10\text{-vol\%}\text{-SiC}$ -whisker composite sintered at 900°C with initial electrical resistivity of $4 \times 10^4 \Omega\text{cm}$ is shown in Figure 7. The plotted points in the figure are for measurements at the time of releasing the load. About 70 % of the fracture load was applied to the composites in one cycle per 40 sec. The test piece fractured after repeated loading of 85 times, and the electrical resistance of the sample increased from 361 k Ω of the initial to 379 k Ω just before fracture. In the initial stage of about ten cycles, the electrical resistance increased largely. Then a gradual increase was observed in next stage, and a relatively large increase was again observed in the last stage, a few cycles before the fracture. The gradual increase of electrical resistance at the intermediate stage indicates the detection of fatigue

of the composites. As the electrical resistance remained at increased value while releasing the loads, fatigue of the composites was able to detect when the load was not applied.

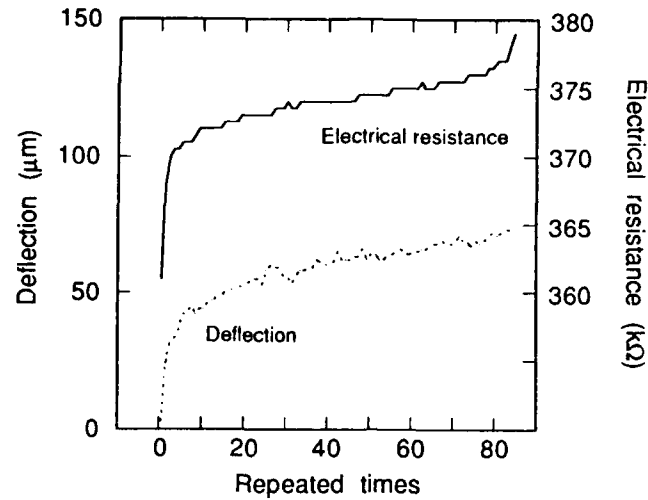


Figure 7. Change of electrical resistance and deflection as a function of repeated times of applying about 70% of fracture strength in $\text{CaF}_2/10\text{-vol\%}\text{-SiC}$ -whisker composites.

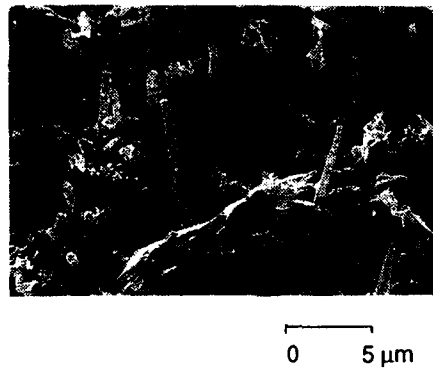


Figure 8. SEM micrograph of $\text{CaF}_2/10\text{-vol\%}\text{-SiC}$ -whisker composite.

SEM micrograph of the fracture surface of $\text{CaF}_2/10\text{-vol\%}\text{-SiC}$ -whisker composite is shown in Figure 8. Many SiC whiskers are observed sticking out from the fracture surface, indicating the sliding of whiskers during the fracture of the composites. The increase in electrical resistance under bending load seems to occur by the breaking of the SiC-whiskers and by the sliding of the SiC-whiskers to disrupt the conduction path.

CONCLUSIONS

Electrical and mechanical properties were investigated on ceramic composites consisting of CaF_2 as insulating matrix and SiC whiskers as conducting additives. Electrical resistivity of the composites decreased markedly from compositions of 2 to 3 vol% of SiC whiskers, indicating the formation of a conduction path in this region. Additions of SiC whiskers resulted in larger deflection up to fracture, and gave no effect in improving the fracture strength of the composites.

When the bending load was applied to the composites with a conduction path ($\text{CaF}_2/10\text{-vol\%}\text{-SiC}$ -whisker), the electrical resistance increased about 7% in average from the initial value. The increase of electrical resistance before the fatal fracture can be used for fracture prediction of the composites. By applying loads repeatedly below the fracture limit, the electrical resistance increased and remained while releasing the load. A relatively large increase of electrical resistance was observed in the initial stage and a few cycles before the fracture, while gradual increase of electrical resistance was observed in the intermediate stage. The gradual increase of electrical resistance suggested the possibility of detecting fatigue. The debonding of whiskers leading to an increase in electrical resistivity was confirmed by SEM observation.

Acknowledgements: The authors thank Dr. Matsubara of the Japan Fine Ceramics Center for many valuable suggestions and discussions during this work. The use of the facilities of the DENKA Research Center is also gratefully acknowledged.

References

- ¹P. F. Becher, "Advances in the Design of Toughened Ceramics," *J. Ceram. Soc. Jpn.*, 99[10]993-1001(1991)

- ²R. C. Garvie, R. H. J. Hannink, and R. T. Pascoe, "Ceramic Steel?" *Nature(London)*, **258**[5537]703-704(1975)
- ³N. Hirotsaki, M. Ando, Y. Akimune, and M. Mitomo, "Gas-Pressure Sintering of β -Silicon Nitride Containing Y_2O_3 and Nd_2O_3 ," *J. Ceram. Soc. Jpn.*, **100**[6]826-829(1992)
- ⁴L. M. Sheppard, "Enhancing Performance of Ceramic Composites," *Am Ceram. Soc. Bull.*, **71**[4]617-631(1992)
- ⁵K. Niihara, "New Design Concept of Structural Ceramics -Ceramic Nanocomposites-," *J. Ceram. Soc. Jpn.*, **99**[10]974-982(1991)
- ⁶G. C. Wei and P. F. Becher, "Development of SiC-Whisker-Reinforced Ceramics," *Am. Ceram. Soc. Bull.*, **64**[2]298-304(1985)
- ⁷N. Claussen, K. L. Weiskopf, and M. Ruhle, "Tetragonal Zirconia Polycrystals Reinforced with SiC Whiskers," *J. Am. Ceram. Soc.*, **69**[3]288-292(1986)
- ⁸P. D. Shalek, J. J. Petrovic, G. F. Hurley, and F. D. Gac, "Hot-Pressed SiC Whisker/Si₃N₄ Matrix Composites," *Am. Ceram. Soc. Bull.*, **65**[2]351-356(1986)
- ⁹H. Yanagida, "Intelligent Ceramics," *Ferroelectrics*, **102**,251-257(1990)
- ¹⁰N. Muto, H. Yanagida, T. Nakatsuji, M. Sugita, and Y. Ohtsuka, "Preventing Fatal Fractures in Carbon-Fiber-Glass-Fiber-Reinforced Plastic Composites by Monitoring Change in Electric Resistance," *J. Am. Ceram. Soc.*, **76**[4]875-879(1993)
- ¹¹S. Kirkpatrick, "Percolation and Conduction" *Rev. Mod. Phys.*, **45**[4]574-588(1973)
- ¹²D. S. McLachlan, M. Blaszkiewicz, and R. E. Newnham, "Electrical Resistivity of Composites," *J. Am. Ceram. Soc.*, **73**[8]2187-2203(1990)

INDEX

1-3 piezocomposite plate and ring structures, 231
1-3 PZT-polymer composites, 239

AC impedance, 343

Actuators

arrays, 231

applications, 231, 239

Agglomeration rate, 183

Alles, Aldo B., 393

Apblett, Allen W., 73

Azimi, M., 55

Baertlein, C.D., 401

Baik, Sunggi, 37

(Ba,Sr)TiO₃ thin films, 67

BaTiO₃, 73, 301

Bearzotti, Andrea, 375

Bending behavior, 385

Bianco, Alessandra, 375

Birefringence, 301

Bismuth titanate film, 55

Boulton, J.M., 401

Bower, L.J., 239

Boyle, Timothy J., 79, 145

Buchanan, Relva C., 137

Buchheit, C.D., 145

CaF₂/SiC-whisker composites, 413

Capurso, Joseph S., 393

Ceramic composites, 277

Ceramic thermal shield support, 249

Characteristics, 137

Characterization, 79

Chu, Peir-Yung, 137

Chu, Sheng-Yuan, 287

Conduction mechanism, 219

nonlinear, 207

Conductive oxides, 165

Cooney, T.G., 197

Cracks, 197

propagation, 277

Cryogenic use, 249

Crystal orientation, 3, 357

Crystallization, 145

behavior, 89

CuO/ZnO pn heterocontact, 343

Dai, Xunhu, 225

DC bias, 343

Defects, 131

Densification, 145

Deposition, 55

Deposition parameters, 55

Device design, 197

Dielectric characteristics, 225

Dielectric constant, 67, 225

Dielectric properties, 55, 67, 401

Electrical properties, 413

Electrode materials, 3, 365

Electron tunneling, 207

Electro-optic effect, 301

Environmental humidity, 385

Epitaxial ferroelectric/metal oxide electrode thin-film heterostructures, 165

Epitaxial ferroelectric thin films, 107

Evaluation, 3

Fabrication, 239

Fatigue detection, 413

Ferroelectric ceramics, 277

Ferroelectric properties, 131, 401

Ferroelectric thin films, 3, 123

Bi₄Ti₃O₁₂, 137

PbTiO₃, 37

Fiore, D.F., 239

Fork, D.K., 165

Fracture prediction techniques, 413

Francis, L.F., 183, 197

French, K.W., 239

Fukagawa, Mitsuru, 27

Gas response, 365

Gas sensing, 343

properties, 357

Gentilman, R.L., 239

Georgieva, Galina D., 73

- Ghonge, Subodh G., 165
 Ghosh, P.K., 55, 301
 Goo, Edward, 165
 Grain boundaries, 207
 Grain size, 67, 131
 effect, 131
 Group IV metal adamantanol
 alkoxides, 79
 Growth, 27
 Gusmano, Gualtiero, 375

 Haakenaasen, R., 165
 Hachfeld, E.A., 197
 Hamagami, Jun-ichi, 331
 Heat treatment, 295
 schedule, 145
 Hikita, Kazuyasu, 343
 Hole transport, 207
 Home appliances, 315
 Honda, T., 67, 219
 Horikawa, T., 67, 219
 Howarth, Thomas R., 231
 Humidity sensors, 375
 Huybrechts, Ben, 331
 Hydroacoustic evaluation, 231
 Hydrolysis, 131
 Hydrophones, 239

 Ichinose, Noboru, 15, 207
 Impact ionization, 207
 Intelligent functions, 207
 Intelligent mechanical behaviors, 277
 Intelligent sensors, 315
 Ion-beam sputtering, 55
 Ishida, Atsumu, 413
 Isogai, Yuji, 385

 Jang, Hyun M., 123

 Kang, C.S., 27
 Kang, Youngmin, 37
 Kawashima, Shunichiro, 315
 Kim, Sangsub, 37
 Kim, Y.J., 183
 Kim, You Song, 123
 Kneer, E.A., 401
 Kuroiwa, T., 67, 219

 LaAlO₃, 165
 Lakeman, Charles D.E., 89
 Large area coverage, 231, 239
 Large area growths, 27
 Laser ablation, 3
 Lead oxide cover coating, 89
 Li, Jie-Fang, 89
 LiNbO₃, 301

 Machinability, 249
 Macrodefects, 197
 Maiwa, Hiroshi, 15
 Makita, T., 67, 219
 Mechanical properties, 413
 Metal-ferroelectric-metal capacitor
 theoretical considerations, 255
 experimental verifications, 267
 Metal methoxyethoxide precursors, 107
 Metallorganic deposition precursor, 73
 MgO(100) substrates, 37
 Microcomputers, 315
 Microelectromechanical systems, 197
 Microstructure, 165
 characteristics, 225
 development, 183
 Mikami, N., 67, 219
 Miyayama, Masaru, 343, 365, 375,
 385, 413
 MOCVD, 27
 Modeling, 255
 Montesperelli, Giampiero, 375

 Nakahira, A., 249
 Nakaya, Kenichi, 27
 Nashimoto, Keiichi, 107
 Niihara, K., 249
 Nishijima, S., 249
 Nitta, Tsuneharu, 315
 Nonaka, Kazuhiro, 295

 Ogawa, Toshio, 3
 Okada, T., 249
 Okazaki, Kiyoshi, 15
 Optical hydrogen sensor, 331

 Particle-particle interactions, 183
 Particulate ceramic coatings, 183

- Payne, David A., 89
 (Pb,La)TiO₃ thin films, 15
 (Pb,La)(Zr,Ti)O₃ ceramics, 287
 Pb(Mg_{1/3}Nb_{2/3})O₃-based relaxor ferroelectrics, 123
 Pd/MoO_x films, 331
 Pearson, Aaron T., 79
 Perovskite-type ceramics, 207
 Pham, H.T., 239
 Phase separation, 183
 Photostriction, 287, 295
 Piezoelectric actuators, 385
 Piezoelectric ceramics, 277
 Piezoelectric composites, 231
 Piezoresistive ceramic sensors, 393
 Platinum, 15
 PLZT
 ceramics, 295
 thin layers, 89
 Polycrystalline film structure, 67
 Pore interconnection, 131
 Potential barriers, 207
 Precursor nature, 145
 Preparation, 3, 15, 73
 Processing, 137
 Projectors, 239
 Properties, 15, 27, 89, 239
 Pt/SiO₂/Si wafer, 219
 PTCR barium titanate, 393
 PTCR effects, 207
 PZT
 films, 267
 built-in field, 267
 precursors, 79
 solid solution, 123
 thin films, 27, 197
 thin layers, 89
 Ramesh, R., 165
 Rapid thermal annealing, 131
 Raygoza-Maceda, Isobel, 73
 Reaction, 183
 Remote control actuators, 287
 RF sputtering, 67, 219
 magnetron, 3, 331
 multiple cathode, 15
 Rittenmyer, Kurt M., 231
 Ruthenium oxide, 15
 Saegusa, K., 131
 Sato, K., 67, 219
 Schulze, Walter A., 393
 Schwartz, Robert W., 79, 145
 Sensing applications, 239
 Sensors, 315
 Shimizu, Masaru, 27
 Shiosaki, Tadashi, 27
 Silicon, 165
 Singh, Raj N., 277
 Smart sensors, 315
 Sol composition, 197
 Sol-gel
 processing, 145
 technology, 123
 Sol-gel-derived PbTiO₃ thin films, 131
 Sol-gel-derived PZT thin films, 401
 Sol-gel-derived PZT and PLZT thin layers, 89
 Spin casting, 137
 Spontaneous switching, 225
 Sputter deposition, 37
 Sputtered SnO₂ films, 357
 SrTiO₃ thin films, 219
 Stoichiometry, 3
 Structural characteristics, 225
 Superconducting magnet system, 249
 Surface structures, 37
 Suzuki, Y., 131
 Synthesis, 79
 Takase, Akira, 295
 Takata, Masasuke, 331, 357
 Tani, Toshihiko, 89
 Tanikawa, Eiki, 27
 Temperature modulation, 301
 Teowee, G., 255, 267, 401
 Tetragonal-structured PLZT relaxors, 225
 Thermal annealing, 37
 Thermal conductivity, 249
 Thermal hysteresis effects, 225
 Thermal penetration, 249
 Ting, Robert Y., 231
 Top metallization, 401

Totally depleted back-to-back Schottky
barriers, 255
Traversa, Enrico, 365, 375

Uchino, Kenji, 287
Uhlmann, D.R., 255, 267, 401
Underwater sonar transducer
applications, 231

VDR effects, 207
Velamakanni, B.V., 183
Vickers indentation technique, 277
Viehland, Dwight, 225
Voigt, J.A., 145

Wang, Hongyu, 277
Wara, N.M., 183
Watanabe, Tadahiko, 295
Watanabe, Yuichi, 331
Watarai, H., 67, 219

Xu, Zhengkui, 89, 225

Yanagida, Hiroaki, 343, 365, 375,
385, 413
Yoshida, Hisayoshi, 295

Zavala-Enriquez, G., 301
Zirconia, 249
thin films, 145
ZnO/La₂CuO₄ heterocontacts, 365, 375